

# The analysis of exclusive semileptonic decays of $\Lambda_b$ –baryons in the Standard Model and Beyond



By

**Aqsa Nasrullah**

**Department of Physics  
Quaid-i-Azam University  
Islamabad 45320  
Pakistan  
2021**

**The analysis of exclusive semileptonic decays of  $\Lambda_b$  –baryons in the  
Standard Model and Beyond**



By

**Aqsa Nasrullah**

Supervised By

**Dr. Muhammad Jamil Aslam**

**Department of Physics  
Quaid-i-Azam University  
Islamabad 45320  
Pakistan  
2021**

**The analysis of exclusive semileptonic decays of  $\Lambda_b$  –baryons in the  
Standard Model and Beyond**



By

**Aqsa Nasrullah**

This work is submitted as a dissertation in the partial fulfillment of  
the requirement for the degree of

DOCTOR OF PHILOSOPHY

In

PHYSICS

Supervised By

**Dr. Muhammad Jamil Aslam**

**Department of Physics  
Quaid-i-Azam University  
Islamabad 45320**

**Pakistan**

**2021**


## Certificate of Approval

This is to certify that the research work presented in this thesis, entitled “**The Analysis of Exclusive Semileptonic Decays of  $\Lambda_b$  - Baryons in the Standard Model and Beyond.**”

Was conducted by Ms. Aqsa Nasrullah under the supervision of Dr. Muhammad Jamil Aslam.

No part of this thesis has been submitted anywhere else for any other degree. This thesis is submitted to the Department of Physics, Quaid-i-Azam University Islamabad, Pakistan in partial fulfillment of the requirements for the degree of Doctor of Philosophy in Physics, Department of Physics Quaid-i-Azam University Islamabad.

Student Name: **Ms. Aqsa Nasrullah**

Signature: 

Examination Committee:

a) Dr. Khunab Gul  
H. No. 38, St. No. 52,  
F-11/3, Islamabad

Signature: 

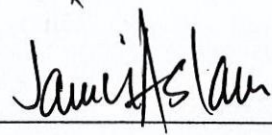
b) Dr. Mahnaz Qader Haseeb  
Professor, Department of Physics  
COMSATS, Institute of Information Technology  
Chak Shahzad, Islamabad.

Signature: 

c) Prof. Dr. Nawazish Ali Khan  
Chairman,  
Department of Physics  
QAU, Islamabad.

Signature: 

Dr. Muhammad Jamil Aslam  
Supervisor,

Signature: 


Chairman

Signature:   
25.2.2021

## AUTHOR'S DECLARATION

I, **Aqsa Nasrullah** hereby state that my PhD thesis entitled “**The analysis of exclusive semileptonic decays of  $\Lambda_b$  –baryons in the Standard Model and Beyond**” is my own work and has not been submitted previously by me for taking any degree from Quaid-i-Azam University, Islamabad or anywhere else in the country/world.

At any time if my statement is found to be incorrect even after my graduation, the university has the right to withdraw my PhD degree.


  
AQSA NASRULLAH

## Plagiarism Undertaking

I solemnly declare that the research work presented in the thesis titled "The analysis of exclusive semileptonic decays of  $\Lambda_b$  -baryons in the Standard Model and Beyond" is solely my research work with no significant contribution from any other person. Small contribution/help wherever has been duly acknowledged and that complete thesis has been written by me.

I understand the zero tolerance policy of the HEC and Quaid-i-Azam University towards plagiarism. Therefore, I as an author of the above titled thesis declare that no portion of my thesis has been plagiarized and any material used as reference is properly referred/cited.

I undertake that if I am found guilty of any formal plagiarism in the above titled thesis even afterward of PhD degree, the university reserves the right to withdraw/revoke my PhD degree and that HEC and University has the right to publish my name on the HEC/University Website on which name of students are placed who submitted plagiarized thesis.

Student/Author Signature:  \_\_\_\_\_

Name: AQSA NASRULLAH

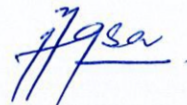
## ACKNOWLEDGEMENT

First of all, I pay special thanks to Almighty Allah, Who assisted me in all walks of life and also assisted and guided me throughout my PhD work and in the accomplishment of this thesis too. Many Salat-o-Salam on our Holy Prophet Hazrat Muhammad (PBUH) Who is a source of knowledge and blessings for the entire creations.

I would like to thank my respectable, honorable, very sincere and dedicated supervisor Dr. Muhammad Jamil Aslam for providing me the opportunity of taking part in PhD Physics Program. I am so grateful for his help, valuable guidance throughout this thesis and through my entire program of study. I do not have enough words to express my deep and sincere appreciation. I am also grateful to my all teachers on directing me to the right path and teaching fruitful courses with their full dedication.

I would like to express my very profound gratitude to my parents , parents in laws and other family members like my sisters Hira Nasrullah, Habiba Nasrullah, Munazza Asghar, my brother Muhammad Talha and my husband Dr. Zaheer Asghar for their prayers and continuous support and encouragement throughout my years of study. This accomplishment would not have been possible without their moral support.

I would like to pay my special thanks to respected Dr. Ishtiaq Ahmed (NCP), Dr. Saba Shafaq (IIU) and Dr. Faisal Munir Bhutta on helping and guiding me in my PhD research work. I am thankful to my all friends and would like to mention the names of Mrs. Fareeha Vardag and Ms. Nadia Sardar for their support.



AQSA NASRULLAH

## Abstract

In this work we analyze a phenomenologically rich four body decay  $\Lambda_b \rightarrow \Lambda(\rightarrow p\pi^-)\mu^+\mu^-$  which provides a large number of physical observables that can be accessed experimentally. In 2015, the LHCb collaboration measured the differential branching ratio  $\frac{d\mathcal{B}}{dq^2}$ , longitudinal polarization fraction of dimuon  $F_L$ , the lepton- and hadron-side forward-backward asymmetries, denoted by  $A_{FB}^\ell$  and  $A_{FB}^\Lambda$ , respectively, in several bins of dimuon mass squared  $s \equiv q^2$ . Motivated by these measurements, we perform an analysis of angular observables for this decay in the SM as well as in family non-universal  $Z'$  model, Randall-Sundrum model with custodial protection ( $RS_c$ ) and in a model independent way.

- Using the full four-folded angular distribution of  $\Lambda_b \rightarrow \Lambda(\rightarrow p\pi^-)\mu^+\mu^-$  decay, first of all we focus on calculations of the experimentally measured observables  $\frac{d\mathcal{B}}{ds}$ ,  $A_{FB}^\ell$  and  $A_{FB}^\Lambda$  in the SM and compare their numerical values with the measurements in appropriate bins of  $s$ . In case of a possible discrepancy between the SM prediction and the measurements, we try to see if these can be accommodated through the extra neutral  $Z'$  boson which modifies the Wilson coefficients (WCs) of the SM. We find that in the dimuon momentum range  $15 < s < 20 \text{ GeV}^2$  the value of  $\frac{d\mathcal{B}}{ds}$  and central value of  $A_{FB}^\ell$  in the  $Z'$  model is compatible with the measured values. In addition, the value of  $F_L$  in  $Z'$  model is closer to LHCb results than the SM in  $15 < s < 20 \text{ GeV}^2$  bin. After comparing the results of these observables, we have proposed the other observables such as  $\alpha_i^{(\prime)}$  with  $i = \theta_\ell, \theta_\Lambda, \xi, L, U$  and coefficients of different foldings  $\mathcal{P}_{1,\dots,9}$  in different bins of  $s$  in the SM and  $Z'$  model.
- The  $RS_c$  model belongs to that class of models where NP is incorporated by the modification of SM WCs. By considering the constraints coming from the direct searches of the lightest Kaluza-Klein (KK) excitation of the gluon, electroweak precision tests, the measurements of the Higgs signal strengths at the LHC and from  $\Delta F = 2$  flavor observables, we perform a scan of the parameter space of the  $RS_c$  model and obtain the maximum allowed deviations of the WCs  $\Delta C_{7,9,10}^{(\prime)}$  for different values of the lightest KK gluon mass  $M_{g(1)}$ . Later, their implications on the observables are discussed for which experimental data is available. It is observed that with the current constraints on the WCs in the  $RS_c$  model show slight deviations from their SM values of these observables and hence cannot accommodate the discrepancies between the SM calculations of various observables and the LHCb measurements in  $\Lambda_b$  decays.
- The exclusive baryonic  $\Lambda_b \rightarrow \Lambda(\rightarrow p\pi^-)\ell^+\ell^-$  decay has been analyzed using model independent approach, where apart from the modification of some of the SM WCs, there are additional vector, axial-vector, scalar, pseudo-scalar, and tensor couplings. We examine the influence of these couplings separately and by taking them together to check whether they satisfy LHCb data and  $B$ -physics constraints simultaneously. We find that most of the available data could be accommodated by the different pairs of  $VA$  and  $SP$  WCs which in result give more severe constraints on the parametric space of these WCs. By using these new constraints, the values of several other angular observables are calculated.

We illustrate that the experimental observations of the  $s$ -dependent angular observables calculated here in several bins of  $s$  can help to test the predictions of the SM and unravel NP contributions arising due to different NP scenarios in  $\Lambda_b \rightarrow \Lambda\mu^+\mu^-$  decay.



# List of Figures

2.1	The sketch of a Unitary triangle. . . . .	12
2.2	Feynmann diagram for the decay $b \rightarrow cs\bar{u}$ which can be replaced by four point effective vertex. . . . .	18
2.3	The quark level transition Feynman diagrams in full theory. . . . .	20
2.4	The SM predictions vs experimental measurements of branching ratio for $B \rightarrow K^*\mu^+\mu^-$ [137]. . . . .	26
2.5	The SM predictions and the measured values of $A_{FB}^\ell$ and $F_L$ by the LHCb for $B \rightarrow K^*\mu^+\mu^-$ decay [198]. . . . .	29
2.6	The SM predictions along with the LHCb measured values of optimized observables for the decay $B \rightarrow K^*\mu^+\mu^-$ [201]. . . . .	31
2.7	The SM predictions along with measured values from LHCb experiment for observables $S_3$ , $S_9$ and $A_9$ for the decay $B \rightarrow K^*\mu^+\mu^-$ [198]. . . . .	33
3.1	$\Lambda_b \rightarrow \Lambda(\rightarrow p\pi^-)\mu^+\mu^-$ decay topology, where $\theta_\ell$ , $\theta_\Lambda$ are the helicity angles and $\xi$ is the azimuthal angle. . . . .	35
4.1	Branching ratio and various asymmetry parameters are plotted as a function of $s$ . The green curve correspond the SM results and red to the $Z'$ model. In both cases, the bands corresponds to the uncertainties in the FFs and other input parameters. . . . .	59
4.2	Different forward-backward asymmetries, $F_L$ , $F_T$ and $\mathcal{P}_1$ are plotted as function of $s$ . The color coding is same as in Fig. 4.1. . . . .	60
4.3	The folded distributions $\mathcal{P}_{2,\dots,9}$ , except $\mathcal{P}_4$ are plotted as function of $s$ . The color coding is same as in Fig. 4.1. . . . .	61
5.1	The $RS_c$ contribution to $ \Delta C_{10} $ as a function of the KK gluon mass $M_{g^{(1)}}$ for two different values of $y_\star$ . The gray region is excluded by the analysis of electroweak precision measurements. . . . .	73
5.2	Correlations plots between the WCs $ \Delta C_{7,9,10}^{(\prime)} $ of the $RS_c$ model for a fixed value of $M_{g^{(1)}} = 4.8$ TeV. The coefficients $\Delta C_7^{(\prime)}$ are calculated at the $\mu_b$ scale. The red and blue points correspond to $y_\star = 1.5$ and 3, respectively. . . . .	74

6.1	Observables for the SM and in the presence of new $VA$ couplings which are compared with LHCb results given in [217]. In all plots the black curves denote the SM results. The orange curve is obtained with $C_V = -1.61$ and $C'_V = C_A = C'_A = 0$ . The blue line is for $C_V = -C_A = -1$ and $C'_V = C'_A = 0$ and green color is for $C_V = -1.34$ , $C'_A = -0.4$ and $C'_V = C_A = 0$ . The solid and dashed lines are for the massive and massless $\mu-$ cases respectively. . . . .	87
6.2	Observables in the SM and in the presence of new $VA$ couplings. The description of different curves is similar to the Fig. 6.1 . . . . .	88
6.3	$\mathcal{P}_3, \mathcal{P}_8$ and $\mathcal{P}_9$ in the SM and in the presence of new $VA$ couplings. The description of different curves is similar to the Fig. 6.1. . . . .	89
6.4	Observables in the presence of new SP couplings which are compared with LHCb results given in [217]. The SM curves are plotted in black color. The orange curve is obtained with $C_S = C_P = -3$ and $C'_S = C'_P = -3.1$ (for $d\mathcal{B}/ds$ orange color is for $C_S = C_P = -1$ and $C'_S = C'_P = -1.1$ ) and the green line is drawn when $C_S = 3$ and $C'_S = 2.9$ (for $d\mathcal{B}/ds$ green color is for $C_S = 1$ and $C'_S = 0.9$ ). The solid and dashed lines are for the massive and massless $\mu-$ cases, respectively. . . . .	92
6.5	Observables in the SM along with SP couplings. The description of different curves is similar to the Fig. 6.4. . . . .	93
6.6	$\mathcal{P}_3, \mathcal{P}_8$ and $\mathcal{P}_9$ in the SM and in the presence of $SP$ couplings. The description of different curves is similar to the Fig. 6.4. . . . .	94
6.7	These plots are constructed by taking $C_T = 0.72$ and $C_{T5} = 0.2$ and the black color curve indicates SM result. Experimental results are taken from [217] . . . . .	95
6.8	(a) The parametric space of $(C_X, C_Y)$ allowed from $B$ -physics constraints on new WCs and that satisfy the data of $d\mathcal{B}/ds, F_L, A_{FB}^\ell$ and $A_{FB}^\Lambda$ simultaneously in the bin $s \in [0.1, 2]$ $\text{GeV}^2$ . Different colors in the plots represent different combinations of new WCs: Red, blue, green, cyan, brown and black dots represent the $(C_X, C_Y) = (C_S, C_V), (C_S, C'_P), (C'_S, C_V), (C'_P, C_V), (C'_S, C_P)$ and $(C_S, C'_S)$ , respectively. The plots (b)-(e) present the predictions of $d\mathcal{B}/ds, F_L, A_{FB}^\ell$ and $A_{FB}^\Lambda$ in the bin $s \in [0.1, 2]$ $\text{GeV}^2$ against the WCs collected in (a) where the pink flat curves reflect the measured values of $d\mathcal{B}/ds, F_L, A_{FB}^\Lambda$ and $A_{FB}^\ell$ , along with the uncertainties at the LHCb. . . . .	98
6.9	Plot (a) shows the parametric space of $(C_X, C_Y)$ allowed from $B$ -physics constraints on new WCs and which also satisfy the data of $d\mathcal{B}/ds, F_L, A_{FB}^\ell$ and $A_{FB}^\Lambda$ , simultaneously, in the bin $s \in [15, 16]$ $\text{GeV}^2$ . (b)-(e) are the predictions of $d\mathcal{B}/ds, F_L, A_{FB}^\ell$ and $A_{FB}^\Lambda$ in the bin $s \in [15, 16]$ $\text{GeV}^2$ against the WCs collected in (a). The legends are same as Fig. 6.8. . . . .	101
6.10	Plot (a) shows the parametric space of $(C_X, C_Y)$ allowed from $B$ -physics constraints on the new WCs which also satisfy the data of $F_L, A_{FB}^\ell$ and $A_{FB}^\Lambda$ simultaneously in the bin $s \in [18 - 20]$ $\text{GeV}^2$ . (b)-(d) are the predictions of $F_L, A_{FB}^\ell$ and $A_{FB}^\Lambda$ in the bin $s \in [18 - 20]$ $\text{GeV}^2$ against the WCs collected in (a). The legends are same as Fig. 6.8. . . . .	102
6.11	$(C'_S, C_P)$ is the most favorable pair of Wilson coefficients. Green, Black, red and blue colors denote $\frac{d\mathcal{B}}{ds}, F_L, A_{FB}^\ell$ and $A_{FB}^\Lambda$ respectively. . . . .	106

# List of Tables

3.1	The values of FFs along with uncertainties calculated in the framework of lattice QCD with $(2 + 1)$ flavor dynamics for $\Lambda_b \rightarrow \Lambda$ transition [44]. . . . .	38
3.2	Pole masses for different FFs [44]. . . . .	38
3.3	Experimentally measured observables for the decay $\Lambda_b \rightarrow \Lambda\mu^+\mu^-$ [217]. . . . .	45
3.4	Foldings required for $\mathcal{P}_i$ 's for which $\theta_\Lambda \in [0, \frac{\pi}{2}]$ , $\theta_\ell \in [0, \frac{\pi}{2}]$ and $\xi$ vary in different range corresponding to different observables [201]. . . . .	47
4.1	Numerical values of the different input parameters corresponding to the SM [44,216]. The WCs are given at the scale $\mu_b = 4.2$ GeV to NNLL accuracy in the SM [111]. .	50
4.2	Numerical values of the parameters corresponding to the different scenarios of $Z'$ model [102]. . . . .	51
4.3	Average values of different observables for $\Lambda_b \rightarrow \Lambda(\rightarrow p\pi)\mu^+\mu^-$ in low and large-recoil regions. . . . .	58
4.4	Numerical results of observables for the decay $\Lambda_b \rightarrow \Lambda(\rightarrow p\pi)\mu^+\mu^-$ for the SM and $Z'$ model in appropriate bins. . . . .	62
4.5	Average values of observables in the SM and $Z'$ model for $\Lambda_b \rightarrow \Lambda(\rightarrow p\pi)\mu^+\mu^-$ in appropriate bins. . . . .	63
4.6	Numerical results of $\mathcal{P}_8$ and $\mathcal{P}_9$ for the decay $\Lambda_b \rightarrow \Lambda(\rightarrow p\pi)\mu^+\mu^-$ for the SM and $Z'$ model in appropriate bins. . . . .	64
5.1	Numerical results of $\frac{d\mathcal{B}}{ds}$ , $F_L$ and $A_{FB}^\ell$ (low $s$ region) in the $\Lambda_b \rightarrow \Lambda(\rightarrow p\pi)\mu^+\mu^-$ decay, obtained for the SM and the $RS_c$ model with $y_\star = 1.5$ case, in different bins of $s$ . Experimentally measured values are taken from [217]. . . . .	76
5.2	Numerical results of $A_{FB}^\Lambda$ and $A_{FB}^{\ell\Lambda}$ (low $s$ region) in the $\Lambda_b \rightarrow \Lambda(\rightarrow p\pi)\mu^+\mu^-$ decay, obtained for the SM and the $RS_c$ model with $y_\star = 1.5$ case, in different bins of $s$ . Experimentally measured values are taken from [217]. . . . .	77
5.3	Numerical results of $\frac{d\mathcal{B}}{ds}$ , $F_L$ and $A_{FB}^\ell$ (high $s$ region) in the $\Lambda_b \rightarrow \Lambda(\rightarrow p\pi)\mu^+\mu^-$ decay, obtained for the SM and the $RS_c$ model with $y_\star = 1.5$ case, in different bins of $s$ . Experimentally measured values are taken from [217]. . . . .	78
5.4	Numerical results of $A_{FB}^\Lambda$ and $A_{FB}^{\ell\Lambda}$ (high $s$ region) in the $\Lambda_b \rightarrow \Lambda(\rightarrow p\pi)\mu^+\mu^-$ decay, obtained for the SM and the $RS_c$ model with $y_\star = 1.5$ case, in different bins of $s$ . Experimentally measured values are taken from [217]. . . . .	79
6.1	Data accommodated by new couplings in different bins based on central values of observables. . . . .	97

6.2	Observables with and without lepton mass for the decay $\Lambda_b \rightarrow \Lambda(\rightarrow p\pi)\tau^+\tau^-$ in the SM and in different scenarios of NP couplings where the case $m_\ell \neq 0$ corresponds to $m_\ell = m_\tau$ in $s \in [15, 20]$ $\text{GeV}^2$ bin. Scenario $VA - 1$ corresponds to $C_V = -1.61$ , $C'_V = C_A = C'_A = 0$ , $VA2$ corresponds to $C_V = -C_A = -1$ , $C'_V = C'_A = 0$ and $VA - 3$ represent $C_V = -1.34$ , $C'_V = C_A = 0$ , $C'_A = -0.4$ . Similarly, in $SP - 1$ case we have taken $C_S = C_P = -3$ , $C'_S = C'_P = -3.1$ whereas $SP - 2$ contains $C_S = 3$ , $C'_S = 2.9$ and $C_P = C'_P = 0$ . Tensor couplings correspond to $C_T = 0.72$ and $C_{T5} = 0.2$ . . . . .	104
6.3	Observables by taking the massive and massless $\tau$ in $\Lambda_b \rightarrow \Lambda(\rightarrow p\pi)\tau^+\tau^-$ decay in the SM and also in different NP scenarios. Description of couplings is similar to Table 6.2. . . . .	105
6.4	Observables by taking the massive and massless $\tau$ in $\Lambda_b \rightarrow \Lambda(\rightarrow p\pi)\tau^+\tau^-$ decay in the SM and also in different NP scenarios. Description of couplings is similar to Table 6.2. . . . .	105
6.5	Observables for the decay $\Lambda_b \rightarrow \Lambda(\rightarrow p\pi)\mu^+\mu^-$ in the SM and in different scenarios of NP couplings along with LHCb results in respective bins. Scenario $VA - 1$ corresponds to $C_V = -1.61$ , $C'_V = C_A = C'_A = 0$ , $VA - 2$ corresponds to $C_V = -C_A = -1$ , $C'_V = C'_A = 0$ and $VA - 3$ corresponds to $C_V = -1.34$ , $C'_V = C_A = 0$ , $C'_A = -0.4$ . Similarly, in $SP - 1$ case we have taken $C_S = C_P = -3$ , $C'_S = C'_P = -3.1$ whereas $SP - 2$ contains $C_S = 3$ , $C'_S = 2.9$ and $C_P = C'_P = 0$ . The tensor couplings correspond to $C_T = 0.72$ and $C_{T5} = 0.2$ . The final state leptons are muons. The experimental results are taken from [217]. . . . .	107
6.6	Observables in the SM and in the presence of new $VA$ and $SP$ couplings for which experimental results are not available. The description of different scenarios is same as in Table 6.5. . . . .	108
6.7	Values of some observables in the SM and in the presence of new $VA$ and $SP$ couplings. Description of different scenarios is same as in Table 6.5. . . . .	109

# Contents

<b>1</b>	<b>Introduction</b>	<b>1</b>
<b>2</b>	<b>Fundamentals</b>	<b>7</b>
2.1	The Standard Model . . . . .	7
2.1.1	The SM Lagrangian . . . . .	9
2.2	CKM matrix . . . . .	10
2.3	Discrepancies of the SM . . . . .	13
2.4	Regularization and Renormalization . . . . .	15
2.5	Operator Product Expansion . . . . .	17
2.6	Effective Field theories . . . . .	18
2.7	$b$ -hadrons . . . . .	22
2.8	Flavor Physics and $B$ Factories . . . . .	23
2.9	Physical Observables in $B \rightarrow K^*(\rightarrow K\pi)\mu^+\mu^-$ . . . . .	25
2.9.1	Decay Rate . . . . .	25
2.9.2	Transverse asymmetries . . . . .	28
2.9.3	Longitudinal polarization fraction . . . . .	29
2.9.4	Forward-Backward Asymmetries . . . . .	29
2.9.5	The Optimized Observables . . . . .	30
2.9.6	Asymmetry parameter $\alpha^{(\prime)}_s$ . . . . .	30
2.9.7	CP symmetries and asymmetries . . . . .	30
<b>3</b>	<b>Helicity Formalism of decay <math>\Lambda_b \rightarrow \Lambda(\rightarrow N\pi)\ell^+\ell^-</math> in the SM</b>	<b>34</b>
3.1	Effective Hamiltonian . . . . .	34
3.2	Helicity amplitudes and Form Factors for $\Lambda_b \rightarrow \Lambda$ transitions . . . . .	36
3.3	Kinematics of Hadronic part . . . . .	37
3.4	Hadron helicity amplitudes . . . . .	39
3.5	Lepton Helicity Amplitude . . . . .	40
3.6	Cascade Decay $\Lambda \rightarrow N\pi$ . . . . .	41
3.7	Angular Decay Distribution . . . . .	42
3.8	Observables . . . . .	43
3.8.1	Differential decay rate and different asymmetry parameters . . . . .	43
3.8.2	Decay foldings and angular coefficients . . . . .	45

<b>4</b>	<b>Analysis of Angular Observables of <math>\Lambda_b \rightarrow \Lambda(\rightarrow p\pi)\mu^+\mu^-</math> Decay in Standard and <math>Z'</math> Models</b>	<b>48</b>
4.1	Family non-universal $Z'$ model . . . . .	48
4.2	Numerical Analysis . . . . .	50
4.2.1	Decay rate . . . . .	51
4.2.2	Forward-backward asymmetries . . . . .	51
4.2.3	Longitudinal and Transverse polarization fractions . . . . .	53
4.2.4	Asymmetry parameters $\alpha's$ . . . . .	54
4.2.5	Angular observables from foldings . . . . .	56
<b>5</b>	<b>The <math>\Lambda_b \rightarrow \Lambda(\rightarrow p\pi^-)\mu^+\mu^-</math> decay in the <math>RS_c</math> model</b>	<b>65</b>
5.1	RS Model with Custodial Symmetry . . . . .	65
5.2	Theoretical Formalism . . . . .	70
5.3	Constraints and generation of the parameter space of the $RS_c$ model . . . . .	71
5.4	Numerical Analysis . . . . .	72
5.4.1	Wilson coefficients . . . . .	72
5.4.2	Angular observables . . . . .	73
<b>6</b>	<b>Probing new physics effects in <math>\Lambda_b \rightarrow \Lambda(\rightarrow p\pi^-)\ell^+\ell^-</math> decay via model independent approach</b>	<b>80</b>
6.1	Effective Hamiltonian for model independent approach . . . . .	81
6.2	Helicity Formalism in model independent approach . . . . .	82
6.3	Four Fold Angular Distribution and Physical Observables . . . . .	85
6.4	Impact of New Couplings on Physical Observables . . . . .	85
6.4.1	Vector and Axial-Vector Part ( $VA$ ) . . . . .	86
6.4.2	Scalar and Pseudo-scalar Part . . . . .	91
6.4.3	Tensor Part . . . . .	95
6.4.4	Combined effects of $VA-SP$ couplings on angular observables . . . . .	96
6.4.5	Lepton mass effects . . . . .	103
6.4.6	Most favorable pair of Wilson coefficients . . . . .	105
<b>7</b>	<b>Conclusions</b>	<b>110</b>
.1	Appendix A . . . . .	114
.2	Appendix B . . . . .	115
.3	Appendix C . . . . .	115

# Chapter 1

## Introduction

Standard model (SM), the theory of fundamental interactions is capable of explaining successfully a huge amount of experimental data however, there are some question marks on the complete validity of the SM. The most pertinent among these are the evidence of dark matter, dark energy, neutrino oscillations, hierarchy problem, strong CP problem, and the exclusion of gravity. In addition, some tensions exist between the SM predictions and the experimental data for the flavor changing neutral current (FCNC) decays involving  $b \rightarrow s\ell^+\ell^-$  and flavor changing charged current (FCCC)  $b \rightarrow c\tau\nu$  processes. It leads to the fact that the SM is not yet a complete theory. A number of searches for the extension of the SM are on the way and the road to **Theory of Everything** passes through the flavor physics. The flavor physics is interesting as it predicted the charm quark and also the masses of charm and top quarks well before their direct experimental observations. Also, the measurements of the flavor changing decays provide us information about new sources of CP violation, which are important because the baryogenesis suggests that there must be sources of CP violation other than the Kobayashi-Maskawa phase ( $\delta_{KM}$ ) present in the SM.

The SM couplings of gauge bosons with different families of leptons; i.e., the lepton-flavor universality (LFU) also invoke agitation between theory and experiments. This important prediction can be tested by measuring the ratio of decay widths of  $B \rightarrow K^{(*)}\mu^+\mu^-$  and  $B \rightarrow K^{(*)}e^+e^-$ , defined as:

$$\mathcal{R}_{K^{(*)}} = \frac{\mathcal{B}r(B \rightarrow K^{(*)}\mu^+\mu^-)}{\mathcal{B}r(B \rightarrow K^{(*)}e^+e^-)} \quad (1.1)$$

in specific bins of the square of momentum transfer  $s(\equiv q^2) \in [s_{\min}, s_{\max}] \text{ GeV}^2$ . In these ratios, the hadronic uncertainties arising from the form factors (FFs) of  $B \rightarrow K^*$  cancel out to a good approximation. Therefore, any possible deviations from the SM predictions; i.e., the value of ratio different from one, will hint towards the New Physics (NP). Due to this reason, these are currently under the spotlight of LHCb and Belle experiments. In 2014, the LHCb collaboration has observed more than  $2\sigma$  mismatch between the experimental observations and the SM predictions in different bins of  $s$  [1]. Recently, the LHCb reported  $R_K = 0.846_{-0.054-0.014}^{+0.060+0.016}$  in the bin  $s \in [1, 6] \text{ GeV}^2$  which is  $2.5\sigma$  away from the corresponding SM value [2].  $R_K^*$  is measured to be  $0.66_{-0.07-0.03}^{+0.11+0.03}$  and  $0.69_{-0.07-0.05}^{+0.11+0.05}$  in the bins  $s \in [0.045, 1.1] \text{ GeV}^2$  and  $s \in [1.1, 6.0] \text{ GeV}^2$  which deviate from the SM prediction by  $2.1\sigma$  and  $2.4\sigma$ , respectively [3]. These hint towards the breakdown of LFU of the SM; i.e., the couplings of gauge bosons with  $\mu$  and  $e$  are not the same [4, 5]. Moreover, the BaBar Collaboration measured the LFU violation [6, 7] for  $R_D$  and  $R_{D^{(*)}}$  ( $R_{D^{(*)}} = \mathcal{B}r(B \rightarrow D^{(*)}\tau\nu_\tau)/\mathcal{B}r(B \rightarrow D^{(*)}\ell\nu_\ell)$ , where  $\ell = e, \mu$ ) and reported  $2\sigma$  and  $2.5\sigma$

deviations from their SM predictions, respectively and  $3.4\sigma$  by taking them together [8]. There are also some other areas where inconsistency between the SM predictions and the experimental observations are found such as the  $\mathcal{P}'_5$  anomaly ( $3.5\sigma$  in one bin  $s \in [4.30, 8.68]$  GeV<sup>2</sup> [9]) that corresponds to the certain coefficient in the angular distribution of the  $B \rightarrow K^*(\rightarrow K\pi)\mu^+\mu^-$  decay [9–11]. This anomaly was again observed at  $3\sigma$  in the LHCb data with  $3 \text{ fb}^{-1}$  luminosity in the two bins  $s \in [4, 6]$  GeV<sup>2</sup> and  $s \in [6, 8]$  GeV<sup>2</sup> [12] and later this is confirmed by Belle in  $s \in [4, 8]$  GeV<sup>2</sup> bin [13]. This anomaly was also accompanied by a  $2.9\sigma$  tension in  $s \in [4, 8]$  GeV<sup>2</sup> region of another angular observable called  $\mathcal{P}_2$  [14]. In addition, there are small but noticeable differences found in the branching ratios of  $B^+ \rightarrow K^{*+}\mu^+\mu^-$  where the SM prediction is  $(26.8 \pm 3.6) \times 10^{-8}$  and the LHCb measurement is  $(15.8^{+3.2}_{-2.9} \pm 1.1) \times 10^{-8}$  [15–17] and  $B_s \rightarrow \phi\mu^+\mu^-$ , which is  $2.0\sigma$  larger than the SM values both in low and high  $\phi$  recoil [18–20]. Similar deviation is seen in the decay of  $B^+ \rightarrow J/\psi\ell^+\nu$  by LHCb [21] which is found to be  $1.7\sigma$  away from the SM predictions [22].

By using the available data and motivated by these tantalizing anomalies observed in  $B$ -meson decays, in addition to explain them in different beyond the SM scenarios [23], the global analyses have also been carried out [10, 14, 24–31]. Incorporating the factorizable (absorbed in the FFs) and non-factorizable contributions, these global analyses favor the negative shift in the Wilson coefficient (WC)  $C_9$  to explain most of the data. However, before we could claim that these are indications of the NP, we have to get full control of the possible hadronic uncertainties arising due to the FFs in the exclusive decays [32–38].

In order to establish the hints of NP, on the experimental side we need to have an improved statistical data which is expected at the Belle II and the LHCb, whereas on the theoretical side we can study some other decays that are governed at quark level by  $b \rightarrow s\ell^+\ell^-$  ( $\ell = \mu, \tau$ ) transitions. In future, it is also possible to have similar deviations in the baryonic partners of these rare  $B$ -meson decays, e.g. in  $\Lambda_b \rightarrow \Lambda(\rightarrow p\pi^-)\mu^+\mu^-$ . Theoretically, the  $b$ -baryon decays are less studied as compared to  $b$ -meson decays because the baryon system includes more degrees of freedom at the quark level. Experimentally, it is easy to detect and isolate heavy baryons than light systems because large mass makes their beam narrow - but the only difficulty in the experiment is due to the fact that in the hadronization process the production rate of  $b$ -baryons is about four times less than that of  $b$ -mesons [39].

The nature of NP in the rare decays can be investigated in two ways: direct detection of new particles and their interactions or indirect detection involving the study of their effects via low energy decay processes. Rare decays involving  $b$ -quark such as  $b \rightarrow (s, d)\gamma$ ,  $b \rightarrow (s, d)\ell^+\ell^-$ , are of prime interest as they are induced by the FCNC transitions involving the quantum number transitions  $|\Delta Q| = 0$  and  $|\Delta B| = 1$ . In the SM, the FCNC transitions are not allowed at the tree level but occur at the loop level because of Glashow-Iliopoulos-Maiani (GIM) mechanism [40]. This makes them sensitive to the masses of particles that run in the loop, e.g.  $m_t$  and  $m_W$  in the SM hence, they play a pivotal role in the determination of Cabibbo-Kobayashi-Masakawa (CKM) [41] matrix elements in an indirect way. In different extensions of the SM, there is a possibility that the new particles can also run in the SM loop diagrams making these rare decays sensitive to their masses and couplings. It can be inferred that the rare decays provide us a rich laboratory to test the predictions of the SM and help us to establish the possible NP indirectly [42, 43].

The study presented in this dissertation is about the flavor sector of the SM and specifically about the bound state of the bottom quark. The decay of the bottom quark takes place via weak



interactions however, the hadronization involves strong interactions. The inclusive decays, e.g.,  $B \rightarrow X_{s,d}(\gamma, \ell^+ \ell^-)$  are easier to calculate theoretically but quite difficult to measure experimentally. Contrary to this, the exclusive decays are easily accessible experimentally because all the decay products are identified but these are quite challenging theoretically due to a lack of deep insight in the low energy QCD. Despite theoretical difficulties in exclusive modes, they have their own advantages to test the SM and to put constraints on the NP scenarios. Just like the exclusive decays of  $B$ -mesons, the decay  $\Lambda_b \rightarrow \Lambda \ell^+ \ell^-$  is prone to the uncertainties arising due to FFs. However, at present the  $\Lambda_b \rightarrow \Lambda$  transition FFs are calculated using lattice QCD (LQCD) calculations with high precision [44] and to have their profile in the full  $s$  range, these FFs are extrapolated using the Bourely-Caprini-Lellouch parametrization [45]. The lattice results are quite consistent with the recent QCD light-cone sum rule calculation [46] with an added benefit of having much smaller uncertainty in most of the kinematical range. However, in contrast to the  $B$ -meson decays, the QCD factorization is not fully developed for the  $b$ -baryon decays, therefore, we will not include these non-factorizable contributions in this work. After having a control on the hadronic uncertainties that mimic in the FFs, the next choice is to find the observables that are relatively clean.

In addition, the decay channel  $\Lambda_b \rightarrow \Lambda(\rightarrow p\pi^-)\ell^+\ell^-$  is interesting to its own regard. On experimental side, this decay was first studied by CDF collaboration [47] and later the LHCb has published the first measurement of  $\Lambda_b$  lifetime [48], differential branching ratio as well as the forward-backward asymmetry of final state muon i.e., the  $A_{FB}^\ell$  [49, 50]. In 2017, the LHCb collaboration has made the observation of  $CP$  violation and the asymmetries arising due to the angle between the  $\mu^+\mu^-$  and  $pK^-$  planes ( $a_{CP}^{\hat{T}^{\text{odd}}}$ ) in  $\Lambda_b \rightarrow pK^-\mu^+\mu^-$  by analyzing the data available at an integrated luminosity of  $3 \text{ fb}^{-1}$  [51]. The LHCb has measured the branching fraction of  $\Lambda_b \rightarrow p\pi^-\mu^+\mu^-$  relative to  $\Lambda_b \rightarrow J/\psi(\rightarrow \mu^+\mu^-)p\pi^-$  [52] and they have also published results of LFU measurement [53], angular moments of polarized  $\Lambda_b$  decay [54] and  $b$ -hadron fractions [55].

On the theoretical front, in the decay  $\Lambda_b \rightarrow \Lambda \ell^+ \ell^-$  the hadrons involved in the initial and final states are the baryons therefore, the study of such decays will help us to understand the helicity structure of the underlying effective Hamiltonian [56–58]. It is because  $\Lambda_b$ -baryon has a non-zero spin, hence it provides a wonderful platform to test the helicity structure which is not possible while studying the  $B$ -meson decays [56, 59]. Like the  $B \rightarrow K^*(\rightarrow K\pi)\mu^+\mu^-$  decay, the above mentioned decay provides a large number of angular observables and is sensitive to all the Dirac structures present in the weak Hamiltonian. Also, this decay is particularly significant as the polarization of  $\Lambda$  is preserved in the parity-violating decay  $\Lambda \rightarrow p\pi^-$  which enables us to make a complementary analysis to that of meson decays. If initial state  $\Lambda_b$  baryons are unpolarized, even then final state  $\Lambda$ 's spin can be used to understand the helicity structure of the weak effective Hamiltonian (WEH) [60, 61]. This motivates us to take into account the cascade decay of  $\Lambda$  that also help us to disentangle the contribution from the individual operators in the WEH of quark level transition  $b \rightarrow s\ell^+\ell^-$  [58, 62–65]. Another feature that makes the semileptonic decay of  $\Lambda_b$  to be more prolific for testing the NP is that the number of angular observables increases when the initial state  $\Lambda_b$  is polarized [66]. Also, the analysis of angular asymmetries in the sequential decay  $\Lambda_b \rightarrow \Lambda(\rightarrow p\pi^-)\mu^+\mu^-$  is expected to complement the different angular asymmetries in the corresponding  $B \rightarrow K^*(\rightarrow K\pi)\ell^+\ell^-$  decays [62, 67, 68]. One important aspect is the stability of  $\Lambda$  under strong interactions and the decay  $\Lambda_b \rightarrow \Lambda(\rightarrow p\pi^-)\ell^+\ell^-$  is theoretically cleaner than the

decay  $B \rightarrow K^*(\rightarrow K\pi)\ell^+\ell^-$ . Due to these reasons  $\Lambda_b \rightarrow \Lambda(\rightarrow p\pi^-)\ell^+\ell^-$  baryon decays have been theoretically well studied in a number of papers [46, 60, 69–100].

In order to address the  $B$ -decays anomalies, several extensions of the SM have been proposed in literature. Presently, applications of these NP models in  $\Lambda_b$  decays become more attractive due to significantly large data from the LHCb experiment. The decays of the  $\Lambda_b$  baryons have been studied in the context of Universal extra dimension (UED) models [90], fourth generation SM [101], top triangle moose [94],  $Z'$  models [102, 103], leptoquark models [99], relativistic quark model [104, 105], G(221) model [106], supersymmetric theories [57, 69], relativistic three quark model [107], covariant confined quark model [108, 109], covariant oscillator quark model [110], aligned two-Higgs doublet model [111], Randall-Sundrum model with custodial protection ( $RS_c$ ) [97, 112] and in a model independent way [65, 75, 77, 78, 113, 114]. In this work we have done the detailed analyses of angular observables of  $\Lambda_b \rightarrow \Lambda(\rightarrow p\pi^-)\ell^+\ell^-$  decay in a family non-universal  $Z'$  model [103],  $RS_c$  model [112] and in a model independent scenario to compare their respective results with the SM predictions and with the LHCb data where available.

In line with the  $B \rightarrow K^*(\rightarrow K\pi)\mu^+\mu^-$  decay, we have calculated the combinations of different angular observables in  $\Lambda_b \rightarrow \Lambda(\rightarrow p\pi^-)\mu^+\mu^-$  decay, namely, forward-backward asymmetries ( $A_{FB}^\ell, A_{FB}^\Lambda, A_{FB}^{\ell\Lambda}$  where the superscripts  $\ell, \Lambda$  and  $\ell\Lambda$  correspond to lepton-side, hadron-side and combined lepton-hadron forward-backward asymmetries, respectively), the longitudinal ( $F_L$ ) and transverse ( $F_T$ ) fractions of dimuon, the longitudinal asymmetry  $\alpha_L$ , the transverse asymmetry  $\alpha_U$ , asymmetry parameters  $\alpha_i$  with  $i = \theta_\ell, \theta_\Lambda, \theta_\xi, \theta'_\xi$  and the observables named as  $\mathcal{P}_i$ 's that are derived from different foldings in the SM at its first right. Keeping in view that among the different hadrons produced at the LHCb, almost 20% will be the  $\Lambda_b$  baryons, it is expected that in the future the results of decay distributions and different angular asymmetries will be available with much better statistics. Therefore, in addition to the SM calculation of the different observables mentioned above, we have studied the impact of different new physics scenarios on these observables in different bins of  $s$ .

First of all, we have analyzed the  $\Lambda_b \rightarrow \Lambda(\rightarrow p\pi^-)\mu^+\mu^-$  decay in the family non-universal  $Z'$  model. It has already been observed that in order to explain the  $R_K$  anomaly in the  $B \rightarrow K\ell^+\ell^-$  decays, the possible candidate is the  $Z'$  model [115]. The economy of these  $Z'$  models is that they can be accommodated to the SM only by extending the electroweak SM group by an additional  $U(1)'$  gauge group to which the extra-gauge boson  $Z'$  is associated. Also, in the grand unification theories (GUTs) such as  $SU(5)$  or string inspired  $E_6$  models [116–120], one of the relevant scenarios is the family non-universal  $Z'$  model [121] and the leptophobic  $Z'$  models [122, 123]. The direct signature of an extra  $Z'$  boson is still missing in the analysis of data taken so far at the LHC [124] experiment, but we already had some indirect constraints on the couplings of  $Z'$  gauge boson through low energy processes that are crucial and complementary for direct searches  $Z' \rightarrow e^+e^-$  at Tevatron [125]. The additional interesting thing that the family non-universal  $Z'$  models have in their account is the new CP-violating phase which has large effects on various FCNC processes [126, 127], such as  $B_s - \bar{B}_s$  mixing [128–132] and rare hadronic and  $B$ -meson decays [102, 133–135]. As extending the SM group by an extra  $U(1)'$  gauge group does not change the operator basis of the SM, therefore, the  $Z'$  model belongs to a class of Minimal Flavor violating models having its imprints in the WCs that correspond to the SM operators.

In the next phase, we study the four body  $\Lambda_b \rightarrow \Lambda(\rightarrow p\pi^-)\mu^+\mu^-$  decay in the framework of the

Randall-Sundrum (RS) model with custodial protection. The RS model features five-dimensional (5D) space-time with a non-trivial warped metric [136]. After performing the KK decomposition and integrating over the fifth dimension the effective 4D theory is obtained which involves new particles appearing as the KK resonances, either of the SM particles or the ones which do not possess SM counterparts. Assuming that the weak effective Hamiltonian of the  $\Lambda_b \rightarrow \Lambda(\rightarrow p\pi^-)\mu^+\mu^-$  decay emerges from the well-defined theory of the  $\text{RS}_c$  model, the WCs of the effective Hamiltonian get modified with respect to the SM values due to additional contributions from the heavy KK excitations and are correlated uniquely. Expecting distinct phenomenological consequences from such a correlation on the angular observables of the  $\Lambda_b \rightarrow \Lambda(\rightarrow p\pi^-)\mu^+\mu^-$  decay, we study whether the current experimental data on  $\Lambda_b$  decays can be explained in the  $\text{RS}_c$  model.

It is well known that the model independent analysis is the most general form to introduce NP in terms of new operators corresponding to vector, axial-vector, scalar, pseudo-scalar, and tensor currents along with their relevant WCs. Contrary to the  $Z'$  and  $\text{RS}_c$  models, in model independent approach the NP enters in two ways; due to the modification of SM WCs  $C_9^{eff}$  and  $C_{10}$  by adding new vector, axial-vector operators and also through the new WCs that correspond to the operators which are missing in the SM. The wealth of data from  $B$ -meson decays has already put some severe constraints on the WCs corresponding to these new operators [137] and the goal here is to see their imprints on several physical observables mentioned above for  $\Lambda_b \rightarrow \Lambda(\rightarrow p\pi^-)\ell^+\ell^-$  decays.

The work presented in this dissertation is organized as follows:

In chapter 2, the contents of the SM, its Lagrangian, and the CKM matrix are reviewed. A brief discussion on the possible limitations of the SM is given in Sect. 2.3. Section 2.4 discusses the regularization and renormalization procedure, the operator product expansion, and its use in the effective theories are presented in Sects. 2.5 and 2.6, respectively. After presenting a short introduction of flavor physics in Sect. 2.8, some of the physical observables which are deduced from the differential decay distribution of  $B \rightarrow K^*\mu^+\mu^-$  along with their experimental measurements are discussed in Sect. 2.9.

Chapter 3 presents a complete derivation of helicity formalism for the four body decay  $\Lambda_b \rightarrow \Lambda(\rightarrow p\pi^-)\ell^+\ell^-$  decay. The kinematics of hadronic part are discussed in Sect. 3.3. In Sects. 3.4 and 3.5 we discussed the helicity amplitudes for both the hadron and lepton parts, respectively whereas, Sect. 3.6 briefly describes the contribution of  $\Lambda \rightarrow p\pi^-$  to the total amplitude. The full expression of four-fold angular distribution obtained from these helicity amplitudes is discussed in Sect. 3.7 and a number of observables  $A_{FB}^\ell, A_{FB}^\Lambda, A_{FB}^{\ell\Lambda}, F_L, F_T, \alpha_i$  with  $i = \theta_\ell, \theta_\Lambda, \theta_\xi, \theta'_\xi$  and  $\mathcal{P}_i$ 's that are derived from different foldings are outlined in Sect. 3.8.

In chapter 4, the salient features of the family non-universal  $Z'$  model are discussed in Sect. 4.1 along with WCs and other parameters of this model. Sect. 4.2 presents the numerical analysis of the above mentioned physical observables performed both in the SM and  $Z'$  model and here we compare the results of certain asymmetries with their measurements from the LHCb experiment. In addition to the tabular form of the results calculated in different bins, these have also been plotted versus  $s$  to see their full profile.

In chapter 5, we describe the main contents of the  $\text{RS}_c$  model, which are particularly relevant for the study of the  $\Lambda_b$  decay under consideration, in Sect. 5.1. In Sect. 5.2, we present the theoretical formalism including the WEH, analytical expressions of the WCs in the  $\text{RS}_c$  model and the angular observables of interest in the four-body  $\Lambda_b \rightarrow \Lambda(\rightarrow p\pi^-)\mu^+\mu^-$  decay. After discussing

the current constraints and subsequently scanning the parameter space of the  $RS_c$  model in Sect. 5.3, we give our numerical results and their discussion in Sect. 5.4.

In chapter 6, Sect. 6.1 discusses the WEH of the SM and its extension to take care of the NP operators arising in the model independent approach. In Sect. 6.2, after giving the matrix elements in terms of the FFs, the helicity formalism corresponding to different quark level currents of WEH is discussed. The four folded angular distribution and the expressions of physical observables for different NP operators are given in Sect. 6.3. The discussion of the impact of new (axial) vector ( $VA$ ), (pseudo) scalar ( $SP$ ) and tensor ( $T$ ) couplings on different physical observables has been done in Sect. 6.4, where the lepton mass effects in  $\Lambda_b \rightarrow \Lambda(\rightarrow p\pi^-)\mu^+\mu^-$  decay are also shown. In the same section, we present the simultaneous fit of observables for which experimental data is available to see if we could find the values of the pairs of NP WCs that could simultaneously satisfy the experimental data and  $B$ -Physics constraints for more than one physical observables in  $\Lambda_b \rightarrow \Lambda(\rightarrow p\pi^-)\mu^+\mu^-$ . At the end of Sect. 6.4, the impact of non-zero lepton mass on different observables is briefly explored for  $\Lambda_b \rightarrow \Lambda(\rightarrow p\pi^-)\tau^+\tau^-$  decay.

Finally, the Chapter 7 concludes all the results of  $\Lambda_b \rightarrow \Lambda(\rightarrow p\pi^-)\ell^+\ell^-$  decay in above discussed NP scenarios.

The work performed here is supplemented with three Appendices which discuss the method adopted to calculate the different helicity fractions of leptons and hadrons in model independent approach along with the full details of their calculation.

# Chapter 2

## Fundamentals

There were five fundamental forces of nature, electric, magnetic, weak, strong, and gravitational force. The Scottish physicist James Clerk-Maxwell and the Dutch physicist Lorentz then proposed the unification of electric and magnetic forces into a single electromagnetic (EM) force thus, making four fundamental forces in terms of which all natural interactions can be explained. All these forces have different strengths and effective ranges with strong force being the strongest and gravitational force being the weakest is almost  $6 \times 10^{-39}$  times weaker than the strong force. The range of the weak force is  $10^{-18}$  m which is 0.1% of the diameter of a proton. The EM, weak, and strong forces are mediated by force carrier particles named bosons. For gravity, graviton may be the corresponding mediator but not yet found.

### 2.1 The Standard Model

The SM is the gauge theory that governs the interactions of fundamental particles in terms of quantum fields. It is not only able to explain most of the particle physics phenomenon but also predicted new particles that were not discovered at the time it was proposed. Below a brief review of the fundamental constituents of the SM is presented.

All particles are categorized depending upon their spin. Particles with half-integer spin are fermions (quarks and leptons) and with integer, spin are bosons (e.g. photons).

- Six quarks with their corresponding antiquarks come in three colors (red, green, and blue). These quarks are classified in three generations: up ( $u$ ) and down ( $d$ ) belong to first, charm ( $c$ ) and strange ( $s$ ) are second and top ( $t$ ) and bottom ( $b$ ) make the third generation (masses increase from first to third generation). They carry a fractional electric charge as well as a color quantum number. The  $u$ ,  $c$  and  $t$  belong to the up-type and each carries an electric charge  $+2/3$  whereas  $d$ ,  $s$  and  $b$ , known as down-type with each having the charge  $-1/3$ . Depending upon their gauge symmetry they can be written in terms of left-handed doublets ( $L$ ) and right-handed singlets ( $R$ ) as:

$$\begin{array}{ccc}
\begin{pmatrix} u \\ d' \end{pmatrix}_L & \begin{pmatrix} c \\ s' \end{pmatrix}_L & \begin{pmatrix} b \\ t' \end{pmatrix}_L \\
u_R & c_R & b_R \\
d_R & s_R & t_R.
\end{array}$$

- Six leptons; i.e., electron, muon, tau, and their respective neutrinos exist along with their anti-particles. Like quarks, leptons also fall in three generations, electron and electron neutrino make the first generation followed by muon and muon neutrino and the heaviest among leptons, tau with its respective neutrino belong to third generation (mass increase from first to third generation). The electron, muon and tau are charged particles whereas neutrinos are chargeless and are massless in the SM. Like quarks, their arrangement in the form of left-handed doublet and right-handed singlet is:

$$\begin{array}{ccc}
\begin{pmatrix} \nu_e \\ e^- \end{pmatrix}_L & \begin{pmatrix} \nu_\mu \\ \mu^- \end{pmatrix}_L & \begin{pmatrix} \nu_\tau \\ \tau^- \end{pmatrix}_L \\
e_R & \mu_R & \tau_R
\end{array}$$

- The photon is a mediator of EM force and has spin 1 and is electrically neutral.
- Eight gluons with non-zero color charge and zero EM charge mediate the strong force.
- $W^+$ ,  $W^-$  and  $Z^0$  bosons are the mediators of the weak force. The  $W^\pm$  bosons were discovered in January 1983 at CERN with mass  $80.379 \pm 0.012 \text{ GeV}/c^2$  [138, 139]. The  $Z$  boson was discovered a few months later, in May 1983 also at the CERN having mass  $91.1876 \pm 0.0021 \text{ GeV}/c^2$  [140, 141].
- The Higgs is the most important particle as it is responsible for giving mass to every fundamental particle via the Higgs mechanism. It was the last missing piece of SM and it was discovered in 2012 at LHC with mass  $125.18 \pm 0.16 \text{ GeV}/c^2$  [142, 143].

The SM proposed by Glashow-Salam-Weinberg [144–146] is based on the  $SU(3)_C \times SU(2)_L \times U(1)_Y$  gauge group where  $C$ ,  $L$  and  $Y$  stand for color, left-handed chirality, and weak hypercharge, respectively. For strong interactions, the gauge group is the non-Abelian  $SU(3)_C$  which has eight generators that correspond to the eight gluons which are mediators of the strong force between color-carrying objects - the subscript  $C$  denotes this fact. Since the gluons themselves are colored, they can directly interact with each other, which leads to the phenomena of "asymptotic freedom" and "confinement". The strong interaction coupling constant  $\alpha_s$  becomes small at the short distance and this allows us to compute the color interactions using perturbative techniques. However, at long distances, the coupling gets large, which causes the quarks to confine into the colorless hadrons that are classified as **mesons** and **baryons**. In Quark Model, the mesons consist of a quark and an anti-quark whereas baryons consist of three quarks or three anti-quarks.

The electroweak interaction is based on the gauge group  $SU(2) \times U(1)$  which is spontaneously broken to  $U(1)_{QED}$  via non-vanishing vacuum expectation value (VEV) of isospin doublet scalar

Higgs field [147]

$$\phi = \begin{pmatrix} \phi^+ \\ \phi^0 \end{pmatrix}, \quad (2.1)$$

which has four scalar degrees of freedom, and three of them give masses to  $W$  and  $Z$  bosons whereas the fourth appears as a physical Higgs boson. In SM, the EM and weak interactions are unified to an electroweak force.

In SM, the fundamental interactions are described in terms of Lagrangian equations which hold local gauge invariance. Mathematically, it means that the Lagrangian remains invariant under the multiplication of a field with an arbitrary phase that varies with space and time, and physically it means that the SM predictions remain the same all over the universe. Below we shall discuss different terms of the SM Lagrangian.

### 2.1.1 The SM Lagrangian

All the information contained in any theory is encoded in the Lagrangian density that is function of fields and their derivatives containing kinetic energy, couplings and interaction terms. It seems more convenient to discuss the Lagrangian for QCD and electroweak theory separately rather than assembling them into full Lagrangian of the SM. The Lagrangian for  $SU(3)$  group is [148]

$$\mathcal{L}_{QCD} = -\frac{1}{4}G_{\mu\nu}^a G^{a\mu\nu} + \sum_f \bar{q}_f i \not{D} q_f, \quad (2.2)$$

with

$$D_\mu = \partial_\mu + ig_s G_\mu^a \frac{T^a}{2}, \quad G_{\mu\nu}^a = \partial_\mu G_\nu^a - \partial_\nu G_\mu^a - g_s f^{abc} G_\mu^b G_\nu^c, \quad (2.3)$$

representing the covariant quark derivative and gluon field strength tensor, respectively. In Eq. (2.2),  $g_s$  and  $f$  in summation stand for strong coupling constant and quark flavors, respectively and  $a, b, c = 1, \dots, 8$  are the eight-bosons of  $SU(3)$ .  $f^{abc}$  are the structure constants defined in terms of generators of  $SU(3)$  group

$$[T^a, T^b] = 4if^{abc}T^c. \quad (2.4)$$

For  $SU(2) \times U(1)$  group, the kinetic energy term for gauge bosons reads as

$$\mathcal{L}_{gauge} = -\frac{1}{4}B_{\mu\nu}B^{\mu\nu} - \frac{1}{4}W_{\mu\nu}^a W^{a\mu\nu} \quad (2.5)$$

with

$$B_{\mu\nu} = \partial_\mu B_\nu - \partial_\nu B_\mu \quad W_{\mu\nu}^a = \partial_\mu W_\nu^a - \partial_\nu W_\mu^a - g\epsilon^{abc}W_\mu^b W_\nu^c \quad (2.6)$$

where  $B_\mu$  and  $W_\mu^a$  represent gauge fields of  $U(1)$  and  $SU(2)$ , respectively and  $a = 1, 2, 3$  denote gauge bosons of weak force and  $g$  is the corresponding coupling.  $B_\mu$  and  $W_\mu^3$  fields ultimately

combine to give the photon and  $Z$  boson. The Higgs part of the Lagrangian is

$$\mathcal{L}_{Higgs} = (D^\mu)\phi D_\mu\phi - \mu^2\phi^\dagger\phi - \lambda(\phi^\dagger\phi)^2, \quad (2.7)$$

where the scalar Higgs field  $\phi$  is defined in Eq. (2.1) with hypercharge  $+1/2$  and the term containing  $\lambda$  leads to quartic self interaction of the scalar fields. The gauge covariant derivative  $D_\mu$  used in Eq. (2.7) is defined as

$$D_\mu = \partial_\mu + ig\frac{\tau^i W_\mu^i}{2} + i\frac{g'}{2}B_\mu \quad (2.8)$$

where  $g'$  is the EM gauge coupling and  $\tau^i$ 's are the Pauli spin matrices. The square of a covariant derivative in Eq. (2.7) represents three and four-point interactions between gauge bosons and the Higgs. In order to break the symmetry spontaneously we must have  $\mu^2 < 0$ .

Fermion interaction term in Lagrangian is

$$\mathcal{L}_{fermion} = \sum_j \left( \bar{q}_L^j i\not{D} q_L^j + \bar{\ell}_L^j i\not{D} \ell_L^j + \bar{u}_R^j i\not{D}' u_R^j + \bar{d}_R^j i\not{D}' d_R^j + \bar{e}_R^j i\not{D}' e_R^j \right) \quad (2.9)$$

where  $j$  stands for family,  $L, R = \frac{1 \mp \gamma_5}{2}$  are chiral projections and

$$D_\mu = \partial_\mu + ig\frac{\tau^i W_\mu^i}{2} + i\frac{g'}{2}Y B_\mu \quad D'_\mu = \partial_\mu + i\frac{g'}{2}Y B_\mu. \quad (2.10)$$

Eq. (2.9) describes the gauge interaction of  $W$  and  $B$  fields with that of the fermions. The fact that left and right-handed fields transform in different manner leads to parity violation in the electroweak interactions. The term in the SM Lagrangian that incorporates the Yukawa interaction is

$$\mathcal{L}_{Yukawa} = - \sum_{f,f'} \left[ \Gamma_{f,f'}^u \bar{q}_L^f \tilde{\phi} u_R^{f'} + \Gamma_{f,f'}^d \bar{q}_L^f \phi d_R^{f'} + \Gamma_{f,f'}^e \bar{\ell}^{f,f'} \phi e_R^{f'} \right] + h.c. \quad (2.11)$$

Here  $\tilde{\phi} = i\tau^2\phi^\dagger$  with  $Y = -\frac{1}{2}$  and  $\Gamma_{f,f'}$  denote Yukawa couplings of Higgs doublet with different fermion flavors.

Finally assembling the different Lagrangian terms given in Eqs. (2.2, 2.5, 2.7, 2.9) and Eq. (2.11), i.e., the complete SM Lagrangian can be obtained as

$$\mathcal{L}_{SM} = \mathcal{L}_{QCD} + \mathcal{L}_{gauge} + \mathcal{L}_{higgs} + \mathcal{L}_{fermions} + \mathcal{L}_{Yukawa}. \quad (2.12)$$

## 2.2 CKM matrix

In SM, the kinetic energy terms of leptons, quarks, and Higgs doublets conserve the Charge-Conjugation-Parity (CP) symmetry and CP violation arises due to interaction terms - usually through the Yukawa couplings. There is no CP violation if the VEV of Higgs doublet vanishes as all fermions are massless in this case. Below the VEV scale of the Higgs doublet, the SM fields get masses and the CP phase can be located in the left-handed currents which couple to  $W_\mu^\pm$  bosons. In this scheme, the charged current couplings are defined using Cabibo-Kabayoshi-Maskawa (CKM)



matrix for quarks and Pontecorvo-Maki-Nakagawa-Sakata (PMNS) matrix for leptons [149].

The CKM matrix is characterized by the three real parameters  $\sin \theta_{ij}$  and a complex phase  $\delta_{KM}$  which is the origin of CP violation in the SM. In 2001, the CP violation was observed in the  $B$ -mesons decays by BaBar [150] and Belle [151] where they have measured the large value of  $\sin 2\beta$  with  $\beta$  corresponding to one of the angles of unitary triangle (c.f. Fig. 2.1). The SM does not estimate the values of these four free parameters and they are determined from the experiments. The measured values of these parameters in different decay processes must be comparable to each other and any mismatch will indicate the existence of the NP. Semileptonic decays are viable to reduce the uncertainties originating from the strong interactions between final state quarks and hence provide an opportunity to predict the values of different CKM elements.

The Yukawa interactions which give masses to quarks can be extracted from Eq. (2.11) and its relevant term can be expressed as

$$\mathcal{L}_{Yukawa} = -\Gamma_{f,f'}^d \bar{q}_{fL}^I \phi d_{f'R}^I - \Gamma_{f,f'}^u \bar{q}_{fL}^I \epsilon \phi^* u_{f'R}^I + h.c., \quad (2.13)$$

where  $\epsilon$  is a  $2 \times 2$  antisymmetric tensor. In weak eigenstate basis,  $q_L^I$  and  $q_R^I$  are the left- and right-handed quark doublets, respectively. When Higgs field acquires VEV  $\langle \phi \rangle = (0, v/\sqrt{2})$ , the above equation gives mass terms for quarks. The physical states can be achieved by diagonalizing  $\Gamma^{u,d}$  with four unitary matrices  $V_{L,R}^{u,d}$  as  $M_{diag}^{u,d} = V_L^{u,d} \Gamma^{u,d} V_R^{u,d} (v/\sqrt{2})$  with a consequence that the charged boson  $W^\pm$  couple with the physical quark states  $u_{fL}, d_{fL}$  as

$$\frac{-g}{\sqrt{2}} (\bar{u}_L, \bar{c}_L, \bar{t}_L) \gamma^\mu W_\mu^+ V_{CKM} \begin{pmatrix} d_L \\ s_L \\ b_L \end{pmatrix} + h.c. \quad (2.14)$$

and  $V_{CKM}$  is a  $3 \times 3$  unitary matrix that govern the transition of one quark to another with the production of a virtual  $W$  boson and it can be written as

$$V_{CKM} \equiv V_L^u V_L^{d\dagger} = \begin{pmatrix} V_{ud} & V_{us} & V_{ub} \\ V_{cd} & V_{cs} & V_{cb} \\ V_{td} & V_{ts} & V_{tb} \end{pmatrix}. \quad (2.15)$$

Here the quarks with  $+2/3$  charge; i.e.,  $u, c$  and  $t$  are taken to be pure states and flavor mixing is expressed in terms of  $3 \times 3$  matrix operating on remaining three quark states  $d, s$  and  $b$ . The CKM matrix has many possible conventions, however a standard one is

$$V_{CKM} = \begin{pmatrix} c_{12}c_{13} & s_{12}c_{13} & s_{13}e^{-i\delta} \\ -s_{12}c_{23} - c_{12}s_{23}s_{13}e^{i\delta} & c_{12}c_{23} - s_{12}s_{23}s_{13}e^{i\delta} & s_{23}c_{13} \\ s_{12}s_{23} - c_{12}c_{23}s_{13}e^{i\delta} & -c_{12}s_{23} - s_{12}c_{23}s_{13}e^{i\delta} & c_{23}c_{13} \end{pmatrix}, \quad (2.16)$$

where  $c_{ij} = \cos \theta_{ij}$ ,  $s_{ij} = \sin \theta_{ij}$  and the phase  $\delta$  is responsible for the CP violation. All  $\theta_{ij}$  lie in first quadrant and it is experimentally verified that  $s_{13} \ll s_{23} \ll s_{12} \ll 1$ . It is convenient to

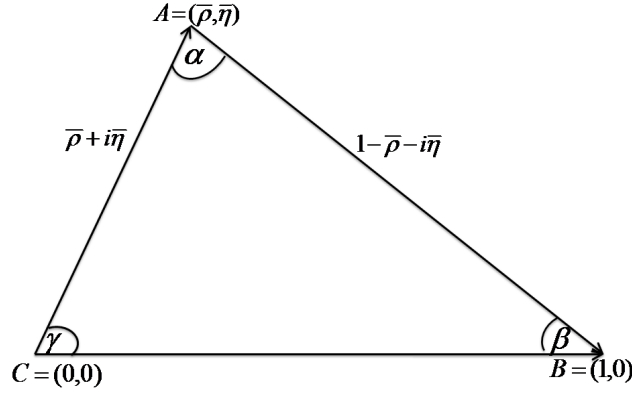


Figure 2.1: The sketch of a Unitary triangle.

relate the parameters with Wolfenstein parametrization [152],

$$s_{12} = \lambda = \frac{|V_{us}|}{\sqrt{|V_{ud}|^2 + |V_{us}|^2}}, \quad s_{23} = A\lambda^2 = \lambda \left| \frac{V_{cb}}{V_{us}} \right|, \quad (2.17)$$

$$s_{13}e^{i\delta} = V_{ub}^* = A\lambda^3(\bar{\rho} + i\bar{\eta}) = \frac{A\lambda^3(\bar{\rho} + i\bar{\eta})\sqrt{1 - A^2\lambda^4}}{\sqrt{1 - \lambda^2[1 - A^2\lambda^4(\bar{\rho} + i\bar{\eta})]}}. \quad (2.18)$$

These relation respect  $(\bar{\rho} + i\bar{\eta}) = -(V_{ud}V_{ub}^*)/(V_{cd}V_{cb}^*)$  with  $\bar{\rho} = -\text{Re} \frac{V_{ud}V_{ub}^*}{V_{cd}V_{cb}^*}$  and  $\bar{\eta} = -\text{Im} \frac{V_{ud}V_{ub}^*}{V_{cd}V_{cb}^*}$ . The CKM matrix given in Eq. (2.16) in terms of Wolfenstein parametrization is written as

$$V_{CKM} = \begin{pmatrix} 1 - \lambda^2/2 & \lambda & A\lambda(\bar{\rho} - i\bar{\eta}) \\ -\lambda & 1 - \lambda^2/2 & A\lambda^2 \\ A\lambda^3(1 - \bar{\rho} - i\bar{\eta}) & -A\lambda^2 & 1 \end{pmatrix} + \mathcal{O}(\lambda^4), \quad (2.19)$$

where the expansion parameter  $\lambda$  is written in terms of Cabbibo angle  $\lambda = \sin \theta_C \approx V_{us}$ . This matrix cannot be forced to be real and its consequence is the CP violation because the couplings for quarks and anti-quarks get different phases  $V_{CKM} \neq V_{CKM}^*$ . In the quark sector, Wolfenstein parameter  $\eta$  is responsible for all CP violation. The unitarity of the CKM matrix implies that  $\sum_i V_{ij}V_{ik}^* = \delta_{jk}$  and  $\sum_j V_{ij}V_{kj}^* = \delta_{ik}$ . The unitary triangle which is most commonly used is the result of relation

$$V_{ud}V_{ub}^* + V_{cd}V_{cb}^* + V_{td}V_{tb}^* = 0. \quad (2.20)$$

By dividing above equation with  $V_{cd}V_{cb}^*$  one gets the unitary triangle represented in Fig. 2.1. The angles  $\alpha, \beta$  and  $\gamma$  are directly related to CP asymmetries which can be written in terms of  $\bar{\rho}$  and  $\bar{\eta}$  as

$$\sin 2\alpha = \frac{2\bar{\eta}(\bar{\eta}^2 + \bar{\rho}^2 - \bar{\rho})}{(\bar{\eta}^2 + \bar{\rho}^2 - \bar{\rho})^2 + \bar{\eta}^2}, \quad \sin 2\beta = \frac{2\bar{\eta}(1 - \bar{\rho})}{(1 - \bar{\rho})^2 + \bar{\eta}^2}. \quad (2.21)$$

The precise determination of CKM matrix elements is important in the study of flavor physics.

## 2.3 Discrepancies of the SM

Although the SM is successful in explaining most of the experimental outcomes but it lacks to address some features of the universe. The main shortcomings of the SM are the following:

**Massive neutrinos:** As a consequence of only left-handed neutrinos, these are massless in the SM because no renormalizable mass term can be added for them in the SM Lagrangian. It is observed that three neutrinos oscillate and transform their flavor as they propagate. Hence present data leads to massive neutrinos which provide evidence of the NP.

**Fermion generations:** The SM is unable to shed light on the fact that why there are three generations of quarks and leptons with the same features but different masses.

**Strong CP problem:** CP is the symmetry combining charge conjugation C (by conjugating all internal quantum numbers, particle transforms to its anti-matter partner) and parity P (handedness of space is inverted; i.e., left-handed to right-handed and vice versa). The laws of physics were the same for matter and anti-matter if CP was an exact symmetry. The CP violation was first observed in 1964 at Brookhaven National laboratory in the decay of neutral kaons decaying into pions [153]. The neutral Kaons come in two versions which have different lifetimes, a long-lived that decays primarily into three pions and a short-lived one that prefers to decay into two pions. However, rarely the long-lived kaons decay into two pions which require CP symmetry to be broken [154]. Then similar CP violation was observed in  $B$  systems i.e. in  $B^0$  [155,156],  $B^+$  [157–159] and  $B_s^0$  [160]. The evidence of CP violation in baryonic decay was observed in  $\Lambda_b$  decay which is found to be at  $3.3\sigma$  level [161]. The very different hierarchies of strong and weak CP violation is termed as strong CP problem. The present measurements of CP violation put strong bounds on quark weak couplings and the future measurements in  $b$ -hadrons and kaons will put even more stringent constraints on the flavor parameters of the SM and can probe the NP.

**General theory of relativity is not included** in the SM. To add the most common force of our daily life to the framework of SM has proved to be a big challenge. But in particle physics, at the subatomic level gravitational effects are negligible. The gravitational effects dominate when the bulk of matter is present.

**Hierarchy Problem:** The question, why the Plank scale ( $\sim 10^{19}$  GeV) is much higher than the electroweak scale ( $\sim 100$  GeV) is not addressed by the SM. Our universe has two scales at two extremes as masses of  $W^\pm$  and  $Z$  boson are very less compared to the Planck scale. In other words, this problem relates to the vast discrepancy (order of  $10^{24}$ ) present between the strengths of weak and gravitational forces.

**Muon anomalous magnetic moment:** A long standing puzzle of particle physics is the significantly larger value of magnetic moment of muon compared to its SM predictions. The muon  $g - 2$  collaboration measured [162]

$$\delta(a_\mu) = (a_\mu)_{exp} - (a_\mu)_{SM} = 261(63)(48) \times 10^{-11}, \quad (2.22)$$

where errors include both from theory and experiment and it shows  $3.3\sigma$  discrepancy between the measurement and SM prediction. Many attempts were made to explain the phenomenon in different NP frameworks such as extra-dimensional models [163–165], non-commutative space-time geometry [166], minimal supersymmetric standard model [167] and little Higgs model [168] in which the observed deviation is addressed by  $a_\mu = (a_\mu)_{SM} + (a_\mu)_{NP}$ .

**Dark energy and dark matter:** Unlike the usual matter, dark matter does not exhibit EM interaction and hence it does not absorb, emit or reflect light which makes it hard to detect. Its existence is inferred from its gravitational effects on the visible matter. The SM does not provide any good dark matter candidate which consists of about 27% of the universe and only explains the 5% content of the universe that make up all stars, planets, and galaxies. Dark matter candidates can arise in some beyond SM scenarios such as supersymmetric theories and extra-dimensional models. About 68% of the universe consists of Dark energy which is related to the vacuum in space. Its effect will not decrease with the expansion of the universe as it is evenly distributed in the whole universe in space-time. Therefore, dark energy does not put local gravitational effects but has global effects throughout the universe. This gravitational repulsive force makes the universe to expand continuously at faster rates. The measurement of the expansion of the universe and other scientific data confirmed the existence of dark matter and approximate how much amount of this exotic substance exists.

**Matter-antimatter asymmetry (Baryogenesis):** Since matter and anti-matter should have been produced in equal amounts at the time of the big-bang, then why the universe is dominated by matter with almost no anti-matter around. This asymmetry can be addressed in terms of the difference in the way how matter and anti-matter interact with the weak force. According to Sakharov, there are three conditions for this asymmetry: C and CP violation, baryon number violation, and departure from thermal equilibrium [169]. The LHCb tried to build the experiment to explain this tension and they have measured some parameters associated with the CKM matrix which measures the CP violation among quarks. The angle  $\gamma$  has been measured using different techniques and its average value is found to be around  $74^\circ$ . The ALPHA team has produced anti-hydrogen atoms by collecting anti-protons from CERN's anti-proton decelerator and combined them with positrons from a Sodium-22 source [170]. If a slight difference is found in the fundamental symmetry charge-parity-time (CPT) between the hydrogen and anti-hydrogen atoms, it would rock the basis of the SM. Until now it has been impossible to produce and trap anti-hydrogen atoms sufficiently long to perform essential optical interrogation technology and to make serious anti-hydrogen spectroscopy possible. The SM predicts the value of CP violation which is far less than that required to address the matter-antimatter asymmetry of the universe.

**Flavor Physics:** A tension exists between the SM predictions and the data for  $b \rightarrow s\mu^+\mu^-$  branching fraction and  $B \rightarrow K^*\mu^+\mu^-$  angular observables which can be solved by introducing the NP effect in  $C_9$  and  $C_{10}$  that interfere destructively in the SM. Since the mismatch exists due to an operator that couple vectorially to leptons involving left-handed quarks which leads to the fact that it may be due to unpredictably large non-factorizable hadronic effect. More accurate measurements of  $s$  dependent observables make it possible to separate the QCD effect from the NP contribution. If the NP violates LFU then the measurement of the ratio of observables of  $b \rightarrow se^+e^-$  to  $b \rightarrow s\mu^+\mu^-$  may provide a clean way to predict it. A more detailed discussion on the deviations observed in a number of physical observables in  $B$ -meson decays at the LHCb experiment is given in section 2.8.

## 2.4 Regularization and Renormalization

Feynman rules can be inferred from the QCD Lagrangian density (2.2) which is used to calculate the amplitude of a process in perturbative QCD. At the loop level, the Feynman diagrams are encountered with ultraviolet divergences because of self-interactions of particles. Renormalization is a useful tool to truncate these divergences from physically accessible quantities. For this purpose, one has to apply the regularization process to modify the theory in such a way that the observables are well-defined and finite to all orders in perturbation theory. After this, we are able to handle the quantities which are divergent only once regularization is eliminated. A direct way to make use of this is the momentum cutoff method that violates Lorentz invariance and Ward identities [171, 172]. But all gauge symmetries are automatically conserved and Ward identities hold to all orders of perturbation theory in dimensional regularization. To regulate the field theory **cut off** is introduced which is an energy scale and by setting it to infinity, original integrals are recovered. For a finite value of cutoff, divergent integrals become convergent but at the cost of showing a dependence on the cutoff. However, these terms are canceled with their cutoff dependent counterparts, and later if the cutoff is made to approach infinity, finite physical results are obtained. If there are no divergences in loop diagrams in a quantum field theory, even then renormalization of mass and fields is required. It is due to the fact that a system of a charged particle is surrounded by a cloud of virtual particles that alter original parameters describing the system such as its mass and charge. It means that long-distance and short-distance parameters are not alike and the relationship between them is provided by renormalization.

The method of dimensional regularization is suitable for gauge theories but potential problems in electroweak theory involve  $\gamma_5$  in  $D \neq 4$  which is defined as  $\gamma_5 = i\epsilon_{\mu\nu\alpha\beta}\gamma^\mu\gamma^\nu\gamma^\alpha\gamma^\beta/4!$  and it is not clean enough to transform the antisymmetric tensor  $\epsilon_{\mu\nu\alpha\beta}$  in  $D \neq 4$  dimensions. In naive dimensional regularization (NDR) [171], the metric tensor is generalized in  $D$  dimensions and anti-commutation relations of 4 dimensional  $\gamma$  matrices are still valid. If these anti-commutation relations are not consistent even then NDR scheme can be applied but evaluation of  $\text{Tr}[\gamma_5\gamma^\mu\gamma^\nu\gamma^\alpha\gamma^\beta]$  must be evaded [173, 174]. Another scheme which is more consistent in the presence of  $\gamma_5$  is proposed by 't Hooft and Veltman and is known as HV scheme [175]. The additional thing in this scheme is the presence of  $-2\epsilon$  dimensional metric tensor  $\hat{g}$  along with already present metric tensors  $g$  (in  $D$  dimensions) and  $\tilde{g}$  (in 4 dimensions). In a similar manner,  $D$  dimensional gamma matrix  $\gamma_\mu$  can be written in terms of  $\tilde{\gamma}_\mu$  (in 4 dimensions) and  $\hat{\gamma}_\mu$  (in  $-2\epsilon$  dimensions). When  $\gamma_5$  is introduced in the scheme, it commutes with  $\hat{\gamma}_\mu$  and anti-commutes with  $\tilde{\gamma}_\mu$  [173].

Once the regularization is achieved, one can proceed with renormalization which connects bare (unphysical) and normalized (physical) quantities such as mass, charge, and couplings, and then observables are expressed in terms of these physical quantities. Bare and physical quantities are related in the following way

$$m^{(0)} = Z_m m, \quad q^{(0)} = Z_q^{1/2} q, \quad g^{(0)} = Z_g g \mu^\epsilon, \quad A_\mu^{(0)} = Z_3^{1/2} A_\mu. \quad (2.23)$$

Here the quantities characterized with superscript (0) are bare and  $m, q, g$  and  $A_\mu$  are renormalized quark mass, charge, QCD coupling, and photon field, respectively.  $Z_m, Z_q, Z_g$  and  $Z_3$  are the renormalization constants in which all divergences are absorbed up to all powers of perturbation. The SM is renormalizable because the gauge invariance of Lagrangian is preserved even in Higgs

mechanism where the symmetry is spontaneously broken [176]. A simplified method to apply renormalization is a counter-term method where QCD bare Lagrangian  $\mathcal{L}_{QCD}^{(0)}$  can be written as

$$\mathcal{L}_{QCD}^{(0)} = \mathcal{L}_{QCD} + \mathcal{L}_{counter}, \quad (2.24)$$

with  $\mathcal{L}_{QCD}$  written in Eq. (2.2) and the newly added term  $\mathcal{L}_{counter}$  is proportional to  $(Z-1)$  that acts as a new interaction term contributing to Green's functions in perturbation theory. Renormalization constants  $Z_{m,q,g,3}$  are fixed in such a way that this new term cancels the contributions of divergences in Green's functions. But a sensible scheme for this cancellation must be defined otherwise convergent terms are also canceled out along with divergent ones. The two schemes designed for this purpose are  $MS$  [177] and  $\overline{MS}$  [178], where the latter one is of prime interest in which renormalization scale  $\mu$  reads as

$$\mu_{\overline{MS}} \rightarrow \frac{\mu e^{\gamma_E/2}}{\sqrt{4\pi}}. \quad (2.25)$$

This scheme is used to proceed so that  $\ln 4\pi - \gamma_E$  terms are no more present and not only the divergent part of radiative corrections is removed by counter terms but also the universal constant appeared in Feynman diagram calculations. In this scheme renormalization constants take the form

$$\begin{aligned} Z_m &= 1 - 3C_F \frac{\alpha_s}{4\pi\varepsilon}, & Z_g &= 1 - \frac{\alpha_s}{4\pi\varepsilon} \left( \frac{11}{6}N_c - \frac{1}{3}N_f \right), \\ Z_q &= 1 - C_F \frac{\alpha_s}{4\pi\varepsilon}, & Z_3 &= 1 - \frac{\alpha_s}{4\pi\varepsilon} \left( \frac{2}{3}N_c - \frac{5}{3}N_f \right), \end{aligned} \quad (2.26)$$

where  $N_c$  and  $N_f$  are colors and flavors of quarks, respectively. Now the parameters of theory depend on renormalization scale  $\mu$  and it must be assigned a certain value to get renormalized parameters from experiment; i.e.,  $g \equiv g(\mu)$ ,  $m \equiv m(\mu)$  and  $q \equiv q(\mu)$ . By varying value of  $\mu$ , one can get different sets of parameters of theory  $m(\mu)$ ,  $q(\mu)$ ,  $g(\mu)$  along with a set of equations which relates parameter set with different values of  $\mu$  and these are called the renormalization group equations (RGE). Using Eq. (2.23) one gets

$$\frac{dm(\mu)}{d\ln(\mu)} = -m(\mu)\gamma_m(g(\mu)), \quad \frac{dg(\mu)}{d\ln(\mu)} = \beta(g(\mu, \varepsilon)), \quad (2.27)$$

where the anomalous dimension of the mass operator and  $\beta$  function are defined as

$$\gamma_m(g(\mu)) = \frac{1}{Z_m} \frac{dZ_m}{d\ln(\mu)}, \quad \beta(g(\mu, \varepsilon)) = -\varepsilon g + \beta(g), \quad (2.28)$$

with

$$\beta(g) = -\frac{1}{Z_g} \frac{dZ_g}{d\ln(\mu)}. \quad (2.29)$$

Up to two loop accuracy one gets

$$\begin{aligned}\gamma_m(\alpha_s) &= \frac{\alpha_s}{4\pi} \gamma_m^{(0)} + \left(\frac{\alpha_s}{4\pi}\right)^2 \gamma_m^{(1)}, \\ \beta(g) &= -\frac{g^3}{16\pi^2} \beta_0 - \frac{g^5}{(16\pi^2)^2} \beta_1,\end{aligned}\tag{2.30}$$

where

$$\begin{aligned}\gamma_m^{(0)} &= 6C_F, & \gamma_m^{(1)} &= C_F(3C_F + \frac{97}{3}N_c - \frac{10}{3}N_f), \\ \beta_{(0)} &= \frac{11N_c - 2N_f}{3}, & \beta_1 &= \frac{34}{3}N_c^2 - \frac{10}{3}N_cN_f - 2C_FN_f, \\ \alpha_s(\mu) &= \frac{g^2(\mu)}{4\pi}, & C_F &= \frac{N_c^2 - 1}{2N_c}.\end{aligned}\tag{2.31}$$

One gets the solutions for  $m(\mu)$  and  $\alpha_s(\mu)$  as

$$m(\mu) = m(\mu_0) \left[ \frac{\alpha_s(\mu)}{\alpha_s(\mu_0)} \right]^{\frac{\gamma_m^{(0)}}{2\beta_0}} \left[ 1 + \left( \frac{\gamma_m^{(1)}}{2\beta_0} - \frac{\beta_1 \gamma_m^{(0)}}{2\beta_0^2} \right) \frac{\alpha_s(\mu) - \alpha_s(\mu_0)}{4\pi} \right],\tag{2.32}$$

$$\alpha_s(\mu) = \frac{4\pi}{\beta_0 \ln(\mu^2/\Lambda_{\overline{MS}}^2)} \left[ 1 - \frac{\beta_1}{\beta_0^2} \frac{\ln(\ln(\mu^2/\Lambda_{\overline{MS}}^2))}{\ln(\mu^2/\Lambda_{\overline{MS}}^2)} \right].\tag{2.33}$$

The cut-off  $\Lambda_{\overline{MS}}$  is a characteristic scale both for QCD and the used  $\overline{MS}$  scheme and depends on the quark flavors present in the  $\beta_0$  and  $\beta_1$ .  $\beta_0$  and  $\gamma_m^{(0)}$  are positive for six quark flavors and three colors which leads to the phenomenon of asymptotic freedom because coupling (also mass) decrease as  $\mu$  increase. Renormalization group has its advantages when we want to sum large logarithms such as the one present in  $\alpha_s$  given in Eq. (2.33) which can be written in the form

$$\alpha_s(\mu) = \frac{\alpha_s(\mu_0)}{v(\mu)} \left[ 1 - \frac{\beta_1}{\beta_0} \frac{\alpha_s(\mu_0)}{4\pi} \frac{\ln v(\mu)}{v(\mu)} \right],\tag{2.34}$$

where  $v(\mu) = 1 - \beta_0 \frac{\alpha_s}{4\pi} \ln \frac{\mu_0^2}{\mu^2}$ .

## 2.5 Operator Product Expansion

In section 2.4 we have seen that in the dimensional regularization we encounter the logarithms of ratios of any scale with the renormalization scale  $\mu$  and these large logarithms can be summed systematically using RGE. It becomes problematic when we have an energy scale with  $\mathcal{O}(1 \text{ GeV})$  i.e., hadron energy scale. Apart from these large logarithms, the strong coupling  $\alpha_s$  is too large for perturbation theory to make sense and hence we need to establish a theory that can describe the weak interactions of quarks. This task can be achieved by using a well established theoretical tool that is known as the Operator Product Expansion (OPE) [179–181].

The OPE can be explained using an example of a quark level  $b \rightarrow cs\bar{u}$  transition with an

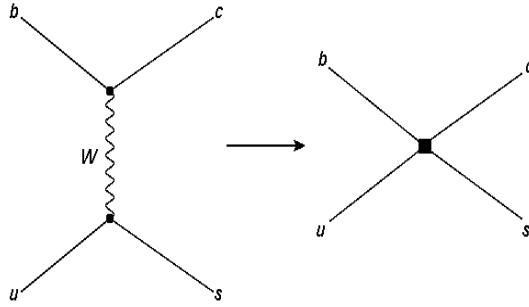


Figure 2.2: Feynmann diagram for the decay  $b \rightarrow cs\bar{u}$  which can be replaced by four point effective vertex.

amplitude

$$\begin{aligned}
 A(b \rightarrow cs\bar{u}) &= -\frac{G_F}{\sqrt{2}} V_{cb} V_{us}^* \frac{M_W^2}{p^2 - M_W^2} (\bar{s}u)_{V-A} (\bar{c}u)_{V-A} \\
 &= \frac{G_F}{\sqrt{2}} V_{cb} V_{us}^* (\bar{s}u)_{V-A} (\bar{c}u)_{V-A} + \mathcal{O}\left(\frac{p^2}{M_W^2}\right)
 \end{aligned} \tag{2.35}$$

where  $W$ -boson propagates the process and  $(\bar{q}_1 q_2)_{V-A} \equiv \bar{q}_1 \gamma_\mu (1 - \gamma_5) q_2$ . As momentum transfer  $p$  is significantly less than  $M_W$  therefore, one can safely ignore the terms of order  $\frac{p^2}{M_W^2}$  and the problem can be tackled by replacing propagator with a four point fermion interaction as shown in Fig. 2.2.

The OPE in quantum field theory is a convergent expansion obtained from the product of two fields lying at different points as a sum of local operators. Consider a state  $\Psi$  that is characterized by  $N$  point functions

$$\langle \mathcal{O}_{A_1}(x_1), \dots, \mathcal{O}_{A_N}(x_N) \rangle \Psi = \sum_B \mathcal{C}_{A_1 \dots A_N}^B(x_1, \dots, x_N) \langle \mathcal{O}_B(x_N) \rangle \Psi$$

where  $\mathcal{C}_{A_1 \dots A_N}^B(x_1, \dots, x_N)$  are the OPE coefficients that are independent of  $\Psi$  and covariant functionals of metric tensor  $g_{\mu\nu}$ . For four dimensional free scalar field having action  $\int |\partial\phi|^2$ , the OPE reads

$$\phi(x_1)\phi(x_2) = \frac{\lambda}{|x_1 - x_2|^2} \cdot 1 + \phi^2(x_2) + \sum \frac{(x_1 - x_2)^{\mu_1} \dots (x_1 - x_2)^{\mu_N}}{N!} \phi \partial_{\mu_1, \dots, \mu_N} \phi(x_2), \tag{2.36}$$

where  $\frac{\lambda}{|x_1 - x_2|^2} = \mathcal{C}_{AB}^C$  and for  $\mathcal{O}_A = \mathcal{O}_B = \phi$  then  $\mathcal{O}_C = 1$ .

## 2.6 Effective Field theories

The processes which take place at energies below the heavy quark masses, charm ( $m_c = 1.4$  GeV), bottom ( $m_b = 4.8$  GeV), and top ( $m_t = 175$  GeV), it is viable to obtain an effective theory by integrating out these heavy degrees of freedom from the Lagrangian of the theory. The flavor changing weak interactions are ruled by the electroweak scale fixed at  $m_W = 80$  GeV. However, the strong interactions that control the underlying forces of final hadronic states occur at the scale  $\Lambda_{QCD} = 0.2$  GeV (non-perturbative QCD), whereas  $b$ -quark mass describes an intermediate



state which lies in between the weak and QCD scales. Due to the involvement of multiple scale dynamics, it is complicated to calculate decay amplitude using the full theory Lagrangian because of the presence of large logarithms  $\ln(m_W/\Lambda_{QCD})$  and hence the perturbation theory collapses. Effective field theory is a good technique for this type of problems. It involves OPE where weak interactions are treated as point-like as from the standpoint of hadronic scales  $\Lambda_{QCD}$  and  $m_b$ . The FCNC interactions are then incorporated in dimension-six operators (comprising of gluons, photons, quarks excluding top quark and leptons) of the theory through the WCs. It is viable to evaluate QCD corrections to weak processes via a perturbative approach. It is supposed that new fields added in the theory will be heavier than the mass of  $b$ -quark and the NP can enter the theory by introducing new operators as well as by the modification of the WCs.

The effective theory is obtained by adopting the following steps:

- Select a cutoff scale  $\Lambda$  and split the field  $\phi$  in high and low energy components  $\phi_H$  and  $\phi_L$ , respectively; i.e.,  $\phi = \phi_H + \phi_L$ . Low energy mode  $\phi_L$  can be written as [182]

$$\langle 0|T(\phi_L(x_1)\dots\phi_L(x_n))|0\rangle = \frac{1}{Z[0]} \left(-\frac{i\delta}{\delta j_L(x_1)}\right) \dots \left(-\frac{i\delta}{\delta j_L(x_n)}\right) Z[j_L]|_{j_L=0}, \quad (2.37)$$

with the generating functional

$$Z[j_L] = \int \mathcal{D}\phi_L \mathcal{D}\phi_H e^{i\int d^d x \mathcal{L}(x) + i\int d^d x j_L(x)\phi_L(x)}. \quad (2.38)$$

- Integrate high energy modes above the scale  $\Lambda$

$$Z[j_L] = \int \mathcal{D}\phi_L \left( \int \mathcal{D}\phi_H e^{i\int d^d x \mathcal{L}(x)} \right) e^{i\int d^d x j_L(x)\phi_L(x)}, \quad (2.39)$$

where  $\int \mathcal{D}\phi_H e^{i\int d^d x \mathcal{L}(x)}$  is called the Wilsonian effective action which is non-local at  $\Delta x^\mu \sim 1/\Lambda$  and is dependent on the selection of cutoff  $\Lambda$ . After integrating on  $\phi_H$ , Eq. (2.39) is independent of fields  $\phi_H$  for which  $E > \Lambda$ .

- Apply OPE on non-local action in low energy regime to expand it in terms of non-local operators comprising of fields for which  $E \ll \Lambda$

$$S_\Lambda(\phi_L) = \int d^d x \mathcal{L}_\Lambda^{eff}(x), \quad (2.40)$$

where

$$\mathcal{L}_\Lambda^{eff}(x) = \sum_i C_i \mathcal{O}_i(\phi_L(x)). \quad (2.41)$$

The above procedure allows us to get the Lagrangian corresponding to a specific scale.

The matrix elements do not involve perturbative QCD whereas the WCs are calculated in perturbation theory at a weak scale  $\mu_0 = m_W$ . The WCs are evaluated using Feynman diagrams of Fig. (2.3) and then matching the computed results onto the effective theory. The matched

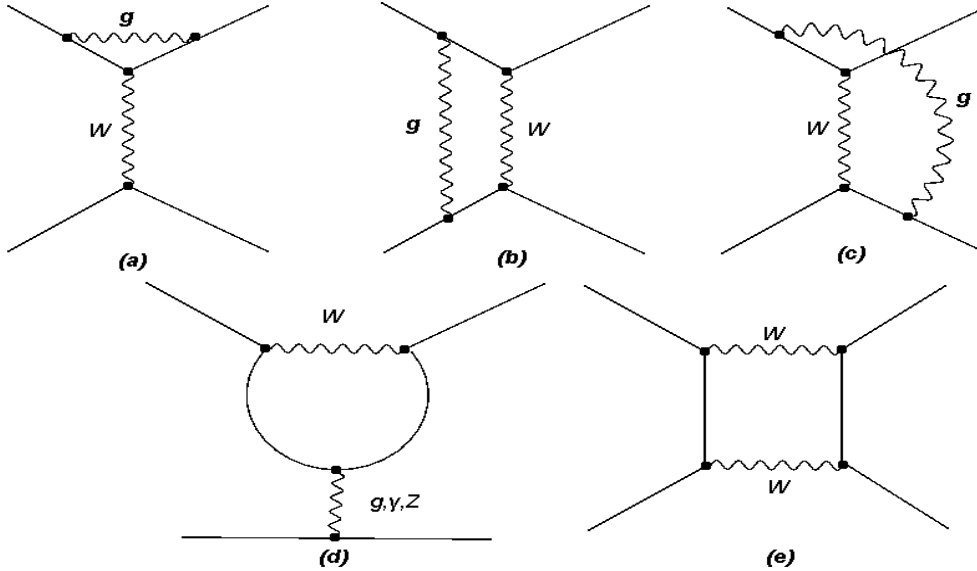


Figure 2.3: The quark level transition Feynman diagrams in full theory.

calculation fixes the initial conditions at high scale  $\sim \mu_{W,t}$ . The RGE

$$\frac{d}{d \ln \mu} C_i(\mu) = \gamma_{ji}(\mu) C_j(\mu) \quad (2.42)$$

is solved which defines the mixing of operators and the evolution at a low scale. In Eq. (2.42) anomalous dimension matrix is defined as

$$\gamma_{ji}(\mu) = Z_{ik}^{-1} \frac{dZ_{kj}}{d \ln \mu}. \quad (2.43)$$

It can expand in terms of powers of strong coupling  $\alpha_s(\mu)$ . The initial conditions are known at next-to-leading order (NLO) for electroweak interaction and next-to-next-to-leading order (NNLO) for the QCD for all the WCs.

To solve Eq. (2.42), one can follow the similar procedure used in Sect. 2.4. It seems straightforward to leading order accuracy but quite cumbersome when one goes beyond leading order as perturbation expansion for  $\gamma_{ij}$  gives

$$\gamma_{ij} = \gamma_{ij}^{(0)} \frac{\alpha_s}{4\pi} + \gamma_{ij}^{(1)} \left(\frac{\alpha_s}{4\pi}\right)^2 + \mathcal{O}(\alpha_s^3), \quad (2.44)$$

where  $\gamma_{ij}^{(0)}$  does not commute with  $\gamma_{ij}^{(1)}$ . Therefore, in order to solve Eq. (2.42) we define an evolution operator such that

$$C_i(\mu) = U_{ij}(\mu, \mu_0) C_j(\mu_0) \quad (2.45)$$

and at the leading order (LO) one can write

$$U^{(0)}(\mu, \mu_0) = \left[ \frac{\alpha(\mu)}{\alpha(\mu_0)} \right]^{-\frac{\gamma^{(0)T}}{2\beta_0}} = V \left( \left[ \frac{\alpha(\mu_0)}{\alpha(\mu)} \right]^{\frac{\gamma^{(0)}}{2\beta_0}} \right)_D V^{-1}, \quad (2.46)$$

where  $V$  diagonalizes the matrix  $\gamma^{(0)T}$  (matrix comprising of eigenvalues of  $\gamma^{(0)}$ ) such that  $\gamma_D^{(0)} = V^{-1}\gamma^{(0)T}V$ . To obtain the solution at the NLO

$$U(\mu, \mu_0) = \left[ 1 + \frac{\alpha_s(\mu)}{4\pi} J \right] U^{(0)}(\mu, \mu_0) \left[ 1 + \frac{\alpha_s(\mu_0)}{4\pi} J \right], \quad (2.47)$$

and if  $J = VHV^{-1}$  then Eq. (2.47) promises the solution of Eq. (2.43). The elements of matrix  $H$  can be written as

$$H_{ij} = \delta_{ij}\gamma_i^{(0)} \frac{\beta_1}{2\beta_0} - \frac{G_{ij}}{2\beta_0 + \gamma_i^{(0)} - \gamma_j^{(0)}}, \quad (2.48)$$

with the property that  $G = V^{-1}\gamma^{(1)T}V$ .

The WCs  $C_{7,8}^{eff}$  are generally used instead of  $C_{7,8}$  that include not only  $C_{7,8}$  but also the contribution of  $C_1$  to  $C_6$  and these can be expressed as

$$C_7^{eff}(\mu) = C_7(\mu) + \sum_{i=1}^6 y_i C_i(\mu), \quad C_8^{eff}(\mu) = C_8(\mu) + \sum_{i=1}^6 z_i C_i(\mu). \quad (2.49)$$

In the NDR scheme  $y = (0, 0, -1/3, -4/9, -20/3, -8/9)$  and  $z = (0, 0, 1, -1/6, 20, -10/3)$  [43]. At the LO,  $C_{7,8}^{eff}$  depend on regularization scheme. The effective Hamiltonian in this case will be expressed in the following form

$$\mathcal{H}_{eff}(b \rightarrow s) = \frac{4G_F}{\sqrt{2}} \left( \lambda_{us} \sum_{i=1}^2 C_i \mathcal{O}_i^u + \lambda_{cs} \sum_{i=1}^2 C_i \mathcal{O}_i^c - \lambda_{ts} \sum_{i=8}^{10} C_i \mathcal{O}_i + h.c \right). \quad (2.50)$$

Here  $\lambda_{qs} = V_{qb}V_{qs}^*$  and the quark operators are defined as,

$$\begin{aligned} \mathcal{O}_1 &= (\bar{s}_L \gamma_\mu T^a q_L)(\bar{q}_L \gamma^\mu T^a b_L), & \mathcal{O}_2 &= (\bar{s}_L \gamma_\mu q_L)(\bar{q}_L \gamma^\mu b_L), \\ \mathcal{O}_3 &= (\bar{s}_L \gamma_\mu b_L) \sum_q (\bar{q} \gamma^\mu q), & \mathcal{O}_4 &= (\bar{s}_L \gamma_\mu T^a b_L) \sum_q (\bar{q} \gamma^\mu T^a q), \\ \mathcal{O}_5 &= (\bar{s}_L \gamma_\mu \gamma_\nu \gamma_\sigma b_L) \sum_q (\bar{q} \gamma^\mu \gamma^\nu \gamma^\sigma q), & \mathcal{O}_6 &= (\bar{s}_L \gamma_\mu \gamma_\nu \gamma_\sigma T^a b_L) \sum_q (\bar{q} \gamma^\mu \gamma^\nu \gamma^\sigma T^a q), \\ \mathcal{O}_7 &= \frac{e}{16\pi^2} m_b (\bar{s}_L \sigma^{\mu\nu} b_R) F_{\mu\nu}, & \mathcal{O}_8 &= \frac{g_s}{16\pi^2} m_b (\bar{s}_L \sigma^{\mu\nu} T^a b_R) G_{\mu\nu}^a, \\ \mathcal{O}_9 &= \frac{e^2}{16\pi^2} (\bar{s}_L \gamma^\mu b_L) \sum_\ell (\bar{\ell} \gamma_\mu \ell), & \mathcal{O}_{10} &= \frac{e^2}{16\pi^2} (\bar{s}_L \gamma^\mu b_L) \sum_\ell (\bar{\ell} \gamma_\mu \gamma_5 \ell). \end{aligned} \quad (2.51)$$

In Eq. (2.51),  $\mathcal{O}_1$  and  $\mathcal{O}_2$  are the current-current operators,  $\mathcal{O}_{3-6}$  are QCD penguin operators,  $\mathcal{O}_7$  is the EM dipole operator,  $\mathcal{O}_8$  is a chromomagnetic dipole operator,  $\mathcal{O}_9$  and  $\mathcal{O}_{10}$  are semileptonic operators and the light quarks are denoted by  $q$ . The letters  $L$  and  $R$  denote left and right-handed chiralities of the fermions. Some of the above operators get significant contributions from renormalisation group mixing with  $\mathcal{O}_2$  generated at tree level and this decrease the NP effects. Hence it is considered sufficient to modify dipole and semileptonic operators in most of the NP

scenarios. The chirality flipped counterparts of these SM operators are

$$\begin{aligned}\mathcal{O}'_7 &= \frac{e}{16\pi^2} m_b (\bar{s}_R \sigma^{\mu\nu} b_L) F_{\mu\nu}, & \mathcal{O}'_8 &= \frac{g_s}{16\pi^2} m_b (\bar{s}_R \sigma^{\mu\nu} T^a b_L) G_{\mu\nu}^a, \\ \mathcal{O}'_9 &= \frac{e^2}{16\pi^2} (\bar{s}_R \gamma^\mu b_R) (\bar{\ell} \gamma_\mu \ell), & \mathcal{O}'_{10} &= \frac{e^2}{16\pi^2} (\bar{s}_R \gamma^\mu b_R) (\bar{\ell} \gamma_\mu \gamma_5 \ell).\end{aligned}$$

The semileptonic unprimed and primed operators with different lepton flavors are

$$\mathcal{O}_9^{(\prime)} = \frac{e^2}{16\pi^2} (\bar{s}_{L,R} \gamma^\mu b_{L,R}) (\bar{\ell}_1 \gamma_\mu \ell_2), \quad \mathcal{O}_{10}^{(\prime)} = \frac{e^2}{16\pi^2} (\bar{s}_{L,R} \gamma^\mu b_{L,R}) (\bar{\ell}_1 \gamma_\mu \gamma_5 \ell_2).$$

The corresponding WCs of four-quark operators hold some symmetry relations such as Minimal flavor violation (MFV) of quarks give  $(C_i)_d = (C_i)_s$  and  $C'_i \approx 0$ . LFU gives  $(C'_i)_q^e = (C'_i)_q^\mu = (C'_i)_q^\tau$  and lepton flavor conservation gives  $(C'_k)_q^{\ell_1 \ell_2}$ . The unitarity of CKM matrix leads to  $\lambda_{us} + \lambda_{cs} + \lambda_{ts} = 0$  which further implies that  $\lambda_{cs,ts} \sim \lambda^2 \gg \lambda_{us} \sim \lambda^4$ . Its consequence is that current-current operators  $\mathcal{O}_1^u$  and  $\mathcal{O}_2^u$  can be neglected and also  $\lambda_{ts} \sim -\lambda_{cs}$  can be predicted which leads to small CP asymmetries in the SM. Including the electroweak corrections, the generalized effective Hamiltonian can be written as

$$\mathcal{H}_{eff} = \frac{G_F}{\sqrt{2}} \sum V_{CKM}^i C_i(\mu) \mathcal{O}_i(\mu) \quad (2.52)$$

where  $V_{CKM}^i$  are the elements of CKM matrix. Decay amplitude for hadron  $H$  is

$$\mathcal{A}(H_i \rightarrow X) = \langle X | \mathcal{H}_{eff} | H_i \rangle = \frac{G_F}{\sqrt{2}} \sum V_{CKM}^i C_i(\mu) \langle X | \mathcal{O}_i(\mu) | H_i \rangle \quad (2.53)$$

where  $X$  is the possible final state and  $C_i(\mu)$  and  $\mathcal{O}_i(\mu)$  are the functions of  $M_W$ , coupling constant  $\alpha_s$  and renormalization scale  $\mu$ . One can get the WCs by matching the results of full theory with an effective theory.

## 2.7 $b$ -hadrons

The bottom quark is lighter among the third generation of quarks and is a weak doublet partner of the top quark. The bottom and top quarks were proposed by Kobayashi and Maskawa in 1973 [41] and their existence was confirmed in 1977 by the production of  $b\bar{b}$  state [183]. The mesons containing a  $b$ -quark with light quarks are  $\bar{b}u$ ,  $\bar{b}d$ ,  $\bar{b}s$  and  $\bar{b}c$  which are called  $B^+$ ,  $B^0$ ,  $B_s^0$  and  $B_c^+$ , respectively. The last one is the heaviest of all bound states and is hard to produce. In 1998, the CDF collaboration has produced it for the very first time [184] and from the decay  $B_c^+ \rightarrow J/\psi \pi^+$  its mass was determined by the CDF collaboration in 2006 [185]. However, the most accurate determination of its mass  $m_{B_c^+} = 6274.28 \pm 1.40 \pm 0.32 \text{ MeV}/c^2$  is made by LHCb through the decay  $B_c^+ \rightarrow J/\psi D^0 K^+$  [186]. One of the  $b$ -quark bound state among baryons is  $\Lambda_b$  which consists of  $udb$  is of prime importance.

The FCNC decays governed by  $b \rightarrow s \ell^+ \ell^-$  are studied as a function of dilepton mass squared  $s$ . In measurements, the regions  $J/\psi$  and  $\psi(2S)$  are usually not included due to dominance of  $b \rightarrow c$  transitions. Hence the most reliable measurements are at low and high  $s$  regions and in these regions, one can compare the experimental measurements with the theoretical predictions.

High energy  $pp$  collisions at the LHC and  $p\bar{p}$  collisions at the Tevatron produce all kinds of  $b$ -hadrons. Tevatron produces cross-section of  $30 \mu\text{b}$  for  $(p\bar{p} \rightarrow bX)$  with pseudorapidity  $\eta < 1$  at  $\sqrt{s} = 1.96 \text{ TeV}$  whereas LHCb produce about  $72 \mu\text{b}$  at  $7 \text{ TeV}$  and about  $144 \mu\text{b}$  at  $13 \text{ TeV}$  with pseudorapidity  $2 < \eta < 5$ . Among the weak decays of  $b$ -hadrons, the dominant decay process is  $b \rightarrow cW^{*+}$  as  $b \rightarrow u$  decay is suppressed by a factor of  $|V_{ub}|/|V_{us}| \sim (0.1)^2$  as compared to the decay  $b \rightarrow c$ . Due to color suppression, the decay modes in which the spectator quark combines with the one quark from virtual  $W$  boson to form bound hadronic state are suppressed by a factor of  $(1/3)^2$  because color of both quarks has to be the same. Decay mode  $B \rightarrow X_c \ell \nu$  is a good way to measure the CKM matrix element  $V_{cb}$  and  $B \rightarrow X_u \ell \nu$  for  $V_{ub}$  as final state with two leptons make the study of strong interactions much easier.

Both inclusive and exclusive analysis can be used for this purpose but both are accompanied by uncertainties. Inclusive analysis includes uncertainties that belong to extrapolation of restricted phase-space to full phase-space whereas exclusive decays have uncertainties belonging to hadronic FFs. For inclusive analysis, differential decay rates of all the  $B$ -meson decays governed by the transition  $b \rightarrow u\ell\nu$  give  $|V_{ub}| = (4.41 \pm 0.15_{-0.17}^{+0.15}) \times 10^{-3}$  where the uncertainties correspond to both the experimental measurements and the theoretical calculations [187]. The analysis of exclusive decays is comparatively simple from experimental point of view in which the branching fraction of a particular decay is used to calculate the CKM matrix element under consideration by using FFs calculated in LQCD or QCD sum rules (QCDSR) approach. The world average of this analysis gives  $|V_{ub}| = (3.28 \pm 0.29) \times 10^{-3}$  which is the average obtained from semileptonic  $B$  decays [188]. An unexpected result was obtained in 2015 when LHCb measured CKM matrix element  $V_{ub}$  by the ratio [189]

$$\frac{|V_{ub}|^2}{|V_{cb}|^2} = \frac{\mathcal{B}r(\Lambda_b^0 \rightarrow p\mu^-\bar{\nu}_\mu)}{\mathcal{B}r(\Lambda_b^0 \rightarrow \Lambda_c^+\mu^-\bar{\nu}_\mu)} R_{FF},$$

where  $R_{FF}$  is the ratio of relevant FFs calculated using LQCD approach. Using  $R_{FF} = 0.68 \pm 0.07$  the above ratio comes out to be  $0.083 \pm 0.004 \pm 0.004$  where the first uncertainty is experimental and the second belongs to LQCD predictions. By using the world average for  $|V_{cb}| = (39.5 \pm 0.8) \times 10^{-3}$ ,  $|V_{ub}|$  is  $(3.27 \pm 0.15 \pm 0.16 \pm 0.06) \times 10^{-3}$  where third uncertainty belongs to  $V_{cb}$  normalization. According to world average presented in [189]

$$V_{cs} = 0.9746 \pm 0.0026, \quad V_{cd} = 0.2140 \pm 0.0097, \quad (2.54)$$

which are compatible with unitary of CKM matrix.

## 2.8 Flavor Physics and $B$ Factories

As we know that in the SM, fermions come in three generations and the study of interactions that distinguish between their generations is the flavor physics. Fermions interact in two ways: when two fermions couple with a scalar, Yukawa interaction occurs and when they couple with the gauge boson, gauge interactions take place. No gauge coupling is present between interaction eigenstates of dissimilar generations and every type of gauge coupling is defined by a single coupling constant. Hence gauge interactions are diagonal and universal when considered on an interaction

basis. But Yukawa couplings include the interaction between different fermion generations and their interaction eigenstates do not have definite masses. However, in a mass eigenstate basis, the Yukawa interactions are diagonal but non-universal and then have definite masses.

Flavor physics, in quark and lepton sectors, is important in the sense that it has the potential to predict the NP before the direct observation through experiments. In the past, some of its predictions were successful [190], such as

- Small ratio of decay width of  $K_L \rightarrow \mu^+\mu^-$  to  $K^+ \rightarrow \mu^+\nu$  predicted charm quark.
- The third generation was predicted by CP violation in the neutral kaon mixing.
- Masses of charm and top quark were successfully predicted by the size of  $\Delta m_K = m_{K_L} - m_{K_S}$  and  $\Delta m_B = m_{B_H^0} - m_{B_L^0}$ , respectively.
- Measurement of flavor transition of neutrino leads towards massive neutrinos.

The very well studied and measured process is the rare  $B_s \rightarrow \mu^+\mu^-, \tau^+\tau^-$ . It is called the rare process because it is not allowed at the tree level in the SM and is produced by the GIM mechanism [40] at the loop level. Such processes are further suppressed by CKM matrix elements whose off-diagonal entries are very small. Further, these leptonic decays with muon and electrons in the final states are also helicity suppressed as two spin-1/2 leptons emitted from a pseudoscalar  $B$ -meson. Some SM predictions of  $B$  decays are

$$\begin{aligned} \mathcal{B}(\bar{B}_s \rightarrow \ell^+\ell^-) &= (8.34 \pm 0.36) \times 10^{-14}, & \mathcal{B}(B^0 \rightarrow \ell^+\ell^-) &= (2.63 \pm 0.32) \times 10^{-15}, \\ \mathcal{B}(\bar{B}_s \rightarrow \mu^+\mu^-) &= (3.52 \pm 0.15) \times 10^{-9}, & \mathcal{B}(B^0 \rightarrow \mu^+\mu^-) &= (1.12 \pm 0.12) \times 10^{-10}, \\ \mathcal{B}(\bar{B}_s \rightarrow \tau^+\tau^-) &= (7.46 \pm 0.30) \times 10^{-7}, & \mathcal{B}(B^0 \rightarrow \tau^+\tau^-) &= (2.35 \pm 0.24) \times 10^{-8}. \end{aligned}$$

During the Run 1 of LHC, the combined results of CMS and LHCb datasets performed in 2014 comes out to be [191]

$$\begin{aligned} \bar{\mathcal{B}}(B_s \rightarrow \mu^+\mu^-) &= (2.8_{-0.6}^{+0.7}) \times 10^{-9} \\ \mathcal{B}(B^0 \rightarrow \mu^+\mu^-) &= (3.9_{-1.4}^{+1.6}) \times 10^{-10} \end{aligned}$$

Since weak and Higgs mediated processes are strongly suppressed in the SM, the FCNCs can take place at higher levels only in electroweak interactions, thus they are good candidates to search for the NP.

At experimental side, the initiative was taken by the CLEO experiment in 1994 which studied the rare radiate decay process  $b \rightarrow s\gamma$  [192]. Later, BaBar and Belle collected a dataset of 467M and 772M  $B^0\bar{B}^0$  pairs in 2008 and 2010, respectively and their combined dataset produced an integrated luminosity of  $1ab^{-1}$  operating at  $\Gamma(4S)$ . At the most efficient  $B$  factory, Large Hadron Collider (LHC),  $b\bar{b}$  cross-section is about  $300\mu b$  at center of mass energy  $\sqrt{s} = 7$  TeV [193] and  $500\mu b$  at  $\sqrt{s} = 14$  TeV. This provides about  $10^{11}$  hadrons produced in a dataset of  $1fb^{-1}$ . At LHC, the experiments contributing to rare  $b$ -hadron decays are the ATLAS, CMS and the LHCb from which the last one is dedicated for production and decays of  $b$ -hadrons. The CMS and ATLAS experiments are able to produce dimuon pair in the final state whereas LHCb can generate photon, dielectron pair and only hadrons as final states. In semileptonic decays, initially  $B$  factories used

to average over neutral and charged  $B$ -mesons and also between  $\mu^+\mu^-$  and  $\ell^+\ell^-$  final states. The LHCb, CMS, ATLAS and CDF experiments measure the decays with  $\mu^+\mu^-$  final states mostly instead of  $\ell^+\ell^-$  final states. In last two decades, the processes  $B \rightarrow K^*(892)^0\ell^+\ell^-$  and  $B^0 \rightarrow K^+\ell^+\ell^-$  have been widely studied. The CDF and LHCb also observed other  $b$ -hadron decays such as  $\Lambda_b^0 \rightarrow \Lambda\mu^+\mu^-$  [47, 50],  $\Lambda_b^0 \rightarrow pK^-\mu^+\mu^-$  [51] and  $B_s^0 \rightarrow \phi\mu^+\mu^-$  [18, 19]. The measured branching fractions of some commonly studied  $b$ -hadron decays are [16, 194]:

$$\begin{aligned}
\mathcal{B}(B^+ \rightarrow K^+\ell^+\ell^-) &= (5.5 \pm 0.7) \times 10^{-7}, \\
\mathcal{B}(B^+ \rightarrow K^+\mu^+\mu^-) &= (4.43 \pm 0.24) \times 10^{-7}, \\
\mathcal{B}(B^0 \rightarrow K^*(892)^0\ell^+\ell^-) &= (1.03_{-0.17}^{+0.19}) \times 10^{-6}, \\
\mathcal{B}(B^0 \rightarrow K^*(892)^0\mu^+\mu^-) &= (1.03 \pm 0.06) \times 10^{-6}, \\
\mathcal{B}(B_s^0 \rightarrow \phi\mu^+\mu^-) &= (8.3 \pm 1.2) \times 10^{-7}, \\
\mathcal{B}(\Lambda_b^0 \rightarrow \Lambda\mu^+\mu^-) &= (1.08 \pm 0.28) \times 10^{-6}.
\end{aligned}$$

Compared to the leptonic and radiative decays of  $B$ -meson the semileptonic one are quite rich in phenomenology. In the next section we will discuss  $B \rightarrow K^*(\rightarrow K\pi)\ell^+\ell^-$  in detail both from the theoretical and experimental point of view.

## 2.9 Physical Observables in $B \rightarrow K^*(\rightarrow K\pi)\mu^+\mu^-$

A lot of information can be extracted from observables constructed from the angular distribution of the hadron decays. Although a renormalization scale  $\mu_b$  is used in the calculations but its dependence cancels between WCs and matrix elements to give the physical observables free from this scale. For this purpose, not only regularization and renormalization schemes should be the same for calculation of WCs and matrix elements but also the evanescent operators that are present at  $D \neq 4$  but die out at  $D = 4$ . Among hadron decays the four body decays are phenomenologically very rich as there are many physical observables extracted from the transversity amplitude and angular coefficients. A large number of angular observables have been studied theoretically for the decay  $B \rightarrow K^*(\rightarrow K\pi)\ell^+\ell^-$  and some of them have been measured experimentally too. The goal of the present dissertation is to work out the analogues observables for  $\Lambda_b \rightarrow \Lambda(\rightarrow p\pi)\ell^+\ell^-$  by following the same lines as both decays are governed by FCNC  $b \rightarrow s\ell^+\ell^-$  transition. Therefore, it will be useful to discuss some physical observables for  $B \rightarrow K^*(\rightarrow K\pi)\ell^+\ell^-$  and then apply a similar procedure to obtain some of them for  $\Lambda_b$  decay in later chapters for the SM and some NP scenarios.

### 2.9.1 Decay Rate

The most important observable which is measured at  $B$  factories for different decay modes of  $b \rightarrow s$  quark level transition is the branching ratio. However, it is difficult to handle theoretically in exclusive analysis due to two reasons; first is the dominance of hadronic uncertainties which are confronted in calculating the FFs and the second is that every FF is integrated over the full spectrum of  $q^2 = s$  namely  $4m_\ell^2 < s < (m_{H_1} - m_{H_2})^2$ , where  $H_1$  and  $H_2$  stands for the parent and the daughter hadrons, respectively. No single method used to calculate the FFs is best working for

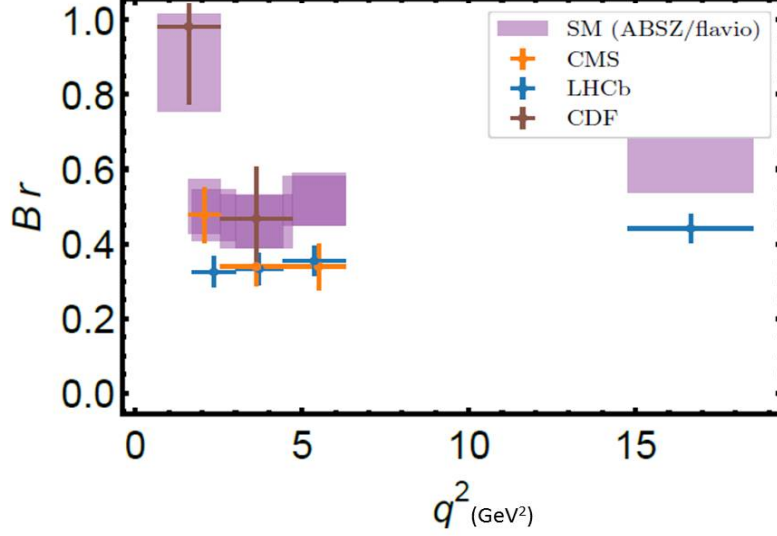


Figure 2.4: The SM predictions vs experimental measurements of branching ratio for  $B \rightarrow K^* \mu^+ \mu^-$  [137].

the full kinematic range and hence partial decay rates integrated over appropriate bins are obtained. It is also required to prevent our calculations from the effects that arise due to  $c\bar{c}$  resonances when dilepton invariant mass squared  $s$  approaches to mass of  $J/\psi$  ( $s = M_{J/\psi}^2 \sim 9.6 GeV^2$ ) and its radial excitations. Hence the theoretical studies are restricted at low and high  $s$  regions to avoid charmonium resonances. The charmless resonances such as  $\rho, \omega$  and their radial excitations can also interrupt but the corresponding effects are very small due to the CKM suppression.

In mesonic decays, the most vastly studied four-body process is  $B \rightarrow K^*(\rightarrow K\pi)\ell^+\ell^-$  with decay rate [195, 196]

$$\begin{aligned}
\frac{d^4\Gamma}{dsd\cos\theta_\ell d\cos\theta^* d\xi} &= \frac{9}{32\pi} \left[ I_{1s} \sin^2\theta^* + I_{1c} \cos^2\theta^* + (I_{2s} \sin^2\theta^* + I_{2c} \cos^2\theta^*) \cos 2\theta_\ell \right. \\
&+ I_3 \sin^2\theta^* \sin^2\theta_\ell \cos 2\xi + I_4 \sin 2\theta^* \sin 2\theta_\ell \cos \xi + I_5 \sin 2\theta^* \sin \theta_\ell \cos \xi \\
&+ (I_{6s} \sin^2\theta^* + I_{6c} \cos^2\theta^*) \cos \theta_\ell + I_7 \sin 2\theta^* \sin \theta_\ell \sin \xi \\
&\left. + I_8 \sin 2\theta^* \sin 2\theta_\ell \sin \xi + I_9 \sin^2\theta^* \sin^2\theta_\ell \sin 2\xi \right]. \tag{2.55}
\end{aligned}$$

where  $I_i$ 's are angular coefficients,  $\theta^*$  is the angle of  $K$  in the CM system of  $K$  and  $\pi$  with respect to direction of flight of  $(K, \pi)$  in  $B$  rest frame,  $\theta_\ell$  is the angle of  $\ell^+$  in the CM system of  $\ell^+$  and  $\ell^-$  with respect to direction of flight of  $(\ell^+, \ell^-)$  in  $B$  rest frame and  $\xi$  is the azimuthal angle between the decaying planes of  $K\pi$  and  $\ell^+\ell^-$ . After integrating Eq. (2.55) over the angles, the measured values and the SM predictions of the branching ratio for this decay are presented in Fig. 2.4. We can see that in the high  $s$  region the measured value of the branching ratio deviates significantly



from the SM predictions. Angular coefficients of Eq. (2.55) are defined as [196]:

$$\begin{aligned}
I_{1s} &= \frac{2+v^2}{4} \left[ |A_{\perp}^L|^2 + |A_{\parallel}^L|^2 + (L \rightarrow R) \right] + \frac{4m_{\ell}^2}{s} \text{Re} \left( A_{\perp}^L + A_{\perp}^{R*} + A_{\parallel}^L + A_{\parallel}^{R*} \right), \\
I_{1c} &= |A_0^L|^2 + |A_0^R|^2 + \frac{4m_{\ell}^2}{s} \left[ |A_t|^2 + 2\text{Re}(A_0^L + A_0^{R*}) \right], \\
I^{2s} &= \frac{v^2}{4} \left[ |A_{\perp}^L|^2 + |A_{\parallel}^L|^2 + (L \rightarrow R) \right], \\
I^{2c} &= -v^2 \left[ |A_0^L|^2 + (L \rightarrow R) \right], \\
I_3 &= \frac{v^2}{2} \left[ |A_{\perp}^L|^2 - |A_{\parallel}^L|^2 + (L \rightarrow R) \right], \\
I_4 &= \frac{v^2}{\sqrt{2}} \left[ \text{Re}(A_0^L A_{\parallel}^{L*} + (L \rightarrow R)) \right], \\
I_5 &= \sqrt{2}v \left[ \text{Re}(A_0^L A_{\perp}^{L*} - (L \rightarrow R)) \right], \\
I_6 &= 2v \left[ \text{Re}(A_{\parallel}^L A_{\perp}^{L*}) - (L \rightarrow R) \right], \\
I_7 &= \sqrt{2}v \left[ \text{Im}(A_0^L A_{\parallel}^{L*}) - (L \rightarrow R) \right], \\
I_8 &= \frac{v^2}{\sqrt{2}} \left[ \text{Im}(A_0^L A_{\perp}^{L*}) + (L \rightarrow R) \right], \\
I_9 &= v^2 \left[ \text{Im}(A_{\parallel}^L A_{\perp}^{L*}) + (L \rightarrow R) \right]
\end{aligned} \tag{2.56}$$

where

$$\begin{aligned}
A_{\perp}^{L,R} &= 4\mathcal{N}\sqrt{2}M_B|\mathbf{P}_2| \left[ (C_9^{eff} \mp C_{10}) \frac{V(s)}{M_B + M_{K^*}} + \frac{2m_b C_7^{eff}}{s} T_1(s) \right], \\
A_{\parallel}^{L,R} &= -\mathcal{N}\sqrt{2}(M_B^2 - M_{K^*}^2) \left[ (C_9^{eff} \mp C_{10}) \frac{A_1(s)}{M_B - M_{K^*}} - 2C_7^{eff} \frac{m_b}{s} T_2(s) \right], \\
A_0^{L,R} &= -\mathcal{N} \frac{(C_9^{eff} \mp C_{10})}{2M_{K^*}\sqrt{s}} \left[ (M_B^2 - M_{K^*}^2 - s)(M_B + M_{K^*})A_1(s) - \frac{4M_B^2|\mathbf{P}_2|^2 V_2(s)}{(M_B + M_{K^*})} \right], \\
&\quad + \mathcal{N} \frac{2m_b C_7^{eff}}{2M_{K^*}\sqrt{s}} \left[ -(M_B^2 + 3M_{K^*}^2 - s)T_2(s) + \frac{4M_B^2|\mathbf{P}_2|^2}{(M_B^2 - M_{K^*}^2)} T_3(s) \right], \\
A_t &= \mathcal{N} \frac{|\mathbf{P}_2| M_B C_{10}}{\sqrt{s}} A_0(s)
\end{aligned} \tag{2.57}$$

and

$$\begin{aligned}
\mathcal{N} &= V_{tb}V_{ts}^* \left( \frac{G_F^2 \alpha^2 |\mathbf{P}_2| s v}{(2\pi)^5 24M_B^2} \right)^{1/2}, \\
v &= \sqrt{1 - \frac{4m_{\ell}^2}{s}}
\end{aligned}$$

$V_{ij}$  is CKM matrix element,  $G_F$  is Fermi coupling constant,  $\alpha$  is EM coupling constant and  $\mathbf{P}_2$  is

the momentum of  $K^*$  meson defined as

$$|\mathbf{P}_2| = \frac{\sqrt{M_B^4 + M_{K^*}^4 + s^2 - 2(M_B^2 M_{K^*}^2 + M_B^2 s + M_{K^*}^2 s)}}{2M_B}.$$

We know that a good physical observable is the one which is theoretically clean; i.e., free from the hadronic uncertainties and hence making it to be a good candidate to hunt for the NP. According to this definition, the decay rate may not be a good observable therefore, one can search for other observables which are the ratios of angular coefficients. In this way, the uncertainties arising due to the hadronic FFs cancel out to a good approximation in these observables, and below we discuss some of them.

### 2.9.2 Transverse asymmetries

The transverse asymmetry  $F_T(s)$  for  $B \rightarrow K^*(\rightarrow K\pi)\mu^+\mu^-$  decay reads as [24]

$$F_T(s) = v^2 \frac{|A_\perp(s)|^2 + |A_\parallel(s)|^2}{d\Gamma/ds}, \quad (2.58)$$

where  $|A_{\perp,\parallel}(s)|^2 = |A_{\perp,\parallel}^L(s)|^2 + |A_{\perp,\parallel}^R(s)|^2$  with

$$\begin{aligned} A_\perp^{L,R} &= N\sqrt{2\lambda} \left[ \left( C_9^{eff} \mp C_{10} \right) \frac{V(s)}{m_B + m_{K^*}} + \frac{2m_b}{s} C_{7eff} T_1(s) \right], \\ A_\parallel^{L,R} &= N\sqrt{2}(m_B^2 - m_{K^*}^2) \left[ \left( C_9^{eff} \mp C_{10} \right) \frac{A_1(s)}{m_B - m_{K^*}} + \frac{2m_b}{s} C_7^{eff} T_2(s) \right]. \end{aligned} \quad (2.59)$$

The  $CP$  conserving transverse asymmetry  $A_T^{(2)}(s)$  is given as:

$$A_T^{(2)}(s) = \frac{|A_\perp(s)|^2 - |A_\parallel(s)|^2}{|A_\perp(s)|^2 + |A_\parallel(s)|^2}. \quad (2.60)$$

This asymmetry satisfies the above conditions of a good observable as it does not include  $A_{0,s,t}$  therefore, easy to handle in the QCD.  $A_T^{(\text{Im})}(s)$  is defined as

$$A_T^{(\text{Im})}(s) = -\frac{2\text{Im}(A_\parallel^L(s)A_\parallel^{L*}(s) + A_\parallel^R(s)A_\parallel^{R*}(s))}{|A_\perp(s)|^2 + |A_\parallel(s)|^2}. \quad (2.61)$$

This observable is important in the context of physics beyond the SM because its value is zero in the SM and if it acquires a non-zero value in the measurements, it will be a clear signature of NP. Its plot against  $s$  can provide information about the origin of the NP phase. One more quantity depending on the similar amplitudes is [197]:

$$A_T^{(5)}(s) = \frac{|A_\parallel^L(s)A_\perp^{R*}(s) + A_\perp^L(s)A_\parallel^{R*}(s)|}{|A_\perp(s)|^2 + |A_\parallel(s)|^2}. \quad (2.62)$$

This observable is independent of  $A_T^{(2)}(s)$  and  $A_T^{(\text{Im})}(s)$ . From  $A_\perp(s)$  and  $A_\parallel(s)$ , only three independent observables can be extracted which are  $A_T^{(2)}(s)$ ,  $A_T^{(\text{Im})}(s)$  and  $A_T^{(5)}(s)$ . It is convenient to

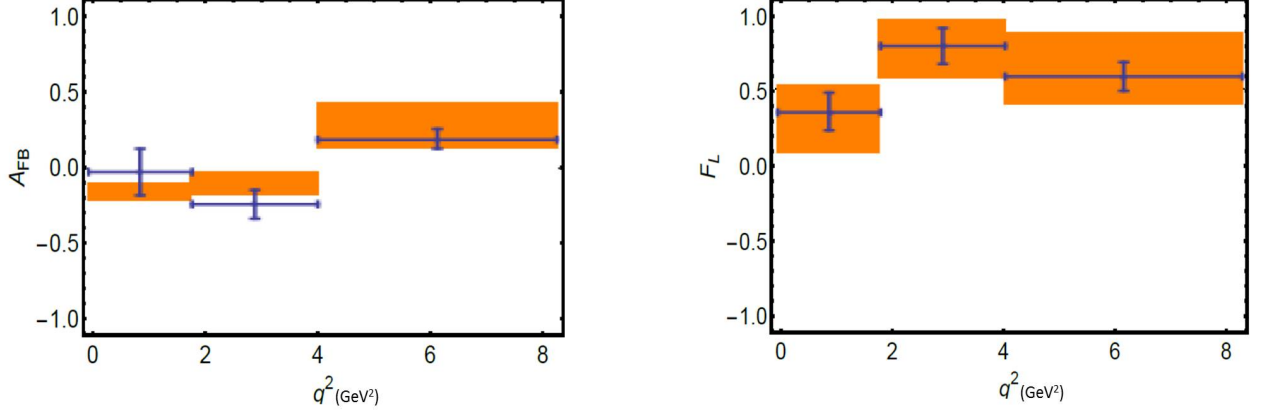


Figure 2.5: The SM predictions and the measured values of  $A_{FB}^\ell$  and  $F_L$  by the LHCb for  $B \rightarrow K^* \mu^+ \mu^-$  decay [198].

introduce one more physical observable

$$A_T^{(\text{Re})}(s) = \frac{2\text{Re}[A_{\parallel}^L(s)A_{\perp}^{L*}(s) - A_{\parallel}^R(s)A_{\perp}^{R*}(s)]}{|A_{\perp}(s)|^2 + |A_{\parallel}(s)|^2} \quad (2.63)$$

such that

$$(A_T^{(2)}(s))^2 + (A_T^{(\text{Im})}(s))^2 + 2(A_T^{(5)}(s))^2 + (A_T^{(\text{Re})}(s))^2 = 1. \quad (2.64)$$

### 2.9.3 Longitudinal polarization fraction

The longitudinal polarization fraction of lepton is obtained by integrating Eq. (2.55) over  $\theta^*$  and  $\xi$  which results

$$F_L = \frac{I_{1c} - (1/3)I_{2c}}{d\Gamma/ds}. \quad (2.65)$$

Knowing this, the transverse polarization fraction can be obtained by using the relation  $F_T + F_L = 1$ . The measured values of  $F_L$  in appropriate bins are presented in Fig. 2.5 for  $B \rightarrow K^* \mu^+ \mu^-$  decay.

### 2.9.4 Forward-Backward Asymmetries

The forward-backward asymmetry with respect to lepton is [199]

$$A_{FB}^\ell(s) = \frac{\int_0^1 d \cos \theta_\ell \frac{d^2\Gamma}{ds d \cos \theta_\ell} - \int_{-1}^0 d \cos \theta_\ell \frac{d^2\Gamma}{ds d \cos \theta_\ell}}{d\Gamma/ds}. \quad (2.66)$$

The experimental measurements for  $A_{FB}^\ell$  for  $B \rightarrow K^* \mu^+ \mu^-$  is shown in Fig. 2.5.

### 2.9.5 The Optimized Observables

It is viable to construct the observables which are ratios of angular coefficient so that the hadronic uncertainties get reduced [200]. Among them the few important asymmetries are given by

$$\begin{aligned}
P_1 &= \frac{|A_{\perp}^L(s)|^2 - |A_{\parallel}^L(s)|^2 + (L \leftrightarrow R)}{|A_{\perp}^L(s)|^2 + |A_{\parallel}^L(s)|^2 + (L \leftrightarrow R)} = \frac{I_3}{2I_{2s}}, \\
P_2 &= \frac{\text{Re}(A_{\perp}^{L*}(s)A_{\parallel}^L(s) - A_{\perp}^R(s)A_{\parallel}^{L*}(s))}{|A_{\perp}^L(s)|^2 + |A_{\parallel}^L(s)|^2 + (L \leftrightarrow R)} = v \frac{I_{6s}}{8I_{2s}}, \\
P_3 &= \frac{\text{Im}(A_{\perp}^{L*}(s)A_{\parallel}^L(s) - A_{\perp}^R(s)A_{\parallel}^{L*}(s))}{|A_{\perp}^L(s)|^2 + |A_{\parallel}^L(s)|^2 + (L \leftrightarrow R)} = v \frac{I_{6s}}{8I_{2s}} = -\frac{I_9}{4I_{2s}}, \\
P_4' &= \frac{\sqrt{2}\text{Re}(A_0^{L*}A_{\parallel}^L + A_0^R A_{\parallel}^{R*})}{(|A_{\perp}^L(s)|^2 + |A_{\parallel}^L(s)|^2 + (L \leftrightarrow R))(|A_0^L|^2 + (L \leftrightarrow R))} = \frac{I_4}{\sqrt{-I_{2c}I_{2s}}}, \\
P_5' &= \frac{\sqrt{2}\text{Re}(A_0^{L*}A_{\perp}^L - A_0^R A_{\perp}^{R*})}{(|A_{\perp}^L(s)|^2 + |A_{\parallel}^L(s)|^2 + (L \leftrightarrow R))(|A_0^L|^2 + (L \leftrightarrow R))} = \frac{v}{2} \frac{I_5}{\sqrt{-I_{2c}I_{2s}}}, \\
P_6' &= \frac{\sqrt{2}\text{Im}(A_0^{L*}A_{\parallel}^L + A_0^R A_{\parallel}^{R*})}{(|A_{\perp}^L(s)|^2 + |A_{\parallel}^L(s)|^2 + (L \leftrightarrow R))(|A_0^L|^2 + (L \leftrightarrow R))} = -\frac{v}{2} \frac{I_7}{\sqrt{-I_{2c}I_{2s}}}. \quad (2.67)
\end{aligned}$$

The expressions of  $A_{\parallel}^{L,R}(s)$ ,  $A_{\perp}^{L,R}(s)$ , and  $A_0^{L,R}$  are defined in Eq. (2.57). The experimentally measured results from LHCb and the SM predictions for above mentioned observables are shown in Fig. 2.6. A worth noted observable is  $P_5'$  [10] that shows deviation from the SM prediction and therefore, a sensitive tool towards the NP scenarios.

### 2.9.6 Asymmetry parameter $\alpha^{(\prime) s}$

From the four-folded angular decay distribution (2.55) the following asymmetry parameters can be extracted [202]:

$$W(\cos^2 \theta^*) = 1 + \alpha_{\theta^*} \cos^2 \theta^*, \quad (2.68)$$

which is obtained by integrating decay distribution over  $\theta_{\ell} \in [0, \pi]$  and  $\xi \in [0, 2\pi]$ . Likewise, by integrating over  $\theta^* \in [0, \pi]$  and  $\xi \in [0, 2\pi]$ , one obtains:

$$W(\cos^2 \theta_{\ell}) = 1 + \alpha_{\theta_{\ell}} \cos^2 \theta_{\ell} + \alpha'_{\theta_{\ell}} \cos \theta. \quad (2.69)$$

Similarly, by integrating over  $\theta^* \in [0, \pi]$  and  $\theta_{\ell} \in [0, \pi]$ , the azimuthal asymmetry parameter  $\beta$  can be defined as:

$$W(\xi) = 1 + \beta \cos 2\xi. \quad (2.70)$$

### 2.9.7 CP symmetries and asymmetries

For the transition  $b \rightarrow s\ell^+\ell^-$ , the relevant CKM matrix element is  $V_{tb}V_{ts}^*$  which is real under the Wolfenstein's parametrization in the SM and therefore, the non-zero CP asymmetries will be a clear signature of the NP. The CP asymmetries arise due to complex CKM matrix element  $V_{ub}V_{us}^*$

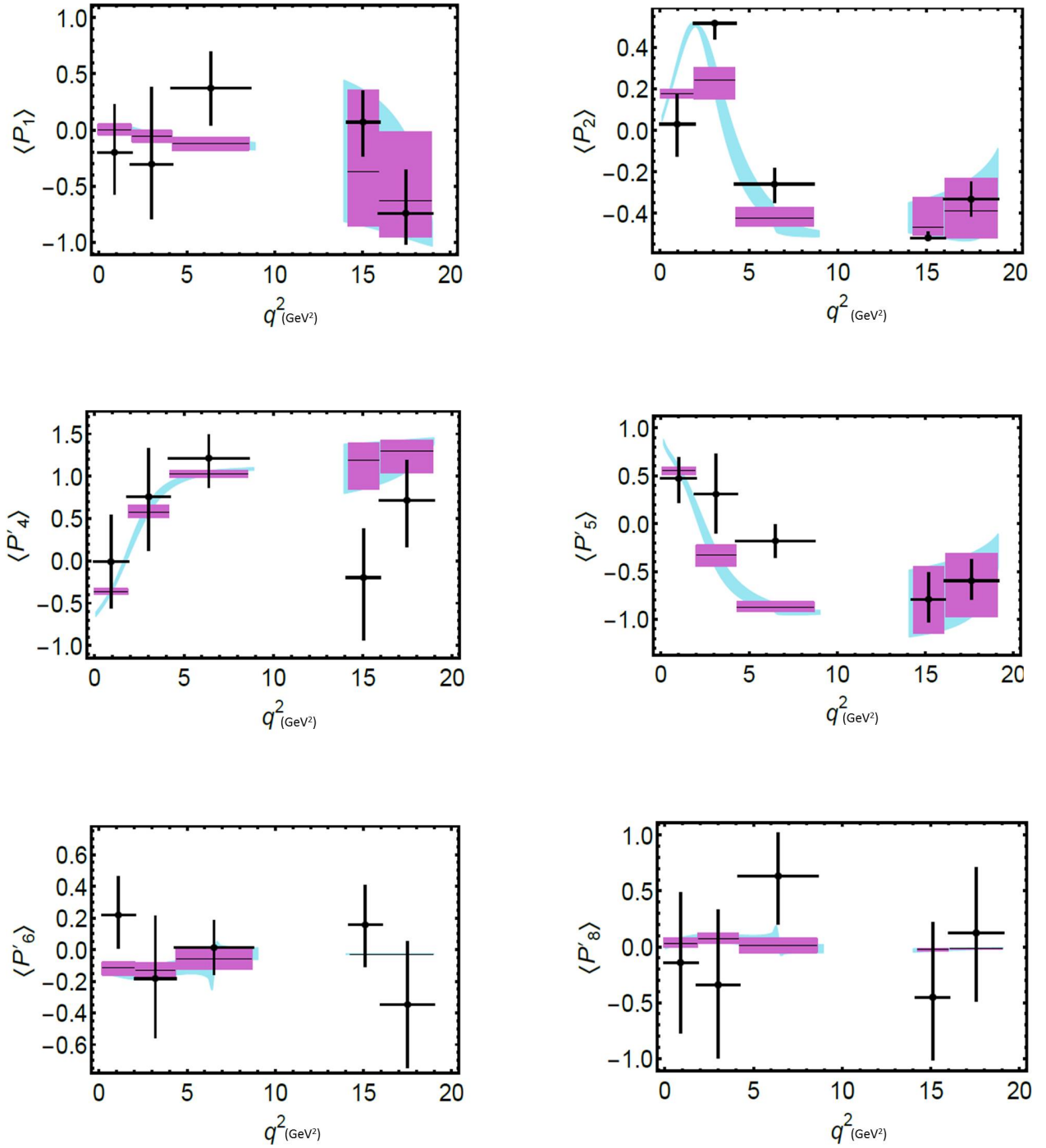


Figure 2.6: The SM predictions along with the LHCb measured values of optimized observables for the decay  $B \rightarrow K^* \mu^+ \mu^-$  [201].

which is also the origin of direct CP asymmetry in  $B \rightarrow X_s \gamma$ . But one can expect that these effects would be smaller in  $B \rightarrow X_s \ell^+ \ell^-$  than  $B \rightarrow X_s \gamma$  because the contributions of the WCs  $C_9$  and  $C_{10}$  are absent in  $B \rightarrow X_s \gamma$ . The CP averaged angular coefficients are [196]:

$$S_i^{(a)} = \frac{(I_i^{(a)} + \bar{I}_i^{(a)})}{d(\Gamma + \bar{\Gamma})/ds}, \quad (2.71)$$

and CP asymmetries are:

$$A_i^{(a)} = \frac{(I_i^{(a)} - \bar{I}_i^{(a)})}{d(\Gamma + \bar{\Gamma})/ds}, \quad (2.72)$$

where  $I_i$  with  $i = 1, \dots, 9$  represent angular coefficients and their explicit expressions can be found in [196]. In this way one can separate the CP conserving and CP violating NP effects. Since  $I_{1,2,3,4,7}$  are even under CP therefore,  $S_{1,2,3,4,7}$  can be obtained directly from angular coefficients and  $I_{5,6,8,9}$  being odd under CP the CP violating observables  $A_{5,6,8,9}$  can be calculated directly from them. The observables which depend on real part of transversity amplitude are  $\{S_{1,2}^{s,c}, S_{3,4}, A_{5,6}\}$ . Among them some of the measured observables are presented in Fig. 2.7 for  $B \rightarrow K^* \mu^+ \mu^-$  decay.

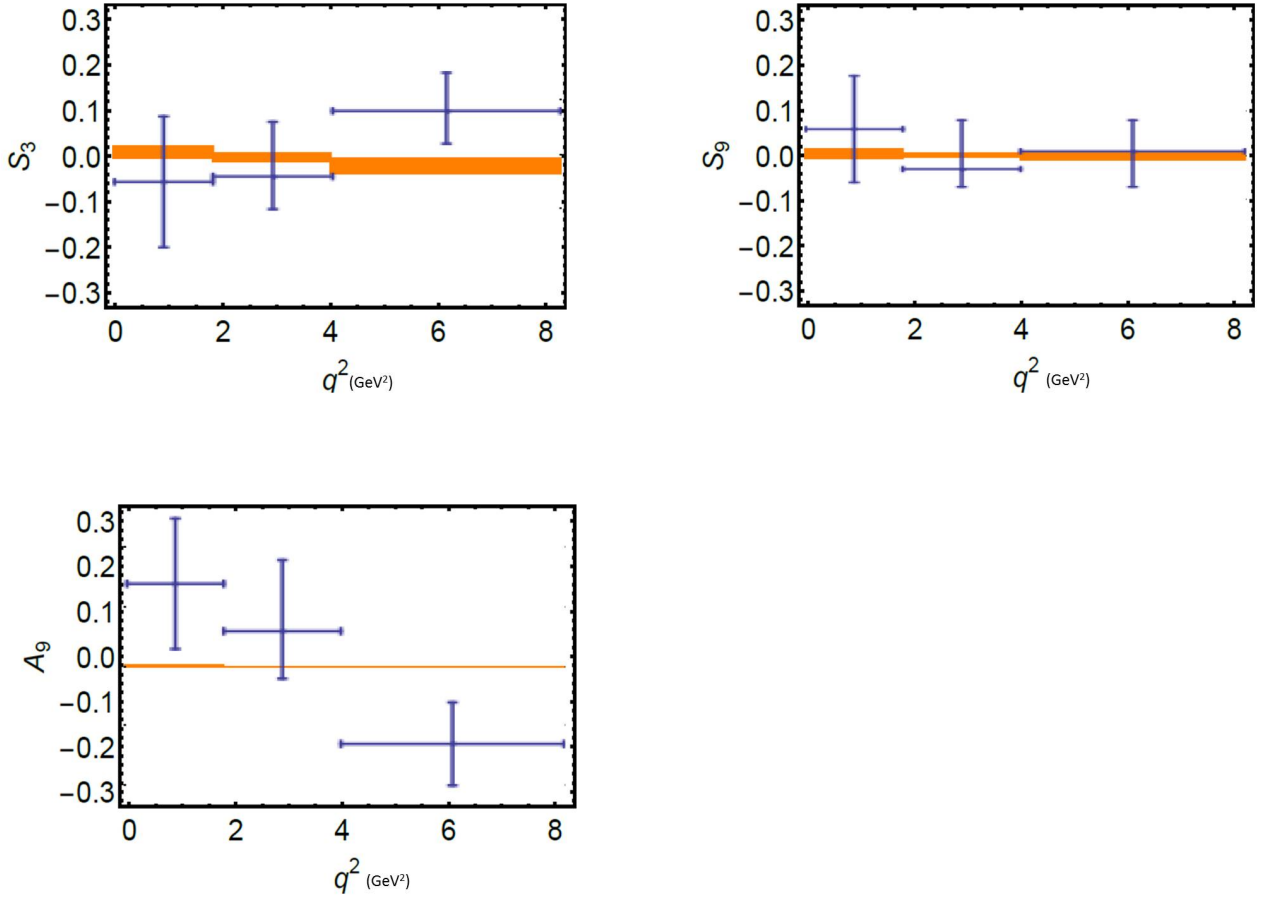


Figure 2.7: The SM predictions along with measured values from LHCb experiment for observables  $S_3$ ,  $S_9$  and  $A_9$  for the decay  $B \rightarrow K^* \mu^+ \mu^-$  [198].

# Chapter 3

## Helicity Formalism of decay

### $\Lambda_b \rightarrow \Lambda(\rightarrow N\pi)\ell^+\ell^-$ in the SM

The  $\Lambda_b$  baryon is an isospin singlet ground state of  $b$ -baryon family which consists of the bottom quark and two light quarks up and down. Its decays are phenomenologically rich as they allow the measurements of many masses, lifetimes, and branching fractions, that can test the underlying QCD physics and provide input for model building. The study of its production and decays provide an opportunity to get analogous information that is obtained from the study of  $B$ -mesons. In the past two decades, a wealth of experimental data was obtained for  $B$ -meson decays but the first measurement of  $b$ -baryon decay  $\Lambda_b \rightarrow \Lambda\mu^+\mu^-$  was made in 2011 by CDF Collaboration [47]. Then, at the Tevatron, characteristics (mass and lifetime) of  $\Lambda_b$  baryon have been measured by two body decay modes such as  $\Lambda_b \rightarrow \Lambda J/\psi$  and  $\Lambda_b \rightarrow \Lambda_c^+\pi^-$  [203–205]. Since December 2009, LHCb is dedicated to the production of  $b$ -hadrons with the ratio  $B^0 : \Lambda_b^0 : B_c^0 = 4 : 2 : 1$ . The high production rate of  $b$ -hadrons at LHCb results in Cabibbo-suppressed decay modes of  $\Lambda_b$  baryons, such as  $\Lambda_b \rightarrow DpK^-$ ,  $\Lambda_b \rightarrow \Lambda_c^+K^-$  [206],  $\Lambda_b \rightarrow \Lambda_c^+D^-$ ,  $\Lambda_b \rightarrow \Lambda_c^+D_s^-$  [207] and  $\Lambda_b \rightarrow J/\psi p\pi^-$  [208]. Later, multi-body decays of  $\Lambda_b$  were measured by LHCb e.g.,  $\Lambda_b \rightarrow \Lambda K^+\pi^-$ ,  $\Lambda_b \rightarrow \Lambda K^+K^-$  [209],  $\Lambda_b \rightarrow pK^-\pi^+\pi^-$ ,  $\Lambda_b \rightarrow pK^-K^+K^-$  [210],  $\Lambda_b \rightarrow \psi(2S)pK^-$  and  $\Lambda_b \rightarrow J/\psi\pi^+\pi^-pK^-$  [211]. The most precise measurement of  $\Lambda_b$  mass was made by LHCb with value  $5620.15 \pm 0.31 \pm 0.47$  where the first uncertainty is statistical and the second is systematic [205]. This chapter is dedicated to study the helicity formalism of the semileptonic four body  $\Lambda_b \rightarrow \Lambda(\rightarrow p\pi)\ell^+\ell^-$  decay.

### 3.1 Effective Hamiltonian

It is well established that a low energy effective theory can be constructed from a full theory by integrating out the heavy degrees of freedom such as  $W, Z$  bosons and top quark at an electroweak scale in the SM (see Sect. 2.6). The weak effective Lagrangian consists of dimension-six local operators of light SM fields (fermions, photons, and gluons) suppressed by inverse powers of  $m_W$ .

The quark level transition governing the

$$\Lambda_b(p_{\Lambda_b}, s_{\Lambda_b}) \rightarrow \Lambda(p_{\Lambda}, s_{\Lambda})(\rightarrow p(p_N, s_N)\pi(p_{\pi}))\ell^+(q_1)\ell^-(q_2),$$

decay is  $b \rightarrow s\ell^+\ell^-$ . In this cascade decay the final state  $\Lambda$  produced in  $\Lambda_b$  decay further decays into  $p\pi$  and the corresponding topology of decay is described in Fig. (3.1). In effective Hamiltonian,



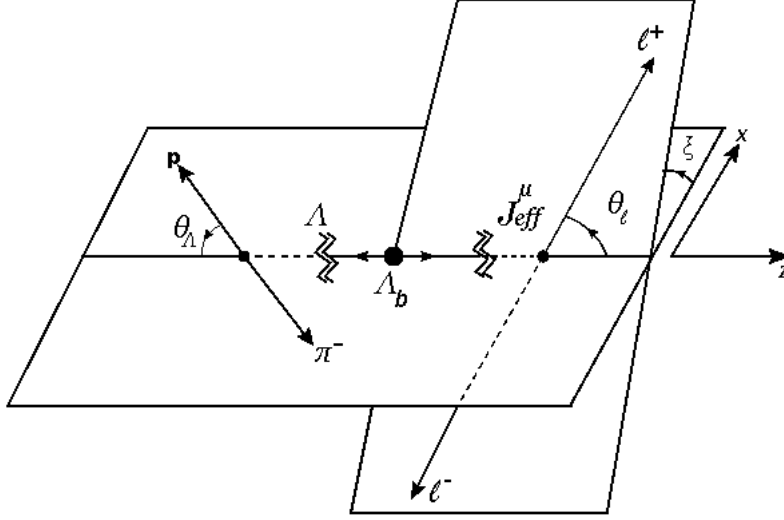


Figure 3.1:  $\Lambda_b \rightarrow \Lambda(\rightarrow p\pi^-)\mu^+\mu^-$  decay topology, where  $\theta_\ell$ ,  $\theta_\Lambda$  are the helicity angles and  $\xi$  is the azimuthal angle.

the short-distance effects are encoded in the WCs, whereas the long-distance contributions are incorporated through the four quark operators. After integrating out the heavy degrees of freedoms, the effective Hamiltonian for this decay is [62, 109, 202]

$$H_{SM}^{eff} = -\frac{4G_F}{\sqrt{2}} \frac{\alpha_e}{4\pi} V_{tb}V_{ts}^* \sum_{i=7,9,10} [C_i(\mu) \mathcal{O}_i + C'_i(\mu) \mathcal{O}'_i], \quad (3.1)$$

where  $G_F$  is the Fermi coupling constant,  $V_{tb}V_{ts}^*$  are the CKM matrix elements,  $\alpha_e$  is the fine structure constant,  $C_i(\mu)$  ( $C'_i(\mu)$ ) with  $i = 7, 9, 10$  are the WCs corresponding to the electromagnetic operator  $\mathcal{O}_7$  ( $\mathcal{O}'_7$ ) and semileptonic operators  $\mathcal{O}_{9,10}$  ( $\mathcal{O}'_{9,10}$ ) that are defined as:

$$\begin{aligned} \mathcal{O}_7 &= \frac{e}{16\pi^2} m_b (\bar{s}_{L\alpha} \sigma^{\mu\nu} b_{R\alpha}) F_{\mu\nu}, \\ \mathcal{O}'_7 &= \frac{e}{16\pi^2} m_b (\bar{s}_{R\alpha} \sigma^{\mu\nu} b_{L\alpha}) F_{\mu\nu}, \\ \mathcal{O}_9 &= \frac{e^2}{16\pi^2} (\bar{s}_{L\alpha} \gamma^\mu b_{L\alpha}) \bar{\ell} \gamma_\mu \ell, \\ \mathcal{O}'_9 &= \frac{e^2}{16\pi^2} (\bar{s}_{R\alpha} \gamma^\mu b_{R\alpha}) \bar{\ell} \gamma_\mu \ell, \\ \mathcal{O}_{10} &= \frac{e^2}{16\pi^2} (\bar{s}_{L\alpha} \gamma^\mu b_{L\alpha}) \bar{\ell} \gamma_\mu \gamma_5 \ell, \\ \mathcal{O}'_{10} &= \frac{e^2}{16\pi^2} (\bar{s}_{R\alpha} \gamma^\mu b_{R\alpha}) \bar{\ell} \gamma_\mu \gamma_5 \ell, \end{aligned} \quad (3.2)$$

where  $e$  is the electromagnetic coupling constant and  $m_b$  is the  $b$  quark running mass in the  $\overline{\text{MS}}$  scheme.

Since QCD factorization at low  $s$  is not fully developed for the  $b$ -baryon decays, therefore, we have ignored the non-factorizable contributions here.<sup>1</sup> The factorizable non-local matrix elements

<sup>1</sup>In case of  $B \rightarrow K^* \mu^+ \mu^-$  decay, it is evident that the non-factorizable charm-loop effects (i.e., corrections that are not described using hadronic FFs) play a sizeable role in the low- $s$  region [38] and the same is expected in case of the decay under consideration. However, in the present study, we shall neglect their contributions because there is no systematic framework available in which these non-factorizable charm-loop effects can be calculated in the baryonic decays [46]. Therefore, our results at low  $s$  are affected by the uncertainties due to these contributions. In

of the four quark operators  $\mathcal{O}_{1-6}$  and  $\mathcal{O}_8^g$  are encoded into effective WCs  $C_7^{eff}(s)$  and  $C_9^{eff}(s)$ , where  $s$  is dilepton squared mass  $s$  ( $q^\mu = p_{\Lambda_b}^\mu - p_\Lambda^\mu$ ).

In high  $s$  region, the WCs  $C_7^{eff}(s)$  and  $C_9^{eff}(s)$  can be written as follows [29]

$$\begin{aligned}
C_7^{eff}(s) &= C_7 - \frac{1}{3} \left( C_3 + \frac{4}{3} C_4 + 20C_5 + \frac{80}{3} C_6 \right) - \frac{\alpha_s}{4\pi} \left[ (C_1 - 6C_2) F_{1,c}^{(7)}(s) + C_8 F_8^{(7)}(s) \right], \\
C_9^{eff}(s) &= C_9 + \frac{4}{3} \left( C_3 + \frac{16}{3} C_5 + \frac{16}{9} C_6 \right) - h(0, s) \left( \frac{1}{2} C_3 + \frac{2}{3} C_4 + 8C_5 + \frac{32}{3} C_6 \right) \\
&\quad - \left( \frac{7}{2} C_3 + \frac{2}{3} C_4 + 38C_5 + \frac{32}{3} C_6 \right) h(m_b, s) + \left( \frac{4}{3} C_1 + C_2 + 6C_3 + 60C_5 \right) h(m_c, s) \\
&\quad - \frac{\alpha_s}{4\pi} \left[ C_1 F_{1,c}^{(9)}(s) + C_2 F_{2,c}^{(9)}(s) + C_8 F_8^{(9)}(s) \right], \tag{3.3}
\end{aligned}$$

where  $h(m_{q'}, s)$  with  $q' = b, c$  correspond to the fermionic loop functions. These  $h(m_{q'}, s)$  along with the functions  $F_8^{(7,9)}$  and  $F_{(1,2,c)}^{(7,9)}$  are calculated in refs. [86, 212].

### 3.2 Helicity amplitudes and Form Factors for $\Lambda_b \rightarrow \Lambda$ transitions

The matrix elements for the  $\Lambda_b \rightarrow \Lambda$  transition for different possible currents, can be straightforwardly parameterized in terms of the FFs. The helicity formalism provides a convenient way to describe these transformations. The helicity amplitudes  $H^i(s_1, s_2)$  with  $i$  corresponding to vector ( $V$ ), axial-vector ( $A$ ), tensor ( $T$ ) and axial-tensor ( $T_5$ ) currents can be written as [67]:

$$H^V(s_{\Lambda_b}, s_\Lambda) \equiv \epsilon_\mu^*(m) \langle \Lambda(p_\Lambda, s_\Lambda) | \bar{s} \gamma^\mu b | \Lambda_b(p_{\Lambda_b}, s_{\Lambda_b}) \rangle,$$

where  $m = t, 0, \pm$  corresponds to time-like, longitudinal and transverse polarizations of daughter baryon  $\Lambda$ . In component form, vector hadronic part reads as

$$\begin{aligned}
H_t^V(s_{\Lambda_b}, s_\Lambda) &= f_0(s) \frac{m_{\Lambda_b} - m_\Lambda}{\sqrt{s}} [\bar{u}(p_\Lambda, s_\Lambda) u(p_{\Lambda_b}, s_{\Lambda_b})], \\
H_0^V(s_{\Lambda_b}, s_\Lambda) &= 2f_+(s) \frac{m_{\Lambda_b} + m_\Lambda}{s_+} (p_\Lambda \cdot \epsilon^*(0)) [\bar{u}(p_\Lambda, s_\Lambda) u(p_{\Lambda_b}, s_{\Lambda_b})], \\
H_\pm^V(s_{\Lambda_b}, s_\Lambda) &= f_\pm(s) [\bar{u}(p_\Lambda, s_\Lambda) \not{\epsilon}^*(\pm) u(p_{\Lambda_b}, s_{\Lambda_b})]. \tag{3.4}
\end{aligned}$$

The axial-vector part of Hamiltonian is

$$H^A(s_{\Lambda_b}, s_\Lambda) \equiv \epsilon_\mu^*(m) \langle \Lambda(p_\Lambda, s_\Lambda) | \bar{s} \gamma^\mu \gamma_5 b | \Lambda_b(p_{\Lambda_b}, s_{\Lambda_b}) \rangle$$

and its helicity components are

$$H_t^A(s_{\Lambda_b}, s_\Lambda) = -g_0(s) \frac{m_{\Lambda_b} + m_\Lambda}{\sqrt{s}} [\bar{u}(p_\Lambda, s_\Lambda) \gamma_5 u(p_{\Lambda_b}, s_{\Lambda_b})], \tag{3.5}$$

---

the whole  $s$  range, the effective WCs are given in Eq. (3.3). According to ref. [44], we use Eq. (3.3) in low and high  $s$  region by increasing 5% uncertainty. Thus having control over the non-factorizable contributions in baryonic decays will help us to hunt the deviations from the SM predictions.

$$\begin{aligned}
H_0^A(s_{\Lambda_b}, s_\Lambda) &= -2g_+(s) \frac{m_{\Lambda_b} - m_\Lambda}{s_-} (p_\Lambda \cdot \epsilon^*(0)) [\bar{u}(p_\Lambda, s_\Lambda) \gamma_5 u(p_{\Lambda_b}, s_{\Lambda_b})], \\
H_\pm^A(s_{\Lambda_b}, s_\Lambda) &= g_\pm(s) [\bar{u}(p_\Lambda, s_\Lambda) \not{\epsilon}^*(\pm) \gamma_5 u(p_{\Lambda_b}, s_{\Lambda_b})].
\end{aligned} \tag{3.6}$$

Part of Hamiltonian corresponding to dipole operator is:

$$\begin{aligned}
H^T(s_{\Lambda_b}, s_\Lambda) &\equiv \epsilon_\mu^*(m) \langle \Lambda(p_\Lambda, s_\Lambda) | \bar{s} i \sigma^{\mu\nu} q_\nu b | \Lambda_b(p_{\Lambda_b}, s_{\Lambda_b}) \rangle \\
H^{T_5}(s_{\Lambda_b}, s_\Lambda) &\equiv \epsilon_\mu^*(m) \langle \Lambda(p_\Lambda, s_\Lambda) | \bar{s} i \sigma^{\mu\nu} q_\nu \gamma_5 b | \Lambda_b(p_{\Lambda_b}, s_{\Lambda_b}) \rangle.
\end{aligned}$$

By examining their polarization states, we can see that the non-zero components read as:

$$\begin{aligned}
H_0^T(s_{\Lambda_b}, s_\Lambda) &= -2h_+(s) \frac{s}{s_+} (p_\Lambda \cdot \epsilon^*(0)) [\bar{u}(p_\Lambda, s_\Lambda) u(p_{\Lambda_b}, s_{\Lambda_b})], \\
H_\pm^T(s_{\Lambda_b}, s_\Lambda) &= -h_\pm(s) (m_{\Lambda_b} + m_\Lambda) [\bar{u}(p_\Lambda, s_\Lambda) \not{\epsilon}^*(\pm) u(p_{\Lambda_b}, s_{\Lambda_b})], \\
H_0^{T_5}(s_{\Lambda_b}, s_\Lambda) &= -2\tilde{h}_+(s) \frac{s}{s_-} (p_\Lambda \cdot \epsilon^*(0)) [\bar{u}(p_\Lambda, s_\Lambda) \gamma_5 u(p_{\Lambda_b}, s_{\Lambda_b})], \\
H_\pm^{T_5}(s_{\Lambda_b}, s_\Lambda) &= \tilde{h}_\pm(s) (m_{\Lambda_b} - m_\Lambda) [\bar{u}(p_\Lambda, s_\Lambda) \not{\epsilon}^*(\pm) \gamma_5 u(p_{\Lambda_b}, s_{\Lambda_b})],
\end{aligned} \tag{3.7}$$

where  $p_{\Lambda_b}(s_{\Lambda_b})$  and  $p_\Lambda(s_\Lambda)$  are the momentum (spin) of  $\Lambda_b$  and  $\Lambda$ , respectively. In Eqs. (3.4, 3.5, 3.6) and (3.7), the functions  $f_i(s)$ ,  $g_i(s)$ ,  $h_i(s)$  and  $\tilde{h}_i(s)$  with  $i = 0, +, \perp$  are the transition FFs. The FFs, being the non-perturbative quantities need to be calculated in some model.  $\Lambda_b \rightarrow \Lambda$  FFs have developed in the framework of QCD light cone sum rule (LCSR) approach [89, 213], soft collinear effective theory (SCET) [71], heavy quark effective theory (HQET) [214], large energy effective theory (LEET) [214] and lattice QCD [44, 215]. In the heavy quark spin symmetry, the symmetry where the spin of spectator-diquark remains same in initial and final state, the number of FFs are reduced. The tensor FFs can be written in terms of vector and axial-vector FFs and with this symmetry we can also equate the longitudinal and transverse FFs. Thus it reduces the number of independent FFs to two i.e., the Isuger-wise relations  $\xi_1$  and  $\xi_2$ . In the decay under consideration here, we will use the FFs that are calculated in LQCD with much better control over the various uncertainties. In full dilepton mass square range these can be expressed as [44]:

$$f(s) = \frac{a_0^f + a_1^f z(s) + a_2^f (z(s))^2}{1 - s/(m_{pole}^f)^2}, \tag{3.8}$$

where, the inputs  $a_0^f, a_1^f$  and  $a_2^f$  are summarized in Tables 3.1 and 3.2. The parameter  $z$  is defined as [44]

$$z(s) = \frac{\sqrt{t_+ - s} - \sqrt{t_+ - t_0}}{\sqrt{t_+ - s} + \sqrt{t_+ - t_0}}, \tag{3.9}$$

with  $t_0 = (m_{\Lambda_b} - m_\Lambda)^2$  and  $t_+ = (m_B + m_K)^2$ .

### 3.3 Kinematics of Hadronic part

In the rest frame of the decaying  $\Lambda_b$  baryon, the momentum of daughter baryon  $\Lambda$  is defined as

$$p_\Lambda = (m_{\Lambda_b} - p_0, 0, 0, |\mathbf{p}|),$$

Table 3.1: The values of FFs along with uncertainties calculated in the framework of lattice QCD with  $(2 + 1)$  flavor dynamics for  $\Lambda_b \rightarrow \Lambda$  transition [44].

Parameter	Input	Parameter	Input	Parameter	Input
$a_0^{f+}$	$0.4229 \pm 0.0274$	$a_1^{f+}$	$-1.3728 \pm 0.3068$	$a_2^{f+}$	$107972 \pm 1.1506$
$a_0^{f0}$	$0.3604 \pm 0.0277$	$a_1^{f0}$	$-0.9284 \pm 0.3453$	$a_2^{f0}$	$0.9861 \pm 1.1988$
$a_0^{f\perp}$	$0.5748 \pm 0.0353$	$a_1^{f\perp}$	$-1.4781 \pm 0.4030$	$a_2^{f\perp}$	$1.2496 \pm 1.6396$
$a_0^{g+}$	$0.3522 \pm 0.5$	$a_1^{g+}$	$-1.2968 \pm 0.2732$	$a_2^{g+}$	$2.7106 \pm 1.0665$
$a_0^{g0}$	$0.4059 \pm 0.0267$	$a_1^{g0}$	$-1.1622 \pm 0.2929$	$a_2^{g0}$	$1.1490 \pm 1.0327$
$a_0^{g\perp}$	$0.3522 \pm 0.0205$	$a_1^{g\perp}$	$-1.3607 \pm 0.2949$	$a_2^{g\perp}$	$2.4621 \pm 1.3711$
$a_0^{h+}$	$0.4753 \pm 0.0423$	$a_1^{h+}$	$-0.8840 \pm 0.3997$	$a_2^{h+}$	$-0.8190 \pm 1.6760$
$a_0^{h\perp}$	$0.3745 \pm 0.0313$	$a_1^{h\perp}$	$-0.9439 \pm 0.2766$	$a_2^{h\perp}$	$1.1606 \pm 1.0757$
$a_0^{\tilde{h}+}$	$0.3256 \pm 0.0248$	$a_1^{\tilde{h}+}$	$-0.9603 \pm 0.2303$	$a_2^{\tilde{h}+}$	$2.9780 \pm 1.0041$
$a_0^{\tilde{h}\perp}$	$0.3256 \pm 0.0248$	$a_1^{\tilde{h}\perp}$	$-0.9634 \pm 0.2268$	$a_2^{\tilde{h}\perp}$	$2.4782 \pm 0.9549$

Table 3.2: Pole masses for different FFs [44].

$f$	$J^P$	$m_{pole}^f$
$f_0$	$0^+$	5.711
$f_+, f_\perp, h_+, h_\perp$	$1^-$	5.416
$g_0$	$0^-$	5.367
$g_+, g_\perp, \tilde{h}_+, \tilde{h}_\perp$	$1^+$	5.750

where  $m_{\Lambda_b}$  is the mass of the  $\Lambda_b$  baryon. In the same frame, momenta of dilepton pair is

$$p = (p_0, 0, 0, -|\mathbf{p}|) \quad (3.10)$$

where  $p_0 = \frac{m_{\Lambda_b}^2 - m_\Lambda^2 + s}{2m_{\Lambda_b}}$  and  $|\mathbf{p}| = \frac{\sqrt{\lambda(m_{\Lambda_b}^2, m_\Lambda^2, s)}}{2m_{\Lambda_b}}$ . Polarization vectors of effective current are written as

$$\begin{aligned} \epsilon^\mu(t) &= \frac{1}{s} (p_0, 0, 0, |\mathbf{p}|), \\ \epsilon^\mu(\pm) &= \frac{1}{\sqrt{2}} (0, \mp 1, -i, 0), \\ \epsilon^\mu(0) &= \frac{1}{s} (|\mathbf{p}|, 0, 0, p_0). \end{aligned} \quad (3.11)$$

In  $N\pi$  rest frame, the momenta of  $N$  and  $\pi$  are defined as

$$\begin{aligned} p_N^\mu &= (E_N, -|\mathbf{k}| \sin \theta_\Lambda \cos \xi, -|\mathbf{k}| \sin \theta_\Lambda \sin \xi, |\mathbf{k}| \cos \theta_\Lambda), \\ p_\pi^\mu &= (E_\pi, |\mathbf{k}| \sin \theta_\Lambda \cos \xi, |\mathbf{k}| \sin \theta_\Lambda \sin \xi, -|\mathbf{k}| \cos \theta_\Lambda), \end{aligned} \quad (3.12)$$

where  $|\mathbf{k}| = \frac{\sqrt{\lambda(k^2, m_N^2, m_\pi^2)}}{2\sqrt{k^2}}$ ,  $E_N = \sqrt{m_N^2 + \frac{\lambda(k^2, m_N^2, m_\pi^2)}{4k^2}}$  and  $E_\pi = \sqrt{m_\pi^2 + \frac{\lambda(k^2, m_N^2, m_\pi^2)}{4k^2}}$ . In  $N\pi$  rest frame  $k^2 = m_\Lambda^2$ ,  $\theta_\Lambda$  is the angle between direction of flight of  $N$  with respect to  $z$ -axis in  $N\pi$  rest frame and  $\xi$  is the azimuthal angle between two decaying planes i.e.  $N\pi$  and  $\ell^+\ell^-$  decaying planes. A Dirac spinor  $u(p, s)$  having momentum

$$p^\mu = (p^0, |\mathbf{p}| \sin \theta \cos \xi, |\mathbf{p}| \sin \theta \sin \xi, |\mathbf{p}| \cos \theta), \quad (3.13)$$

in its rest frame is defined as

$$u(p, +1/2) = \frac{1}{\sqrt{2(p^0 + m)}} \begin{pmatrix} (p^0 + m - |\mathbf{p}|) \cos(\theta/2) \\ (p^0 + m - |\mathbf{p}|) \sin(\theta/2) e^{i\xi} \\ (p^0 + m + |\mathbf{p}|) \cos(\theta/2) \\ (p^0 + m + |\mathbf{p}|) \sin(\theta/2) e^{i\xi} \end{pmatrix}, \quad (3.14)$$

$$u(p, -1/2) = \frac{1}{\sqrt{2(p^0 + m)}} \begin{pmatrix} -(p^0 + m + |\mathbf{p}|) \sin(\theta/2) e^{-i\xi} \\ (p^0 + m + |\mathbf{p}|) \cos(\theta/2) \\ -(p^0 + m - |\mathbf{p}|) \sin(\theta/2) e^{-i\xi} \\ (p^0 + m - |\mathbf{p}|) \cos(\theta/2) \end{pmatrix}, \quad (3.15)$$

Non-zero components of vector and axial-vector currents are

$$\bar{u}(p', \pm 1/2) \gamma^\mu u(p, \pm 1/2) = (\sqrt{s_+}, 0, 0, \sqrt{s_-}), \quad (3.16)$$

$$\bar{u}(p', \mp 1/2) \gamma^\mu u(p, \mp 1/2) = \sqrt{2s_-} \epsilon^\mu(\pm), \quad (3.17)$$

$$\bar{u}(p', \pm 1/2) \gamma^\mu \gamma_5 u(p, \pm 1/2) = \pm(\sqrt{s_-}, 0, 0, \sqrt{s_+}), \quad (3.18)$$

$$\bar{u}(p', \pm 1/2) \gamma^\mu \gamma_5 u(p, \mp 1/2) = \mp \sqrt{2s_+} \epsilon^\mu(\mp), \quad (3.19)$$

### 3.4 Hadron helicity amplitudes

Using Eqs. (3.16)-(3.19) in Eqs. (3.4)-(3.7), we get the following helicity amplitudes in terms of  $\Lambda_b \rightarrow \Lambda$  transition FFs [67]:

$$\begin{aligned} H_{t(+1/2,+1/2)}^V &= H_{t(-1/2,-1/2)}^V = f_0(s) \frac{m_{\Lambda_b} - m_\Lambda}{\sqrt{s}} \sqrt{s_+}, \\ H_{0(+1/2,+1/2)}^V &= H_{0(-1/2,-1/2)}^V = f_+(s) \frac{m_{\Lambda_b} + m_\Lambda}{\sqrt{s}} \sqrt{s_-}, \\ H_{+(-1/2,+1/2)}^V &= H_{-(+1/2,-1/2)}^V = -f_\perp(s) \sqrt{2s_-}, \\ H_{t(+1/2,+1/2)}^A &= -H_{t(-1/2,-1/2)}^A = g_0(s) \frac{m_{\Lambda_b} + m_\Lambda}{\sqrt{s}} \sqrt{s_-}, \\ H_{0(+1/2,+1/2)}^A &= -H_{0(-1/2,-1/2)}^A = g_+(s) \frac{m_{\Lambda_b} - m_\Lambda}{\sqrt{s}} \sqrt{s_+}, \\ H_{+(-1/2,+1/2)}^A &= -H_{-(+1/2,-1/2)}^A = -g_\perp(s) \sqrt{2s_+}, \\ H_{0(+1/2,+1/2)}^T &= H_{0(-1/2,-1/2)}^T = -h_+(s) \sqrt{s} \sqrt{s_-}, \\ H_{+(-1/2,+1/2)}^T &= H_{-(+1/2,-1/2)}^T = h_\perp(s) (m_{\Lambda_b} + m_\Lambda) \sqrt{2s_-}, \\ H_{0(+1/2,+1/2)}^{T5} &= -H_{0(-1/2,-1/2)}^{T5} = \tilde{h}_+(s) \sqrt{s} \sqrt{s_+}, \\ H_{+(-1/2,+1/2)}^{T5} &= -H_{-(+1/2,-1/2)}^{T5} = -\tilde{h}_\perp(s) (m_{\Lambda_b} - m_\Lambda) \sqrt{2s_+}, \end{aligned} \quad (3.20)$$

where  $f_0(g_0)$ ,  $f_+(g_+)$  and  $f_\perp(g_\perp)$  denotes time-like, longitudinal, and transverse components of vector (axial-vector) currents. The kinematic functions used in the above equation are defined as  $s_\pm \equiv (m_{\Lambda_b} \pm m_\Lambda)^2 - s$ .

The transversity amplitude can be written in terms of helicity amplitudes as [67]

$$\begin{aligned}
A_{\perp 1}^{L(R)} &= +\sqrt{2}\mathcal{N} \left( (C_9^+ \mp C_{10}^+) H_{+(-1/2,+1/2)}^V - \frac{2m_b C_7^+}{s} H_{+(-1/2,+1/2)}^T \right), \\
A_{\parallel 1}^{L(R)} &= -\sqrt{2}\mathcal{N} \left( (C_9^- \mp C_{10}^-) H_{+(-1/2,+1/2)}^A + \frac{2m_b C_7^-}{s} H_{+(-1/2,+1/2)}^{T5} \right), \\
A_{\perp 0}^{L(R)} &= +\sqrt{2}\mathcal{N} \left( (C_9^+ \mp C_{10}^+) H_{0(+1/2,+1/2)}^V - \frac{2m_b C_7^+}{s} H_{0(+1/2,+1/2)}^T \right), \\
A_{\parallel 0}^{L(R)} &= -\sqrt{2}\mathcal{N} \left( (C_9^- \mp C_{10}^-) H_{0(+1/2,+1/2)}^A + \frac{2m_b C_7^-}{s} H_{0(+1/2,+1/2)}^{T5} \right). \tag{3.21}
\end{aligned}$$

where  $\mathcal{N} = G_F V_{tb} V_{ts}^* \alpha_e \sqrt{\frac{s\lambda^{1/2}(m_{\Lambda_b}^2, m_{\Lambda}^2, s)}{3 \cdot 2^{11} m_{\Lambda_b}^3 \pi^5}}$  and

$$\begin{aligned}
C_9^+ &= C_9 + C_9', & C_9^- &= C_9 - C_9', & C_{10}^+ &= C_{10} + C_{10}' \\
C_{10}^- &= C_{10} - C_{10}', & C_7^+ &= C_7 + C_7', & C_7^- &= C_7 - C_7'.
\end{aligned}$$

In case of the SM, all the primed WCs are zero.

### 3.5 Lepton Helicity Amplitude

The lepton polarization vectors in the dilepton rest frame are given as

$$\begin{aligned}
\epsilon_+^\mu &= \frac{1}{\sqrt{2}}(0, 1, -i, 0), & \epsilon_-^\mu &= \frac{1}{\sqrt{2}}(0, -1, -i, 0), \\
\epsilon_t^\mu &= (1, 0, 0, 0), & \epsilon_0^\mu &= (0, 0, 0, 1)
\end{aligned} \tag{3.22}$$

and the corresponding Lepton momentum vectors in dilepton rest frame are [67]

$$\begin{aligned}
q_1^\mu &= (E_\ell, -|\mathbf{q}| \sin \theta_\ell, 0, -|\mathbf{q}| \cos \theta_\ell), \\
q_2^\mu &= (E_\ell, |\mathbf{q}| \sin \theta_\ell, 0, |\mathbf{q}| \cos \theta_\ell),
\end{aligned}$$

with  $E_\ell = \frac{\sqrt{s}}{2}$  and  $|\mathbf{q}| = \sqrt{E_\ell^2 - m_\ell^2}$ .

Helicity amplitudes for leptons are defined as

$$\begin{aligned}
L_{m,n}^{L(R),r} &= \bar{\epsilon}^\mu(r) \langle \bar{\ell}_1(m) \ell_2(n) | \bar{\ell}_1 \gamma_\mu (1 \mp \gamma_5) \ell_2 | 0 \rangle \\
&= \bar{\epsilon}^\mu(r) \bar{u}_{\ell_1}(\vec{p}, m) \gamma_\mu (1 \mp \gamma_5) v_{\ell_2}(-\vec{p}', n), \tag{3.23}
\end{aligned}$$

where  $\ell_1 = \ell^+$  and  $\ell_2 = \ell^-$ . The dilepton polarization vector is written as  $\epsilon_\mu^*(m)$  with  $m = t, 0, \pm$  and their explicit definitions are given in Eq. (3.22) [67]. In dilepton rest frame, spinors are written as:

$$u_{\ell^-}(s) = \begin{pmatrix} \sqrt{E_\ell + m_\ell} \chi_u(s) \\ 2s \sqrt{E_\ell - m_\ell} \chi_u(s) \end{pmatrix}, \tag{3.24}$$

$$v_{\ell^+}(s) = \begin{pmatrix} \sqrt{E_\ell - m_\ell} \chi_v(s) \\ -2s \sqrt{E_\ell + m_\ell} \chi_v(s) \end{pmatrix}, \tag{3.25}$$

where

$$\chi_u(+1/2) = \begin{pmatrix} \cos \theta_\ell/2 \\ \sin \theta_\ell/2 \end{pmatrix}, \quad \chi_u(-1/2) = \begin{pmatrix} -\sin \theta_\ell/2 \\ \cos \theta_\ell/2 \end{pmatrix}, \quad (3.26)$$

$$\chi_v(+1/2) = \begin{pmatrix} \sin \theta_\ell/2 \\ \cos \theta_\ell/2 \end{pmatrix}, \quad \chi_v(-1/2) = \begin{pmatrix} -\cos \theta_\ell/2 \\ \sin \theta_\ell/2 \end{pmatrix}. \quad (3.27)$$

Using above spinors in Eq. (3.23), we get

$$\begin{aligned} L_+^L(+1/2, +1/2) &= L_+^R(+1/2, +1/2) = L_-^L(-1/2, -1/2) = L_-^R(-1/2, -1/2) = \sqrt{2}m_\ell \sin \theta_\ell, \\ L_+^L(-1/2, -1/2) &= L_+^R(-1/2, -1/2) = L_-^L(+1/2, +1/2) = L_-^R(+1/2, +1/2) = -\sqrt{2}m_\ell \sin \theta_\ell, \\ L_+^L(+1/2, -1/2) &= -L_-^R(-1/2, +1/2) = -\sqrt{\frac{s}{2}}(1-v)(1-\cos \theta_\ell), \\ L_+^L(-1/2, -1/2) &= -L_-^R(+1/2, -1/2) = \sqrt{\frac{s}{2}}(1+v)(1+\cos \theta_\ell), \\ L_+^R(+1/2, -1/2) &= -L_-^L(-1/2, +1/2) = -\sqrt{\frac{s}{2}}(1+v)(1-\cos \theta_\ell), \\ L_+^R(-1/2, +1/2) &= -L_-^L(+1/2, -1/2) = \sqrt{\frac{s}{2}}(1-v)(1+\cos \theta_\ell), \\ L_0^L(+1/2, +1/2) &= -L_0^L(-1/2, -1/2) = L_0^R(+1/2, +1/2) = -L_0^R(-1/2, -1/2) = -2m_\ell \cos \theta_\ell, \\ L_0^L(+1/2, -1/2) &= L_0^R(-1/2, +1/2) = -\sqrt{s}(1-v) \sin \theta_\ell, \\ L_0^L(-1/2, +1/2) &= L_0^R(+1/2, -1/2) = \sqrt{s}(1+v) \sin \theta_\ell, \\ L_t^L(+1/2, +1/2) &= -L_t^R(+1/2, +1/2) = L_t^L(-1/2, -1/2) = -L_t^R(-1/2, -1/2) = 2m_\ell. \end{aligned} \quad (3.28)$$

### 3.6 Cascade Decay $\Lambda \rightarrow N\pi$

The daughter baryon  $\Lambda$  produced in decay  $\Lambda_b \rightarrow \Lambda \ell^+ \ell^-$  subsequently decays to  $p\pi^-$  and governed by the effective Hamiltonian [67]

$$H_\Lambda^{eff} = \frac{4G_F}{\sqrt{2}} V_{us} V_{ud}^* (\bar{d}\gamma^\mu P_L u) (\bar{u}\gamma^\mu P_L s). \quad (3.29)$$

Matrix element for this decay is given as

$$H_2(s_\Lambda, s_N) = \langle N(p_N, s_N) \pi(p_\pi) | (\bar{d}\gamma^\mu P_L u) (\bar{u}\gamma^\mu P_L s) | \Lambda(p_\Lambda, s_\Lambda) \rangle = [\bar{u}(k_N, s_N) (\xi \gamma_5 + \omega) u(p_\Lambda, s_\Lambda)].$$

It involves two independent parameters,  $\xi$  and  $\omega$ , extracted from  $\Lambda \rightarrow N\pi$  decay width and polarization measurements. Using the kinematics defined in Sect. 3.3, one can write the contribution of secondary decay to total decay width as:

$$\Gamma'(s_\Lambda, s'_\Lambda) = |\mathcal{N}'|^2 \frac{\sqrt{r_+ r_-}}{16\pi m_\Lambda^3} \sum_{s_N} H'(s_\Lambda, s_N) H'^*(s'_\Lambda, s_N) \quad (3.30)$$

with  $r_{\pm} = (m_{\Lambda} \pm m_N)^2 - m_{\pi}^2$  and

$$\begin{aligned} H'(\pm 1/2, \pm 1/2) &= (\sqrt{r_+}\omega + \sqrt{r_-}\xi) \cos(\theta_{\Lambda}/2), \\ H'(+1/2, -1/2) &= (\sqrt{r_+}\omega + \sqrt{r_-}\xi) \sin(\theta_{\Lambda}/2)e^{i\xi}, \\ H'(-1/2, +1/2) &= (-\sqrt{r_+}\omega + \sqrt{r_-}\xi) \sin(\theta_{\Lambda}/2)e^{-i\xi}. \end{aligned} \quad (3.31)$$

By using these relations, Eq. (3.30) gives

$$\begin{aligned} \Gamma'(+1/2, +1/2) &= (1 + \alpha \cos \theta_{\Lambda})\Gamma_{\Lambda} & \Gamma'(+1/2, -1/2) &= -\alpha \sin \theta_{\Lambda} e^{i\xi} \Gamma_{\Lambda}, \\ \Gamma'(-1/2, -1/2) &= (1 - \alpha \cos \theta_{\Lambda})\Gamma_{\Lambda} & \Gamma'(-1/2, +1/2) &= -\alpha \sin \theta_{\Lambda} e^{-i\xi} \Gamma_{\Lambda}, \end{aligned} \quad (3.32)$$

with

$$\Gamma_{\Lambda} = |\mathcal{N}'|^2 \frac{\sqrt{r_+ r_-}}{16\pi m_{\Lambda}^3} (r_- |\xi|^2 + r_+ |\omega|^2), \quad (3.33)$$

and parity violating decay parameter

$$\alpha = \frac{2\Re[\omega^* \xi]}{\sqrt{\frac{r_-}{r_+}} |\xi|^2 + \sqrt{\frac{r_+}{r_-}} |\omega|^2}. \quad (3.34)$$

### 3.7 Angular Decay Distribution

Now we are in a position to combine hadron and lepton helicity amplitudes to get the four-fold angular decay distribution. We can assemble the hadronic and leptonic parts given in Eqs. (3.20) and (3.28) in the following way

$$|M|^2 = \frac{1}{4} \sum_{s_{\Lambda_b}, s_{\Lambda}^{(\prime)}} \sum_{s_{\ell_1}, s_{\ell_2}} H^m(s_{\Lambda_b}, s_{\Lambda}) H^{n*}(s_{\Lambda_b}, s'_{\Lambda}) g_{m,m'} g_{n,n'} L^{m'}(s_{\ell_1}, s_{\ell_2}) L^{n'*}(s_{\ell_1}, s_{\ell_2}) \Gamma'(s_{\Lambda}, s'_{\Lambda}),$$

where sum over polarization indices  $m^{(\prime)}, n^{(\prime)}$  is understood. Differential decay distribution is written in terms of amplitude square as

$$\frac{d^4\Gamma}{ds d\cos\theta_{\Lambda} d\cos\theta_{\ell} d\xi} = G_F^2 |V_{tb} V_{ts}^*|^2 \alpha_e \frac{s\lambda^{1/2}(m_{\Lambda_b}^2, m_{\Lambda}^2, s)}{3 \cdot 2^{11} m_{\Lambda_b}^3 \pi^5} |M|^2, \quad (3.35)$$

which results

$$\begin{aligned} \frac{d^4\Gamma}{ds d\cos\theta_{\Lambda} d\cos\theta_{\ell} d\xi} &= \frac{3}{8\pi} \left[ K_{1ss} \sin^2 \theta_{\ell} + K_{1cc} \cos^2 \theta_{\ell} + K_{1c} \cos \theta_{\ell} + (K_{2ss} \sin^2 \theta_{\ell} + K_{2cc} \cos^2 \theta_{\ell} \right. \\ &+ K_{2c} \cos \theta_{\ell}) \cos \theta_{\Lambda} + (K_{3sc} \sin \theta_{\ell} \cos \theta_{\ell} + K_{3s} \sin \theta_{\ell}) \sin \theta_{\Lambda} \sin \xi \\ &\left. + (K_{4sc} \sin \theta_{\ell} \cos \theta_{\ell} + K_{4s} \sin \theta_{\ell}) \sin \theta_{\Lambda} \cos \xi \right]. \end{aligned} \quad (3.36)$$

For angular variable  $K_{l,m}$ , the  $l$  and  $m$  denote the relative angular momentum and its third component for  $p\pi$  and  $\ell^+\ell^-$  systems, respectively. In Eq. (3.36),  $\theta_{\ell}$  and  $\theta_{\Lambda}$  are the helicity angles,  $\xi$  is the azimuthal angle and  $s$  is the dilepton mass square. The different angular coefficients



correspond to the particular values of the  $(l, m)$ , e.g., the coefficients of  $\cos^2 \theta_\ell$ ,  $\sin^2 \theta_\ell$  and  $\cos \theta_\ell$  correspond to  $K_{0,0}$  whereas coefficients of  $\cos^2 \theta_\ell \cos \theta_\Lambda$ ,  $\sin^2 \theta_\ell \cos \theta_\Lambda$  and  $\cos \theta_\ell \cos \theta_\Lambda$  correspond to  $K_{1,0}$  and the last four terms correspond to  $K_{1,1}$ . These angular parameters  $K_{ij}$ , where  $i = 1, \dots, 4$  and  $j = ss, cc, c, sc, s$  are functions of the square of momentum transfer  $s$ . Angular coefficients that are introduced in Eq. (3.36) can be written in terms of transversity amplitudes as:

$$\begin{aligned}
K_{1ss}(s) &= \frac{1}{4} \left[ |A_{\perp 1}^R|^2 + |A_{\parallel 1}^R|^2 + 2|A_{\perp 0}^R|^2 + 2|A_{\parallel 0}^R|^2 + (R \leftrightarrow L) \right] \\
&\quad - \frac{m_\ell^2}{s} \left[ |A_{\perp 0}^R|^2 + |A_{\parallel 0}^R|^2 + (R \leftrightarrow L) \right] + \frac{2m_\ell^2}{s} \text{Re} \left[ A_{\perp 0}^R A_{\perp 0}^{*L} + A_{\perp 1}^R A_{\perp 1}^{*L} + (\perp \leftrightarrow \parallel) \right], \\
K_{1cc}(s) &= \frac{1}{2} \left[ |A_{\perp 1}^R|^2 + |A_{\parallel 1}^R|^2 + (R \leftrightarrow L) \right] + \frac{m_\ell^2}{s} \left[ |A_{\perp 0}^R|^2 - |A_{\perp 1}^R|^2 + |A_{\parallel 0}^R|^2 - |A_{\parallel 1}^R|^2 + (R \leftrightarrow L) \right] \\
&\quad + \frac{2m_\ell^2}{s} \text{Re} \left[ A_{\perp 0}^R A_{\perp 0}^{*L} + A_{\perp 1}^R A_{\perp 1}^{*L} + (\perp \leftrightarrow \parallel) \right], \\
K_{1c}(s) &= -v \text{Re} \left\{ A_{\perp 1}^R A_{\parallel 1}^{*R} - (R \leftrightarrow L) \right\} \\
K_{2ss}(s) &= \frac{\alpha}{2} \text{Re} \left\{ A_{\perp 1}^R A_{\parallel 1}^{*R} + 2A_{\perp 0}^R A_{\parallel 0}^{*R} + (R \leftrightarrow L) \right\} - \frac{2\alpha m_\ell^2}{s} \text{Re} \left[ A_{\perp 0}^R A_{\parallel 0}^{*R} + A_{\perp 0}^L A_{\parallel 0}^{*L} \right] \\
&\quad + \frac{2\alpha m_\ell^2}{s} \text{Re} \left[ A_{\perp 0}^R A_{\parallel 0}^{*L} + A_{\parallel 0}^R A_{\perp 0}^{*L} + A_{\perp 1}^R A_{\parallel 1}^{*L} + A_{\parallel 1}^R A_{\perp 1}^{*L} \right], \\
K_{2cc}(s) &= \alpha \text{Re} \left\{ A_{\perp 1}^R A_{\parallel 1}^{*R} + (R \leftrightarrow L) \right\} + \frac{2\alpha m_\ell^2}{s} \text{Re} \left[ A_{\perp 0}^R A_{\parallel 0}^{*R} - A_{\perp 1}^R A_{\parallel 1}^{*R} + (R \leftrightarrow L) \right] \\
&\quad + \frac{2\alpha m_\ell^2}{s} \text{Re} \left[ A_{\perp 0}^R A_{\parallel 0}^{*L} + A_{\perp 1}^R A_{\parallel 1}^{*L} + A_{\parallel 0}^R A_{\perp 0}^{*L} + A_{\parallel 1}^R A_{\perp 1}^{*L} \right], \\
K_{2c}(s) &= -\frac{\alpha v}{2} \left[ |A_{\perp 1}^R|^2 + |A_{\parallel 1}^R|^2 - (R \leftrightarrow L) \right], \\
K_{3sc}(s) &= \frac{2\sqrt{2}\alpha m_\ell^2}{s} \text{Im} \left\{ A_{\parallel 1}^R A_{\parallel 0}^{*R} - A_{\perp 1}^R A_{\perp 0}^{*R} + (R \leftrightarrow L) \right\} \\
&\quad + \frac{\alpha}{\sqrt{2}} \text{Im} \left\{ A_{\perp 1}^R A_{\perp 0}^{*R} - A_{\parallel 1}^R A_{\parallel 0}^{*R} + (R \leftrightarrow L) \right\}, \\
K_{3s}(s) &= \frac{\alpha}{\sqrt{2}} \text{Im} \left\{ A_{\perp 1}^R A_{\parallel 0}^{*R} - A_{\parallel 1}^R A_{\perp 0}^{*R} - (R \leftrightarrow L) \right\}, \\
K_{4sc}(s) &= \frac{2\sqrt{2}\alpha m_\ell^2}{s} \text{Re} \left\{ A_{\parallel 1}^R A_{\perp 0}^{*R} - A_{\perp 1}^R A_{\parallel 0}^{*R} + (R \leftrightarrow L) \right\} \\
&\quad + \frac{\alpha}{\sqrt{2}} \text{Re} \left\{ A_{\perp 1}^R A_{\parallel 0}^{*R} - A_{\parallel 1}^R A_{\perp 0}^{*R} + (R \leftrightarrow L) \right\}, \\
K_{4s}(s) &= \frac{\alpha}{\sqrt{2}} \text{Re} \left\{ A_{\perp 1}^R A_{\perp 0}^{*R} - A_{\parallel 1}^R A_{\parallel 0}^{*R} - (R \leftrightarrow L) \right\}. \tag{3.37}
\end{aligned}$$

### 3.8 Observables

From the four-fold angular decay distribution, a number of physical observables can be obtained after integrating on different parameters among  $\theta_\ell$ ,  $\theta_\Lambda$ ,  $\xi$  and  $s$ .

#### 3.8.1 Differential decay rate and different asymmetry parameters

One of the most important observables from the theoretical and experimental point of view, is the differential decay distribution. By integrating over  $\theta_\ell \in [0, \pi]$ ,  $\theta_\Lambda \in [0, \pi]$  and  $\xi \in [0, 2\pi]$ , the

expression for the differential decay rate becomes

$$\frac{d\Gamma}{ds} = K_{1cc} + 2K_{1ss}. \quad (3.38)$$

In addition to the decay rate, we can extract several asymmetry parameters that correspond to different angles and can be separated by doing different integrations one by one. For example, by integrating on  $\theta_\ell \in [0, \pi]$  and  $\xi \in [0, 2\pi]$ , the expression for the differential decay rate takes the form

$$\frac{d\Gamma}{dsd\cos\theta_\Lambda} = (K_{1cc} + 2K_{1ss})[1 + \alpha_{\theta_\Lambda} \cos\theta_\Lambda], \quad (3.39)$$

where  $\alpha_{\theta_\Lambda}$  is the asymmetry parameter for the longitudinal polarization of the  $\Lambda$  baryon. It can be noticed that if we integrate Eq. (3.39) on  $\theta_\Lambda \in [0, \pi]$ , we get back the Eq. (3.38). In terms of the helicity parameters  $K_{ij}$ , the asymmetry parameter  $\alpha_{\theta_\Lambda}$  can be expressed as follows:

$$\alpha_{\theta_\Lambda} = \frac{\tilde{K}_{2cc} + 2\tilde{K}_{2ss}}{K_{1cc} + 2K_{1ss}}, \quad (3.40)$$

with  $\tilde{K}_{i,j} = \frac{K_{i,j}}{\alpha_\Lambda}$ . Here  $\alpha_\Lambda$  is the asymmetry parameter corresponding to the parity violating  $\Lambda \rightarrow p\pi^-$  decay and its experimental value is  $\alpha_\Lambda = 0.642 \pm 0.013$  [216].

Similarly, by performing an integration on  $\theta_\Lambda \in [0, \pi]$  and  $\xi \in [0, 2\pi]$  and leaving the angle  $\theta_\ell$ , we will have asymmetries corresponding to angle  $\theta_\ell$ . In terms of  $\alpha_{\theta_\ell}$  and  $\alpha'_{\theta_\ell}$ , the differential decay rate can be formulated as

$$\frac{d\Gamma}{dsd\cos\theta_\ell} = K_{1ss}[1 + \alpha_{\theta_\ell} \cos^2\theta_\ell + \alpha'_{\theta_\ell} \cos\theta_\ell], \quad (3.41)$$

with

$$\alpha_{\theta_\ell} = \frac{K_{1cc} - K_{1ss}}{K_{1ss}}, \quad \alpha'_{\theta_\ell} = \frac{K_{1c}}{K_{1ss}}. \quad (3.42)$$

On the same lines, if we perform integration on the helicity angles  $\theta_\ell \in [0, \pi]$  and  $\theta_\Lambda \in [0, \pi]$ , Eq. (3.36) can be written in terms of asymmetries corresponding to the angle  $\xi$  as

$$\frac{d\Gamma}{dsd\xi} = (K_{1cc} + 2K_{1ss})[1 + \alpha_\xi \cos\xi + \alpha'_\xi \sin\xi], \quad (3.43)$$

where

$$\alpha_\xi = \frac{3\pi^2\tilde{K}_{4s}}{16(K_{1cc} + 2K_{1ss})}, \quad \alpha'_\xi = \frac{3\pi^2\tilde{K}_{3s}}{16(K_{1cc} + 2K_{1ss})}. \quad (3.44)$$

From Eq. (3.36), the  $s$  dependence of the transverse ( $\alpha_U$ ) and longitudinal ( $\alpha_L$ ) asymmetry parameters are written in the following form [218]:

$$\alpha_U = \frac{\tilde{K}_{2cc}}{K_{1cc}}, \quad \alpha_L = \frac{\tilde{K}_{2ss}}{K_{1ss}}. \quad (3.45)$$

Even though one of the important observables is the decay rate, but it is prone to the uncertainties arising from different input parameters where the major contributors are the FFs. It is a well-

Table 3.3: Experimentally measured observables for the decay  $\Lambda_b \rightarrow \Lambda \mu^+ \mu^-$  [217].

$s$	$\mathcal{B}r$	$F_L$	$A_{FB}^\ell$	$A_{FB}^\Lambda$
[0.1, 2]	$0.36_{-0.011-0.02}^{+0.012+0.02} \pm 0.07$	$0.56_{-0.56}^{+0.23} \pm 0.08$	$0.37_{-0.48}^{+0.37} \pm 0.03$	$-0.12_{-0.28}^{+0.31} \pm 0.15$
[15, 16]	$1.12_{-0.018-0.05}^{+0.019+0.05} \pm 0.23$	$0.49_{-0.30}^{+0.30} \pm 0.05$	$-0.10_{-0.16}^{+0.18} \pm 0.03$	$-0.19_{-0.16}^{+0.14} \pm 0.03$
[16, 18]	$1.22_{-0.14-0.06}^{+0.14+0.03} \pm 0.25$	$0.68_{-0.21}^{+0.15} \pm 0.05$	$-0.07_{-0.12}^{+0.13} \pm 0.04$	$-0.44_{-0.05}^{+0.10} \pm 0.03$
[18, 20]	$1.24_{-0.14-0.05}^{+0.14+0.06} \pm 0.26$	$0.62_{-0.27}^{+0.24} \pm 0.04$	$0.01_{-0.14}^{+0.15} \pm 0.04$	$-0.13_{-0.12}^{+0.09} \pm 0.03$
[15, 20]	$1.20_{-0.09-0.04}^{+0.09+0.02} \pm 0.25$	$0.61_{-0.14}^{+0.11} \pm 0.03$	$-0.05_{-0.09}^{+0.09} \pm 0.03$	$-0.29_{-0.07}^{+0.07} \pm 0.03$

established fact that the zero position of the forward-backward asymmetry in the different semileptonic decays of  $B$ -meson has minimal dependence on the FFs [219]. Based on these observations the different forward-backward asymmetries are exploited in the  $\Lambda_b$  decays [62,67–70]. The forward-backward asymmetries corresponding to the lepton angle  $\theta_\ell$  is defined as  $A_{FB}^\ell = (F - B)/(F + B)$ . Similarly, the hadron-side forward-backward asymmetry, i.e., the asymmetry corresponding to the hadronic angle  $\theta_\Lambda$  is  $A_{FB}^\Lambda = (F - B)/(F + B)$ . In both cases,  $F$  and  $B$  are the forward and backward hemispheres, respectively. From Eq. (3.36), these forward-backward asymmetries become

$$A_{FB}^\ell = \frac{3K_{1c}}{4K_{1ss} + 2K_{1cc}}, \quad A_{FB}^\Lambda = \frac{2K_{2ss} + K_{2cc}}{4K_{1ss} + 2K_{1cc}}. \quad (3.46)$$

We take this opportunity to mention that in case of the  $\Lambda_b \rightarrow \Lambda(\rightarrow p\pi)\mu^+\mu^-$  decay, the sequential decay  $\Lambda \rightarrow p\pi$  is parity-violating. Therefore, the helicity components with the polarizations of the proton to be  $\pm\frac{1}{2}$  are not the same and hence the hadron-side forward-backward asymmetry is non-zero in these  $b$ -baryon decays. This is contrary to what we have seen in the  $B \rightarrow K^*(\rightarrow K\pi)\mu^+\mu^-$  decay. In addition to this, the combined lepton-hadron forward-backward asymmetry can be expressed as

$$A_{FB}^{\ell\Lambda} = \frac{3K_{2c}}{8K_{1ss} + 4K_{1cc}}. \quad (3.47)$$

According to experimental point of view, the other interesting observables are the fractions of longitudinal ( $F_L$ ) and transverse ( $F_T$ ) polarized dimuons in  $\Lambda_b \rightarrow \Lambda \mu^+ \mu^-$  decay and  $F_L$  has already been measured in different bins by the LHCb Collaboration [217]. In order to achieve the mathematical formula of these helicity fractions we have to integrate the four-folded differential decay rate given in Eq. (3.36) on  $\theta_\Lambda \in [0, \pi]$  and  $\xi \in [0, 2\pi]$ . Their explicit expressions in terms of  $K_{ij}$  are

$$F_T = \frac{2K_{1cc}}{2K_{1ss} + K_{1cc}}, \quad F_L = 1 - F_T = \frac{2K_{1ss} - K_{1cc}}{2K_{1ss} + K_{1cc}}. \quad (3.48)$$

Experimentally measured values of observables are given in Table 3.3.

### 3.8.2 Decay foldings and angular coefficients

The four-fold decay distribution defined in Eq. (3.36) gives us a chance to single out the different physical observables by studying different foldings. In semileptonic  $B$ -meson decays, such foldings

have been studied in detail especially the penguin asymmetries  $\mathcal{P}$ , where  $P_5^{(\prime)}$  is the most important [201]. On the same lines, by using the foldings defined in Table 3.4, corresponding to different variations of azimuthal angle  $\xi$  while taking  $\theta_\ell \in [0, \frac{\pi}{2}]$  and  $\theta_\Lambda \in [0, \frac{\pi}{2}]$ , these foldings can be expressed in terms of different angular coefficients as:

$$\begin{aligned}
\frac{d\Gamma_1}{\widehat{\Gamma}} &= \frac{3}{8\pi} \left[ 2\frac{K_{1cc}}{\widehat{\Gamma}} + \mathcal{P}_1 \sin^2 \theta_\ell + \frac{1}{2}\mathcal{P}_9 \cos \theta_\Lambda + \mathcal{P}_2 \sin^2 \theta_\ell \cos \theta_\Lambda + \frac{1}{2}\mathcal{P}_8 \cos \theta_\ell + \mathcal{P}_3 \cos \theta_\ell \cos \theta_\Lambda \right], \\
\frac{d\Gamma_2}{\widehat{\Gamma}} &= \frac{3}{8\pi} \left[ 4\frac{K_{1cc}}{\widehat{\Gamma}} + 2\mathcal{P}_1 \sin^2 \theta_\ell + \mathcal{P}_6 \sin \theta_\ell \sin \theta_\Lambda \cos \xi + 2\mathcal{P}_4 \sin \theta_\ell \cos \theta_\ell \sin \theta_\Lambda \sin \xi \right], \\
\frac{d\Gamma_3}{\widehat{\Gamma}} &= \frac{3}{8\pi} \left[ 4\frac{K_{1cc}}{\widehat{\Gamma}} + 2\mathcal{P}_1 \sin^2 \theta_\ell + \mathcal{P}_6 \sin \theta_\ell \sin \theta_\Lambda \cos \xi + 2\mathcal{P}_5 \sin \theta_\ell \cos \theta_\ell \sin \theta_\Lambda \cos \xi + \mathcal{P}_8 \cos \theta_\ell \right], \\
\frac{d\Gamma_4}{\widehat{\Gamma}} &= \frac{3}{8\pi} \left[ 4\frac{K_{1cc}}{\widehat{\Gamma}} + 2\mathcal{P}_1 \sin^2 \theta_\ell + \mathcal{P}_6 \sin \theta_\ell \sin \theta_\Lambda \cos \xi + \mathcal{P}_7 \sin \theta_\ell \sin \theta_\Lambda \sin \xi \right], \\
\frac{d\Gamma_5}{\widehat{\Gamma}} &= \frac{3}{8\pi} \left[ 4\frac{K_{1cc}}{\widehat{\Gamma}} + 2\mathcal{P}_1 \sin^2 \theta_\ell + \mathcal{P}_6 \sin \theta_\ell \sin \theta_\Lambda \cos \xi + 2\mathcal{P}_3 \cos \theta_\ell \cos \theta_\Lambda \right], \\
\frac{d\Gamma_6}{\widehat{\Gamma}} &= \frac{3}{8\pi} \left[ 4\frac{K_{1cc}}{\widehat{\Gamma}} + 2\mathcal{P}_1 \sin^2 \theta_\ell + \mathcal{P}_9 \cos \theta_\Lambda + 2\mathcal{P}_2 \sin^2 \theta_\ell \cos \theta_\Lambda + \mathcal{P}_6 \sin \theta_\ell \sin \theta_\Lambda \cos \xi \right]. \quad (3.49)
\end{aligned}$$

Following things can be noticed from Eq. (3.49):

- The coefficients of  $\sin^2 \theta_\ell$  and  $\sin^2 \theta_\ell \cos \theta_\Lambda$  correspond to the angular coefficients named as  $\mathcal{P}_1$  and  $\mathcal{P}_2$ , respectively.
- The coefficient of  $\cos \theta_\ell \cos \theta_\Lambda$  corresponds to the angular coefficient  $\mathcal{P}_3$  and that of  $\sin \theta_\ell \cos \theta_\ell \sin \theta_\Lambda \sin \xi$  is  $\mathcal{P}_4$ .
- $\mathcal{P}_5$  is the coefficient of  $\sin \theta_\ell \cos \theta_\ell \sin \theta_\Lambda \cos \xi$ , where as  $\mathcal{P}_6$  is the coefficient of  $\sin \theta_\ell \sin \theta_\Lambda \cos \xi$ .
- $\mathcal{P}_7$ ,  $\mathcal{P}_8$  and  $\mathcal{P}_9$  are the coefficients of  $\sin \theta_\ell \sin \theta_\Lambda \sin \xi$ ,  $\cos \theta_\ell$  and  $\cos \theta_\Lambda$ , respectively.

In terms of the different helicity components, the angular coefficients  $\mathcal{P}_i$ ,  $i = 1, \dots, 9$  are

$$\begin{aligned}
\mathcal{P}_1 &= \frac{2}{\widehat{\Gamma}} (K_{1ss} - K_{1cc}), & \mathcal{P}_2 &= \frac{2}{\widehat{\Gamma}} (K_{2ss} - K_{2cc}), & \mathcal{P}_3 &= \frac{2K_{2c}}{\widehat{\Gamma}}, \\
\mathcal{P}_4 &= \frac{2K_{3sc}}{\widehat{\Gamma}}, & \mathcal{P}_5 &= \frac{2K_{4sc}}{\widehat{\Gamma}}, & \mathcal{P}_6 &= \frac{4K_{4s}}{\widehat{\Gamma}}, \\
\mathcal{P}_7 &= \frac{4K_{3s}}{\widehat{\Gamma}}, & \mathcal{P}_8 &= \frac{4K_{1c}}{\widehat{\Gamma}}, & \mathcal{P}_9 &= \frac{4K_{2cc}}{\widehat{\Gamma}}, \quad (3.50)
\end{aligned}$$

where  $\widehat{\Gamma} = \frac{d\Gamma}{ds}$ . It is worth mentioning that while obtaining the different  $\mathcal{P}_i$ 's, we have used the first six foldings defined in Table 3.4, because the last two foldings do not add any new observable.

In order to compare the results with some of the experimentally measured observables and to propose possible candidates that might be useful to establish new physics, the interesting quantities are the normalized fractions calculated in different bins of square of dimuon momentum i.e.,  $s = q^2$ . The normalized branching ratio, various asymmetry observables, and different angular coefficients can be calculated as

$$\langle X \rangle = \frac{\int_{s_{min}}^{s_{max}} X ds}{\int_{s_{min}}^{s_{max}} \left( \frac{d\Gamma}{ds} \right) ds}. \quad (3.51)$$

Table 3.4: Foldings required for  $\mathcal{P}_i$ 's for which  $\theta_\Lambda \in [0, \frac{\pi}{2}]$ ,  $\theta_\ell \in [0, \frac{\pi}{2}]$  and  $\xi$  vary in different range corresponding to different observables [201].

	Folding	$\xi$ Range
1-	$d\Gamma(\xi, \theta_l, \theta_\Lambda) + d\Gamma(\xi - \pi, \theta_l, \theta_\Lambda)$	$[0, \pi]$
2-	$d\Gamma(\xi, \theta_l, \theta_\Lambda) + d\Gamma(\xi, \theta_l, \pi - \theta_\Lambda) + d\Gamma(-\xi, \pi - \theta_l, \theta_\Lambda) + d\Gamma(-\xi, \pi - \theta_l, \pi - \theta_\Lambda)$	$[0, \pi]$
3-	$d\Gamma(\xi, \theta_l, \theta_\Lambda) + d\Gamma(\xi, \theta_l, \pi - \theta_\Lambda) + d\Gamma(-\xi, \theta_l, \theta_\Lambda) + d\Gamma(-\xi, \theta_l, \pi - \theta_\Lambda)$	$[0, \pi]$
4-	$d\Gamma(\xi, \theta_l, \theta_\Lambda) + d\Gamma(\xi, \theta_l, \pi - \theta_\Lambda) + d\Gamma(\xi, \pi - \theta_l, \theta_\Lambda) + d\Gamma(\xi, \pi - \theta_l, \pi - \theta_\Lambda)$	$[0, \pi]$
5-	$d\Gamma(\xi, \theta_l, \theta_\Lambda) + d\Gamma(-\xi, \theta_l, \theta_\Lambda) + d\Gamma(\xi, \pi - \theta_l, \pi - \theta_\Lambda) + d\Gamma(-\xi, \pi - \theta_l, \pi - \theta_\Lambda)$	$[0, \pi]$
6-	$d\Gamma(\xi, \theta_l, \theta_\Lambda) + d\Gamma(-\xi, \theta_l, \theta_\Lambda) + d\Gamma(\xi, \pi - \theta_l, \theta_\Lambda) + d\Gamma(-\xi, \pi - \theta_l, \theta_\Lambda)$	$[0, \pi]$
7-	$d\Gamma(\xi, \theta_l, \theta_\Lambda) + d\Gamma(\pi - \xi, \theta_l, \theta_\Lambda) + d\Gamma(\xi, \pi - \theta_l, \theta_\Lambda) + d\Gamma(\pi - \xi, \pi - \theta_l, \theta_\Lambda)$	$[-\pi/2, \pi/2]$
8-	$d\Gamma(\xi, \theta_l, \theta_\Lambda) + d\Gamma(\pi - \xi, \theta_l, \theta_\Lambda) + d\Gamma(\xi, \pi - \theta_l, \pi - \theta_\Lambda) + d\Gamma(\pi - \xi, \pi - \theta_l, \pi - \theta_\Lambda)$	$[-\pi/2, \pi/2]$

In the next chapters 4 and 5 we perform the numerical analysis of these observables in the SM,  $Z'$ , and RSc models. In chapter 6 we re-derive some of these observables by using the most general model independent Hamiltonian and then discuss them numerically.

## Chapter 4

# Analysis of Angular Observables of $\Lambda_b \rightarrow \Lambda(\rightarrow p\pi)\mu^+\mu^-$ Decay in Standard and $Z'$ Models

The  $Z'$  models are among the minimal extensions of the SM, where an additional  $U(1)'$  gauge boson is introduced. In grand unified theories, extra-dimensional models, and superstring theories, this coupling is incorporated naturally. In this chapter, after summarizing the main features of family non-universal  $Z'$  model, we analyze  $\Lambda_b \rightarrow \Lambda(\rightarrow p\pi)\mu^+\mu^-$  decay in the framework of this model and compare the numerical results of different physical observables with that of the SM predictions and experimental measurements where available.

### 4.1 Family non-universal $Z'$ model

If  $Z'$  gauge couplings are assumed to be family universal, they appear diagonal in mass eigenstate basis even if fermion flavor mixing occurs due to the GIM mechanism. However, it is possible to have a non-diagonal chiral coupling matrix leading to family non-universal  $Z'$  model where the coupling of  $Z'$  boson to different fermion families is different. These couplings favor FCNC processes at the tree level which are stringently forbidden according to the SM. When quark and lepton mixing occur, flavor changing and CP-violating  $Z'$  vertices are generated due to these non-universal  $Z'$  couplings.  $Z - Z'$  mixing is also a cause of flavor violating  $Z$  couplings. Flavor changing and CP-violating processes can constrain  $Z'$  couplings, the mass of  $Z'$  boson, and  $Z - Z'$  mixing angle. The Lagrangian of neutral current in gauge eigenstate basis [220]

$$\mathcal{L}_{NC} = -eJ_\mu^{em} A^\mu - g_1 J_\mu^{(1)} Z_1^\mu - g_2 J_\mu^{(2)} Z_2^\mu, \quad (4.1)$$

where  $Z_1$  and  $Z_2$  are gauge bosons of  $SU(2) \times U(1)$  and additional  $U(1)'$  gauge groups, respectively and  $g_1$  and  $g_2$  are their corresponding gauge couplings. The current corresponding to  $U(1)'$  gauge symmetry reads as:

$$J_\mu^{(2)} = \sum_{i,j} \bar{\psi}_i \gamma_\mu \left[ \epsilon_{\psi L_{ij}}^{(2)} P_L + \epsilon_{\psi R_{ij}}^{(2)} P_R \right] \psi_j, \quad (4.2)$$

where  $\epsilon_{\psi L,R ij}^{(2)}$  is a chiral coupling between  $U(1)'$  gauge boson and fermions and indices  $i, j$  denote quark or lepton flavors. Flavor changing currents can arise either from non-diagonal couplings  $\epsilon^{(2)}$  or non-universal diagonal couplings with fermion mixing. Current in gauge eigenstate basis can be transformed into fermion mass eigenstate basis by diagonalizing  $\epsilon^{(2)}$  by unitary matrices  $V_{L,R}^\psi$  and can be rewritten as

$$J_\mu^{(2)} = \sum_{i,j} \bar{\chi}_i \gamma_\mu \left[ B_{ij}^{\psi L} P_L + B_{ij}^{\psi R} P_R \right] \chi_j, \quad (4.3)$$

where

$$B_{ij}^{\psi L,R} = \left( V_{L,R}^\psi \epsilon_{\psi L,R}^{(2)} V_{L,R}^{\psi \dagger} \right)_{ij}. \quad (4.4)$$

These off-diagonal elements  $B_{ij}^{\psi L,R}$  are generally complex and corresponding phases are independent for different fermion flavors but hermiticity of Lagrangian implies that diagonal elements must be real. For  $b \rightarrow s$  process, the corresponding coupling includes  $b - s - Z'$  vertex which are  $B_{sb}^{L,R} = |B_{sb}^{L,R}| e^{i\phi_s^{L,R}}$  where  $\phi_s^{L,R}$  are weak phases. In the presence of lepton and quark mixing,  $Z'$  vertices corresponding to flavor changing and CP-violating currents are induced.  $Z - Z'$  mixing also leads to flavor violating  $Z$  couplings. There are stringent bounds on the mass of extra  $Z'$  boson and  $Z - Z'$  mixing angle from collider search experiments at Tevatron and precision data respectively.

Long ago Langacker and Plümacher included a family non-universal  $Z'$  boson through additional  $U(1)'$  gauge symmetry [126]. In contrast to the SM, having a non-diagonal chiral coupling matrix; in a family non-universal  $Z'$  model, the FCNC transitions  $b \rightarrow s\ell^+\ell^-$  could be induced at tree level. Ignoring  $Z - Z'$  mixing, along with the assumption that the couplings of right handed quark flavors with  $Z'$  boson are diagonal, the effective Hamiltonian for the  $b \rightarrow s\ell^+\ell^-$  transition corresponding to the  $Z'$  boson becomes [221–223]:

$$\mathcal{H}_{eff}^{Z'}(b \rightarrow s\ell^+\ell^-) = -\frac{2G_F}{\sqrt{2}} V_{tb} V_{ts}^* \left[ \frac{B_{sb} S_{\ell\ell}^L}{V_{tb} V_{ts}^*} (\bar{s}b)_{V-A} (\bar{\ell}\ell)_{V-A} + \frac{B_{sb} S_{\ell\ell}^R}{V_{tb} V_{ts}^*} (\bar{s}b)_{V-A} (\bar{\ell}\ell)_{V+A} \right]. \quad (4.5)$$

In Eq. (4.5),  $S_{\ell\ell}^L$  and  $S_{\ell\ell}^R$  represent the couplings of  $Z'$  boson with the left- and right-handed leptons, respectively. The corresponding off-diagonal left-handed coupling of quarks with the new  $Z'$  boson is taken care of by  $B_{sb} = |\mathcal{B}_{sb}| e^{-i\phi_{sb}}$ , with  $\phi_{sb}$  a new weak phase. In a more sophisticated form, Eq. (4.5) can be written as

$$\mathcal{H}_{eff}^{Z'}(b \rightarrow s\ell^+\ell^-) = -\frac{4G_F}{\sqrt{2}} V_{tb} V_{ts}^* \left[ \Lambda_{sb} C_9^{Z'} O_9 + \Lambda_{sb} C_{10}^{Z'} O_{10} \right], \quad (4.6)$$

where

$$\Lambda_{sb} = \frac{4\pi e^{-i\phi_{sb}}}{\alpha_{EM} V_{tb} V_{ts}^*}; \quad C_9^{Z'} = |\mathcal{B}_{sb}| S_{LL}; \quad C_{10}^{Z'} = |\mathcal{B}_{sb}| D_{LL} \quad (4.7)$$

and

$$S_{LL} = S_{\ell\ell}^L + S_{\ell\ell}^R; \quad D_{LL} = S_{\ell\ell}^L - S_{\ell\ell}^R. \quad (4.8)$$

By comparing Eq. (3.1) and Eq. (4.6) it can be noticed that except  $C_7^{eff}$ , which is absent in the  $Z'$  model, the operator basis of the family non-universal  $Z'$  model is the same as that of the SM

Table 4.1: Numerical values of the different input parameters corresponding to the SM [44, 216]. The WCs are given at the scale  $\mu_b = 4.2$  GeV to NNLL accuracy in the SM [111].

$G_F$	$1.16638 \times 10^{-5}$	$\alpha_s(m_Z)$	0.1182	$m_b^{pole}$	4.78
$\mu$	4.2	$m_Z$	91.1876	$\alpha_e$	$\frac{1}{128}$
$m_\pi$	0.135	$m_K$	0.494	$m_{\Lambda_b}$	5.619
$m_B$	5.279	$V_{tb}V_{ts}^*$	0.04152	$m_\Lambda$	1.116
$\tau_{\Lambda_b}$	1.466ps	$\alpha_\Lambda$	0.64	$C_1$	-0.294
$C_2$	1.017	$C_3$	-0.0059	$C_4$	-0.087
$C_5$	0.0004	$C_6$	0.001	$C_7$	-0.324
$C_8$	-0.176	$C_9$	4.114	$C_{10}$	-4.193

for  $O_{9,10}$ . Hence the contribution arising due to the extra  $Z'$  boson is absorbed in the WCs  $C_9^{eff}$  and  $C_{10}$  leaving the operator basis to be the same as that of the SM.

The total amplitude for the decay  $\Lambda_b \rightarrow \Lambda \ell^+ \ell^-$  is the sum of the SM and  $Z'$  contributions, and it can be formulated in terms of  $\Lambda_b \rightarrow \Lambda$  matrix elements as

$$\begin{aligned} \mathcal{M}^{tot}(\Lambda_b \rightarrow \Lambda \ell^+ \ell^-) &= -\frac{G_F \alpha}{2\sqrt{2}\pi} V_{tb} V_{ts}^* \langle \Lambda(p_\Lambda) | \bar{s} \gamma_\mu (1 - \gamma_5) b | \Lambda_b(p_{\Lambda_b}) \rangle \{ C_9^{tot}(\bar{\ell} \gamma^\mu \ell) + C_{10}^{tot}(\bar{\ell} \gamma^\mu \gamma^5 \ell) \} \\ &\quad - \frac{2m_b}{s} C_7^{eff} \langle \Lambda(p_\Lambda) | \bar{s} i \sigma_{\mu\nu} q^\nu (1 + \gamma^5) b | \Lambda_b(p_{\Lambda_b}) \rangle \bar{\ell} \gamma^\mu \ell, \end{aligned} \quad (4.9)$$

where  $C_9^{tot} = C_9^{eff} + \Lambda_{sb} C_9^{Z'}$  and  $C_{10}^{tot} = C_{10}^{SM} + \Lambda_{sb} C_{10}^{Z'}$ , with  $C_9^{eff}$  defined in Eq. (3.3). Therefore, this leaves the helicity formalism to obtain decay distribution, similar to that mentioned in chapter 3, except the difference that  $C_9^{eff}$  and  $C_{10}$  are replaced with  $C_9^{tot}$  and  $C_{10}^{tot}$  as given in Eq. (4.9).

## 4.2 Numerical Analysis

In this section, we discuss the numerical results obtained for the different observables defined in Sect. 2.9 in both the Standard and  $Z'$  models for the  $\Lambda_b \rightarrow \Lambda(\rightarrow p\pi^-)\mu^+\mu^-$  decay. In  $\Lambda_b \rightarrow \Lambda$  decays, the final state  $\Lambda \rightarrow p\pi^-$  is a parity-violating decay and the corresponding asymmetry parameter ( $\alpha_\Lambda$ ) has been measured experimentally [216]. This is really helpful in disentangling the direct  $\Lambda_b \rightarrow p\pi^-\mu^+\mu^-$  from the one that occurs through the intermediate  $\Lambda$  decay that subsequently decays to  $p\pi^-$ . This is contrary to  $B \rightarrow K^*(\rightarrow K\pi)\mu^+\mu^-$  decay, where the final state  $K^*$  meson decays to  $K\pi$  via the strong interaction. Therefore, the angular analysis of  $\Lambda_b \rightarrow \Lambda(\rightarrow p\pi^-)\mu^+\mu^-$  decay is quite interesting from both theoretical and experimental point of view [62,67]. In addition to the input parameters given in Table 4.1, the other important ingredient in the numerical calculations of  $\Lambda_b$  decays is the FFs. In the numerical calculation, we will use one of the most accurately calculated FFs at the QCD lattice [44] with 2+1 flavor dynamics (c.f. Table 3.1) along with the next-to-next-to-leading logarithmic (NNLL) corrections to the FFs for the SM that are given in [224].

In addition to the FFs, the numerical values of the other input parameters that correspond to the  $Z'$  model are given in Table 4.2. Using these values a quantitative analysis of above calculated observables in various bins of  $s$  is presented in Tables 4.3, 4.4, 4.5 and 4.6. In the whole analysis, we have observed that the results are not sensitive to the different scenarios of the  $Z'$  model; therefore, we have used only the scenario  $\mathcal{S}_1$  to generate the results in various bins of  $s$ .



Table 4.2: Numerical values of the parameters corresponding to the different scenarios of  $Z'$  model [102].

	$ \mathcal{B}_{sb}  \times 10^{-3}$	$\phi_{sb}$ (in degrees)	$S_{LL} \times 10^{-2}$	$D_{LL} \times 10^{-2}$
$\mathcal{S}_1$	$1.09 \pm 0.22$	$-72 \pm 7$	$-2.8 \pm 3.9$	$-6.7 \pm 2.6$
$\mathcal{S}_2$	$2.20 \pm 0.15$	$-82 \pm 4$	$-1.2 \pm 1.4$	$-2.5 \pm 0.9$
$\mathcal{S}_3$	$4.0 \pm 1.5$	$150 \pm 10$	0.8	-2.6

### 4.2.1 Decay rate

The first observable that is of prime interest from both theoretical and experimental points of view is the branching ratio in different bins of  $s$  that can be set up by the experimentalists. From Eq. (3.38), in a bin  $s \in [1.1, 6]$  (large-recoil) the average value of branching ratio in the SM and  $Z'$  model reads:

$$\begin{aligned}\langle \mathcal{B}r \rangle_{\text{SM}} &= (0.466_{-0.394}^{+0.760}) \times 10^{-7}, \\ \langle \mathcal{B}r \rangle_{Z'} &= (0.709_{-0.601}^{+0.115}) \times 10^{-7},\end{aligned}\tag{4.10}$$

whereas the measured value at the LHCb experiment in this particular bin is [217]

$$\langle \mathcal{B}r \rangle_{\text{exp}} = (0.09_{-0.05}^{+0.06}) \times 10^{-7}.\tag{4.11}$$

By looking at Eqs. (4.10) and (4.11), we can say that the deviations from the measured value in this bin are quite large in the SM and ever larger in the  $Z'$  model. One possible reason for such a large deviation is that the FFs are not very precisely calculated in this region. Contrary to this, the calculation of FFs is more precise in  $s \in [15, 20]$  (low-recoil). In this bin the average value of the branching ratio in the SM and  $Z'$  model becomes:

$$\begin{aligned}\langle \mathcal{B}r \rangle_{\text{SM}} &= (0.731_{-0.187}^{+0.198}) \times 10^{-7} \\ \langle \mathcal{B}r \rangle_{Z'} &= (1.179_{-0.233}^{+0.271}) \times 10^{-7}.\end{aligned}\tag{4.12}$$

The experimentally measured value in this bin is [217]

$$\langle \mathcal{B}r \rangle_{\text{exp}} = (1.20 \pm 0.25) \times 10^{-7}.\tag{4.13}$$

This can be reconciled because, in this region, the deviations from the measured values are small compared to that of the large-recoil bin: the deviations are  $3.2\sigma$  and  $0.1\sigma$  in the SM and  $Z'$  model, respectively. Hence, the results of the branching ratio in the  $Z'$  model for the low-recoil bin look more promising when compared with the corresponding experimental value. In the future, when we shall have more data from the LHCb experiment and Belle II, on one hand, it will give us a chance to see possible hints of the extra neutral  $Z'$  boson and on the other hand, it will help us to test the SM predictions with better accuracy.

### 4.2.2 Forward-backward asymmetries

It is a well-known fact that the branching ratio is prone to uncertainties arising due to the FFs. In order to cope with some of the uncertainties, there are observables such as the  $\Lambda$  baryon forward-

backward asymmetry ( $A_{FB}^\Lambda$ ) and lepton forward-backward asymmetry ( $A_{FB}^\ell$ ) that are measured with respect to the baryon angle  $\theta_\Lambda$  and lepton angle  $\theta_\ell$ , respectively. The asymmetry  $A_{FB}^\Lambda$  can be expressed in terms of the ratio of a linear combination of the angular coefficients  $K_{2ss}$  and  $K_{2cc}$  to a linear combination of the angular coefficients  $K_{1ss}$  and  $K_{1cc}$ , as given in Eq. (3.46). Owing to change in the value of Wilson coefficient  $C_9$  in the  $Z'$  model,  $K_{2ss}$  and  $K_{2cc}$  get more contribution as compared to  $K_{1ss}$  and  $K_{1cc}$ . Hence, this will result in significantly different values of  $A_{FB}^\Lambda$  in the SM and  $Z'$  model. In the first large-recoil bin  $s \in [0.1, 2]$  GeV<sup>2</sup>, our results for  $A_{FB}^\Lambda$  in the SM and  $Z'$  model are

$$\langle A_{FB}^\Lambda \rangle_{\text{SM}} = -0.311_{-0.001}^{+0.002}, \quad \langle A_{FB}^\Lambda \rangle_{Z'} = -0.067_{-0.002}^{+0.009},$$

whereas the experimental result in this bin is [217]

$$\langle A_{FB}^\Lambda \rangle_{\text{exp}} = -0.12_{-0.28}^{+0.31}.$$

It can be noticed that in comparison with the central values of the experimental measurements in  $s \in [0.1, 2]$  GeV<sup>2</sup>, the value of  $Z'$  model is 1.8 times smaller, whereas the one in the SM is 2.5 times higher. In the low-recoil region ( $s \in [15, 20]$  GeV<sup>2</sup>) the calculated values of  $A_{FB}^\Lambda$  are

$$\langle A_{FB}^\Lambda \rangle_{\text{SM}} = -0.273_{-0.002}^{+0.003}, \quad \langle A_{FB}^\Lambda \rangle_{Z'} = -0.137_{-0.001}^{+0.001}$$

and the experimental value in this particular bin is [217]

$$\langle A_{FB}^\Lambda \rangle_{\text{exp}} = -0.29_{-0.07}^{+0.07}.$$

It can be seen easily that at low-recoil, the SM prediction is close to the experimentally measured value and the deviation is  $0.2\sigma$ . The  $Z'$  value of  $A_{FB}^\Lambda$  exceeds the experimental result by  $2.2\sigma$ . From the above discussion, it is clear that in the first large-recoil bin both the values of the SM and  $Z'$  model deviate significantly from the experimental result for this bin, whereas at low-recoil the SM prediction is much closer to the experimental result compared with the  $Z'$  model. We hope that in the future when more data comes from the LHCb, the results of measurements will become more concrete to compare with the SM and to see if the deviations can be accommodated with the  $Z'$  model.

Another observable which is clean from the QCD uncertainties and that has been experimentally measured is  $A_{FB}^\ell$ , which is an asymmetry with respect to the lepton scattering angle ( $\theta_\ell$ ); its mathematical expression is given in Eq. (3.46). Here, it can be noticed that  $A_{FB}^\ell$  depends on the angular coefficient  $K_{1c}$  and its denominator is the same as that of  $A_{FB}^\Lambda$ . The angular coefficient  $K_{1c}$  is higher for the SM than the  $Z'$  model for  $s < 4$  GeV<sup>2</sup>, whereas its behavior reverses when  $s > 4$  GeV<sup>2</sup>. For  $s < 4$  GeV<sup>2</sup>,  $K_{1c}$  is dominated by  $C_9^{Z'}$  whereas for  $s > 4$  GeV<sup>2</sup>, the terms containing  $C_7^{Z'}$  dominate over the one that contains  $C_9^{Z'}$ . Therefore,  $A_{FB}^\ell$  increases with  $s$  at the start of the large-recoil and then it starts decreasing and crosses the zero point at around 4 GeV<sup>2</sup>. Our results for  $\langle A_{FB}^\ell \rangle$  in the SM and  $Z'$  model calculated in the experimentally set-up bin  $[0.1, 2]$  GeV<sup>2</sup> are

$$\langle A_{FB}^\ell \rangle_{\text{SM}} = 0.083_{-0.035}^{+0.001}, \quad \langle A_{FB}^\ell \rangle_{Z'} = 0.040_{-0.024}^{+0.003}.$$

The experimental value of  $A_{FB}^\ell$  in the corresponding bin is [217]:

$$\langle A_{FB}^\ell \rangle_{\text{exp}} = 0.37_{-0.48}^{+0.37}. \quad (4.14)$$

In Eq. (4.14), one can see that the errors are significant, and it is likely to improve with future data from LHCb. However, the current central values are significantly away from the SM and  $Z'$  values. In low-recoil region ( $s \in [15, 20]$  GeV<sup>2</sup>) the results for this asymmetry are:

$$\langle A_{FB}^\ell \rangle_{\text{SM}} = -0.180_{-0.005}^{+0.007}, \quad \langle A_{FB}^\ell \rangle_{Z'} = -0.135_{-0.002}^{+0.003}$$

and for comparison the corresponding experimental value in this bin is

$$\langle A_{FB}^\ell \rangle_{\text{exp}} = -0.05_{-0.09}^{+0.09}.$$

It can be deduced that in this particular bin the average value of  $A_{FB}^\ell$  in  $Z'$  is comparable to the lower limit of the experimentally measured value, i.e.,  $-0.14$ .

The last in the category of the forward-backward asymmetry is  $A_{FB}^{\ell\Lambda}$  which mainly depends on the angular coefficient  $K_{2c}$  (c.f. Eq. (3.47)). Compared to the SM, the value of  $K_{2c}$  is higher in the  $Z'$  model. At large-recoil our results in the SM and  $Z'$  model are

$$\langle A_{FB}^{\ell\Lambda} \rangle_{\text{SM}} = -0.011_{-0.006}^{+0.003}, \quad \langle A_{FB}^{\ell\Lambda} \rangle_{Z'} = -0.009_{-0.003}^{+0.002},$$

whereas at the low-recoil, the combined lepton-hadron forward-backward asymmetry is

$$\langle A_{FB}^{\ell\Lambda} \rangle_{\text{SM}} = 0.069_{-0.002}^{+0.002}, \quad \langle A_{FB}^{\ell\Lambda} \rangle_{Z'} = 0.087_{-0.002}^{+0.001}.$$

It can be seen that at large-recoil the deviations between the SM and  $Z'$  model are small, and it grows significantly in the low-recoil region.

### 4.2.3 Longitudinal and Transverse polarization fractions

The next observable to be discussed here is the fraction of longitudinal polarization ( $F_L$ ) of the dilepton system. Due to linear combinations of the same angular coefficients ( $K_{1ss}$  and  $K_{1cc}$ ) in both numerator and denominator of  $F_L$ , the  $Z'$  model is not much different from the SM. The values in one of the large-recoil bins,  $[0.1, 2]$ , for the SM and  $Z'$  model are:

$$\langle F_L \rangle_{\text{SM}} = 0.576_{-0.174}^{+0.031}, \quad \langle F_L \rangle_{Z'} = 0.463_{-0.095}^{+0.018}$$

and the corresponding experimental result is:

$$\langle F_L \rangle_{\text{exp}} = 0.56_{-0.56}^{+0.23}.$$

It can be observed that it is in good agreement with the SM value and somewhat differs from the corresponding value in  $Z'$  model for this bin.

At low-recoil, the values for SM and  $Z'$  are:

$$\langle F_L \rangle_{\text{SM}} = 0.713_{-0.008}^{+0.010}, \quad \langle F_L \rangle_{Z'} = 0.590_{-0.005}^{+0.007}$$

and the corresponding experimental result for this bin is:

$$\langle F_L \rangle_{\text{exp}} = 0.61_{-0.14}^{+0.11}.$$

In contrast to the large-recoil, at low-recoil, the results of  $F_L$  in the  $Z'$  model are closer to the experimentally measured results. Therefore, to uncover the imprints of the neutral boson in the longitudinal helicity fraction of the dimuon system in  $\Lambda_b \rightarrow \Lambda(\rightarrow p\pi)\mu^+\mu^-$  decay, the low-recoil bin might provide fertile ground.

Having compared the SM and  $Z'$  model with the experimentally measured values of the different observables as discussed above, we will now exploit some other observables that may be of interest in the future at the LHCb and different B-factories. In connection with  $F_L$ , the fraction of transverse polarization  $F_T$  depends on  $K_{1cc}$  and  $K_{1ss}$  and its value at the large-recoil is:

$$\langle F_T \rangle_{\text{SM}} = 0.136_{-0.002}^{+0.021}, \quad \langle F_T \rangle_{Z'} = 0.134_{-0.000}^{+0.012},$$

where it can be seen that the value in the  $Z'$  is very close to the SM result. However, at low-recoil,

$$\langle F_T \rangle_{\text{SM}} = 0.287_{-0.010}^{+0.008}, \quad \langle F_T \rangle_{Z'} = 0.410_{-0.007}^{+0.005},$$

the results for the  $Z'$  model significantly differ from those of the SM. Hence, measurement of the fraction of transverse polarization in the low-recoil region will help us to see the possible contribution of the neutral  $Z'$  boson in these  $b$ - baryon decays.

#### 4.2.4 Asymmetry parameters $\alpha'$ s

It is well known that in the case of the  $\Lambda_b \rightarrow \Lambda J/\psi$  the different asymmetries have been experimentally measured. Motivated by this fact, let us explore the asymmetries corresponding to the hadronic angle  $\theta_\Lambda$  and  $\theta_\ell$  one by one. The asymmetry arising due to the angle  $\theta_\Lambda$  is defined as  $\alpha_{\theta_\Lambda}$  and its explicit expression is given in Eq. (3.40); the corresponding numerical values at low- and large-recoil bins are tabulated in Table 4.3. In the large-recoil bin  $s \in [1, 6]$  GeV<sup>2</sup> the value reads:

$$\langle \alpha_{\theta_\Lambda} \rangle_{\text{SM}} = -0.984_{-0.001}^{+0.007}, \quad \langle \alpha_{\theta_\Lambda} \rangle_{Z'} = -0.390_{-0.006}^{+0.027}.$$

Similarly, in the low-recoil bin  $s \in [15, 20]$  GeV<sup>2</sup>, our calculated results for this observable are:

$$\langle \alpha_{\theta_\Lambda} \rangle_{\text{SM}} = -0.851_{-0.007}^{+0.010}, \quad \langle \alpha_{\theta_\Lambda} \rangle_{Z'} = -0.427_{-0.001}^{+0.001}.$$

Here we can see that  $\alpha_{\theta_\Lambda}$  differs in the  $Z'$  model from the SM results significantly in both low- and large-recoil bins.

Likewise, the asymmetry  $\alpha'_{\theta_\ell}$  that corresponds to angle  $\theta_\ell$  given in Eq. (3.42) depends on the angular coefficient  $K_{1c}$ , and therefore its behavior is similar to  $A_{FB}^\ell$ . The results in the large-recoil bin  $s \in [1, 6]$  GeV<sup>2</sup> for the SM and  $Z'$  model are:

$$\langle \alpha'_{\theta_\ell} \rangle_{\text{SM}} = 0.047_{-0.016}^{+0.039}, \quad \langle \alpha'_{\theta_\ell} \rangle_{Z'} = 0.027_{-0.002}^{+0.001},$$

where the value of  $\alpha'_{\theta_\ell}$  in the SM is 1.7 times that of the  $Z'$  model. Similarly in the low-recoil bin

( $s \in [15, 20]$  GeV<sup>2</sup>) the results are:

$$\langle \alpha'_{\theta_\ell} \rangle_{\text{SM}} = -0.280_{-0.010}^{+0.012}, \quad \langle \alpha'_{\theta_\ell} \rangle_{Z'} = -0.225_{-0.004}^{+0.006}.$$

It can be noticed that the results in the low-recoil bin are an order of magnitude large than the corresponding values in the large-recoil bin both in the SM and in the  $Z'$  model. These values are quite large to be measured at the LCHb experiment to test the predictions of the SM.

We now discuss  $\alpha_{\theta_\ell}$ , which depends upon the angular coefficients  $K_{1ss}$  and  $K_{1cc}$ . This is not significantly affected by the couplings of the  $Z'$  model and hence shows little deviations from the SM, especially in the large-recoil region. In this region, the numerical values are:

$$\langle \alpha_{\theta_\ell} \rangle_{\text{SM}} = -0.854_{-0.002}^{+0.024}, \quad \langle \alpha_{\theta_\ell} \rangle_{Z'} = -0.857_{-0.001}^{+0.014},$$

where it is clear that the values in both the models are almost the same. Similarly in low-recoil region, the results in the SM and  $Z'$  model are:

$$\langle \alpha_{\theta_\ell} \rangle_{\text{SM}} = -0.665_{-0.014}^{+0.010}, \quad \langle \alpha_{\theta_\ell} \rangle_{Z'} = -0.485_{-0.011}^{+0.008}.$$

In comparison to the low- $s$  region, here the values of  $\alpha'_{\theta_\ell}$  in the SM and  $Z'$  model differ significantly. Therefore, to establish the possible new physics arising in the  $Z'$  model, an analysis of  $\alpha_{\theta_\ell}$  in the high- $s$  region will serve as a useful probe.

Looking at  $\alpha_\xi$  discloses that it depends upon  $K_{4s}$ . At very low- $s$ ,  $C_7$  term dominates in the SM which results in negative  $K_{4s}$  but for  $s > 2$  GeV<sup>2</sup>, the Wilson Coefficient  $C_9$  term dominates, giving positive results. For the  $Z'$  model  $C_9^{Z'}$  gets affected much more than  $C_7^{Z'}$  for the entire range of  $s$  and hence  $\alpha_\xi$  is expected to change significantly with  $s$  in the  $Z'$  model from the corresponding SM result. The values of  $\alpha_\xi$  in the bin  $s \in [1, 6]$  GeV<sup>2</sup> for the SM and  $Z'$  model are:

$$\langle \alpha_\xi \rangle_{\text{SM}} = 0.040_{-0.016}^{+0.070}, \quad \langle \alpha_\xi \rangle_{Z'} = 0.130_{-0.060}^{+0.015}$$

and for the low-recoil region  $s \in [15, 20]$  GeV<sup>2</sup>, the values of the observable are:

$$\langle \alpha_\xi \rangle_{\text{SM}} = 0.047_{-0.004}^{+0.003}, \quad \langle \alpha_\xi \rangle_{Z'} = -0.448_{-0.006}^{+0.004}.$$

Hence, it can be revealed that in the SM the value of  $\alpha_\xi$  is almost the same in the low- and large-recoil bins, which is not the case for the  $Z'$  model where a large deviation is observed in both bins. Also, in both these bins, the results of the  $Z'$  model are quite large compared to the SM results, and experimental observation of  $\alpha_\xi$  will act as a useful observable.

The longitudinal (transverse) asymmetry parameter  $\alpha_L$  ( $\alpha_U$ ) is the ratio of the helicity combinations  $K_{2ss}$  ( $K_{2cc}$ ) to  $K_{1ss}$  as depicted in Eq. (3.45). Their values in the large-recoil region are:

$$\langle \alpha_L(\alpha_U) \rangle_{\text{SM}} = -0.989_{-0.000}^{+0.006}(-0.916_{-0.004}^{+0.010}) \quad \langle \alpha_L(\alpha_U) \rangle_{Z'} = -0.386_{-0.003}^{+0.016}(-0.445_{-0.040}^{+0.168})$$

where we can see that in this bin the values of both the longitudinal and the transverse asymmetry parameters in the  $Z'$  model differ significantly from their respective values in the SM. This is due

to the fact that the contribution of the extra neutral boson  $Z'$  affects the value of  $K_{1ss}$  lesser than  $K_{2ss}(K_{2cc})$ . Now, in the low-recoil region

$$\langle\alpha_L(\alpha_U)\rangle_{\text{SM}} = -0.852^{+0.011}_{-0.008}(-0.844^{+0.003}_{-0.002}) \quad \langle\alpha_L(\alpha_U)\rangle_{Z'} = -0.458^{+0.001}_{-0.001}(-0.307^{+0.002}_{-0.002}).$$

It can be deduced that the value of  $\alpha_L(\alpha_U)$  in the  $Z'$  is half that of the SM model in this bin. With the current luminosity of the LHCb experiment, the values of these observables are in the measurable range. Hence the experimental observation of these observables will give us a chance to test the predictions of the SM and the possibility of exploring the imprints of the  $Z'$  boson in  $\Lambda_b \rightarrow \Lambda\mu^+\mu^-$  decays.

#### 4.2.5 Angular observables from foldings

It is a well-established fact that certain asymmetries, such as  $\mathcal{P}_5^{(\prime)}$ , that correspond to different foldings in  $B \rightarrow K^*\mu^+\mu^-$  have shown significant deviations from the SM predictions. It makes them a fertile hunting ground to dig for the various beyond-SM scenarios that give possible explanations and  $Z'$  is one of them [225]. Motivated by this fact, we have calculated such foldings in the decay under consideration; their expressions in terms of the helicity combinations are given in Eq. (3.50). Among them, the first one is the  $\mathcal{P}_1$  which behaves very similar to  $F_T$ . The average values of  $\mathcal{P}_1$  at large-recoil in the SM and  $Z'$  model are

$$\langle\mathcal{P}_1\rangle_{\text{SM}} = 0.796^{+0.002}_{-0.031}, \quad \langle\mathcal{P}_1\rangle_{Z'} = 0.799^{+0.001}_{-0.018}$$

and at low-recoil, the values are

$$\langle\mathcal{P}_1\rangle_{\text{SM}} = 0.569^{+0.017}_{-0.009}, \quad \langle\mathcal{P}_1\rangle_{Z'} = 0.386^{+0.010}_{-0.008}.$$

Here, we can see that in the large-recoil region, the values in the SM and  $Z'$  model are very close, which is not the situation in the low-recoil region where the value of the SM is 1.5 times that of the  $Z'$  model.

$\mathcal{P}_2$  is the ratio of a linear combination of  $K_{2ss}$  and  $K_{2cc}$  to the total decay rate. In most of the bins, the SM results are more than twice the  $Z'$  model values, and this can be seen in the results at large-recoil, which are:

$$\langle\mathcal{P}_2\rangle_{\text{SM}} = 0.512^{+0.001}_{-0.022}, \quad \langle\mathcal{P}_2\rangle_{Z'} = 0.193^{+0.001}_{-0.002}.$$

The situation persists similarly at the low-recoil:

$$\langle\mathcal{P}_2\rangle_{\text{SM}} = 0.316^{+0.003}_{-0.002}, \quad \langle\mathcal{P}_2\rangle_{Z'} = 0.153^{+0.004}_{-0.003}.$$

The behavior of  $\mathcal{P}_3$  is similar to  $A_{FB}^\Lambda$ . The average values of  $\mathcal{P}_3$  at large-recoil are:

$$\langle\mathcal{P}_3\rangle_{\text{SM}} = -0.030^{+0.009}_{-0.015}, \quad \langle\mathcal{P}_3\rangle_{Z'} = -0.025^{+0.004}_{-0.009},$$

whereas the results at low-recoil become:

$$\langle \mathcal{P}_3 \rangle_{\text{SM}} = 0.184_{-0.007}^{+0.004} \quad \langle \mathcal{P}_3 \rangle_{Z'} = 0.232_{-0.004}^{+0.003}$$

It can be observed that just like  $\mathcal{P}_1$ , for the asymmetry defined by  $\mathcal{P}_3$  the average values in the SM and  $Z'$  model, are comparable at large-recoil but differ significantly at low-recoil. We have observed that with  $3\text{fb}^{-1}$  of data, the LHCb collaboration has measured the  $A_{FB}^h$  which is of the same order as  $\mathcal{P}_3$ . Therefore, it is expected that in the future  $\mathcal{P}_3$  will be measured.

Average values of  $\mathcal{P}_5$  at large-recoil read as:

$$\langle \mathcal{P}_5 \rangle_{\text{SM}} = 0.030_{-0.013}^{+0.048}, \quad \langle \mathcal{P}_5 \rangle_{Z'} = 0.034_{-0.004}^{+0.013},$$

and results at low-recoil are

$$\langle \mathcal{P}_5 \rangle_{\text{SM}} = 0.163_{-0.000}^{+0.001} \quad \langle \mathcal{P}_5 \rangle_{Z'} = 0.091_{-0.001}^{+0.002}$$

This case is similar to  $\mathcal{P}_1$  and  $\mathcal{P}_3$  as the values in both models are very close at large-recoil and deviations started to appear in the low-recoil region of  $s$ .

Now we come to  $\mathcal{P}_6$ , which depends on the angular coefficient  $K_{4s}$  and hence behaves as  $\alpha_\xi$ . The values of the observable in the SM and  $Z'$  at large-recoil become

$$\langle \mathcal{P}_6 \rangle_{\text{SM}} = 0.056_{-0.023}^{+0.097}, \quad \langle \mathcal{P}_6 \rangle_{Z'} = 0.180_{-0.083}^{+0.021},$$

and the results at low-recoil are

$$\langle \mathcal{P}_6 \rangle_{\text{SM}} = 0.066_{-0.007}^{+0.002}, \quad \langle \mathcal{P}_6 \rangle_{Z'} = 0.621_{-0.008}^{+0.005}.$$

From the above results, it can be easily deduced that the value of  $\mathcal{P}_6$  in the  $Z'$  model differs significantly from the SM results both at large- and low-recoil, which is also the case for  $\alpha_\xi$ . In particular, in the low-recoil region, the value of this asymmetry is an order of magnitude larger than in the large-recoil bin and it is in the experimentally measurable range with the current luminosity of the LHCb experiment.

The next observable to be discussed is  $\mathcal{P}_8$  which mainly depends on the angular coefficient  $K_{1c}$  and therefore its behavior is exactly the same as  $A_{FB}^\ell$ . Its results in large-recoil bin are:

$$\langle \mathcal{P}_8 \rangle_{\text{SM}} = 0.088_{-0.032}^{+0.070}, \quad \langle \mathcal{P}_8 \rangle_{Z'} = 0.051_{-0.003}^{+0.003},$$

and at low-recoil:

$$\langle \mathcal{P}_8 \rangle_{\text{SM}} = -0.480_{-0.012}^{+0.020}, \quad \langle \mathcal{P}_8 \rangle_{Z'} = -0.359_{-0.006}^{+0.007}.$$

We can see that there is an order of magnitude difference between the results in the large- and low-recoil region. Therefore, the number of events required to see the deviations in the low-recoil region is much smaller compared to the large-recoil region.

The last observable in this list is  $\mathcal{P}_9$ , which depends upon the angular coefficient  $K_{2cc}$ . Its

values at large-recoil are:

$$\langle \mathcal{P}_9 \rangle_{SM} = -0.160_{-0.023}^{+0.001}, \quad \langle \mathcal{P}_9 \rangle_{Z'} = -0.076_{-0.007}^{+0.024},$$

and at low-recoil the results become:

$$\langle \mathcal{P}_9 \rangle_{SM} = -0.308_{-0.008}^{+0.013}, \quad \langle \mathcal{P}_9 \rangle_{Z'} = -0.161_{-0.004}^{+0.003}.$$

We can see that the value of the SM is almost twice of the  $Z'$  model in both regions.

In the case of  $\Lambda_b \rightarrow \Lambda(\rightarrow p\pi)\mu^+\mu^-$  decay, the LHCb experiment has measured the value of the branching ratio, forward-backward asymmetries, and longitudinal dimuon helicity fraction in small bins of  $s$ . Therefore, we have tabulated the values of the above-mentioned observables in large- and low-recoil regions in Table 4.3, and various small bins in Tables 4.4, 4.5 and 4.6. In addition, to see the profile of these asymmetries we have plotted them graphically in Figs. 4.1, 4.2 and Fig. 4.3 with the square of the dimuon momentum  $s$ . We hope that in the future when more precise results for various asymmetries come from the LHCb, it will give us a chance to compare the profile of various asymmetries calculated here with the experiments both for the SM and the  $Z'$  model.

Table 4.3: Average values of different observables for  $\Lambda_b \rightarrow \Lambda(\rightarrow p\pi)\mu^+\mu^-$  in low and large-recoil regions.

		$\langle \alpha_{\theta_\Lambda} \rangle$	$\langle \alpha'_{\theta_\Lambda} \rangle$	$\langle \alpha_{\theta_l} \rangle$	$\langle \alpha_\xi \rangle$
[1, 6]	SM	$-0.984_{-0.001}^{+0.007}$	$0.047_{-0.016}^{+0.039}$	$-0.854_{-0.002}^{+0.024}$	$0.040_{-0.016}^{+0.070}$
	$Z'$	$-0.390_{-0.006}^{+0.027}$	$0.027_{-0.002}^{+0.001}$	$-0.857_{-0.001}^{+0.014}$	$0.130_{-0.060}^{+0.015}$
[15, 20]	SM	$-0.851_{-0.007}^{+0.010}$	$-0.280_{-0.010}^{+0.012}$	$-0.665_{-0.014}^{+0.010}$	$0.047_{-0.004}^{+0.003}$
	$Z'$	$-0.427_{-0.001}^{+0.001}$	$-0.225_{-0.004}^{+0.006}$	$-0.485_{-0.011}^{+0.008}$	$0.448_{-0.006}^{+0.004}$
		$\langle \alpha'_\xi \rangle$	$\langle \alpha_U \rangle$	$\langle \alpha_L \rangle$	$\langle d\mathcal{B}/ds \rangle \times 10^{-7}$
[1, 6]	SM	$0.000_{-0.001}^{+0.000}$	$-0.916_{-0.004}^{+0.010}$	$-0.989_{-0.000}^{+0.006}$	$0.466_{-0.394}^{+0.760}$
	$Z'$	$-0.002_{-0.000}^{+0.001}$	$-0.445_{-0.040}^{+0.168}$	$-0.386_{-0.003}^{+0.016}$	$0.709_{-0.601}^{+0.115}$
[15, 20]	SM	$-0.056_{-0.002}^{+0.001}$	$-0.844_{-0.002}^{+0.003}$	$-0.852_{-0.008}^{+0.011}$	$0.731_{-0.187}^{+0.198}$
	$Z'$	$-0.049_{-0.002}^{+0.002}$	$-0.307_{-0.002}^{+0.002}$	$-0.458_{-0.001}^{+0.001}$	$1.179_{-0.233}^{+0.271}$
		$\langle F_T \rangle$	$\langle F_L \rangle$	$\langle A_{FB}^{\ell\Lambda} \rangle$	$\langle \mathcal{P}_1 \rangle$
[1, 6]	SM	$0.136_{-0.002}^{+0.021}$	$0.864_{-0.021}^{+0.002}$	$-0.011_{-0.006}^{+0.003}$	$0.796_{-0.031}^{+0.002}$
	$Z'$	$0.134_{-0.000}^{+0.012}$	$0.866_{-0.012}^{+0.000}$	$-0.009_{-0.003}^{+0.002}$	$0.799_{-0.018}^{+0.001}$
[15, 20]	SM	$0.287_{-0.010}^{+0.008}$	$0.713_{-0.008}^{+0.010}$	$0.069_{-0.002}^{+0.002}$	$0.569_{-0.009}^{+0.017}$
	$Z'$	$0.410_{-0.007}^{+0.005}$	$0.590_{-0.005}^{+0.007}$	$0.087_{-0.002}^{+0.001}$	$0.386_{-0.008}^{+0.010}$
		$\langle \mathcal{P}_2 \rangle$	$\langle \mathcal{P}_3 \rangle$	$\langle \mathcal{P}_5 \rangle$	$\langle \mathcal{P}_6 \rangle$
[1, 6]	SM	$0.512_{-0.022}^{+0.001}$	$-0.030_{-0.015}^{+0.009}$	$0.030_{-0.013}^{+0.048}$	$0.056_{-0.023}^{+0.097}$
	$Z'$	$0.193_{-0.002}^{+0.001}$	$-0.025_{-0.009}^{+0.004}$	$0.034_{-0.004}^{+0.013}$	$0.180_{-0.083}^{+0.021}$
[15, 20]	SM	$0.316_{-0.002}^{+0.003}$	$0.184_{-0.007}^{+0.004}$	$0.163_{-0.000}^{+0.001}$	$0.066_{-0.007}^{+0.002}$
	$Z'$	$0.153_{-0.003}^{+0.004}$	$0.232_{-0.004}^{+0.003}$	$0.091_{-0.001}^{+0.002}$	$0.621_{-0.008}^{+0.005}$
		$\langle \mathcal{P}_8 \rangle$	$\langle \mathcal{P}_9 \rangle$		
[1, 6]	SM	$0.088_{-0.032}^{+0.070}$	$-0.160_{-0.023}^{+0.001}$		
	$Z'$	$0.051_{-0.003}^{+0.003}$	$-0.076_{-0.007}^{+0.024}$		
[15, 20]	SM	$-0.480_{-0.012}^{+0.020}$	$-0.308_{-0.008}^{+0.013}$		
	$Z'$	$-0.359_{-0.006}^{+0.007}$	$-0.161_{-0.003}^{+0.004}$		



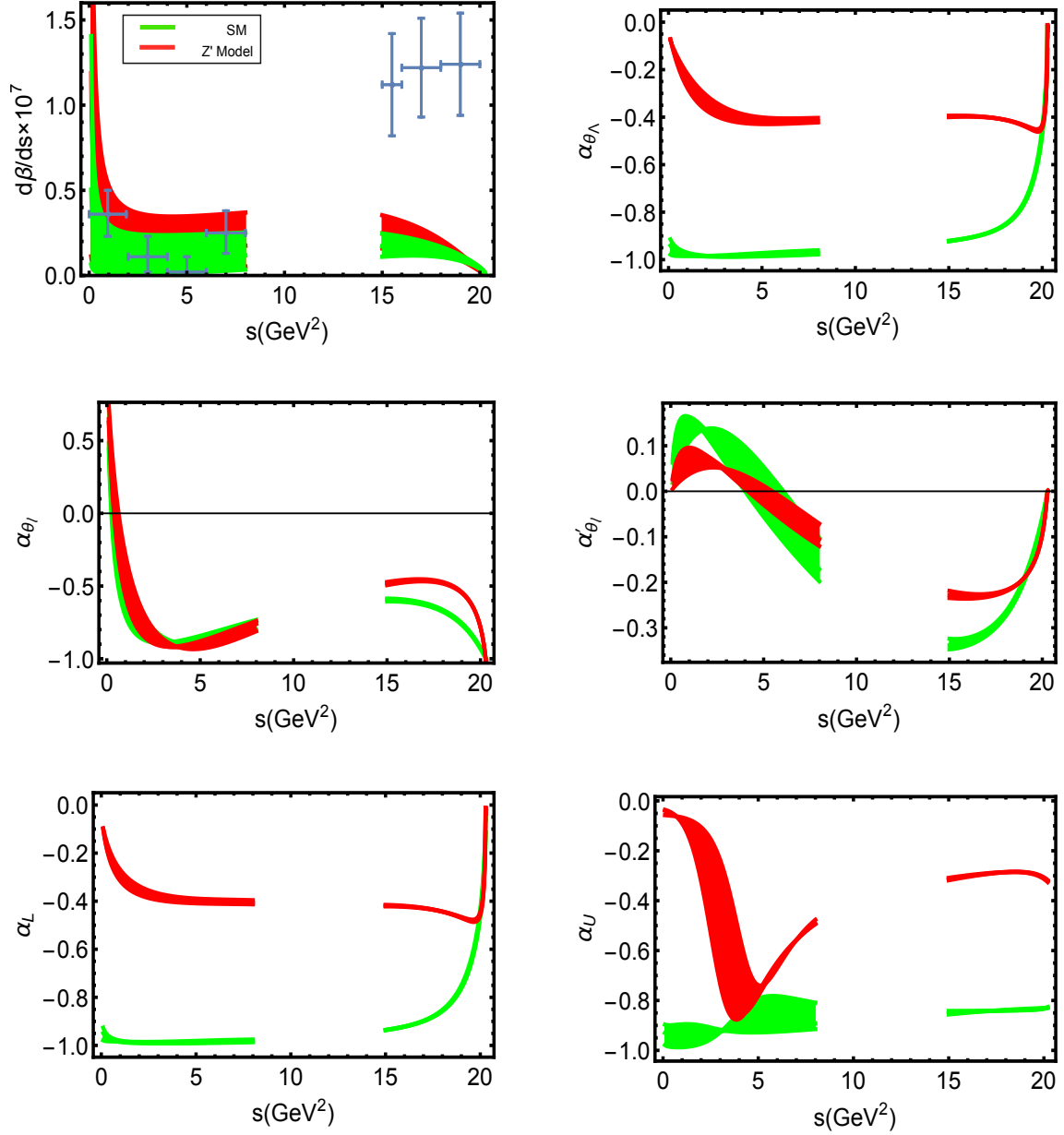


Figure 4.1: Branching ratio and various asymmetry parameters are plotted as a function of  $s$ . The green curve correspond the SM results and red to the  $Z'$  model. In both cases, the bands corresponds to the uncertainties in the FFs and other input parameters.

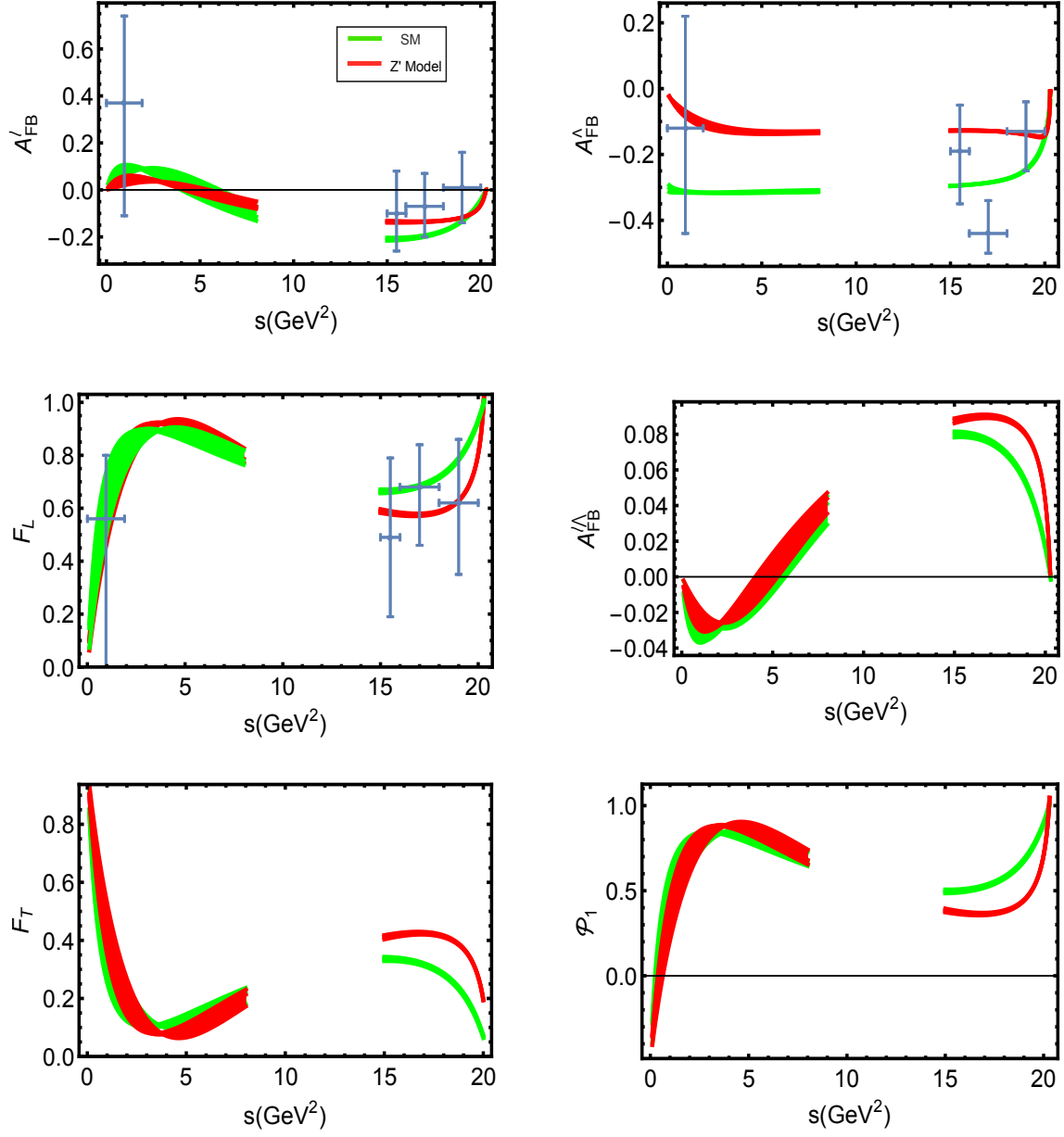


Figure 4.2: Different forward-backward asymmetries,  $F_L$ ,  $F_T$  and  $\mathcal{P}_1$  are plotted as function of  $s$ . The color coding is same as in Fig. 4.1.

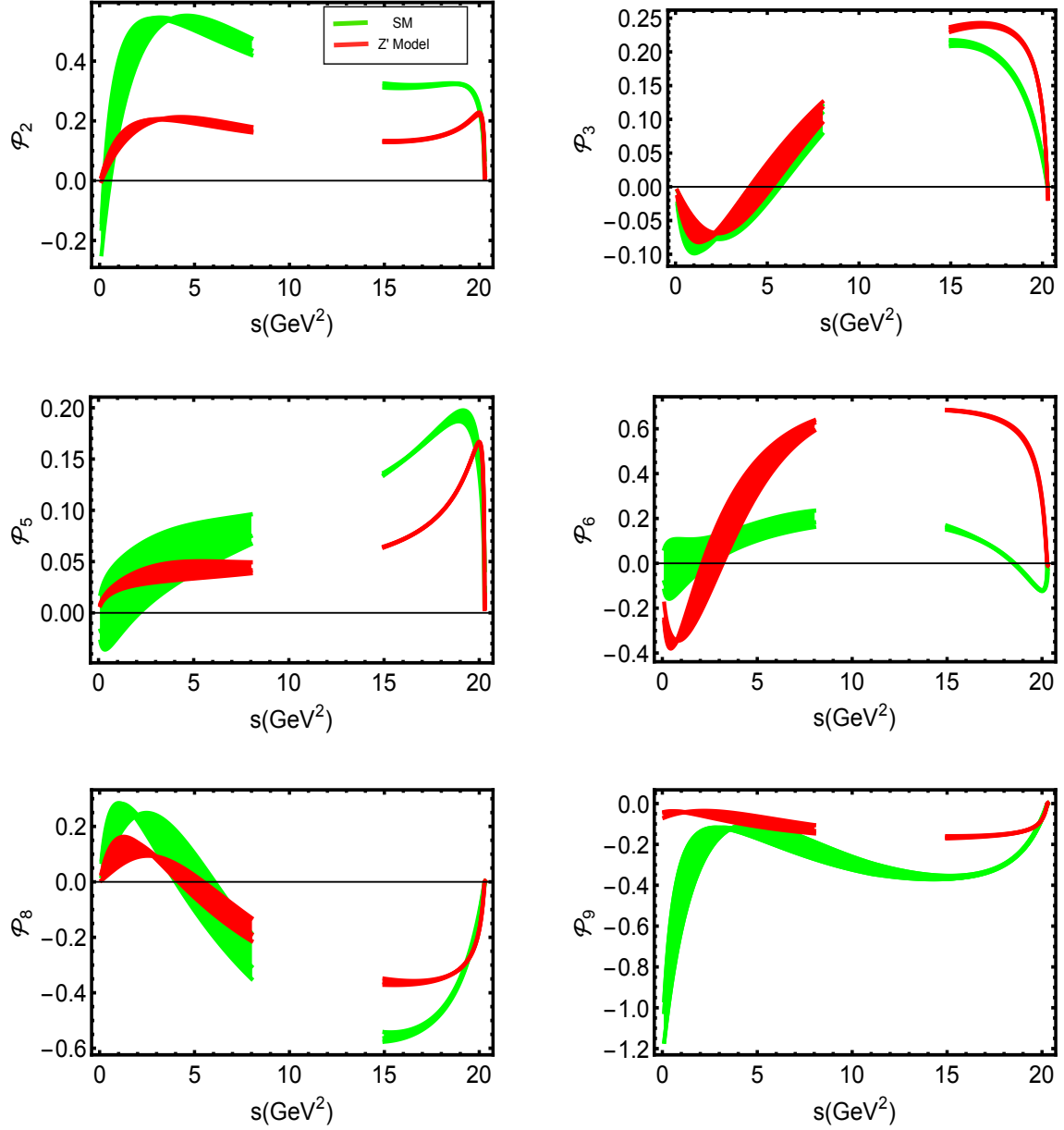


Figure 4.3: The folded distributions  $\mathcal{P}_{2,\dots,9}$ , except  $\mathcal{P}_4$  are plotted as function of  $s$ . The color coding is same as in Fig. 4.1.

Table 4.4: Numerical results of observables for the decay  $\Lambda_b \rightarrow \Lambda(\rightarrow p\pi)\mu^+\mu^-$  for the SM and  $Z'$  model in appropriate bins.

		$\langle\alpha_{\theta_\Lambda}\rangle$	$\langle\alpha'_{\theta_i}\rangle$	$\langle\alpha_{\theta_i}\rangle$	$\langle\alpha_\xi\rangle$
[0.1, 2]	SM	$-0.970^{+0.012}_{-0.014}$	$0.140^{+0.001}_{-0.049}$	$-0.463^{+0.315}_{-0.049}$	$-0.058^{+0.129}_{-0.026}$
	$Z'$	$-0.209^{+0.028}_{-0.005}$	$0.073^{+0.005}_{-0.042}$	$-0.265^{+0.191}_{-0.033}$	$-0.208^{+0.003}_{-0.001}$
[1, 2]	SM	$-0.983^{+0.005}_{-0.002}$	$0.141^{+0.008}_{-0.013}$	$-0.788^{+0.223}_{-0.028}$	$-0.032^{+0.110}_{-0.020}$
	$Z'$	$-0.318^{+0.054}_{-0.010}$	$0.086^{+0.003}_{-0.040}$	$-0.710^{+0.193}_{-0.030}$	$-0.137^{+0.020}_{-0.074}$
[2, 4]	SM	$-0.987^{+0.006}_{-0.001}$	$0.076^{+0.048}_{-0.020}$	$-0.887^{+0.046}_{-0.001}$	$0.030^{+0.064}_{-0.013}$
	$Z'$	$-0.397^{+0.040}_{-0.008}$	$0.046^{+0.001}_{-0.004}$	$-0.899^{+0.048}_{-0.003}$	$0.100^{+0.029}_{-0.120}$
[4, 6]	SM	$-0.984^{+0.012}_{-0.002}$	$-0.030^{+0.079}_{-0.028}$	$-0.858^{+0.016}_{-0.035}$	$0.086^{+0.046}_{-0.013}$
	$Z'$	$-0.423^{+0.023}_{-0.006}$	$-0.018^{+0.028}_{-0.011}$	$-0.892^{+0.014}_{-0.034}$	$0.308^{+0.022}_{-0.083}$
[6, 8]	SM	$-0.977^{+0.014}_{-0.004}$	$-0.128^{+0.075}_{-0.028}$	$-0.789^{+0.020}_{-0.049}$	$0.200^{+0.041}_{-0.014}$
	$Z'$	$-0.420^{+0.016}_{-0.005}$	$-0.078^{+0.034}_{-0.014}$	$-0.809^{+0.020}_{-0.050}$	$0.418^{+0.012}_{-0.038}$
[14, 16]	SM	$-0.922^{+0.002}_{-0.001}$	$-0.338^{+0.014}_{-0.009}$	$-0.596^{+0.008}_{-0.012}$	$0.114^{+0.007}_{-0.005}$
	$Z'$	$-0.409^{+0.004}_{-0.003}$	$-0.231^{+0.010}_{-0.006}$	$-0.482^{+0.008}_{-0.012}$	$0.484^{+0.000}_{-0.001}$
[16, 18]	SM	$-0.889^{+0.002}_{-0.001}$	$-0.312^{+0.007}_{-0.005}$	$-0.627^{+0.006}_{-0.008}$	$0.067^{+0.001}_{-0.001}$
	$Z'$	$-0.420^{+0.001}_{-0.001}$	$-0.235^{+0.004}_{-0.003}$	$-0.461^{+0.006}_{-0.008}$	$0.462^{+0.001}_{-0.002}$
[18, 20]	SM	$-0.747^{+0.010}_{-0.008}$	$-0.195^{+0.005}_{-0.004}$	$-0.767^{+0.006}_{-0.007}$	$-0.023^{+0.002}_{-0.003}$
	$Z'$	$-0.459^{+0.002}_{-0.002}$	$-0.198^{+0.002}_{-0.001}$	$-0.544^{+0.006}_{-0.007}$	$0.382^{+0.005}_{-0.006}$
		$\langle\alpha'_\xi\rangle$	$\langle\alpha_U\rangle$	$\langle\alpha_L\rangle$	$\langle dB/ds\rangle$ $\times 10^{-7}$
[0.1, 2]	SM	$0.002^{+0.000}_{-0.001}$	$-0.933^{+0.034}_{-0.051}$	$-0.980^{+0.008}_{-0.004}$	$0.251^{+0.451}_{-0.222}$
	$Z'$	$0.000^{+0.000}_{-0.000}$	$-0.063^{+0.001}_{-0.001}$	$-0.262^{+0.027}_{-0.004}$	$0.479^{+0.880}_{-0.430}$
[1, 2]	SM	$0.001^{+0.000}_{-0.001}$	$-0.932^{+0.036}_{-0.051}$	$-0.986^{+0.001}_{-0.003}$	$0.095^{+0.172}_{-0.084}$
	$Z'$	$0.000^{+0.000}_{-0.001}$	$-0.140^{+0.061}_{-0.024}$	$-0.344^{+0.036}_{-0.005}$	$0.158^{+0.283}_{-0.140}$
[2, 4]	SM	$0.000^{+0.000}_{-0.001}$	$-0.923^{+0.007}_{-0.005}$	$-0.991^{+0.006}_{-0.000}$	$0.178^{+0.302}_{-0.153}$
	$Z'$	$-0.001^{+0.000}_{-0.001}$	$-0.561^{+0.333}_{-0.088}$	$-0.389^{+0.022}_{-0.004}$	$0.268^{+4.490}_{-0.231}$
[4, 6]	SM	$-0.001^{+0.000}_{-0.001}$	$-0.908^{+0.110}_{-0.020}$	$-0.989^{+0.008}_{-0.001}$	$0.193^{+0.286}_{-0.157}$
	$Z'$	$-0.002^{+0.000}_{-0.001}$	$-0.754^{+0.060}_{-0.008}$	$-0.404^{+0.015}_{-0.004}$	$0.283^{+0.041}_{-0.229}$
[6, 8]	SM	$-0.002^{+0.000}_{-0.001}$	$-0.897^{+0.100}_{-0.023}$	$-0.986^{+0.009}_{-0.002}$	$0.220^{+0.275}_{-0.164}$
	$Z'$	$-0.002^{+0.000}_{-0.000}$	$-0.556^{+0.010}_{-0.000}$	$-0.407^{+0.013}_{-0.004}$	$0.325^{+0.040}_{-0.240}$
[14, 16]	SM	$-0.038^{+0.000}_{-0.000}$	$-0.851^{+0.009}_{-0.006}$	$-0.936^{+0.001}_{-0.001}$	$0.353^{+0.153}_{-0.127}$
	$Z'$	$-0.030^{+0.000}_{-0.001}$	$-0.321^{+0.006}_{-0.004}$	$-0.432^{+0.004}_{-0.002}$	$0.720^{+0.217}_{-0.178}$
[16, 18]	SM	$-0.052^{+0.000}_{-0.000}$	$-0.843^{+0.002}_{-0.002}$	$-0.896^{+0.002}_{-0.001}$	$0.328^{+0.095}_{-0.086}$
	$Z'$	$-0.044^{+0.000}_{-0.000}$	$-0.304^{+0.002}_{-0.002}$	$-0.451^{+0.001}_{-0.001}$	$0.562^{+0.129}_{-0.112}$
[18, 20]	SM	$-0.072^{+0.002}_{-0.002}$	$-0.840^{+0.000}_{-0.000}$	$-0.735^{+0.011}_{-0.009}$	$0.226^{+0.033}_{-0.042}$
	$Z'$	$-0.078^{+0.003}_{-0.003}$	$-0.302^{+0.001}_{-0.001}$	$-0.494^{+0.002}_{-0.002}$	$0.270^{+0.043}_{-0.040}$

Table 4.5: Average values of observables in the SM and  $Z'$  model for  $\Lambda_b \rightarrow \Lambda(\rightarrow p\pi)\mu^+\mu^-$  in appropriate bins.

		$\langle F_T \rangle$	$\langle F_L \rangle$	$\langle A_{FB}^{\ell\Lambda} \rangle$	$\langle \mathcal{P}_1 \rangle$
[0.1, 2]	$SM$	$0.424^{+0.174}_{-0.031}$	$0.576^{+0.031}_{-0.174}$	$-0.028^{+0.013}_{-0.001}$	$0.364^{+0.047}_{-0.260}$
	$Z'$	$0.537^{+0.095}_{-0.018}$	$0.463^{+0.018}_{-0.095}$	$-0.021^{+0.008}_{-0.001}$	$0.194^{+0.027}_{-0.143}$
[1, 2]	$SM$	$0.192^{+0.166}_{-0.023}$	$0.808^{+0.023}_{-0.166}$	$-0.034^{+0.009}_{-0.001}$	$0.711^{+0.035}_{-0.248}$
	$Z'$	$0.253^{+0.136}_{-0.023}$	$0.747^{+0.023}_{-0.136}$	$-0.030^{+0.007}_{-0.000}$	$0.620^{+0.035}_{-0.203}$
[2, 4]	$SM$	$0.107^{+0.040}_{-0.001}$	$0.893^{+0.001}_{-0.040}$	$-0.019^{+0.004}_{-0.008}$	$0.839^{+0.001}_{-0.061}$
	$Z'$	$0.096^{+0.042}_{-0.003}$	$0.904^{+0.003}_{-0.042}$	$-0.017^{+0.002}_{-0.006}$	$0.856^{+0.005}_{-0.064}$
[4, 6]	$SM$	$0.133^{+0.014}_{-0.031}$	$0.867^{+0.031}_{-0.014}$	$0.007^{+0.005}_{-0.015}$	$0.801^{+0.047}_{-0.021}$
	$Z'$	$0.102^{+0.013}_{-0.031}$	$0.897^{+0.031}_{-0.013}$	$0.009^{+0.004}_{-0.012}$	$0.846^{+0.046}_{-0.019}$
[6, 8]	$SM$	$0.191^{+0.016}_{-0.041}$	$0.809^{+0.041}_{-0.016}$	$0.031^{+0.005}_{-0.013}$	$0.714^{+0.061}_{-0.025}$
	$Z'$	$0.175^{+0.016}_{-0.042}$	$0.825^{+0.042}_{-0.016}$	$0.034^{+0.003}_{-0.010}$	$0.738^{+0.063}_{-0.024}$
[14, 16]	$SM$	$0.336^{+0.005}_{-0.008}$	$0.664^{+0.008}_{-0.005}$	$0.080^{+0.001}_{-0.002}$	$0.496^{+0.013}_{-0.006}$
	$Z'$	$0.411^{+0.005}_{-0.008}$	$0.589^{+0.008}_{-0.005}$	$0.088^{+0.001}_{-0.002}$	$0.383^{+0.012}_{-0.008}$
[16, 18]	$SM$	$0.315^{+0.004}_{-0.005}$	$0.685^{+0.005}_{-0.004}$	$0.076^{+0.001}_{-0.001}$	$0.528^{+0.011}_{-0.003}$
	$Z'$	$0.424^{+0.004}_{-0.005}$	$0.576^{+0.005}_{-0.004}$	$0.090^{+0.001}_{-0.001}$	$0.363^{+0.008}_{-0.006}$
[18, 20]	$SM$	$0.209^{+0.004}_{-0.005}$	$0.791^{+0.005}_{-0.004}$	$0.051^{+0.001}_{-0.001}$	$0.686^{+0.012}_{-0.002}$
	$Z'$	$0.371^{+0.004}_{-0.004}$	$0.629^{+0.004}_{-0.004}$	$0.079^{+0.001}_{-0.001}$	$0.443^{+0.007}_{-0.005}$
		$\langle \mathcal{P}_2 \rangle$	$\langle \mathcal{P}_3 \rangle$	$\langle \mathcal{P}_5 \rangle$	$\langle \mathcal{P}_6 \rangle$
[0.1, 2]	$SM$	$0.240^{+0.034}_{-0.176}$	$-0.076^{+0.036}_{-0.002}$	$-0.011^{+0.054}_{-0.014}$	$-0.079^{+0.178}_{-0.038}$
	$Z'$	$0.102^{+0.004}_{-0.024}$	$-0.056^{+0.021}_{-0.002}$	$0.019^{+0.005}_{-0.002}$	$-0.288^{+0.005}_{-0.001}$
[1, 2]	$SM$	$0.458^{+0.024}_{-0.166}$	$-0.090^{+0.024}_{-0.002}$	$0.001^{+0.057}_{-0.014}$	$-0.044^{+0.151}_{-0.029}$
	$Z'$	$0.170^{+0.004}_{-0.030}$	$-0.079^{+0.020}_{-0.001}$	$0.027^{+0.008}_{-0.003}$	$-0.191^{+0.028}_{-0.102}$
[2, 4]	$SM$	$0.539^{+0.001}_{-0.041}$	$-0.050^{+0.011}_{-0.020}$	$0.025^{+0.050}_{-0.012}$	$0.042^{+0.088}_{-0.019}$
	$Z'$	$0.202^{+0.001}_{-0.003}$	$-0.045^{+0.007}_{-0.015}$	$0.033^{+0.013}_{-0.004}$	$0.138^{+0.040}_{-0.167}$
[4, 6]	$SM$	$0.516^{+0.030}_{-0.013}$	$0.020^{+0.015}_{-0.041}$	$0.049^{+0.038}_{-0.010}$	$0.119^{+0.064}_{-0.018}$
	$Z'$	$0.196^{+0.013}_{-0.005}$	$0.024^{+0.010}_{-0.031}$	$0.037^{+0.013}_{-0.004}$	$0.427^{+0.030}_{-0.115}$
[6, 8]	$SM$	$0.463^{+0.041}_{-0.016}$	$0.082^{+0.014}_{-0.035}$	$0.067^{+0.027}_{-0.009}$	$0.166^{+0.057}_{-0.020}$
	$Z'$	$0.176^{+0.014}_{-0.005}$	$0.089^{+0.009}_{-0.025}$	$0.040^{+0.010}_{-0.003}$	$0.579^{+0.016}_{-0.053}$
[14, 16]	$SM$	$0.318^{+0.009}_{-0.005}$	$0.214^{+0.003}_{-0.006}$	$0.135^{+0.002}_{-0.001}$	$0.158^{+0.008}_{-0.008}$
	$Z'$	$0.136^{+0.002}_{-0.002}$	$0.234^{+0.003}_{-0.004}$	$0.066^{+0.001}_{-0.000}$	$0.672^{+0.000}_{-0.001}$
[16, 18]	$SM$	$0.317^{+0.005}_{-0.002}$	$0.202^{+0.002}_{-0.003}$	$0.163^{+0.000}_{-0.000}$	$0.090^{+0.002}_{-0.001}$
	$Z'$	$0.146^{+0.002}_{-0.001}$	$0.240^{+0.002}_{-0.003}$	$0.085^{+0.000}_{-0.000}$	$0.641^{+0.002}_{-0.003}$
[18, 20]	$SM$	$0.313^{+0.001}_{-0.002}$	$0.135^{+0.000}_{-0.005}$	$0.180^{+0.002}_{-0.003}$	$-0.032^{+0.001}_{-0.007}$
	$Z'$	$0.187^{+0.002}_{-0.002}$	$0.210^{+0.002}_{-0.003}$	$0.127^{+0.000}_{-0.000}$	$0.531^{+0.007}_{-0.008}$

Table 4.6: Numerical results of  $\mathcal{P}_8$  and  $\mathcal{P}_9$  for the decay  $\Lambda_b \rightarrow \Lambda(\rightarrow p\pi)\mu^+\mu^-$  for the SM and  $Z'$  model in appropriate bins.

		$\langle \mathcal{P}_8 \rangle$	$\langle \mathcal{P}_9 \rangle$
[0.1, 2]	<i>SM</i>	$0.221^{+0.003}_{-0.093}$	$-0.511^{+0.056}_{-0.247}$
	$Z'$	$0.107^{+0.008}_{-0.065}$	$-0.043^{+0.001}_{-0.009}$
[1, 2]	<i>SM</i>	$0.257^{+0.012}_{-0.048}$	$-0.231^{+0.036}_{-0.222}$
	$Z'$	$0.150^{+0.007}_{-0.076}$	$-0.046^{+0.006}_{-0.003}$
[2, 4]	<i>SM</i>	$0.145^{+0.084}_{-0.039}$	$-0.126^{+0.000}_{-0.050}$
	$Z'$	$0.089^{+0.003}_{-0.006}$	$-0.069^{+0.028}_{-0.008}$
[4, 6]	<i>SM</i>	$-0.055^{+0.149}_{-0.051}$	$-0.155^{+0.051}_{-0.020}$
	$Z'$	$-0.034^{+0.053}_{-0.021}$	$-0.100^{+0.036}_{-0.011}$
[6, 8]	<i>SM</i>	$-0.231^{+0.133}_{-0.049}$	$-0.220^{+0.066}_{-0.025}$
	$Z'$	$-0.143^{+0.060}_{-0.024}$	$-0.125^{+0.032}_{-0.011}$
[14, 16]	<i>SM</i>	$-0.564^{+0.022}_{-0.012}$	$-0.365^{+0.014}_{-0.007}$
	$Z'$	$-0.368^{+0.013}_{-0.009}$	$-0.169^{+0.007}_{-0.004}$
[16, 18]	<i>SM</i>	$-0.527^{+0.013}_{-0.005}$	$-0.338^{+0.008}_{-0.003}$
	$Z'$	$-0.371^{+0.006}_{-0.004}$	$-0.165^{+0.003}_{-0.002}$
[18, 20]	<i>SM</i>	$-0.350^{+0.013}_{-0.002}$	$-0.222^{+0.009}_{-0.002}$
	$Z'$	$-0.323^{+0.002}_{-0.002}$	$-0.143^{+0.001}_{-0.001}$

## Chapter 5

# The $\Lambda_b \rightarrow \Lambda (\rightarrow p\pi^-)\mu^+\mu^-$ decay in the $\text{RS}_c$ model

Although  $B$ -meson decays have been investigated extensively in different variants of the Randall-Sundrum (RS) model [97, 112, 226–239], not many studies are devoted to the  $\Lambda_b$  decay in the RS model [97]. Additionally, the present chapter includes new considerations and results which were not available in the previous studies of the  $\Lambda_b$  decays entertaining the RS model. Firstly, we summarize the main features of the RS model with custodial symmetry ( $\text{RS}_c$ ). Secondly, we consider the current constraints on the parameter space of the  $\text{RS}_c$  model coming from the direct searches of the lightest Kaluza-Klein (KK) gluon, electroweak precision tests, and the measurements of the Higgs signal strengths at the LHC, which yield much stricter constraints on the mass scale of the lowest KK gluon  $M_{g(1)}$ , which in turn, prevent sizable deviations of the WCs from the SM predictions. At a third step, we have not adopted the simplification of treating the elements of the 5D Yukawa coupling matrices to be real numbers as considered in [97, 235], rather we take these entries to be complex numbers as taken in [230, 237] leading to the complex WCs instead of real ones. Last but not the least, we use the helicity parametrization of the  $\Lambda_b \rightarrow \Lambda$  hadronic matrix elements and for the involved FFs, the most recent lattice QCD calculations, both in the low and high  $s$  regions, which yield much smaller uncertainties in most of the kinematic range [44] will be used.

### 5.1 RS Model with Custodial Symmetry

In this section, we will describe some of the salient features of the RS model [136]. The RS model, also known as a warped extra dimension, offers a geometrical solution of the gauge hierarchy problem along with naturally explaining the observed hierarchies in the SM fermion masses and mixing angles. In RS model, five-dimensional space-time is assumed with warped geometry in such a way that when it is lowered to four dimensions new particles appear which may be excitations of the SM particles or new particles beyond the SM. Five dimensional non-factorisable metric with coordinates  $(x, y)$  is given as [97, 232]

$$ds^2 = e^{-2ky}\eta_{\mu\nu}dx^\mu dx^\nu - dy^2, \quad (5.1)$$

where  $k \sim \mathcal{O}(M_{\text{Pl}}) \simeq 10^{19}$  GeV is the curvature scale,  $\eta_{\mu\nu} = \text{diag}(+1, -1, -1, -1)$  is the 4D Minkowski metric and  $y$  is the extra-dimensional (fifth) coordinate which varies in the finite interval  $0 \leq y \leq L$ ; the end points of the interval  $y = 0$  and  $y = L$  represent the boundaries of the extra dimension and are known as *ultraviolet* (UV) and *Infrared* (IR) brane, respectively. The region in between the UV and IR brane is denoted as the bulk of the warped extra dimension. In order to solve the gauge hierarchy problem, let's take  $kL = 36$  and define

$$M_{\text{KK}} \equiv ke^{-kL} \sim \mathcal{O}(\text{TeV}), \quad (5.2)$$

as the only free parameter coming from space-time geometry representing the effective NP scale.

In the present study, we consider a specific setup of the RS model in which the SM gauge group is enlarged to the bulk gauge group

$$SU(3)_c \times SU(2)_L \times U(1)_X \times SU(2)_R \times P_{LR}. \quad (5.3)$$

This gauge group along with metric (5.1) describes the model.  $P_{LR}$  is discrete left-right symmetry that implies mirror action of two symmetry groups  $SU(2)_L$  and  $SU(2)_R$  and protects  $Zb_L\bar{b}_L$  vertex to avoid large  $Z$  couplings to left-handed fermions (which are not allowed experimentally). In the chosen setup, all the SM fields are allowed to propagate in the 5D bulk, except the Higgs field, which is localized near or on the IR brane. In the present study, we consider the case in which the Higgs boson is completely localized on the IR brane at  $y = L$ . The  $RS_c$  model features two symmetry breakings. First, the enlarged gauge group of the model is broken down to the SM gauge group after imposing suitable boundary conditions (BCs) on the UV brane.

$$\begin{aligned} SU(3)_c \times O(4) \times U(1)_X &\sim SU(3)_c \times SU(2)_L \times U(1)_X \times SU(2)_R \times P_{LR} \\ &\longrightarrow SU(3)_c \times SU(2)_L \times U(1)_Y. \end{aligned} \quad (5.4)$$

Later on, the spontaneous symmetry breaking occurs through Higgs mechanism on the IR brane. As a natural consequence in all the extra-dimensional models, we have an infinite tower of KK excitations in this model. For this, each 5D field  $F(x^\mu, y)$  is KK decomposed to generic form

$$F(x^\mu, y) = \frac{1}{\sqrt{L}} \sum_{n=0}^{\infty} F^{(n)}(x^\mu) f^{(n)}(y), \quad (5.5)$$

where  $F^{(n)}(x^\mu)$  represent the effective four-dimensional fields and  $f^{(n)}(y)$  are called as the 5D profiles or the shape functions.  $n = 0$  case, called as zero mode in the KK mode expansion of a given field, corresponds to the SM particle. Appropriate choices for BCs help to distinguish between fields with and without a zero mode. Fields with the Neumann BCs on both branes, denoted as  $(++)$ , have a zero-mode that can be identified with an SM particle while fields with the Dirichlet BC on the UV brane and Neumann BC on the IR brane, denoted as  $(-+)$ , do not have the SM partners. Profiles for different fields are obtained by solving the corresponding 5D bulk equations of motion (EOM). In a perturbative approach as described in [97, 232], EOMs can be solved before the electroweak symmetry breaking (EWSB) and after the Higgs field develops a vacuum expectation value (VEV), the ratio  $v/M_{g(1)}$  of the Higgs VEV  $v$  and the mass of the



lowest KK excitation mode of gauge bosons  $M_{g^{(1)}}$  can be taken as perturbation.<sup>1</sup> Starting with the action of 5D theory, we integrate over the fifth dimension  $y$  to obtain the 4D effective field theory, and the Feynman rules of the model are obtained by neglecting terms of  $\mathcal{O}(v^2/M_{g^{(1)}}^2)$  or higher. On similar grounds, the mixing that occurs between the SM fermions and the higher KK fermion modes can be neglected as it leads to  $\mathcal{O}(v^2/M_{g^{(1)}}^2)$  modifications of the relevant couplings.

Next, we discuss the particle content of the gauge sector of the  $RS_c$  model and the mixing between SM gauge bosons and the first higher KK modes after the EWSB. For gauge bosons, following the analyses performed in [230, 235], we have neglected the  $n > 1$  KK modes as it is observed that the model becomes non-perturbative already for scales corresponding to the first few KK modes. Corresponding to the enlarged gauge group of the model, we have a large number of gauge bosons. For  $SU(3)_c$ , we have  $G_\mu^A$  ( $A = 1, \dots, 8$ ) corresponding to the SM gluons with 5D coupling  $g_s$ . The gauge bosons corresponding to  $SU(2)_L$  and  $SU(2)_R$  are denoted as  $W_{L\mu}^a$  and  $W_{R\mu}^a$  ( $a = 1, 2, 3$ ), respectively, with 5D gauge coupling  $g$  where the equality of the  $SU(2)_L$  and  $SU(2)_R$  couplings is imposed by  $P_{LR}$  symmetry. The gauge field corresponding to  $U(1)_X$  is denoted as  $X_\mu$  with 5D coupling  $g_X$ . All 5D gauge couplings are dimensionful and the relation between 5D and its 4D counterpart is given by  $g_s^{4D} = g_s/\sqrt{L}$ , with similar expressions also existing for  $g^{4D}$  and  $g_X^{4D}$ . Charged gauge bosons are defined as

$$W_{L(R)\mu}^\pm = \frac{W_{L(R)\mu}^1 \mp iW_{L(R)\mu}^2}{\sqrt{2}}. \quad (5.6)$$

Mixing between the bosons  $W_{R\mu}^3$  and  $X_\mu$  results in fields  $Z_{X\mu}$  and  $B_\mu$ ,

$$\begin{aligned} Z_{X\mu} &= \cos \phi W_{R\mu}^3 - \sin \phi X_\mu, \\ B_\mu &= \sin \phi W_{R\mu}^3 + \cos \phi X_\mu, \end{aligned} \quad (5.7)$$

where

$$\cos \phi = \frac{g}{\sqrt{g^2 + g_X^2}}, \quad \sin \phi = \frac{g_X}{\sqrt{g^2 + g_X^2}}. \quad (5.8)$$

Further, mixing between  $W_{L\mu}^3$  and  $B_\mu$  yields the fields  $Z_\mu$  and  $A_\mu$  in analogy to the SM,

$$\begin{aligned} Z_\mu &= \cos \psi W_{L\mu}^3 - \sin \psi B_\mu, \\ A_\mu &= \sin \psi W_{L\mu}^3 + \cos \psi B_\mu, \end{aligned} \quad (5.9)$$

with

$$\cos \psi = \frac{1}{\sqrt{1 + \sin^2 \phi}}, \quad \sin \psi = \frac{\sin \phi}{\sqrt{1 + \sin^2 \phi}}. \quad (5.10)$$

Along with eight gluons  $G_\mu^A(++)$ , after the mixing pattern, we have four charged bosons which are specified as  $W_L^\pm(++)$  and  $W_R^\pm(-+)$  while three neutral gauge bosons are given as  $A(++)$ ,  $Z(++)$  and  $Z_X(-+)$ . Moreover, we mention the following remarks about the masses and profiles of various

---

<sup>1</sup>Here we mention that we have employed a different notation for the mass of the first KK gauge bosons than in [97, 232] such that our  $M_{KK}$  corresponds to their  $f$ .

gauge boson fields that are obtained after solving the corresponding EOMs. Before EWSB, gauge bosons with  $(++)$  BCs have massless zero modes, which correspond to the SM gauge fields, with flat profiles along the extra dimension. On the other hand gauge bosons with  $(-+)$  BCs do not have a zero-mode and the lightest mode in the KK tower starts at  $n = 1$ . The profiles of the first KK mode of gauge bosons having a zero-mode are denoted by  $g(y)$  and the mass of such modes is denoted as  $M_{++}$  while the first mode profiles of the gauge bosons without a zero-mode are given by  $\tilde{g}(y)$  and the mass of such modes is denoted as  $M_{-+}$  before EWSB. The expressions are given by [240],

$$g(y) = \frac{e^{ky}}{N_1} \left[ J_1 \left( \frac{M_{g^{(1)}}}{k} e^{ky} \right) + b_1(M_{g^{(1)}}) Y_1 \left( \frac{M_{g^{(1)}}}{k} e^{ky} \right) \right], \quad (5.11)$$

$$\tilde{g}(y) = \frac{e^{ky}}{N_1} \left[ J_1 \left( \frac{\tilde{M}_{g^{(1)}}}{k} e^{ky} \right) + \tilde{b}_1(\tilde{M}_{g^{(1)}}) Y_1 \left( \frac{\tilde{M}_{g^{(1)}}}{k} e^{ky} \right) \right], \quad (5.12)$$

where  $J_1$  and  $Y_1$  are the Bessel functions of first and second kinds, respectively. The coefficients  $b_1(M_{g^{(1)}})$ ,  $\tilde{b}_1(\tilde{M}_{g^{(1)}})$  and  $N_1$  are

$$b_1(M_{g^{(1)}}) = -\frac{J_1 \left( M_{g^{(1)}}/k \right) + M_{g^{(1)}}/k J_1' \left( M_{g^{(1)}}/k \right)}{Y_1 \left( M_{g^{(1)}}/k \right) + M_{g^{(1)}}/k Y_1' \left( M_{g^{(1)}}/k \right)}, \quad (5.13)$$

$$\tilde{b}_1(\tilde{M}_{g^{(1)}}) = -\frac{J_1 \left( \tilde{M}_{g^{(1)}}/k \right)}{Y_1 \left( \tilde{M}_{g^{(1)}}/k \right)}, \quad (5.14)$$

$$N_1 = \frac{e^{kL/2}}{\sqrt{\pi L M_{g^{(1)}}}}. \quad (5.15)$$

The masses of the lowest KK gauge excitations are numerically given to be  $M_{g^{(1)}} \simeq 2.45 M_{\text{KK}} \equiv M_{++}$  and  $\tilde{M}_{g^{(1)}} \simeq 2.40 M_{\text{KK}} \equiv M_{-+}$ . Notice that the presented KK masses for the gauge bosons are universal for all gauge bosons with the same BCs. After EWSB, the zero-mode gauge bosons with  $(++)$  BCs, other than gluons, and photon, acquire masses while the massive KK gauge excitations of all the gauge bosons, except KK gluons and KK photons receive mass corrections. Due to the unbroken gauge invariance of  $SU(3)$  and  $U(1)_Q$ , gluons and photon do not obtain masses such that their zero modes remain massless while their higher KK excitations that are massive do not get a mass correction as a result of EWSB and hence remain mass eigenstates. Furthermore, we have mixing among zero modes and the higher KK modes. Considering only the first KK modes, the charged and neutral mass eigenstates are related to their corresponding gauge KK eigenstates via

$$\begin{pmatrix} W^\pm \\ W_H^\pm \\ W'^\pm \end{pmatrix} = \mathcal{G}_W \begin{pmatrix} W_L^{\pm(0)} \\ W_L^{\pm(1)} \\ W_R^{\pm(1)} \end{pmatrix}, \quad \begin{pmatrix} Z \\ Z_H \\ Z' \end{pmatrix} = \mathcal{G}_Z \begin{pmatrix} Z^{(0)} \\ Z^{(1)} \\ Z_X^{(1)} \end{pmatrix}. \quad (5.16)$$

The expressions of the orthogonal mixing matrices  $\mathcal{G}_W$  and  $\mathcal{G}_Z$  and the masses of the mass eigen-

states are given explicitly in [97, 232].

Next, the SM fermions are embedded in three possible representations of  $SU(2)_L \times SU(2)_R$ , that are  $(\mathbf{2}, \mathbf{2})$ ,  $(\mathbf{1}, \mathbf{1})$  and  $(\mathbf{3}, \mathbf{1}) \oplus (\mathbf{1}, \mathbf{3})$ . Which field belong to which multiplet is chosen according to the guidelines provided by phenomenology. For the realization of the SM quark and lepton sector in the  $RS_c$  model, we refer the reader to ref. [97, 232]. Moreover, other than SM fields, several additional vector-like fermion fields with electric charge  $2/3$ ,  $-1/3$ , and  $5/3$  are required to fill in the three representations of the  $SU(2)_L \times SU(2)_R$  gauge group. Since we only consider the fermion fields with  $(++)$  BCs, we do not discuss the new fermions which are introduced with  $(-+)$  or  $(+-)$  choices of the BCs. Furthermore, we will restrict ourselves only to the zero modes in the KK mode expansion of the fermionic fields with  $(++)$  BCs, which are massless before EWSB and up to small mixing effects with other massive modes after the EWSB, due to the transformation to mass eigenstates, are identified as the SM quarks and leptons. We have neglected the higher KK fermion modes because their impact is sub-leading as pointed out previously. The solution of the EOMs of the left and right-handed fermionic zero modes leads to their bulk profiles, which we denote as  $f_{L,R}^{(0)}(y, c_\Psi)$  and their expressions are given by

$$f_L^{(0)}(y, c_\Psi) = \sqrt{\frac{(1 - 2c_\Psi)kL}{e^{(1-2c_\Psi)kL} - 1}} e^{-c_\Psi ky}, \quad f_R^{(0)}(y, c_\Psi) = f_L^{(0)}(y, -c_\Psi). \quad (5.17)$$

The bulk mass parameter  $c_\Psi$  controls the localization of the fermionic zero modes such as for  $c_\Psi > 1/2$ , the left-handed fermionic zero mode is localized towards the UV brane, while for  $c_\Psi < 1/2$ , it is localized towards the IR brane. Similarly, from the expression of the  $f_R^{(0)}(y, c_\Psi)$ , the localization of the right-handed fermion zero mode depends on whether  $c_\Psi < -1/2$  or  $c_\Psi > -1/2$ . For the SM quarks we will denote the bulk mass parameters  $c_Q^i$  for the three left-handed zero mode embedded into bi-doublets of  $SU(2)_L \times SU(2)_R$ , while for the right-handed zero mode up and down-type quarks which belong to  $(\mathbf{1}, \mathbf{1})$  and  $(\mathbf{3}, \mathbf{1}) \oplus (\mathbf{1}, \mathbf{3})$  representations, respectively [97, 232, 241], we assign bulk mass parameters  $c_{u,d}^i$ , respectively.

The effective 4D Yukawa couplings, relevant for the SM fermion masses and mixings, for the Higgs sector residing on the IR brane, are given by [230]

$$Y_{ij}^{u(d)} = \lambda_{ij}^{u(d)} \frac{e^{kL}}{kL} f_L^{(0)}(y=L, c_Q^i) f_R^{(0)}(y=L, c_u^j(c_d^j)) \equiv \lambda_{ij}^{u(d)} \frac{e^{kL}}{kL} f_i^Q f_j^{u(d)}, \quad (5.18)$$

where  $\lambda^{u(d)}$  are the fundamental 5D Yukawa coupling matrices. Since the fermion profiles depend exponentially on the bulk mass parameters, one can recognize from the above relation that the strong hierarchies of quark masses and mixings originate from the  $\mathcal{O}(1)$  bulk mass parameters and anarchic 5D Yukawa couplings  $\lambda_{ij}^{u(d)}$ . The transformation from the quark flavor eigenbasis to the mass eigenbasis is performed by means of unitary mixing matrices, which are presented by  $\mathcal{U}_{L(R)}$  and  $\mathcal{D}_{L(R)}$  for the up-type left (right) and down-type left (right) quarks, respectively. Moreover, the CKM matrix is given by  $V_{\text{CKM}} = \mathcal{U}_L^\dagger \mathcal{D}_L$  and the FCNCs are induced already at tree level in this model. This happens because the couplings of the fermions with the gauge bosons involve overlap integrals which contain the profiles of the corresponding fermions and gauge boson leading to non-universal flavor diagonal couplings. These non-universal flavor diagonal couplings induce off-diagonal entries in the interaction matrix after going to the fermion mass basis, resulting in tree level FCNCs. These are mediated by the three neutral electroweak gauge bosons  $Z$ ,  $Z'$  and

$Z_H$  as well as by the first KK excitations of the photon and the gluons, although the last one does not contribute to the processes with leptons in the final state. The expressions of the masses of the SM quarks and the flavor mixing matrices  $\mathcal{U}_{L(R)}$ ,  $\mathcal{D}_{L(R)}$  are given explicitly in terms of the quark profiles and the five-dimensional Yukawa couplings  $\lambda_{ij}^{u(d)}$  in [230].

Moreover, for this particular scenario, it has been shown that all existing  $\Delta F = 2$  and electroweak (EW) precision constraints can be satisfied, without requiring too much fine-tuning, for the masses of the lightest KK excitations of the order of a few TeV [230], in the reach of the LHC. However, after the ATLAS and the CMS measurements of the Higgs signal strengths, the bounds on the masses of the lightest KK modes arising from Higgs physics have grown much stronger than those stemming from EW precision measurements [242]. In view of this, we have performed a scan for the allowed parameter space of the model by considering all existing constraints, which will be discussed later on.

## 5.2 Theoretical Formalism

The effective weak Hamiltonian for  $b \rightarrow s\mu^+\mu^-$  transition in the  $\text{RS}_c$  model can be written as

$$H_{\text{eff}}^{\text{RS}_c} = -\frac{4G_F}{\sqrt{2}}V_{tb}V_{ts}^* \left[ C_7^{\text{RS}_c} O_7 + C_7'^{\text{RS}_c} O_7' + C_9^{\text{RS}_c} O_9 + C_9'^{\text{RS}_c} O_9' + C_{10}^{\text{RS}_c} O_{10} + C_{10}'^{\text{RS}_c} O_{10}' \right], \quad (5.19)$$

where  $G_F$  is the Fermi coupling constant and  $V_{tb}$ ,  $V_{ts}^*$  are the elements of the CKM mixing matrix. In the  $\text{RS}_c$  model the WCs in the above effective Hamiltonian can be written as

$$C_i^{(\prime)\text{RS}_c} = C_i^{(\prime)\text{SM}} + \Delta C_i^{(\prime)}, \quad (5.20)$$

where  $i = 7, 9, 10$ . In the SM case, ignoring tiny contribution, when present, the primed coefficients are zero while the unprimed WCs  $C_i$  incorporating short-distance physics are evaluated through perturbative approach. The factorizable contributions from operators  $O_{1-6,8}$  have been absorbed in the effective WCs  $C_7^{\text{eff}}$  and  $C_9^{\text{eff}}$  (c.f. Eq. (3.3) [29]). The expressions of these effective coefficients involve the functions  $h(m_q, s)$ ,  $F_8^{(7,9)}(s)$  defined in [86], and the functions  $F_{1,c}^{(7,9)}(q^2)$ ,  $F_{1,c}'^{(7,9)}(q^2)$  given in [224] for low  $s$  and in [212] for high  $s$ . The quark masses appearing in these functions are defined in the pole scheme. The long-distance non-factorizable contributions of charm loop effects can alter the value of  $C_7^{\text{eff}}$  to some extent particularly in the region of charmonium resonances. Modifications  $\Delta C_{9,10}^{(\prime)}$ , in the  $\text{RS}_c$  model, evaluated at the scale  $\mathcal{O}(M_{g(1)})$  are given by [231]

$$\begin{aligned} \Delta C_9 &= \frac{\Delta Y_s}{\sin^2 \theta_W} - 4\Delta Z_s, \\ \Delta C_9' &= \frac{\Delta Y_s'}{\sin^2 \theta_W} - 4\Delta Z_s', \\ \Delta C_{10} &= -\frac{\Delta Y_s}{\sin^2 \theta_W}, \\ \Delta C_{10}' &= \frac{\Delta Y_s'}{\sin^2 \theta_W}, \end{aligned} \quad (5.21)$$

where

$$\begin{aligned}
\Delta Y_s &= -\frac{1}{V_{tb}V_{ts}^*} \sum_X \frac{\Delta_L^{\mu\mu}(X) - \Delta_R^{\mu\mu}(X)}{4M_X^2 g_{SM}^2} \Delta_L^{bs}(X), \\
\Delta Y'_s &= -\frac{1}{V_{tb}V_{ts}^*} \sum_X \frac{\Delta_L^{\mu\mu}(X) - \Delta_R^{\mu\mu}(X)}{4M_X^2 g_{SM}^2} \Delta_R^{bs}(X), \\
\Delta Z_s &= \frac{1}{V_{tb}V_{ts}^*} \sum_X \frac{\Delta_R^{\mu\mu}(X)}{8M_X^2 g_{SM}^2 \sin^2 \theta_W} \Delta_L^{bs}(X), \\
\Delta Z'_s &= \frac{1}{V_{tb}V_{ts}^*} \sum_X \frac{\Delta_R^{\mu\mu}(X)}{8M_X^2 g_{SM}^2 \sin^2 \theta_W} \Delta_R^{bs}(X).
\end{aligned} \tag{5.22}$$

The sums run over the neutral gauge bosons  $X = Z, Z', Z_H$  and  $A^{(1)}$  with  $g_{SM}^2 = \frac{G_F}{\sqrt{2}} \frac{\alpha}{2\pi \sin^2 \theta_W}$ .  $\Delta C_9^{(\prime)}$  and  $\Delta C_{10}^{(\prime)}$  evaluated at the scale  $M_{g^{(1)}}$  do not need to be evolved to  $\mu_b$  scale. In the case of  $\Delta C_7^{(\prime)}$ , detailed calculation with the set of assumptions consistent with the calculations of  $\Delta C_{9,10}^{(\prime)}$  is given in Appendix C of ref. [235], where  $\Delta C_7$  and  $\Delta C_7'$  are evaluated at the  $M_{g^{(1)}}$  scale. The evolution at the scale  $\mu_b$  is given by the following master formula [234]

$$\Delta C_7^{(\prime)}(\mu_b) = 0.429 \Delta C_7^{(\prime)}(M_{g^{(1)}}) + 0.128 \Delta C_8^{(\prime)}(M_{g^{(1)}}). \tag{5.23}$$

The decay amplitude for  $\Lambda_b \rightarrow \Lambda \mu^+ \mu^-$  can be obtained by sandwiching the effective Hamiltonian displayed in Eq. (5.19) within the baryonic states

$$\begin{aligned}
\mathcal{M}_{\text{RS}_c}(\Lambda_b \rightarrow \Lambda \mu^+ \mu^-) &= \frac{G_F \alpha}{\sqrt{2\pi}} V_{tb} V_{ts}^* \left[ \langle \Lambda(p_\Lambda) | \bar{s} \gamma_\mu (C_9^{\text{RS}_c} P_L + C_9'^{\text{RS}_c} P_R) b | \Lambda_b(p_{\Lambda_b}) \rangle (\bar{\mu} \gamma^\mu \mu) \right. \\
&\quad + \langle \Lambda(p_\Lambda) | \bar{s} \gamma_\mu (C_{10}^{\text{RS}_c} P_L + C_{10}'^{\text{RS}_c} P_R) b | \Lambda_b(p_{\Lambda_b}) \rangle (\bar{\mu} \gamma^\mu \gamma^5 \mu) \\
&\quad \left. - \frac{2m_b}{s} \langle \Lambda(p_\Lambda) | \bar{s} i \sigma_{\mu\nu} q^\nu (C_7^{\text{RS}_c} P_R + C_7'^{\text{RS}_c} P_L) b | \Lambda_b(p_{\Lambda_b}) \rangle \bar{\mu} \gamma^\mu \mu \right].
\end{aligned} \tag{5.24}$$

The matrix elements involved in the expression of decay amplitude are given in [67] written in helicity basis in terms of FFs. The detailed calculation of FFs in lattice QCD is carried out in [44], which will be used in our numerical analysis.

### 5.3 Constraints and generation of the parameter space of the $\text{RS}_c$ model

In this section, we consider the relevant constraints on the parameter space of the  $\text{RS}_c$  model coming from the direct searches at the LHC [243, 244], EW precision tests [242, 245], the latest measurements of the Higgs signal strengths at the LHC [242] and from  $\Delta F = 2$  flavor observables.

Starting with the direct searches, current measurements at the LHC for resonances decaying to  $t\bar{t}$  pair constrain the lightest KK gluon mass  $M_{g^{(1)}} > 3.3$  TeV at 95% confidence level [244]. Further, in the  $\text{RS}_c$  model, EW precision measurements permit to have masses of the lowest KK gauge bosons in the few TeV range. For example, a tree-level analysis of the S and T parameters leads to  $M_{g^{(1)}} > 4.8$  TeV for the lightest KK gluon and KK photon masses [245]. Furthermore, a comparison of the predictions of all relevant Higgs decays in the  $\text{RS}_c$  model with the latest data from the LHC shows that the signal rates for  $pp \rightarrow h \rightarrow ZZ^*, WW^*$  provide the most stringent

bounds, such that KK gluon masses lighter than  $22.7 \text{ TeV} \times (y_\star/3)$  in the brane-Higgs case and  $13.2 \text{ TeV} \times (y_\star/3)$  in the narrow bulk-Higgs scenario are excluded at 95% probability [242], where  $y_\star = \mathcal{O}(1)$  free parameter is defined as the upper bound on the anarchic 5D Yukawa couplings such that  $|\lambda_{ij}^{u(d)}| \leq y_\star$ . This implies that  $y_\star = 3$  value, coming from the perturbativity bound of the RS model, will lead to much stronger bounds from Higgs physics than those emerging from the EW precision tests. In general, one can lower these bounds by considering smaller values of  $y_\star$ . However one should keep in mind that lowering the bounds up to KK gauge bosons masses implied by EW precision constraints,  $M_{g(1)} = 4.8 \text{ TeV}$ , will require too-small Yukawa couplings,  $y_\star < 0.3$  for the brane-Higgs scenario [242], which will reinforce the RS flavor problem because of enhanced corrections to  $\epsilon_K$ . Therefore, moderate bounds on the value of the  $y_\star$  should be considered by relatively increasing the KK scale, in order to avoid constraints from both flavor observables and Higgs physics.

Next, in analogy to our previous analysis [237], we explore the parameter space of the  $\text{RS}_c$  model by generating two sets of anarchic 5D Yukawa matrices, whose entries satisfy  $|\lambda_{ij}^{u(d)}| \leq y_\star$  with  $y_\star = 1.5$  and 3. Further, we choose the nine quark bulk-mass parameters  $c_{Q,u,d}$ , which together with the 5D Yukawa matrices reproduce the correct values of the quark masses evaluated at the scale  $\mu = 3 \text{ TeV}$ , CKM mixing angles and the Jarlskog determinant, all within their respective  $2\sigma$  ranges. For muon, we take  $c_\mu = 0.7$  as lepton flavor-conserving couplings are found to be almost independent of the chosen value as far as  $c_l > 0.5$  [231]. Additionally, from the  $\Delta F = 2$  flavor observables, we apply the constraints from  $\epsilon_K$ ,  $\Delta M_K$  and  $\Delta M_{B_s}$  observables, where we can set the required input parameters, as given in Table 2 of [237], to their central values and allow the resulting observables to deviate by  $\pm 30\%$ ,  $\pm 50\%$  and  $\pm 30\%$ , respectively in analogy to the analysis [230]. For further details on the parameter scan, we refer the reader to [230, 237].

## 5.4 Numerical Analysis

### 5.4.1 Wilson coefficients

The generated 5D parameter points consisting of Yukawa coupling matrices and bulk mass parameters, fulfilling all the relevant constraints, are used to evaluate the WCs in the  $\text{RS}_c$  model. In Fig. 5.1, we show the dependence of  $|\Delta C_{10}|$  Wilson coefficient on the mass of lowest KK gluon  $M_{g(1)}$  taken in the range 2.45 to 20 TeV. The red and blue scatter points represent the cases of  $y_\star = 1.5$  and 3, respectively. The gray region is excluded by the analysis of EW precision observables. It is clear that the smaller values of  $M_{g(1)}$  give larger deviations. Moreover, for a fixed value of  $M_{g(1)}$  a range of predictions for possible deviations are present for both cases of  $y_\star$  such that the maximum allowed deviation for  $|\Delta C_{10}|$  in the case of  $y_\star = 1.5$  are generally greater than the case of  $y_\star = 3$ . This is due to the fact that in the case of  $y_\star = 3$ , the SM fermions are more elementary as their profiles are localized towards the UV brane to a greater extent compared to the  $y_\star = 1.5$  case leading to more suppressed FCNC and subsequently smaller deviations in comparison to the case of  $y_\star = 1.5$ . Observing the fact that the deviations for all  $|\Delta C_i^{(\prime)}|$  for  $M_{g(1)} > 10 \text{ TeV}$  are so small, as clear from Fig. 5.1 in the case of  $|\Delta C_{10}|$ , that the observables will almost remain unaffected, we limit the range for  $M_{g(1)}$  from 4.8 TeV to 10 TeV, where the lower value is implied by the EW precision constraints. As we are interested in the largest possible deviations of  $|\Delta C_i^{(\prime)}|$ , for a given allowed value of  $M_{g(1)}$ , so we will take the  $y_\star = 1.5$  case and by considering five different values

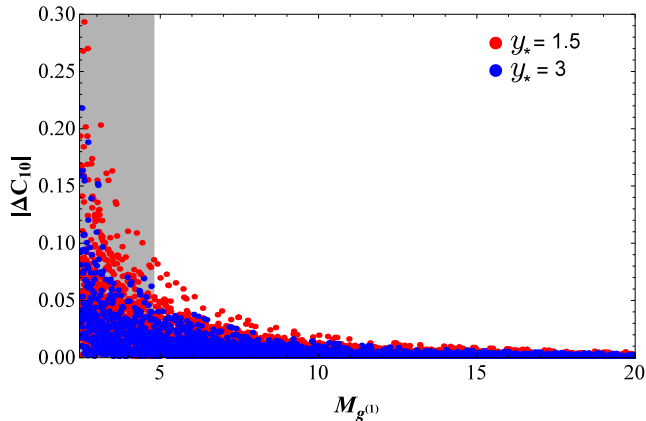


Figure 5.1: The  $RS_c$  contribution to  $|\Delta C_{10}|$  as a function of the KK gluon mass  $M_{g^{(1)}}$  for two different values of  $y_*$ . The gray region is excluded by the analysis of electroweak precision measurements.

of  $M_{g^{(1)}} \in [4.8, 10]$ , we obtain the maximum possible deviation of each Wilson coefficient. The resultant values will be used for evaluating the effects on the angular observables of interest for each considered value of  $M_{g^{(1)}}$  in the next section i.e., Sect. 5.4.2.

In Fig. 5.2, we show the correlation plots between  $|\Delta C_{7,9,10}^{(i)}|$  obtained for the fixed value of  $M_{g^{(1)}} = 4.8$  TeV. The maximum possible deviations from the SM values in this case are

$$\begin{aligned} |\Delta C_7|_{max} &= 0.011, & |\Delta C_9|_{max} &= 0.006, & |\Delta C_{10}|_{max} &= 0.085, \\ |\Delta C_7'|_{max} &= 0.004, & |\Delta C_9'|_{max} &= 0.047, & |\Delta C_{10}'|_{max} &= 0.621. \end{aligned}$$

It is found that  $|\Delta C_9|$  and  $|\Delta C_{10}|$  are linearly correlated, as shown in Fig. 5.2(f), and same is true for each pair  $|\Delta C_i^{(i)}|$  with  $i = 9, 10$ .

### 5.4.2 Angular observables

In this section, we discuss the numerical results computed for different angular observables both in the SM and for the  $RS_c$  model. The input parameters used in the calculations are included in Table 4.1. The presented results include the uncertainty in the hadronic FFs, which are non-perturbative quantities. For this, we utilize the lattice QCD calculations [44], both in the low- and high- $s$  ranges, which till to date are considered as most accurate in the literature. To improve the accuracy, we have used the numerical values for the short-distance WCs, with NNLL accuracy, at the low energy scale  $\mu_b = 4.2$  GeV, shown in Table 4.1.

The numerical results for the angular observables in appropriate bins are shown in Tables 5.1, 5.2, 5.3 and 5.4, where a comparison is presented between the predictions obtained for five different values of  $M_{g^{(1)}}$  in the  $RS_c$  model (for  $y_* = 1.5$ ) to that of the SM estimates and with the experimental measurements, where available. The whole spectrum of dimuon mass squared ( $s \in \{s_{min} = 4m_\mu^2, s_{max} = (m_{\Lambda_b} - m_\Lambda)^2\}$ ) has not been discussed as the region  $s \in [8, 15]$  GeV<sup>2</sup> is expected to receive sizable corrections from charmonium loops that violate quark-hadron duality. Hence the regions  $s \in [0.1, 8]$  GeV<sup>2</sup> and  $s \in [15, 20]$  GeV<sup>2</sup> have been considered in order to avoid the long-distance effects of charmonium resonances arising when lepton pair momenta

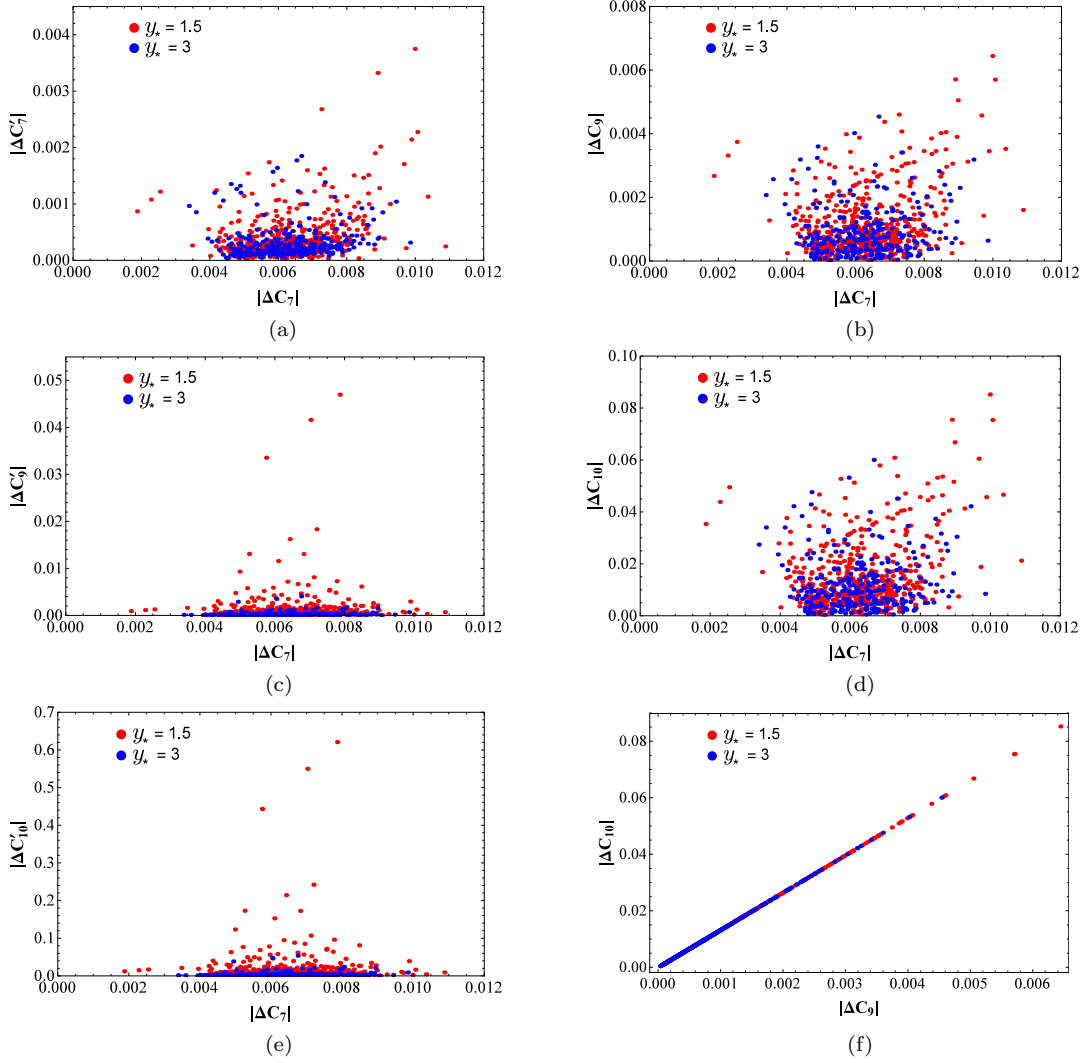


Figure 5.2: Correlations plots between the WCs  $|\Delta C_{7,9,10}^{(r)}|$  of the  $RS_c$  model for a fixed value of  $M_{g(1)} = 4.8$  TeV. The coefficients  $\Delta C_7^{(r)}$  are calculated at the  $\mu_b$  scale. The red and blue points correspond to  $y_* = 1.5$  and 3, respectively.

approaches the masses of  $J/\psi$  family. It can be seen that the results in the  $RS_c$  model for most of the observables show little deviation from the SM predictions. Maximum deviation from the SM results has been observed for  $M_{g(1)} = 4.8$  TeV and the difference gradually decreases as one moves from  $M_{g(1)} = 4.8$  TeV to  $M_{g(1)} = 10$  TeV.

Next, we compare our results of observables in the SM and the  $RS_c$  model with the measurements from the LHCb experiment [217]. For most of the observables, results in the  $RS_c$  model are close to that obtained for the SM in all bins of  $s$  and this can be seen in Tables 5.1, 5.2, 5.3 and 5.4. The branching ratio for the four body decay process  $\Lambda_b \rightarrow \Lambda(\rightarrow p\pi)\mu^+\mu^-$  in the  $RS_c$  model (for  $M_{g(1)} = 4.8$  TeV) shows a slight deviation at low-recoil and almost no deviation at large-recoil. For the bin  $[1.1, 6]$ , the branching ratio in the SM and the  $RS_c$  are  $0.199_{-0.12}^{+0.12}$  and  $0.190_{-0.119}^{+0.120}$  respectively, which are  $1.8\sigma$  and  $1.9\sigma$  away from the measured value  $0.09_{-0.051}^{+0.061}$ . The situation is quite similar for all other bins for large-recoil where values of observables do not change much even for  $M_{g(1)} = 4.8$  TeV. For low-recoil bin  $[15, 20]$ , the SM and the  $RS_c$  model results  $0.753_{-0.069}^{+0.069}$  and  $0.807_{-0.069}^{+0.069}$  deviate from the measured value by  $4.7\sigma$  and  $4.1\sigma$ . It is noted that the differential



branching ratio in the  $RS_c$  model is lower than the SM at large-recoil and higher than the SM at low-recoil.

In case of  $F_L$ , maximum deviation has been observed for the first bin  $[0.1, 2]$   $\text{GeV}^2$  where predictions in the SM and the  $RS_c$  model are  $\langle F_L \rangle_{SM} = 0.535_{-0.078}^{+0.065}$  and  $\langle F_L \rangle_{RS_c} = 0.552_{-0.084}^{+0.069}$ , respectively which vary from the measured value  $0.56_{-0.566}^{+0.244}$  by  $0.1\sigma$  and  $0.02\sigma$ , respectively. For most of the bins, deviation of  $F_L$  in the  $RS_c$  model from the SM is negligible. For low-recoil bin  $[15, 20]$   $\text{GeV}^2$ , the values in both models  $\langle F_L \rangle_{SM} = 0.409_{-0.018}^{+0.033}$ ,  $\langle F_L \rangle_{RS_c} = 0.403_{-0.019}^{+0.034}$  deviate from the experimental result  $0.61_{-0.143}^{+0.114}$  in the same bin by  $1.6\sigma$ . At lower values of  $s$  up to  $4 \text{ GeV}^2$ , the  $RS_c$  model results deviate from the SM values to a greater extent, whereas almost similar values of the  $RS_c$  model are obtained for the rest of the spectrum.

For  $A_{FB}^\ell$ , small deviation in the  $RS_c$  model exists from the SM both at low- and high-recoil. In the first bin  $[0.1, 2]$   $\text{GeV}^2$  our calculated results in both models differ from the measured value by  $0.6\sigma$ . For large  $s$  bin  $[15, 20]$   $\text{GeV}^2$ , the values in both models  $\langle A_{FB}^\ell \rangle_{SM} = -0.358_{-0.007}^{+0.012}$  and  $\langle A_{FB}^\ell \rangle_{RS_c} = -0.332_{-0.009}^{+0.008}$  are very close to each other and are  $3.2\sigma$  and  $3.0\sigma$  away from the measured value  $-0.05_{-0.095}^{+0.095}$  in the same bin.

For  $A_{FB}^\Lambda$  in the bin  $[15, 20]$   $\text{GeV}^2$  results of the SM and the  $RS_c$  model are  $\langle A_{FB}^\Lambda \rangle_{SM} = -0.271_{-0.011}^{+0.011}$  and  $\langle A_{FB}^\Lambda \rangle_{RS_c} = -0.247_{-0.011}^{+0.011}$  and deviate from the measured value of LHCb  $-0.29_{-0.081}^{+0.076}$  by  $0.2\sigma$  and  $0.5\sigma$ . For  $A_{FB}^{\ell\Lambda}$ , no sizable deviation from the SM has been observed in any  $s$  bin for the  $RS_c$  model.

Table 5.1: Numerical results of  $\frac{d\mathcal{B}}{ds}$ ,  $F_L$  and  $A_{FB}^\ell$  (low  $s$  region) in the  $\Lambda_b \rightarrow \Lambda(\rightarrow p\pi)\mu^+\mu^-$  decay, obtained for the SM and the  $RS_c$  model with  $y_* = 1.5$  case, in different bins of  $s$ . Experimentally measured values are taken from [217].

		$\langle \frac{d\mathcal{B}}{ds} \times 10^{-7} \rangle$	$\langle F_L \rangle$	$\langle A_{FB}^\ell \rangle$
[0.1, 2]	SM	$0.238^{+0.230}_{-0.230}$	$0.535^{+0.065}_{-0.078}$	$0.097^{+0.006}_{-0.007}$
	$RS_c _{M_{g^{(1)}} = 4.8}$	$0.219^{+0.218}_{-0.217}$	$0.552^{+0.069}_{-0.084}$	$0.093^{+0.005}_{-0.006}$
	$RS_c _{M_{g^{(1)}} = 6.1}$	$0.225^{+0.219}_{-0.217}$	$0.545^{+0.067}_{-0.082}$	$0.095^{+0.005}_{-0.006}$
	$RS_c _{M_{g^{(1)}} = 7.4}$	$0.229^{+0.224}_{-0.222}$	$0.542^{+0.067}_{-0.081}$	$0.095^{+0.006}_{-0.007}$
	$RS_c _{M_{g^{(1)}} = 8.7}$	$0.232^{+0.224}_{-0.223}$	$0.540^{+0.066}_{-0.080}$	$0.096^{+0.006}_{-0.007}$
	$RS_c _{M_{g^{(1)}} = 10}$	$0.233^{+0.228}_{-0.225}$	$0.539^{+0.066}_{-0.080}$	$0.096^{+0.006}_{-0.007}$
	LHCb	$0.36^{+0.122}_{-0.112}$	$0.56^{+0.244}_{-0.566}$	$0.37^{+0.371}_{-0.481}$
[2, 4]	SM	$0.180^{+0.123}_{-0.123}$	$0.855^{+0.008}_{-0.012}$	$0.054^{+0.037}_{-0.030}$
	$RS_c _{M_{g^{(1)}} = 4.8}$	$0.171^{+0.118}_{-0.117}$	$0.860^{+0.008}_{-0.006}$	$0.040^{+0.035}_{-0.026}$
	$RS_c _{M_{g^{(1)}} = 6.1}$	$0.173^{+0.118}_{-0.117}$	$0.859^{+0.008}_{-0.008}$	$0.045^{+0.036}_{-0.028}$
	$RS_c _{M_{g^{(1)}} = 7.4}$	$0.175^{+0.119}_{-0.118}$	$0.858^{+0.008}_{-0.009}$	$0.048^{+0.036}_{-0.028}$
	$RS_c _{M_{g^{(1)}} = 8.7}$	$0.176^{+0.119}_{-0.119}$	$0.857^{+0.008}_{-0.010}$	$0.050^{+0.036}_{-0.029}$
	$RS_c _{M_{g^{(1)}} = 10}$	$0.177^{+0.120}_{-0.120}$	$0.857^{+0.008}_{-0.011}$	$0.051^{+0.037}_{-0.030}$
	LHCb	$0.11^{+0.120}_{-0.091}$	—	—
[4, 6]	SM	$0.232^{+0.110}_{-0.110}$	$0.807^{+0.018}_{-0.012}$	$-0.063^{+0.038}_{-0.026}$
	$RS_c _{M_{g^{(1)}} = 4.8}$	$0.224^{+0.108}_{-0.108}$	$0.806^{+0.021}_{-0.016}$	$-0.078^{+0.034}_{-0.021}$
	$RS_c _{M_{g^{(1)}} = 6.1}$	$0.227^{+0.109}_{-0.108}$	$0.807^{+0.019}_{-0.015}$	$-0.072^{+0.036}_{-0.022}$
	$RS_c _{M_{g^{(1)}} = 7.4}$	$0.228^{+0.109}_{-0.109}$	$0.807^{+0.019}_{-0.014}$	$-0.069^{+0.037}_{-0.024}$
	$RS_c _{M_{g^{(1)}} = 8.7}$	$0.229^{+0.109}_{-0.109}$	$0.807^{+0.019}_{-0.013}$	$-0.068^{+0.037}_{-0.024}$
	$RS_c _{M_{g^{(1)}} = 10}$	$0.230^{+0.110}_{-0.110}$	$0.807^{+0.019}_{-0.013}$	$-0.067^{+0.037}_{-0.025}$
	LHCb	$0.02^{+0.091}_{-0.010}$	—	—
[6, 8]	SM	$0.312^{+0.094}_{-0.094}$	$0.724^{+0.025}_{-0.014}$	$-0.162^{+0.025}_{-0.017}$
	$RS_c _{M_{g^{(1)}} = 4.8}$	$0.306^{+0.094}_{-0.093}$	$0.720^{+0.026}_{-0.016}$	$-0.174^{+0.021}_{-0.013}$
	$RS_c _{M_{g^{(1)}} = 6.1}$	$0.307^{+0.094}_{-0.093}$	$0.721^{+0.026}_{-0.016}$	$-0.170^{+0.022}_{-0.014}$
	$RS_c _{M_{g^{(1)}} = 7.4}$	$0.308^{+0.094}_{-0.093}$	$0.722^{+0.025}_{-0.015}$	$-0.168^{+0.023}_{-0.015}$
	$RS_c _{M_{g^{(1)}} = 8.7}$	$0.309^{+0.094}_{-0.094}$	$0.723^{+0.025}_{-0.015}$	$-0.166^{+0.024}_{-0.016}$
	$RS_c _{M_{g^{(1)}} = 10}$	$0.310^{+0.094}_{-0.094}$	$0.723^{+0.025}_{-0.014}$	$-0.165^{+0.024}_{-0.016}$
	LHCb	$0.25^{+0.120}_{-0.111}$	—	—
[1.1, 6]	SM	$0.199^{+0.120}_{-0.120}$	$0.818^{+0.011}_{-0.011}$	$0.009^{+0.027}_{-0.018}$
	$RS_c _{M_{g^{(1)}} = 4.8}$	$0.190^{+0.120}_{-0.119}$	$0.824^{+0.010}_{-0.007}$	$-0.005^{+0.025}_{-0.014}$
	$RS_c _{M_{g^{(1)}} = 6.1}$	$0.193^{+0.120}_{-0.119}$	$0.821^{+0.010}_{-0.008}$	$0.001^{+0.026}_{-0.015}$
	$RS_c _{M_{g^{(1)}} = 7.4}$	$0.195^{+0.120}_{-0.119}$	$0.820^{+0.010}_{-0.010}$	$0.003^{+0.026}_{-0.016}$
	$RS_c _{M_{g^{(1)}} = 8.7}$	$0.196^{+0.120}_{-0.119}$	$0.819^{+0.010}_{-0.010}$	$0.005^{+0.026}_{-0.016}$
	$RS_c _{M_{g^{(1)}} = 10}$	$0.197^{+0.120}_{-0.120}$	$0.819^{+0.011}_{-0.011}$	$0.006^{+0.026}_{-0.017}$
	LHCb	$0.09^{+0.061}_{-0.051}$	—	—

Table 5.2: Numerical results of  $A_{FB}^\Lambda$  and  $A_{FB}^{\ell\Lambda}$  (low  $s$  region) in the  $\Lambda_b \rightarrow \Lambda(\rightarrow p\pi)\mu^+\mu^-$  decay, obtained for the SM and the  $RS_c$  model with  $y_\star = 1.5$  case, in different bins of  $s$ . Experimentally measured values are taken from [217].

		$\langle A_{FB}^\Lambda \rangle$	$\langle A_{FB}^{\ell\Lambda} \rangle$
[0.1, 2]	SM	$-0.310^{+0.015}_{-0.008}$	$-0.031^{+0.003}_{-0.002}$
	$RS_c _{M_{g^{(1)}} = 4.8}$	$-0.313^{+0.013}_{-0.004}$	$-0.030^{+0.003}_{-0.002}$
	$RS_c _{M_{g^{(1)}} = 6.1}$	$-0.313^{+0.014}_{-0.006}$	$-0.030^{+0.003}_{-0.002}$
	$RS_c _{M_{g^{(1)}} = 7.4}$	$-0.312^{+0.015}_{-0.007}$	$-0.030^{+0.003}_{-0.002}$
	$RS_c _{M_{g^{(1)}} = 8.7}$	$-0.312^{+0.015}_{-0.007}$	$-0.031^{+0.003}_{-0.002}$
	$RS_c _{M_{g^{(1)}} = 10}$	$-0.311^{+0.015}_{-0.007}$	$-0.031^{+0.003}_{-0.002}$
	LHCb	$-0.12^{+0.344}_{-0.318}$	—
[2, 4]	SM	$-0.306^{+0.022}_{-0.012}$	$-0.016^{+0.008}_{-0.009}$
	$RS_c _{M_{g^{(1)}} = 4.8}$	$-0.311^{+0.016}_{-0.005}$	$-0.013^{+0.009}_{-0.010}$
	$RS_c _{M_{g^{(1)}} = 6.1}$	$-0.311^{+0.018}_{-0.008}$	$-0.014^{+0.008}_{-0.009}$
	$RS_c _{M_{g^{(1)}} = 7.4}$	$-0.310^{+0.020}_{-0.009}$	$0.015^{+0.008}_{-0.009}$
	$RS_c _{M_{g^{(1)}} = 8.7}$	$-0.310^{+0.020}_{-0.010}$	$-0.015^{+0.008}_{-0.009}$
	$RS_c _{M_{g^{(1)}} = 10}$	$-0.309^{+0.021}_{-0.010}$	$-0.016^{+0.008}_{-0.009}$
	LHCb	—	—
[4, 6]	SM	$-0.311^{+0.014}_{-0.008}$	$0.021^{+0.007}_{-0.009}$
	$RS_c _{M_{g^{(1)}} = 4.8}$	$-0.314^{+0.008}_{-0.002}$	$0.024^{+0.008}_{-0.009}$
	$RS_c _{M_{g^{(1)}} = 6.1}$	$-0.314^{+0.010}_{-0.004}$	$0.023^{+0.007}_{-0.009}$
	$RS_c _{M_{g^{(1)}} = 7.4}$	$-0.314^{+0.012}_{-0.005}$	$0.023^{+0.007}_{-0.009}$
	$RS_c _{M_{g^{(1)}} = 8.7}$	$-0.314^{+0.012}_{-0.006}$	$0.022^{+0.007}_{-0.009}$
	$RS_c _{M_{g^{(1)}} = 10}$	$-0.313^{+0.013}_{-0.006}$	$0.022^{+0.007}_{-0.009}$
	LHCb	—	—
[6, 8]	SM	$-0.317^{+0.007}_{-0.004}$	$0.052^{+0.005}_{-0.007}$
	$RS_c _{M_{g^{(1)}} = 4.8}$	$-0.314^{+0.002}_{-0.001}$	$0.054^{+0.005}_{-0.007}$
	$RS_c _{M_{g^{(1)}} = 6.1}$	$-0.317^{+0.004}_{-0.001}$	$0.054^{+0.005}_{-0.007}$
	$RS_c _{M_{g^{(1)}} = 7.4}$	$-0.317^{+0.005}_{-0.002}$	$0.054^{+0.005}_{-0.007}$
	$RS_c _{M_{g^{(1)}} = 8.7}$	$-0.317^{+0.006}_{-0.002}$	$0.053^{+0.005}_{-0.007}$
	$RS_c _{M_{g^{(1)}} = 10}$	$-0.317^{+0.006}_{-0.003}$	$0.053^{+0.006}_{-0.007}$
	LHCb	—	—
[1.1, 6]	SM	$-0.309^{+0.018}_{-0.010}$	$-0.002^{+0.004}_{-0.005}$
	$RS_c _{M_{g^{(1)}} = 4.8}$	$-0.312^{+0.012}_{-0.004}$	$0.001^{+0.005}_{-0.006}$
	$RS_c _{M_{g^{(1)}} = 6.1}$	$-0.312^{+0.014}_{-0.006}$	$0.000^{+0.005}_{-0.006}$
	$RS_c _{M_{g^{(1)}} = 7.4}$	$-0.312^{+0.016}_{-0.007}$	$-0.001^{+0.005}_{-0.005}$
	$RS_c _{M_{g^{(1)}} = 8.7}$	$-0.311^{+0.016}_{-0.008}$	$-0.001^{+0.005}_{-0.005}$
	$RS_c _{M_{g^{(1)}} = 10}$	$-0.311^{+0.017}_{-0.008}$	$-0.001^{+0.004}_{-0.005}$
	LHCb	—	—

Table 5.3: Numerical results of  $\frac{d\mathcal{B}}{ds}$ ,  $F_L$  and  $A_{FB}^\ell$  (high  $s$  region) in the  $\Lambda_b \rightarrow \Lambda(\rightarrow p\pi)\mu^+\mu^-$  decay, obtained for the SM and the  $RS_c$  model with  $y_\star = 1.5$  case, in different bins of  $s$ . Experimentally measured values are taken from [217].

		$\langle \frac{d\mathcal{B}}{ds} \times 10^{-7} \rangle$	$\langle F_L \rangle$	$\langle A_{FB}^\ell \rangle$
[15, 16]	SM			
	$RS_c _{M_{g(1)} = 4.8}$	$0.798^{+0.073}_{-0.073}$	$0.454^{+0.032}_{-0.017}$	$-0.382^{+0.017}_{-0.008}$
	$RS_c _{M_{g(1)} = 6.1}$	$0.832^{+0.073}_{-0.073}$	$0.447^{+0.033}_{-0.017}$	$-0.365^{+0.014}_{-0.006}$
	$RS_c _{M_{g(1)} = 7.4}$	$0.816^{+0.073}_{-0.073}$	$0.450^{+0.033}_{-0.017}$	$-0.372^{+0.015}_{-0.007}$
	$RS_c _{M_{g(1)} = 8.7}$	$0.810^{+0.073}_{-0.073}$	$0.451^{+0.032}_{-0.017}$	$-0.375^{+0.015}_{-0.007}$
	$RS_c _{M_{g(1)} = 10}$	$0.806^{+0.074}_{-0.074}$	$0.452^{+0.032}_{-0.017}$	$-0.377^{+0.016}_{-0.007}$
	LHCb	$0.804^{+0.074}_{-0.074}$	$0.452^{+0.032}_{-0.017}$	$-0.378^{+0.016}_{-0.008}$
[16, 18]	SM			
	$RS_c _{M_{g(1)} = 4.8}$	$1.12^{+0.30}_{-0.30}$	$0.49^{+0.304}_{-0.304}$	$-0.10^{+0.183}_{-0.163}$
	$RS_c _{M_{g(1)} = 6.1}$	$0.825^{+0.075}_{-0.075}$	$0.418^{+0.033}_{-0.017}$	$-0.381^{+0.013}_{-0.006}$
	$RS_c _{M_{g(1)} = 7.4}$	$0.877^{+0.075}_{-0.075}$	$0.411^{+0.033}_{-0.017}$	$-0.356^{+0.010}_{-0.004}$
	$RS_c _{M_{g(1)} = 8.7}$	$0.855^{+0.075}_{-0.075}$	$0.414^{+0.033}_{-0.017}$	$-0.366^{+0.011}_{-0.005}$
	$RS_c _{M_{g(1)} = 10}$	$0.844^{+0.075}_{-0.075}$	$0.415^{+0.033}_{-0.017}$	$-0.371^{+0.012}_{-0.005}$
	LHCb	$0.838^{+0.075}_{-0.075}$	$0.416^{+0.033}_{-0.017}$	$-0.374^{+0.012}_{-0.005}$
[18, 20]	SM			
	$RS_c _{M_{g(1)} = 4.8}$	$0.835^{+0.075}_{-0.075}$	$0.416^{+0.033}_{-0.017}$	$-0.376^{+0.012}_{-0.006}$
	$RS_c _{M_{g(1)} = 6.1}$	$1.22^{+0.29}_{-0.29}$	$0.68^{+0.158}_{-0.216}$	$-0.07^{+0.136}_{-0.127}$
	$RS_c _{M_{g(1)} = 7.4}$	$0.658^{+0.066}_{-0.066}$	$0.371^{+0.034}_{-0.019}$	$-0.317^{+0.010}_{-0.010}$
	$RS_c _{M_{g(1)} = 8.7}$	$0.726^{+0.066}_{-0.066}$	$0.367^{+0.034}_{-0.020}$	$-0.286^{+0.010}_{-0.010}$
	$RS_c _{M_{g(1)} = 10}$	$0.698^{+0.066}_{-0.066}$	$0.368^{+0.034}_{-0.019}$	$-0.297^{+0.010}_{-0.010}$
	LHCb	$0.685^{+0.066}_{-0.066}$	$0.369^{+0.034}_{-0.019}$	$-0.303^{+0.010}_{-0.010}$
[15, 20]	SM			
	$RS_c _{M_{g(1)} = 4.8}$	$0.677^{+0.066}_{-0.066}$	$0.370^{+0.034}_{-0.019}$	$-0.307^{+0.010}_{-0.010}$
	$RS_c _{M_{g(1)} = 6.1}$	$0.672^{+0.066}_{-0.066}$	$0.370^{+0.034}_{-0.019}$	$-0.309^{+0.010}_{-0.010}$
	$RS_c _{M_{g(1)} = 7.4}$	$1.24^{+0.30}_{-0.30}$	$0.62^{+0.243}_{-0.273}$	$0.01^{+0.155}_{-0.146}$
	$RS_c _{M_{g(1)} = 8.7}$	$0.753^{+0.069}_{-0.069}$	$0.409^{+0.033}_{-0.018}$	$-0.358^{+0.012}_{-0.007}$
	$RS_c _{M_{g(1)} = 10}$	$0.807^{+0.069}_{-0.069}$	$0.403^{+0.034}_{-0.019}$	$-0.332^{+0.008}_{-0.009}$
	LHCb	$0.785^{+0.069}_{-0.069}$	$0.405^{+0.034}_{-0.019}$	$-0.343^{+0.010}_{-0.008}$
[15, 20]	SM			
	$RS_c _{M_{g(1)} = 4.8}$	$0.774^{+0.069}_{-0.069}$	$0.406^{+0.033}_{-0.019}$	$-0.348^{+0.010}_{-0.007}$
	$RS_c _{M_{g(1)} = 6.1}$	$0.767^{+0.069}_{-0.069}$	$0.407^{+0.033}_{-0.019}$	$-0.351^{+0.011}_{-0.007}$
	$RS_c _{M_{g(1)} = 7.4}$	$0.764^{+0.069}_{-0.069}$	$0.407^{+0.033}_{-0.019}$	$-0.353^{+0.011}_{-0.007}$
	$RS_c _{M_{g(1)} = 8.7}$	$1.20^{+0.27}_{-0.27}$	$0.61^{+0.114}_{-0.143}$	$-0.05^{+0.095}_{-0.095}$
	$RS_c _{M_{g(1)} = 10}$			
	LHCb			

Table 5.4: Numerical results of  $A_{FB}^\Lambda$  and  $A_{FB}^{\ell\Lambda}$  (high  $s$  region) in the  $\Lambda_b \rightarrow \Lambda(\rightarrow p\pi)\mu^+\mu^-$  decay, obtained for the SM and the  $RS_c$  model with  $y_\star = 1.5$  case, in different bins of  $s$ . Experimentally measured values are taken from [217].

		$\langle A_{FB}^\Lambda \rangle$	$\langle A_{FB}^{\ell\Lambda} \rangle$
[15, 16]	SM	$-0.307^{+0.002}_{-0.004}$	$0.131^{+0.004}_{-0.008}$
	$RS_c _{M_{g^{(1)}} = 4.8}$	$-0.287^{+0.003}_{-0.005}$	$0.132^{+0.004}_{-0.008}$
	$RS_c _{M_{g^{(1)}} = 6.1}$	$-0.296^{+0.003}_{-0.005}$	$0.132^{+0.004}_{-0.008}$
	$RS_c _{M_{g^{(1)}} = 7.4}$	$-0.300^{+0.003}_{-0.004}$	$0.132^{+0.004}_{-0.008}$
	$RS_c _{M_{g^{(1)}} = 8.7}$	$-0.302^{+0.003}_{-0.004}$	$0.132^{+0.004}_{-0.008}$
	$RS_c _{M_{g^{(1)}} = 10}$	$-0.304^{+0.002}_{-0.004}$	$0.132^{+0.004}_{-0.008}$
	LHCb	$-0.19^{+0.143}_{-0.163}$	—
[16, 18]	SM	$-0.289^{+0.005}_{-0.006}$	$0.141^{+0.004}_{-0.008}$
	$RS_c _{M_{g^{(1)}} = 4.8}$	$-0.265^{+0.005}_{-0.006}$	$0.140^{+0.004}_{-0.009}$
	$RS_c _{M_{g^{(1)}} = 6.1}$	$-0.276^{+0.005}_{-0.006}$	$0.141^{+0.004}_{-0.008}$
	$RS_c _{M_{g^{(1)}} = 7.4}$	$-0.280^{+0.005}_{-0.006}$	$0.141^{+0.004}_{-0.008}$
	$RS_c _{M_{g^{(1)}} = 8.7}$	$-0.283^{+0.005}_{-0.006}$	$0.141^{+0.004}_{-0.008}$
	$RS_c _{M_{g^{(1)}} = 10}$	$-0.284^{+0.005}_{-0.006}$	$0.141^{+0.004}_{-0.008}$
	LHCb	$-0.44^{+0.104}_{-0.058}$	—
[18, 20]	SM	$-0.227^{+0.011}_{-0.011}$	$0.153^{+0.005}_{-0.009}$
	$RS_c _{M_{g^{(1)}} = 4.8}$	$-0.201^{+0.010}_{-0.010}$	$0.151^{+0.005}_{-0.009}$
	$RS_c _{M_{g^{(1)}} = 6.1}$	$-0.211^{+0.010}_{-0.010}$	$0.152^{+0.005}_{-0.009}$
	$RS_c _{M_{g^{(1)}} = 7.4}$	$-0.216^{+0.011}_{-0.011}$	$0.152^{+0.005}_{-0.009}$
	$RS_c _{M_{g^{(1)}} = 8.7}$	$-0.219^{+0.011}_{-0.011}$	$0.153^{+0.005}_{-0.009}$
	$RS_c _{M_{g^{(1)}} = 10}$	$-0.221^{+0.011}_{-0.011}$	$0.153^{+0.005}_{-0.009}$
	LHCb	$-0.13^{+0.095}_{-0.124}$	—
[15, 20]	SM	$-0.271^{+0.011}_{-0.011}$	$0.143^{+0.005}_{-0.008}$
	$RS_c _{M_{g^{(1)}} = 4.8}$	$-0.247^{+0.011}_{-0.011}$	$0.142^{+0.005}_{-0.009}$
	$RS_c _{M_{g^{(1)}} = 6.1}$	$-0.257^{+0.011}_{-0.011}$	$0.143^{+0.005}_{-0.009}$
	$RS_c _{M_{g^{(1)}} = 7.4}$	$-0.262^{+0.011}_{-0.011}$	$0.143^{+0.005}_{-0.009}$
	$RS_c _{M_{g^{(1)}} = 8.7}$	$-0.264^{+0.011}_{-0.011}$	$0.143^{+0.005}_{-0.009}$
	$RS_c _{M_{g^{(1)}} = 10}$	$-0.266^{+0.011}_{-0.011}$	$0.143^{+0.005}_{-0.008}$
	LHCb	$-0.29^{+0.076}_{-0.081}$	—

## Chapter 6

# Probing new physics effects in $\Lambda_b \rightarrow \Lambda(\rightarrow p\pi^-)\ell^+\ell^-$ decay via model independent approach

In order to test the SM to better accuracy and to explain the possible mismatch with its predictions in different  $B$ -meson decays, the theoretical physicists are trying to construct other successful models than the SM and experimentalists are trying to build more powerful machines for this purpose. The wealth of data from LHC compel the theoretical community to adopt a fundamental approach that is not along a defined path but has open ends. This leads to model independent approach which is most general, exploratory, and sensitive to data-driven methods. It is designed in such a way that the possible NP effects can be captured and any discrepancies between the data and the SM predictions can be accommodated. In this situation, it becomes easy to predict a set of models that favors the data and also helps us to see which class of models is excluded with a high confidence level.

This chapter is devoted to the study of  $\Lambda_b \rightarrow \Lambda(\rightarrow p\pi^-)\ell^+\ell^-$  decay in a model independent approach where new  $VA$ ,  $SP$  and  $(T)$  operators are introduced. The  $VA$  operators modify the existing WCs, in case they have the same form as the SM  $VA$  operators, whereas the  $SP$  and  $T$  operators are absent in the SM. These modifications lead to interesting results for branching fraction ( $d\mathcal{B}/ds$ ), forward-backward asymmetries ( $A_{FB}^\ell$ ,  $A_{FB}^\Lambda$ ,  $A_{FB}^{\ell\Lambda}$ ), longitudinal and transverse polarization fractions ( $F_L$ ,  $F_T$ ), asymmetry parameters  $\alpha$ 's and some other foldings ( $\mathcal{P}_i$ ). Most of the WCs corresponding to these new operators have already been constrained from experimental measurements of different physical observables in  $B$ -mesons decays. The measured results of different observables in  $\Lambda_b$  decays further constrain these new WCs and hence make their parametric space even narrower than  $B$ -meson decays. Therefore, this approach will prove fruitful to check which type of NP contributions should be added to the SM to match with experimental measurements in  $B$  and  $\Lambda_b$  sector.

This chapter is organized as follows: after presenting the effective Hamiltonian for model independent approach in Sect. 6.1 we discuss the helicity formalism for the decay under consideration in Sect. 6.2. In terms of these helicity fractions, the expressions of decay rate and other physical observables are obtained in Sect. 6.3 and their numerical analysis is performed in Sect. 6.4.

## 6.1 Effective Hamiltonian for model independent approach

The exclusive  $\Lambda_b(P_{\Lambda_b}) \rightarrow \Lambda(P_{\Lambda})\ell^+(q_1)\ell^-(q_2)$  decay is governed by the quark level  $b \rightarrow s\ell^+\ell^-$  transition. In order to incorporate the NP, the effective Hamiltonian of the SM is modified in such a way that not only new operators and their corresponding WCs are introduced but in some cases the SM WCs are modified provided the form of the new operators matches to that of the SM operators. Just to emphasis, here the additional terms are of two types: the first one corresponds to add the scalar ( $\mathcal{O}_S = \bar{s}b$ ), pseudo-scalar ( $\mathcal{O}_P = \bar{s}\gamma_5 b$ ) and tensor ( $\mathcal{O}_T = \bar{s}\sigma^{\mu\nu}b$ ) operators along with their respective WCs ( $C_S^{(\prime)}$ ,  $C_P^{(\prime)}$ ,  $C_T$  and  $C_{T_5}$ ) and the other is related to the addition of new vector and axial-vector operators to the already existing SM  $VA$  operators, hence modifying the respective SM WCs by adding ( $C_V^{(\prime)}$ ,  $C_A^{(\prime)}$ ). The most general Hamiltonian in this case will take the form

$$\begin{aligned} \mathcal{H}_{eff} = & -\frac{G_F\alpha_e}{\sqrt{2}\pi}V_{tb}V_{ts}^*\left[\left(C_9^{eff}\bar{s}\gamma^\mu P_L b - \frac{2m_b}{s}C_7^{eff}\bar{s}i q_\nu\sigma^{\mu\nu}P_R b + C_V\bar{s}\gamma^\mu P_L b + C_V'\bar{s}\gamma^\mu P_R b\right)\bar{\ell}\gamma_\mu\ell\right. \\ & + \left.(C_{10}\bar{s}\gamma^\mu P_L b + C_A\bar{s}\gamma^\mu P_L b + C_A'\bar{s}\gamma^\mu P_R b\right)\bar{\ell}\gamma_\mu\gamma_5\ell + \left.(C_S'\bar{s}P_L b + C_S\bar{P}R b\right)\bar{\ell}\ell \\ & + \left.(C_P'\bar{s}P_L b + C_P\bar{P}R b\right)\bar{\ell}\gamma_5\ell + C_T(\bar{s}\sigma^{\mu\nu}b)\bar{\ell}\sigma_{\mu\nu}\ell + C_{T_5}(\bar{s}\sigma^{\mu\nu}b)\bar{\ell}\sigma_{\mu\nu}\gamma_5\ell\left. \right], \end{aligned} \quad (6.1)$$

where  $G_F$  is Fermi-constant,  $\alpha_e$  is fine structure constant,  $V_{tb}V_{ts}^*$  are the corresponding elements of CKM matrix and  $s$  is dilepton mass squared. The new WCs  $C_V^{(\prime)}$ ,  $C_A^{(\prime)}$ ,  $C_S^{(\prime)}$ ,  $C_P^{(\prime)}$ ,  $C_T$  and  $C_{T_5}$  represent the vector, axial-vector, scalar, pseudo-scalar, tensor and pseudo-tensor currents, respectively. The part of Hamiltonian (6.1) representing  $VA$  current is

$$\begin{aligned} \mathcal{H}_{VA} = & -\frac{G_F\alpha_e}{\sqrt{2}\pi}V_{tb}V_{ts}^*\left[\left(C_9^{eff}(H_V^\mu - H_A^\mu) - \frac{2m_b}{s}C_7^{eff}(H_T^\mu + H_{T_5}^\mu) + C_V(H_V^\mu - H_A^\mu) + C_V'(H_V^\mu + H_A^\mu)\right)\right. \\ & \left.\times\bar{\ell}\gamma_\mu\ell + \left(C_{10}^{eff}(H_V^\mu - H_A^\mu) + C_A(H_V^\mu - H_A^\mu) + C_A'(H_V^\mu + H_A^\mu)\right)\bar{\ell}\gamma_\mu\gamma_5\ell\right], \end{aligned} \quad (6.2)$$

where  $H_V^\mu = \frac{1}{2}(\bar{s}\gamma^\mu b)$  and  $H_A^\mu = \frac{1}{2}(\bar{s}\gamma^\mu\gamma_5 b)$ . Writing  $\tilde{C}_9^+ = C_9^{eff} + C_V + C_V'$ ,  $\tilde{C}_9^- = C_9^{eff} + C_V - C_V'$ ,  $\tilde{C}_{10}^+ = C_{10}^{eff} + C_A + C_A'$  and  $\tilde{C}_{10}^- = C_{10}^{eff} + C_A - C_A'$ , Eq. (6.2) takes the form

$$\mathcal{H}_{VA} = -\frac{G_F\alpha_e}{\sqrt{2}\pi}V_{tb}V_{ts}^*\left[\left(H_V^\mu\tilde{C}_9^+ - H_A^\mu\tilde{C}_9^- - \frac{2m_b}{s}C_7^{eff}(H_T^\mu + H_{T_5}^\mu)\right)\bar{\ell}\gamma_\mu\ell + \left(H_V^\mu\tilde{C}_{10}^+ - H_A^\mu\tilde{C}_{10}^-\right)\bar{\ell}\gamma_\mu\gamma_5\ell\right]. \quad (6.3)$$

The  $SP$  part of effective Hamiltonian is

$$\mathcal{H}_{SP} = -\frac{G_F\alpha_e}{\sqrt{2}\pi}V_{tb}V_{ts}^*\left[\left(C_S'(H_S - H_P) + C_S(H_S + H_P)\right)\bar{\ell}\ell + \left(C_P'(H_S - H_P) + C_P(H_S + H_P)\right)\bar{\ell}\gamma_5\ell\right], \quad (6.4)$$

with  $H_S = \bar{s}b$  and  $H_P = \bar{s}\gamma_5 b$ . In a more compact form it becomes

$$\mathcal{H}_{SP} = [C_S^+ H_S + C_S^- H_P]\bar{\ell}\ell + [C_P^+ H_S + C_P^- H_P]\bar{\ell}\gamma_5\ell, \quad (6.5)$$

where  $C_{S,P}^\pm = C_{S,P} \pm C_{S,P}'$ . Likewise, we can write the tensor ( $T'$ ) part from Eq. (6.1) as

$$\mathcal{H}_{T'} = -\frac{G_F\alpha_e}{\sqrt{2}\pi}V_{tb}V_{ts}^*\left[(\bar{s}\sigma^{\mu\nu}b)\bar{\ell}\sigma_{\mu\nu}(C_T + C_{T_5}\gamma_5)\ell\right]. \quad (6.6)$$

## 6.2 Helicity Formalism in model independent approach

As an exclusive process, the matrix elements for  $\Lambda_b \rightarrow \Lambda$  transition for different possible currents can be parameterized in terms of FFs,  $f_{t,0,\perp}^V$ ,  $f_{t,0,\perp}^A$ ,  $f_{0,\perp}^T$  and  $f_{0,\perp}^{T_5}$  [71]. It is well known fact that the helicity formalism provides a convenient way to describe these parameterizations therefore, we will adopt it to express the different matrix elements. In case of vector current it becomes

$$H_V^t(s_{\Lambda_b}, s_\Lambda) = \varepsilon_t^{\mu*} \langle \Lambda(P_\Lambda, s_\Lambda) | \bar{s} \gamma^\mu b | \Lambda_b(P_{\Lambda_b}, s_{\Lambda_b}) \rangle, \quad (6.7)$$

where  $\varepsilon_t^{\mu*}$  denotes the time-like polarization of the virtual gauge boson and  $s_{\Lambda_b}$  and  $s_\Lambda$  are the spin-projections on the  $z$ -axis in the respective rest frames of initial and final state baryons, respectively. In terms of the FFs, the matrix elements for  $\Lambda_b \rightarrow \Lambda$  appearing in Eq. (6.7) become

$$\begin{aligned} \langle \Lambda(P_\Lambda, s_\Lambda) | \bar{s} \gamma^\mu b | \Lambda_b(P_{\Lambda_b}, s_{\Lambda_b}) \rangle &= \bar{u}(P_{\Lambda_b}, s_{\Lambda_b}) \left[ f_t^V(s) (m_{\Lambda_b} - m_\Lambda) \frac{q^\mu}{s} + f_0^V(s) \frac{m_{\Lambda_b} + m_\Lambda}{s_+} \right. \\ &\quad \times \left( P_{\Lambda_b}^\mu + P_\Lambda^\mu - \frac{q^\mu}{s} (m_{\Lambda_b}^2 - m_\Lambda^2) \right) \\ &\quad \left. + f_\perp^V(s) \left( \gamma^\mu - \frac{2m_\Lambda}{s_+} P_{\Lambda_b}^\mu - \frac{2m_{\Lambda_b}}{s_+} P_\Lambda^\mu \right) \right] u(P_\Lambda, s_\Lambda), \quad (6.8) \end{aligned}$$

with  $s_+ = (m_{\Lambda_b} + m_\Lambda)^2 - s$  and  $q = P_{\Lambda_b} - P_\Lambda$ . Using the kinematical relations defined in [62, 113] and taking polarization vector from Eq. (3.11), the non-zero helicity components for time-like polarization from Eq. (6.8) read as

$$H_V^t(+1/2, +1/2) = H_V^t(-1/2, -1/2) = f_V^t(s) \frac{m_{\Lambda_b} - m_\Lambda}{\sqrt{s}} \sqrt{s_+}. \quad (6.9)$$

In case of longitudinal polarization (c.f. Eq. (3.11)), the corresponding helicity amplitude becomes

$$H_V^0(s_{\Lambda_b}, s_\Lambda) = \varepsilon_0^{\mu*} \langle \Lambda(P_\Lambda, s_\Lambda) | \bar{s} \gamma^\mu b | \Lambda_b(P_{\Lambda_b}, s_{\Lambda_b}) \rangle \quad (6.10)$$

and using Eq. (6.8), the non-zero longitudinal components for vector current become

$$H_V^0(+1/2, +1/2) = H_V^0(-1/2, -1/2) = f_V^0(s) \frac{m_{\Lambda_b} + m_\Lambda}{\sqrt{s}} \sqrt{s_-}, \quad (6.11)$$

with  $s_- = (m_{\Lambda_b} - m_\Lambda)^2 - s$ . Likewise, for the transverse polarization

$$H_V^\pm(s_{\Lambda_b}, s_\Lambda) = \varepsilon_\pm^{\mu*} \langle \Lambda(P_\Lambda, s_\Lambda) | \bar{s} \gamma^\mu b | \Lambda_b(P_{\Lambda_b}, s_{\Lambda_b}) \rangle, \quad (6.12)$$

the corresponding non-zero helicity components are

$$H_V^\pm(-1/2, +1/2) = H_V^\mp(+1/2, -1/2) = -f_V^\pm(s) \sqrt{2s_-}. \quad (6.13)$$



Similarly the matrix elements for the axial-vector currents are

$$\begin{aligned}
\langle \Lambda(P_\Lambda, s_\Lambda) | \bar{s} \gamma^\mu \gamma_5 b | \Lambda_b(P_{\Lambda_b}, s_{\Lambda_b}) \rangle &= -\bar{u}(P_{\Lambda_b}, s_{\Lambda_b}) \left[ f_t^A(s) (m_{\Lambda_b} + m_\Lambda) \frac{q^\mu}{s} + f_0^A(s) \frac{m_{\Lambda_b} - m_\Lambda}{s_-} \right. \\
&\times \left( P_{\Lambda_b}^\mu + P_\Lambda^\mu - \frac{q^\mu}{s} (m_{\Lambda_b}^2 - m_\Lambda^2) \right) \\
&\left. + f_\perp^V(s) \left( \gamma^\mu + \frac{2m_\Lambda}{s_+} P_{\Lambda_b}^\mu - \frac{2m_{\Lambda_b}}{s_-} P_\Lambda^\mu \right) \right] u(P_\Lambda, s_\Lambda). \quad (6.14)
\end{aligned}$$

The corresponding non-zero components for time-like polarization of virtual boson are

$$H_A^t(s_{\Lambda_b}, s_\Lambda) = \varepsilon_t^{\mu*} \langle \Lambda(P_\Lambda, s_\Lambda) | \bar{s} \gamma^\mu \gamma_5 b | \Lambda(P_{\Lambda_b}, s_{\Lambda_b}) \rangle, \quad (6.15)$$

$$H_A^t(+1/2, +1/2) = -H_A^t(-1/2, -1/2) = f_A^t(s) \frac{m_{\Lambda_b} + m_\Lambda}{\sqrt{s}} \sqrt{s_-}. \quad (6.16)$$

The corresponding longitudinally polarized components are

$$H_A^0(s_{\Lambda_b}, s_\Lambda) = \varepsilon_0^{\mu*} \langle \Lambda(P_\Lambda, s_\Lambda) | \bar{s} \gamma^\mu \gamma_5 b | \Lambda(P_{\Lambda_b}, s_{\Lambda_b}) \rangle, \quad (6.17)$$

$$H_A^0(+1/2, +1/2) = -H_A^0(-1/2, -1/2) = f_A^0(s) \frac{m_{\Lambda_b} - m_\Lambda}{\sqrt{s}} \sqrt{s_+} \quad (6.18)$$

and the results for the transverse polarization are

$$H_A^\pm(s_{\Lambda_b}, s_\Lambda) = \varepsilon_\pm^{\mu*} \langle \Lambda(P_\Lambda, s_\Lambda) | \bar{s} \gamma^\mu \gamma_5 b | \Lambda(P_{\Lambda_b}, s_{\Lambda_b}) \rangle, \quad (6.19)$$

$$H_A^+(-1/2, +1/2) = -H_A^-(-1/2, -1/2) = -f_A^\pm(s) \sqrt{2s_+}. \quad (6.20)$$

For the dipole operators  $i\bar{s}q_\nu\sigma^{\mu\nu}b$  and  $i\bar{s}q_\nu\sigma^{\mu\nu}\gamma_5b$ , the respective transition matrix elements are

$$\begin{aligned}
\langle \Lambda(P_\Lambda, s_\Lambda) | \bar{s} i \sigma^{\mu\nu} q_\nu b | \Lambda_b(P_{\Lambda_b}, s_{\Lambda_b}) \rangle &= -\bar{u}(P_{\Lambda_b}, s_{\Lambda_b}) \left[ f_0^T(s) \frac{s}{s_+} \left( P_{\Lambda_b}^\mu + P_\Lambda^\mu - \frac{q^\mu}{s} (m_{\Lambda_b}^2 - m_\Lambda^2) \right) \right. \\
&\left. + f_\perp^T(s) (m_{\Lambda_b} + m_\Lambda) \left( \gamma^\mu - \frac{2m_\Lambda}{s_+} P_{\Lambda_b}^\mu - \frac{2m_{\Lambda_b}}{s_+} P_\Lambda^\mu \right) \right] u(P_\Lambda, s_\Lambda) \quad (6.21)
\end{aligned}$$

and

$$\begin{aligned}
\langle \Lambda(P_\Lambda, s_\Lambda) | \bar{s} i \sigma^{\mu\nu} q_\nu \gamma_5 b | \Lambda_b(P_{\Lambda_b}, s_{\Lambda_b}) \rangle &= -\bar{u}(P_{\Lambda_b}, s_{\Lambda_b}) \gamma_5 \left[ f_0^{T_5}(s) \frac{s}{s_-} \left( P_{\Lambda_b}^\mu + P_\Lambda^\mu - \frac{q^\mu}{s} (m_{\Lambda_b}^2 - m_\Lambda^2) \right) \right. \\
&\left. + f_\perp^{T_5}(s) (m_{\Lambda_b} - m_\Lambda) \left( \gamma^\mu + \frac{2m_\Lambda}{s_-} P_{\Lambda_b}^\mu - \frac{2m_{\Lambda_b}}{s_-} P_\Lambda^\mu \right) \right] u(P_\Lambda, s_\Lambda). \quad (6.22)
\end{aligned}$$

In this case, the corresponding non-zero helicity components for different polarizations of virtual boson are

$$H_T^0(s_{\Lambda_b}, s_\Lambda) = \varepsilon_0^{\mu*} \langle \Lambda(P_\Lambda, s_\Lambda) | \bar{s} i \sigma^{\mu\nu} q_\nu b | \Lambda_b(P_{\Lambda_b}, s_{\Lambda_b}) \rangle, \quad (6.23)$$

$$H_{T_5}^0(s_{\Lambda_b}, s_\Lambda) = \varepsilon_0^{\mu*} \langle \Lambda(P_\Lambda, s_\Lambda) | \bar{s} i \sigma^{\mu\nu} q_\nu \gamma_5 b | \Lambda_b(P_{\Lambda_b}, s_{\Lambda_b}) \rangle, \quad (6.24)$$

$$H_T^0(+1/2, +1/2) = H_T^0(-1/2, -1/2) = -f_T^0(s) \sqrt{ss_-}, \quad (6.25)$$

$$H_{T_5}^0(+1/2, +1/2) = H_{T_5}^0(-1/2, -1/2) = f_{T_5}^0(s) \sqrt{ss_+}. \quad (6.26)$$

The helicity amplitude for the tensor current; i.e.,  $\bar{s}\sigma^{\mu\nu}b$  becomes

$$H_{T'}^{m,n}(s_{\Lambda_b}, s_{\Lambda}) = \varepsilon_m^{\mu*} \varepsilon_n^{\mu*} \langle \Lambda(P_{\Lambda}, s_{\Lambda}) | \bar{s}i\sigma^{\mu\nu}b | \Lambda(P_{\Lambda_b}, s_{\Lambda_b}) \rangle, \quad (6.27)$$

where  $m, n = t, 0, \pm$ . Using the expression of  $\langle \Lambda(P_{\Lambda}, s_{\Lambda}) | \bar{s}i\sigma^{\mu\nu}b | \Lambda_b(P_{\Lambda_b}, s_{\Lambda_b}) \rangle$  from [113] (c.f. Eq. (C.7)), the non-zero components for virtual bosons's time-like, longitudinal, transverse and the possible combinations of these polarizations become

$$H_{T'}^{0t}(+1/2, +1/2) = H_{T'}^{0t}(-1/2, -1/2) = -f_T^0(s)\sqrt{s_-}, \quad (6.28)$$

$$H_{T'}^{+t}(-1/2, +1/2) = H_{T'}^{-t}(+1/2, -1/2) = f_{T_5}^{\perp}(s) \frac{m_{\Lambda_b} + m_{\Lambda}}{\sqrt{s}} \sqrt{2s_-}, \quad (6.29)$$

$$H_{T'}^{+0}(-1/2, +1/2) = H_{T'}^{-0}(+1/2, -1/2) = f_{T_5}^{\perp}(s) \frac{m_{\Lambda_b} - m_{\Lambda}}{\sqrt{s}} \sqrt{2s_+}, \quad (6.30)$$

$$H_{T'}^{+-}(+1/2, +1/2) = -H_{T'}^{+ -}(-1/2, -1/2) = -f_{T_5}^0(s)\sqrt{s_+}. \quad (6.31)$$

The remaining components can be obtained by using the relation  $H_{T'}^{m,n}(s_{\Lambda_b}, s_{\Lambda}) = -H_{T'}^{n,m}(s_{\Lambda_b}, s_{\Lambda})$ .

In order to obtain the matrix elements for the scalar and pseudo-scalar currents, we have to contract Eq. (6.8) and Eq. (6.14) with  $q_{\mu}$ . Using the Dirac equation and ignoring the mass of strange quark we have

$$\langle \Lambda(P_{\Lambda}, s_{\Lambda}) | \bar{s}b | \Lambda_b(P_{\Lambda_b}, s_{\Lambda_b}) \rangle = f_t^V(s) \frac{m_{\Lambda_b} - m_{\Lambda}}{m_b} \bar{u}(P_{\Lambda_b}, s_{\Lambda_b}) u(P_{\Lambda}, s_{\Lambda}), \quad (6.32)$$

$$\langle \Lambda(P_{\Lambda}, s_{\Lambda}) | \bar{s}\gamma_5 b | \Lambda_b(P_{\Lambda_b}, s_{\Lambda_b}) \rangle = f_t^A(s) \frac{m_{\Lambda_b} + m_{\Lambda}}{m_b} \bar{u}(P_{\Lambda_b}, s_{\Lambda_b}) \gamma_5 u(P_{\Lambda}, s_{\Lambda}). \quad (6.33)$$

Here, we can see that the matrix elements for these currents do not add any new FF. The corresponding helicity amplitudes along with their non-zero components are

$$H_S^t(s_{\Lambda_b}, s_{\Lambda}) = \varepsilon_t^{\mu*} \langle \Lambda(P_{\Lambda}, s_{\Lambda}) | \bar{s}b | \Lambda_b(P_{\Lambda_b}, s_{\Lambda_b}) \rangle, \quad (6.34)$$

$$H_S^t(+1/2, +1/2) = H_S^t(-1/2, -1/2) = f_V^t(s) \frac{m_{\Lambda_b} - m_{\Lambda}}{m_b} \sqrt{s_+}, \quad (6.35)$$

$$H_P^t(s_{\Lambda_b}, s_{\Lambda}) = \varepsilon_t^{\mu*} \langle \Lambda(P_{\Lambda}, s_{\Lambda}) | \bar{s}\gamma_5 b | \Lambda_b(P_{\Lambda_b}, s_{\Lambda_b}) \rangle, \quad (6.36)$$

$$H_P^t(+1/2, +1/2) = -H_P^t(-1/2, -1/2) = -f_A^t(s) \frac{m_{\Lambda_b} - m_{\Lambda}}{m_b} \sqrt{s_-}. \quad (6.37)$$

In the theoretical study of the exclusive decays the FFs being the non-perturbative quantities are the major source of uncertainties and hence having a good control on their precise calculations is always a need of time. To address this, several approaches have been opted to compute them, e.g., the quark models [63, 110, 246], the Lattice QCD [44], LCSR [89, 247] and the perturbative QCD approach [248]. In order to reduce the number of independent FFs, some effective theories are used, e.g., the HQET [249, 250] helps to reduce the number of independent FFs from ten to two; i.e., the Isuger-wise relations  $\xi_1$  and  $\xi_2$ . Similarly, in SCET the evaluation of the FFs [71] reduces this number to one. In our analysis, we use the FFs calculated by using Lattice QCD for full dilepton mass square range and the expression is given in Eq. (3.8) in Sect. 3.2. The values of parameters used in Eq. (3.8) are listed in Table 3.1 with the replacement  $f_V^t \rightarrow f_0$ ,  $f_V^0 \rightarrow f_+$ ,  $f_V^{\perp} \rightarrow f_{\perp}$ ,  $f_A^t \rightarrow g_0$ ,  $f_A^0 \rightarrow g_+$ ,  $f_A^{\perp} \rightarrow g_{\perp}$ ,  $f_T^0 \rightarrow h_+$ ,  $f_T^{\perp} \rightarrow h_{\perp}$ ,  $f_{T_5}^0 \rightarrow \tilde{h}_+$ ,  $f_{T_5}^{\perp} \rightarrow \tilde{h}_{\perp}$ .

### 6.3 Four Fold Angular Distribution and Physical Observables

The four fold differential decay width for the four-body decay process  $\Lambda_b \rightarrow \Lambda(\rightarrow p\pi)\ell^+\ell^-$  is

$$\frac{d^4\Gamma}{ds d\cos\theta d\cos\theta_\Lambda d\xi} = d\Gamma_{VA} + d\Gamma_{SP} + d\Gamma_{T'} + d\Gamma_{VA-SP} + d\Gamma_{VA-T'} + d\Gamma_{SP-T'} \quad (6.38)$$

denoting

$$d\Gamma_i = \frac{d^4\Gamma_i}{ds d\cos\theta d\cos\theta_\Lambda d\xi} \quad (6.39)$$

with  $i = VA, SP, T', VA-SP, VA-T'$  and  $SP-T'$ . Eq. (6.38) can be written in the form of different matrix elements as

$$\frac{d^4\Gamma}{ds d\cos\theta d\cos\theta_\Lambda d\xi} = \mathcal{N} [ |M_{VA}|^2 + |M_{SP}|^2 + |M_{T'}|^2 + (M_{VA}M_{SP}^* + M_{VA}M_{T'}^* + M_{SP}M_{T'}^* + h.c.) ],$$

and the normalization constant  $\mathcal{N}$  is given by

$$\mathcal{N} = \frac{(G_F\alpha_e V_{tb}V_{ts}^*)^2 \lambda v}{3 \times 2^{11} m_{\Lambda_b}^3 \pi^5}, \quad (6.40)$$

where  $v = \sqrt{1 - \frac{4m_\ell^2}{s}}$  and  $\lambda = (m_{\Lambda_b}^2 - m_\Lambda^2 - s)^2 + 4sm_\Lambda^2$ . The non-zero helicity components of leptonic current are given in Appendix A. Here, we would like to mention that our expressions of the lepton helicities corresponding to different currents include the lepton mass term and by setting it equal to zero, it can be easily verified that they are reduced to the form given in [113].

We know that in the SM the currents corresponding to  $\Lambda_b \rightarrow \Lambda\ell^+\ell^-$  are vector and axial-vector therefore, the contribution of  $VA$  operators only modify some of the angular coefficients appearing in the SM. However, the contributions from the scalar and pseudo-scalar operators, being missing in the SM, may introduce new angular coefficients. In the case of the SM like currents, the four-fold angular decay distribution for the decay under consideration is given in Eq. (3.36). However, the contributions from the model independent NP scalar and tensor type operators in Eq. (6.38) are given in Appendix B. The expressions of observables of interest are given in Eqs. (3.38, 3.40, 3.42, 3.44, 3.45, 3.46, 3.47) and Eq. (3.50) [103] along with  $Y_i$  which are obtained to be [111]

$$Y_2 = \frac{3(K_{2cc} - K_{2ss})}{8\hat{\Gamma}}, \quad Y_{3sc} = \frac{K_{3sc}}{2\hat{\Gamma}}, \quad Y_{4sc} = \frac{K_{4sc}}{2\hat{\Gamma}}, \quad (6.41)$$

where  $\tilde{K}_{i,j} = \frac{K_{i,j}}{\alpha_\Lambda}$  and  $\hat{\Gamma} = \frac{d\Gamma}{ds}$ . The detailed expressions of  $K_{i,j}$  for NP in terms of helicity amplitudes are given in the Appendix C. In Eq. (6.41),  $\alpha_\Lambda$  is the asymmetry parameter corresponding to the parity violating  $\Lambda \rightarrow p\pi^-$  decay and its experimentally measured value is  $0.642 \pm 0.013$  [216].

### 6.4 Impact of New Couplings on Physical Observables

In this section, we will discuss the impact of the NP couplings corresponding to  $VA, SP$  and  $T$  operators on the different physical observables discussed above. First we start with  $d\mathcal{B}/ds, F_L, A_{FB}^\ell$ , and  $A_{FB}^\Lambda$  for which the experimental data is available. By using the most recent constraints

on NP couplings from [137], the idea behind this approach is to see whether these NP couplings accommodate the currently available data [217] or not. To accomplish this task, first of all, we discuss the impact of individual NP couplings on the above mentioned observables and later we analyze their simultaneous impact. In doing so, we will explore all the available range of new couplings constrained by  $B$ -meson decays in different bins of  $s$ . After this, we will discuss the observables  $Y_{2, 3sc, 4sc}$ ,  $\mathcal{P}_{3, 8, 9}$  and  $\alpha_i^{(\prime)}$  where,  $i = \theta_\ell, \theta_\Lambda, \xi, L, U$  which show minimum dependence on the FFs and hence are the potential candidates to search for NP in some ongoing and future experiments. In order to present our results of different physical observables, we plot them against the square of the momentum transfer  $s$  in the SM as well as in the presence of NP couplings. In these plots, we have presented our results both for the zero and non-zero lepton ( $\mu$ ) mass. Therefore, our formalism is more general from the previous study of the same decay presented in ref. [113]. Just to distinguish the lepton mass effect [251], we have also discussed the different physical observables for  $\Lambda_b \rightarrow \Lambda(\rightarrow p\pi)\tau^+\tau^-$  decay where the mass of final state  $\tau$ 's is significantly large as compared to the  $\mu$ 's case. Here, we would like to emphasize that all the plots are drawn for the central values of the FFs however, to quantify the uncertainties arising due to the FFs and other input parameters we have calculated these observables in different bins of  $s$  and tabulated them in Tables 6.5, 6.6, and 6.7. Furthermore, to see whether the NP couplings,  $VA$ ,  $SP$ , and  $T$  could simultaneously accommodate all available data for the observables  $d\mathcal{B}/ds$ ,  $F_L$ ,  $A_{FB}^\ell$  and  $A_{FB}^\Lambda$  of  $\Lambda_b \rightarrow \Lambda(\rightarrow p\pi^-)\mu^+\mu^-$  decay, we have plotted them against the new WCs.

#### 6.4.1 Vector and Axial-Vector Part ( $VA$ )

It is a well-established fact that in order to accommodate the discrepancies between the SM predictions and the experimental measurements in different  $B$ -meson decays, some models with new  $VA$  couplings have been proposed [252, 253]. As these couplings are already present in the SM therefore, they will only modify the SM WCs and leave the operator bases to be the same. Hence, no new angular coefficient arises in this particular case. In case of the massless lepton and varying the  $VA$  couplings in the range  $C_V = [-1.61, -1]$ ,  $C'_V = 0$ ,  $C_A = 1$  and  $C'_A = -0.4$  which take care of the global fit sign, the observables  $d\mathcal{B}/ds$ ,  $A_{FB}^\ell$  and  $F_L$  have already been discussed in [113]. We have taken three scenarios of new  $VA$  couplings following [113]. As a first step, we have repeated their analysis for the massless lepton case (dashed lines in all plots) in our formalism and found the same results. Later, the same analysis has been done by setting the non-zero mass for our final state leptons that is muons (solid lines of all colors). Fig. 6.1(a) shows that by using available range of  $C_{V,A}^{(\prime)}$  couplings mentioned above, the available data of the branching ratio could be accommodated only in three low  $s$  bins ( $s \in [0.1, 2]$  GeV<sup>2</sup>,  $s \in [2, 4]$  GeV<sup>2</sup> and  $s \in [6, 8]$  GeV<sup>2</sup>) for which SM also satisfies the LHCb results. In case of high  $s$  region, no combination of new  $VA$  couplings satisfy experimental results as LHCb values in this region are greater than the SM results but due to the negative value of  $C_V$ , the value of the branching ratio in the presence of these couplings is smaller than the corresponding SM value in the whole  $s$  region. This can also be noticed quantitatively from Table 6.5 (c.f. column 1) where we can see that in the high  $s$  bins the results are suppressed significantly from the SM predictions and even further from the experimental measurements. In addition, the  $\mu$ -mass does not add any visible deviation for this observable.

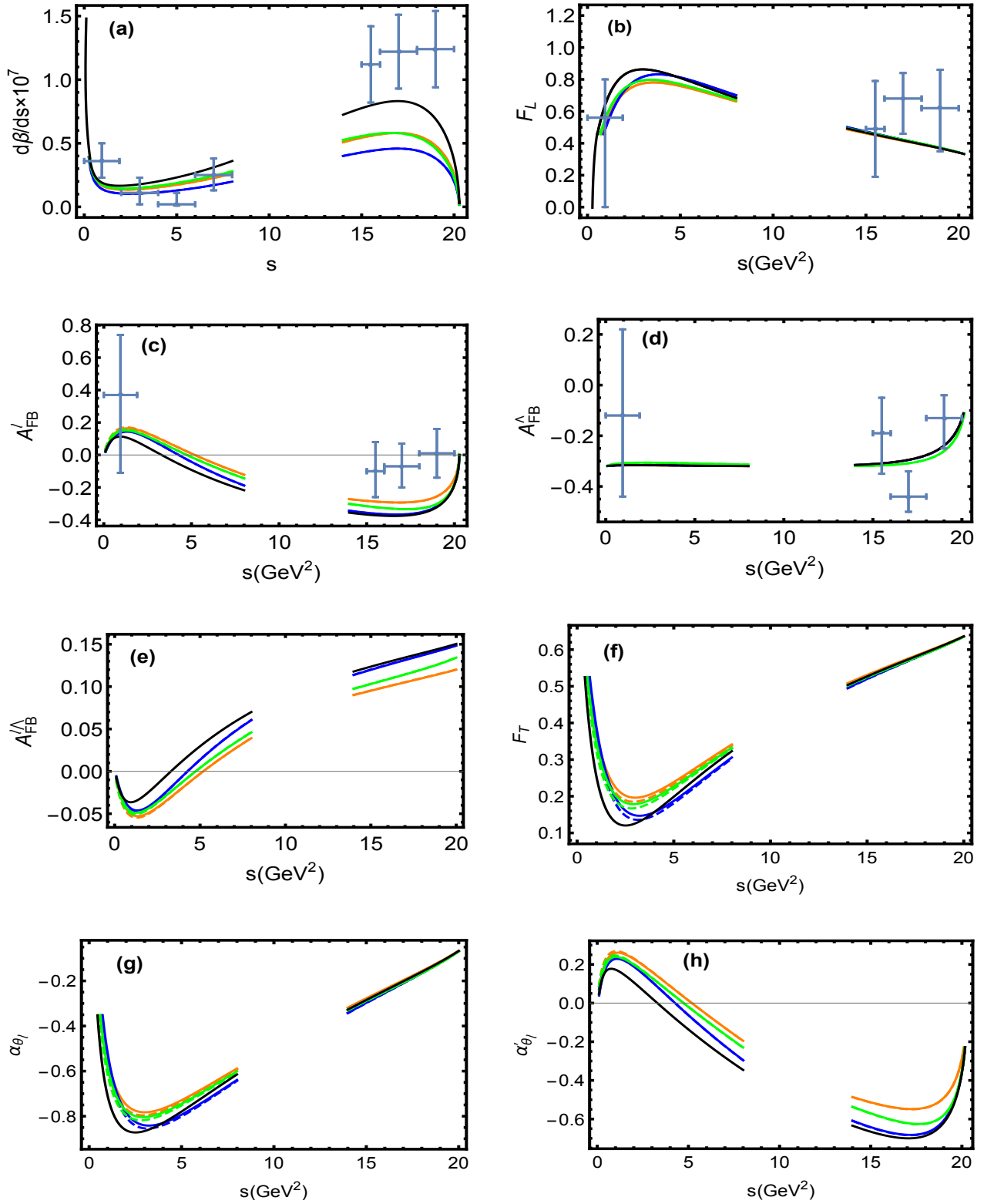


Figure 6.1: Observables for the SM and in the presence of new  $VA$  couplings which are compared with LHCb results given in [217]. In all plots the black curves denote the SM results. The orange curve is obtained with  $C_V = -1.61$  and  $C'_V = C_A = C'_A = 0$ . The blue line is for  $C_V = -C_A = -1$  and  $C'_V = C'_A = 0$  and green color is for  $C_V = -1.34$ ,  $C'_A = -0.4$  and  $C'_V = C_A = 0$ . The solid and dashed lines are for the massive and massless  $\mu^-$  cases respectively.

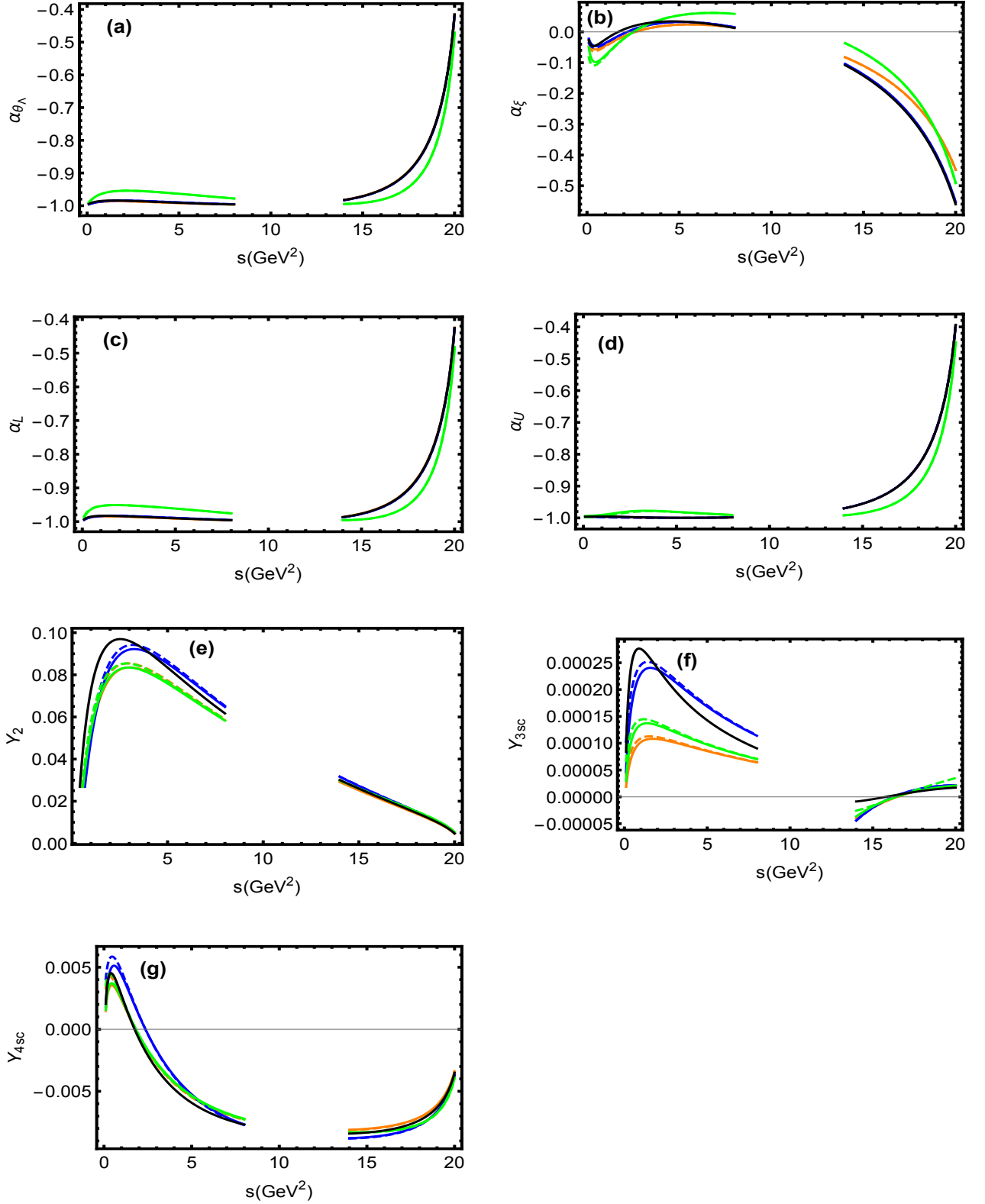


Figure 6.2: Observables in the SM and in the presence of new  $VA$  couplings. The description of different curves is similar to the Fig. 6.1 .

In Table 6.5 we can observe that the uncertainties due to FFs are quite significant in the calculation of the branching ratio in the SM as well as in any of the NP scenarios. Hence, we can look for the observables which show minimal dependence on the FFs, and  $A_{FB}^\ell$  is one of them. In

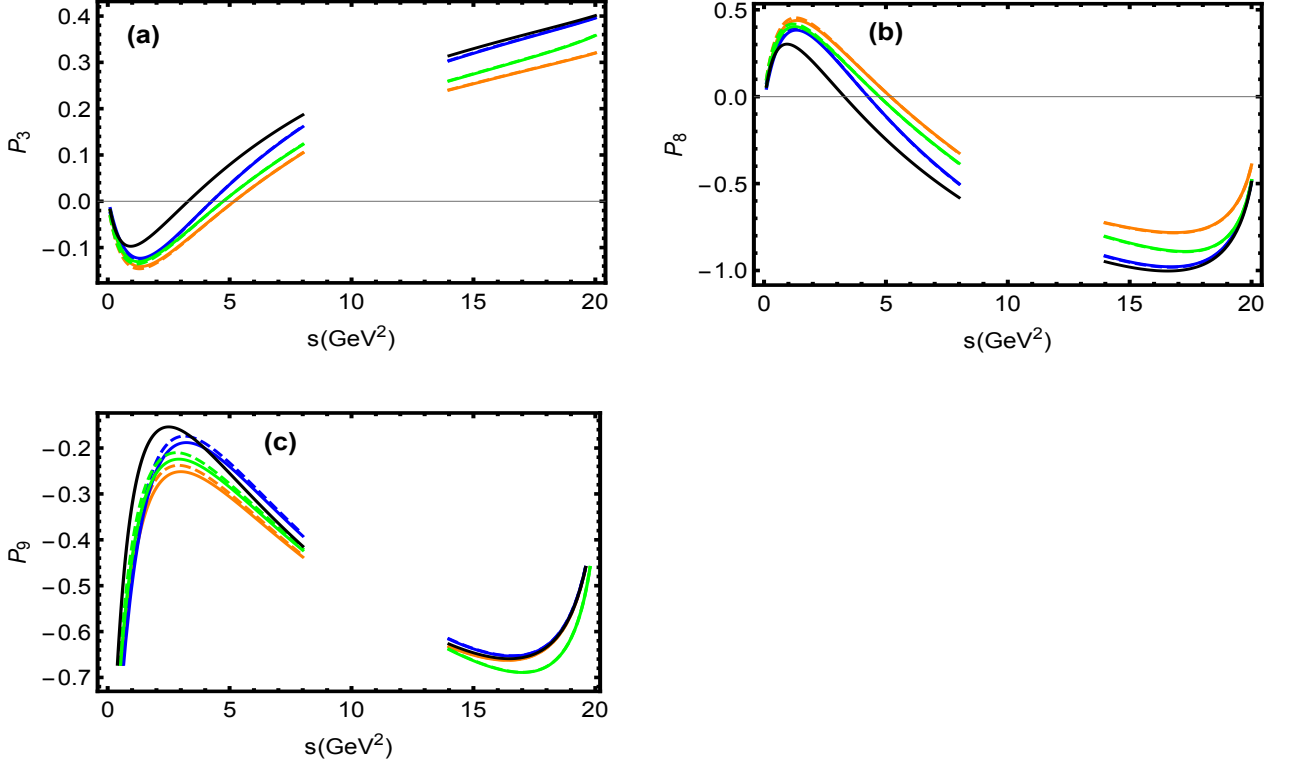


Figure 6.3:  $\mathcal{P}_3$ ,  $\mathcal{P}_8$  and  $\mathcal{P}_9$  in the SM and in the presence of new  $VA$  couplings. The description of different curves is similar to the Fig. 6.1.

the case of  $A_{FB}^\ell$  though, the NP couplings enhanced its average value but still, it is small enough to accommodate the data (c.f. second column in Table 6.6). As the zero position of this asymmetry is proportional to the vector-current coefficients  $C_7^{\text{eff}}/C_9^{\text{eff}}$  therefore, the shift in the zero-position is expected after the addition of any new vector type couplings and it can be seen in Fig. 6.1(c). We hope that the future data of the zero-position of  $A_{FB}^\ell$  in  $\Lambda_b \rightarrow \Lambda \mu^+ \mu^-$  decay will further improve the constraints on  $VA$  couplings. Like the branching ratio, the  $\mu$ -mass effects are also invisible in this case too.

The situation is slightly different for  $F_L$  (Fig. 6.1(b)) and  $A_{FB}^\Lambda$  (Fig. 6.1(d)) where the above constraints on  $VA$  couplings satisfy the data within errors in the measurements especially for  $F_L$  in the  $s \in [1, 3]$   $\text{GeV}^2$  and  $s \in [15, 16]$   $\text{GeV}^2$  bins. Again, going from massless to massive  $\mu$ -case did not lead to any significant change. It is also worth mentioning that just like  $A_{FB}^\ell$  the hadronic uncertainties due to FFs in  $F_L$ , and  $A_{FB}^\Lambda$  are negligible for all low-recoil bins both for the SM and when the new  $VA$  couplings are considered (c.f. Table 6.5). This can provide a clean way to test the SM and NP models with additional  $VA$  couplings.

Besides the above mentioned observables we show that there are some other interesting physical observables; e.g., the combined lepton-baryon forward-backward asymmetry  $A_{FB}^{\ell\Lambda}$ , the fractions of transverse ( $F_T$ ) polarized dimuons, the asymmetry parameters  $\alpha_{\theta_\ell}^{(\prime)}$ ,  $\alpha_{\theta_\Lambda}$ ,  $\alpha_\xi$ ,  $\alpha_L$ ,  $\alpha_U$  and angular coefficients  $Y_{2, 3sc, 4sc}$  and  $\mathcal{P}_{3, 8, 9}$  which are influenced by these new couplings. These observables are also interesting from the experimental point of view as they have minimum dependence on the FFs and hence these are not significantly prone by the uncertainties. Therefore, these observables will provide an optimal ground to test the SM as well as to explore the possible NP. The values of

these observables are plotted against  $s$  in Figs. 6.1, 6.2 and 6.3 for the SM and in the presence of  $C_{V,A}^{(\prime)}$  couplings. Quantitatively, by considering different  $VA$  scenarios their values are compared with the SM predictions which are collected in Tables 6.5, 6.6 and 6.7. The main effects of  $C_{V,A}^{(\prime)}$  on these observables can be summarized as:

- Fig. 6.1(e) depicts that the value of  $A_{FB}^{\ell\Lambda}$  is an order of magnitude smaller than the experimentally measured  $A_{FB}^{\ell}$  and  $A_{FB}^{\Lambda}$ . After including the new  $VA$  operators, we can see that its value decreases compared to its SM predictions in almost all the  $s$  range. Just like  $A_{FB}^{\ell}$  its zero position also shifts to the right and it increases when  $C_V$  becomes more negative. The value of this observable is changed throughout the  $s$  region due to the change in the value of  $VA$  couplings however, this value is insensitive to the mass of the final state  $\mu$ . It can be seen from Table 6.6 that in the low-recoil bin its value is almost free from the uncertainties.
- In case of  $F_T$  which is plotted in Fig. 6.1(f), the impact of new  $VA$  couplings along with the final state  $\mu$ -mass effects are visible only in the low  $s$  region. Like  $F_L$ , this observable has minimal dependence on the FFs especially in the bin  $[15, 20]$   $\text{GeV}^2$  and this can be seen clearly from Table 6.6. As we know that  $F_L + F_T \approx 1$  therefore, the behavior of  $F_T$  and  $F_L$  are expected to be opposite to each other in the presence of  $VA$  couplings and it can be seen in Fig. 6.1.
- The observables  $\alpha_{\theta_\ell}$  and  $\alpha'_{\theta_\ell}$  are plotted in Figs. 6.1(g) and 6.1(h), respectively. From these plots, one can see that the  $\mu$ -mass effects are visible in low  $s$  region for  $\alpha_{\theta_\ell}$  but not for the  $\alpha'_{\theta_\ell}$ . However, both observables are sensitive to the  $VA$  couplings and to extract the imprints of NP both are significant to be measured precisely at LHCb and Belle-II experiments. Furthermore, the behavior of  $\alpha'_{\theta_\ell}$  is similar to the  $A_{FB}^{\ell}$  and it also passes from the zero-position at a specific value of  $s$  in the SM. Also this zero-position is shifted towards the higher value of  $s$  when  $C_V$  is set to higher negative value. In order to quantify the impact of new  $VA$  couplings their numerical values along with the SM predictions are given in Table 6.6.
- For the observables  $\alpha_{\theta_\Lambda}$ ,  $\alpha_\xi$ ,  $\alpha_L$  and  $\alpha_U$  the maximum deviations from the SM predictions come only when we set  $C_V = -1.34$ ,  $C'_A = -0.4$  and  $C'_V = C_A = 0$  as shown by the green curves in Fig. 6.2(a,b,c,d). However, in  $Y_2$  this is the case for  $C_V = -1.61$  and  $C'_V = C_A = C'_A = 0$  which is drawn as an orange curve in Fig. 6.2(e). It can also be noticed from Table 6.6 that  $Y_2$  has negligible uncertainties due to FFs. While the value of  $Y_{4sc}$  is suppressed in the SM and even after adding the new  $VA$  couplings it is still not in a reasonable range to be measured experimentally. The  $\mu$ -mass effect is also insignificant for all these observables at large-recoil.
- The four-folded decay distribution defined in Eq. (3.36) gives us a chance to single out the different physical observables by studying different foldings. In semileptonic  $B$ -meson decays, such foldings have been studied in detail, especially the penguin asymmetries ( $P_i$ ). Among them the  $P_5^{(\prime)}$  is the most important as highlighted in the Section 2.9.5 and these foldings have been discussed in detail in ref. [103]. However, in the current study of the  $\Lambda_b$  baryon, we consider only  $\mathcal{P}_3$ ,  $\mathcal{P}_8$  and  $\mathcal{P}_9$  which are the coefficients of  $\cos\theta_\ell \cos\theta_\Lambda$ ,  $\cos\theta_\ell$  and  $\cos\theta_\Lambda$ , respectively. We can see from Eq. (6.41), together with the expressions given in



Appendix C, that these observables depend heavily on the  $VA$  couplings. We find that the values of  $\mathcal{P}_3$  and  $\mathcal{P}_8$  change maximally from their SM predictions when we set  $C_V = -1.61$  and  $C'_V = C_A = C'_A = 0$  in almost all the  $s$  region and it is shown by the orange curve in Fig. 6.3 and numerically it can be seen in Table 6.7. Similar to the case of  $A_{FB}^\ell$  and  $\alpha'_{\theta_\ell}$ , the zero-positions of  $\mathcal{P}_3$  and  $\mathcal{P}_8$  also move to the right from their SM zero-positions. But the effects of  $VA$  couplings on  $\mathcal{P}_9$  are prominent only for low values of  $s$  and for this particular observable, the  $\mu$ -mass term contribution is also quite visible in this region. In addition, from Table 6.7, it is clear that the uncertainties in  $P_3$ ,  $P_8$  and  $P_9$  are comparatively large in the large-recoil region.

#### 6.4.2 Scalar and Pseudo-scalar Part

In order to constraint the  $SP$  couplings, the golden channel is the  $B_s \rightarrow \mu^+\mu^-$ . In this decay we do not have any contributions from  $C'_V$  and the one proportional to  $C'_A$  is helicity suppressed ( $\mathcal{O}(m_\ell^2/m_B^2)$ ). Therefore, by using the available experimental data of  $B_s \rightarrow \mu^+\mu^-$  and  $B \rightarrow X_s\mu^+\mu^-$  decay channels, the constraints on  $SP$  couplings are already obtained in [113] and these are  $C_{S,P}^{(\prime)} = [-4.0, 4.0]$ . In the present study, we use these constraints to see the dependence of different physical observables on  $SP$  couplings.

As the  $SP$  couplings are absent in the SM, therefore, in contrast to the new  $VA$  couplings mentioned in the previous section, a new angular coefficient arises which corresponds to  $\cos\theta_\Lambda$ . In addition to this coefficient, all the SM angular coefficients are modified except  $K_{3sc}$  and  $K_{4sc}$  and hence we expect that most of the physical observables show strong dependence on these  $SP$  couplings. Hence, by taking  $C_{S,P}^{(\prime)} = [-3.1, 3]$  with the condition  $|C_{S,P} - C'_{S,P}| \lesssim 0.1$  [113] due to having a large pull in global fits to  $B$ -Physics data and the corresponding results are plotted in Figs. 6.4, 6.5 and Fig. 6.6. We have considered two scenarios of  $SP$  couplings and their results for all observables are presented in Tables 6.5, 6.6 and 6.7 along with uncertainties. The important observations can be summarized as:

- In the massless  $\mu$ - limit, we can see that our results of the  $d\mathcal{B}/ds$ ,  $A_{FB}^\ell$  and  $F_L$  for the  $SP$  couplings are in agreement with the trend shown in [113] and the values of these observables mainly change in the high  $s$  region. It is clear from Fig. 6.4(a) that the results of  $d\mathcal{B}/ds$  are SM like in the low  $s$  region but get closer to LHCb data for the bins  $s \in [15, 16]$  GeV<sup>2</sup> and  $s \in [16, 18]$  GeV<sup>2</sup> when  $SP$  couplings are introduced. This can also be noticed from the numerical values of  $d\mathcal{B}/ds$  appended in the first column of Table 6.5. From Fig. 6.4(c), it can be seen that for  $A_{FB}^\ell$ , a good agreement to the data is achieved when we set  $C_S = 3.0$  and  $C'_S = 2.9$  and it is displayed by the green curve. Just to mention, in contrast to the  $SP$  couplings, the  $VA$  couplings do not accommodate the data of  $A_{FB}^\ell$  in high  $s$  bins. However, the zero-position is not affected because the contributions from the  $SP$  couplings do not contain any odd power term in  $\cos\theta_\ell$ . On the other hand, after inclusion of  $SP$  couplings,  $F_L$  agrees with the data only in  $s \in [0.1, 2]$  GeV<sup>2</sup> bin (c.f. Fig. 6.4(b)) and for this particular observable the SM predictions show better trend with the data as can be read from Table 6.5. However, more data of these observable will reveal the future status of  $SP$  couplings. For the  $A_{FB}^\Lambda$ , in contrast to the  $VA$  coupling, this observable is sensitive to the  $SP$  couplings and it can be observed from Fig. 6.4(d). It is important to emphasize that the changed

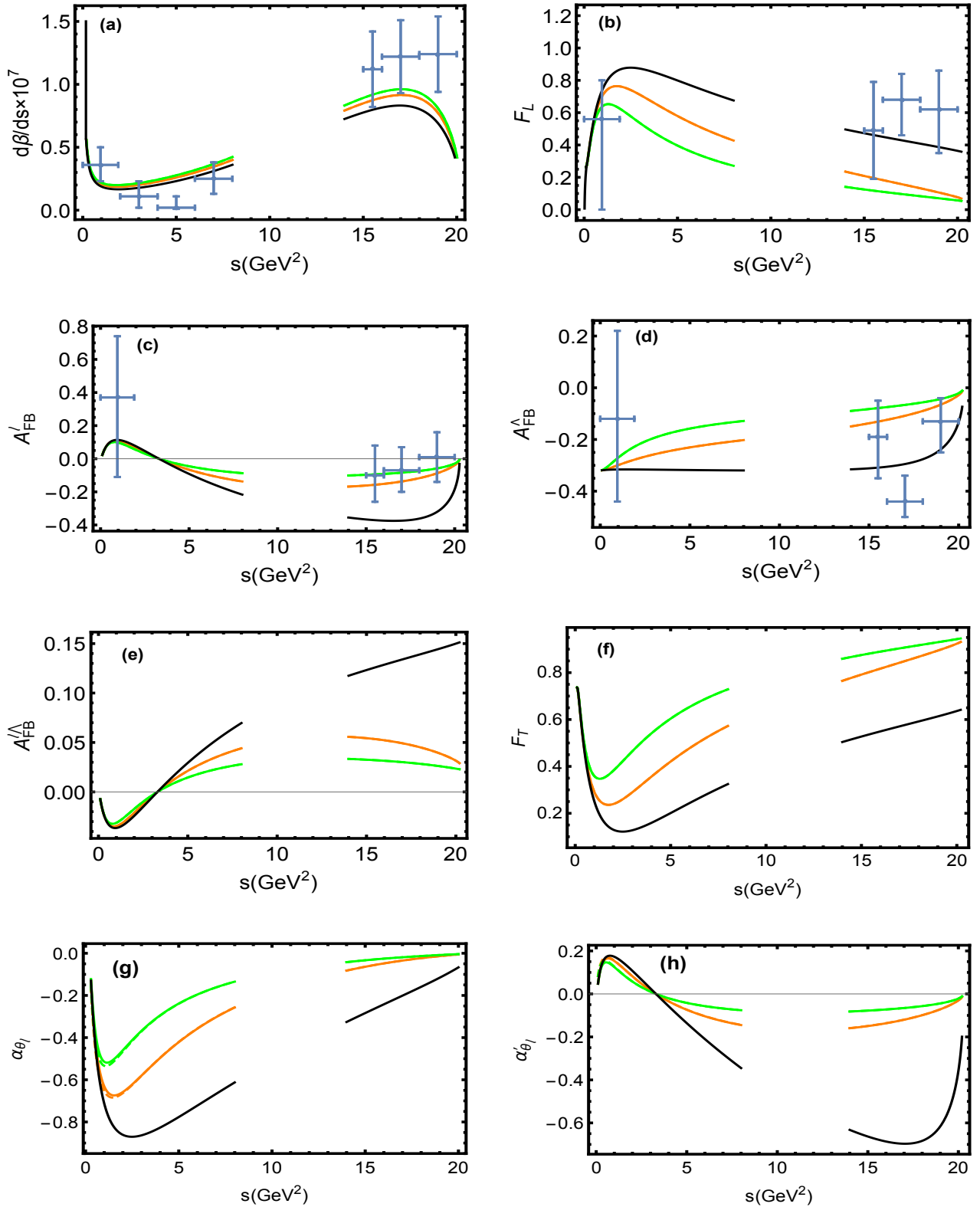


Figure 6.4: Observables in the presence of new SP couplings which are compared with LHCb results given in [217]. The SM curves are plotted in black color. The orange curve is obtained with  $C_S = C_P = -3$  and  $C'_S = C'_P = -3.1$  (for  $d\mathcal{B}/ds$  orange color is for  $C_S = C_P = -1$  and  $C'_S = C'_P = -1.1$ ) and the green line is drawn when  $C_S = 3$  and  $C'_S = 2.9$  (for  $d\mathcal{B}/ds$  green color is for  $C_S = 1$  and  $C'_S = 0.9$ ). The solid and dashed lines are for the massive and massless  $\mu$ -cases, respectively.

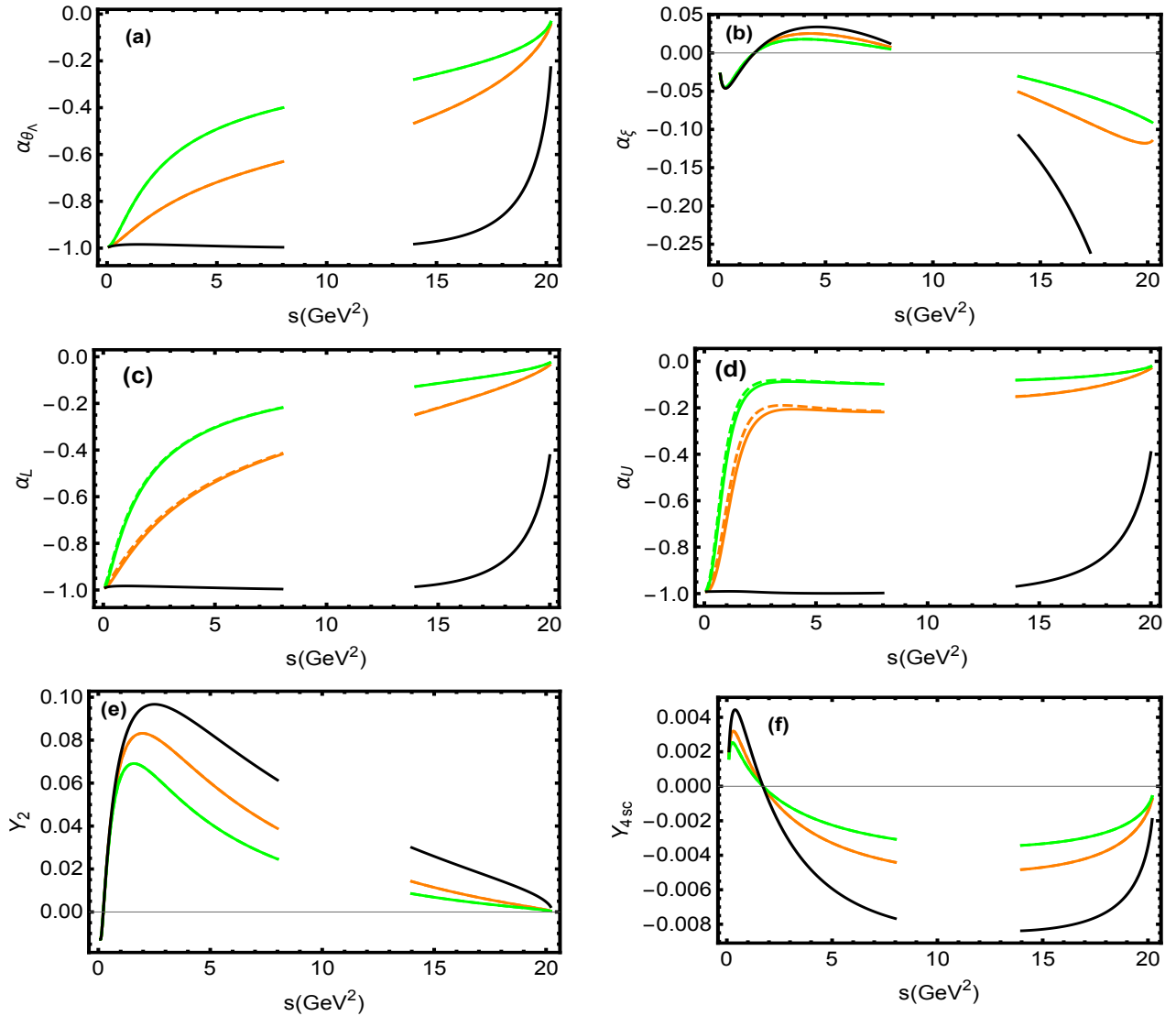


Figure 6.5: Observables in the SM along with  $SP$  couplings. The description of different curves is similar to the Fig. 6.4.

values are still within the errors in the measurements except in one high  $s$  bin; i.e., [16, 18]  $\text{GeV}^2$ . Similar to the  $F_L$ , in the high  $s$  bins, the SM  $A_{FB}^\Lambda$  curve has shown better agreement with the data than the curves with  $SP$  couplings. It is found that these observables are also insensitive to the mass of the final state  $\mu$ .

- Compared to  $VA$  couplings, the profile of  $A_{FB}^{\ell\Lambda}$  is quite sensitive to the  $SP$  couplings and it can be observed in Fig. 6.4(e). Particularly, in the high  $s$  region, we can notice from Table 6.6 that its value is approximately decreased by an order of magnitude from the corresponding SM prediction. However, similar to the  $A_{FB}^\ell$ , its zero-position is not changed because it is also proportional to the  $VA$  and not to the  $SP$  couplings. Also, the massless or massive  $\mu$  considerations do not lead to any visible change in this particular observable.
- In the presence of  $SP$  couplings, the behavior of  $F_T$  is opposite to that of  $F_L$  as it is expected due to  $F_L + F_T = 1$  for every value of  $s$ . This can be noticed in Fig. 6.4(f) and from the second column of Tables 6.5 and 6.6.

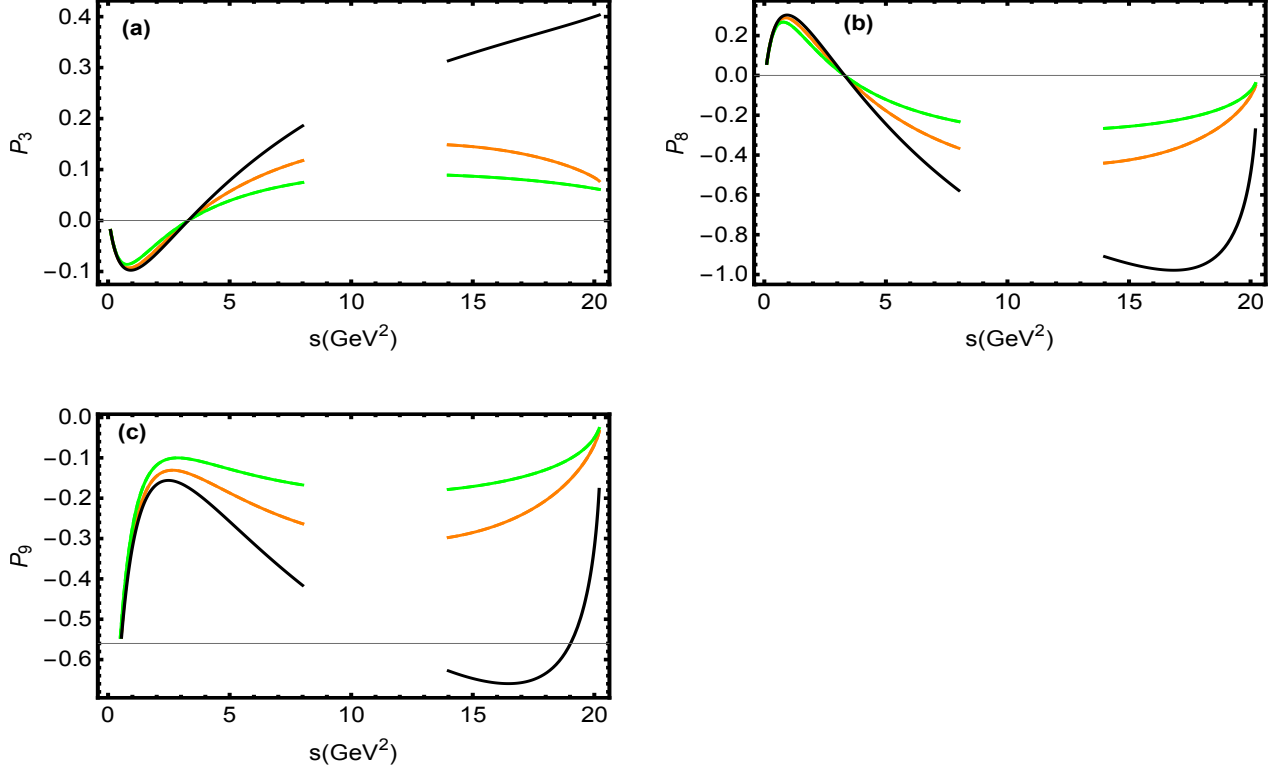


Figure 6.6:  $\mathcal{P}_3$ ,  $\mathcal{P}_8$  and  $\mathcal{P}_9$  in the SM and in the presence of  $SP$  couplings. The description of different curves is similar to the Fig. 6.4.

- In contrast to the  $VA$  couplings, one can see from Fig. 6.4(g) and the Fig. 6.5(a, c, d) that  $\alpha_{\theta_\ell}$ ,  $\alpha_{\theta_\Lambda}$ ,  $\alpha_L$  and  $\alpha_U$  are quite sensitive to the  $SP$  couplings. These plots show that due to the  $SP$  couplings, the values of these observables are significantly suppressed from that of the SM predictions in almost all the  $s$  region. For  $\alpha'_{\theta_\ell}$ , similar to the  $A_{FB}^\ell$  and  $A_{FB}^{\ell\Lambda}$ , the zero-position depends only on  $VA$  couplings and hence is not expected to be changed due to consideration of the  $SP$  couplings and it can be seen in Fig. 6.4(h). However,  $\alpha'_{\theta_\ell}$  is looking more sensitive to the  $SP$  coupling as compared to the  $VA$  couplings. Particularly, in  $s \in [15, 20]$   $\text{GeV}^2$  bin the value of  $\alpha'_{\theta_\ell}$  is almost 80% suppressed from its SM predictions and it can also be read from Table 6.6. In line with this, Fig. 6.5(b) shows that in the high  $s$  region,  $\alpha_\xi$  is also quite sensitive to the  $SP$  couplings. From Table 6.7, one can notice that for the  $SP$  couplings the uncertainties in the value of  $\alpha_\xi$  are even larger than the actual value at the large-recoil. Just like other observables, these are also insensitive to the  $\mu$  mass.
- For the angular observables  $Y$ 's only the value of  $Y_2$  is significant to be measured at the LHCb and the future experiments therefore, we have only plotted it in Fig. 6.5(e). From Table 6.6, one can notice that similar to the  $\alpha$ 's the value of  $Y_2$  is significantly reduced from its numbers calculated using the SM operators. Here, we can also see that inspite  $Y_{4sc}$  is sensitive to  $SP$  couplings at low-recoil its value is still too small to be measured experimentally.
- Similar to  $\alpha$ 's,  $\mathcal{P}_{3, 8, 9}$  are also very sensitive to the  $SP$  couplings as compared to that of the  $VA$  couplings and it can be noticed from Fig. (6.6). We can see that the values of  $\mathcal{P}$ 's are changed from their SM predictions by a factor of 4 – 6 (c.f. Table 6.7). Again, the position

of the zero-crossing in  $\mathcal{P}_3$  and  $\mathcal{P}_8$  are unchanged after the inclusion of  $SP$  couplings, and the numerical results presented in Table 6.7 stay the same even if we take the non-zero mass for the final state  $\mu$ .

Thus, together with the  $B$ -meson decays, we hope that it will be interesting to look for the angular asymmetries of  $\Lambda_b$  baryon decay at the LHCb which help us to get better constraints on the  $SP$  couplings. In short, when experimental data of these angular observables will be available for  $\Lambda_b$  baryon, we would be in a better position to draw a conclusion about the future status of these couplings.

### 6.4.3 Tensor Part

Just like  $SP$  couplings, the one corresponding to the tensor currents are also absent in the SM, hence they also modify the SM angular coefficients except  $K_{3sc}$  and  $K_{4sc}$ . In [113], it has been discussed in detail that  $B_s \rightarrow X_s \mu^+ \mu^-$  along with  $B \rightarrow X_c \ell \nu_\ell$  are the most important channels to obtain the constraints on these NP couplings and by using these channels the equation of constraints is obtained to be  $C_T^2 + C_{T5}^2 = 0.55$  [113]. As the constraints on these couplings are quite stringent, therefore, to see their impact on physical observables we vary the values  $C_T$  and  $C_{T5}$  such that the above equation of constraints is satisfied. Doing this we find that the maximum impact on the different observables is achieved when we select  $C_T = 0.72$  and  $C_{T5} = 0.2$  [113].

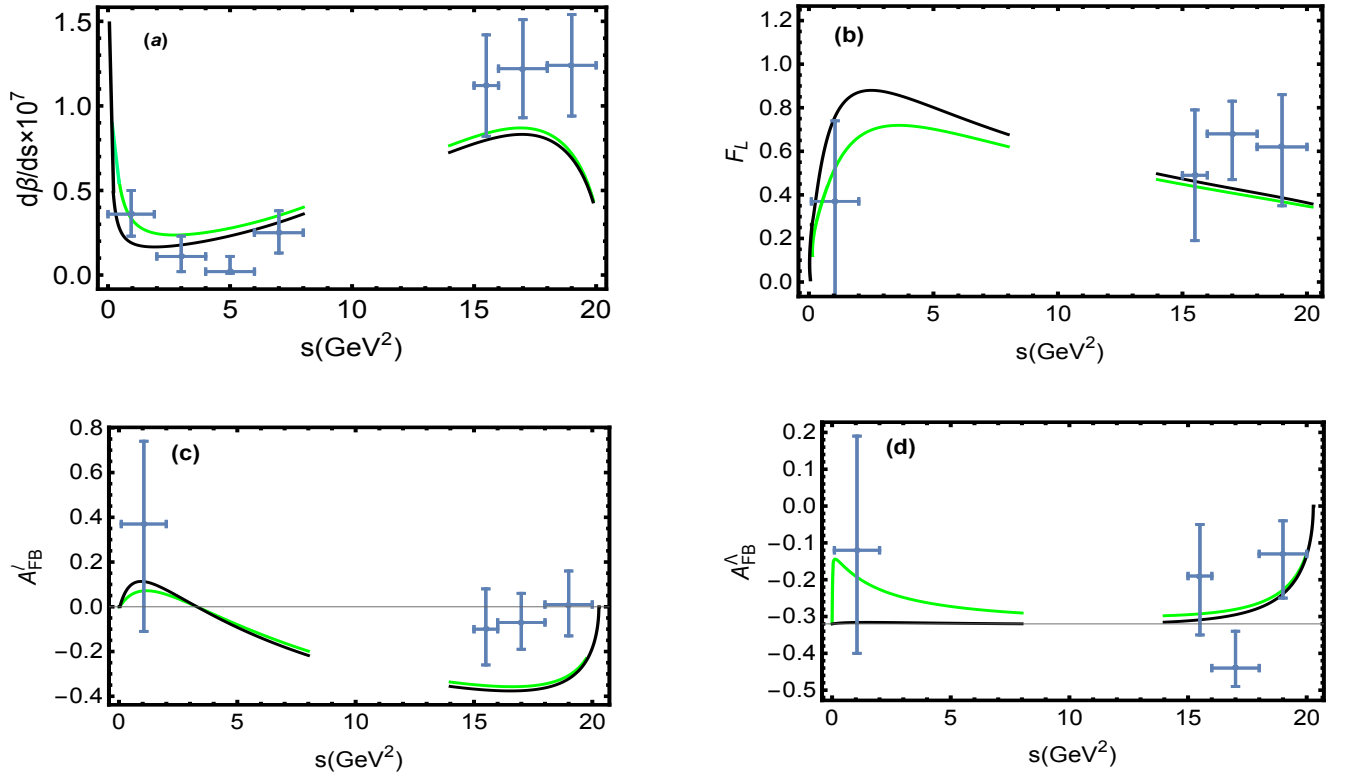


Figure 6.7: These plots are constructed by taking  $C_T = 0.72$  and  $C_{T5} = 0.2$  and the black color curve indicates SM result. Experimental results are taken from [217]

We have also explored that in contrast to the  $VA$  and  $SP$  couplings, very few observables are affected by the tensor couplings only in the low  $s$  region. The values of most of the observables do

not show any dependence on the tensor couplings and remain close to their SM predictions. For example, in case  $d\mathcal{B}/ds$ ,  $F_L$ ,  $A_{FB}^\ell$  and  $A_{FB}^\Lambda$  on which the experimental data is available, the imprints of tensor couplings are shown in Fig. 6.7 and the numerical results in different experimental bins are provided in Table 6.5. Here, we can observe that our analysis coincides with [113] for  $d\mathcal{B}/ds$  and  $F_L$ . One can also see that these four observables are sensitive to tensor couplings only in the low  $s$  region. However, the effects on  $d\mathcal{B}/ds$  and  $A_{FB}^\ell$  are mild as compared to  $F_L$  and  $A_{FB}^\Lambda$ , particularly in  $s \in [0.1, 3]$  GeV<sup>2</sup> bin where the effects in the  $A_{FB}^\Lambda$  are very prominent. In this region, after the inclusion of tensor coupling, the value of  $A_{FB}^\Lambda$  looks slightly better in agreement with the experimental observations as compared to that of the SM predictions. In short, our analysis shows that the effects of the tensor couplings are not prominent for the angular observables except  $F_L$  and  $A_{FB}^\Lambda$  in the low  $s$  region.

#### 6.4.4 Combined effects of $VA$ - $SP$ couplings on angular observables

As the uncertainties in the experimental data of  $d\mathcal{B}/ds$ ,  $A_{FB}^\ell$ ,  $F_L$  and  $A_{FB}^\Lambda$  are significantly large and based on the analysis performed above, we can say that any individual set of new couplings can not accommodate all the available data. This situation is somewhat more problematic in high  $s$  bins. In this case, from Figs. 6.1, 6.4 and 6.7 one can quantify the situation for these observables in Table 6.1 that lead to the following findings:

- The  $VA$  coupling accommodate  $d\mathcal{B}/ds$  data only in three bins of  $s$  at large-recoil. The data of  $F_L$  and  $A_{FB}^\Lambda$  can be accommodated in low and high  $s$  bins except  $s \in [16, 18]$  GeV<sup>2</sup> bin. The data of  $A_{FB}^\ell$  can be taken care of only in  $s \in [0.1, 2]$  GeV<sup>2</sup> bin. It means that the  $VA$  couplings only satisfy LHCb data in those bins where the SM can also accommodate the data to the same extent. Hence, the addition of new  $VA$  couplings to the SM is not sufficient alone.
- Just like the SM, the  $SP$  couplings satisfy the  $d\mathcal{B}/ds$  data in three low  $s$  bins. In addition, these  $SP$  couplings accommodate the data in  $s \in [15, 16]$  GeV<sup>2</sup> where the SM predictions do not match with experimental measurements. The data of  $F_L$  can be taken care of in only low  $s$  bin  $s \in [0.1, 2]$  GeV<sup>2</sup>. The LHCb data of  $A_{FB}^\ell$  could be fully accommodated but in case of  $A_{FB}^\Lambda$  it is possible in all bins except for  $s \in [16, 18]$  GeV<sup>2</sup> region.
- Similar to the results of the SM, the  $T$  coupling only accommodate  $d\mathcal{B}/ds$  data in three low  $s$  bins. The data of  $A_{FB}^\ell$  is satisfied in  $s \in [0.1, 2]$  GeV<sup>2</sup> bin only however, for that of  $F_L$  and  $A_{FB}^\Lambda$  it can be accommodated in all bins except  $s \in [16, 18]$  GeV<sup>2</sup>.

Based on these observations, we can see that taking new couplings separately is not a favorable option in the presence of available data of the different physical observables in  $\Lambda_b \rightarrow \Lambda(\rightarrow p\pi^-)\mu^+\mu^-$  decay. Therefore, it is useful to see if two new couplings are turned on together, does this situation improve or not? In order to do so, the constraints on new WCs corresponding to vector, axial-vector, scalar, and pseudo-scalar operators are once again chosen from the one adopted by [113] and by using the global fit presented in [137]; i.e.,

$$C_V = [-1.61, -1] \quad C_S^{(\prime)} = [-4, 4] \quad C_P^{(\prime)} = [-4, 4] \quad (6.42)$$

Table 6.1: Data accommodated by new couplings in different bins based on central values of observables.

$\mathcal{O}$ bins (GeV <sup>2</sup> )	$d\mathcal{B}/ds$				$F_L$				$A_{FB}^\ell$				$A_{FB}^\Lambda$				
	SM	VA	SP	T	SM	VA	SP	T	SM	VA	SP	T	SM	VA	SP	T	
[0.1, 2]	✓	✓	✓	✓	✓	✓	✓	✓	✓	✓	✓	✓	✓	✓	✓	✓	✓
[2, 4]	✓	✓	✓	✓	–	–	–	–	–	–	–	–	–	–	–	–	–
[4, 6]	✗	✗	✗	✗	–	–	–	–	–	–	–	–	–	–	–	–	–
[6, 8]	✓	✓	✓	✓	–	–	–	–	–	–	–	–	–	–	–	–	–
[15, 16]	✗	✗	✓	✓	✓	✓	✓	✓	✗	✗	✓	✓	✓	✓	✓	✓	✓
[16, 18]	✗	✗	✓	✗	✗	✗	✗	✗	✗	✗	✓	✓	✗	✗	✗	✗	✗
[18, 20]	✗	✗	✗	✗	✓	✓	✗	✓	✗	✗	✓	✗	✓	✓	✓	✓	✓

with  $|C_{S,P} - C'_{S,P}| \leq 0.1$ . We have not included  $C'_V$ ,  $C_A$ ,  $C'_A$ ,  $C_T$  and  $C_{T5}$  in the forthcoming numerical analysis as the severe constraints from  $B$ -physics on these WCs do not allow us to vary them significantly. Thus, from Eq. (6.42) the following ten combinations are possible:

$$\begin{aligned}
 & \text{(i)} : (C_S, C_V), \quad \text{(ii)} : (C'_S, C_V), \quad \text{(iii)} : (C_P, C_V), \quad \text{(iv)} : (C'_P, C_V), \quad \text{(v)} : (C_S, C_{S'}) \quad (6.43) \\
 & \text{(vi)} : (C_S, C'_P), \quad \text{(vii)} : (C'_S, C_P), \quad \text{(viii)} : (C_S, C_P), \quad \text{(ix)} : (C_{S'}, C_{P'}), \quad \text{(x)} : (C_P, C'_P).
 \end{aligned}$$

Among these combinations, we are interested in looking for the combination(s) which maximally accommodate the currently available data of all the four observables mentioned above. With this condition, by exploring the various combinations given in Eq. (6.43), it is found that there is not a single choice which could explain the full data of all four observables simultaneously. However, we found from Eq. (6.44) there are six combinations of new WCs that could accommodate the data of the four observables; i.e.,  $d\mathcal{B}/ds$ ,  $F_L$ ,  $A_{FB}^\ell$  and  $A_{FB}^\Lambda$  simultaneously in the bins  $s \in [0.1, 2]$  GeV<sup>2</sup> and  $s \in [15, 16]$  GeV<sup>2</sup> and three observables (excluding  $d\mathcal{B}/ds$ ) in  $s \in [18, 20]$  GeV<sup>2</sup> bin. In this case, for the bin  $s \in [16, 18]$  GeV<sup>2</sup> only  $F_L$  and  $A_{FB}^\Lambda$  can be taken care of. On the other hand, if we would like to accommodate the data of  $d\mathcal{B}/ds$  as well, we have to choose one from the other three observables. Therefore, based on these observations the six possible combinations of new couplings which accommodate almost all the data of above mentioned three or four observables simultaneously are

$$\begin{aligned}
 & \text{(i)} : (C_S, C_V), \quad \text{(ii)} : (C'_S, C_V), \quad \text{(iii)} : (C'_P, C_V), \\
 & \text{(iv)} : (C_S, C'_S), \quad \text{(v)} : (C_S, C'_P), \quad \text{(vi)} : (C'_S, C_P) \quad . \quad (6.44)
 \end{aligned}$$

The impact of these combinations of new couplings on the experimentally measured and other physical observables in low (high-recoil region) and high (low-recoil region)  $s$  bins will be discussed from here onwards. The whole analysis is performed by taking the central values of the FFs and that of the experimental data of  $d\mathcal{B}/ds$ ,  $F_L$ ,  $A_{FB}^\ell$  and  $A_{FB}^\Lambda$ .

### High-recoil region

In this region, we focus only on the bin  $s \in [0.1, 2]$  GeV<sup>2</sup> because the LHCb data in this particular region is available for all the four observables mentioned above. First, we have examined all the six combinations given in Eq. (6.44) by tweaking them in their current allowed ranges (c.f. Eq. (6.42)), to see if they could simultaneously accommodate the available data of these observables or not. At the next step, we have calculated the values of these observables for these combinations

accordingly and their results are presented in Fig. 6.8. From these plots, we have made the following observations:

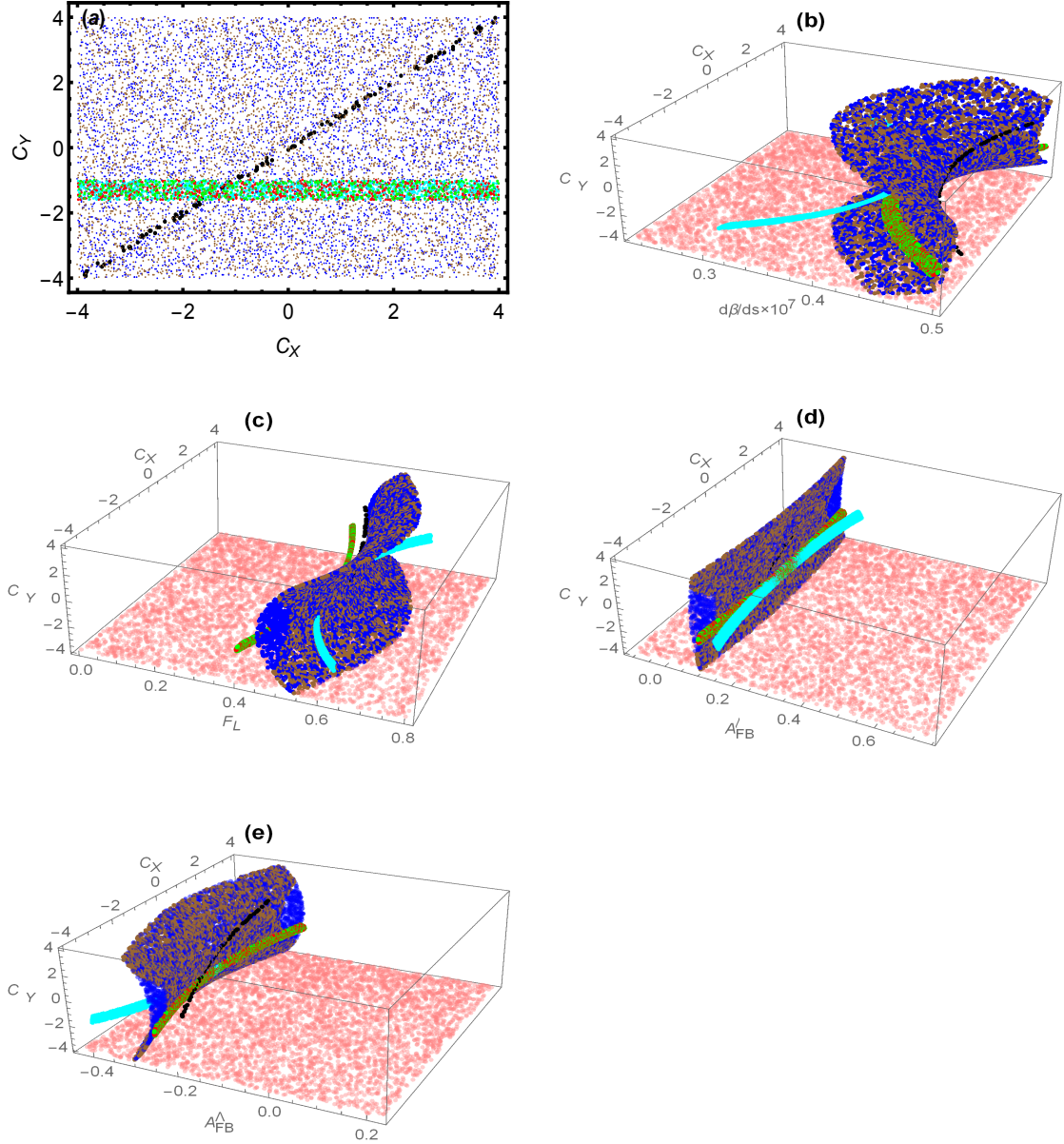


Figure 6.8: (a) The parametric space of  $(C_X, C_Y)$  allowed from  $B$ -physics constraints on new WCs and that satisfy the data of  $d\mathcal{B}/ds$ ,  $F_L$ ,  $A_{FB}^{\ell}$  and  $A_{FB}^{\Lambda}$  simultaneously in the bin  $s \in [0.1, 2]$   $\text{GeV}^2$ . Different colors in the plots represent different combinations of new WCs: Red, blue, green, cyan, brown and black dots represent the  $(C_X, C_Y) = (C_S, C_V)$ ,  $(C_S, C'_P)$ ,  $(C'_S, C_V)$ ,  $(C'_P, C_V)$ ,  $(C'_S, C_P)$  and  $(C_S, C'_S)$ , respectively. The plots (b)-(e) present the predictions of  $d\mathcal{B}/ds$ ,  $F_L$ ,  $A_{FB}^{\ell}$  and  $A_{FB}^{\Lambda}$  in the bin  $s \in [0.1, 2]$   $\text{GeV}^2$  against the WCs collected in (a) where the pink flat curves reflect the measured values of  $d\mathcal{B}/ds$ ,  $F_L$ ,  $A_{FB}^{\Lambda}$  and  $A_{FB}^{\ell}$ , along with the uncertainties at the LHCb.

- Fig. 6.8(a) reflects the complete range of each combination of new WCs given in Eq. (6.44) which is allowed by  $B$ -physics data (c.f. Eq. (6.42)) with the condition  $|C_S - C'_S| \leq 0.1$ . The range of  $C_X$ ,  $C_Y$  and the corresponding color schemes are given in the caption of the



figure. We found that the full allowed ranges of WCs from  $B$ -meson decays simultaneously satisfy the the data of  $d\mathcal{B}/ds$ ,  $F_L$ ,  $A_{FB}^\ell$  and  $A_{FB}^\Lambda$  in  $s \in [0.1, 2]$   $\text{GeV}^2$  bin.

- By using these allowed values for each combination of new WCs, we predict the values of  $d\mathcal{B}/ds$ ,  $F_L$ ,  $A_{FB}^\ell$  and  $A_{FB}^\Lambda$  by plotting them against the  $C_X$  and  $C_Y$  in Fig. 6.8(b)-(e). The pink plane in each plot corresponds to the measured experimental range of the observable. The central SM values of  $d\mathcal{B}/ds$ ,  $F_L$ ,  $A_{FB}^\ell$  and  $A_{FB}^\Lambda$  are  $0.24 \times 10^{-7}$ , 0.54, 0.10 and  $-0.31$ , respectively in  $s \in [0.1, 2]$   $\text{GeV}^2$  as shown in Table 6.5.
- Fig. 6.8(b) shows that the value of  $d\mathcal{B}/ds$  varies from  $0.27 \times 10^{-7}$  to  $0.50 \times 10^{-7}$  inside the experimentally allowed region when  $C_X$  and  $C_Y$  are varied in their range constrained by the analysis of different  $B$ - meson decays. Hence it can be inferred that the experimentally allowed region  $0.22 \times 10^{-7} < d\mathcal{B}/ds < 0.27 \times 10^{-7}$  is excluded by the present analysis.
- Fig. 6.8(c) represents the variation in the values of  $F_L$  against each combination of  $C_X$  and  $C_Y$ . It can be noticed that the value of  $F_L$  approximately varies from 0.39 – 0.77 when we vary the values of  $C_X$  and  $C_Y$  in their allowed ranges. It means current constraints on the new WCs suggest that the value of  $F_L$  is  $0.39 < F_L < 0.77$  therefore, it excludes the experimentally measured ranges that are above and below this range of  $F_L$ .
- Fig. 6.8(d) depicts that the value of  $A_{FB}^\ell$  is not very sensitive to the combinations of NP couplings and its value remains close to its SM prediction which is 0.097 (central value). Therefore, the larger experimental values of this observable cannot be accommodated in light of the current constraints on new WCs.
- In case of  $A_{FB}^\Lambda$ , the combinations  $(C'_P, C_V)$  and  $(C_S, C'_S)$  (cyan and black dots) change the value of this observable from its SM predictions to some extent while for other combinations of new WCs this value remains close to the SM predictions and it can be seen in Fig. 6.8(e). In this high-recoil bin, the maximum and the minimum values of  $A_{FB}^\Lambda$  are found to be  $-0.25$  and  $-0.4$ , respectively. Therefore, the positive value of this observable and the value greater than  $-0.25$  seems to be excluded by the current constraints on these new WCs.

In short, the observables  $d\mathcal{B}/ds$ ,  $F_L$ ,  $A_{FB}^\ell$  and  $A_{FB}^\Lambda$  in high recoil region are very interesting to tell us more about the possible values of the new  $VA$  and  $SP$  couplings. Particularly, in this bin, the study of the observables of  $\Lambda_b$  decay do not put additional constraints on the range of WCs obtained from the analysis of  $B$ -meson decays.

### Low-recoil region

For the low-recoil **bin**  $s \in [15, 16]$   $\text{GeV}^2$ , one can make the following observations from Fig. 6.9

- In this bin, the available data of all four observables could be accommodated by the combinations of  $VA$  and  $SP$  couplings given in Eq. (6.44) with the exception of  $(C'_P, C_V)$ . However, when we try to accommodate the available data of the observables by these combinations the range of new WCs allowed by  $B$ -physics is further reduced and it can be seen from Fig. 6.9(a).

- It can be noticed from the blue and brown dots in Fig. 6.9(a) that for the combinations  $(C_S, C'_P)$  and  $(C'_S, C_P)$ , the parametric space of  $C_S$  is reduced to  $[\pm 4, \pm 2.6]$  and when  $C_S$  is close to its maximum value, i.e.,  $\pm 4$ , then full range of  $C'_P \in [+4, -4]$  is allowed. On the other hand when  $C'_S$  is close to  $\pm 4$ , the  $C'_P$  is allowed to be varied between  $[\pm 3, \pm 4]$  (see brown dots). It can be further seen that if  $C'_S$  reaches to  $\pm 2.6$  then  $C'_P$  goes to zero.
- In the combinations of  $(C_S^{(\prime)}, C_V)$ , the parametric space of  $C_V$  is unchanged which can be seen from the red and green dots in Fig. 6.9(a) while the parametric ranges of  $C_S, C'_S$  are reduced to  $\pm 4 < C_S < \pm 0.5$  and  $\pm 2 < C'_S < \pm 0.5$  which can be observed from the red and green dots, respectively.
- The constraint on the combination  $(C_S, C'_S)$  is already severe due to the condition  $|C_S - C'_S| \leq 0.1$  and it further narrow down when we try to explore the data of above mentioned observables. The new allowed range of this combination is between  $\pm 2$  to  $\pm 1$  with  $|C_S - C'_S| \leq 0.1$  condition. This can be seen from the black dots in Fig. 6.9(a).
- By using these new allowed ranges of model independent WCs, we have predicted the values of all four observables in the bin  $s \in [15, 16]$  GeV<sup>2</sup> and plotted them in Fig. 6.9(b-e). In this bin the SM value of  $d\mathcal{B}/ds$  is  $0.80 \times 10^{-7}$  and from Fig. 6.9(b) we can see that this value varies between  $(0.82 - 1.42) \times 10^{-7}$  by varying the values of the combinations  $(C_S, C'_P)$ ,  $(C'_S, C_P)$  and  $(C_S, C'_S)$  in their allowed parametric space shown in Fig. 6.9(a). It can also be noticed that the combinations  $(C_S, C'_P)$ ,  $(C'_S, C_P)$  and  $(C_S, C'_S)$  allow full experimental range of  $d\mathcal{B}/ds$  which can be seen by blue, brown and black dots. In contrast to this, the combinations  $(C_S^{(\prime)}, C_V)$  allow the region  $(0.82 - 1.15) \times 10^{-7}$  of experimental measurements that is displayed by red and green dots in the same plot.
- Just like  $d\mathcal{B}/ds$ , the values of  $F_L$  are also predicted in  $s \in [15, 16]$  GeV<sup>2</sup> bin and plotted in Fig. 6.9(c). The SM value of  $F_L$  is 0.45 and it varies in the range  $0.19 - 0.32$  for the combinations  $(C_S, C'_P)$ ,  $(C'_S, C_P)$  and  $(C_S, C'_S)$  (see blue, brown and black dots). On the other hand choosing the combinations  $(C_S^{(\prime)}, C_V)$  the value of  $F_L$  does not vary too much and predicted to be about  $0.19 - 0.24$ . This is displayed by the red and green color dots in the plot.
- Similarly, the values of  $A_{FB}^\ell$  are predicted and plotted in Fig. 6.9(d). The SM value of this observable in this bin is  $-0.38$  and by using the values of combinations  $(C_S, C'_P)$  and  $(C'_S, C_P)$  it varies between  $-0.15$  to  $-0.26$  which is shown by blue and brown dots. For the combinations  $(C_S^{(\prime)}, C_V)$ , the predicted range of the value of  $A_{FB}^\ell$  is  $-0.19$  to  $-0.12$  (red and green dots).
- Fig. 6.9(e) represents the predicted values of  $A_{FB}^\Lambda$  by using the combinations of new WCs. The SM value of this observable in this bin is  $-0.31$  and by using the allowed values of  $(C_S, C'_P)$  and  $(C'_S, C_P)$  combinations, it changes from  $-0.22$  to  $-0.13$  (blue and brown dots) and by  $(C_S^{(\prime)}, C_V)$  combinations the range of the value of  $A_{FB}^\Lambda$  is found to be  $-0.17$  to  $-0.12$  (red and green dots).

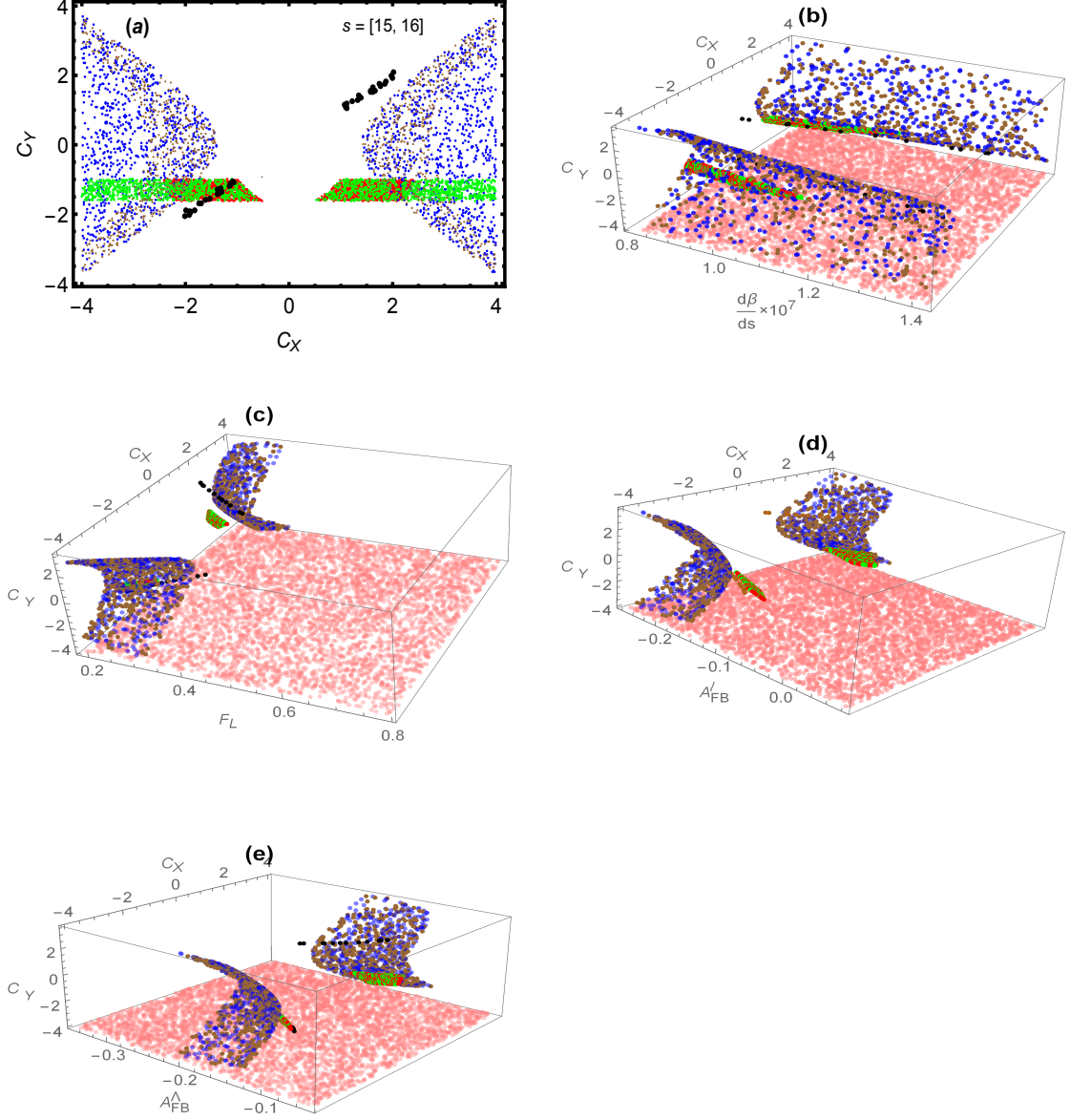


Figure 6.9: Plot (a) shows the parametric space of  $(C_X, C_Y)$  allowed from  $B$ -physics constraints on new WCs and which also satisfy the data of  $d\mathcal{B}/ds$ ,  $F_L$ ,  $A_{FB}^\ell$  and  $A_{FB}^\Lambda$ , simultaneously, in the bin  $s \in [15, 16]$   $\text{GeV}^2$ . (b)-(e) are the predictions of  $d\mathcal{B}/ds$ ,  $F_L$ ,  $A_{FB}^\ell$  and  $A_{FB}^\Lambda$  in the bin  $s \in [15, 16]$   $\text{GeV}^2$  against the WCs collected in (a). The legends are same as Fig. 6.8.

It is important to mention here that the values of the observables do not depend on the signs of the new WCs and it can be observed from Fig. 6.9(b - e). However, when more precise data will be available from the Run 3 of the LHC, we expect that the values of the observables in this bin can be used to further constraining the new WCs particularly, the scalar type couplings.

**In  $s \in [16, 18]$   $\text{GeV}^2$  bin:**

- The SM values of the  $d\mathcal{B}/ds$ ,  $F_L$ ,  $A_{FB}^\ell$  and  $A_{FB}^\Lambda$  in this bin are  $0.82 \times 10^{-7}$ , 0.42,  $-0.38$  and  $-0.29$ , respectively. As we have mentioned earlier that we are interested only in those bins where all four and if not at least three observables could be accommodated simultaneously by using the parametric space of new WCs which is allowed by the  $B$ -physics data. In this

particular bin, we have found that only the data of two observables,  $F_L$  and  $A_{FB}^\ell$  favor our choice. Therefore, based on this fact we can say that this region is not good to predict the values of different angular observables. However, in the future when more accurate data will be available in this range of  $s$ ; it will be looking for the possible NP effects due to these new WCs in the decay under consideration.

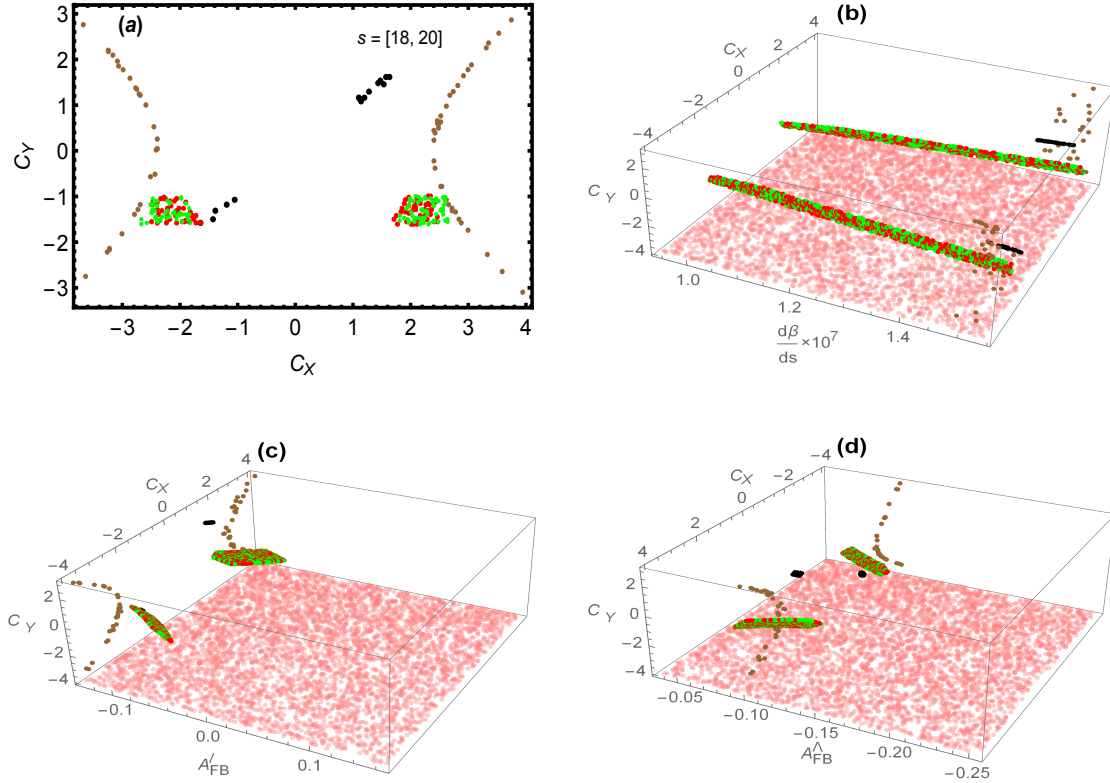


Figure 6.10: Plot (a) shows the parametric space of  $(C_X, C_Y)$  allowed from  $B$ -physics constraints on the new WCs which also satisfy the data of  $F_L$ ,  $A_{FB}^\ell$  and  $A_{FB}^\Delta$  simultaneously in the bin  $s \in [18 - 20]$   $\text{GeV}^2$ . (b)-(d) are the predictions of  $F_L$ ,  $A_{FB}^\ell$  and  $A_{FB}^\Delta$  in the bin  $s \in [18 - 20]$   $\text{GeV}^2$  against the WCs collected in (a). The legends are same as Fig. 6.8.

**In  $s \in [18 - 20]$   $\text{GeV}^2$  bin:**

In this bin, by excluding the data of  $F_L$  the available data of remaining three observables; i.e.,  $d\mathcal{B}/ds$ ,  $A_{FB}^\ell$  and  $A_{FB}^\Delta$  could be accommodated simultaneously for the combinations of new WCs given in Eq. (6.44). However, except  $(C'_S, C'_P)$  and  $(C'_P, C'_V)$  the other four combinations of new WCs can take care of LHCb data of these observables. We have also explored the case by including the data of  $F_L$  but in this situation, it is found that only one more observable can be accommodated at a time with it. Furthermore, as a result of satisfying the data, this bin provides more severe constraints on the new WCs that are still allowed by  $B$ -physics and it can be seen from Fig. 6.10(a). The important observations, in this case, are the following:

- It can be noticed from the brown dots in Fig. 6.10(a) that for the combination  $(C'_S, C'_P)$  the parametric space of  $C'_S$  is reduced to  $[\pm 4, \pm 2.4]$  and that of  $C'_P$  is  $[+3, -3]$  with the severe parabolic condition  $5.057(C'_S - 2.384) \simeq C'_P{}^2$ . On the other hand, for the other combinations the allowed region of  $C'_S$  is further narrow down (black and brown dots) while the region of

$C_V$  still remains the same as restricted by  $B$ -physics data (red and green dots). Therefore, similar to the  $s \in [15, 16]$  GeV<sup>2</sup> bin, the  $s \in [18 - 20]$  GeV<sup>2</sup> is also important for the scalar type new WCs.

- By using the allowed ranges of new WCs shown in Fig. 6.10(a) and discussed above, the predictions of the observables  $d\mathcal{B}/ds$ ,  $A_{FB}^\ell$  and  $A_{FB}^\Lambda$  are plotted in Fig. 6.10(b-d) in  $s \in [18 - 20]$  GeV<sup>2</sup> bin. In this bin the SM value of  $d\mathcal{B}/ds$  is  $0.66 \times 10^{-7}$  and it can be observed from Fig. 6.10(b) that by using the allowed values of  $(C'_S, C_P)$  and  $(C_S, C'_S)$  combinations, the value of  $d\mathcal{B}/ds$  varies in a very small region of experimental range, i.e., roughly  $(1.47 - 1.54) \times 10^{-7}$  (brown and black dots, respectively). In contrast, the combinations  $(C_S^{(\prime)}, C_V)$  allow the full region of experimental values and in this case the range of the value is found to be  $(0.94 - 1.54) \times 10^{-7}$  that is displayed by the red and green dots in Fig. 6.10(b).
- Similarly, the values of  $A_{FB}^\ell$  are predicted and plotted in Fig. 6.10(c). The SM value of  $A_{FB}^\ell$  in this bin is  $-0.32$  and by using the allowed values of the combinations  $(C'_S, C_P)$  and  $(C_S, C'_S)$  the value is found to be  $\simeq -0.13$  which is shown by brown and black dots. For the combinations  $(C_S^{(\prime)}, C_V)$  the predicted range of  $A_{FB}^\ell$  is  $-0.07$  to  $-0.14$  which is plotted by red and green dots. One can further notice that the allowed range of combinations predicts only the negative value of  $A_{FB}^\ell$  which satisfies a very small experimental region of this observable, particularly, the positive experimental value of this observable is not possible to accommodate if we use the above six combinations.
- Fig. 6.10(d) represents the predicted values of  $A_{FB}^\Lambda$  by using the combinations of new WCs. The SM value of  $A_{FB}^\Lambda$  in this particular bin is  $-0.23$  and by using the allowed values of  $(C'_S, C_P)$  and  $(C_S, C'_S)$  combinations, this value is roughly to be  $-0.10$  (see the brown and black dots) and by  $(C_S^{(\prime)}, C_V)$  combinations its values change from  $-0.07$  to  $-0.12$  which can be seen by the red and green dots. The higher experimental values of this observable are also not possible to be reproduced by using the current constraints on any possible combination of new WCs.

To summarize, in this particular bin, the analysis of the above-mentioned observables helps us to put the additional constraints on the new scalar type couplings. On the other hand, the parametric space of the vector type couplings does not change and remains to be the same as constrained by the  $B$ -physics data. Moreover, similar to the case of  $s \in [15, 16]$  GeV<sup>2</sup> bin, the numerical values of the observables, in this case, are also independent of the sign of new WCs.

#### 6.4.5 Lepton mass effects

It has already been mentioned that we have calculated the expressions of different physical observables by taking the mass of final state leptons to be non-zero which is not the case in [113] and hence our study can be extended easily to the semileptonic  $\Lambda_b \rightarrow \Lambda \tau^+ \tau^-$  case. Based on our analysis of  $\Lambda_b \rightarrow \Lambda \mu^+ \mu^-$  we find that  $\mu$ -mass effects in the angular observables of the four body decay  $\Lambda_b \rightarrow \Lambda(\rightarrow p\pi^-)\mu^+\mu^-$  are not prominent consequently in the case of muons, the lepton mass terms can be safely ignored like in [113]. For the sake of completeness, we have also calculated the values of angular observables in the low-recoil region for the case of  $\Lambda_b \rightarrow \Lambda(\rightarrow p\pi^-)\tau^+\tau^-$  decay in SM and also by considering the new WCs corresponding to the model independent approach.

Table 6.2: Observables with and without lepton mass for the decay  $\Lambda_b \rightarrow \Lambda(\rightarrow p\pi)\tau^+\tau^-$  in the SM and in different scenarios of NP couplings where the case  $m_\ell \neq 0$  corresponds to  $m_\ell = m_\tau$  in  $s \in [15, 20]$  GeV<sup>2</sup> bin. Scenario  $VA - 1$  corresponds to  $C_V = -1.61$ ,  $C'_V = C_A = C'_A = 0$ ,  $VA2$  corresponds to  $C_V = -C_A = -1$ ,  $C'_V = C'_A = 0$  and  $VA - 3$  represent  $C_V = -1.34$ ,  $C'_V = C_A = 0$ ,  $C'_A = -0.4$ . Similarly, in  $SP - 1$  case we have taken  $C_S = C_P = -3$ ,  $C'_S = C'_P = -3.1$  whereas  $SP - 2$  contains  $C_S = 3$ ,  $C'_S = 2.9$  and  $C_P = C'_P = 0$ . Tensor couplings correspond to  $C_T = 0.72$  and  $C_{T5} = 0.2$ .

	$\frac{d\mathcal{B}}{ds} \times 10^{-7}$	$F_L$	$A_{FB}^\ell$	$A_{FB}^\Lambda$	$A_{FB}^{\ell\Lambda}$	$F_T$
$SM_{m_\ell=0}$	0.75	0.41	-0.35	-0.26	0.14	0.60
$SM_{m_\ell \neq 0}$	0.53	0.35	-0.13	-0.26	0.06	0.65
$VA - 1_{m_\ell=0}$	0.52	0.40	-0.28	-0.26	0.12	0.60
$VA - 1_{m_\ell \neq 0}$	0.37	0.35	-0.11	-0.26	0.04	0.65
$VA - 2_{m_\ell=0}$	0.42	0.41	-0.35	-0.26	0.14	0.59
$VA - 2_{m_\ell \neq 0}$	0.29	0.35	-0.13	-0.26	0.06	0.65
$VA - 3_{m_\ell=0}$	0.52	0.41	-0.33	-0.28	0.13	0.59
$VA - 3_{m_\ell \neq 0}$	0.36	0.35	-0.12	-0.28	0.05	0.65
$SP - 1_{m_\ell=0}$	0.91	0.22	-0.20	-0.15	0.14	0.59
$SP - 1_{m_\ell \neq 0}$	0.68	0.15	-0.05	-0.12	0.03	0.85
$SP - 2_{m_\ell=0}$	0.87	0.16	-0.14	-0.11	0.06	0.84
$SP - 2_{m_\ell \neq 0}$	0.90	0.21	-0.08	-0.16	0.03	0.79
$T'_{m_\ell=0}$	0.79	0.39	-0.33	-0.25		
$T'_{m_\ell \neq 0}$	0.54	0.34	-0.13	-0.26		

By using the central values of the FFs the calculated values of different physical observables are listed in Tables 6.2 - 6.4. From the first row in each of the Tables 6.2 - 6.4, one can notice that the magnitude of the SM values of observables  $A_{FB}^\ell$ ,  $F_T$ ,  $Y_{4sc}$ ,  $\alpha_{\theta_\ell}$ ,  $\alpha'_{\theta_\ell}$ ,  $\alpha_\xi$ ,  $\alpha'_\xi$  and  $P_8$  are increased due to the non-zero  $\tau$ 's mass whereas the values of  $A_{FB}^\Lambda$  and  $\alpha_{\theta_\Lambda}$  do not receive tauon mass effect. Similar effects can also be noticed in these tables when we include the  $VA$  (rows 2 - 4) and  $T$  (row 7) couplings along with the SM couplings. It is noticed that in the case of  $SP - 1$ , the values of  $F_L$ ,  $A_{FB}^\ell$ ,  $A_{FB}^\Lambda$ ,  $F_T$ ,  $Y_{4sc}$ ,  $\alpha_{\theta_\Lambda}$ ,  $\alpha_{\theta_\ell}$ ,  $\alpha'_{\theta_\ell}$ ,  $\alpha_\xi$ ,  $\alpha'_\xi$ ,  $\alpha_L$ ,  $P_8$  and  $P_9$  increase when tau mass effects are included whereas  $d\mathcal{B}/ds$ ,  $A_{FB}^{\ell\Lambda}$ ,  $\alpha_U$  and  $P_3$  values decrease.

For the second possibility of scalar couplings ( $SP - 2$ ), the values of the observables  $A_{FB}^\ell$ ,  $Y_{4sc}$ ,  $\alpha_{\theta_\ell}$ ,  $\alpha'_{\theta_\ell}$ ,  $\alpha_\xi$ ,  $\alpha'_\xi$ ,  $\alpha_U$  and  $P_8$  are increased due to the  $\tau$  mass while the values of the observables  $d\mathcal{B}/ds$ ,  $F_L$ ,  $A_{FB}^\Lambda$ ,  $A_{FB}^{\ell\Lambda}$ ,  $F_T$ ,  $\alpha_{\theta_\Lambda}$ ,  $\alpha_L$ ,  $P_3$  and  $P_9$  are decreased. However, there are no effects of non-zero tauon mass observed in the calculated values of  $Y_2$  and  $Y_{3sc}$  in both scenarios of SP couplings (c.f. sixth row of Table 6.4). In short, we have found that the effects of  $\tau$  mass are significantly large in the decay  $\Lambda_b \rightarrow \Lambda(\rightarrow p\pi)\tau^+\tau^-$  therefore, in contrast to the case of muons, to pursue the NP effects in the angular observables of  $\Lambda_b \rightarrow \Lambda(\rightarrow p\pi)\tau^+\tau^-$  decay it is indispensable to include the lepton mass terms in the expressions of different physical observables. Consequently, it is worthy to derive the expressions by taking the lepton mass to be non zero in the semileptonic decay  $\Lambda_b \rightarrow \Lambda(\rightarrow p\pi)\ell^+\ell^-$  where  $\ell = e, \mu, \tau$ .

Table 6.3: Observables by taking the massive and massless  $\tau$  in  $\Lambda_b \rightarrow \Lambda(\rightarrow p\pi)\tau^+\tau^-$  decay in the SM and also in different NP scenarios. Description of couplings is similar to Table 6.2.

	$Y_{3sc} \times 10^{-3}$	$Y_{4sc} \times 10^{-2}$	$Y_2$	$\alpha_{\theta_\Lambda}$	$\alpha_{\theta_\ell}$	$\alpha'_{\theta_\ell}$
$SM_{m_\ell=0}$	0.02	-0.96	0.02	-0.82	-0.15	-0.67
$SM_{m_\ell \neq 0}$	0.00	-0.19	0.00	-0.82	-0.03	-0.26
$VA - 1_{m_\ell=0}$	0.02	-0.94	0.02	-0.82	-0.15	-0.54
$VA - 1_{m_\ell \neq 0}$	0.00	-0.18	0.00	-0.82	-0.03	-0.21
$VA - 2_{m_\ell=0}$	0.03	-1.00	0.02	-0.82	-0.16	-0.67
$VA - 2_{m_\ell \neq 0}$	0.00	-0.19	0.00	-0.82	-0.03	-0.26
$VA - 3_{m_\ell=0}$	0.02	-1.00	0.02	-0.87	-0.16	-0.62
$VA - 3_{m_\ell \neq 0}$	0.00	-0.19	0.00	-0.87	-0.03	-0.24
$SP - 1_{m_\ell=0}$	0.01	-0.10	0.01	-0.46	-0.05	-0.21
$SP - 1_{m_\ell \neq 0}$	0.00	-0.07	0.00	-0.32	-0.01	-0.05
$SP - 2_{m_\ell=0}$	0.01	-0.50	0.01	-0.34	-0.03	-0.13
$SP - 2_{m_\ell \neq 0}$	0.00	-0.11	0.00	-0.51	-0.01	-0.09

Table 6.4: Observables by taking the massive and massless  $\tau$  in  $\Lambda_b \rightarrow \Lambda(\rightarrow p\pi)\tau^+\tau^-$  decay in the SM and also in different NP scenarios. Description of couplings is similar to Table 6.2.

	$\alpha_\xi$	$\alpha'_\xi \times 10^{-3}$	$\alpha_U$	$\alpha_L$	$\mathcal{P}_3$	$\mathcal{P}_8$	$\mathcal{P}_9$
$SM_{m_\ell=0}$	-0.32	-0.20	-0.79	-0.84	0.38	-0.94	-0.60
$SM_{m_\ell \neq 0}$	-0.13	-0.07	-0.82	-0.83	0.14	-0.35	-0.69
$VA - 1_{m_\ell=0}$	-0.26	-0.29	-0.79	-0.84	0.31	-0.76	-0.60
$VA - 1_{m_\ell \neq 0}$	-0.11	-0.11	-0.82	-0.83	0.12	-0.29	-0.69
$VA - 2_{m_\ell=0}$	-0.32	-0.27	-0.79	-0.84	0.37	-0.94	-0.59
$VA - 2_{m_\ell \neq 0}$	-0.13	-0.01	-0.82	-0.83	0.15	-0.36	-0.58
$VA - 3_{m_\ell=0}$	-0.25	-4.69	-0.85	-0.89	0.34	-0.87	-0.64
$VA - 3_{m_\ell \neq 0}$	-0.10	-1.78	-0.87	-0.88	0.13	-0.33	-0.73
$SP - 1_{m_\ell=0}$	-0.16	-0.12	-0.21	-0.26	0.20	-0.52	-0.34
$SP - 1_{m_\ell \neq 0}$	-0.05	-0.03	-0.14	-0.14	0.06	-0.14	-0.27
$SP - 2_{m_\ell=0}$	-0.12	-0.08	-0.13	-0.16	0.15	-0.37	-0.24
$SP - 2_{m_\ell \neq 0}$	-0.07	-0.05	-0.28	-0.30	0.09	-0.21	-0.44

#### 6.4.6 Most favorable pair of Wilson coefficients

We have extracted the most favorable pair of new WC's which is  $(C'_S, C_P)$  as shown in Fig. 6.11. This pair satisfies individual observables  $\frac{dB}{ds}$ ,  $F_L$ ,  $A_{FB}^\ell$  and  $A_{FB}^\Lambda$  in large-recoil bin  $s \in [0.1, 2]$  GeV<sup>2</sup> and low-recoil bins  $s \in [15, 16]$  GeV<sup>2</sup>,  $[16, 18]$  GeV<sup>2</sup> and  $[18, 20]$  GeV<sup>2</sup>. It means that it can satisfy all experimental data available for  $\Lambda_b$  decay observables respecting the  $B$ -physics constraints. Density of plots in Fig. 6.11 shows how the respective parametric space of  $(C'_S, C_P)$  is favorable by these decay observables.

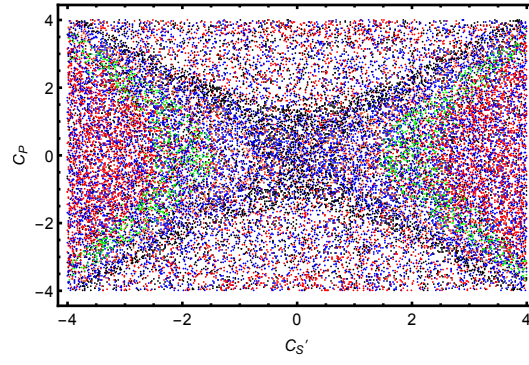


Figure 6.11:  $(C'_S, C_P)$  is the most favorable pair of Wilson coefficients. Green, Black, red and blue colors denote  $\frac{dB}{ds}$ ,  $F_L$ ,  $A_{FB}^\ell$  and  $A_{FB}^\Lambda$  respectively.



Table 6.5: Observables for the decay  $\Lambda_b \rightarrow \Lambda(\rightarrow p\pi)\mu^+\mu^-$  in the SM and in different scenarios of NP couplings along with LHCb results in respective bins. Scenario  $VA-1$  corresponds to  $C_V = -1.61$ ,  $C'_V = C_A = C'_A = 0$ ,  $VA-2$  corresponds to  $C_V = -C_A = -1$ ,  $C'_V = C'_A = 0$  and  $VA-3$  corresponds to  $C_V = -1.34$ ,  $C'_V = C_A = 0$ ,  $C'_A = -0.4$ . Similarly, in  $SP-1$  case we have taken  $C_S = C_P = -3$ ,  $C'_S = C'_P = -3.1$  whereas  $SP-2$  contains  $C_S = 3$ ,  $C'_S = 2.9$  and  $C_P = C'_P = 0$ . The tensor couplings correspond to  $C_T = 0.72$  and  $C_{T5} = 0.2$ . The final state leptons are muons. The experimental results are taken from [217].

	$\langle \frac{d\mathcal{B}}{ds} \times 10^{-7} \rangle$	$\langle F_L \rangle$	$\langle A_{FB}^\ell \rangle$	$\langle A_{FB}^\Lambda \rangle$	
[0.1, 2]	<i>SM</i>	$0.238^{+0.185}_{-0.131}$	$0.535^{+0.025}_{-0.051}$	$0.097^{+0.006}_{-0.003}$	$-0.310^{+0.011}_{-0.004}$
	<i>VA-1</i>	$0.214^{+0.163}_{-0.116}$	$0.453^{+0.024}_{-0.048}$	$0.122^{+0.003}_{-0.010}$	$-0.312^{+0.008}_{-0.003}$
	<i>VA-2</i>	$0.187^{+0.136}_{-0.100}$	$0.398^{+0.025}_{-0.046}$	$0.101^{+0.003}_{-0.009}$	$-0.312^{+0.008}_{-0.003}$
	<i>VA-3</i>	$0.222^{+0.168}_{-0.120}$	$0.459^{+0.022}_{-0.042}$	$0.117^{+0.002}_{-0.007}$	$-0.303^{+0.010}_{-0.004}$
	<i>SP-1</i>	$0.280^{+0.255}_{-0.167}$	$0.335^{+0.084}_{-0.045}$	$0.060^{+0.020}_{-0.010}$	$-0.194^{+0.031}_{-0.064}$
	<i>SP-2</i>	$0.268^{+0.236}_{-0.157}$	$0.241^{+0.116}_{-0.044}$	$0.043^{+0.025}_{-0.009}$	$-0.139^{+0.029}_{-0.081}$
	<i>T'</i>	$0.434^{+0.318}_{-0.232}$	$0.293^{+0.020}_{-0.039}$	$0.053^{+0.002}_{-0.003}$	$-0.167^{+0.016}_{-0.002}$
	<i>LHCb</i>	$0.36^{+0.14}_{-0.13}$	$0.56^{+0.24}_{-0.57}$	$0.37^{+0.37}_{-0.48}$	$-0.12^{+0.34}_{-0.32}$
[15, 16]	<i>SM</i>	$0.797^{+0.172}_{-0.155}$	$0.454^{+0.005}_{-0.004}$	$-0.382^{+0.002}_{-0.001}$	$-0.307^{+0.001}_{-0.001}$
	<i>VA-1</i>	$0.558^{+0.120}_{-0.108}$	$0.450^{+0.004}_{-0.004}$	$-0.301^{+0.002}_{-0.002}$	$-0.307^{+0.001}_{-0.001}$
	<i>VA-2</i>	$0.439^{+0.087}_{-0.086}$	$0.460^{+0.005}_{-0.004}$	$-0.379^{+0.002}_{-0.002}$	$-0.307^{+0.001}_{-0.001}$
	<i>VA-3</i>	$0.568^{+0.168}_{-0.110}$	$0.458^{+0.004}_{-0.004}$	$-0.337^{+0.002}_{-0.002}$	$-0.316^{+0.001}_{-0.001}$
	<i>SP-1</i>	$0.960^{+0.236}_{-0.208}$	$0.261^{+0.025}_{-0.019}$	$-0.220^{+0.014}_{-0.018}$	$-0.177^{+0.012}_{-0.016}$
	<i>SP-2</i>	$0.917^{+0.220}_{-0.195}$	$0.187^{+0.023}_{-0.017}$	$-0.157^{+0.012}_{-0.017}$	$-0.126^{+0.011}_{-0.014}$
	<i>T'</i>	$0.837^{+0.172}_{-0.167}$	$0.432^{+0.007}_{-0.000}$	$-0.362^{+0.004}_{-0.002}$	$-0.292^{+0.001}_{-0.001}$
	<i>LHCb</i>	$1.12^{+0.30}_{-0.30}$	$0.49^{+0.30}_{-0.30}$	$-0.10^{+0.18}_{-0.16}$	$-0.19^{+0.14}_{-0.16}$
[16, 18]	<i>SM</i>	$0.824^{+0.141}_{-0.130}$	$0.418^{+0.003}_{-0.002}$	$-0.381^{+0.001}_{-0.001}$	$-0.289^{+0.001}_{-0.001}$
	<i>VA-1</i>	$0.576^{+0.098}_{-0.091}$	$0.415^{+0.002}_{-0.002}$	$-0.306^{+0.001}_{-0.001}$	$-0.289^{+0.001}_{-0.001}$
	<i>VA-2</i>	$0.454^{+0.060}_{-0.072}$	$0.422^{+0.003}_{-0.002}$	$-0.381^{+0.001}_{-0.001}$	$-0.289^{+0.001}_{-0.001}$
	<i>VA-3</i>	$0.574^{+0.098}_{-0.090}$	$0.422^{+0.002}_{-0.002}$	$-0.349^{+0.001}_{-0.001}$	$-0.304^{+0.000}_{-0.001}$
	<i>SP-1</i>	$0.998^{+0.196}_{-0.177}$	$0.234^{+0.018}_{-0.014}$	$-0.213^{+0.012}_{-0.014}$	$-0.162^{+0.009}_{-0.012}$
	<i>SP-2</i>	$0.953^{+0.182}_{-0.165}$	$0.168^{+0.016}_{-0.012}$	$-0.153^{+0.010}_{-0.013}$	$-0.116^{+0.008}_{-0.011}$
	<i>T'</i>	$0.862^{+0.130}_{-0.148}$	$0.406^{+0.005}_{-0.006}$	$-0.361^{+0.002}_{-0.004}$	$-0.276^{+0.001}_{-0.001}$
	<i>LHCb</i>	$1.22^{+0.29}_{-0.29}$	$0.68^{+0.16}_{-0.22}$	$-0.07^{+0.14}_{-0.13}$	$-0.44^{+0.10}_{-0.06}$
[18, 20]	<i>SM</i>	$0.658^{+0.078}_{-0.073}$	$0.371^{+0.001}_{-0.001}$	$-0.317^{+0.001}_{-0.001}$	$-0.227^{+0.000}_{-0.000}$
	<i>VA-1</i>	$0.459^{+0.054}_{-0.051}$	$0.370^{+0.001}_{-0.001}$	$-0.260^{+0.001}_{-0.001}$	$-0.227^{+0.000}_{-0.000}$
	<i>VA-2</i>	$0.354^{+0.009}_{-0.031}$	$0.373^{+0.001}_{-0.001}$	$-0.318^{+0.001}_{-0.001}$	$-0.226^{+0.000}_{-0.000}$
	<i>VA-3</i>	$0.438^{+0.052}_{-0.049}$	$0.375^{+0.001}_{-0.001}$	$-0.307^{+0.001}_{-0.001}$	$-0.248^{+0.000}_{-0.000}$
	<i>SP-1</i>	$0.808^{+0.110}_{-0.103}$	$0.192^{+0.010}_{-0.009}$	$-0.164^{+0.007}_{-0.008}$	$-0.117^{+0.005}_{-0.006}$
	<i>SP-2</i>	$0.771^{+0.102}_{-0.096}$	$0.141^{+0.009}_{-0.008}$	$-0.120^{+0.006}_{-0.007}$	$-0.086^{+0.004}_{-0.005}$
	<i>T'</i>	$0.684^{+0.029}_{-0.118}$	$0.385^{+0.003}_{-0.028}$	$-0.286^{+0.001}_{-0.019}$	$-0.215^{+0.000}_{-0.001}$
	<i>LHCb</i>	$1.24^{+0.30}_{-0.30}$	$0.62^{+0.24}_{-0.27}$	$0.01^{+0.16}_{-0.15}$	$-0.13^{+0.10}_{-0.12}$
[15, 20]	<i>SM</i>	$0.752^{+0.122}_{-0.112}$	$0.409^{+0.001}_{-0.001}$	$-0.359^{+0.002}_{-0.002}$	$-0.271^{+0.001}_{-0.001}$
	<i>VA-1</i>	$0.525^{+0.085}_{-0.078}$	$0.407^{+0.001}_{-0.001}$	$-0.289^{+0.002}_{-0.002}$	$-0.271^{+0.001}_{-0.001}$
	<i>VA-2</i>	$0.415^{+0.038}_{-0.062}$	$0.412^{+0.001}_{-0.001}$	$-0.359^{+0.002}_{-0.002}$	$-0.271^{+0.001}_{-0.001}$
	<i>VA-3</i>	$0.518^{+0.084}_{-0.078}$	$0.414^{+0.001}_{-0.001}$	$-0.332^{+0.002}_{-0.002}$	$-0.287^{+0.001}_{-0.001}$
	<i>SP-1</i>	$0.914^{+0.169}_{-0.153}$	$0.224^{+0.015}_{-0.012}$	$-0.196^{+0.009}_{-0.011}$	$-0.149^{+0.007}_{-0.009}$
	<i>SP-2</i>	$0.873^{+0.158}_{-0.143}$	$0.162^{+0.014}_{-0.011}$	$-0.142^{+0.009}_{-0.011}$	$-0.107^{+0.007}_{-0.008}$
	<i>T'</i>	$0.786^{+0.098}_{-0.140}$	$0.404^{+0.004}_{-0.016}$	$-0.337^{+0.004}_{-0.003}$	$-0.257^{+0.002}_{-0.001}$
	<i>LHCb</i>	$1.20^{+0.27}_{-0.27}$	$0.61^{+0.11}_{-0.14}$	$-0.05^{+0.09}_{-0.09}$	$-0.29^{+0.08}_{-0.08}$

Table 6.6: Observables in the SM and in the presence of new  $VA$  and  $SP$  couplings for which experimental results are not available. The description of different scenarios is same as in Table 6.5.

		$\langle A_{FB}^{\ell\Lambda} \rangle$	$\langle F_T \rangle$	$\langle Y_{3sc} \times 10^{-3} \rangle$	$\langle Y_{4sc} \rangle$
[1.1, 6]	$SM$	$-0.002^{+0.003}_{-0.004}$	$0.182^{+0.002}_{-0.001}$	$0.326^{+0.101}_{-0.053}$	$0.004^{+0.008}_{-0.004}$
	$VA - 1$	$-0.034^{+0.002}_{-0.003}$	$0.266^{+0.502}_{-0.011}$	$0.238^{+0.071}_{-0.037}$	$0.003^{+0.007}_{-0.004}$
	$VA - 2$	$-0.022^{+0.003}_{-0.004}$	$0.236^{+0.517}_{-0.019}$	$0.524^{+0.118}_{-0.063}$	$0.006^{+0.009}_{-0.005}$
	$VA - 3$	$-0.026^{+0.002}_{-0.003}$	$0.240^{+0.008}_{-0.003}$	$0.250^{+0.071}_{-0.038}$	$0.004^{+0.007}_{-0.004}$
	$SP - 1$	$-0.001^{+0.001}_{-0.003}$	$0.581^{+0.073}_{-0.165}$	$0.167^{+0.138}_{-0.051}$	$0.002^{+0.007}_{-0.002}$
	$SP - 2$	$-0.001^{+0.001}_{-0.001}$	$0.722^{+0.057}_{-0.158}$	$0.111^{+0.117}_{-0.037}$	$0.001^{+0.005}_{-0.001}$
[15, 20]	$SM$	$0.143^{+0.000}_{-0.000}$	$0.591^{+0.001}_{-0.001}$	$0.018^{+0.001}_{-0.001}$	$-0.010^{+0.000}_{-0.000}$
	$VA - 1$	$0.116^{+0.000}_{-0.000}$	$0.593^{+0.001}_{-0.001}$	$0.020^{+0.001}_{-0.001}$	$-0.010^{+0.000}_{-0.000}$
	$VA - 2$	$0.144^{+0.000}_{-0.000}$	$0.587^{+0.001}_{-0.001}$	$0.027^{+0.002}_{-0.002}$	$-0.010^{+0.000}_{-0.000}$
	$VA - 3$	$0.126^{+0.000}_{-0.000}$	$0.586^{+0.001}_{-0.001}$	$0.021^{+0.002}_{-0.002}$	$-0.010^{+0.000}_{-0.000}$
	$SP - 1$	$0.078^{+0.005}_{-0.004}$	$0.776^{+0.012}_{-0.015}$	$0.010^{+0.000}_{-0.000}$	$-0.005^{+0.000}_{-0.000}$
	$SP - 2$	$0.057^{+0.004}_{-0.004}$	$0.838^{+0.011}_{-0.014}$	$0.007^{+0.000}_{-0.000}$	$-0.004^{+0.000}_{-0.000}$
		$\langle Y_2 \rangle$	$\langle \alpha_{\theta_\Lambda} \rangle$	$\langle \alpha_{\theta_l} \rangle$	$\langle \alpha'_{\theta_l} \rangle$
[1.1, 6]	$SM$	$0.084^{+0.001}_{-0.003}$	$-0.961^{+0.039}_{-0.015}$	$-0.800^{+0.003}_{-0.001}$	$0.014^{+0.031}_{-0.017}$
	$VA - 1$	$0.071^{+0.002}_{-0.004}$	$-0.966^{+0.034}_{-0.013}$	$-0.704^{+0.011}_{-0.004}$	$0.163^{+0.024}_{-0.015}$
	$VA - 2$	$0.076^{+0.002}_{-0.005}$	$-0.961^{+0.039}_{-0.015}$	$-0.750^{+0.018}_{-0.006}$	$0.107^{+0.030}_{-0.017}$
	$VA - 3$	$0.070^{+0.002}_{-0.004}$	$-0.920^{+0.044}_{-0.020}$	$-0.727^{+0.011}_{-0.004}$	$0.131^{+0.027}_{-0.016}$
	$SP - 1$	$0.043^{+0.015}_{-0.007}$	$-0.492^{+0.078}_{-0.168}$	$-0.259^{+0.058}_{-0.167}$	$0.004^{+0.019}_{-0.005}$
	$SP - 2$	$0.028^{+0.015}_{-0.006}$	$-0.327^{+0.062}_{-0.167}$	$-0.152^{+0.036}_{-0.122}$	$0.003^{+0.013}_{-0.003}$
[15, 20]	$SM$	$0.016^{+0.000}_{-0.000}$	$-0.844^{+0.003}_{-0.002}$	$-0.161^{+0.002}_{-0.002}$	$-0.679^{+0.004}_{-0.004}$
	$VA - 1$	$0.015^{+0.000}_{-0.000}$	$-0.844^{+0.003}_{-0.002}$	$-0.159^{+0.002}_{-0.002}$	$-0.548^{+0.004}_{-0.003}$
	$VA - 2$	$0.016^{+0.000}_{-0.000}$	$-0.844^{+0.003}_{-0.002}$	$-0.168^{+0.002}_{-0.002}$	$-0.677^{+0.004}_{-0.004}$
	$VA - 3$	$0.016^{+0.000}_{-0.000}$	$-0.895^{+0.002}_{-0.002}$	$-0.171^{+0.002}_{-0.002}$	$-0.626^{+0.004}_{-0.004}$
	$SP - 1$	$0.009^{+0.001}_{-0.001}$	$-0.463^{+0.023}_{-0.028}$	$-0.048^{+0.004}_{-0.006}$	$-0.212^{+0.017}_{-0.022}$
	$SP - 2$	$0.006^{+0.001}_{-0.000}$	$-0.335^{+0.021}_{-0.026}$	$-0.030^{+0.003}_{-0.003}$	$-0.126^{+0.010}_{-0.014}$

Table 6.7: Values of some observables in the SM and in the presence of new VA and SP couplings. Description of different scenarios is same as in Table 6.5.

		$\langle\alpha_\xi\rangle$	$\langle\alpha'_\xi \times 10^{-2}\rangle$	$\langle\alpha_U\rangle$	$\langle\alpha_L\rangle$
[1.1, 6]	<i>SM</i>	$0.087^{+0.050}_{-0.030}$	$-0.202^{+0.057}_{-0.110}$	$-0.973^{+0.063}_{-0.018}$	$-0.960^{+0.037}_{-0.015}$
	<i>VA</i> - 1	$0.042^{+0.029}_{-0.019}$	$-0.260^{+0.072}_{-0.138}$	$-0.983^{+0.038}_{-0.011}$	$-0.963^{+0.034}_{-0.013}$
	<i>VA</i> - 2	$0.069^{+0.042}_{-0.026}$	$-0.262^{+0.073}_{-0.138}$	$-0.979^{+0.046}_{-0.014}$	$-0.959^{+0.038}_{-0.015}$
	<i>VA</i> - 3	$0.053^{+0.028}_{-0.018}$	$-0.242^{+0.066}_{-0.125}$	$-0.944^{+0.053}_{-0.021}$	$-0.917^{+0.043}_{-0.020}$
	<i>SP</i> - 1	$0.044^{+0.054}_{-0.021}$	$-0.103^{+0.042}_{-0.120}$	$-0.084^{+0.022}_{-0.087}$	$-0.310^{+0.066}_{-0.182}$
	<i>SP</i> - 2	$0.029^{+0.044}_{-0.014}$	$-0.069^{+0.029}_{-0.098}$	$-0.043^{+0.011}_{-0.044}$	$-0.182^{+0.041}_{-0.135}$
[15, 20]	<i>SM</i>	$-0.304^{+0.002}_{-0.002}$	$-0.021^{+0.004}_{-0.005}$	$-0.805^{+0.003}_{-0.008}$	$-0.860^{+0.003}_{-0.002}$
	<i>VA</i> - 1	$-0.251^{+0.001}_{-0.001}$	$-0.030^{+0.006}_{-0.007}$	$-0.807^{+0.003}_{-0.002}$	$-0.860^{+0.003}_{-0.002}$
	<i>VA</i> - 2	$-0.308^{+0.002}_{-0.002}$	$-0.028^{+0.006}_{-0.007}$	$-0.803^{+0.002}_{-0.002}$	$-0.861^{+0.003}_{-0.002}$
	<i>VA</i> - 3	$-0.228^{+0.001}_{-0.002}$	$-0.030^{+0.006}_{-0.006}$	$-0.864^{+0.002}_{-0.002}$	$-0.908^{+0.002}_{-0.002}$
	<i>SP</i> - 1	$-0.167^{+0.001}_{-0.012}$	$-0.012^{+0.003}_{-0.004}$	$-0.211^{+0.017}_{-0.022}$	$-0.256^{+0.020}_{-0.025}$
	<i>SP</i> - 2	$-0.120^{+0.008}_{-0.011}$	$-0.008^{+0.002}_{-0.003}$	$-0.130^{+0.011}_{-0.015}$	$-0.161^{+0.013}_{-0.018}$
		$\langle P_3 \rangle$	$\langle P_8 \rangle$	$\langle P_9 \rangle$	
[1.1, 6]	<i>SM</i>	$-0.005^{+0.008}_{-0.011}$	$0.025^{+0.055}_{-0.030}$	$-0.226^{+0.011}_{-0.005}$	
	<i>VA</i> - 1	$-0.089^{+0.007}_{-0.008}$	$0.284^{+0.041}_{-0.025}$	$-0.325^{+0.002}_{-0.001}$	
	<i>VA</i> - 2	$-0.059^{+0.008}_{-0.010}$	$0.190^{+0.051}_{-0.030}$	$-0.279^{+0.002}_{-0.004}$	
	<i>VA</i> - 3	$-0.070^{+0.006}_{-0.007}$	$0.231^{+0.046}_{-0.027}$	$-0.291^{+0.007}_{-0.003}$	
	<i>SP</i> - 1	$-0.003^{+0.004}_{-0.000}$	$0.013^{+0.045}_{-0.015}$	$-0.116^{+0.018}_{-0.038}$	
	<i>SP</i> - 2	$-0.002^{+0.002}_{-0.007}$	$0.008^{+0.034}_{-0.010}$	$-0.077^{+0.014}_{-0.038}$	
[15, 20]	<i>SM</i>	$0.382^{+0.001}_{-0.001}$	$-0.956^{+0.005}_{-0.004}$	$-0.611^{+0.003}_{-0.003}$	
	<i>VA</i> - 1	$0.310^{+0.001}_{-0.001}$	$-0.770^{+0.005}_{-0.004}$	$-0.614^{+0.003}_{-0.003}$	
	<i>VA</i> - 2	$0.383^{+0.001}_{-0.001}$	$-0.956^{+0.005}_{-0.004}$	$-0.606^{+0.003}_{-0.003}$	
	<i>VA</i> - 3	$0.336^{+0.001}_{-0.001}$	$-0.885^{+0.005}_{-0.004}$	$-0.650^{+0.003}_{-0.002}$	
	<i>SP</i> - 1	$0.198^{+0.011}_{-0.197}$	$-0.523^{+0.025}_{-0.030}$	$-0.335^{+0.016}_{-0.019}$	
	<i>SP</i> - 2	$0.151^{+0.012}_{-0.010}$	$-0.375^{+0.023}_{-0.029}$	$-0.242^{+0.015}_{-0.018}$	

# Chapter 7

## Conclusions

In this dissertation we have investigated the full four-folded angular distributions for the semi-leptonic  $b$ -baryon decay  $\Lambda_b \rightarrow \Lambda(\rightarrow p\pi^-)\mu^+\mu^-$  in the SM,  $Z'$  model, Randall-Sundrum model with custodial protection ( $RS_c$ ) and using the most general model independent approach. This chapter summarizes the main findings of our study.

### $Z'$ model

At the quark level, the decay  $\Lambda_b \rightarrow \Lambda(\rightarrow p\pi^-)\mu^+\mu^-$  is mediated by the FCNC  $b \rightarrow s\mu^+\mu^-$  transition, which is same for the well studied  $B \rightarrow K^*\mu^+\mu^-$  decay. For  $\Lambda_b \rightarrow \Lambda$  transitions, we have used the high precision FFs calculated in the lattice QCD using  $2+1$  dynamical flavors along with the factorizable non-local matrix elements of the four quark operators  $\mathcal{O}_{1-6}$  and  $\mathcal{O}_8^g$  encoded into effective WCs  $C_7^{eff}(s)$  and  $C_9^{eff}(s)$ . By using them we have numerically calculated the differential branching ratio ( $\frac{dB}{ds}$ ), the lepton, hadron, and combined hadron-lepton forward-backward asymmetries ( $A_{FB}^\ell, A_{FB}^\Lambda, A_{FB}^{\ell\Lambda}$ ), the various asymmetry parameters ( $\alpha_i^{(\prime)}$ ), the fractions of longitudinal ( $F_L$ ) and transverse ( $F_T$ ) polarized dimuons and different angular asymmetry observables denoted by  $\mathcal{P}_i$  in different bins of  $s$ .

- In the low-recoil bin  $s \in [15, 20]$  GeV<sup>2</sup> the FFs from lattice are known most precisely, the results of  $\frac{dB}{ds}$  in the  $Z'$  model lie close to the experimental measurements in this bin. The SM results are significantly smaller than the measurements in this low-recoil bin.
- In the large-recoil region the results of hadron-side forward-backward asymmetry ( $A_{FB}^\Lambda$ ) is significantly away from the experimental observations for both the SM and  $Z'$  model. However, in the low-recoil region, the results of the SM lie close to the experimental observations.
- The experimental measurements of lepton-side forward-backward asymmetry ( $A_{FB}^\ell$ ) in both low- and large-recoil regions have significant errors. However, in the bin  $s \in [15, 20]$  GeV<sup>2</sup> the lower limit is comparable to the  $Z'$  model. We hope that in the future when the statistics of the data are improved, it will help us to find the signatures of the extra neutral  $Z'$  boson.
- We have also predicted the values of the lepton-hadron combined forward-backward asymmetry ( $A_{FB}^{\ell\Lambda}$ ) both in the SM and the  $Z'$  model. It has been found that in the low-recoil bin the value of the  $Z'$  model deviates significantly from the SM result.

- The longitudinal polarization fraction  $F_L$  of the dimuon system is measured experimentally where the statistics are not good enough in the large-recoil bin as compared to the low-recoil region. In the region  $s \in [1, 6]$  GeV<sup>2</sup> the central value of the SM is compatible with the central value of the experimental measurements. However, in the bin  $s \in [15, 20]$  GeV<sup>2</sup>, where uncertainties in the FFs are better controlled, the experimental observations favor the results of the  $Z'$  model.
- In line with these asymmetries, we have also calculated the transverse polarization fraction of the dimuon system  $F_T$ , the asymmetry parameters  $\alpha$ , and different angular asymmetry observables  $\mathcal{P}_i$  for  $i = 1, \dots, 9$  in the SM and  $Z'$  model. We have found significantly large values of some of these observables that can be measured in the future at LHCb and Belle II.

It is worth emphasizing that some of the asymmetries calculated here were also reported in the SM and aligned 2HDM in ref. [111] and our SM results match with these results. We hope that in the future, the precise measurement of some of the asymmetries reported here in the four-folded distribution of  $\Lambda_b \rightarrow \Lambda(\rightarrow p\pi^-)\mu^+\mu^-$  decay, in fine bins of  $s$  at the LHCb and Belle II will help us to test the SM predictions in  $\Lambda_b$  decays with significantly improved statistics. It will also give us a chance to hunt for the indirect signals of NP arising due to the neutral  $Z'$  boson, especially where the SM mismatched with the experimental predictions.

### Randall-Sundrum Model with Custodial Protection

Our work on the analysis of angular observables of the theoretically clean decay  $\Lambda_b \rightarrow \Lambda(\rightarrow p\pi^-)\mu^+\mu^-$  in the SM and the RS model with custodial protection is presented in Chapter 5. After performing the scan of the parameter space of the model in the light of current constraints, we have worked out the largest possible deviations in the WCs  $|\Delta C_{7,9,10}^{(\ell)}|$  from the SM predictions for different allowed values of KK gluon mass  $M_{g(1)}$ . The resultant deviations are small and do not allow for large effects in the angular observables. Although for maximum possible deviations in WCs, for  $M_{g(1)} = 4.8$  TeV, in the  $RS_c$  model, some of the observables receive considerable change in particular bins such as  $\frac{dB}{ds}$  and  $A_{FB}^\ell$  in low-recoil bin  $[15, 20]$  GeV<sup>2</sup> and  $F_L$  in the bin  $[0.1, 2]$  GeV<sup>2</sup> but these deviations are still small enough to explain the large gap between the theoretical and experimental data. Therefore, it is concluded that under the present bounds on the mass of first KK gluon state  $M_{g(1)}$ , observables are largely unaffected by the NP arises due to custodially protected RS model. Hence, the current constraints on the parameters of  $RS_c$  are too strict to explain the observed deviations in different observables of  $\Lambda_b \rightarrow \Lambda(\rightarrow p\pi^-)\mu^+\mu^-$  decay.

### Model Independent Approach

In Chapter 6, the investigation on NP is not restricted to operators that already appear in the SM; i.e., the four-fermion ones built out of  $V - A$   $b \rightarrow s$  and vector/axial leptonic currents - but actually also considers (pseudo)scalar and tensor operators, and the  $V + A$  combination for the  $b \rightarrow s$  current. In literature, it is known as the model independent approach. By taking the most general weak interaction Hamiltonian, we have discussed the impact of new  $VA$ ,  $SP$  and tensor  $T$  couplings on above mentioned physical observables in  $\Lambda_b \rightarrow \Lambda(\rightarrow p\pi^-)\mu^+\mu^-$  decay. Most of them are the ratios of angular coefficients and hence show little dependence on the uncertainties

involved in the calculation of hadronic FFs therefore, in the future these observables can serve as a tool to look for the imprints of currents which are beyond the SM physics.

First of all we have plotted  $d\mathcal{B}/ds$ ,  $A_{FB}^\ell$ ,  $A_{FB}^\Lambda$ ,  $A_{FB}^{\ell\Lambda}$ ,  $F_{L,T}$ ,  $Y_{2,3sc,4sc}$ ,  $\mathcal{P}_{3,8,9}$  and  $\alpha_i^{(\prime)}$  where,  $i = \theta_\ell, \theta_\Lambda, \xi, L, U$  by considering the non-zero mass for the final state leptons. We deduce that in case of  $\mu$  as final state lepton the mass effects are negligible at low-recoil for all the observables - but mildly affected some observables, such as  $F_T$ ,  $\alpha_{\theta_\ell}$ ,  $Y_2$ ,  $Y_{4sc}$  and  $\mathcal{P}_9$  in high-recoil region. Therefore, based on our analysis it can be inferred that one can safely ignore the muon mass terms in the expressions of the lepton helicity fractions as was done in [113]. By using the following ranges of new WCs that are allowed by the  $B$ -physics data with the global fit sign suggestions

$$\begin{aligned} C_V &= [-1.61, -1], & C'_V &= 0, & C_A &= 1, & C'_A &= -0.4 \\ C_S^{(\prime)} &= C_P^{(\prime)} = [-4, 4], & C_T &= 0.72, & C_{T5} &= 0.2, \end{aligned} \quad (7.1)$$

we have the following findings:

- There is a mismatch between the SM predictions and the LHCb data of  $d\mathcal{B}/ds$ , particularly in the high  $s$  region. Only new  $VA$  couplings in three low  $s$  bins,  $[0.1, 2]$  GeV<sup>2</sup>,  $[2, 4]$  GeV<sup>2</sup> and  $[6, 8]$  GeV<sup>2</sup> are able to accommodate this data.
- The SM values of  $F_L$  and  $A_{FB}^\Lambda$  fall within the error bars of the LHCb data in all bins except in  $s \in [16, 18]$  GeV<sup>2</sup> where  $VA$ ,  $SP$  and  $T$  couplings are also unable to accommodate the data.
- The data of  $A_{FB}^\ell$  deviates from the SM values in the high  $s$  region and only  $SP$  couplings show some promising effect to accommodate it.

It is also observed that the zero-crossing of observables shift towards the high  $s$  region when new  $VA$  couplings are introduced in addition to the SM WCs which is not the case for the  $SP$  couplings. In case of  $\alpha_{\theta_\ell}, \alpha_U$  and  $\alpha_L$  when we include  $VA$  couplings their values are modified slightly for the combination  $C_V = -1.34, C'_A = -0.4, C'_V = C_A = 0$ . However, the data of  $A_{FB}^\ell$ , particularly in the high  $s$  region favors the new  $VA$  couplings in comparison to the SM couplings alone. Now compared to  $VA$  and  $T$  couplings, the constraints are less stringent on  $SP$  WCs therefore, their influence on the above discussed observables is more prominent. Also, the data of  $d\mathcal{B}/ds$ ,  $A_{FB}^\ell$  and  $A_{FB}^\Lambda$  in some high  $s$  bins favors the  $SP$  couplings. In the case of the WCs corresponding to the tensor currents, the value of  $A_{FB}^\Lambda$  in high  $s$  region come closer to the experimental value which is neither the case for the SM nor for any other NP couplings. Hence, one can deduce that there is not a single new coupling among  $VA$ ,  $SP$ , and  $T$  operators that can simultaneously accommodate the whole available LHCb data of these four observables in all  $s$  bins.

To overcome this difficulty, we have also examined the impact of  $C_V, C_S, C'_S, C_P$  and  $C'_P$  by considering these couplings in pairs  $(C_X, C_Y)$  where  $X, Y = V, S, S', P, P'$ . The goal was to explore their allowed parametric space to see whether the combinations of these new couplings satisfy the available LHCb data for all the four observables in large-recoil bin  $s \in [0.1, 2]$  GeV<sup>2</sup> and in low-recoil bins  $s \in [15, 16]$ ,  $[16, 18]$  GeV<sup>2</sup> and  $s \in [18, 20]$  GeV<sup>2</sup> or not. We observed that at large-recoil  $s \in [0.1, 2]$  GeV<sup>2</sup> region, the measured values of  $d\mathcal{B}/ds$ ,  $F_L$ ,  $A_{FB}^\ell$  and  $A_{FB}^\Lambda$  could be justified simultaneously by taking the combinations given in Eq. (6.44) while the ranges of WCs mentioned in Eq. (7.1) remain unchanged. At low-recoil, for the bin  $s \in [15, 16]$  GeV<sup>2</sup>, these

combinations also accommodate LHCb data for all four observables simultaneously but the ranges of  $SP$  WCs mentioned in Eq. (7.1) are further constrained while the ranges of  $VA$  WCs remain the same. It reflects that these two bins can provide a good opportunity to search for the NP when more accurate data will be available from the Run 3 of the LHC. In the  $s \in [16, 18]$  GeV<sup>2</sup> bin, the measurements of all observables cannot be accommodated by any of the combinations of NP WCs. In this region, only a few combinations satisfy the measured ranges of  $F_L$  and  $A_{FB}^\Lambda$  simultaneously but none of them satisfies  $A_{FB}^\ell$ . In last bin of low-recoil region; i.e.,  $s \in [18, 20]$  GeV<sup>2</sup> we tried to accommodate the data of  $A_{FB}^\ell$ ,  $A_{FB}^\Lambda$  and  $d\mathcal{B}/ds$  simultaneously and found that it is still possible for the several combinations of NP WCs. However, doing so for these three observables we got more severe constraints on the  $SP$  WCs as compared to the one in  $s \in [15, 16]$  GeV<sup>2</sup> bin while the range of  $VA$  WCs remains the same as allowed by the  $B$ -physics data. Finally, by using the allowed parametric space of these WCs constrained by the data of above mentioned observables in  $\Lambda_b$  decays, we predicted the values of these four observables in their corresponding bins and find that they could be potentially measured in the future at the LHCb and other planned experiments.

It has already been discussed that in this study we have calculated the expressions of the lepton helicity fractions in the presence of lepton mass therefore, this analysis can be easily extended to the  $\Lambda_b \rightarrow \Lambda \tau^+ \tau^-$  decays. Doing so, we found that the non-zero mass of tauons significantly modifies the values of different physical observables both in the SM as well as in the presence of new WCs. Finally, by considering the uncertainties involved in the FFs and other input parameters, we have calculated the values of all the 19 observables for  $\Lambda_b \rightarrow \Lambda(\rightarrow p\pi^-)\tau^+\tau^-$  decay.

Concluding, we hope that our results will be scrutinized after the Run 3 of the LHC, in particular at the LHCb and the future  $B$  factories.

## .1 Appendix A

### Lepton Helicity Amplitudes

Leptonic part of scalar, pseudo-scalar, vector and axial-vector currents having non-zero contribution are [254]

$$\begin{aligned}
L_S(+1/2, +1/2) &= -L_S(-1/2, -1/2) = s\beta_\ell \\
L_P(+1/2, +1/2) &= L_P(-1/2, -1/2) = -s \\
L_V^\pm(+1/2, +1/2) &= L_V^\mp(-1/2, -1/2) = \mp\sqrt{2}m_\ell \sin\theta_\ell \\
L_V^0(+1/2, +1/2) &= -L_V^0(-1/2, -1/2) = -2m_\ell \cos\theta_\ell \\
L_V^0(+1/2, -1/2) &= L_V^0(-1/2, +1/2) = s \sin\theta_\ell \\
L_V^+(+1/2, -1/2) &= -L_V^-(+1/2, +1/2) = \frac{s}{\sqrt{2}}(1 - \cos\theta_\ell) \\
L_V^-(+1/2, -1/2) &= -L_V^+(+1/2, +1/2) = \frac{s}{\sqrt{2}}(1 + \cos\theta_\ell) \\
L_A^t(+1/2, +1/2) &= L_A^t(-1/2, -1/2) = -2m_\ell \\
L_A^+(+1/2, -1/2) &= L_A^-(+1/2, +1/2) = \frac{sv}{\sqrt{2}}(1 - \cos\theta_\ell) \\
L_A^-(+1/2, -1/2) &= L_A^+(-1/2, +1/2) = \frac{sv}{\sqrt{2}}(1 + \cos\theta_\ell) \\
L_A^0(+1/2, -1/2) &= -L_A^0(-1/2, +1/2) = sv \sin\theta_\ell.
\end{aligned} \tag{2}$$

Tensor part of leptonic current read as

$$\begin{aligned}
L_{T'}^{t,\pm}(+1/2, +1/2) &= -L_{T'}^{t,\pm}(-1/2, -1/2) = \mp\frac{s}{\sqrt{2}} \sin\theta_\ell, \\
L_{T'}^{t,+}(-1/2, +1/2) &= -L_{T'}^{t,-}(+1/2, -1/2) = \sqrt{2}(1 - \cos\theta_\ell)m_\ell, \\
L_{T'}^{t,-}(-1/2, +1/2) &= -L_{T'}^{t,+}(+1/2, -1/2) = \sqrt{2}m_\ell(1 + \cos\theta_\ell), \\
L_{T'}^{t,0}(+1/2, +1/2) &= -L_{T'}^{t,0}(-1/2, -1/2) = -s \cos\theta_\ell, \\
L_{T'}^{+,-}(+1/2, +1/2) &= L_{T'}^{+,-}(-1/2, -1/2) = -s \cos\theta_\ell\beta_\ell, \\
L_{T'}^{\pm,0}(+1/2, +1/2) &= L_{T'}^{\pm,0}(-1/2, -1/2) = -\frac{s}{\sqrt{2}} \sin\theta_\ell\beta_\ell, \\
L_{T'}^{t,0}(-1/2, +1/2) &= L_{T'}^{t,0}(+1/2, -1/2) = 2m_\ell \sin\theta_\ell \\
L_{T5'}^{t,\pm}(+1/2, +1/2) &= -L_{T5'}^{t,\pm}(-1/2, -1/2) = \pm\frac{s}{\sqrt{2}} \sin\theta_\ell\beta_\ell \\
L_{T5'}^{t,0}(+1/2, +1/2) &= L_{T5'}^{t,0}(-1/2, -1/2) = s \cos\theta_\ell\beta_\ell \\
L_{T5'}^{+,-}(+1/2, +1/2) &= -L_{T5'}^{+,-}(-1/2, -1/2) = s \cos\theta_\ell, \\
L_{T5'}^{-,+}(+1/2, -1/2) &= L_{T5'}^{-,+}(-1/2, +1/2) = 2m_\ell \sin\theta_\ell, \\
L_{T5'}^{+,0}(+1/2, -1/2) &= -L_{T5'}^{-,0}(-1/2, +1/2) = \sqrt{2}(1 + \cos\theta_\ell)m_\ell, \\
L_{T5'}^{\pm,0}(+1/2, +1/2) &= -L_{T5'}^{\pm,0}(-1/2, -1/2) = \frac{s}{\sqrt{2}} \sin\theta_\ell, \\
L_{T5'}^{-,0}(+1/2, -1/2) &= L_{T5'}^{+,0}(-1/2, +1/2) = -\sqrt{2}(1 - \cos\theta_\ell)m_\ell,
\end{aligned} \tag{3}$$

where  $\beta = \frac{2m_\ell}{\sqrt{s}}$  and  $v = \sqrt{1 - \beta^2}$ . It can be seen that if we put the lepton mass  $m_\ell$  to be zero, we can get back the relations given in [113].



## .2 Appendix B

### Total amplitude

In terms of the hadronic and leptonic currents, the square of amplitudes corresponding to different currents can be assembled as

$$|M_{VA}|^2 = \frac{1}{4} \sum_{s_{\Lambda_b}, s_{\Lambda}} \sum_{s'_{\Lambda}} \sum_{s_{\ell_1}, s_{\ell_2}} \sum_{m, n} \sum_{m', n'} H^m(s_{\Lambda_b}, s_{\Lambda}) H^{n*}(s_{\Lambda_b}, s_{\Lambda}') g_{m, m'} g_{n, n'} L^{m'}(s_{\ell_1}, s_{\ell_2}) \times L^{n'*}(s_{\ell_1}, s_{\ell_2}) \Gamma'(s_{\Lambda}, s'_{\Lambda}), \quad (4)$$

where  $\lambda = (m_{\Lambda_b}^2 - m_{\Lambda}^2 - s)^2 + 4sm_{\Lambda}^2$  and  $L^{m', n'}$  are the helicity amplitudes for the leptonic part given in Eq. (??). Likewise

$$\begin{aligned} |M_{SP}|^2 &= \frac{1}{4} \sum_{s_{\Lambda_b}, s_{\Lambda}} \sum_{s'_{\Lambda}} \sum_{s_{\ell_1}, s_{\ell_2}} H(s_{\Lambda_b}, s_{\Lambda}) H^*(s_{\Lambda_b}, s_{\Lambda}') L(s_{\ell_1}, s_{\ell_2}) L^*(s_{\ell_1}, s_{\ell_2}) \Gamma'(s_{\Lambda}, s'_{\Lambda}) \\ |M_{T'}|^2 &= \sum_{s_{\Lambda_b}, s_{\Lambda}} \sum_{s'_{\Lambda}} \sum_{s_{\ell_1}, s_{\ell_2}} H^{mn}(s_{\Lambda_b}, s_{\Lambda}) H^{rs*}(s_{\Lambda_b}, s_{\Lambda}') g_{mm'} g_{nn'} g_{rr'} g_{ss'} L^{m'n'}(s_{\ell_1}, s_{\ell_2}) \\ &\quad \times L^{r's'*}(s_{\ell_1}, s_{\ell_2}) \Gamma'(s_{\Lambda}, s'_{\Lambda}) \\ M_{VA} M_{SP}^* &= \frac{1}{4} \sum_{s_{\Lambda_b}, s_{\Lambda}} \sum_{s'_{\Lambda}} \sum_{s_{\ell_1}, s_{\ell_2}} \left[ H^m(s_{\Lambda_b}, s_{\Lambda}) H^*(s_{\Lambda_b}, s_{\Lambda}') L^{m'}(s_{\ell_1}, s_{\ell_2}) L^*(s_{\ell_1}, s_{\ell_2}) \right] \Gamma'(s_{\Lambda}, s'_{\Lambda}) \\ M_{VA} M_{T'}^* &= \frac{1}{2} \sum_{s_{\Lambda_b}, s_{\Lambda}} \sum_{s'_{\Lambda}} \sum_{s_{\ell_1}, s_{\ell_2}} \left[ H^m(s_{\Lambda_b}, s_{\Lambda}) H^{*rs}(s_{\Lambda_b}, s_{\Lambda}') L^{m'}(s_{\ell_1}, s_{\ell_2}) L^{r's'*}(s_{\ell_1}, s_{\ell_2}) \right] \Gamma'(s_{\Lambda}, s'_{\Lambda}) \\ M_{SP} M_{T'}^* &= \frac{1}{2} \sum_{s_{\Lambda_b}, s_{\Lambda}} \sum_{s'_{\Lambda}} \sum_{s_{\ell_1}, s_{\ell_2}} \left[ H(s_{\Lambda_b}, s_{\Lambda}) H^{mn*}(s_{\Lambda_b}, s_{\Lambda}') L(s_{\ell_1}, s_{\ell_2}) L^{r's'*}(s_{\ell_1}, s_{\ell_2}) \right] \Gamma'(s_{\Lambda}, s'_{\Lambda}) \end{aligned} \quad (5)$$

where summation over the repeated indices is understood.

## .3 Appendix C

### Angular coefficients

The various angular coefficients appearing in Eq. (3.36) are defined as

$$\begin{aligned} \hat{K}_{1ss} &= |\tilde{C}_9^+|^2 H_{1V}^{0,+} + |\tilde{C}_9^-|^2 H_{1A}^{0,+} + |C_7^+|^2 H_{1T}^{0,+} + |C_7^-|^2 H_{1T5}^{0,+} + |\tilde{C}_{10}^+|^2 H_V^{t,0,+} + |\tilde{C}_{10}^-|^2 H_A^{t,0,+} \\ &\quad + \Re [C_7^+ C_9^{+*}] H_{4(V,T)} + \Re [C_7^- C_9^{-*}] H_{4(A,T5)}, \\ \hat{K}_{1cc} &= |\tilde{C}_9^+|^2 H_{2V}^{0,+} + |\tilde{C}_9^-|^2 H_{2A}^{0,+} + |\tilde{C}_{10}^+|^2 H_{3V}^{t,+} + |\tilde{C}_{10}^-|^2 H_{3A}^{t,+} + (|C_7^+|^2 + |C_7^-|^2) H_{2T}^{0,+} \\ &\quad + 2\Re [C_7^+ C_9^{+*}] H_{5(V,T)} + 2\Re [C_7^- C_9^{-*}] H_{5(A,T5)}, \\ \hat{K}_{2ss} &= \alpha \left[ \Re [\tilde{C}_{10}^+ \tilde{C}_{10}^{-*}] \left( 2\beta^2 H_{A,V}^{t,t} (+1/2, +1/2) + 2v^2 H_{A,V}^{0,0} (+1/2, +1/2) + v^2 H_{A,V}^{+,+} (-1/2, +1/2) \right) \right. \\ &\quad \left. + \Re [\tilde{C}_9^+ \tilde{C}_9^{-*}] H_{4(A,V)} + \Re [C_7^+ C_7^{-*}] H_{4(T,T5)} + \Re [C_7^+ \tilde{C}_9^{-*}] H_{4(A,T)} + \Re [C_7^- \tilde{C}_9^{+*}] H_{4(V,T5)} \right] \\ \hat{K}_{2cc} &= 2\alpha \Re [\tilde{C}_9^+ \tilde{C}_9^{-*}] H_{5(A,V)} + 2\alpha \Re [\tilde{C}_{10}^+ \tilde{C}_{10}^{-*}] \left( \beta^2 H_{A,V}^{t,t} (+1/2, +1/2) + v^2 H_{A,V}^{+,+} (-1/2, +1/2) \right) \\ &\quad + 2\alpha \left( \Re [C_7^+ C_7^{-*}] H_{5(T,T5)} + \Re [C_7^+ \tilde{C}_9^{-*}] H_{5(A,T)} + \Re [C_7^- \tilde{C}_9^{+*}] H_{5(V,T5)} \right), \end{aligned} \quad (6)$$

$$\begin{aligned}
\hat{K}_{1c} &= -2v \left[ \Re \left[ C_7^+ \tilde{C}_{10}^{-*} \right] H_{A,T}^{+,+}(-1/2, +1/2) + \Re \left[ C_7^- \tilde{C}_{10}^{+*} \right] H_{V,T5}^{+,+}(-1/2, +1/2) \right. \\
&\quad \left. + \Re \left[ \tilde{C}_9^+ \tilde{C}_{10}^{-*} \right] H_{A,V}^{+,+}(-1/2, +1/2) + \Re \left[ \tilde{C}_9^- \tilde{C}_{10}^{+*} \right] H_{A,V}^{+,+}(-1/2, +1/2) \right], \\
\hat{K}_{2c} &= -2v\alpha \left[ \Re \left[ C_7^+ \tilde{C}_{10}^{+*} \right] H_{V,T}^{+,+}(-1/2, +1/2) + \Re \left[ C_7^- \tilde{C}_{10}^{-*} \right] H_{A,T5}^{+,+}(-1/2, +1/2) \right. \\
&\quad \left. + \Re \left[ \tilde{C}_9^+ \tilde{C}_{10}^{+*} \right] |H_V^+(-1/2, +1/2)|^2 + \Re \left[ \tilde{C}_9^- \tilde{C}_{10}^{-*} \right] |H_A^+(-1/2, +1/2)|^2 \right] \\
\hat{K}_{3s} &= \sqrt{2}v\alpha \left( \text{Im} \left[ C_7^+ \tilde{C}_{10}^{-*} \right] H_{6(A,T)}^R + \Im \left[ C_7^- \tilde{C}_{10}^{+*} \right] H_{6(V,T5)}^R + \Im \left[ \tilde{C}_9^+ \tilde{C}_{10}^{-*} \right] H_{6(A,V)}^R \right. \\
&\quad \left. + \Im \left[ \tilde{C}_{10}^+ \tilde{C}_9^{-*} \right] H_{6(A,V)}^R \right), \\
\hat{K}_{4s} &= \sqrt{2}v\alpha \left[ \text{Re} \left[ C_7^+ \tilde{C}_{10}^{+*} \right] H_{6(T,V)}^R + 2\Re \left[ \tilde{C}_9^+ \tilde{C}_{10}^{+*} \right] H_V^0(+1/2, +1/2) H_V^{+*}(-1/2, -1/2) \right. \\
&\quad \left. - \text{Re} \left[ C_7^- \tilde{C}_{10}^{-*} \right] H_{6(A,T5)}^R - 2\Re \left[ \tilde{C}_9^- \tilde{C}_{10}^{-*} \right] H_A^0(+1/2, +1/2) H_A^{+*}(-1/2, -1/2) \right] \\
\hat{K}_{3sc} &= \sqrt{2}v^2\alpha \left( -\Im \left[ \tilde{C}_9^+ C_7^{+*} \right] H_{6(V,T)}^L + \Im \left[ \tilde{C}_9^- C_7^{-*} \right] H_{6(A,T5)}^L \right), \\
\hat{K}_{4sc} &= -\sqrt{2}v^2\alpha \left[ \Re \left[ C_7^+ C_7^{-*} \right] H_{6(T,T5)}^L + \Re \left[ \tilde{C}_9^+ C_7^{-*} \right] H_{6(T5,V)}^L \right. \\
&\quad \left. - \Re \left[ \tilde{C}_9^+ \tilde{C}_9^{-*} \right] H_{6(A,V)}^L - \Re \left[ \tilde{C}_9^- C_7^{+*} \right] H_{6(A,T)}^L \right] \tag{7}
\end{aligned}$$

where  $v' = \sqrt{1 + \beta^2}$ ,  $\hat{K}_{ij} = \mathcal{N}K_{i,j}$  ( $\mathcal{N}$  is defined in Eq. (6.40)) and

$$\begin{aligned}
H_{x,y}^{m,n}(s_{\Lambda_b}, s_{\Lambda}) &= H_x^m(s_{\Lambda_b}, s_{\Lambda}) H_y^{n*}(s_{\Lambda_b}, s_{\Lambda}) \\
H_{1x}^{0,+} &= |H_x^0(+1/2, +1/2)|^2 + \frac{1}{2}v'^2 |H_x^+(-1/2, +1/2)| \\
H_{2x}^{0,+} &= \beta^2 |H_x^0(+1/2, +1/2)|^2 + |H_x^+(-1/2, +1/2)|^2 \\
H_{3x}^{t,+} &= \beta^2 |H_x^t(+1/2, +1/2)|^2 + v^2 |H_x^+(-1/2, +1/2)|^2 \\
H_{4(x,y)} &= 2H_{x,y}^{0,0}(+1/2, +1/2) + v'^2 H_{x,y}^{+,+}(-1/2, +1/2) \\
H_{5(x,y)} &= \beta^2 H_{x,y}^{0,0}(+1/2, +1/2) + H_{x,y}^{+,+}(-1/2, +1/2) \\
H_{6(x,y)}^{R,L} &= H_x^0(+1/2, +1/2) H_y^{+*}(-1/2, +1/2) \pm H_x^+(-1/2, +1/2) H_y^{0*}(+1/2, +1/2), \\
H_x^{t,0,+} &= \beta^2 |H_x^t(+1/2, +1/2)|^2 + v^2 |H_x^0(+1/2, +1/2)|^2 + \frac{1}{2}v^2 |H_x^+(-1/2, +1/2)|^2
\end{aligned} \tag{8}$$

with  $x, y = V, A, T, T5$  and

$$\begin{aligned}
H_{7,T'} &= v'^2 |H_{T'}^{t,-}(+1/2, -1/2)|^2 + v^2 |H_{T'}^{0,-}(+1/2, -1/2)|^2 + \beta^2 |H_{T'}^{t,0}(+1/2, +1/2)|^2 \\
H_{8,T'} &= v^2 |H_{T'}^{t,-}(+1/2, -1/2)|^2 + v'^2 |H_{T'}^{0,-}(+1/2, -1/2)|^2 + \beta^2 |H_{T'}^{+,-}(+1/2, +1/2)|^2 \\
H_{9,T'} &= v^2 |H_{T'}^{+,-}(+1/2, +1/2)|^2 + |H_{T'}^{t,0}(+1/2, +1/2)|^2 + \beta^2 |H_{T'}^{t,-}(+1/2, -1/2)|^2 \\
H_{10,T'} &= |H_{T'}^{+,-}(+1/2, +1/2)|^2 + v^2 |H_{T'}^{t,0}(+1/2, +1/2)|^2 + \beta^2 |H_{T'}^{0,-}(+1/2, -1/2)|^2 \\
H_{11,T'} &= \beta^2 H_{T'}^{+,-}(+1/2, +1/2) (H_{T'}^{t,0}(+1/2, +1/2))^* - H_{T'}^{0,-}(+1/2, -1/2) (H_{T'}^{t,-}(+1/2, -1/2))^* \\
H_{12,T'} &= \left( 1 - \frac{\beta^2}{2} \right) H_{T'}^{+,-}(+1/2, +1/2) (H_{T'}^{t,0}(+1/2, +1/2))^* \\
&\quad - \frac{\beta^2}{2} H_{T'}^{0,-}(+1/2, -1/2) (H_{T'}^{t,-}(+1/2, -1/2))^* \\
H_{13,T'} &= H_{T'}^{+,-}(+1/2, +1/2) (H_{T'}^{t,-}(+1/2, -1/2))^* + H_{T'}^{0,-}(+1/2, -1/2) (H_{T'}^{t,0}(+1/2, +1/2))^*
\end{aligned} \tag{9}$$

Angular coefficients defined in Eq. (7) correspond to the SM when one use  $C_V^{(\prime)} = C_A^{(\prime)} = 0$  as they have been absorbed in  $\tilde{C}_9^\pm$  and  $\tilde{C}_{10}^\pm$ . Contribution of other NP effects to the differential decay rate which are not present in the SM is written in terms of following NP coefficients:

$$\begin{aligned}
\hat{K}_{1ss}^{NP} &= 8 [|C_T|^2 H_{7,T'} + |C_{T5}|^2 H_{8,T'}] \\
\hat{K}_{1cc}^{NP} &= 16 [|C_T|^2 H_{9,T'} + |C_{T5}|^2 H_{10,T'}] \\
\hat{K}_{2ss}^{NP} &= 32\alpha \Re [C_{T5} C_T^*] H_{11,T'} \\
\hat{K}_{2cc}^{NP} &= 64\alpha \Re [C_{T5} C_T^*] H_{12,T'} \\
\hat{K}_{1c}^{NP} &= 2v\beta \left[ \Re [C_S^+ \tilde{C}_9^{+*}] H_{S,V}^0(+1/2, +1/2) + \Re [C_S^- \tilde{C}_9^{-*}] H_{P,A}^0(+1/2, +1/2) \right] \\
&\quad + 2v\beta \left[ \Re [C_S^+ \tilde{C}_7^{+*}] H_{S,T}^0(+1/2, +1/2) + \Re [C_S^- \tilde{C}_7^{-*}] H_{P,T5}^0(+1/2, +1/2) \right] \\
&\quad + 8v \left[ \Re [C_T C_P^{-*} + C_{T5} C_S^{-*}] H_P(+1/2, +1/2) (H_{T'}^{+,-} (+1/2, +1/2))^* \right. \\
&\quad + \Re [C_T C_S^{+*} + C_{T5} C_P^{+*}] H_S(+1/2, +1/2) (H_{T'}^{t,0} (+1/2, +1/2))^* \\
&\quad + \beta \Re [C_T \tilde{C}_{10}^{+*}] \left( H_A^t(+1/2, +1/2) (H_{T'}^{+,-} (+1/2, +1/2))^* \right. \\
&\quad \left. - H_A^+(-1/2, +1/2) (H_{T'}^{t,-} (+1/2, -1/2))^* \right) \\
&\quad + \beta \Re [C_{T5} \tilde{C}_{10}^{+*}] \left( H_V^t(+1/2, +1/2) (H_{T'}^{t,0} (+1/2, +1/2))^* \right. \\
&\quad \left. + H_V^+(-1/2, +1/2) (H_{T'}^{0,-} (+1/2, -1/2))^* \right) \Big] \\
\hat{K}_{2c}^{NP} &= 2\alpha v\beta \left[ \Re [C_S^+ \tilde{C}_9^{-*}] H_{S,A}^0(+1/2, +1/2) + \Re [C_S^- \tilde{C}_9^{+*}] H_{P,V}^0(+1/2, +1/2) \right] \\
&\quad + 2\alpha v\beta \left[ \Re [C_S^+ \tilde{C}_7^{-*}] H_{S,T5}^0(+1/2, +1/2) + \Re [C_S^- \tilde{C}_7^{+*}] H_{P,T}^0(+1/2, +1/2) \right] \\
&\quad + 8\alpha v \left[ \Re [C_T C_S^{-*} + C_{T5} C_P^{-*}] H_P(+1/2, +1/2) (H_{T'}^{t,0} (+1/2, +1/2))^* \right. \\
&\quad + \Re [C_T C_P^{+*} + C_{T5} C_S^{+*}] H_S(+1/2, +1/2) (H_{T'}^{+,-} (+1/2, +1/2))^* \\
&\quad + \beta \Re [C_T \tilde{C}_{10}^{+*}] \left( H_V^t(+1/2, +1/2) (H_{T'}^{+,-} (+1/2, +1/2))^* \right. \\
&\quad \left. - H_V^+(-1/2, +1/2) (H_{T'}^{t,-} (+1/2, -1/2))^* \right) \\
&\quad + \beta \Re [C_{T5} \tilde{C}_{10}^{-*}] \left( H_A^t(+1/2, +1/2) (H_{T'}^{t,0} (+1/2, +1/2))^* \right. \\
&\quad \left. + H_A^+(-1/2, +1/2) (H_{T'}^{0,-} (+1/2, -1/2))^* \right) \Big] \\
\hat{K}_{3s}^{NP} &= \sqrt{2}\alpha v\beta \left[ \Im [C_S^+ \tilde{C}_9^{+*}] H_S(+1/2, +1/2) (H_V^+(-1/2, +1/2))^* \right. \\
&\quad - \Im [C_S^- \tilde{C}_9^{-*}] H_P(+1/2, +1/2) (H_A^+(-1/2, +1/2))^* \\
&\quad + \Im [C_S^+ \tilde{C}_7^{+*}] H_S(+1/2, +1/2) (H_T^+(-1/2, +1/2))^* \\
&\quad \left. - \Im [C_S^- \tilde{C}_7^{-*}] H_P(+1/2, +1/2) (H_{T5}^+(-1/2, +1/2))^* \right] \\
&\quad - 4\sqrt{2}\alpha v \left[ \Im [C_T C_P^{-*} + C_{T5} C_S^{-*}] H_P(+1/2, +1/2) (H_{T'}^{0,-} (+1/2, -1/2))^* \right. \\
&\quad + \Im [C_T C_S^{+*} + C_{T5} C_P^{+*}] H_S(+1/2, +1/2) (H_{T'}^{t,-} (+1/2, -1/2))^* \\
&\quad + \beta \Im [C_T \tilde{C}_{10}^{-*}] \left( H_A^t(+1/2, +1/2) (H_{T'}^{0,-} (+1/2, -1/2))^* \right. \\
&\quad + H_A^0(+1/2, +1/2) (H_{T'}^{t,-} (+1/2, -1/2))^* \\
&\quad \left. - \beta H_A^+(-1/2, +1/2) (H_{T'}^{t,0} (+1/2, +1/2))^* \right) \Big]
\end{aligned} \tag{10}$$

$$\begin{aligned}
& + \Im[C_{T5}\tilde{C}_{10}^{+*}] \left( H_V^t(+1/2, +1/2)(H_{T'}^{t,-}(+1/2, -1/2))^* \right. \\
& \left. - \beta H_V^0(+1/2, +1/2)(H_{T'}^{0,-}(+1/2, -1/2))^* - \beta H_V^+(-1/2, +1/2)(H_{T'}^{+,-}(+1/2, +1/2))^* \right) \\
\hat{K}_{4s}^{NP} = & \sqrt{2}\alpha v \beta \left[ \Re[C_S^+\tilde{C}_9^{-*}] H_S(+1/2, +1/2)(H_A^+(-1/2, +1/2))^* \right. \\
& - \Re[C_S^-\tilde{C}_9^{+*}] H_P(+1/2, +1/2)(H_V^+(-1/2, +1/2))^* \\
& + \Re[C_S^+\tilde{C}_7^{-*}] H_S(+1/2, +1/2)(H_{T5}^+(-1/2, +1/2))^* \\
& \left. - \Re[C_S^-\tilde{C}_7^{+*}] H_P(+1/2, +1/2)(H_T^+(-1/2, +1/2))^* \right] \\
& + 4\sqrt{2}\alpha v \left[ -\Re[C_T C_S^{-*} + C_{T5} C_P^{-*}] H_P(+1/2, +1/2)(H_{T'}^{t,-}(+1/2, -1/2))^* \right. \\
& - \Re[C_T C_P^{+*} + C_{T5} C_S^{+*}] H_S(+1/2, +1/2)(H_{T'}^{0,-}(+1/2, -1/2))^* \\
& + \beta \Re[C_T \tilde{C}_{10}^{+*}] \left( -H_V^t(+1/2, +1/2)(H_{T'}^{0,-}(+1/2, -1/2))^* \right. \\
& + H_V^0(+1/2, +1/2)(H_{T'}^{t,-}(+1/2, -1/2))^* \\
& + H_V^+(-1/2, +1/2)(H_{T'}^{t,0}(+1/2, +1/2))^* \left. \right) \\
& + \beta \Re[C_{T5} \tilde{C}_{10}^{-*}] \left( -H_A^t(+1/2, +1/2)(H_{T'}^{t,-}(+1/2, -1/2))^* \right. \\
& + H_A^0(+1/2, +1/2)(H_{T'}^{0,-}(+1/2, -1/2))^* - H_A^+(-1/2, +1/2)(H_{T'}^{+,-}(+1/2, +1/2))^* \left. \right) \\
\hat{K}_{4sc}^{NP} = & -32\sqrt{2}v^2\alpha \Re[C_{T5} C_T^*] H_{13,T'} \tag{11}
\end{aligned}$$

Other terms which do not correspond to any angular coefficient of Eq. (3.36) but contribute to differential decay distribution are

$$\begin{aligned}
\hat{K}^{NP} = & [(v^2|C_S^+|^2 + |C_P^+|^2)|H_S(+1/2, +1/2)|^2 + (v^2|C_S^-|^2 + |C_P^-|^2)|H_P(+1/2, +1/2)|^2] \\
& + 2\alpha \left[ \Re[C_P^+ C_P^{-*} + C_S^+ C_S^{-*}] H_S(+1/2, +1/2) H_P^*(+1/2, +1/2) \right] \cos \theta_\Lambda \\
& + 2\beta \left[ \Re[C_P^+ \tilde{C}_{10}^{+*}] H_S(+1/2, +1/2) H_V^{t*}(+1/2, +1/2) \right. \\
& + \Re[C_P^- \tilde{C}_{10}^{-*}] H_P(+1/2, +1/2) H_A^{t*}(+1/2, +1/2) \left. \right] \\
& + 2\alpha\beta \left[ \Re[C_P^+ \tilde{C}_{10}^{-*}] H_S(+1/2, +1/2) H_A^{t*}(+1/2, +1/2) \right. \\
& + \Re[C_P^- \tilde{C}_{10}^{+*}] H_P(+1/2, +1/2) H_V^{t*}(+1/2, +1/2) \left. \right] \cos \theta_\Lambda \\
& + 8\beta \Re[C_T \tilde{C}_9^{+*}] \left( H_V^+(-1/2, +1/2)(H_{T'}^{t,-}(+1/2, -1/2))^* \right. \\
& + H_V^0(+1/2, +1/2)(H_{T'}^{t,0}(+1/2, +1/2))^* \left. \right) \\
& + 8\beta \Re[C_{T5} \tilde{C}_9^{-*}] \left( -H_A^+(-1/2, +1/2)(H_{T'}^{0,-}(+1/2, -1/2))^* \right. \\
& + H_A^0(+1/2, +1/2)(H_{T'}^{+,-}(+1/2, +1/2))^* \left. \right) \\
& + 8\alpha\beta \Re[C_T \tilde{C}_9^{-*}] \left( H_A^+(-1/2, +1/2)(H_{T'}^{t,-}(+1/2, -1/2))^* \right. \\
& + H_A^0(+1/2, +1/2)(H_{T'}^{t,0}(+1/2, +1/2))^* \left. \right) \cos \theta_\Lambda \\
& + 8\alpha\beta \Re[C_{T5} \tilde{C}_9^{+*}] \left( -H_V^+(-1/2, +1/2)(H_{T'}^{0,-}(+1/2, -1/2))^* \right. \\
& + H_V^0(+1/2, +1/2)(H_{T'}^{+,-}(+1/2, +1/2))^* \left. \right) \cos \theta_\Lambda \tag{12}
\end{aligned}$$

$$\begin{aligned}
& +8\beta\Re \left[ C_T \tilde{C}_7^{+*} \right] \left( H_T^+(-1/2, +1/2)(H_{T'}^{t,-}(+1/2, -1/2))^* \right. \\
& \left. + H_T^0(+1/2, +1/2)(H_{T'}^{t,0}(+1/2, +1/2))^* \right) \\
& +8\beta\Re \left[ C_{T5} \tilde{C}_7^{-*} \right] \left( -H_T^+(-1/2, +1/2)(H_{T'}^{0,-}(+1/2, -1/2))^* \right. \\
& \left. + H_T^0(+1/2, +1/2)(H_{T'}^{+,-}(+1/2, +1/2))^* \right) \\
& +8\alpha\beta\Re \left[ C_T \tilde{C}_7^{-*} \right] \left( H_T^+(-1/2, +1/2)(H_{T'}^{t,-}(+1/2, -1/2))^* \right. \\
& \left. + H_T^0(+1/2, +1/2)(H_{T'}^{t,0}(+1/2, +1/2))^* \right) \cos \theta_\Lambda \\
& +8\alpha\beta\Re \left[ C_{T5} \tilde{C}_7^{+*} \right] \left( -H_T^+(-1/2, +1/2)(H_{T'}^{0,-}(+1/2, -1/2))^* \right. \\
& \left. + H_T^0(+1/2, +1/2)(H_{T'}^{+,-}(+1/2, +1/2))^* \right) \cos \theta_\Lambda
\end{aligned} \tag{13}$$

# Bibliography

- [1] R. Aaij *et al.* [LHCb Collaboration], Phys. Rev. Lett. **113** (2014) 151601 [arXiv:1406.6482 [hep-ex]].
- [2] R. Aaij *et al.* [LHCb Collaboration], Phys. Rev. Lett. **122** (2019) no.19, 191801 [arXiv:1903.09252 [hep-ex]].
- [3] R. Aaij *et al.* [LHCb Collaboration], JHEP **1708** (2017) 055 [arXiv:1705.05802 [hep-ex]].
- [4] M. Bordone, G. Isidori and A. Pattori, Eur. Phys. J. C **76** (2016) no.8, 440 [arXiv:1605.07633 [hep-ph]].
- [5] A. Celis, J. Fuentes-Martin, A. Vicente and J. Virto, Phys. Rev. D **96** (2017) no.3, 035026 [arXiv:1704.05672 [hep-ph]].
- [6] M. Huschle *et al.* [Belle Collaboration], Phys. Rev. D **92** (2015) no.7, 072014 [arXiv:1507.03233 [hep-ex]].
- [7] R. Aaij *et al.* [LHCb Collaboration], Phys. Rev. Lett. **120** (2018) no.17, 171802 [arXiv:1708.08856 [hep-ex]].
- [8] J. P. Lees *et al.* [BaBar Collaboration], Phys. Rev. Lett. **109** (2012) 101802 [arXiv:1205.5442 [hep-ex]].
- [9] R. Aaij *et al.* [LHCb Collaboration], Phys. Rev. Lett. **111** (2013) 191801 [arXiv:1308.1707 [hep-ex]].
- [10] S. Descotes-Genon, J. Matias, M. Ramon and J. Virto, JHEP **1301** (2013) 048 [arXiv:1207.2753 [hep-ph]].
- [11] S. Descotes-Genon, T. Hurth, J. Matias and J. Virto, JHEP **1305** (2013) 137 [arXiv:1303.5794 [hep-ph]].
- [12] R. Aaij *et al.* [LHCb Collaboration], JHEP **1602** (2016) 104 [arXiv:1512.04442 [hep-ex]].
- [13] A. Abdesselam *et al.* [Belle Collaboration], arXiv:1604.04042 [hep-ex].
- [14] U. Egede, T. Hurth, J. Matias, M. Ramon and W. Reece, JHEP **1010** (2010) 056 [arXiv:1005.0571 [hep-ph]].
- [15] R. Aaij *et al.* [LHCb Collaboration], JHEP **1308** (2013) 131 [arXiv:1304.6325 [hep-ex]].
- [16] R. Aaij *et al.* [LHCb Collaboration], JHEP **1406** (2014) 133 [arXiv:1403.8044 [hep-ex]].

- [17] C. Bouchard *et al.* [HPQCD Collaboration], Phys. Rev. Lett. **111** (2013) no.16, 162002  
Erratum: [Phys. Rev. Lett. **112** (2014) no.14, 149902] [arXiv:1306.0434 [hep-ph]].
- [18] R. Aaij *et al.* [LHCb Collaboration], JHEP **1307** (2013) 084 [arXiv:1305.2168 [hep-ex]].
- [19] R. Aaij *et al.* [LHCb Collaboration], JHEP **1509** (2015) 179 [arXiv:1506.08777 [hep-ex]].
- [20] R. R. Horgan, Z. Liu, S. Meinel and M. Wingate, Phys. Rev. Lett. **112** (2014) 212003  
[arXiv:1310.3887 [hep-ph]].
- [21] R. Aaij *et al.* [LHCb Collaboration], Phys. Rev. Lett. **120** (2018) no.12, 121801  
[arXiv:1711.05623 [hep-ex]].
- [22] W. F. Wang, Y. Y. Fan and Z. J. Xiao, Chin. Phys. C **37** (2013) 093102 [arXiv:1212.5903  
[hep-ph]]; R. Dutta and A. Bhol, Phys. Rev. D **96** (2017) no.7, 076001 [arXiv:1701.08598  
[hep-ph]].
- [23] G. Hiller and M. Schmaltz, Phys. Rev. D **90** (2014) 054014 [arXiv:1408.1627 [hep-ph]];  
M. Bauer and M. Neubert, Phys. Rev. Lett. **116** (2016) no.14, 141802 [arXiv:1511.01900  
[hep-ph]]; R. Barbieri, G. Isidori, A. Pattori and F. Senia, Eur. Phys. J. C **76** (2016) no.2,  
67 [arXiv:1512.01560 [hep-ph]].
- [24] D. Becirevic and E. Schneider, Nucl. Phys. B **854** (2012) 321 [arXiv:1106.3283 [hep-ph]].
- [25] T. Hurth and F. Mahmoudi, JHEP **1404** (2014) 097 [arXiv:1312.5267 [hep-ph]].
- [26] W. Altmannshofer and D. M. Straub, Eur. Phys. J. C **75** (2015) no.8, 382 [arXiv:1411.3161  
[hep-ph]].
- [27] T. Hurth, F. Mahmoudi and S. Neshatpour, JHEP **1412** (2014) 053 [arXiv:1410.4545 [hep-  
ph]].
- [28] F. Beaujean, C. Bobeth and S. Jahn, Eur. Phys. J. C **75** (2015) no.9, 456 [arXiv:1508.01526  
[hep-ph]].
- [29] D. Du, A. X. El-Khadra, S. Gottlieb, A. S. Kronfeld, J. Laiho, E. Lunghi, R. S. Van de  
Water and R. Zhou, Phys. Rev. D **93** (2016) no.3, 034005 [arXiv:1510.02349 [hep-ph]].
- [30] S. Descotes-Genon, L. Hofer, J. Matias and J. Virto, JHEP **1606** (2016) 092  
[arXiv:1510.04239 [hep-ph]].
- [31] T. Hurth, F. Mahmoudi and S. Neshatpour, Nucl. Phys. B **909** (2016) 737 [arXiv:1603.00865  
[hep-ph]].
- [32] A. Khodjamirian, T. Mannel, A. A. Pivovarov and Y.-M. Wang, JHEP **1009** (2010) 089  
[arXiv:1006.4945 [hep-ph]].
- [33] A. Khodjamirian, T. Mannel and Y. M. Wang, JHEP **1302** (2013) 010 [arXiv:1211.0234  
[hep-ph]].
- [34] S. Jäger and J. Martin Camalich, JHEP **1305** (2013) 043 [arXiv:1212.2263 [hep-ph]].

- [35] S. Jäger and J. Martin Camalich, Phys. Rev. D **93** (2016) no.1, 014028 [arXiv:1412.3183 [hep-ph]].
- [36] M. Ciuchini, M. Fedele, E. Franco, S. Mishima, A. Paul, L. Silvestrini and M. Valli, JHEP **1606** (2016) 116 [arXiv:1512.07157 [hep-ph]].
- [37] J. Lyon and R. Zwicky, arXiv:1406.0566 [hep-ph].
- [38] S. Descotes-Genon, L. Hofer, J. Matias and J. Virto, JHEP **1412** (2014) 125 [arXiv:1407.8526 [hep-ph]].
- [39] Y. Oh, C. M. Ko, S. H. Lee and S. Yasui, Phys. Rev. C **79** (2009), 044905 [arXiv:0901.1382 [nucl-th]].
- [40] S. L. Glashow, J. Iliopoulos and L. Maiani, Phys. Rev. D **2** (1970) 1285.
- [41] M. Kobayashi and T. Maskawa, Prog. Theor. Phys. **49** (1973) 652.
- [42] T. Hurth and M. Nakao, Ann. Rev. Nucl. Part. Sci. **60** (2010) 645 [arXiv:1005.1224 [hep-ph]].
- [43] T. Blake, G. Lanfranchi and D. M. Straub, Prog. Part. Nucl. Phys. **92** (2017) 50 [arXiv:1606.00916 [hep-ph]].
- [44] W. Detmold and S. Meinel, Phys. Rev. D **93** (2016) no.7, 074501 [arXiv:1602.01399 [hep-lat]].
- [45] C. Bourrely, I. Caprini and L. Lellouch, Phys. Rev. D **79** (2009) 013008 Erratum: [Phys. Rev. D **82** (2010) 099902] [arXiv:0807.2722 [hep-ph]].
- [46] Y. M. Wang and Y. L. Shen, JHEP **1602** (2016) 179 [arXiv:1511.09036 [hep-ph]].
- [47] T. Aaltonen *et al.* [CDF Collaboration], Phys. Rev. Lett. **107** (2011) 201802 [arXiv:1107.3753 [hep-ex]].
- [48] R. Aaij *et al.* [LHCb Collaboration], Phys. Rev. Lett. **111** (2013) 102003 [arXiv:1307.2476 [hep-ex]].
- [49] R. Aaij *et al.* [LHCb Collaboration], Phys. Rev. D **85** (2012) 032008 [arXiv:1111.2357 [hep-ex]].
- [50] R. Aaij *et al.* [LHCb Collaboration], Phys. Lett. B **725** (2013) 25 [arXiv:1306.2577 [hep-ex]].
- [51] R. Aaij *et al.* [LHCb Collaboration], JHEP **1706** (2017) 108 [arXiv:1703.00256 [hep-ex]].
- [52] R. Aaij *et al.* [LHCb Collaboration], JHEP **1704** (2017) 029 [arXiv:1701.08705 [hep-ex]].
- [53] R. Aaij *et al.* [LHCb Collaboration], arXiv:1912.08139 [hep-ex].
- [54] R. Aaij *et al.* [LHCb Collaboration], JHEP **1809** (2018) 146 [arXiv:1808.00264 [hep-ex]].
- [55] R. Aaij *et al.* [LHCb Collaboration], Phys. Rev. D **100** (2019) no.3, 031102 [arXiv:1902.06794 [hep-ex]].
- [56] T. Mannel and S. Recksiegel, J. Phys. G **24** (1998) 979 [hep-ph/9701399].



- [57] C. H. Chen and C. Q. Geng, Phys. Rev. D **64** (2001) 074001 [hep-ph/0106193].
- [58] C. S. Huang and H. G. Yan, Phys. Rev. D **59** (1999) 114022 Erratum: [Phys. Rev. D **61** (2000) 039901] [hep-ph/9811303].
- [59] G. Hiller, M. Knecht, F. Legger and T. Schietinger, Phys. Lett. B **649** (2007) 152 [hep-ph/0702191].
- [60] Y. m. Wang, Y. Li and C. D. Lu, Eur. Phys. J. C **59** (2009) 861 [arXiv:0804.0648 [hep-ph]].
- [61] C. H. Chen and C. Q. Geng, Phys. Rev. D **63** (2001) 114024 [hep-ph/0101171].
- [62] T. Gutsche, M. A. Ivanov, J. G. Korner, V. E. Lyubovitskij and P. Santorelli, Phys. Rev. D **87** (2013) 074031 [arXiv:1301.3737 [hep-ph]].
- [63] L. Mott and W. Roberts, Int. J. Mod. Phys. A **27** (2012) 1250016 [arXiv:1108.6129 [nucl-th]].
- [64] S. Roy, R. Sain and R. Sinha, Phys. Rev. D **96** (2017) no.11, 116005 [arXiv:1710.01335 [hep-ph]].
- [65] D. Das, JHEP **1807** (2018) 063 [arXiv:1804.08527 [hep-ph]].
- [66] S. Bhattacharya, S. Nandi, S. K. Patra and R. Sain, arXiv:1912.06148 [hep-ph].
- [67] P. Böer, T. Feldmann and D. van Dyk, JHEP **1501** (2015) 155 [arXiv:1410.2115 [hep-ph]].
- [68] G. Kumar and N. Mahajan, arXiv:1511.00935 [hep-ph].
- [69] M. J. Aslam, Y. M. Wang and C. D. Lu, Phys. Rev. D **78**, 114032 (2008) [arXiv:0808.2113 [hep-ph]].
- [70] Y. M. Wang, M. J. Aslam and C. D. Lu, Eur. Phys. J. C **59** (2009) 847 [arXiv:0810.0609 [hep-ph]].
- [71] T. Feldmann and M. W. Y. Yip, Phys. Rev. D **85** (2012) 014035 Erratum: [Phys. Rev. D **86** (2012) 079901] [arXiv:1111.1844 [hep-ph]].
- [72] W. Wang, Phys. Lett. B **708** (2012) 119 [arXiv:1112.0237 [hep-ph]].
- [73] M. Beneke, T. Feldmann and D. Seidel, Eur. Phys. J. C **41** (2005) 173 [hep-ph/0412400].
- [74] C. H. Chen, C. Q. Geng and J. N. Ng, Phys. Rev. D **65** (2002) 091502 [hep-ph/0202103].
- [75] T. M. Aliev, A. Ozpineci and M. Savci, Nucl. Phys. B **649** (2003) 168 [hep-ph/0202120].
- [76] T. M. Aliev, A. Ozpineci and M. Savci, Phys. Rev. D **65** (2002) 115002 [hep-ph/0203045].
- [77] T. M. Aliev, A. Ozpineci and M. Savci, Phys. Rev. D **67** (2003) 035007 [hep-ph/0211447].
- [78] T. M. Aliev, V. Bashiry and M. Savci, Nucl. Phys. B **709** (2005) 115 [hep-ph/0407217].
- [79] T. M. Aliev, V. Bashiry and M. Savci, Eur. Phys. J. C **38** (2004) 283 [hep-ph/0409275].
- [80] T. M. Aliev and M. Savci, JHEP **0605** (2006) 001 [hep-ph/0507324].

- [81] A. K. Giri and R. Mohanta, *J. Phys. G* **31** (2005) 1559.
- [82] A. K. Giri and R. Mohanta, *Eur. Phys. J. C* **45** (2006) 151 [hep-ph/0510171].
- [83] G. Turan, *JHEP* **0505** (2005) 008.
- [84] G. Turan, *J. Phys. G* **31** (2005) 525.
- [85] T. M. Aliev and M. Savci, *Eur. Phys. J. C* **50** (2007) 91 [hep-ph/0606225].
- [86] M. Beneke, T. Feldmann and D. Seidel, *Nucl. Phys. B* **612** (2001) 25 [hep-ph/0106067].
- [87] V. Bashiry and K. Azizi, *JHEP* **0707** (2007) 064 [hep-ph/0702044 [HEP-PH]].
- [88] F. Zolfagharpour and V. Bashiry, *Nucl. Phys. B* **796** (2008) 294 [arXiv:0707.4337 [hep-ph]].
- [89] T. M. Aliev, K. Azizi and M. Savci, *Phys. Rev. D* **81** (2010) 056006 [arXiv:1001.0227 [hep-ph]].
- [90] K. Azizi and N. Katirci, *JHEP* **1101** (2011) 087 [arXiv:1011.5647 [hep-ph]].
- [91] T. M. Aliev and M. Savci, *Phys. Lett. B* **718** (2012) 566 [arXiv:1202.5444 [hep-ph]].
- [92] L. F. Gan, Y. L. Liu, W. B. Chen and M. Q. Huang, *Commun. Theor. Phys.* **58** (2012) 872 [arXiv:1212.4671 [hep-ph]].
- [93] K. Azizi, S. Kartal, A. T. Olgun and Z. Tavukoglu, *Phys. Rev. D* **88** (2013) no.7, 075007 [arXiv:1307.3101 [hep-ph]].
- [94] Y. L. Wen, C. X. Yue and J. Zhang, *Int. J. Mod. Phys. A* **28** (2013) 1350075 [arXiv:1307.5320 [hep-ph]].
- [95] Y. Liu, L.-L. Liu and X.-H. Guo, arXiv:1503.06907 [hep-ph].
- [96] L. Mott and W. Roberts, *Int. J. Mod. Phys. A* **30** (2015) no.27, 1550172 [arXiv:1506.04106 [nucl-th]].
- [97] K. Azizi, A. T. Olgun and Z. Tavukoğlu, *Phys. Rev. D* **92** (2015) no.11, 115025 [arXiv:1508.03980 [hep-ph]].
- [98] S. Sahoo and R. Mohanta, *New J. Phys.* **18** (2016) no.9, 093051 [arXiv:1607.04449 [hep-ph]].
- [99] S. W. Wang and Y. D. Yang, *Adv. High Energy Phys.* **2016** (2016) 5796131 [arXiv:1608.03662 [hep-ph]].
- [100] S. Meinel and D. van Dyk, *Phys. Rev. D* **94** (2016) no.1, 013007 [arXiv:1603.02974 [hep-ph]].
- [101] V. Bashiry, N. Shirkhaghah and K. Zeynali, *Chin. Phys. Lett.* **27** (2010) 041201.
- [102] M. A. Paracha, I. Ahmed and M. J. Aslam, *PTEP* **2015** (2015) no.3, 033B04 [arXiv:1408.4318 [hep-ph]].
- [103] A. Nasrullah, M. Jamil Aslam and S. Shafaq, *PTEP* **2018** (2018) no. 4, 043B08 [arXiv:1803.06885 [hep-ph]].

- [104] R. N. Faustov and V. O. Galkin, Phys. Rev. D **96** (2017) no.5, 053006 [arXiv:1705.07741 [hep-ph]].
- [105] R. N. Faustov and V. O. Galkin, Phys. Rev. D **94** (2016) no.7, 073008 [arXiv:1609.00199 [hep-ph]].
- [106] S. W. Wang, Int. J. Mod. Phys. A **31** (2016) no.36, 1650197.
- [107] M. A. Ivanov, V. E. Lyubovitskij, J. G. Körner and P. Kroll, Phys. Rev. D **56** (1997) 348 [hep-ph/9612463].
- [108] T. Gutsche, M. A. Ivanov, J. G. Körner, V. E. Lyubovitskij and P. Santorelli, Phys. Rev. D **90** (2014) no.11, 114033 Erratum: [Phys. Rev. D **94** (2016) no.5, 059902] [arXiv:1410.6043 [hep-ph]].
- [109] T. Gutsche, M. A. Ivanov, J. G. Körner, V. E. Lyubovitskij and P. Santorelli, Phys. Rev. D **88** (2013) no.11, 114018 [arXiv:1309.7879 [hep-ph]].
- [110] R. Mohanta, A. K. Giri, M. P. Khanna, M. Ishida and S. Ishida, Prog. Theor. Phys. **102** (1999) 645 [hep-ph/9908291].
- [111] Q. Y. Hu, X. Q. Li and Y. D. Yang, Eur. Phys. J. C **77** (2017) no.4, 228 [arXiv:1701.04029 [hep-ph]].
- [112] A. Nasrullah, F. M. Bhutta and M. J. Aslam, J. Phys. G **45**, no. 9, 095007 (2018) [arXiv:1805.01393 [hep-ph]].
- [113] D. Das, Eur. Phys. J. C **78** (2018) no. 3, 230 [arXiv:1802.09404 [hep-ph]].
- [114] A. Ray, S. Sahoo and R. Mohanta, Phys. Rev. D **99** (2019) no.1, 015015 [arXiv:1812.08314 [hep-ph]].
- [115] C. W. Chiang, X. G. He and G. Valencia, Phys. Rev. D **93** (2016) no.7, 074003 [arXiv:1601.07328 [hep-ph]]; S. Di Chiara, A. Fowlie, S. Fraser, C. Marzo, L. Marzola, M. Raidal and C. Spethmann, Nucl. Phys. B **923** (2017) 245 [arXiv:1704.06200 [hep-ph]]; J. F. Kamenik, Y. Soreq and J. Zupan, Phys. Rev. D **97** (2018) no.3, 035002 [arXiv:1704.06005 [hep-ph]].
- [116] C. S. Kalman, Lett. Nuovo Cim. **21** (1978) 291.
- [117] G. Buchalla, G. Burdman, C. T. Hill and D. Kominis, Phys. Rev. D **53** (1996) 5185 [hep-ph/9510376].
- [118] E. Nardi, Phys. Rev. D **48** (1993) 1240 [hep-ph/9209223].
- [119] J. Bernabeu, E. Nardi and D. Tommasini, Nucl. Phys. B **409** (1993) 69 [hep-ph/9306251].
- [120] V. D. Barger, M. S. Berger and R. J. N. Phillips, Phys. Rev. D **52** (1995) 1663 [hep-ph/9503204].
- [121] E. Eichten, I. Hinchliffe, K. D. Lane and C. Quigg, Rev. Mod. Phys. **56** (1984) 579 Addendum: [Rev. Mod. Phys. **58** (1986) 1065].

- [122] J. L. Lopez and D. V. Nanopoulos, Phys. Rev. D **55** (1997) 397 [hep-ph/9605359].
- [123] B. B. Sirvanli, Mod. Phys. Lett. A **23** (2008) 347 [hep-ph/0701173].
- [124] T. G. Rizzo, hep-ph/0610104.
- [125] A. Abulencia *et al.* [CDF Collaboration], Phys. Rev. Lett. **96** (2006) 211801 [hep-ex/0602045].
- [126] P. Langacker and M. Plumacher, Phys. Rev. D **62** (2000) 013006 [hep-ph/0001204].
- [127] V. Barger, L. Everett, J. Jiang, P. Langacker, T. Liu and C. Wagner, Phys. Rev. D **80** (2009) 055008 [arXiv:0902.4507 [hep-ph]]; V. Barger, L. L. Everett, J. Jiang, P. Langacker, T. Liu and C. E. M. Wagner, JHEP **0912** (2009) 048 [arXiv:0906.3745 [hep-ph]].
- [128] Q. Chang, X. Q. Li and Y. D. Yang, JHEP **1002** (2010) 082 [arXiv:0907.4408 [hep-ph]].
- [129] V. Barger, C. W. Chiang, J. Jiang and P. Langacker, Phys. Lett. B **596** (2004) 229 [hep-ph/0405108]; X. G. He and G. Valencia, Phys. Rev. D **74** (2006) 013011 [hep-ph/0605202]; S. Baek, J. H. Jeon and C. S. Kim, Phys. Lett. B **664** (2008) 84 [arXiv:0803.0062 [hep-ph]]; S. Sahoo, C. K. Das and L. Maharana, Int. J. Mod. Phys. A **26** (2011) 3347 [arXiv:1112.0460 [hep-ph]].
- [130] M. Bona *et al.* [UTfit Collaboration], PMC Phys. A **3** (2009) 6 [arXiv:0803.0659 [hep-ph]]; M. Bona *et al.*, arXiv:0906.0953 [hep-ph]; N. G. Deshpande, X. G. He and G. Valencia, Phys. Rev. D **82** (2010) 056013 [arXiv:1006.1682 [hep-ph]]; P. J. Fox, J. Liu, D. Tucker-Smith and N. Weiner, Phys. Rev. D **84** (2011) 115006 [arXiv:1104.4127 [hep-ph]]; Q. Chang, R. M. Wang, Y. G. Xu and X. W. Cui, Chin. Phys. Lett. **28** (2011) 081301.
- [131] C. Bobeth and U. Haisch, Acta Phys. Polon. B **44** (2013) 127 [arXiv:1109.1826 [hep-ph]].
- [132] A. K. Alok, S. Baek and D. London, JHEP **1107** (2011) 111 [arXiv:1010.1333 [hep-ph]]; X. Q. Li, Y. M. Li, G. R. Lu and F. Su, JHEP **1205** (2012) 049 [arXiv:1204.5250 [hep-ph]].
- [133] V. Barger, C. W. Chiang, P. Langacker and H. S. Lee, Phys. Lett. B **580** (2004) 186 [hep-ph/0310073]; C. W. Chiang, R. H. Li and C. D. Lu, Chin. Phys. C **36** (2012) 14 [arXiv:0911.2399 [hep-ph]]; J. Hua, C. S. Kim and Y. Li, Eur. Phys. J. C **69** (2010) 139 [arXiv:1002.2531 [hep-ph]]; Q. Chang, X. Q. Li and Y. D. Yang, JHEP **1004** (2010) 052 [arXiv:1002.2758 [hep-ph]].
- [134] V. Barger, C. W. Chiang, P. Langacker and H. S. Lee, Phys. Lett. B **598** (2004) 218 [hep-ph/0406126]; Q. Chang, X. Q. Li and Y. D. Yang, Int. J. Mod. Phys. A **26** (2011) 1273 [arXiv:1003.6051 [hep-ph]]; Q. Chang and Y. D. Yang, Nucl. Phys. B **852** (2011) 539 [arXiv:1010.3181 [hep-ph]].
- [135] I. Ahmed, Phys. Rev. D **86** (2012) 095022 [arXiv:1208.0549 [hep-ph]];
- [136] L. Randall and R. Sundrum, Phys. Rev. Lett. **83** (1999) 3370 [hep-ph/9905221].
- [137] W. Altmannshofer, C. Niehoff, P. Stangl and D. M. Straub, Eur. Phys. J. C **77** (2017) no. 6, 377 [arXiv:1703.09189 [hep-ph]].

- [138] G. Arnison *et al.* [UA1], Phys. Lett. B **122** (1983), 103
- [139] M. Banner *et al.* [UA2], Phys. Lett. B **122** (1983), 476
- [140] G. Arnison *et al.* [UA1], Phys. Lett. B **126** (1983), 398
- [141] P. Bagnaia *et al.* [UA2], Phys. Lett. B **129** (1983), 130
- [142] G. Aad *et al.* [ATLAS], Phys. Lett. B **716** (2012), 1-29 [arXiv:1207.7214 [hep-ex]].
- [143] S. Chatrchyan *et al.* [CMS], Phys. Lett. B **716** (2012), 30-61 [arXiv:1207.7235 [hep-ex]].
- [144] S. L. Glashow, Nucl. Phys. **22** (1961), 579-588
- [145] S. Weinberg, Phys. Rev. Lett. **19** (1967), 1264-1266
- [146] A. Salam, Conf. Proc. C **680519** (1968), 367-377
- [147] P. W. Higgs, Phys. Rev. Lett. **13** (1964) 508.
- [148] P. Langacker, Adv. Ser. Direct. High Energy Phys. **14** (1995) 15 [hep-ph/0304186].
- [149] Z. Maki, M. Nakagawa and S. Sakata, Prog. Theor. Phys. **28** (1962) 870.
- [150] B. Aubert *et al.* [BaBar Collaboration], Phys. Rev. Lett. **87** (2001) 091801 [hep-ex/0107013].
- [151] K. Abe *et al.* [Belle Collaboration], Phys. Rev. Lett. **87** (2001) 091802 [hep-ex/0107061].
- [152] L. Wolfenstein, Phys. Rev. Lett. **51** (1983) 1945
- [153] J. H. Christenson, J. W. Cronin, V. L. Fitch and R. Turlay, Phys. Rev. Lett. **13** (1964) 138.
- [154] A. Alavi-Harati *et al.* [KTeV Collaboration], Phys. Rev. Lett. **83** (1999) 22 [hep-ex/9905060].
- [155] B. Aubert *et al.* [BaBar Collaboration], Phys. Rev. Lett. **93** (2004) 131801 [hep-ex/0407057].
- [156] Y. Chao *et al.* [Belle Collaboration], Phys. Rev. Lett. **93** (2004) 191802 [hep-ex/0408100].
- [157] A. Poluektov *et al.* [Belle Collaboration], Phys. Rev. D **81** (2010) 112002 [arXiv:1003.3360 [hep-ex]].
- [158] P. del Amo Sanchez *et al.* [BaBar Collaboration], Phys. Rev. D **82** (2010) 072004 [arXiv:1007.0504 [hep-ex]].
- [159] R. Aaij *et al.* [LHCb Collaboration], Phys. Lett. B **712** (2012) 203 Erratum: [Phys. Lett. B **713** (2012) 351] [arXiv:1203.3662 [hep-ex]].
- [160] R. Aaij *et al.* [LHCb Collaboration], Phys. Rev. Lett. **110** (2013) no.22, 221601 [arXiv:1304.6173 [hep-ex]].
- [161] R. Aaij *et al.* [LHCb Collaboration], Nature Phys. **13** (2017) 391 [arXiv:1609.05216 [hep-ex]].
- [162] M. Tanabashi *et al.* [Particle Data Group], Phys. Rev. D **98** (2018) no.3, 030001
- [163] G. C. McLaughlin and J. N. Ng, Phys. Lett. B **493** (2000) 88 [hep-ph/0008209].

- [164] G. Cacciapaglia, M. Cirelli and G. Cristadoro, Nucl. Phys. B **634** (2002) 230 [hep-ph/0111288].
- [165] M. Beneke, P. Moch and J. Rohrwild, Int. J. Mod. Phys. A **29** (2014) 1444011 [arXiv:1404.7157 [hep-ph]].
- [166] A. Joseph, Phys. Rev. D **79** (2009) 096004 [arXiv:0811.3972 [hep-ph]]; T. C. Adorno, D. M. Gitman and A. E. Shabad, Phys. Rev. D **86** (2012) 027702 [arXiv:1207.1743 [hep-th]]; M. Haghghat and M. Khorsandi, Eur. Phys. J. C **75** (2015) no.1, 4 [arXiv:1410.0836 [hep-ph]].
- [167] T. Li, S. Raza and K. Wang, Phys. Rev. D **93** (2016) no.5, 055040 [arXiv:1601.00178 [hep-ph]]; F. V. Flores-Baez, M. Gómez Bock and M. Mondragón, Eur. Phys. J. C **76** (2016) no.10, 561 [arXiv:1512.00902 [hep-ph]]; M. Endo, K. Hamaguchi, S. Iwamoto and K. Yanagi, JHEP **1706** (2017) 031 [arXiv:1704.05287 [hep-ph]].
- [168] S. C. Park and J. h. Song, Phys. Rev. D **69** (2004) 115010 [hep-ph/0306112]; S. R. Choudhury, A. S. Cornell, A. Deandrea, N. Gaur and A. Goyal, Phys. Rev. D **75** (2007) 055011 [hep-ph/0612327].
- [169] A. D. Sakharov, JETP Lett. **5** (1967) 24.
- [170] M. Ahmadi, B.X.R Alves, C.J. *et al.*, Nature, **561** (2018) 211.
- [171] M. S. Chanowitz, M. Furman and I. Hinchliffe, Nucl. Phys. B **159** (1979) 225.
- [172] C. G. Bollini and J. J. Giambiagi, Nuovo Cim. B **12** (1972) 20; G. M. Cicutta and E. Montaldi, Lett. Nuovo Cim. **4** (1972) 329.
- [173] P. Breitenlohner and D. Maison, Commun. Math. Phys. **52** (1977) 11.
- [174] A. J. Buras and P. H. Weisz, Nucl. Phys. B **333** (1990) 66.
- [175] Gerard't Hooft, M.J.G Veltman, Nucl. Phys. B **44** (1972) 189.
- [176] G. 't Hooft, Nucl. Phys. B **33** (1971) 173.
- [177] G. 't Hooft, Nucl. Phys. B **61** (1973) 455.
- [178] W. A. Bardeen, A. J. Buras, D. W. Duke and T. Muta, Phys. Rev. D **18** (1978) 3998.
- [179] K. G. Wilson, Phys. Rev. **179** (1969), 1499-1512
- [180] K. G. Wilson and W. Zimmermann, Commun. Math. Phys. **24** (1972), 87-106
- [181] E. Witten, Nucl. Phys. B **120** (1977), 189-202
- [182] B. Grinstein, arXiv:1501.05283 [hep-ph].
- [183] S. W. Herb *et al.*, Phys. Rev. Lett. **39** (1977) 252.
- [184] F. Abe *et al.* [CDF Collaboration], Phys. Rev. Lett. **81** (1998) 2432 [hep-ex/9805034]; F. Abe *et al.* [CDF Collaboration], Phys. Rev. D **58** (1998) 112004 [hep-ex/9804014].

- [185] A. Abulencia *et al.* [CDF Collaboration], Phys. Rev. Lett. **96** (2006) 082002 [hep-ex/0505076].
- [186] R. Aaij *et al.* [LHCb Collaboration], Phys. Rev. D **95** (2017) no.3, 032005 [arXiv:1612.07421 [hep-ex]].
- [187] K. A. Olive *et al.* [Particle Data Group], Chin. Phys. C **38** (2014) 090001.
- [188] Y. Amhis *et al.* [Heavy Flavor Averaging Group (HFAG)], arXiv:1412.7515 [hep-ex].
- [189] R. Aaij *et al.* [LHCb Collaboration], Nature Phys. **11** (2015) 743 [arXiv:1504.01568 [hep-ex]].
- [190] Y. Nir, arXiv:0708.1872 [hep-ph].
- [191] V. Khachatryan *et al.* [CMS and LHCb Collaborations], Nature **522** (2015) 68 [arXiv:1411.4413 [hep-ex]]. S. Chatrchyan *et al.* [CMS Collaboration], Phys. Rev. Lett. **111** (2013) 101804 [arXiv:1307.5025 [hep-ex]]. R. Aaij *et al.* [LHCb Collaboration], Phys. Rev. Lett. **111** (2013) 101805 [arXiv:1307.5024 [hep-ex]].
- [192] J. A. Ernst, UMI-95-30386.
- [193] R. Aaij *et al.* [LHCb Collaboration], Phys. Lett. B **694** (2010) 209 [arXiv:1009.2731 [hep-ex]].
- [194] J.-T. Wei *et al.* [Belle Collaboration], Phys. Rev. Lett. **103** (2009) 171801 [arXiv:0904.0770 [hep-ex]]. J. P. Lees *et al.* [BaBar Collaboration], Phys. Rev. D **86** (2012) 032012 [arXiv:1204.3933 [hep-ex]]; R. Aaij *et al.* [LHCb Collaboration], JHEP **1611** (2016) 047 Erratum: [JHEP **1704** (2017) 142] [arXiv:1606.04731 [hep-ex]].
- [195] Kruger, Frank and Sehgal, Lalit M. and Sinha, Nita and Sinha, Rahul”, Phys. Rev. D **61** (2000) 114028 [arXiv:hep-ph/9907386].
- [196] W. Altmannshofer, P. Ball, A. Bharucha, A. J. Buras, D. M. Straub and M. Wick, JHEP **0901** (2009) 019 [arXiv:0811.1214 [hep-ph]].
- [197] U. Egede, T. Hurth, J. Matias, M. Ramon and W. Reece, JHEP **0811** (2008) 032 [arXiv:0807.2589 [hep-ph]].
- [198] S. Descotes-Genon, T. Hurth, J. Matias and J. Virto, [arXiv:1305.4808 [hep-ph]].
- [199] P. Colangelo, F. De Fazio, R. Ferrandes and T. N. Pham, Phys. Rev. D **73** (2006) 115006 [hep-ph/0604029]; P. Colangelo, F. De Fazio, R. Ferrandes and T. N. Pham, Phys. Rev. D **73** (2006) 115006 [hep-ph/0604029]. A. Hovhannisyan, W. S. Hou and N. Mahajan, Phys. Rev. D **77** (2008) 014016 [hep-ph/0701046]; A. K. Alok, A. Dighe, D. Ghosh, D. London, J. Matias, M. Nagashima and A. Szynekman, JHEP **1002** (2010) 053 [arXiv:0912.1382 [hep-ph]]; A. Bharucha and W. Reece, Eur. Phys. J. C **69** (2010) 623 [arXiv:1002.4310 [hep-ph]].
- [200] J. Matias, Phys. Rev. D **86** (2012) 094024 [arXiv:1209.1525 [hep-ph]].
- [201] S. Descotes-Genon, J. Matias and J. Virto, Phys. Rev. D **88** (2013) 074002 [arXiv:1307.5683 [hep-ph]].

- [202] A. Faessler, T. Gutsche, M. A. Ivanov, J. G. Korner and V. E. Lyubovitskij, *Eur. Phys. J. direct* **4** (2002) no.1, 18 [hep-ph/0205287].
- [203] A. Abulencia *et al.*, *Phys. Rev. Lett.* **98** (2007) 122002 [hep-ex/0601003].
- [204] V. M. Abazov *et al.* [D0], *Phys. Rev. D* **84** (2011) 031102 [arXiv:1105.0690 [hep-ex]].
- [205] T. A. Aaltonen *et al.* [CDF], *Phys. Rev. D* **89** (2014) no.7, 072014 [arXiv:1403.8126 [hep-ex]].
- [206] R. Aaij *et al.* [LHCb], *Phys. Rev. D* **89** (2014) no.3, 032001 [arXiv:1311.4823 [hep-ex]].
- [207] R. Aaij *et al.* [LHCb], *Phys. Rev. Lett.* **112** (2014), 202001 [arXiv:1403.3606 [hep-ex]].
- [208] R. Aaij *et al.* [LHCb], *JHEP* **07** (2014), 103 [arXiv:1406.0755 [hep-ex]].
- [209] D. O’Hanlon [LHCb], [arXiv:1605.06990 [hep-ex]] (2016).
- [210] R. Aaij *et al.* [LHCb], *JHEP* **02** (2018) 098 [arXiv:1711.05490 [hep-ex]]
- [211] R. Aaij *et al.* [LHCb], *JHEP* **05** (2016) 132 [arXiv:1603.06961 [hep-ex]].
- [212] C. Greub, V. Pilipp and C. Schupbach, *JHEP* **0812** (2008) 040 [arXiv:0810.4077 [hep-ph]].
- [213] Y. M. Wang, Y. L. Shen and C. D. Lu, *Phys. Rev. D* **80** (2009) 074012 [arXiv:0907.4008 [hep-ph]].
- [214] G. Hiller and A. Kagan, *Phys. Rev. D* **65** (2002) 074038 [hep-ph/0108074].
- [215] W. Detmold, C.-J. D. Lin, S. Meinel and M. Wingate, *Phys. Rev. D* **87** (2013) no.7, 074502 [arXiv:1212.4827 [hep-lat]].
- [216] C. Patrignani *et al.* [Particle Data Group], *Chin. Phys. C* **40** (2016) no.10, 100001.
- [217] R. Aaij *et al.* [LHCb Collaboration], *JHEP* **1506** (2015) 115 [arXiv:1503.07138 [hep-ex]].
- [218] J. G. Korner, M. Kramer and D. Pirjol, *Prog. Part. Nucl. Phys.* **33**, 787 (1994) [hep-ph/9406359].
- [219] G. Burdman, *Phys. Rev. D* **57** (1998) 4254 [hep-ph/9710550]; A. Ali, P. Ball, L. T. Handoko and G. Hiller, *Phys. Rev. D* **61** (2000) 074024 [hep-ph/9910221].
- [220] Q. Chang, X. Q. Li and Y. D. Yang, *J. Phys. G* **41** (2014) 105002 [arXiv:1312.1302 [hep-ph]]; C. W. Chiang, N. G. Deshpande and J. Jiang, *JHEP* **0608** (2006) 075 [hep-ph/0606122]; R. Foot, X. G. He, H. Lew and R. R. Volkas, *Phys. Rev. D* **50** (1994) 4571 [hep-ph/9401250].
- [221] Q. Chang and Y. H. Gao, *Nucl. Phys. B* **845** (2011) 179 [arXiv:1101.1272 [hep-ph]].
- [222] K. Cheung, C. W. Chiang, N. G. Deshpande and J. Jiang, *Phys. Lett. B* **652** (2007) 285 [hep-ph/0604223].
- [223] R. Mohanta and A. K. Giri, *Phys. Rev. D* **79** (2009) 057902 [arXiv:0812.1842 [hep-ph]].
- [224] H. H. Asatryan, H. M. Asatrian, C. Greub and M. Walker, *Phys. Rev. D* **65** (2002) 074004 [hep-ph/0109140].



- [225] I. Ahmed and A. Rehman, *Chin. Phys. C* **42** (2018) no.6, 063103 [arXiv:1703.09627 [hep-ph]].
- [226] G. Burdman, *Phys. Lett. B* **590** (2004) 86 [hep-ph/0310144].
- [227] K. Agashe, G. Perez and A. Soni, *Phys. Rev. D* **71** (2005) 016002 [hep-ph/0408134].
- [228] G. Moreau and J. I. Silva-Marcos, *JHEP* **0603** (2006) 090 [hep-ph/0602155].
- [229] S. Casagrande, F. Goertz, U. Haisch, M. Neubert and T. Pfoh, *JHEP* **0810** (2008) 094 [arXiv:0807.4937 [hep-ph]].
- [230] M. Blanke, A. J. Buras, B. Duling, S. Gori and A. Weiler, *JHEP* **0903** (2009) 001 [arXiv:0809.1073 [hep-ph]].
- [231] M. Blanke, A. J. Buras, B. Duling, K. Gemmler and S. Gori, *JHEP* **0903** (2009) 108 [arXiv:0812.3803 [hep-ph]].
- [232] M. E. Albrecht, M. Blanke, A. J. Buras, B. Duling and K. Gemmler, *JHEP* **0909** (2009) 064 [arXiv:0903.2415 [hep-ph]].
- [233] M. Bauer, S. Casagrande, U. Haisch and M. Neubert, *JHEP* **1009** (2010) 017 [arXiv:0912.1625 [hep-ph]].
- [234] M. Blanke, B. Shakya, P. Tanedo and Y. Tsai, *JHEP* **1208** (2012) 038 [arXiv:1203.6650 [hep-ph]].
- [235] P. Biancofiore, P. Colangelo and F. De Fazio, *Phys. Rev. D* **89** (2014) no.9, 095018 [arXiv:1403.2944 [hep-ph]].
- [236] P. Biancofiore, P. Colangelo, F. De Fazio and E. Scrimieri, *Eur. Phys. J. C* **75** (2015) 134 [arXiv:1408.5614 [hep-ph]].
- [237] C. D. Lü, F. Munir and Q. Qin, *Chin. Phys. C* **41** (2017) no.5, 053106 [arXiv:1607.07713 [hep-ph]].
- [238] G. D'Ambrosio and A. M. Iyer, *Eur. Phys. J. C* **78** (2018) no.6, 448 [arXiv:1712.08122 [hep-ph]].
- [239] M. Blanke and A. Crivellin, *Phys. Rev. Lett.* **121** (2018) no.1, 011801 [arXiv:1801.07256 [hep-ph]].
- [240] T. Gherghetta and A. Pomarol, *Nucl. Phys. B* **586** (2000) 141 [hep-ph/0003129].
- [241] M. Carena, E. Ponton, J. Santiago and C. E. M. Wagner, *Nucl. Phys. B* **759** (2006) 202 [hep-ph/0607106].
- [242] R. Malm, M. Neubert and C. Schmell, *JHEP* **1502** (2015) 008 [arXiv:1408.4456 [hep-ph]].
- [243] G. Aad *et al.* [ATLAS Collaboration], *JHEP* **1508** (2015) 148 [arXiv:1505.07018 [hep-ex]].
- [244] A. M. Sirunyan *et al.* [CMS Collaboration], *JHEP* **1707** (2017) 001 [arXiv:1704.03366 [hep-ex]].

- [245] R. Malm, M. Neubert, K. Novotny and C. Schmell, *JHEP* **1401** (2014) 173 [arXiv:1303.5702 [hep-ph]].
- [246] H. Y. Cheng and B. Tseng, *Phys. Rev. D* **53** (1996) 1457 Erratum: [*Phys. Rev. D* **55** (1997) 1697] [hep-ph/9502391].
- [247] A. Khodjamirian, C. Klein, T. Mannel and Y.-M. Wang, *JHEP* **1109** (2011) 106 [arXiv:1108.2971 [hep-ph]].
- [248] X. G. He, T. Li, X. Q. Li and Y. M. Wang, *Phys. Rev. D* **74** (2006) 034026 [hep-ph/0606025].
- [249] F. Hussain, J. G. Korner, M. Kramer and G. Thompson, *Z. Phys. C* **51** (1991) 321.
- [250] F. Hussain, D. S. Liu, M. Kramer, J. G. Korner and S. Tawfiq, *Nucl. Phys. B* **370** (1992) 259.
- [251] T. Gutsche, M. A. Ivanov, J. G. Körner, V. E. Lyubovitskij, P. Santorelli and N. Habył, *Phys. Rev. D* **91** (2015) no.7, 074001 [arXiv:1502.04864 [hep-ph]].
- [252] R. Dutta, *Phys. Rev. D* **100** (2019) no.7, 075025 [arXiv:1906.02412 [hep-ph]].
- [253] F. U. Bernlochner, Z. Ligeti and D. J. Robinson, *Phys. Rev. D* **97** (2018) no.7, 075011 [arXiv:1711.03110 [hep-ph]].
- [254] H. Yan, [arXiv:1911.11568 [hep-ph]].

## List of Publications

This dissertation comprises of the following publications/submissions:

- 1) **Title:** The  $\Lambda_b \rightarrow \Lambda(\rightarrow p\pi^-)\mu^+\mu^-$  decay in the RSc model  
**Authors:** Aqsa Nasrullah, Faisal Munir Bhutta, M. Jamil Aslam  
**Journal Details:** Journal of Physics G 45 (2018) no. 9, 095007 (I. F. 3.534)  
**Status:** Online
- 2) **Title:** Analysis of angular observables of  $\Lambda_b \rightarrow \Lambda(\rightarrow p\pi^-)\mu^+\mu^-$  decay in the Standard and  $Z'$  models  
**Authors:** Aqsa Nasrullah, M. Jamil Aslam, Saba Shafaq  
**Journal Detail:** Progress in Theoretical and Experimental Physics 2018 (2018) no. 4, 043B08 (I. F. 2.091)  
**Status:** Online
- 3) **Title:** Probing new physics effects in  $\Lambda_b \rightarrow \Lambda(\rightarrow p\pi^-)l^+l^-$  decay via model independent approach  
**Authors:** Aqsa Nasrullah, Ishtiaq Ahmed, M. Jamil Aslam, Z. Asghar, Saba Shafaq  
**arXiv Details:** 2006.15513 [hep-ph]  
**Status:** Under Review in Physica Scripta

# Analysis of angular observables of $\Lambda_b \rightarrow \Lambda(\rightarrow p\pi)\mu^+\mu^-$ decay in the standard and $Z'$ models

Aqsa Nasrullah<sup>1</sup>, M. Jamil Aslam<sup>1,2,\*</sup>, and Saba Shafaq<sup>3</sup>

<sup>1</sup>Department of Physics, Quaid-i-Azam University, Islamabad 45320, Pakistan

<sup>2</sup>Institute of High Energy Physics, P.O. Box 918(4), Chinese Academy of Sciences, Beijing 100049, China

<sup>3</sup>Department of Physics, International Islamic University, Islamabad 45320, Pakistan

\*E-mail: muhammadjamil@gmail.com

Received August 12, 2017; Revised March 18, 2018; Accepted March 18, 2018; Published April 27, 2018

In 2015, the LHCb collaboration measured the differential branching ratio  $\frac{d\mathcal{B}}{dq^2}$ , the lepton- and hadron-side forward–backward asymmetries, denoted by  $A_{\text{FB}}^{\ell}$  and  $A_{\text{FB}}^{\Lambda}$ , respectively, in the range  $15 < q^2 (= s) < 20 \text{ GeV}^2$  with  $3 \text{ fb}^{-1}$  of data. Motivated by these measurements, we perform an analysis of  $q^2$ -dependent  $\Lambda_b \rightarrow \Lambda(\rightarrow p\pi)\mu^+\mu^-$  angular observables at large- and low-recoil in the standard model (SM) and in a family non-universal  $Z'$  model. The exclusive  $\Lambda_b \rightarrow \Lambda$  transition is governed by the form factors, and in the present study we use the recently performed high-precision lattice QCD calculations that have well-controlled uncertainties, especially in the  $15 < s < 20 \text{ GeV}^2$  bin. Using the full four-folded angular distribution of  $\Lambda_b \rightarrow \Lambda(\rightarrow p\pi)\mu^+\mu^-$  decay, first of all we focus on calculations of the experimentally measured  $\frac{d\mathcal{B}}{ds}$ ,  $A_{\text{FB}}^{\ell}$ , and  $A_{\text{FB}}^{\Lambda}$  in the SM and compare their numerical values with the measurements in appropriate bins of  $s$ . In case of a possible discrepancy between the SM prediction and the measurements, we try to see if these can be accommodated through the extra neutral  $Z'$  boson. We find that in the dimuon momentum range  $15 < s < 20 \text{ GeV}^2$  the value of  $\frac{d\mathcal{B}}{ds}$  and central value of  $A_{\text{FB}}^{\ell}$  in the  $Z'$  model is compatible with the measured values. In addition, the fraction of longitudinal polarization of the dimuon  $F_L$  was measured to be  $0.61_{-0.14}^{+0.11} \pm 0.03$  in  $15 < s < 20 \text{ GeV}^2$  at the LHCb. We find that in this bin the value found in the  $Z'$  model is close to the observed values. After comparing the results of these observables, we have proposed other observables such as  $\alpha_i$  and  $\alpha_i^{(\prime)}$  with  $i = \theta_{\ell}, \theta_{\Lambda}, \phi, L, U$  and coefficients of different foldings  $\mathcal{P}_{1,\dots,9}$  in different bins of  $s$  in the SM and  $Z'$  model. We illustrate that the experimental observations of the  $s$ -dependent angular observables calculated here in several bins of  $s$  can help to test the predictions of the SM and unravel new physics contributions arising due to the  $Z'$  model in  $\Lambda_b \rightarrow \Lambda(\rightarrow p\pi)\mu^+\mu^-$  decays.

Subject Index B56, B57, C18

## 1. Introduction

Rare decays involving  $b$ -quarks, such as  $b \rightarrow (s, d)\gamma$ ,  $b \rightarrow (s, d)\ell^+\ell^-$ , have been of immense interest in recent decades. This is because these decays are induced by flavor-changing neutral current transitions (FCNC) involving the quantum number transitions  $|\Delta Q| = 0$  and  $|\Delta B| = 1$ . In the standard model (SM), FCNC transitions are not allowed at the tree level but occur at loop level because of the Glashow–Iliopoulos–Maiani (GIM) mechanism [1]. This makes them sensitive to the masses of particles that run in the loop, e.g.  $m_t$  and  $m_W$  in the SM. As a consequence, these decays play a pivotal role in the determination of Cabibbo–Kobayashi–Masakawa (CKM) [2,3] matrix elements in an indirect way. In different extensions of the SM, there is a possibility that the new particles can also run in the SM loop diagrams, making these rare decays sensitive to the masses and couplings

of the new particles. Hence, rare decays provide a rich laboratory to test the predictions of the SM and help us to establish possible new physics (NP) indirectly [4,5].

As long as the inclusive radiative and semi-leptonic decays are concerned, there are hardly any open issues that could lead us towards evidence of NP. However, experimental precision is limited at present and it is expected that these bounds will be improved significantly at Belle II [6]. The situation for exclusive semi-leptonic  $B$ -meson decays is different, with a lot of open issues. Among them, the most pertinent is lepton flavor universality (LFU), i.e., the couplings of gauge bosons in the SM are the same for different families of leptons. This important prediction of the SM can be tested by measuring the ratio of the decay widths of  $B \rightarrow K^{(*)}\mu^+\mu^-$  and  $B \rightarrow K^{(*)}e^+e^-$ , defined as

$$\mathcal{R}_{K^{(*)}} = \frac{B \rightarrow K^{(*)}\mu^+\mu^-}{B \rightarrow K^{(*)}e^+e^-}, \quad (1)$$

in specific bins of the dilepton invariant mass squared, written as  $s \in [s_{\min}, s_{\max}]$  from here onwards. As this ratio involves the same  $B \rightarrow K^{(*)}$  transition, the hadronic uncertainties arising from the form factors cancel out to a good approximation. Therefore, any possible deviations from the SM predictions, i.e., a value of the ratio different from one, will hint towards the NP. In 2014, the LHCb collaboration observed more than a  $2\sigma$  mismatch between experimental observations and SM predictions in different bins of the square of momentum transfer  $s = q^2$  [7]. This hints at the breakdown of the SM LFU, i.e., the couplings of gauge bosons with  $\mu$  and  $e$  are not the same [8,9]. There are also some other areas where tensions between SM predictions and experimental observations are found, such as the  $\mathcal{P}_5$  anomaly ( $3.5\sigma$  in one bin  $s \in [4.30, 8.68] \text{ GeV}^2$  [10], which corresponds to a certain coefficient in the angular distribution of the  $B \rightarrow K^*(\rightarrow K\pi)\mu^+\mu^-$  decay [10–12]. This anomaly was again observed at  $3\sigma$  in the data with  $3 \text{ fb}^{-1}$  luminosity in the two bins  $s \in [4, 6] \text{ GeV}^2$  and  $s \in [6, 8] \text{ GeV}^2$  [13], and this was later confirmed by Belle in the bin  $s \in [4, 8] \text{ GeV}^2$  [14]. This anomaly was accompanied by a  $2.9\sigma$  tension in the second bin of another angular observable called  $\mathcal{P}_2$  [15]. In addition, a small but noticeable difference was found in the branching ratio of  $B \rightarrow K^*\mu^+\mu^-$  [16–18] and  $B_s \rightarrow \phi\mu^+\mu^-$  ( $2.0\sigma$  larger than the SM prediction both in low- and large- $\phi$  recoil) [19–21]. Making use of the available data and motivated by these tantalizing anomalies observed in these  $B$  decays, in addition to explaining them in different beyond-the-SM scenarios [22–24], global analyses have also been carried out [15,25–33]. Incorporating the factorizable (absorbed in the form factors) and non-factorizable contributions, these global analyses favor a negative shift in the Wilson coefficient  $C_9$  to explain most of the data. However, before we could claim that these are indications of NP, we have to get full control of the possible hadronic uncertainties arising due to form factors in the exclusive decays [34–40]. In order to establish the hints of NP, on the experimental side we need to have the improved statistical data that is expected at Belle II and the LHCb, whereas on the theoretical side we can study some other decays that are governed at quark level by  $b \rightarrow s\ell^+\ell^-$  ( $\ell = \mu, \tau$ ) transitions.

In the present study, we have considered the  $\Lambda_b \rightarrow \Lambda(\rightarrow p\pi)\ell^+\ell^-$  decay that is interesting to its own regard. On the experimental side, this decay was first studied by the CDF collaboration [41], and the LHCb later published the first measurement of the differential branching ratio as well as the forward–backward asymmetry of the final state muon, i.e.,  $\mathcal{A}_{\text{FB}}$  [42,43]. Recently, the LHCb collaboration has made an observation of CP violation and the asymmetries arising due to the angle between the  $\mu^+\mu^-$  and  $pK^-$  planes ( $a_{\text{CP}}^{\hat{T}\text{odd}}$ ) in  $\Lambda_b \rightarrow pK^-\mu^+\mu^-$  by analyzing the data available at an integrated luminosity of  $3 \text{ fb}^{-1}$  [44]. On the theoretical front, at first in the decay  $\Lambda_b \rightarrow \Lambda\ell^+\ell^-$ , the hadrons involved in the initial and final states are the baryons, therefore the study of such decays

will help us to understand the helicity structure of the underlying effective Hamiltonian [45–47]. Another added benefit is that analysis of the angular asymmetries in the sequential decay  $\Lambda_b \rightarrow \Lambda(\rightarrow p\pi)\mu^+\mu^-$  is expected to complement the different angular asymmetries in the corresponding  $B \rightarrow K^*(\rightarrow K\pi)\ell^+\ell^-$  decays [48–50]. One important aspect is the stability of  $\Lambda$  under strong interactions, and the decay  $\Lambda_b \rightarrow \Lambda(\rightarrow p\pi)\ell^+\ell^-$  is theoretically cleaner than the decay  $B \rightarrow K^*(\rightarrow K\pi)\ell^+\ell^-$ . Hence, the decay  $\Lambda_b \rightarrow \Lambda\ell^+\ell^-$  has been theoretically studied in a number of papers [51–88].

Just like the exclusive decays of  $B$ -mesons, the decay  $\Lambda_b \rightarrow \Lambda\ell^+\ell^-$  is prone to the uncertainties arising due to form factors. However, at present the  $\Lambda_b \rightarrow \Lambda$  transition form factors are calculated using lattice QCD calculations with high precision [89]; to have their profile in the full  $q^2$  range, these form factors are extrapolated using the Bourrely–Caprini–Lellouch parametrization [90]. The lattice results are quite consistent with the recent QCD light-cone sum rule calculation [53], with the added benefit of a much smaller uncertainty in most of the kinematic range. However, in contrast to the  $B$  decays, the QCD factorization is not fully developed for the  $b$ -baryon decays; therefore, we will not include these non-factorizable contributions in the present study. After having control of the hadronic uncertainties in the form factors, the next choice is to find observables that are relatively clean. In line with the  $B \rightarrow K^*(\rightarrow K\pi)\mu^+\mu^-$  decays, we have calculated combinations of different angular observables in  $\Lambda_b \rightarrow \Lambda(\rightarrow p\pi)\mu^+\mu^-$  decays, namely, forward–backward asymmetries ( $A_{\text{FB}}^\ell, A_{\text{FB}}^\Lambda, A_{\text{FB}}^{\Lambda\ell}$ ), the longitudinal ( $F_L$ ) and transverse ( $F_T$ ) fractions of the dimuon, the longitudinal asymmetry  $\alpha_L$ , the transverse asymmetry  $\alpha_U$ , and the observables named as  $\mathcal{P}_i$  that are derived from different foldings, in the SM at its first right.

It has been observed that in order to explain the  $R_K$  anomaly in  $B \rightarrow K\ell^+\ell^-$  decays, a possible candidate is the  $Z'$  model [91–93]. The economy of these  $Z'$  models is that they can be accommodated to the SM just by extending the electroweak SM group by an additional  $U(1)'$  gauge group with which the extra gauge boson  $Z'$  is associated. Also, in the grand unification theories (GUTs) such as  $SU(5)$  or string-inspired  $E_6$  models [94–98], relevant scenarios are the family non-universal  $Z'$  model [99,100] and the leptophobic  $Z'$  models [101,102]. The direct signature of an extra  $Z'$  boson is still missing in the analysis of data taken so far at the LHC [103] experiment, but we already have some indirect constraints on the couplings of the  $Z'$  gauge boson through low-energy processes that are crucial and complementary for direct searches  $Z' \rightarrow e^+e^-$  at Tevatron [104]. The additional interesting thing that the family non-universal  $Z'$  models have in their favor is the new CP-violating phase, which has large effects on various FCNC processes [100,105,106], such as  $B_s-\bar{B}_s$  mixing [107–121] and rare hadronic and  $B$ -meson decays [122–140]. As extending the SM group by an extra  $U(1)'$  gauge group does not change the operator basis of the SM, the  $Z'$  model therefore belongs to a class of minimal flavor-violating models having its imprints in the Wilson coefficients that correspond to the SM operators. Keeping in view that among the different hadrons produced at the LHCb, almost 20% will be  $\Lambda_b$  baryons, it is expected that in future the results of decay distributions and different angular asymmetries will be available with much better statistics. Therefore, in addition to the SM calculation of the different observables mentioned above, we have studied the impact of different  $Z'$  parameters on these observables in different bins of  $s$ .

The paper is organized as follows: In Sect. 2, the theoretical framework for the decay  $\Lambda_b \rightarrow \Lambda(\rightarrow p\pi)\ell^+\ell^-$  is discussed. Helicity amplitudes for the decay are written in terms of transition form factors and four-fold differential decay distributions. After summarizing the Wilson coefficients and other parameters of the  $Z'$  model in Sect. 3, we present the calculation of several observables that have been obtained using four-folded angular distributions in Sect. 4. Section 5 presents numerical

analysis of the observables done in the SM and in the  $Z'$  model, and here we compare the results of certain asymmetries with the measurements available from the LHCb experiment. In addition to the tabular form of the results, these are also plotted graphically here. Finally, the main findings are summarized in the last section.

## 2. Effective Hamiltonian formalism for the SM and $Z'$ model

The quark-level decay governing  $\Lambda_b \rightarrow \Lambda(\rightarrow p\pi)\mu^+\mu^-$  is  $b \rightarrow s\mu^+\mu^-$ . In this decay of the  $b$ -baryon, the short-distance effects are encoded in the Wilson coefficients, whereas the long-distance contributions are incorporated through the four-quark operators. After integrating out the heavy degrees of freedom,  $W^\pm$ ,  $Z$  bosons, and top quark, the SM effective Hamiltonian for these decays is

$$H_{\text{SM}}^{\text{eff}} = -\frac{4G_F}{\sqrt{2}} \frac{\alpha_e}{4\pi} V_{tb}V_{ts}^* \sum_{i=7,9,10} C_i(\mu) \mathcal{O}_i, \quad (2)$$

where  $G_F$  is the Fermi coupling constant,  $V_{tb}V_{ts}^*$  are the CKM matrix elements,  $\alpha_e$  is the fine structure constant, and  $C_i(\mu)$  with  $i = 7, 9, 10$  are the Wilson coefficients corresponding to the electromagnetic operator  $\mathcal{O}_7$  and semi-leptonic operators  $\mathcal{O}_{9,10}$  that are defined as

$$\mathcal{O}_7 = \frac{m_b}{e} [\bar{s}\sigma^{\mu\nu}P_R b] F_{\mu\nu}, \quad \mathcal{O}_9 = [\bar{s}\gamma^\mu P_L b] [\bar{\ell}\gamma_\mu \ell], \quad \mathcal{O}_{10} = [\bar{s}\gamma^\mu P_L b] [\bar{\ell}\gamma_\mu \gamma_5 \ell].$$

It has already been mentioned that QCD factorization at low- $q^2$  is not fully developed for the hadronic  $b$ -baryon decay; therefore, we have ignored the non-factorizable contributions here.<sup>1</sup> The factorizable non-local matrix elements of the four-quark operators  $\mathcal{O}_{1-6}$  and  $\mathcal{O}_8^g$  are encoded into effective Wilson coefficients  $C_7^{\text{eff}}(s)$  and  $C_9^{\text{eff}}(s)$ , where  $s$  is the dilepton squared mass  $q^2$  ( $q^\mu = p_1^\mu - p_2^\mu$ ). In the high- $q^2$  region, the Wilson coefficients  $C_7^{\text{eff}}(s)$  and  $C_9^{\text{eff}}(s)$  can be written as [31]

$$\begin{aligned} C_7^{\text{eff}}(s) &= C_7 - \frac{1}{3} \left( C_3 + \frac{4}{3}C_4 + 20C_5 + \frac{80}{3}C_6 \right) - \frac{\alpha_s}{4\pi} \left[ (C_1 - 6C_2)F_{1,c}^{(7)}(s) + C_8F_8^{(7)}(s) \right], \\ C_9^{\text{eff}}(s) &= C_9 + \frac{4}{3} \left( C_3 + \frac{16}{3}C_5 + \frac{16}{9}C_6 \right) - h(0, s) \left( \frac{1}{2}C_3 + \frac{2}{3}C_4 + 8C_5 + \frac{32}{3}C_6 \right) \\ &\quad - \left( \frac{7}{2}C_3 + \frac{2}{3}C_4 + 38C_5 + \frac{32}{3}C_6 \right) h(m_b, s) + \left( \frac{4}{3}C_1 + C_2 + 6C_3 + 60C_5 \right) h(m_c, s) \\ &\quad - \frac{\alpha_s}{4\pi} \left[ C_1F_{1,c}^{(9)}(s) + C_2F_{2,c}^{(9)}(s) + C_8F_8^{(9)}(s) \right], \end{aligned} \quad (3)$$

where  $h(m_{q'}, s)$  with  $q' = b, c$  corresponds to the fermionic loop functions. These  $h(m_{q'}, s)$  along with the functions  $F_8^{(7,9)}$  and  $F_{(1,2,c)}^{(7,9)}$  are calculated in Refs. [54,141].

Long ago, Langacker and Plümacher included a family non-universal  $Z'$  boson through additional  $U(1)'$  gauge symmetry [100]. In contrast to the SM, having a non-diagonal chiral coupling matrix,

<sup>1</sup> In the case of  $B \rightarrow K^*\mu^+\mu^-$  decay, it is evident that the non-factorizable charm-loop effects (i.e., corrections that are not described using hadronic form factors) play a sizeable role in the low- $q^2$  region [40] and the same is expected in case of the decay under consideration. However, in the present study we shall neglect their contributions because there is no systematic framework available in which these non-factorizable charm-loop effects can be calculated in baryonic decays [53]. Therefore, our results at low- $q^2$  are affected by the uncertainties due to these contributions. In the whole  $q^2$  range, the effective Wilson coefficients are given in Eq. (3). According to Ref. [89], we use Eq. (3) in the low- and high- $q^2$  regions by increasing the 5% uncertainty. Thus, having a control on the non-factorizable contributions in baryonic decays will help us to hunt for deviations from the SM predictions.

in a family non-universal  $Z'$  model, the FCNC transitions  $b \rightarrow s\ell^+\ell^-$  could be induced at tree level. Ignoring  $Z-Z'$  mixing, along with the assumption that the couplings of right-handed quark flavors with  $Z'$  boson are diagonal, the effective Hamiltonian for the  $b \rightarrow s\ell^+\ell^-$  transition corresponding to the  $Z'$  boson becomes [142–146]

$$\mathcal{H}_{\text{eff}}^{Z'}(b \rightarrow s\ell^+\ell^-) = -\frac{2G_F}{\sqrt{2}}V_{tb}V_{ts}^* \left[ \frac{B_{sb}S_{\ell\ell}^L}{V_{tb}V_{ts}^*}(\bar{s}b)_{V-A}(\bar{\ell}\ell)_{V-A} + \frac{B_{sb}S_{\ell\ell}^R}{V_{tb}V_{ts}^*}(\bar{s}b)_{V-A}(\bar{\ell}\ell)_{V+A} \right]. \quad (4)$$

In Eq. (4),  $S_{\ell\ell}^L$  and  $S_{\ell\ell}^R$  represent the couplings of the  $Z'$  boson with the left- and right-handed leptons, respectively. The corresponding off-diagonal left-handed coupling of quarks with the new  $Z'$  boson is taken care of by  $B_{sb} = |\mathcal{B}_{sb}|e^{-i\phi_{sb}}$ , with  $\phi_{sb}$  a new weak phase. In a more sophisticated form, Eq. (4) can be written as

$$\mathcal{H}_{\text{eff}}^{Z'}(b \rightarrow s\ell^+\ell^-) = -\frac{4G_F}{\sqrt{2}}V_{tb}V_{ts}^* \left[ \Lambda_{sb}C_9^{Z'}O_9 + \Lambda_{sb}C_{10}^{Z'}O_{10} \right], \quad (5)$$

where

$$\Lambda_{sb} = \frac{4\pi e^{-i\phi_{sb}}}{\alpha_{EM}V_{tb}V_{ts}^*}, \quad C_9^{Z'} = |\mathcal{B}_{sb}|S_{LL}, \quad C_{10}^{Z'} = |\mathcal{B}_{sb}|D_{LL}, \quad (6)$$

and

$$S_{LL} = S_{\ell\ell}^L + S_{\ell\ell}^R, \quad D_{LL} = S_{\ell\ell}^L - S_{\ell\ell}^R. \quad (7)$$

By comparing Eqs. (2) and (5) it can be noticed that except for  $C_7^{\text{eff}}$ , which is absent in the  $Z'$  model, the operator basis of the family non-universal  $Z'$  model is the same as that of the SM for  $O_{9,10}$ . Hence, the contribution arising due to the extra  $Z'$  boson is absorbed in the Wilson coefficients  $C_9^{\text{eff}}$  and  $C_{10}$ .

The total amplitude for the decay  $\Lambda_b \rightarrow \Lambda\ell^+\ell^-$  is the sum of the SM and  $Z'$  contributions, and it can be formulated in terms of  $\Lambda_b \rightarrow \Lambda$  matrix elements as

$$\begin{aligned} \mathcal{M}^{\text{tot}}(\Lambda_b \rightarrow \Lambda\ell^+\ell^-) &= -\frac{G_F\alpha}{2\sqrt{2}\pi}V_{tb}V_{ts}^*[\langle\Lambda(k)|\bar{s}\gamma_\mu(1-\gamma_5)b|\Lambda_b(p)\rangle\{C_9^{\text{tot}}(\bar{\ell}\gamma^\mu\ell) + C_{10}^{\text{tot}}(\bar{\ell}\gamma^\mu\gamma^5\ell)\} \\ &\quad - \frac{2m_b}{q^2}C_7^{\text{eff}}\langle\Lambda(k)|\bar{s}i\sigma_{\mu\nu}q^\nu(1+\gamma^5)b|\Lambda_b(p)\rangle\bar{\ell}\gamma^\mu\ell], \end{aligned} \quad (8)$$

where  $C_9^{\text{tot}} = C_9^{\text{eff}} + \Lambda_{sb}C_9^{Z'}$  and  $C_{10}^{\text{tot}} = C_{10}^{\text{SM}} + \Lambda_{sb}C_{10}^{Z'}$ , with  $C_9^{\text{eff}}$  defined in Eq. (3).

### 3. Helicity amplitudes and form factors for $\Lambda_b \rightarrow \Lambda$ transitions

The matrix elements for the  $\Lambda_b \rightarrow \Lambda$  transition for different possible currents can be straightforwardly parameterized in terms of the form factors. The helicity formalism provides a convenient way to describe these transformations. The helicity amplitudes  $H^i(s_1, s_2)$  with  $i$  corresponding to



vector ( $V$ ), axial-vector ( $A$ ), tensor ( $T$ ), and axial-tensor ( $T_5$ ) currents can be written as [48]

$$\begin{aligned}
 H^V(s_1, s_2) &\equiv \epsilon_\mu^*(\lambda) \langle \Lambda(p_2, s_2) | \bar{s} \gamma^\mu b | \Lambda_b(p_1, s_1) \rangle \\
 &= f_0(s) \frac{m_{\Lambda_b} - m_\Lambda}{\sqrt{s}} [\bar{u}(p_2, s_2) u(p_1, s_1)] \\
 &\quad + 2f_+(s) \frac{m_{\Lambda_b} + m_\Lambda}{s_+} (p_2 \cdot \epsilon^*(0)) [\bar{u}(p_2, s_2) u(p_1, s_1)] \\
 &\quad + f_\perp(s) [\bar{u}(p_2, s_2) \not{\epsilon}^*(\pm) u(p_1, s_1)], \tag{9}
 \end{aligned}$$

$$\begin{aligned}
 H^A(s_1, s_2) &\equiv \epsilon_\mu^*(\lambda) \langle \Lambda(p_2, s_2) | \bar{s} \gamma^\mu \gamma_5 b | \Lambda_b(p_1, s_1) \rangle \\
 &= -g_0(s) \frac{m_{\Lambda_b} + m_\Lambda}{\sqrt{s}} [\bar{u}(p_2, s_2) \gamma_5 u(p_1, s_1)] \\
 &\quad - 2g_+(s) \frac{m_{\Lambda_b} - m_\Lambda}{s_-} (p_2 \cdot \epsilon^*(0)) [\bar{u}(p_2, s_2) \gamma_5 u(p_1, s_1)] \\
 &\quad + g_\perp(s) [\bar{u}(p_2, s_2) \not{\epsilon}^*(\pm) \gamma_5 u(p_1, s_1)], \tag{10}
 \end{aligned}$$

$$\begin{aligned}
 H^T(s_1, s_2) &\equiv \epsilon_\mu^*(\lambda) \langle \Lambda(p_2, s_2) | \bar{s} i \sigma^{\mu\nu} q_\nu b | \Lambda_b(p_1, s_1) \rangle \\
 &= -2h_+(s) \frac{s}{s_+} (p_2 \cdot \epsilon^*(0)) [\bar{u}(p_2, s_2) u(p_1, s_1)] \\
 &\quad - h_\perp(s) (m_{\Lambda_b} + m_\Lambda) [\bar{u}(p_2, s_2) \not{\epsilon}^*(\pm) u(p_1, s_1)], \tag{11}
 \end{aligned}$$

$$\begin{aligned}
 H^{T_5}(s_1, s_2) &\equiv \epsilon_\mu^*(\lambda) \langle \Lambda(p_2, s_2) | \bar{s} i \sigma^{\mu\nu} q_\nu \gamma_5 b | \Lambda_b(p_1, s_1) \rangle \\
 &= -2\tilde{h}_+(s) \frac{s}{s_-} (p_2 \cdot \epsilon^*(0)) [\bar{u}(p_2, s_2) \gamma_5 u(p_1, s_1)] \\
 &\quad + \tilde{h}_\perp(s) (m_{\Lambda_b} - m_\Lambda) [\bar{u}(p_2, s_2) \not{\epsilon}^*(\pm) \gamma_5 u(p_1, s_1)], \tag{12}
 \end{aligned}$$

where  $p_1(s_1)$  and  $p_2(s_2)$  are the momentum (spin) of  $\Lambda_b$  and  $\Lambda$ , respectively. The dilepton polarization vector is written as  $\epsilon_\mu^*(\lambda)$  with  $\lambda = t, 0, \pm$ ; their explicit definitions are given in Ref. [48] and summarized in the appendix.

In Eqs. (9)–(12), the functions  $f_i(s)$ ,  $g_i(s)$ ,  $h_i(s)$ , and  $\tilde{h}_i(s)$  with  $i = 0, +, \perp$  are the transition form factors. In the heavy quark spin symmetry, the symmetry where the spin of a spectator diquark remains the same in the initial and final states, the number of form factors is reduced. The tensor form factors can be written in terms of vector and axial-vector form factors, and with this symmetry we can also equate the longitudinal and transverse form factors. Thus it reduces the number of independent form factors to two, i.e., the Isgur–Wise relations  $\xi_1$  and  $\xi_2$ ; the form factors being the non-perturbative quantities needed to be calculated in some model. In the decay under consideration here, we will use the form factors that are calculated in lattice QCD with much better control on the various uncertainties. In the full dilepton mass squared range these can be expressed as [89]

$$f(s) = \frac{d_0^f + d_1^f z(s) + d_2^f (z(s))^2}{1 - s/(m_{\text{pole}}^f)^2}, \tag{13}$$

where the inputs  $d_0^f$ ,  $d_1^f$ , and  $d_2^f$  are summarized in Tables 1 and 2. The parameter  $z$  is defined as [89]

$$z(s) = \frac{\sqrt{t_+ - s} - \sqrt{t_+ - t_0}}{\sqrt{t_+ - s} + \sqrt{t_+ - t_0}}, \tag{14}$$

with  $t_0 = (m_{\Lambda_b} - m_\Lambda)^2$  and  $t_+ = (m_B + m_K)^2$ .

**Table 1.** The values of form factors along with uncertainties calculated in the framework of lattice QCD with  $(2 + 1)$ -flavor dynamics for the  $\Lambda_b \rightarrow \Lambda$  transition [89].

Parameter	Input	Parameter	Input	Parameter	Input
$a_0^{f_+}$	$0.4229 \pm 0.0274$	$a_1^{f_+}$	$-1.3728 \pm 0.3068$	$a_2^{f_+}$	$107972 \pm 1.1506$
$a_0^{f_0}$	$0.3604 \pm 0.0277$	$a_1^{f_0}$	$-0.9284 \pm 0.3453$	$a_2^{f_0}$	$0.9861 \pm 1.1988$
$a_0^{f_\perp}$	$0.5748 \pm 0.0353$	$a_1^{f_\perp}$	$-1.4781 \pm 0.4030$	$a_2^{f_\perp}$	$1.2496 \pm 1.6396$
$a_0^{g_+}$	$0.3522 \pm 0.0205$	$a_1^{g_+}$	$-1.2968 \pm 0.2732$	$a_2^{g_+}$	$2.7106 \pm 1.0665$
$a_0^{g_0}$	$0.4059 \pm 0.0267$	$a_1^{g_0}$	$-1.1622 \pm 0.2929$	$a_2^{g_0}$	$1.1490 \pm 1.0327$
$a_0^{g_\perp}$	$0.3522 \pm 0.0205$	$a_1^{g_\perp}$	$-1.3607 \pm 0.2949$	$a_2^{g_\perp}$	$2.4621 \pm 1.3711$
$a_0^{h_+}$	$0.4753 \pm 0.0423$	$a_1^{h_+}$	$-0.8840 \pm 0.3997$	$a_2^{h_+}$	$-0.8190 \pm 1.6760$
$a_0^{h_\perp}$	$0.3745 \pm 0.0313$	$a_1^{h_\perp}$	$-0.9439 \pm 0.2766$	$a_2^{h_\perp}$	$1.1606 \pm 1.0757$
$a_0^{\tilde{h}_+}$	$0.3256 \pm 0.0248$	$a_1^{\tilde{h}_+}$	$-0.9603 \pm 0.2303$	$a_2^{\tilde{h}_+}$	$2.9780 \pm 1.0041$
$a_0^{\tilde{h}_\perp}$	$0.3256 \pm 0.0248$	$a_1^{\tilde{h}_\perp}$	$-0.9634 \pm 0.2268$	$a_2^{\tilde{h}_\perp}$	$2.4782 \pm 0.9549$

**Table 2.** Pole masses for different form factors [89].

$f$	$J^P$	$m_{\text{pole}}^f$
$f_0$	$0^+$	5.711
$f_+, f_\perp, h_+, h_\perp$	$1^-$	5.416
$g_0$	$0^-$	5.367
$g_+, g_\perp, \tilde{h}_+, \tilde{h}_\perp$	$1^+$	5.750

#### 4. Angular distribution and physical observables

The four-folded angular distribution of the four-body  $\Lambda_b \rightarrow \Lambda(\rightarrow p\pi)\mu^+\mu^-$  decay, with an unpolarized  $\Lambda_b$ , can be written in terms of  $K_{l,m}$ , where  $l$  and  $m$  denote the relative angular momentum and its third component for  $p\pi$  and  $\mu^+\mu^-$  systems, respectively, as [48]

$$\frac{d^4\Gamma}{ds d \cos \theta_\Lambda d \cos \theta_\ell d \phi} = \frac{3}{8\pi} \left[ K_{1s's'} \sin^2 \theta_\ell + K_{1cc} \cos^2 \theta_\ell + K_{1c} \cos \theta_\ell \right. \\ \left. + (K_{2s's'} \sin^2 \theta_\ell + K_{2cc} \cos^2 \theta_\ell + K_{2c} \cos \theta_\ell) \cos \theta_\Lambda \right. \\ \left. + (K_{3s'c} \sin \theta_\ell \cos \theta_\ell + K_{3s'} \sin \theta_\ell) \sin \theta_\Lambda \sin \phi \right. \\ \left. + (K_{4s'c} \sin \theta_\ell \cos \theta_\ell + K_{4s'} \sin \theta_\ell) \sin \theta_\Lambda \cos \phi \right]. \quad (15)$$

In Eq. (15),  $\theta_\ell$  and  $\theta_\Lambda$  are the helicity angles,  $\phi$  is the azimuthal angle, and  $s$  is the dilepton mass squared (see also Fig. 1). The different kinematic relations are defined in Ref. [48]. The different angular coefficients correspond to the particular values of  $(l, m)$ : e.g., the coefficients of  $\cos^2 \theta_\ell$ ,  $\sin^2 \theta_\ell$ , and  $\cos \theta_\ell$  correspond to  $K_{0,0}$ , whereas the coefficients of  $\cos^2 \theta_\ell \cos \theta_\Lambda$ ,  $\sin^2 \theta_\ell \cos \theta_\Lambda$ , and  $\cos \theta_\ell \cos \theta_\Lambda$  correspond to  $K_{1,0}$  and the last four terms correspond to  $K_{1,1}$ . These angular parameters  $K_{ij}$ , where  $i = 1, \dots, 4$  and  $j = s's', cc, c, s'c, s'$  are functions of the square of momentum transfer  $s$ . In terms of the transversity amplitudes, their explicit expressions are summarized in the appendix.

From the four-fold angular decay distribution, a number of physical observables can be obtained after integrating on different parameters among  $\theta_\ell$ ,  $\theta_\Lambda$ ,  $\phi$ , and  $s$ .

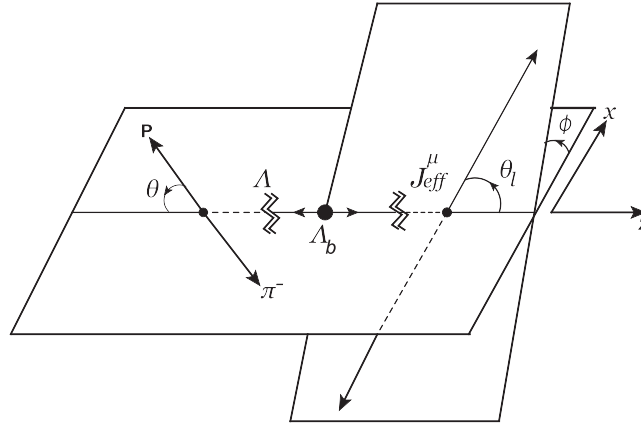


**Fig. 1.**  $\Lambda_b \rightarrow \Lambda(\rightarrow p\pi)\mu^+\mu^-$  decay topology, where  $\theta_\ell, \theta = \theta_\Lambda$  are the helicity angles and  $\phi$  is the azimuthal angle.

#### 4.1. Differential decay rate and different asymmetry parameters

One of the most important observables, from both the theoretical and experimental points of view, is the differential decay distribution. By integrating over  $\theta_\ell \in [0, \pi]$ ,  $\theta_\Lambda \in [0, \pi]$ , and  $\phi \in [0, 2\pi]$ , the expression for the differential decay rate becomes

$$\frac{d\Gamma}{ds} = K_{1cc} + 2K_{1s's'}. \tag{16}$$

In addition to the decay rate, we can extract a number of asymmetry parameters that correspond to different angles and they can be separated out by doing different integrations one by one. For example, by integrating on  $\theta_\ell \in [0, \pi]$  and  $\phi \in [0, 2\pi]$ , the expression for the differential decay rate takes the form

$$\frac{d\Gamma}{dsd \cos \theta_\Lambda} = (K_{1cc} + 2K_{1s's'})[1 + \alpha_{\theta_\Lambda} \cos \theta_\Lambda], \tag{17}$$

where  $\alpha_{\theta_\Lambda}$  is the asymmetry parameter for the longitudinal polarization of the  $\Lambda$  baryon. It can be noticed that if we integrate Eq. (17) on  $\theta_\Lambda \in [0, \pi]$ , we get back Eq. (16). In terms of the helicity parameters  $K_{ij}$ , the asymmetry parameter  $\alpha_{\theta_\Lambda}$  can be expressed as follows:

$$\alpha_{\theta_\Lambda} = \frac{\tilde{K}_{2cc} + 2\tilde{K}_{2s's'}}{K_{1cc} + 2K_{1s's'}}, \tag{18}$$

with  $\tilde{K}_{ij} = \frac{K_{ij}}{\alpha_\Lambda}$ . Here,  $\alpha_\Lambda$  is the asymmetry parameter corresponding to the parity-violating  $\Lambda \rightarrow p\pi^-$  decay, and its experimental value is  $\alpha_\Lambda = 0.642 \pm 0.013$  [151].

Similarly, by performing an integration on  $\theta_\Lambda \in [0, \pi]$  and  $\phi \in [0, 2\pi]$  and leaving the angle  $\theta_\ell$ , we will have asymmetries corresponding to the angle  $\theta_\ell$ . In terms of  $\alpha_{\theta_\ell}$  and  $\alpha'_{\theta_\ell}$ , the differential decay rate can be formulated as

$$\frac{d\Gamma}{dsd \cos \theta_\ell} = K_{1s's'}[1 + \alpha_{\theta_\ell} \cos^2 \theta_\ell + \alpha'_{\theta_\ell} \cos \theta_\ell], \tag{19}$$

with

$$\alpha_{\theta_\ell} = \frac{K_{1cc} - K_{1s's'}}{K_{1s's'}}, \quad \alpha'_{\theta_\ell} = \frac{K_{1c}}{K_{1s's'}}. \tag{20}$$

On the same lines, if we perform integration on the helicity angles  $\theta_\ell \in [0, \pi]$  and  $\theta_\Lambda \in [0, \pi]$ , Eq. (15) can be written in terms of asymmetries corresponding to the angle  $\phi$  as

$$\frac{d\Gamma}{dsd\phi} = (K_{1cc} + 2K_{1s's'})[1 + \alpha_\phi \cos \phi + \alpha'_\phi \sin \phi], \quad (21)$$

where

$$\alpha_\phi = \frac{3\pi^2 \tilde{K}_{4s'}}{16(K_{1cc} + 2K_{1s's'})}, \quad \alpha'_\phi = \frac{3\pi^2 \tilde{K}_{3s'}}{16(K_{1cc} + 2K_{1s's'})}. \quad (22)$$

From Eq. (15), the  $s$  dependence of the transverse ( $\alpha_U$ ) and longitudinal ( $\alpha_L$ ) asymmetry parameters is written in the following form [147]:

$$\alpha_U = \frac{\tilde{K}_{2cc}}{K_{1cc}}, \quad \alpha_L = \frac{\tilde{K}_{2s's'}}{K_{1s's'}}. \quad (23)$$

Even though one of the important observables is the decay rate, it is affected by the uncertainties arising from different input parameters, where the major contributors are the form factors. It is a well-established fact that the zero position of the forward–backward asymmetry in the different semi-leptonic decays of the  $B$ -meson have a minimal dependence on the form factors [148–150]. Based on these observations the different forward–backward asymmetries are exploited in the  $\Lambda_b$  decays [48–50, 75, 76]. The forward–backward asymmetries corresponding to the lepton angle  $\theta_\ell$  is defined as  $A_{\text{FB}}^\ell = (F - B)/(F + B)$ . Similarly, the hadron-side forward–backward asymmetry, i.e., the asymmetry corresponding to the hadronic angle  $\theta_\Lambda$ , is  $A_{\text{FB}}^\Lambda = (F - B)/(F + B)$ . In both cases,  $F$  and  $B$  are the forward and backward hemispheres, respectively. From Eq. (15), these forward–backward asymmetries become

$$A_{\text{FB}}^\ell = \frac{3K_{1c}}{4K_{1s's'} + 2K_{1cc}}, \quad A_{\text{FB}}^\Lambda = \frac{2K_{2s's'} + K_{2cc}}{4K_{1s's'} + 2K_{1cc}}. \quad (24)$$

We take this opportunity to mention that in the case of the  $\Lambda_b \rightarrow \Lambda(\rightarrow p\pi)\mu^+\mu^-$  decay, the sequential decay  $\Lambda \rightarrow p\pi$  is parity violating. Therefore, the helicity components with the polarizations of the proton being  $\pm\frac{1}{2}$  are not the same, and hence the hadron-side forward–backward asymmetry is non-zero in these  $b$ -baryon decays. This is contrary to what we have seen in the  $B \rightarrow K^*(\rightarrow K\pi)\mu^+\mu^-$  decay. In addition to this, the combined lepton–hadron forward–backward asymmetry can be expressed as

$$A_{\text{FB}}^{\ell\Lambda} = \frac{3K_{2c}}{8K_{1s's'} + 4K_{1cc}}. \quad (25)$$

According to the experimental point of view, the other interesting observables are the fractions of longitudinal ( $F_L$ ) and transverse ( $F_T$ ) polarized dimuons in  $\Lambda_b \rightarrow \Lambda\mu^+\mu^-$  decay, and these have already been measured in different bins by the LHCb Collaboration [153]. In order to achieve the mathematical formula for these helicity fractions we have to integrate the four-folded differential decay rate given in Eq. (15) on  $\theta_\Lambda \in [0, \pi]$  and  $\phi \in [0, 2\pi]$ . Their explicit expressions in terms of  $K_{ij}$  are

$$F_T = \frac{2K_{1cc}}{2K_{1s's'} + K_{1cc}}, \quad F_L = 1 - F_T = \frac{2K_{1s's'} - K_{1cc}}{2K_{1s's'} + K_{1cc}}. \quad (26)$$

**Table 3.** Foldings required for  $\mathcal{P}_i$  for which  $\theta_\Lambda \in [0, \frac{\pi}{2}]$ ,  $\theta_\ell \in [0, \frac{\pi}{2}]$ , and  $\phi$  vary in different ranges corresponding to different observables [15].

Sr. no.	Folding	$\phi$ range
1	$d\Gamma(\phi, \theta_\ell, \theta_\Lambda) + d\Gamma(\phi - \pi, \theta_\ell, \theta_\Lambda)$	$[0, \pi]$
2	$d\Gamma(\phi, \theta_\ell, \theta_\Lambda) + d\Gamma(\phi, \theta_\ell, \pi - \theta_\Lambda) + d\Gamma(-\phi, \pi - \theta_\ell, \theta_\Lambda) + d\Gamma(-\phi, \pi - \theta_\ell, \pi - \theta_\Lambda)$	$[0, \pi]$
3	$d\Gamma(\phi, \theta_\ell, \theta_K) + d\Gamma(\phi, \theta_\ell, \pi - \theta_\Lambda) + d\Gamma(-\phi, \theta_\ell, \theta_\Lambda) + d\Gamma(-\phi, \theta_\ell, \pi - \theta_\Lambda)$	$[0, \pi]$
4	$d\Gamma(\phi, \theta_\ell, \theta_\Lambda) + d\Gamma(\phi, \theta_\ell, \pi - \theta_\Lambda) + d\Gamma(\phi, \pi - \theta_\ell, \theta_\Lambda) + d\Gamma(\phi, \pi - \theta_\ell, \pi - \theta_\Lambda)$	$[0, \pi]$
5	$d\Gamma(\phi, \theta_\ell, \theta_\Lambda) + d\Gamma(-\phi, \theta_\ell, \theta_\Lambda) + d\Gamma(\phi, \pi - \theta_\ell, \pi - \theta_\Lambda) + d\Gamma(-\phi, \pi - \theta_\ell, \pi - \theta_\Lambda)$	$[0, \pi]$
6	$d\Gamma(\phi, \theta_\ell, \theta_\Lambda) + d\Gamma(-\phi, \theta_\ell, \theta_\Lambda) + d\Gamma(\phi, \pi - \theta_\ell, \theta_\Lambda) + d\Gamma(-\phi, \pi - \theta_\ell, \theta_\Lambda)$	$[0, \pi]$
7	$d\Gamma(\phi, \theta_\ell, \theta_\Lambda) + d\Gamma(\pi - \phi, \theta_\ell, \theta_\Lambda) + d\Gamma(\phi, \pi - \theta_\ell, \theta_\Lambda) + d\Gamma(\pi - \phi, \pi - \theta_\ell, \theta_\Lambda)$	$[-\pi/2, \pi/2]$
8	$d\Gamma(\phi, \theta_\ell, \theta_\Lambda) + d\Gamma(\pi - \phi, \theta_\ell, \theta_\Lambda) + d\Gamma(\phi, \pi - \theta_\ell, \pi - \theta_\Lambda) + d\Gamma(\pi - \phi, \pi - \theta_\ell, \pi - \theta_\Lambda)$	$[-\pi/2, \pi/2]$

### 4.2. Decay foldings and angular coefficients

The four-fold decay distribution defined in Eq. (15) gives us a chance to single out the different physical observables by studying different foldings. In semi-leptonic  $B$ -meson decays, such foldings have been studied in detail, especially the penguin asymmetries  $\mathcal{P}$ , where  $\mathcal{P}_5^{(\prime)}$  is the most important [15]. On the same lines, by using the foldings defined in Table 3, corresponding to different variations of azimuthal angle  $\phi$ , while taking  $\theta_\ell \in [0, \frac{\pi}{2}]$  and  $\theta_\Lambda \in [0, \frac{\pi}{2}]$ , these foldings can be expressed in terms of different angular coefficients as:

$$\begin{aligned}
 \frac{d\Gamma_1}{\widehat{\Gamma}} &= \frac{3}{8\pi} \left[ 2 \frac{K_{1cc}}{\widehat{\Gamma}} + \mathcal{P}_1 \sin^2 \theta_\ell + \frac{1}{2} \mathcal{P}_9 \cos \theta_\Lambda + \mathcal{P}_2 \sin^2 \theta_\ell \cos \theta_\Lambda + \frac{1}{2} \mathcal{P}_8 \cos \theta_\ell + \mathcal{P}_3 \cos \theta_\ell \cos \theta_\Lambda \right], \\
 \frac{d\Gamma_2}{\widehat{\Gamma}} &= \frac{3}{8\pi} \left[ 4 \frac{K_{1cc}}{\widehat{\Gamma}} + 2\mathcal{P}_1 \sin^2 \theta_\ell + \mathcal{P}_6 \sin \theta_\ell \sin \theta_\Lambda \cos \phi + 2\mathcal{P}_4 \sin \theta_\ell \cos \theta_\ell \sin \theta_\Lambda \sin \phi \right], \\
 \frac{d\Gamma_3}{\widehat{\Gamma}} &= \frac{3}{8\pi} \left[ 4 \frac{K_{1cc}}{\widehat{\Gamma}} + 2\mathcal{P}_1 \sin^2 \theta_\ell + \mathcal{P}_6 \sin \theta_\ell \sin \theta_\Lambda \cos \phi + 2\mathcal{P}_5 \sin \theta_\ell \cos \theta_\ell \sin \theta_\Lambda \cos \phi + \mathcal{P}_8 \cos \theta_\ell \right], \\
 \frac{d\Gamma_4}{\widehat{\Gamma}} &= \frac{3}{8\pi} \left[ 4 \frac{K_{1cc}}{\widehat{\Gamma}} + 2\mathcal{P}_1 \sin^2 \theta_\ell + \mathcal{P}_6 \sin \theta_\ell \sin \theta_\Lambda \cos \phi + \mathcal{P}_7 \sin \theta_\ell \sin \theta_\Lambda \sin \phi \right], \\
 \frac{d\Gamma_5}{\widehat{\Gamma}} &= \frac{3}{8\pi} \left[ 4 \frac{K_{1cc}}{\widehat{\Gamma}} + 2\mathcal{P}_1 \sin^2 \theta_\ell + \mathcal{P}_6 \sin \theta_\ell \sin \theta_\Lambda \cos \phi + 2\mathcal{P}_3 \cos \theta_\ell \cos \theta_\Lambda \right], \\
 \frac{d\Gamma_6}{\widehat{\Gamma}} &= \frac{3}{8\pi} \left[ 4 \frac{K_{1cc}}{\widehat{\Gamma}} + 2\mathcal{P}_1 \sin^2 \theta_\ell + \mathcal{P}_9 \cos \theta_\Lambda + 2\mathcal{P}_2 \sin^2 \theta_\ell \cos \theta_\Lambda + \mathcal{P}_6 \sin \theta_\ell \sin \theta_\Lambda \cos \phi \right]. \tag{27}
 \end{aligned}$$

The following things can be noticed from Eq. (27):

- The coefficients of  $\sin^2 \theta_\ell$  and  $\sin^2 \theta_\ell \cos \theta_\Lambda$  correspond to the angular coefficients named as  $\mathcal{P}_1$  and  $\mathcal{P}_2$ , respectively.
- The coefficient of  $\cos \theta_\ell \cos \theta_\Lambda$  corresponds to the angular coefficient  $\mathcal{P}_3$ , and that of  $\sin \theta_\ell \cos \theta_\ell \sin \theta_\Lambda \sin \phi$  is  $\mathcal{P}_4$ .
- $\mathcal{P}_5$  is the coefficient of  $\sin \theta_\ell \cos \theta_\ell \sin \theta_\Lambda \cos \phi$ , whereas  $\mathcal{P}_6$  is the coefficient of  $\sin \theta_\ell \sin \theta_\Lambda \cos \phi$ .
- $\mathcal{P}_7$ ,  $\mathcal{P}_8$ , and  $\mathcal{P}_9$  are the coefficients of  $\sin \theta_\ell \sin \theta_\Lambda \sin \phi$ ,  $\cos \theta_\ell$ , and  $\cos \theta_\Lambda$ , respectively.

In terms of the different helicity components, the angular coefficients  $\mathcal{P}_i$ ,  $i = 1, \dots, 9$  are

$$\begin{aligned} \mathcal{P}_1 &= \frac{2}{\widehat{\Gamma}} (K_{1ss} - K_{1cc}), & \mathcal{P}_2 &= \frac{2}{\widehat{\Gamma}} (K_{2ss} - K_{2cc}), & \mathcal{P}_3 &= \frac{2K_{2c}}{\widehat{\Gamma}}, \\ \mathcal{P}_4 &= \frac{2K_{3sc}}{\widehat{\Gamma}}, & \mathcal{P}_5 &= \frac{2K_{4sc}}{\widehat{\Gamma}}, & \mathcal{P}_6 &= \frac{4K_{4s}}{\widehat{\Gamma}}, \\ \mathcal{P}_7 &= \frac{4K_{3s}}{\widehat{\Gamma}}, & \mathcal{P}_8 &= \frac{4K_{1c}}{\widehat{\Gamma}}, & \mathcal{P}_9 &= \frac{4K_{2cc}}{\widehat{\Gamma}}, \end{aligned} \quad (28)$$

where  $\widehat{\Gamma} = \frac{d\Gamma}{ds}$ . It is worth mentioning that while obtaining the different  $\mathcal{P}_i$  we have used the first six foldings defined in Table 3, because the last two foldings do not add any new observable.

In order to compare the results with some of the experimentally measured observables and to propose possible candidates that might be useful to establish new physics, the interesting quantities are the normalized fractions calculated in different bins of the square of the dimuon momentum, i.e.,  $s = q^2$ . The normalized branching ratio, various asymmetry observables, and different angular coefficients can be calculated as

$$\langle X \rangle = \frac{\int_{s_{\min}}^{s_{\max}} X ds}{\int_{s_{\min}}^{s_{\max}} \left( \frac{d\Gamma}{ds} \right) ds}. \quad (29)$$

## 5. Numerical analysis

In this section we discuss the numerical results obtained for the different observables defined in Sect. 4 in both the standard and  $Z'$  models for the  $\Lambda_b \rightarrow \Lambda(\rightarrow p\pi)\mu^+\mu^-$  decay. In  $\Lambda_b \rightarrow \Lambda$  decays, the final state  $\Lambda \rightarrow p\pi^-$  is a parity-violating decay and the corresponding asymmetry parameter ( $\alpha_\Lambda$ ) has been measured experimentally [151]. This is really helpful in disentangling the direct  $\Lambda_b \rightarrow p\pi^-\mu^+\mu^-$  from the one that occurs through the intermediate  $\Lambda$  decay that subsequently decays to  $p\pi^-$ . This is contrary to  $B \rightarrow K^*(\rightarrow K\pi)\mu^+\mu^-$  decay, where the final-state  $K^*$  meson decays to  $K\pi$  via the strong interaction. Therefore, the angular analysis of  $\Lambda_b \rightarrow \Lambda(\rightarrow p\pi^-\mu^+\mu^-)$  decay is quite interesting from both theoretical and experimental points of view [48,49]. In addition to the input parameters given above, the other important ingredient in the numerical calculations in  $\Lambda_b$  decays is the form factors. In the numerical calculation, we will use one of the most accurately calculated form factors at the QCD lattice [89] with 2+1-flavor dynamics (cf. Table 1) along with the next-to-next-to-leading (NNLL) corrections to the form factors for the SM that are given in [141,152].

In addition to the form factors, the numerical values of the other input parameters that correspond to the standard and  $Z'$  models are given in Tables 4 and 5, respectively. Using these values a quantitative analysis of the above-calculated observables in various bins of  $s$  is presented in Tables 6, 7, and 8. In the whole analysis, we have observed that the results are not sensitive to the different scenarios of the  $Z'$  model; therefore, we have used only the scenario  $\mathcal{S}_1$  to generate the results in various bins of  $s$ .

The first observable that is of prime interest from both theoretical and experimental points of view is the branching ratio in different bins of  $s$  that can be set up by the experimentalists. From Eq. (16), in a bin  $s \in [1.1, 6] \text{ GeV}^2$  (large-recoil) the average value of the branching ratio in the SM and  $Z'$

**Table 4.** Numerical values of the different input parameters corresponding to the SM [89,151]. The Wilson coefficients are given at the scale  $\mu_b = 4.2$  GeV to NNLL accuracy in the SM [155].

$G_F$	$1.16638 \times 10^{-5}$	$\alpha_s(m_Z)$	0.1182	$m_b^{\text{pole}}$	4.78
$\mu$	4.2	$m_Z$	91.1876	$\alpha_e$	$\frac{1}{128}$
$m_\pi$	0.135	$m_K$	0.494	$m_{\Lambda_b}$	5.619
$m_B$	5.279	$V_{tb}V_{ts}^*$	0.04152	$m_\Lambda$	1.116
$\tau_{\Lambda_b}$	1.466ps	$\alpha_\Lambda$	0.64	$C_1$	-0.294
$C_2$	1.017	$C_3$	-0.0059	$C_4$	-0.087
$C_5$	0.0004	$C_6$	0.001	$C_7$	-0.324
$C_8$	-0.176	$C_9$	4.114	$C_{10}$	-4.193

**Table 5.** Numerical values of the parameters corresponding to the different scenarios of the  $Z'$  model [139,140].

	$ \mathcal{B}_{sb}  \times 10^{-3}$	$\phi_{sb}$ (degrees)	$S_{LL} \times 10^{-2}$	$D_{LL} \times 10^{-2}$
$\mathcal{S}_1$	$1.09 \pm 0.22$	$-72 \pm 7$	$-2.8 \pm 3.9$	$-6.7 \pm 2.6$
$\mathcal{S}_2$	$2.20 \pm 0.15$	$-82 \pm 4$	$-1.2 \pm 1.4$	$-2.5 \pm 0.9$
$\mathcal{S}_3$	$4.0 \pm 1.5$	$150 \pm 10$	0.8	-2.6

**Table 6.** Average values of different observables for  $\Lambda_b \rightarrow \Lambda(\rightarrow p\pi)\mu^+\mu^-$  in low- and large-recoil regions.

	$\langle\alpha_{\theta_\Lambda}\rangle$	$\langle\alpha'_{\theta_l}\rangle$	$\langle\alpha_{\theta_l}\rangle$	$\langle\alpha_\phi\rangle$	$\langle\alpha'_\phi\rangle$	$\langle\alpha_U\rangle$
[1, 6] SM	$-0.984^{+0.007}_{-0.001}$	$0.047^{+0.039}_{-0.016}$	$-0.854^{+0.024}_{-0.002}$	$0.040^{+0.070}_{-0.016}$	$0.000^{+0.000}_{-0.001}$	$-0.916^{+0.010}_{-0.004}$
[1, 6] $Z'$	$-0.390^{+0.027}_{-0.006}$	$0.027^{+0.001}_{-0.002}$	$-0.857^{+0.014}_{-0.001}$	$0.130^{+0.015}_{-0.060}$	$-0.002^{+0.001}_{-0.000}$	$-0.445^{+0.168}_{-0.040}$
[15, 20.25] SM	$-0.851^{+0.010}_{-0.007}$	$-0.280^{+0.012}_{-0.010}$	$-0.665^{+0.010}_{-0.014}$	$0.047^{+0.003}_{-0.004}$	$-0.056^{+0.001}_{-0.002}$	$-0.844^{+0.003}_{-0.002}$
[15, 20.25] $Z'$	$-0.427^{+0.001}_{-0.001}$	$-0.225^{+0.006}_{-0.004}$	$-0.485^{+0.008}_{-0.011}$	$0.448^{+0.004}_{-0.006}$	$-0.049^{+0.002}_{-0.002}$	$-0.307^{+0.002}_{-0.002}$
	$\langle\alpha_L\rangle$	$\langle d\mathcal{B}/ds \rangle \times 10^{-7}$	$\langle F_T \rangle$	$\langle F_L \rangle$	$\langle A_{FB}^{\ell\Lambda} \rangle$	$\langle \mathcal{P}_1 \rangle$
[1, 6] SM	$-0.989^{+0.006}_{-0.000}$	$0.466^{+0.760}_{-0.394}$	$0.136^{+0.021}_{-0.002}$	$0.864^{+0.002}_{-0.021}$	$-0.011^{+0.003}_{-0.006}$	$0.796^{+0.002}_{-0.031}$
[1, 6] $Z'$	$-0.386^{+0.016}_{-0.003}$	$0.709^{+0.115}_{-0.601}$	$0.134^{+0.012}_{-0.000}$	$0.866^{+0.000}_{-0.012}$	$-0.009^{+0.002}_{-0.003}$	$0.799^{+0.001}_{-0.018}$
[15, 20.25] SM	$-0.852^{+0.011}_{-0.008}$	$0.731^{0.198}_{0.187}$	$0.287^{+0.008}_{-0.010}$	$0.713^{+0.010}_{-0.008}$	$0.069^{+0.002}_{-0.002}$	$0.569^{+0.017}_{-0.009}$
[15, 20.25] $Z'$	$-0.458^{+0.001}_{-0.001}$	$1.179^{0.271}_{0.233}$	$0.410^{+0.005}_{-0.007}$	$0.590^{+0.007}_{-0.005}$	$0.087^{+0.001}_{-0.002}$	$0.386^{+0.010}_{-0.008}$
	$\langle \mathcal{P}_2 \rangle$	$\langle \mathcal{P}_3 \rangle$	$\langle \mathcal{P}_5 \rangle$	$\langle \mathcal{P}_6 \rangle$	$\langle \mathcal{P}_8 \rangle$	$\langle \mathcal{P}_9 \rangle$
[1, 6] SM	$0.512^{+0.001}_{-0.022}$	$-0.030^{+0.009}_{-0.015}$	$0.030^{+0.048}_{-0.013}$	$0.056^{+0.097}_{-0.023}$	$0.088^{+0.070}_{-0.032}$	$-0.160^{+0.001}_{-0.023}$
[1, 6] $Z'$	$0.193^{+0.001}_{-0.002}$	$-0.025^{+0.004}_{-0.009}$	$0.034^{+0.013}_{-0.004}$	$0.180^{+0.021}_{-0.083}$	$0.051^{+0.003}_{-0.003}$	$-0.076^{+0.024}_{-0.007}$
[15, 20.25] SM	$0.316^{+0.003}_{-0.002}$	$0.184^{+0.004}_{-0.007}$	$0.163^{+0.001}_{-0.000}$	$0.066^{+0.002}_{-0.007}$	$-0.480^{+0.020}_{-0.012}$	$-0.308^{+0.013}_{-0.008}$
[15, 20.25] $Z'$	$0.153^{+0.004}_{-0.003}$	$0.232^{+0.003}_{-0.004}$	$0.091^{+0.002}_{-0.001}$	$0.621^{+0.005}_{-0.008}$	$-0.359^{+0.007}_{-0.006}$	$-0.161^{+0.004}_{-0.003}$

model read

$$\begin{aligned} \langle \mathcal{B}r \rangle_{\text{SM}} &= (0.466^{+0.760}_{-0.394}) \times 10^{-7}, \\ \langle \mathcal{B}r \rangle_{Z'} &= (0.709^{+0.115}_{-0.601}) \times 10^{-7}, \end{aligned} \quad (30)$$

whereas the measured value at the LHCb experiment in this particular bin is [153]

$$\langle \mathcal{B}r \rangle_{\text{exp}} = (0.09^{+0.06}_{-0.05}) \times 10^{-7}. \quad (31)$$

**Table 7.** Numerical results for observables for the decay  $\Lambda_b \rightarrow \Lambda(\rightarrow p\pi)\mu^+\mu^-$  for the SM and  $Z'$  in appropriate bins.

		$\langle\alpha_{\theta_\Lambda}\rangle$	$\langle\alpha'_{\theta'_1}\rangle$	$\langle\alpha_{\theta_1}\rangle$	$\langle\alpha_\phi\rangle$	$\langle\alpha'_\phi\rangle$	$\langle\alpha_U\rangle$
[0.1, 2]	SM	$-0.970^{+0.012}_{-0.014}$	$0.140^{+0.001}_{-0.049}$	$-0.463^{+0.315}_{-0.049}$	$-0.058^{+0.129}_{-0.026}$	$0.002^{+0.000}_{-0.001}$	$-0.933^{+0.034}_{-0.051}$
	$Z'$	$-0.209^{+0.028}_{-0.005}$	$0.073^{+0.005}_{-0.042}$	$-0.265^{+0.191}_{-0.033}$	$-0.208^{+0.003}_{-0.001}$	$0.000^{+0.000}_{-0.000}$	$-0.063^{+0.001}_{-0.001}$
[1, 2]	SM	$-0.983^{+0.005}_{-0.002}$	$0.141^{+0.008}_{-0.013}$	$-0.788^{+0.223}_{-0.028}$	$-0.032^{+0.110}_{-0.020}$	$0.001^{+0.000}_{-0.001}$	$-0.932^{+0.036}_{-0.051}$
	$Z'$	$-0.318^{+0.054}_{-0.010}$	$0.086^{+0.003}_{-0.040}$	$-0.710^{+0.193}_{-0.030}$	$-0.137^{+0.020}_{-0.074}$	$0.000^{+0.000}_{-0.001}$	$-0.140^{+0.061}_{-0.024}$
[2, 4]	SM	$-0.987^{+0.006}_{-0.001}$	$0.076^{+0.048}_{-0.020}$	$-0.887^{+0.046}_{-0.001}$	$0.030^{+0.064}_{-0.013}$	$0.000^{+0.000}_{-0.001}$	$-0.923^{+0.007}_{-0.005}$
	$Z'$	$-0.397^{+0.040}_{-0.008}$	$0.046^{+0.001}_{-0.004}$	$-0.899^{+0.048}_{-0.003}$	$0.100^{+0.029}_{-0.120}$	$-0.001^{+0.000}_{-0.001}$	$-0.561^{+0.333}_{-0.088}$
[4, 6]	SM	$-0.984^{+0.012}_{-0.002}$	$-0.030^{+0.079}_{-0.028}$	$-0.858^{+0.016}_{-0.035}$	$0.086^{+0.046}_{-0.013}$	$-0.001^{+0.000}_{-0.001}$	$-0.908^{+0.110}_{-0.020}$
	$Z'$	$-0.423^{+0.023}_{-0.006}$	$-0.018^{+0.028}_{-0.011}$	$-0.892^{+0.014}_{-0.034}$	$0.308^{+0.022}_{-0.083}$	$-0.002^{+0.000}_{-0.001}$	$-0.754^{+0.060}_{-0.008}$
[6, 8]	SM	$-0.977^{+0.014}_{-0.004}$	$-0.128^{+0.075}_{-0.028}$	$-0.789^{+0.020}_{-0.049}$	$0.200^{+0.041}_{-0.014}$	$-0.002^{+0.000}_{-0.001}$	$-0.897^{+0.100}_{-0.023}$
	$Z'$	$-0.420^{+0.016}_{-0.005}$	$-0.078^{+0.034}_{-0.014}$	$-0.809^{+0.020}_{-0.050}$	$0.418^{+0.012}_{-0.038}$	$-0.002^{+0.000}_{-0.000}$	$-0.556^{+0.010}_{-0.000}$
[14, 16]	SM	$-0.922^{+0.002}_{-0.001}$	$-0.338^{+0.014}_{-0.009}$	$-0.596^{+0.008}_{-0.012}$	$0.114^{+0.007}_{-0.005}$	$-0.038^{+0.000}_{-0.000}$	$-0.851^{+0.009}_{-0.006}$
	$Z'$	$-0.409^{+0.004}_{-0.003}$	$-0.231^{+0.010}_{-0.006}$	$-0.482^{+0.008}_{-0.012}$	$0.484^{+0.000}_{-0.001}$	$-0.030^{+0.000}_{-0.001}$	$-0.321^{+0.006}_{-0.004}$
[16, 18]	SM	$-0.889^{+0.002}_{-0.001}$	$-0.312^{+0.007}_{-0.005}$	$-0.627^{+0.006}_{-0.008}$	$0.067^{+0.001}_{-0.001}$	$-0.052^{+0.000}_{-0.000}$	$-0.843^{+0.002}_{-0.002}$
	$Z'$	$-0.420^{+0.001}_{-0.001}$	$-0.235^{+0.004}_{-0.003}$	$-0.461^{+0.006}_{-0.008}$	$0.462^{+0.001}_{-0.002}$	$-0.044^{+0.000}_{-0.000}$	$-0.304^{+0.002}_{-0.002}$
[18, 20.25]	SM	$-0.747^{+0.010}_{-0.008}$	$-0.195^{+0.005}_{-0.004}$	$-0.767^{+0.006}_{-0.007}$	$-0.023^{+0.002}_{-0.003}$	$-0.072^{+0.002}_{-0.002}$	$-0.840^{+0.000}_{-0.000}$
	$Z'$	$-0.459^{+0.002}_{-0.002}$	$-0.198^{+0.002}_{-0.001}$	$-0.544^{+0.006}_{-0.007}$	$0.382^{+0.005}_{-0.006}$	$-0.078^{+0.003}_{-0.003}$	$-0.302^{+0.001}_{-0.001}$
		$\langle\alpha_L\rangle$	$\langle dB/ds\rangle \times 10^{-7}$	$\langle F_T\rangle$	$\langle F_L\rangle$	$\langle A_{FB}^{\ell\Lambda}\rangle$	$\langle \mathcal{P}_1\rangle$
[0.1, 2]	SM	$-0.980^{+0.008}_{-0.004}$	$0.251^{+0.451}_{-0.222}$	$0.424^{+0.174}_{-0.031}$	$0.576^{+0.031}_{-0.174}$	$-0.028^{+0.013}_{-0.001}$	$0.364^{+0.047}_{-0.260}$
	$Z'$	$-0.262^{+0.027}_{-0.004}$	$0.479^{+0.880}_{-0.430}$	$0.537^{+0.095}_{-0.018}$	$0.463^{+0.018}_{-0.095}$	$-0.021^{+0.008}_{-0.001}$	$0.194^{+0.027}_{-0.143}$
[1, 2]	SM	$-0.986^{+0.001}_{-0.003}$	$0.095^{+0.172}_{-0.084}$	$0.192^{+0.166}_{-0.023}$	$0.808^{+0.023}_{-0.166}$	$-0.034^{+0.009}_{-0.001}$	$0.711^{+0.035}_{-0.248}$
	$Z'$	$-0.344^{+0.036}_{-0.005}$	$0.158^{+0.283}_{-0.140}$	$0.253^{+0.136}_{-0.023}$	$0.747^{+0.023}_{-0.136}$	$-0.030^{+0.007}_{-0.000}$	$0.620^{+0.035}_{-0.203}$
[2, 4]	SM	$-0.991^{+0.006}_{-0.000}$	$0.178^{+0.302}_{-0.153}$	$0.107^{+0.040}_{-0.001}$	$0.893^{+0.001}_{-0.040}$	$-0.019^{+0.004}_{-0.008}$	$0.839^{+0.001}_{-0.061}$
	$Z'$	$-0.389^{+0.022}_{-0.004}$	$0.268^{+4.490}_{-0.231}$	$0.096^{+0.042}_{-0.003}$	$0.904^{+0.003}_{-0.042}$	$-0.017^{+0.002}_{-0.006}$	$0.856^{+0.005}_{-0.064}$
[4, 6]	SM	$-0.989^{+0.008}_{-0.001}$	$0.193^{+0.286}_{-0.157}$	$0.133^{+0.014}_{-0.031}$	$0.867^{+0.031}_{-0.014}$	$0.007^{+0.005}_{-0.015}$	$0.801^{+0.047}_{-0.021}$
	$Z'$	$-0.404^{+0.015}_{-0.004}$	$0.283^{+0.041}_{-0.229}$	$0.102^{+0.013}_{-0.031}$	$0.897^{+0.031}_{-0.013}$	$0.009^{+0.004}_{-0.012}$	$0.846^{+0.046}_{-0.019}$
[6, 8]	SM	$-0.986^{+0.009}_{-0.002}$	$0.220^{+0.275}_{-0.164}$	$0.191^{+0.016}_{-0.041}$	$0.809^{+0.041}_{-0.016}$	$0.031^{+0.005}_{-0.013}$	$0.714^{+0.061}_{-0.025}$
	$Z'$	$-0.407^{+0.013}_{-0.004}$	$0.325^{+0.040}_{-0.240}$	$0.175^{+0.016}_{-0.042}$	$0.825^{+0.042}_{-0.016}$	$0.034^{+0.003}_{-0.010}$	$0.738^{+0.063}_{-0.024}$
[14, 16]	SM	$-0.936^{+0.001}_{-0.001}$	$0.353^{+0.153}_{-0.127}$	$0.336^{+0.005}_{-0.008}$	$0.664^{+0.008}_{-0.005}$	$0.080^{+0.001}_{-0.002}$	$0.496^{+0.013}_{-0.006}$
	$Z'$	$-0.432^{+0.004}_{-0.002}$	$0.720^{+0.217}_{-0.178}$	$0.411^{+0.005}_{-0.008}$	$0.589^{+0.008}_{-0.005}$	$0.088^{+0.001}_{-0.002}$	$0.383^{+0.012}_{-0.008}$
[16, 18]	SM	$-0.896^{+0.002}_{-0.001}$	$0.328^{+0.095}_{-0.086}$	$0.315^{+0.004}_{-0.005}$	$0.685^{+0.005}_{-0.004}$	$0.076^{+0.001}_{-0.001}$	$0.528^{+0.011}_{-0.003}$
	$Z'$	$-0.451^{+0.001}_{-0.001}$	$0.562^{+0.129}_{-0.112}$	$0.424^{+0.004}_{-0.005}$	$0.576^{+0.005}_{-0.004}$	$0.090^{+0.001}_{-0.001}$	$0.363^{+0.008}_{-0.006}$
[18, 20.25]	SM	$-0.735^{+0.011}_{-0.009}$	$0.226^{+0.033}_{-0.042}$	$0.209^{+0.004}_{-0.005}$	$0.791^{+0.005}_{-0.004}$	$0.051^{+0.001}_{-0.001}$	$0.686^{+0.012}_{-0.002}$
	$Z'$	$-0.494^{+0.002}_{-0.002}$	$0.270^{+0.043}_{-0.040}$	$0.371^{+0.004}_{-0.004}$	$0.629^{+0.004}_{-0.004}$	$0.079^{+0.001}_{-0.001}$	$0.443^{+0.007}_{-0.005}$

By looking at Eqs. (30) and (31), we can say that the deviations from the measured value in this bin are quite large in the SM and even larger in the  $Z'$  model. One possible reason for such a large deviation is that the form factors are not very precisely calculated in this region. Contrary to this, the calculation of form factors is more precise in  $s \in [15, 20] \text{ GeV}^2$  (low-recoil). In this bin the average



**Table 8.** Average values of observables  $\mathcal{P}_i$ ,  $i = 2, \dots, 9$  (for real observables) for  $\Lambda_b \rightarrow \Lambda(\rightarrow p\pi)\mu^+\mu^-$  in appropriate bins.

	$\langle \mathcal{P}_2 \rangle$	$\langle \mathcal{P}_3 \rangle$	$\langle \mathcal{P}_5 \rangle$	$\langle \mathcal{P}_6 \rangle$	$\langle \mathcal{P}_8 \rangle$	$\langle \mathcal{P}_9 \rangle$
[0.1, 2] SM	$0.240^{+0.034}_{-0.176}$	$-0.076^{+0.036}_{-0.002}$	$-0.011^{+0.054}_{-0.014}$	$-0.079^{+0.178}_{-0.038}$	$0.221^{+0.003}_{-0.093}$	$-0.511^{+0.056}_{-0.247}$
[0.1, 2] $Z'$	$0.102^{+0.004}_{-0.024}$	$-0.056^{+0.021}_{-0.002}$	$0.019^{+0.005}_{-0.002}$	$-0.288^{+0.005}_{-0.001}$	$0.107^{+0.008}_{-0.065}$	$-0.043^{+0.001}_{-0.009}$
[1, 2] SM	$0.458^{+0.024}_{-0.166}$	$-0.090^{+0.024}_{-0.002}$	$0.001^{+0.057}_{-0.014}$	$-0.044^{+0.151}_{-0.029}$	$0.257^{+0.012}_{-0.048}$	$-0.231^{+0.036}_{-0.222}$
[1, 2] $Z'$	$0.170^{+0.004}_{-0.030}$	$-0.079^{+0.020}_{-0.001}$	$0.027^{+0.008}_{-0.003}$	$-0.191^{+0.028}_{-0.102}$	$0.150^{+0.007}_{-0.076}$	$-0.046^{+0.006}_{-0.003}$
[2, 4] SM	$0.539^{+0.001}_{-0.041}$	$-0.050^{+0.011}_{-0.020}$	$0.025^{+0.050}_{-0.012}$	$0.042^{+0.088}_{-0.019}$	$0.145^{+0.084}_{-0.039}$	$-0.126^{+0.000}_{-0.050}$
[2, 4] $Z'$	$0.202^{+0.001}_{-0.003}$	$-0.045^{+0.007}_{-0.015}$	$0.033^{+0.013}_{-0.004}$	$0.138^{+0.040}_{-0.167}$	$0.089^{+0.003}_{-0.006}$	$-0.069^{+0.028}_{-0.008}$
[4, 6] SM	$0.516^{+0.030}_{-0.013}$	$0.020^{+0.015}_{-0.041}$	$0.049^{+0.038}_{-0.010}$	$0.119^{+0.064}_{-0.018}$	$-0.055^{+0.149}_{-0.051}$	$-0.155^{+0.051}_{-0.020}$
[4, 6] $Z'$	$0.196^{+0.013}_{-0.005}$	$0.024^{+0.010}_{-0.031}$	$0.037^{+0.013}_{-0.004}$	$0.427^{+0.030}_{-0.115}$	$-0.034^{+0.053}_{-0.021}$	$-0.100^{+0.036}_{-0.011}$
[6, 8] SM	$0.463^{+0.041}_{-0.016}$	$0.082^{+0.014}_{-0.035}$	$0.067^{+0.027}_{-0.009}$	$0.166^{+0.057}_{-0.020}$	$-0.231^{+0.133}_{-0.049}$	$-0.220^{+0.066}_{-0.025}$
[6, 8] $Z'$	$0.176^{+0.014}_{-0.005}$	$0.089^{+0.009}_{-0.025}$	$0.040^{+0.010}_{-0.003}$	$0.579^{+0.016}_{-0.053}$	$-0.143^{+0.060}_{-0.024}$	$-0.125^{+0.032}_{-0.011}$
[14, 16] SM	$0.318^{+0.009}_{-0.005}$	$0.214^{+0.003}_{-0.006}$	$0.135^{+0.002}_{-0.001}$	$0.158^{+0.008}_{-0.008}$	$-0.564^{+0.022}_{-0.012}$	$-0.365^{+0.014}_{-0.007}$
[14, 16] $Z'$	$0.136^{+0.002}_{-0.002}$	$0.234^{+0.003}_{-0.004}$	$0.066^{+0.001}_{-0.000}$	$0.672^{+0.000}_{-0.001}$	$-0.368^{+0.013}_{-0.009}$	$-0.169^{+0.007}_{-0.004}$
[16, 18] SM	$0.317^{+0.005}_{-0.002}$	$0.202^{+0.002}_{-0.003}$	$0.163^{+0.000}_{-0.000}$	$0.090^{+0.002}_{-0.001}$	$-0.527^{+0.013}_{-0.005}$	$-0.338^{+0.008}_{-0.003}$
[16, 18] $Z'$	$0.146^{+0.002}_{-0.001}$	$0.240^{+0.002}_{-0.003}$	$0.085^{+0.000}_{-0.000}$	$0.641^{+0.002}_{-0.003}$	$-0.371^{+0.006}_{-0.004}$	$-0.165^{+0.003}_{-0.002}$
[18, 20.25] SM	$0.313^{+0.001}_{-0.002}$	$0.135^{+0.000}_{-0.005}$	$0.180^{+0.002}_{-0.003}$	$-0.032^{+0.001}_{-0.007}$	$-0.350^{+0.013}_{-0.002}$	$-0.222^{+0.009}_{-0.002}$
[18, 20.25] $Z'$	$0.187^{+0.002}_{-0.002}$	$0.210^{+0.002}_{-0.003}$	$0.127^{+0.000}_{-0.000}$	$0.531^{+0.007}_{-0.008}$	$-0.323^{+0.002}_{-0.002}$	$-0.143^{+0.001}_{-0.001}$

value of the branching ratio in the SM and  $Z'$  model become

$$\begin{aligned} \langle \mathcal{B}r \rangle_{\text{SM}} &= (0.731^{+0.198}_{-0.187}) \times 10^{-7}, \\ \langle \mathcal{B}r \rangle_{Z'} &= (1.179^{+0.271}_{-0.233}) \times 10^{-7}. \end{aligned} \quad (32)$$

The experimentally measured value in this bin is [153]

$$\langle \mathcal{B}r \rangle_{\text{exp}} = (1.20 \pm 0.25) \times 10^{-7}. \quad (33)$$

This can be reconciled because in this region, the deviations from the measured values are small compared to that of the large-recoil bin; in this case, the deviations are  $3.2\sigma$  and  $0.1\sigma$  in the SM and  $Z'$  model, respectively. Hence, the results of the branching ratio in the  $Z'$  model for the low-recoil bin look more promising when compared with the corresponding experimental value. In future, when we have more data from the LHCb experiment and Belle II, on one hand it will give us a chance to see possible hints of the extra neutral  $Z'$  boson and on the other hand it will help us to test the SM predictions with better accuracy.

It is a well-known fact that the branching ratio is prone to uncertainties arising due to the form factors. In order to cope with some of the uncertainties, there are observables such as the  $\Lambda$  baryon forward–backward asymmetry ( $A_{\text{FB}}^{\Lambda}$ ) and lepton forward–backward asymmetry ( $A_{\text{FB}}^{\ell}$ ) that are measured with respect to the baryon angle  $\theta_{\Lambda}$  and lepton angle  $\theta_{\ell}$ , respectively. The asymmetry  $A_{\text{FB}}^{\Lambda}$  can be expressed in terms of the ratio of a linear combination of the angular coefficients  $K_{2ss}$  and  $K_{2cc}$  to a linear combination of the angular coefficients  $K_{1ss}$  and  $K_{1cc}$ , as given in Eq. (24). Due to the change in the value of Wilson coefficient  $C_9$  in the  $Z'$  model,  $K_{2ss}$  and  $K_{2cc}$  get more contribution

as compared to  $K_{1ss}$  and  $K_{1cc}$ . Hence, this will result in significantly different values of  $\langle A_{\text{FB}}^{\Lambda} \rangle$  in the SM and  $Z'$  model. In the first large-recoil bin  $s \in [0.1, 2] \text{ GeV}^2$ , our results for  $\langle A_{\text{FB}}^{\Lambda} \rangle$  in the SM and  $Z'$  model are

$$\langle A_{\text{FB}}^{\Lambda} \rangle_{\text{SM}} = -0.311_{-0.001}^{+0.002}, \quad \langle A_{\text{FB}}^{\Lambda} \rangle_{Z'} = -0.067_{-0.002}^{+0.009},$$

whereas the experimental result in this bin is [153]

$$\langle A_{\text{FB}}^{\Lambda} \rangle_{\text{exp}} = -0.12_{-0.28}^{+0.31}.$$

It can be noticed that in comparison with the central values of the experimental measurements in  $s \in [0.1, 2] \text{ GeV}^2$ , the value of the  $Z'$  model is 1.8 times smaller, whereas the one in the SM is 2.5 times higher. In the low-recoil region ( $s \in [15, 20] \text{ GeV}^2$ ) the calculated values of  $\langle A_{\text{FB}}^{\Lambda} \rangle$  are

$$\langle A_{\text{FB}}^{\Lambda} \rangle_{\text{SM}} = -0.273_{-0.002}^{+0.003}, \quad \langle A_{\text{FB}}^{\Lambda} \rangle_{Z'} = -0.137_{-0.001}^{+0.001},$$

and the experimental value in this particular bin is [153]

$$\langle A_{\text{FB}}^{\Lambda} \rangle_{\text{exp}} = -0.29_{-0.07}^{+0.07}.$$

It can easily be seen that at low-recoil, the SM prediction is close to the experimentally measured value and the deviation is  $0.2 \sigma$ . The  $Z'$  value of  $\langle A_{\text{FB}}^{\Lambda} \rangle$  exceeds the experimental result by  $2.2 \sigma$ . From the above discussion, it is clear that in the first large-recoil bin both the SM and  $Z'$  model values deviate significantly from the experimental result for this bin, whereas at low-recoil the SM prediction is much closer to the experimental result compared with the  $Z'$  model. We hope that in the future, when more data comes from the LHCb, the results of measurements will become more concrete to compare with the SM and to see if the deviations can be accommodated with the  $Z'$  model.

Another observable which is clean from the QCD uncertainties and that has been experimentally measured is the lepton forward–backward asymmetry ( $A_{\text{FB}}^{\ell}$ ), which is an asymmetry with respect to the lepton scattering angle ( $\theta_l$ ); its mathematical expression is given in Eq. (24). Here, it can be noticed that  $\langle A_{\text{FB}}^{\ell} \rangle$  depends on the angular coefficient  $K_{1c}$  and its denominator is same as that of  $A_{\text{FB}}^{\Lambda}$ . The angular coefficient  $K_{1c}$  is higher for the SM than the  $Z'$  model for  $s < 4 \text{ GeV}^2$ , whereas its behavior reverses when  $s > 4 \text{ GeV}^2$ . For  $s < 4 \text{ GeV}^2$   $K_{1c}$  is dominated by  $C_9^{Z'}$ , whereas for  $s > 4 \text{ GeV}^2$  the terms containing  $C_7^{Z'}$  dominate over the one that contains  $C_9^{Z'}$ . Therefore,  $A_{\text{FB}}^{\ell}$  increases with  $s$  at the start of the large-recoil and then it starts decreasing and crosses the zero point at around  $4 \text{ GeV}^2$ . Our results for  $\langle A_{\text{FB}}^{\ell} \rangle$  in the SM and  $Z'$  model calculated in the experimentally set-up bin  $[0.1, 2] \text{ GeV}^2$  are

$$\langle A_{\text{FB}}^{\ell} \rangle_{\text{SM}} = 0.083_{-0.035}^{+0.001}, \quad \langle A_{\text{FB}}^{\ell} \rangle_{Z'} = 0.040_{-0.024}^{+0.003}.$$

The experimental value of  $\langle A_{\text{FB}}^{\ell} \rangle$  in the corresponding bin is [153]

$$\langle A_{\text{FB}}^{\ell} \rangle_{\text{exp}} = 0.37_{-0.48}^{+0.37}. \quad (34)$$

In Eq. (34), one can see that the errors are significant, and this is likely to improve with future data from LHCb. However, the current central values are significantly away from the SM and  $Z'$  values, respectively. In the low-recoil region ( $s \in [15, 20] \text{ GeV}^2$ ) the results for this asymmetry are

$$\langle A_{\text{FB}}^{\ell} \rangle_{\text{SM}} = -0.180_{-0.005}^{+0.007}, \quad \langle A_{\text{FB}}^{\ell} \rangle_{Z'} = -0.135_{-0.002}^{+0.003},$$

and for comparison the corresponding experimental value in this bin is

$$\langle A_{\text{FB}}^{\ell} \rangle_{\text{exp}} = -0.05_{-0.09}^{+0.09}.$$

It can be deduced that in this particular bin the average value of  $A_{\text{FB}}^{\ell}$  in  $Z'$  is comparable to the lower limit of the experimentally measured value, i.e.,  $-0.14$ .

The last in the category of the forward–backward asymmetry is the combined forward–backward asymmetry  $A_{\text{FB}}^{\ell\Lambda}$ , which mainly depends on the angular coefficient  $K_{2c}$  [cf. Eq. (25)]. Compared to the SM, the value of  $K_{2c}$  is higher in the  $Z'$  model. At large-recoil our results in the SM and  $Z'$  model are

$$\langle A_{\text{FB}}^{\ell\Lambda} \rangle_{\text{SM}} = -0.011_{-0.006}^{+0.003}, \quad \langle A_{\text{FB}}^{\ell\Lambda} \rangle_{Z'} = -0.009_{-0.003}^{+0.002},$$

whereas at low-recoil, the combined hadron–lepton forward–backward asymmetry is

$$\langle A_{\text{FB}}^{\ell\Lambda} \rangle_{\text{SM}} = 0.069_{-0.002}^{+0.002}, \quad \langle A_{\text{FB}}^{\ell\Lambda} \rangle_{Z'} = 0.087_{-0.002}^{+0.001}.$$

It can be seen that at large-recoil the deviations between the SM and  $Z'$  model are small, and it grows significantly in the low-recoil region.

The next observable to be discussed here is the fraction of longitudinal polarization ( $F_L$ ) of the dilepton system. Due to linear combinations of the same angular coefficients ( $K_{1ss}$  and  $K_{1cc}$ ) in both numerator and denominator of  $F_L$ , the  $Z'$  model is not much different from the SM. The values in one of the large-recoil bins, [0.1, 2], for the SM and  $Z'$  model are

$$\langle F_L \rangle_{\text{SM}} = 0.576_{-0.174}^{+0.031}, \quad \langle F_L \rangle_{Z'} = 0.463_{-0.095}^{+0.018},$$

and the corresponding experimental result is

$$\langle F_L \rangle_{\text{exp}} = 0.56_{-0.56}^{+0.23}.$$

It can be observed that this is in good agreement with the SM value and somewhat different from the corresponding value in the  $Z'$  model for this bin.

At low-recoil, the values for SM and  $Z'$  are

$$\langle F_L \rangle_{\text{SM}} = 0.713_{-0.008}^{+0.010}, \quad \langle F_L \rangle_{Z'} = 0.590_{-0.005}^{+0.007},$$

and the corresponding experimental result for this bin is

$$\langle F_L \rangle_{\text{exp}} = 0.61_{-0.14}^{+0.11}.$$

In contrast to the large-recoil, at low-recoil the results of  $F_L$  in the  $Z'$  model are closer to the experimentally measured results. Therefore, to uncover the imprints of the neutral boson in the longitudinal helicity fraction of the dimuon system in  $\Lambda_b \rightarrow \Lambda(\rightarrow p\pi)\mu^+\mu^-$  decays, the low-recoil bin might provide fertile ground.

Having compared the SM and  $Z'$  model with the experimentally measured values of the different observables as discussed above, we will now exploit some other observables that may be of interest in future at the LHCb and different B-factories. In connection with  $F_L$ , the fraction of transverse polarization  $F_T$  depends on  $K_{1cc}$  and  $K_{1ss}$  and its value at the large-recoil is

$$\langle F_T \rangle_{\text{SM}} = 0.136_{-0.002}^{+0.021}, \quad \langle F_T \rangle_{Z'} = 0.134_{-0.000}^{+0.012},$$

where it can be seen that the value in the  $Z'$  model is very close to the SM result. However, at low-recoil,

$$\langle F_T \rangle_{\text{SM}} = 0.287^{+0.008}_{-0.010}, \quad \langle F_T \rangle_{Z'} = 0.410^{+0.005}_{-0.007},$$

the results for the  $Z'$  model significantly differ from those of the SM. Hence, measurement of the fraction of transverse polarization in the low-recoil region will help us to see the possible contribution of the neutral  $Z'$  boson in these  $b$ -baryon decays.

It is well known that in the case of  $\Lambda_b \rightarrow \Lambda J/\psi$  the different asymmetries have been experimentally measured. Motivated by this fact, let us explore the asymmetries corresponding to the hadronic angle  $\theta_\Lambda$  and  $\theta_l$  one by one. The asymmetry arising due to the angle  $\theta_\Lambda$  is defined as  $\alpha_{\theta_\Lambda}$  and its explicit expression is given in Eq. (18); the corresponding numerical values in low- and large-recoil bins are tabulated in Table 6. In the large-recoil bin  $s \in [1, 6] \text{ GeV}^2$  the value reads

$$\langle \alpha_{\theta_\Lambda} \rangle_{\text{SM}} = -0.984^{+0.007}_{-0.001}, \quad \langle \alpha_{\theta_\Lambda} \rangle_{Z'} = -0.390^{+0.027}_{-0.006}.$$

Similarly, in the low-recoil bin  $s \in [15, 20] \text{ GeV}^2$ , our calculated results for this observable are

$$\langle \alpha_{\theta_\Lambda} \rangle_{\text{SM}} = -0.851^{+0.010}_{-0.007}, \quad \langle \alpha_{\theta_\Lambda} \rangle_{Z'} = -0.427^{+0.001}_{-0.001}.$$

Here we can see that  $\alpha_{\theta_\Lambda}$  differs in the  $Z'$  model from the SM results significantly in both low- and large-recoil bins.

Likewise, the asymmetry  $\alpha'_{\theta_\ell}$  that corresponds to angle  $\theta_\ell$  given in Eq. (20) depends on the angular coefficient  $K_{1c}$ , and therefore its behavior is similar to  $A_{\text{FB}}^\ell$ . The results in the large-recoil bin  $s \in [1, 6] \text{ GeV}^2$  for the SM and  $Z'$  model are

$$\langle \alpha'_{\theta_\ell} \rangle_{\text{SM}} = 0.047^{+0.039}_{-0.016}, \quad \langle \alpha'_{\theta_\ell} \rangle_{Z'} = 0.027^{+0.001}_{-0.002},$$

where the value of  $\alpha'_{\theta_\ell}$  in the SM is 1.7 times that of the  $Z'$  model. Similarly, in the low-recoil bin ( $s \in [15, 20] \text{ GeV}^2$ ) the results are

$$\langle \alpha'_{\theta_\ell} \rangle_{\text{SM}} = -0.280^{+0.012}_{-0.010}, \quad \langle \alpha'_{\theta_\ell} \rangle_{Z'} = -0.225^{+0.006}_{-0.004}.$$

It can be noticed that the results in the low-recoil bin are an order of magnitude large than the corresponding values in the large-recoil bin both in the SM and in the  $Z'$  model. These values are quite large to be measured at the LCHb experiment to test the predictions of the SM.

We now discuss  $\alpha_{\theta_\ell}$ , which depends upon the angular coefficients  $K_{1ss}$  and  $K_{1cc}$ . This is not significantly affected by the couplings of the  $Z'$  model and hence show little deviation from the SM, especially in the large-recoil region. In this region the numerical values are

$$\langle \alpha_{\theta_\ell} \rangle_{\text{SM}} = -0.854^{+0.024}_{-0.002}, \quad \langle \alpha_{\theta_\ell} \rangle_{Z'} = -0.857^{+0.014}_{-0.001},$$

where it is clear that the values in both models are almost the same. Similarly, in low-recoil region the results in the SM and  $Z'$  model are

$$\langle \alpha_{\theta_\ell} \rangle_{\text{SM}} = -0.665^{+0.010}_{-0.014}, \quad \langle \alpha_{\theta_\ell} \rangle_{Z'} = -0.485^{+0.008}_{-0.011}.$$

In comparison with the low- $s$  region, here the values of  $\alpha'_{\theta_\ell}$  in the SM and  $Z'$  model differ significantly. Therefore, to establish the possible new physics arising in the  $Z'$  model, analysis of  $\alpha_{\theta_\ell}$  in the high- $s$  region will serve as a useful probe.

Looking at  $\alpha_\phi$  discloses that it depends upon  $K_{4s}$ . At very low- $s$ , the  $C_7$  term dominates in the SM which results in negative  $K_{4s}$ , but for  $s > 2 \text{ GeV}^2$  the Wilson coefficient  $C_9$  term dominates, giving positive results. For the  $Z'$  model  $C_9^{Z'}$  gets affected much more than  $C_7^{Z'}$  for the entire range of  $s$  and hence  $\alpha_\phi$  is expected to change significantly with  $s$  in the  $Z'$  model from the corresponding SM result. The values of  $\alpha_\phi$  in the bin  $s \in [1, 6] \text{ GeV}^2$  for the SM and  $Z'$  model are

$$\langle \alpha_\phi \rangle_{\text{SM}} = 0.040_{-0.016}^{+0.070}, \quad \langle \alpha_\phi \rangle_{Z'} = 0.130_{-0.060}^{+0.015},$$

and for the low-recoil region  $s \in [15, 20] \text{ GeV}^2$ , the values of the observable are

$$\langle \alpha_\phi \rangle_{\text{SM}} = 0.047_{-0.004}^{+0.003}, \quad \langle \alpha_\phi \rangle_{Z'} = -0.448_{-0.006}^{+0.004}.$$

Hence, it can be revealed that in the SM the value of  $\alpha_\phi$  is almost the same in the low- and large-recoil bins, which is not the case for the  $Z'$  model where a large deviation is observed in both bins. Also, in both these bins the results of the  $Z'$  model are quite large compared to the SM results and experimental observation of  $\alpha_\phi$  will act as a useful observable.

The longitudinal (transverse) asymmetry parameter  $\alpha_L$  ( $\alpha_U$ ) is the ratio of the helicity combinations  $K_{2ss}$  ( $K_{2cc}$ ) to  $K_{1ss}$  as depicted in Eq. (23). Their values in the large-recoil region are

$$\langle \alpha_L(\alpha_U) \rangle_{\text{SM}} = -0.989_{-0.000}^{+0.006}(-0.916_{-0.004}^{+0.010}), \quad \langle \alpha_L(\alpha_U) \rangle_{Z'} = -0.386_{-0.003}^{+0.016}(-0.445_{-0.040}^{+0.168}),$$

where we can see that in this bin the values of both the longitudinal and the transverse asymmetry parameters in the  $Z'$  model differ significantly from their respective values in the SM. This is due to the fact that the contribution of the extra neutral boson  $Z'$  affects the value of  $K_{1ss}$  less than  $K_{2ss}$  ( $K_{2cc}$ ). Now, in the low-recoil region

$$\langle \alpha_L(\alpha_U) \rangle_{\text{SM}} = -0.852_{-0.008}^{+0.011}(-0.844_{-0.002}^{+0.003}), \quad \langle \alpha_L(\alpha_U) \rangle_{Z'} = -0.458_{-0.001}^{+0.001}(-0.307_{-0.002}^{+0.002}).$$

It can be deduced that the value of  $\alpha_L$  ( $\alpha_U$ ) in the  $Z'$  model is half that of the SM model in this bin. With the current luminosity of the LHCb experiment, the values of these observables are in the measurable range. Hence, experimental observation of these observables will give us a chance to test the predictions of the SM and the possibility of exploring the imprints of the  $Z'$  boson in  $\Lambda_b \rightarrow \Lambda \mu^+ \mu^-$  decays.

It is a well-established fact that certain asymmetries, such as  $\mathcal{P}_5^{(\prime)}$ , that correspond to different foldings in  $B \rightarrow K^* \mu^+ \mu^-$  have shown significant deviations from the SM predictions. This makes them a fertile hunting ground to dig for the various beyond-SM scenarios that give possible explanations, and  $Z'$  is one of them [154]. Motivated by this fact, we have calculated such foldings in the decay under consideration; their expressions in terms of the helicity combinations are given in Eq. (28). Among them the first one is  $\mathcal{P}_1$ , which behaves very similarly to  $F_T$ . The average values of  $\mathcal{P}_1$  at large-recoil in the SM and  $Z'$  model are

$$\langle \mathcal{P}_1 \rangle_{\text{SM}} = 0.796_{-0.031}^{+0.002}, \quad \langle \mathcal{P}_1 \rangle_{Z'} = 0.799_{-0.018}^{+0.001},$$

and at low-recoil, the values are

$$\langle \mathcal{P}_1 \rangle_{\text{SM}} = 0.569_{-0.009}^{+0.017}, \quad \langle \mathcal{P}_1 \rangle_{Z'} = 0.386_{-0.008}^{+0.010}.$$

Here, we can see that in the large-recoil region, the values in the SM and  $Z'$  model are very close, which is not the situation in the low-recoil region where the value of the SM is 1.5 times that of the  $Z'$  model.

$\mathcal{P}_2$  is the ratio of a linear combination of  $K_{2ss}$  and  $K_{2cc}$  to the total decay rate. In most of the bins the SM results are more than twice the  $Z'$  model values, and this can be seen in the results at large-recoil, which are

$$\langle \mathcal{P}_2 \rangle_{\text{SM}} = 0.512^{+0.001}_{-0.022}, \quad \langle \mathcal{P}_2 \rangle_{Z'} = 0.193^{+0.001}_{-0.002}.$$

The situation persists similarly at low-recoil:

$$\langle \mathcal{P}_2 \rangle_{\text{SM}} = 0.316^{+0.003}_{-0.002}, \quad \langle \mathcal{P}_2 \rangle_{Z'} = 0.153^{+0.004}_{-0.003}.$$

The behavior of  $\mathcal{P}_3$  is similar to  $A_{\text{FB}}^{\Lambda}$ . The average values of  $\mathcal{P}_3$  at large-recoil are

$$\langle \mathcal{P}_3 \rangle_{\text{SM}} = -0.030^{+0.009}_{-0.015}, \quad \langle \mathcal{P}_3 \rangle_{Z'} = -0.025^{+0.004}_{-0.009},$$

whereas the results at low-recoil become

$$\langle \mathcal{P}_3 \rangle_{\text{SM}} = 0.184^{+0.004}_{-0.007}, \quad \langle \mathcal{P}_3 \rangle_{Z'} = 0.232^{+0.003}_{-0.004}.$$

It can be observed that just like  $\mathcal{P}_1$ , for the asymmetry defined by  $\mathcal{P}_3$  the average values in the SM and  $Z'$  model are comparable at large-recoil but differ significantly at low-recoil. We have observed that with  $3 \text{ fb}^{-1}$  of data, the LHCb Collaboration has measured  $A_{\text{FB}}^h$ , which is of the same order as  $\mathcal{P}_3$ . Therefore, it is expected that in future  $\mathcal{P}_3$  will be measured.

Average values of  $\mathcal{P}_5$  at large-recoil are

$$\langle \mathcal{P}_5 \rangle_{\text{SM}} = 0.030^{+0.048}_{-0.013}, \quad \langle \mathcal{P}_5 \rangle_{Z'} = 0.034^{+0.013}_{-0.004},$$

and the results at low-recoil are

$$\langle \mathcal{P}_5 \rangle_{\text{SM}} = 0.163^{+0.001}_{-0.000}, \quad \langle \mathcal{P}_5 \rangle_{Z'} = 0.091^{+0.002}_{-0.001}.$$

This case is similar to  $\mathcal{P}_1$  and  $\mathcal{P}_3$  as the values in both models are very close at large-recoil and deviations started to appear in the low-recoil region of  $s$ .

Now we come to  $\mathcal{P}_6$ , which depends on the angular coefficient  $K_{4s}$  and hence behaves as  $\alpha_{\phi}$ . The values of the observable in the SM and  $Z'$  at large-recoil become

$$\langle \mathcal{P}_6 \rangle_{\text{SM}} = 0.056^{+0.097}_{-0.023}, \quad \langle \mathcal{P}_6 \rangle_{Z'} = 0.180^{+0.021}_{-0.083},$$

and the results at low-recoil are

$$\langle \mathcal{P}_6 \rangle_{\text{SM}} = 0.066^{+0.002}_{-0.007}, \quad \langle \mathcal{P}_6 \rangle_{Z'} = 0.621^{+0.005}_{-0.008}.$$

From the above results, it can be easily deduced that the value of  $\mathcal{P}_6$  in the  $Z'$  model differs significantly from the SM results both at large- and low-recoil, which is also the case for  $\alpha_{\phi}$ . In particular, in the low-recoil region, the value of an asymmetry is an order of magnitude larger from that in the large-recoil bin and it is in the experimentally measurable range with the current luminosity of the LHCb experiment.

The next observable to be discussed is  $\mathcal{P}_8$ , which mainly depends on the angular coefficient  $K_{1c}$  and therefore its behavior is exactly the same as  $A_{\text{FB}}^l$ . Its results in the large-recoil bin are

$$\langle \mathcal{P}_8 \rangle_{\text{SM}} = 0.088^{+0.070}_{-0.032}, \quad \langle \mathcal{P}_8 \rangle_{Z'} = 0.051^{+0.003}_{-0.003},$$

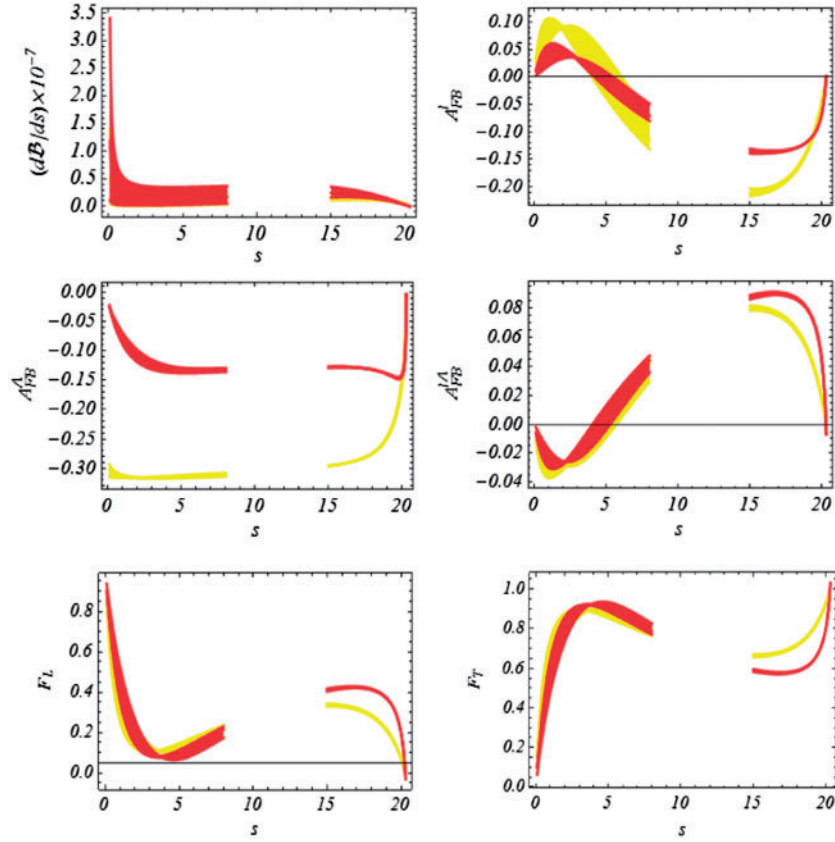


**Fig. 2.** Branching ratio and various forward–backward asymmetries plotted as functions of  $s$ . The yellow curve corresponds to the SM results and the red to the  $Z'$  model. In both cases, the bands correspond to the uncertainties in the form factors and other input parameters.

and at low-recoil:

$$\langle \mathcal{P}_8 \rangle_{\text{SM}} = -0.480^{+0.020}_{-0.012}, \quad \langle \mathcal{P}_8 \rangle_{Z'} = -0.359^{+0.007}_{-0.006}.$$

We can see that there is an order of magnitude difference between the results in the large- and low-recoil regions. Therefore, the number of events required to see the deviations in the low-recoil region is much smaller compared to the large-recoil region.

The last observable in this list is  $\mathcal{P}_9$ , which depends on the angular coefficient  $K_{2cc}$ . Its values at large-recoil are

$$\langle \mathcal{P}_9 \rangle_{\text{SM}} = -0.160^{+0.001}_{-0.023}, \quad \langle \mathcal{P}_9 \rangle_{Z'} = -0.076^{+0.024}_{-0.007},$$

and at low-recoil the results become

$$\langle \mathcal{P}_9 \rangle_{\text{SM}} = -0.308^{+0.013}_{-0.008}, \quad \langle \mathcal{P}_9 \rangle_{Z'} = -0.161^{+0.003}_{-0.004}.$$

We can see that the value of the SM is almost twice that of the  $Z'$  model in both regions.

In the case of  $\Lambda_b \rightarrow \Lambda(\rightarrow p\pi)\mu^+\mu^-$  decay, the LHCb experiment has measured the values of the branching ratio, forward–backward asymmetries, and longitudinal dimuon helicity fraction in small bins of  $s$ . Therefore, we have tabulated the values of the abovementioned observables in the large- and low-recoil regions in Table 6, and various small bins in Tables 7 and 8. In addition, to see the profile of these asymmetries we have plotted them graphically in Figs. 2, 3, and 4 with the square of the dimuon

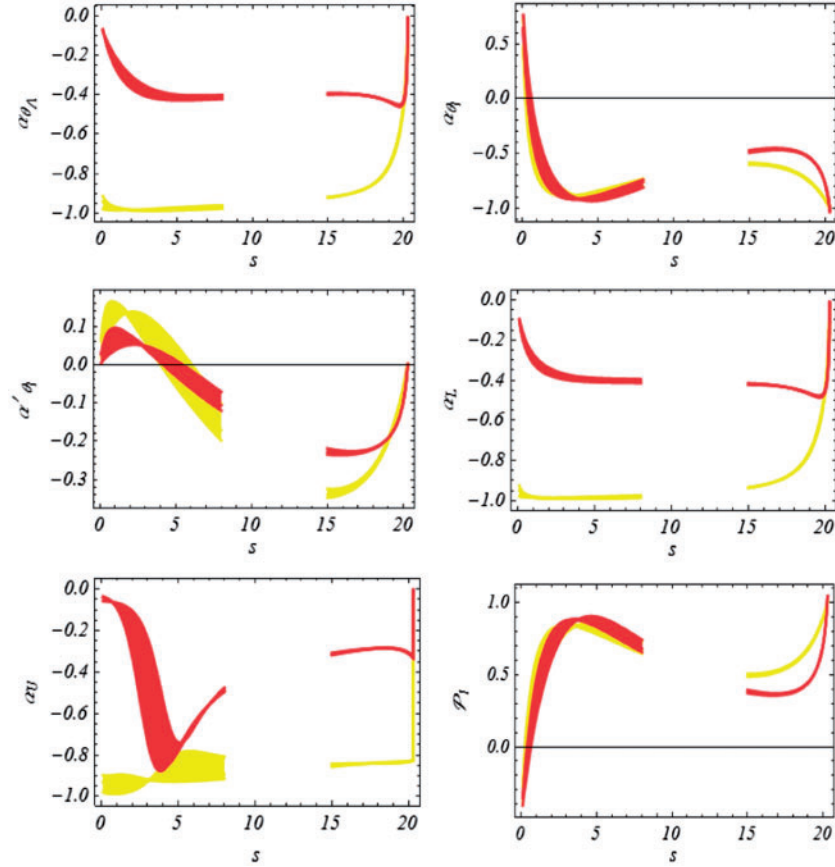


**Fig. 3.** Different asymmetry parameters denoted by  $\alpha$  and  $\mathcal{P}_1$  plotted as functions of  $s$ . The color coding is the same as in Fig. 2.

momentum  $s$ . We hope that in future, when more precise results for various asymmetries come from the LHCb, it will give us a chance to compare the profile of various asymmetries calculated here with the experiments for both the SM and the  $Z'$  model.

## 6. Conclusion

In this study we have investigated the full four-folded angular distributions for the semi-leptonic  $b$ -baryon decay  $\Lambda_b \rightarrow \Lambda(\rightarrow p\pi)\mu^+\mu^-$  in the SM and  $Z'$  model. At the quark level, this decay is mediated by the quark-level transition  $b \rightarrow s\mu^+\mu^-$ , which is same for the well-studied meson decay  $B \rightarrow K^*\mu^+\mu^-$ . For  $\Lambda_b \rightarrow \Lambda$  transitions, we have used the high-precision form factors calculated in the lattice QCD using  $2+1$  dynamical flavors along with the factorizable non-local matrix elements of the four-quark operators  $\mathcal{O}_{1-6}$  and  $\mathcal{O}_8^g$  encoded into effective Wilson coefficients  $C_7^{\text{eff}}(s)$  and  $C_9^{\text{eff}}(s)$ . By using them we have numerically calculated the differential branching ratio  $\frac{d\mathcal{B}}{ds}$ , the lepton, hadron, and combined hadron-lepton forward-backward asymmetries ( $A_{\text{FB}}^\ell, A_{\text{FB}}^\Lambda, A_{\text{FB}}^{\ell\Lambda}$ ), the various asymmetry parameters ( $\alpha$ ), the fractions of longitudinal ( $F_L$ ) and transverse ( $F_T$ ) polarized dimuons, and different angular asymmetry observables denoted by  $\mathcal{P}$  in different bins of  $s$ .

- In the low-recoil bin  $s \in [15, 20]\text{GeV}^2$  the form factors from the lattice are known most precisely, and the results of  $\frac{d\mathcal{B}}{ds}$  in the  $Z'$  model lie close to the experimental measurements in this bin. The SM results are significantly smaller than the measurements in this low-recoil bin.



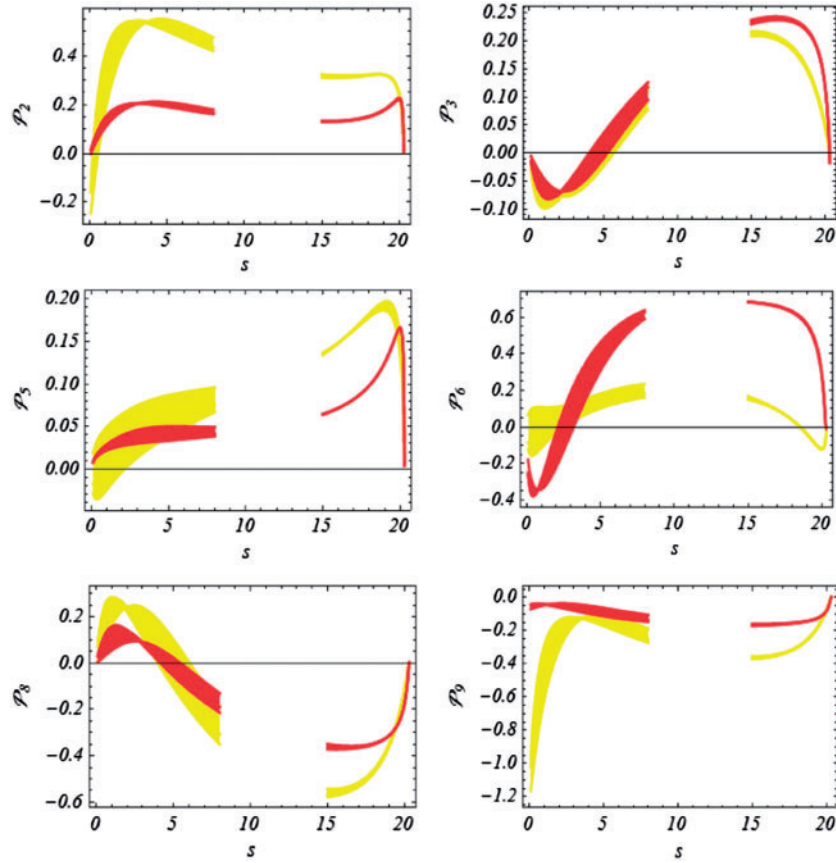


**Fig. 4.** The folded distributions  $\mathcal{P}_{2,\dots,9}$ , except  $\mathcal{P}_4$ , plotted as functions of  $s$ . The color coding is the same as in Fig. 2.

- In the large-recoil region the results of hadron-side forward–backward asymmetry ( $A_{\text{FB}}^{\Lambda}$ ) are significantly away from the experimental observations for both the SM and  $Z'$  model. However, in the low-recoil region the results of the SM lie close to the experimental observations.
- The experimental measurements of lepton-side forward–backward asymmetry ( $A_{\text{FB}}^{\ell}$ ) in both low- and large-recoil regions have significant errors. However, in the bin  $s \in [15, 20]$  GeV<sup>2</sup> the lower limit is comparable to the  $Z'$  model. We hope that in the future, when the statistics of the data are improved, it will help us to find the signatures of the extra neutral  $Z'$  boson.
- We have also predicted the values of the lepton–hadron combined forward–backward asymmetry ( $A_{\text{FB}}^{\ell\Lambda}$ ) both in the SM and the  $Z'$  model. It has been found that in the low-recoil bin the value of the  $Z'$  model deviates significantly from the SM result.
- The longitudinal polarization fraction  $F_L$  of the dimuon system is measured experimentally where the statistics is not good enough in the large-recoil bin as compared to the low-recoil region. In the region  $s \in [1, 6]$  GeV<sup>2</sup> the central value of the SM is compatible with the central value of the experimental measurements. However, in the bin  $s \in [15, 20]$  GeV<sup>2</sup>, where uncertainties in the form factors are better controlled, the experimental observations favor the results of the  $Z'$  model.
- In line with these asymmetries, we have also calculated the transverse polarization fraction of the dimuon system  $F_T$ , the asymmetry parameters  $\alpha$  and different angular asymmetry observables

$\mathcal{P}_i$  for  $i = 1, \dots, 9$  in the SM and the  $Z'$  model. We have found significantly large values of some of these observables that can be measured in the future at LHCb and Belle II.

In the end we would like to emphasize that some of the asymmetries calculated here were also reported in the SM and aligned 2HDM in Ref. [155], and our SM results match these results. We hope that in future, the precise measurement of some of the asymmetries reported here in the four-folded distribution of  $\Lambda_b \rightarrow \Lambda(\rightarrow p\pi)\mu^+\mu^-$  decay, in fine bins of  $s$ , at the LHCb and Belle II will help us to test the SM predictions in  $\Lambda_b$  decays with significantly improved statistics. It will also give us a chance to hunt for the indirect signals of NP arising due to the neutral  $Z'$  boson, especially where the SM is mismatched with the experimental predictions.

### Acknowledgements

The authors would like to thank Wei Wang and Ishtiaq Ahmed for useful discussions and suggestions to improve the work. In addition, MJA and SS would like to thank D. Van Dyk for his help in understanding the uncertainties arising due to different inputs. MJA would like to acknowledge the support of Quaid-i-Azam University through the University Research Funds and the funds from the Centre for Future High Energy Physics, Beijing, China through its visiting scientist scheme.

### Funding

Open Access funding: SCOAP<sup>3</sup>.

### Appendix. Definitions

In the rest frame of the decaying  $\Lambda_b$  baryon, the momentum of the daughter baryon  $\Lambda$  is defined as

$$p_2 = (m_{\Lambda_b} - q_0, 0, 0, |\mathbf{q}|),$$

where  $m_{\Lambda_b}$  is the mass of the  $\Lambda_b$  baryon. The lepton polarization vectors in the dilepton rest frame are given as

$$\begin{aligned} \epsilon_+^\mu &= \frac{1}{\sqrt{2}}(0, 1, -i, 0), & \epsilon_-^\mu &= \frac{1}{\sqrt{2}}(0, -1, -i, 0), \\ \epsilon_t^\mu &= (1, 0, 0, 0), & \epsilon_0^\mu &= (0, 0, 0, 1), \end{aligned}$$

and the corresponding lepton momentum vectors are [48]

$$\begin{aligned} q_1^\mu &= (E_\ell, -|\mathbf{q}| \sin \theta_1, \mathbf{0}, -|\mathbf{q}| \cos \theta_1), \\ q_2^\mu &= (E_\ell, |\mathbf{q}| \sin \theta_1, \mathbf{0}, |\mathbf{q}| \cos \theta_1), \end{aligned}$$

with  $E_\ell = \frac{\sqrt{s}}{2}$  and  $|\mathbf{q}| = E_\ell^2 - m_\ell^2$ .

The helicity amplitudes for the decay  $\Lambda_b \rightarrow \Lambda$  transitions can be expressed in terms of the form factors as [48]

$$\begin{aligned}
H_{t(+1/2,+1/2)}^V &= H_{t(-1/2,-1/2)}^V = f_0(s) \frac{m_{\Lambda_b} - m_{\Lambda}}{\sqrt{s}} \sqrt{s_+}, \\
H_{0(+1/2,+1/2)}^V &= H_{0(-1/2,-1/2)}^V = f_+(s) \frac{m_{\Lambda_b} + m_{\Lambda}}{\sqrt{s}} \sqrt{s_-}, \\
H_{+(-1/2,+1/2)}^V &= H_{-(+1/2,-1/2)}^V = -f_{\perp}(s) \sqrt{2s_-}, \\
H_{t(+1/2,+1/2)}^A &= -H_{t(-1/2,-1/2)}^A = g_0(s) \frac{m_{\Lambda_b} + m_{\Lambda}}{\sqrt{s}} \sqrt{s_-}, \\
H_{0(+1/2,+1/2)}^A &= -H_{0(-1/2,-1/2)}^A = g_+(s) \frac{m_{\Lambda_b} - m_{\Lambda}}{\sqrt{s}} \sqrt{s_+}, \\
H_{+(-1/2,+1/2)}^A &= -H_{-(+1/2,-1/2)}^A = -g_{\perp}(s) \sqrt{2s_+}, \\
H_{0(+1/2,+1/2)}^T &= H_{0(-1/2,-1/2)}^T = -h_+(s) \sqrt{s} \sqrt{s_-}, \\
H_{+(-1/2,+1/2)}^T &= H_{-(+1/2,-1/2)}^T = h_{\perp}(s) (m_{\Lambda_b} + m_{\Lambda}) \sqrt{2s_-}, \\
H_{0(+1/2,+1/2)}^{T5} &= -H_{0(-1/2,-1/2)}^{T5} = \tilde{h}_+(s) \sqrt{s} \sqrt{s_+}, \\
H_{+(-1/2,+1/2)}^{T5} &= -H_{-(+1/2,-1/2)}^{T5} = -\tilde{h}_{\perp}(s) (m_{\Lambda_b} - m_{\Lambda}) \sqrt{2s_+},
\end{aligned}$$

where  $f_0$ ,  $f_+$ , and  $f_{\perp}$  denote time-like, longitudinal, and transverse components of vector currents. The kinematic functions used in the above equation are defined as  $s_{\pm} \equiv (m_{\Lambda_b} \pm m_{\Lambda})^2 - s$ .

The transversity amplitude can be written in terms of helicity amplitudes as [48]

$$\begin{aligned}
A_{\perp 1}^{L(R)} &= +\sqrt{2}\mathcal{N} \left( (C_9^+ \mp C_{10}^+) H_{+(-1/2,+1/2)}^V - \frac{2m_b C_7^+}{s} H_{+(-1/2,+1/2)}^T \right), \\
A_{\parallel 1}^{L(R)} &= -\sqrt{2}\mathcal{N} \left( (C_9^- \mp C_{10}^-) H_{+(-1/2,+1/2)}^A + \frac{2m_b C_7^-}{s} H_{+(-1/2,+1/2)}^{T5} \right), \\
A_{\perp 0}^{L(R)} &= +\sqrt{2}\mathcal{N} \left( (C_9^+ \mp C_{10}^+) H_{0(+1/2,+1/2)}^V - \frac{2m_b C_7^+}{s} H_{0(+1/2,+1/2)}^T \right), \\
A_{\parallel 0}^{L(R)} &= -\sqrt{2}\mathcal{N} \left( (C_9^- \mp C_{10}^-) H_{0(+1/2,+1/2)}^A + \frac{2m_b C_7^-}{s} H_{0(+1/2,+1/2)}^{T5} \right),
\end{aligned} \tag{A.1}$$

where  $\mathcal{N} = G_F V_{tb} V_{ts}^* \alpha_e \sqrt{\frac{s\lambda^{1/2}(m_{\Lambda_b}^2, m_{\Lambda}^2, s)}{3 \cdot 2^{11} m_{\Lambda_b}^3 \pi^5}}$  and  $C_9^+ = C_9 + C_9'$ ,  $C_9^- = C_9 - C_9'$ ,  $C_{10}^+ = C_{10} + C_{10}'$ ,  $C_{10}^- = C_{10} - C_{10}'$ ,  $C_7^+ = C_7 + C_7'$ , and  $C_7^- = C_7 - C_7'$ . In the case of the SM and  $Z'$  model, all the primed Wilson coefficients are zero.

The angular variable  $K_{lm}$ , with  $l$  and  $m$  denoting the relative angular momentum and its third component for  $p\pi$  and  $\mu^+\mu^-$  systems, respectively, introduced in Eq. (15) can be written in terms

of transversality amplitudes as [48]:

$$\begin{aligned}
 K_{1ss}(s) &= \frac{1}{4} \left[ |A_{\perp 1}^R|^2 + |A_{\parallel 1}^R|^2 + 2|A_{\perp 0}^R|^2 + 2|A_{\parallel 0}^R|^2 + (R \leftrightarrow L) \right], \\
 K_{1cc}(s) &= \frac{1}{2} \left[ |A_{\perp 1}^R|^2 + |A_{\parallel 1}^R|^2 + (R \leftrightarrow L) \right], \\
 K_{1c}(s) &= -\text{Re} \left\{ A_{\perp 1}^R A_{\parallel 1}^{*R} - (R \leftrightarrow L) \right\}, \\
 K_{2ss}(s) &= \frac{\alpha}{2} \text{Re} \left\{ A_{\perp 1}^R A_{\parallel 1}^{*R} + 2A_{\perp 0}^R A_{\parallel 0}^{*R} + (R \leftrightarrow L) \right\}, \\
 K_{2cc}(s) &= +\alpha \text{Re} \left\{ A_{\perp 1}^R A_{\parallel 1}^{*R} + (R \leftrightarrow L) \right\}, \\
 K_{2c}(s) &= -\frac{\alpha}{2} \left[ |A_{\perp 1}^R|^2 + |A_{\parallel 1}^R|^2 - (R \leftrightarrow L) \right], \\
 K_{2sc}(s) &= +\frac{\alpha}{\sqrt{2}} \text{Im} \left\{ A_{\perp 1}^R A_{\perp 0}^{*R} - A_{\parallel 1}^R A_{\parallel 0}^{*R} + (R \leftrightarrow L) \right\}, \\
 K_{3s}(s) &= \frac{\alpha}{\sqrt{2}} \text{Im} \left\{ A_{\perp 1}^R A_{\parallel 0}^{*R} - A_{\parallel 1}^R A_{\perp 0}^{*R} - (R \leftrightarrow L) \right\}, \\
 K_{4sc}(s) &= +\frac{\alpha}{\sqrt{2}} \text{Re} \left\{ A_{\perp 1}^R A_{\parallel 0}^{*R} - A_{\parallel 1}^R A_{\perp 0}^{*R} + (R \leftrightarrow L) \right\}, \\
 K_{4s}(s) &= \frac{\alpha}{\sqrt{2}} \text{Re} \left\{ A_{\perp 1}^R A_{\perp 0}^{*R} - A_{\parallel 1}^R A_{\parallel 0}^{*R} - (R \leftrightarrow L) \right\}.
 \end{aligned}$$

## References

- [1] S. L. Glashow, J. Iliopoulos, and L. Maiani, *Phys. Rev. D* **2**, 1285 (1970).
- [2] N. Cabibbo, *Phys. Rev. Lett.* **10**, 531 (1963).
- [3] M. Kobayashi and T. Maskawa, *Prog. Theor. Phys.* **49**, 652 (1973).
- [4] T. Hurth and M. Nakao, *Ann. Rev. Nucl. Part. Sci.* **60**, 645 (2010) [arXiv:1005.1224 [hep-ph]] [Search INSPIRE].
- [5] T. Blake, G. Lanfranchi, and D. M. Straub, *Prog. Part. Nucl. Phys.* **92**, 50 (2017) [arXiv:1606.00916 [hep-ph]] [Search INSPIRE].
- [6] A. Ali, *Int. J. Mod. Phys. A* **31**, 1630036 (2016) [arXiv:1607.04918 [hep-ph]] [Search INSPIRE].
- [7] R. Aaij et al. (LHCb Collaboration), *Phys. Rev. Lett.* **113**, 151601 (2014) [arXiv:1406.6482 [hep-ex]] [Search INSPIRE].
- [8] M. Bordone, G. Isidori, and A. Pattori, *Eur. Phys. J. C* **76**, 440 (2016) [arXiv:1605.07633 [hep-ph]] [Search INSPIRE].
- [9] A. Celis, J. Fuentes-Martín, A. Vicente, and J. Virto, *Phys. Rev. D* **96**, 035026 (2017) [arXiv:1704.05672 [hep-ph]] [Search INSPIRE].
- [10] R. Aaij et al. (LHCb Collaboration), *Phys. Rev. Lett.* **111**, 191801 (2013) [arXiv:1308.1707 [hep-ex]] [Search INSPIRE].
- [11] S. Descotes-Genon, J. Matias, M. Ramon, and J. Virto, *J. High Energy Phys.* **01**, 048 (2013) [arXiv:1207.2753 [hep-ph]] [Search INSPIRE].
- [12] S. Descotes-Genon, T. Hurth, J. Matias, and J. Virto, *J. High Energy Phys.* **05**, 137 (2013) [arXiv:1303.5794 [hep-ph]] [Search INSPIRE].
- [13] LHCb Collaboration, *J. High Energy Phys.* **02**, 104 (2016) [arXiv:1512.04442 [hep-ex]] [Search INSPIRE].
- [14] Belle Collaboration, arXiv:1604.04042 [hep-ex] [Search INSPIRE].
- [15] S. Descotes-Genon, J. Matias, and J. Virto, *Phys. Rev. D* **88**, 074002 (2013) [arXiv:1307.5683 [hep-ph]] [Search INSPIRE].
- [16] LHCb Collaboration, *J. High Energy Phys.* **08**, 131 (2013) [arXiv:1304.6325 [hep-ex]] [Search INSPIRE].

- [17] LHCb Collaboration, *J. High Energy Phys.* **06**, 133 (2014) [[arXiv:1403.8044 \[hep-ex\]](#)] [[Search INSPIRE](#)].
- [18] C. Bouchard, G. P. Lepage, C. Monahan, H. Na, and J. Shigemitsu, *Phys. Rev. Lett.* **111**, 162002 (2013); **112**, 149902 (2014) [erratum] [[arXiv:1306.0434 \[hep-ph\]](#)] [[Search INSPIRE](#)].
- [19] LHCb Collaboration, *J. High Energy Phys.* **07**, 084 (2013) [[arXiv:1305.2168 \[hep-ex\]](#)] [[Search INSPIRE](#)].
- [20] LHCb Collaboration, *J. High Energy Phys.* **09**, 179 (2015) [[arXiv:1506.08777 \[hep-ex\]](#)] [[Search INSPIRE](#)].
- [21] R. R. Horgan, Z. Liu, S. Meinel, and M. Wingate, *Phys. Rev. Lett.* **112**, 212003 (2014) [[arXiv:1310.3887 \[hep-ph\]](#)].
- [22] G. Hiller and M. Schmaltz, *Phys. Rev. D* **90**, 054014 (2014) [[arXiv:1408.1627 \[hep-ph\]](#)] [[Search INSPIRE](#)].
- [23] M. Bauer and M. Neubert, *Phys. Rev. Lett.* **116**, 141802 (2016) [[arXiv:1511.01900 \[hep-ph\]](#)] [[Search INSPIRE](#)].
- [24] R. Barbieri, G. Isidori, A. Pattori, and F. Senia, *Eur. Phys. J. C* **76**, 67 (2016) [[arXiv:1512.01560 \[hep-ph\]](#)] [[Search INSPIRE](#)].
- [25] W. Altmannshofer and D. M. Straub, *Eur. Phys. J. C* **73**, 2646 (2013) [[arXiv:1308.1501 \[hep-ph\]](#)] [[Search INSPIRE](#)].
- [26] F. Beaujean, C. Bobeth, and D. van Dyk, *Eur. Phys. J. C* **74**, 2897 (2014); **74**, 3179 (2014) [erratum] [[arXiv:1310.2478 \[hep-ph\]](#)] [[Search INSPIRE](#)].
- [27] T. Hurth and F. Mahmoudi, *J. High Energy Phys.* **04**, 097 (2014) [[arXiv:1312.5267 \[hep-ph\]](#)] [[Search INSPIRE](#)].
- [28] W. Altmannshofer and D. M. Straub, *Eur. Phys. J. C* **75**, 382 (2015) [[arXiv:1411.3161 \[hep-ph\]](#)] [[Search INSPIRE](#)].
- [29] T. Hurth, F. Mahmoudi, and S. Neshatpour, *J. High Energy Phys.* **12**, 053 (2014) [[arXiv:1410.4545 \[hep-ph\]](#)] [[Search INSPIRE](#)].
- [30] F. Beaujean, C. Bobeth, and S. Jahn, *Eur. Phys. J. C* **75**, 456 (2015) [[arXiv:1508.01526 \[hep-ph\]](#)] [[Search INSPIRE](#)].
- [31] D. Du, A. X. El-Khadra, S. Gottlieb, A. S. Kronfeld, J. Laiho, E. Lunghi, R. S. Van de Water, and R. Zhou [Fermilab Lattice and MILC Collaborations], *Phys. Rev. D* **93**, 034005 (2016) [[arXiv:1510.02349 \[hep-ph\]](#)] [[Search INSPIRE](#)].
- [32] S. Descotes-Genon, L. Hofer, J. Matias, and J. Virto, *J. High Energy Phys.* **06**, 092 (2016) [[arXiv:1510.04239 \[hep-ph\]](#)] [[Search INSPIRE](#)].
- [33] T. Hurth, F. Mahmoudi, and S. Neshatpour, *Nucl. Phys. B* **909**, 737 (2016) [[arXiv:1603.00865 \[hep-ph\]](#)] [[Search INSPIRE](#)].
- [34] A. Khodjamirian, Th. Mannel, A. A. Pivovarov, and Y.-M. Wang, *J. High Energy Phys.* **09**, 089 (2010) [[arXiv:1006.4945 \[hep-ph\]](#)] [[Search INSPIRE](#)].
- [35] A. Khodjamirian, Th. Mannel, and Y.-M. Wang, *J. High Energy Phys.* **02**, 010 (2013) [[arXiv:1211.0234 \[hep-ph\]](#)] [[Search INSPIRE](#)].
- [36] S. Jäger and J. Martin Camalich, *J. High Energy Phys.* **05**, 043 (2013) [[arXiv:1212.2263 \[hep-ph\]](#)] [[Search INSPIRE](#)].
- [37] S. Jäger and J. Martin Camalich, *Phys. Rev. D* **93**, 014028 (2016) [[arXiv:1412.3183 \[hep-ph\]](#)] [[Search INSPIRE](#)].
- [38] M. Ciuchini, M. Fedele, E. Franco, S. Mishima, A. Paul, L. Silvestrini, and M. Valli, *J. High Energy Phys.* **06**, 116 (2016) [[arXiv:1512.07157 \[hep-ph\]](#)] [[Search INSPIRE](#)].
- [39] J. Lyon and R. Zwicky, [[arXiv:1406.0566 \[hep-ph\]](#)] [[Search INSPIRE](#)].
- [40] S. Descotes-Genon, L. Hofer, J. Matias, and J. Virto, *J. High Energy Phys.* **12**, 125 (2014) [[arXiv:1407.8526 \[hep-ph\]](#)] [[Search INSPIRE](#)].
- [41] T. Aaltonen et al. [CDF Collaboration], *Phys. Rev. Lett.* **107**, 201802 (2011) [[arXiv:1107.3753 \[hep-ex\]](#)] [[Search INSPIRE](#)].
- [42] R. Aaji et al. [The LHCb Collaboration], *Phys. Rev. D* **85**, 032008 (2012) [[arXiv:1111.2357 \[hep-ex\]](#)] [[Search INSPIRE](#)].
- [43] LHCb Collaboration, *Phys. Lett. B* **725**, 25 (2013) [[arXiv:1306.2577 \[hep-ex\]](#)] [[Search INSPIRE](#)].
- [44] R. Aaji et al. [The LHCb Collaboration], *J. High Energy Phys.* **06**, 108 (2017) [[arXiv:1703.00256 \[hep-ex\]](#)] [[Search INSPIRE](#)].
- [45] T. Mannel and S. Recksiegel, *J. Phys. G* **24**, 979 (1998) [[arXiv:hep-ph/9701399](#)] [[Search INSPIRE](#)].

- [46] C.-H. Chen and C. Q. Geng, Phys. Rev. D **64**, 074001 (2001) [arXiv:hep-ph/0106193] [Search INSPIRE].
- [47] C.-S. Huang and H.-G. Yan, Phys. Rev. D **59**, 114022 (1999); **61**, 039901 (2000) [erratum] [arXiv:hep-ph/9811303] [Search INSPIRE].
- [48] P. Böer, T. Feldmann, and D. van Dyk, J. High Energy Phys. **01**, 155 (2015) [arXiv:1410.2115 [hep-ph]] [Search INSPIRE].
- [49] T. Gutsche, M. A. Ivanov, J. G. Körner, V. E. Lyubovitskij, and P. Santorelli, Phys. Rev. D **87**, 074031 (2013) [arXiv:1301.3737 [hep-ph]] [Search INSPIRE].
- [50] G. Kumar and N. Mahajan, arXiv:1511.00935 [hep-ph] [Search INSPIRE].
- [51] T. Feldmann and M. W. Y. Yip, Phys. Rev. D **85**, 014035 (2012); **86**, 079901 (2012) [erratum] [arXiv:1111.1844 [hep-ph]] [Search INSPIRE].
- [52] W. Wang, Phys. Lett. B **708**, 119 (2012) [arXiv:1112.0237 [hep-ph]] [Search INSPIRE].
- [53] Y.-M. Wang and Y.-L. Shen, J. High Energy Phys. **02**, 179 (2016) [arXiv:1511.09036 [hep-ph]] [Search INSPIRE].
- [54] M. Beneke, Th. Feldmann, and D. Seidel, Nucl. Phys. B **612**, 25 (2001) [arXiv:hep-ph/0106067] [Search INSPIRE].
- [55] M. Beneke, Th. Feldmann, and D. Seidel, Eur. Phys. J. C **41**, 173 (2005) [arXiv:hep-ph/0412400] [Search INSPIRE].
- [56] B. Grinstein and D. Pirjol, Phys. Rev. D **70**, 114005 (2004) [arXiv:hep-ph/0404250] [Search INSPIRE].
- [57] M. Beylich, G. Buchalla, and T. Feldmann, Eur. Phys. J. C **71**, 1635 (2011) [arXiv:1101.5118 [hep-ph]] [Search INSPIRE].
- [58] B. Grinstein, M. J. Savage, and M. B. Wise, Nucl. Phys. B **319**, 271 (1989).
- [59] W. Altmannshofer, P. Ball, A. Bharucha, A. J. Buras, D. M. Straub, and M. Wick, J. High Energy Phys. **01**, 019 (2009) [arXiv:0811.1214 [hep-ph]] [Search INSPIRE].
- [60] C.-H. Chen, C. Q. Geng, and J. N. Ng, Phys. Rev. D **65**, 091502(R) (2002) [arXiv:hep-ph/0202103] [Search INSPIRE].
- [61] T. M. Aliev, A. Özpıneci, and M. Savcı, Nucl. Phys. B **649**, 168 (2003) [arXiv:hep-ph/0202120] [Search INSPIRE].
- [62] T. M. Aliev, A. Özpıneci, and M. Savcı, Phys. Rev. D **65**, 115002 (2002) [arXiv:hep-ph/0203045] [Search INSPIRE].
- [63] T. M. Aliev, A. Özpıneci, and M. Savcı, Phys. Rev. D **67**, 035007 (2003) [arXiv:hep-ph/0211447] [Search INSPIRE].
- [64] T. M. Aliev, V. Bashiry, and M. Savcı, Nucl. Phys. B **709**, 115 (2005) [arXiv:hep-ph/0407217] [Search INSPIRE].
- [65] T. M. Aliev, V. Bashiry, and M. Savcı, Eur. Phys. J. C **38**, 283 (2004) [arXiv:hep-ph/0409275] [Search INSPIRE].
- [66] T. M. Aliev and M. Savcı, J. High Energy Phys. **05**, 001 (2006) [arXiv:hep-ph/0507324] [Search INSPIRE].
- [67] A. K. Giri and R. Mohanta, J. Phys. G **31**, 1559 (2005).
- [68] A. K. Giri and R. Mohanta, Eur. Phys. J. C **45**, 151 (2006) [arXiv:hep-ph/0510171] [Search INSPIRE].
- [69] G. Turan, J. High Energy Phys. **05**, 008 (2005).
- [70] G. Turan, J. Phys. G **31**, 525 (2005).
- [71] T. M. Aliev and M. Savcı, Eur. Phys. J. C **50**, 91 (2007) [arXiv:hep-ph/0606225] [Search INSPIRE].
- [72] V. Bashiry and K. Azizi, J. High Energy Phys. **07**, 064 (2007) [arXiv:hep-ph/0702044] [Search INSPIRE].
- [73] F. Zolfagharpour and V. Bashiry, Nucl. Phys. B **796**, 294 (2008) [arXiv:0707.4337 [hep-ph]] [Search INSPIRE].
- [74] Y.-M. Wang, Y. Li, and C.-D. Lü, Eur. Phys. J. C **59**, 861 (2009) [arXiv:0804.0648 [hep-ph]] [Search INSPIRE].
- [75] M. J. Aslam, Y.-M. Wang, and C.-D. Lü, Phys. Rev. D **78**, 114032 (2008) [arXiv:0808.2113 [hep-ph]] [Search INSPIRE].
- [76] Y.-M. Wang, M. J. Aslam, and C.-D. Lü, Eur. Phys. J. C **59**, 847 (2009) [arXiv:0810.0609 [hep-ph]] [Search INSPIRE].
- [77] T. M. Aliev, K. Azizi, and M. Savcı, Phys. Rev. D **81**, 056006 (2010) [arXiv:1001.0227 [hep-ph]] [Search INSPIRE].

- [78] K. Azizi and N. Katirci, *High Energy Phys.* **01**, 087 (2011) [arXiv:1011.5647 [hep-ph]] [Search INSPIRE].
- [79] T. M. Aliev and M. Savcı, *Phys. Lett. B* **718**, 566 (2012) [arXiv:1202.5444 [hep-ph]] [Search INSPIRE].
- [80] L.-F. Gan, Y.-L. Liu, W.-B. Chen, and M.-Q. Huang, *Commun. Theor. Phys.* **58**, 872 (2012) [arXiv:1212.4671 [hep-ph]] [Search INSPIRE].
- [81] K. Azizi, S. Katirci, A. T. Olgun, and Z. Tavukoğlu, *Phys. Rev. D* **88**, 075007 (2013) [arXiv:1307.3101 [hep-ph]] [Search INSPIRE].
- [82] Y.-L. Wen, C.-X. Yue, and J. Zhang, *Int. J. Mod. Phys. A* **28**, 1350075 (2013) [arXiv:1307.5320 [hep-ph]] [Search INSPIRE].
- [83] Y. Liu, L.-L. Liu, and X.-H. Guo, arXiv:1503.06907 [Search INSPIRE].
- [84] L. Mott and W. Roberts, *Int. J. Mod. Phys. A* **30**, 1550172 (2015) [arXiv:1506.04106 [nucl-th]] [Search INSPIRE].
- [85] K. Azizi, A. T. Olgun, and Z. Tavukoğlu, *Phys. Rev. D* **92**, 115025 (2015) [arXiv:1508.03980 [hep-ph]] [Search INSPIRE].
- [86] S. Sahoo and R. Mohanta, *New J. Phys.* **18**, 093051 (2016) [arXiv:1607.04449 [hep-ph]] [Search INSPIRE].
- [87] S.-W. Wang and Y.-D. Yang, *Adv. High Energy Phys.* **2016**, 5796131 (2016) [arXiv:1608.03662 [hep-ph]] [Search INSPIRE].
- [88] S. Meinel and D. van Dyk, *Phys. Rev. D* **94**, 013007 (2016) [arXiv:1603.02974 [hep-ph]] [Search INSPIRE].
- [89] W. Detmold and S. Meinel, *Phys. Rev. D* **93**, 074501 (2016) [arXiv:1602.01399 [hep-lat]] [Search INSPIRE].
- [90] C. Bourrely, L. Lellouch, and I. Caprini, *Phys. Rev. D* **79**, 013008 (2009); **82**, 099902 (2010) [erratum] [arXiv:0807.2722 [hep-ph]] [Search INSPIRE].
- [91] C.-W. Chiang, X.-G. He, and G. Valencia, *Phys. Rev. D* **93**, 074003 (2016) [arXiv:1601.07328 [hep-ph]] [Search INSPIRE].
- [92] S. Di Chiara, A. Fowlie, S. Fraser, C. Marzo, L. Marzola, M. Raidal, and C. Spethmann, *Nucl. Phys. B* **923**, 245 (2017) [arXiv:1704.06200 [hep-ph]] [Search INSPIRE].
- [93] J. F. Kamenik, Y. Soreq, and J. Zupan, *Phys. Rev. D* **97**, 035002 (2018) [arXiv:1704.06005 [hep-ph]] [Search INSPIRE].
- [94] F. Gursey and M. Serdaroglu, *Lett. Nuo. Cim.* **21**, 28 (1978).
- [95] G. Buchalla, G. Burdman, C. T. Hill, and D. Kominis, *Phys. Rev. D* **53**, 5185 (1996) [arXiv:hep-ph/9510376] [Search INSPIRE].
- [96] E. Nardi, *Phys. Rev. D* **48**, 1240 (1993) [arXiv:hep-ph/9209223] [Search INSPIRE].
- [97] J. Bernabéu, E. Nardi, and D. Tommasini, *Nucl. Phys. B* **409**, 69 (1993) [arXiv:hep-ph/9306251] [Search INSPIRE].
- [98] V. Barger, M. S. Berger, and R. J. N. Phillips, *Phys. Rev. D* **52**, 1663 (1995) [arXiv:hep-ph/9503204] [Search INSPIRE].
- [99] E. Eichten, I. Hinchliffe, K. Lane, and C. Quigg, *Rev. Mod. Phys.* **56**, 579 (1984); **58**, 1065 (1986) [erratum].
- [100] P. Langacker and M. Plümacher, *Phys. Rev. D* **62**, 013006 (2000).
- [101] J. L. Lopez and D. V. Nanopoulos, *Phys. Rev. D* **55**, 397 (1997) [arXiv:hep-ph/9605359] [Search INSPIRE].
- [102] B. B. Şirvanli, *Mod. Phys. Lett. A* **23**, 347 (2008) [arXiv:hep-ph/0701173] [Search INSPIRE].
- [103] T. G. Rizzo, arXiv:hep-ph/0610104 [Search INSPIRE].
- [104] A. Abulencia et al. [CDF Collaboration], *Phys. Rev. Lett.* **96**, 211801 (2006) [arXiv:hep-ex/0602045] [Search INSPIRE].
- [105] V. Barger, L. Everett, J. Jiang, P. Langacker, T. Liu, and C. E. M. Wagner, *Phys. Rev. D* **80**, 055008 (2009) [arXiv:0902.4507 [hep-ph]] [Search INSPIRE].
- [106] L. V. Barger, L. L. Everett, J. Jiang, P. Langacker, T. Liu, and C. E. M. Wagner, *J. High Energy Phys.* **12**, 048 (2009) [arXiv:0906.3745 [hep-ph]] [Search INSPIRE].
- [107] Q. Chang, X.-Q. Lic, and Y.-D. Yang, *J. High Energy Phys.* **02**, 082 (2010) [arXiv:0907.4408 [hep-ph]] [Search INSPIRE].
- [108] V. Barger, C.-W. Chiang, J. Jiang, and P. Langacker, *Phys. Lett. B* **596**, 229 (2004) [arXiv:hep-ph/0405108] [Search INSPIRE].

- [109] X.-G. He and G. Valencia, Phys. Rev. D **74**, 013011 (2006) [arXiv:hep-ph/0605202] [Search INSPIRE].
- [110] S. Baek, J. H. Jeon, and C. S. Kim, Phys. Lett. B **664**, 84 (2008) [arXiv:0803.0062 [hep-ph]] [Search INSPIRE].
- [111] S. Sahoo, C. K. Das, and L. Maharana, Int. J. Mod. Phys. A **26**, 3347 (2011) [arXiv:1112.0460 [hep-ph]] [Search INSPIRE].
- [112] M. Bona et al. PMC Phys. A **3**, 6 (2009) [arXiv:0803.0659 [hep-ph]] [Search INSPIRE].
- [113] M. Bona et al., arXiv:0906.0953 [hep-ph] [Search INSPIRE].
- [114] C.-H. Chen, Phys. Lett. B **683**, 160 (2010) [arXiv:0911.3479 [hep-ph]] [Search INSPIRE].
- [115] N. G. Deshpande, X.-G. He, and G. Valencia, Phys. Rev. D **82**, 056013 (2010) [arXiv:1006.1682 [hep-ph]] [Search INSPIRE].
- [116] J. E. Kim, M.-S. Seo, and S. Shin, Phys. Rev. D **83**, 036003 (2011) [arXiv:1010.5123 [hep-ph]] [Search INSPIRE].
- [117] P. J. Fox, J. Liu, D. Tucker-Smith, and N. Weiner, Phys. Rev. D **84**, 115006 (2011) [arXiv:1104.4127 [hep-ph]] [Search INSPIRE].
- [118] Q. Chang, R.-M. Wang, Y.-G. Xu, and X.-W. Cui, Chin. Phys. Lett. **28**, 081301 (2011).
- [119] C. Bobeth and U. Haisch, arXiv:1109.1826 [hep-ph] [Search INSPIRE].
- [120] A. K. Alok, S. Baek, and D. London, J. High Energy Phys. **07**, 111 (2011) [arXiv:1010.1333 [hep-ph]] [Search INSPIRE].
- [121] X.-Q. Li, Y.-M. Li, G.-R. Lu, and F. Su, J. High Energy Phys. **05**, 049 (2012) [arXiv:1204.5250 [hep-ph]] [Search INSPIRE].
- [122] V. Barger, C.-W. Chiang, P. Langacker, and H.-S. Lee, Phys. Lett. B **580**, 186 (2004) [arXiv:hep-ph/0310073] [Search INSPIRE].
- [123] C.-W. Chiang, R.-H. Li, and C.-D. Lü, Chin. Phys. C **36**, 14 (2012) [arXiv:0911.2399 [hep-ph]] [Search INSPIRE].
- [124] J. Hua, C. S. Kim, and Y. Li, Eur. Phys. J. C **69**, 139 (2010) [arXiv:1002.2531 [hep-ph]] [Search INSPIRE].
- [125] Q. Chang, X.-Q. Li, and Y.-D. Yang, J. High Energy Phys. **04**, 052 (2010) [arXiv:1002.2758 [hep-ph]] [Search INSPIRE].
- [126] Y. Li, J. Hua, and K.-C. Yang, Eur. Phys. J. C **71**, 1775 (2011) [arXiv:1107.0630 [hep-ph]] [Search INSPIRE].
- [127] C.-W. Chiang, Y.-F. Lin, and J. Tandean, J. High Energy Phys. **11**, 083 (2011) [arXiv:1108.3969 [hep-ph]] [Search INSPIRE].
- [128] S. Sahoo, C. K. Das, and L. Maharana, Int. J. Mod. Phys. A **24**, 6223 (2009) [arXiv:1112.4563 [hep-ph]] [Search INSPIRE].
- [129] N. Katirci and K. Azizi, J. Phys. G **40**, 085005 (2013) arXiv:1207.4053 [hep-ph] [Search INSPIRE].
- [130] V. Barger, C.-W. Chiang, P. Langacker, and H.-S. Lee, Phys. Lett. B **598**, 218 (2004) [arXiv:hep-ph/0406126] [Search INSPIRE].
- [131] Q. Chang, X.-Q. Li, and Y.-D. Yang, J. High Energy Phys. **05**, 056 (2009) [arXiv:0903.0275 [hep-ph]] [Search INSPIRE].
- [132] J. Hua, C. S. Kim, and Y. Li, Phys. Lett. B **690**, 508 (2010) [arXiv:1002.2532 [hep-ph]] [Search INSPIRE].
- [133] Q. Chang, X.-Q. Li, and Y.-D. Yang, Int. J. Mod. Phys. A **26**, 1273 (2011) [arXiv:1003.6051 [hep-ph]] [Search INSPIRE].
- [134] Q. Chang and Y.-D. Yang, Nucl. Phys. B **852**, 539 (2011) [arXiv:1010.3181 [hep-ph]] [Search INSPIRE].
- [135] L. Hofer, D. Scherer, and L. Vernazza, J. High Energy Phys. **02**, 080 (2011) [arXiv:1011.6319 [hep-ph]] [Search INSPIRE].
- [136] Y. Li, X.-J. Fan, J. Hua, and E.-L. Wang, Phys. Rev. D **85**, 074010 (2012) [arXiv:1111.7153 [hep-ph]] [Search INSPIRE].
- [137] S. Sahoo, C. K. Das, and L. Maharana, Phys. Atom. Nucl. **74**, 1032 (2011) [arXiv:1112.2246 [hep-ph]] [Search INSPIRE].
- [138] S. Sahoo and L. Maharana, Indian J. Pure Appl. Phys. **46**, 306 (2008).
- [139] I. Ahmed, Phys. Rev. D **86**, 095022 (2012).
- [140] M. A. Paracha, I. Ahmed, and M. J. Aslam, Prog. Theor. Exp. Phys. **2015**, 033B04 (2015) [arXiv:1408.4318 [hep-ph]] [Search INSPIRE].



- [141] C. Greub, V. Pilipp, and C. Schüpbach, *J. High Energy Phys.* **12**, 040 (2008) [[arXiv:0810.4077 \[hep-ph\]](#)] [[Search INSPIRE](#)].
- [142] Q. Chang and Y.-H. Gao, *Nucl. Phys. B* **845**, 179 (2011) [[arXiv:1101.1272 \[hep-ph\]](#)] [[Search INSPIRE](#)].
- [143] K. Cheung, C.-W. Chiang, N.G. Deshpande, and J. Jiang, *Phys. Lett. B* **652**, 285 (2007).
- [144] C.-H. Chen and H. Hatanaka, *Phys. Rev. D* **73**, 075003 (2006).
- [145] C.-W. Chiang, N. G. Deshpande, and J. Jiang, *J. High Energy Phys.* **08**, 075 (2006).
- [146] R. Mohanta and A. K. Giri, *Phys. Rev. D* **79**, 057902 (2009).
- [147] J. G. Körner, M. Krämer, and D. Pirjol, *Prog. Part. Nucl. Phys.* **33**, 787 (1994) [[arXiv:hep-ph/9406359](#)] [[Search INSPIRE](#)].
- [148] A. Ali, T. Mannel, and T. Morozumi, *Phys. Lett. B* **273**, 505 (1991).
- [149] G. Burdman, *Phys. Rev. D* **57**, 4254 (1998) [[arXiv:hep-ph/9710550](#)] [[Search INSPIRE](#)].
- [150] A. Ali, P. Ball, L. T. Handoko, and G. Hiller, *Phys. Rev. D* **61**, 074024 (2000) [[arXiv:hep-ph/9910221](#)] [[Search INSPIRE](#)].
- [151] C. Patrignani et al. [Particle Data Group], *Chin. Phys. C* **40**, 100001 (2016).
- [152] H. H. Asatryan, H. M. Asatrian, C. Greub, and M. Walker, *Phys. Rev. D* **65**, 074004 (2002).
- [153] The LHCb Collaboration, *J. High Energy Phys.* **06**, 115 (2015) [[arXiv:1503.07138 \[hep-ex\]](#)] [[Search INSPIRE](#)].
- [154] I. Ahmed and A. Rehman, [arXiv:1703.09627 \[hep-ph\]](#) [[Search INSPIRE](#)].
- [155] Q.-Y. Hu, X.-Q. Li, and Y.-D. Yang, *Eur. Phys. J. C* **77**, 228 (2017) [[arXiv:1701.04029 \[hep-ph\]](#)] [[Search INSPIRE](#)].

PAPER

## The $\Lambda_b \rightarrow \Lambda (\rightarrow p \pi^-) \mu^+ \mu^-$ decay in the $RS_e$ model

To cite this article: Aqsa Nasrullah *et al* 2018 *J. Phys. G: Nucl. Part. Phys.* **45** 095007

View the [article online](#) for updates and enhancements.

### Related content

- [b<sub>s</sub> ssd decay in Randall-Sundrum models](#)  
Cai-Dian Lü, Faisal Munir and Qin Qin
- [Impact of vector leptiquarks on  \$\bar{B} \rightarrow \bar{K} \gamma^\* \gamma^\* \gamma^\* \gamma^\*\$  anomalies](#)  
Suchismita Sahoo and Rukmani Mohanta
- [Study of the rare decays  \$B \rightarrow \(s, d\) \gamma^\* \gamma^\* \gamma^\* \gamma^\* \rightarrow \mu^+ \mu^- \mu^+ \mu^-\$](#)   
Suchismita Sahoo and Rukmani Mohanta

# The $\Lambda_b \rightarrow \Lambda (\rightarrow p\pi^-) \mu^+ \mu^-$ decay in the $RS_c$ model

Aqsa Nasrullah<sup>1</sup>, Faisal Munir Bhutta<sup>2,3,4</sup>  and M Jamil Aslam<sup>1</sup> 

<sup>1</sup> Physics Department, Quaid-i-Azam University, Islamabad, Pakistan

<sup>2</sup> Institute of High Energy Physics, Chinese Academy of Sciences, Beijing 100049, People's Republic of China

<sup>3</sup> University of Chinese Academy of Sciences, Beijing 100049, People's Republic of China

E-mail: [aqsanasrullah54@gmail.com](mailto:aqsanasrullah54@gmail.com), [faisalmunir@ihep.ac.cn](mailto:faisalmunir@ihep.ac.cn) and [jamil@qau.edu.pk](mailto:jamil@qau.edu.pk)

Received 3 June 2018, revised 16 July 2018

Accepted for publication 23 July 2018

Published 8 August 2018



CrossMark

## Abstract

We study the four-body decay  $\Lambda_b \rightarrow \Lambda (\rightarrow p\pi^-) \mu^+ \mu^-$  in the Randall–Sundrum model with custodial protection ( $RS_c$ ). By considering the constraints coming from the direct searches of the lightest Kaluza–Klein (KK) excitation of the gluon, electroweak precision tests, the measurements of the Higgs signal strengths at the LHC and from  $\Delta F = 2$  flavor observables, we perform a scan of the parameter space of the  $RS_c$  model and obtain the maximum allowed deviations of the Wilson coefficients  $\Delta C_{7,9,10}^{(\prime)}$  for different values of the lightest KK gluon mass  $M_g^{(1)}$ . Later, their implications on the observables such as differential branching fraction, longitudinal polarization of the daughter baryon  $\Lambda$ , forward–backward asymmetry with respect to leptonic, hadronic and combined lepton–hadron angles are discussed where we present the analysis of these observables in different bins of di-muon invariant mass squared  $s (= q^2)$ . It is observed that with the current constraints the Wilson coefficients in the  $RS_c$  model show slight deviations from their Standard Model values and hence cannot accommodate the discrepancies between the Standard Model calculations of various observables and the LHCb measurements in  $\Lambda_b$  decays.

Keywords: rare flavor-changing neutral-current decays, beyond standard model, new physics

(Some figures may appear in colour only in the online journal)

<sup>4</sup> Author to whom any correspondence should be addressed.

## 1. Introduction

Although the Large Hadron Collider (LHC) has so far not observed any new particles directly, that are predicted by many beyond Standard Model (SM) scenarios, it has certainly provided some intriguing discrepancies from the SM expectations in semi-leptonic rare  $B$ -meson decays. In this context, a persistent pattern of deviations in tension with the SM predictions has been emerging from observables in a number of  $b \rightarrow sl^+l^-$  processes. In particular, LHCb measurements [1, 2] of the observables  $R_K$  and  $R_{K^*}$  representing the ratios of branching fractions  $B^+ \rightarrow K^+\mu^+\mu^-$  to  $B^+ \rightarrow K^+e^+e^-$  and  $B^0 \rightarrow K^{*0}\mu^+\mu^-$  to  $B^0 \rightarrow K^{*0}e^+e^-$ , respectively, show deviations from the SM predictions  $\sim 1$  and together they indicate the lepton flavor universality violation with the significance at the  $4\sigma$  level [3–6]. Further, the LHCb results for the branching fractions of the  $B \rightarrow K^{(*)}\mu^+\mu^-$  and  $B_s \rightarrow \phi\mu^+\mu^-$  decays [7–9], suggest the smaller values compared to their SM estimates. Moreover, mismatch between the LHCb findings and the SM predictions in the angular analysis of the  $B^0 \rightarrow K^{*0}\mu^+\mu^-$  decay [10, 11], with the confirmation by the Belle collaboration later on [12], has become a longstanding issue. In this context, recent phenomenological analyses have explored the underlying new physics (NP) possibilities behind these anomalies [3–6, 13–18]. However, to establish the claim that the deviations in the angular asymmetries in  $B \rightarrow K^{*}(\rightarrow K\pi)\mu^+\mu^-$  decays are indications of NP, an improvement is needed both on the theoretical and the experimental sides. On the theoretical front we have to get better control on the hadronic uncertainties arising mainly due to form factors (FF) and on the experimental end, some more data with improved statistics is needed which is expected from the Belle II and LHCb. Another possibility that exists on the theoretical side is to analyze more processes which are mediated by the same quark level transition  $b \rightarrow s\mu^+\mu^-$ .

Among them, the rare baryonic decay  $\Lambda_b \rightarrow \Lambda\mu^+\mu^-$  is particularly important as it can provide complementary information and additionally offers a unique opportunity to understand the helicity structure of the effective weak Hamiltonian for  $b \rightarrow s$  transition [19, 20]. The branching ratio for this decay was first measured by CDF collaboration [21]. Recently, the LHCb has reported its measurements for branching ratio and three angular observables [22] in the  $\Lambda_b \rightarrow \Lambda(\rightarrow p\pi^-)\mu^+\mu^-$  decay. Theoretically challenging aspect in the study of the  $\Lambda_b \rightarrow \Lambda\mu^+\mu^-$  decay is the evaluation of the hadronic  $\Lambda_b \rightarrow \Lambda$  transition form factors. In this context, recent progress is made by performing the high precision lattice QCD calculations [23]. Moreover, these FF have been estimated using various models or approximations such as quark models [24, 25], perturbative QCD [26], SCET [27] and QCD light cone sum-rules [28–30]. Furthermore, extensive studies of the semi-leptonic decays of  $\Lambda_b$  baryon ( $\Lambda_b \rightarrow \Lambda\ell^+\ell^-$ ), both within the SM and in many different NP scenarios, have been performed [31–56]. Recently, the angular distributions for polarized  $\Lambda_b$  are presented in [57].

In the present work, we study the four-body  $\Lambda_b \rightarrow \Lambda(\rightarrow p\pi^-)\mu^+\mu^-$  decay in the framework of the Randall–Sundrum (RS) model with custodial protection. The RS model features five-dimensional (5D) space–time with a non-trivial warped metric [58]. After performing the Kaluza–Klein (KK) decomposition and integrating over the fifth dimension the effective 4D theory is obtained which involves new particles appearing as the KK resonances, either of the SM particles or the ones which do not possess SM counterparts. Assuming that the weak effective Hamiltonian of the  $\Lambda_b \rightarrow \Lambda(\rightarrow p\pi^-)\mu^+\mu^-$  decay emerges from the well-defined theory of the  $RS_c$  model, the Wilson coefficients of the effective Hamiltonian get modified with respect to the SM values due to additional contributions from the heavy KK excitations and are correlated in a unique way. Expecting distinct phenomenological consequences from such a correlation on the angular observables of the  $\Lambda_b \rightarrow \Lambda(\rightarrow p\pi^-)\mu^+\mu^-$

decay, we study whether the current experimental data on this decay can be explained in the  $RS_c$  model.

Although  $B$ -meson decays have been investigated extensively in different variants of the RS model [59–72], not many studies are devoted to the  $\Lambda_b$  decays in the RS model [73]. Additionally, our present study includes new considerations and results which were not available in the previous studies of the  $\Lambda_b$  decays entertaining the RS model. Firstly, we will consider the current constraints on the parameter space of the  $RS_c$  model coming from the direct searches of the lightest KK gluon, electroweak precision tests and from the measurements of the Higgs signal strengths at the LHC, which yield much stricter constraints on the mass scale of the lowest KK gluon  $M_g^{(0)}$ , which in turn prevent sizeable deviations of the Wilson coefficients from the SM predictions. Secondly, we will not adopt the simplification of treating the elements of the 5D Yukawa coupling matrices to be real numbers as considered in [68, 73], rather we will take these entries to be complex numbers as considered in [63, 70] leading to the complex Wilson coefficients instead of real ones. Last but not the least, we will use the helicity parametrization of the  $\Lambda_b \rightarrow \Lambda$  hadronic matrix elements and for the involved FF, we will use the most recent lattice QCD calculations, both in the low and high  $q^2$  regions, which yield much smaller uncertainties in most of the kinematic range [23].

The rest of the paper is organized as follows. In section 2, we describe the essential features of the  $RS_c$  model especially relevant for the study of the considered decay. In section 3, we present the theoretical formalism including the effective weak Hamiltonian, analytical expressions of the Wilson coefficients in the  $RS_c$  model and the angular observables of interest in the four-body  $\Lambda_b \rightarrow \Lambda(\rightarrow p\pi^-)\mu^+\mu^-$  decay. After discussing the current constraints and subsequently scanning the parameter space of the  $RS_c$  model in section 4, we give our numerical results and their discussion in section 5. Finally, in section 6, we conclude our findings.

## 2. RS model with custodial symmetry

In this section we will describe some of the salient features of the RS model [58]. The RS model, also known as warped extra dimension, offers a geometrical solution of the gauge hierarchy problem along with naturally explaining the observed hierarchies in the SM fermion masses and mixing angles. The model is described in a 5D space–time, where the fifth dimension is compactified on an orbifold and the non-factorizable RS metric is given by

$$ds^2 = e^{-2ky}\eta_{\mu\nu}dx^\mu dx^\nu - dy^2, \quad (1)$$

where  $k \sim \mathcal{O}(M_{\text{Pl}}) \simeq 10^{19}$  GeV is the curvature scale,  $\eta_{\mu\nu} = \text{diag}(+1, -1, -1, -1)$  is the 4D Minkowski metric and  $y$  is the extra-dimensional (fifth) coordinate which varies in the finite interval  $0 \leq y \leq L$ ; the endpoints of the interval  $y = 0$  and  $y = L$  represent the boundaries of the extra dimension and are known as *ultraviolet* (UV) and *infrared* (IR) brane, respectively. The region in between the UV and IR brane is denoted as the bulk of the warped extra dimension. In order to solve the gauge hierarchy problem, we take  $kL = 36$  and define

$$M_{\text{KK}} \equiv ke^{-kL} \sim \mathcal{O}(\text{TeV}), \quad (2)$$

as the only free parameter coming from space–time geometry representing the effective NP scale.

In the present study, we consider a specific setup of the RS model in which the SM gauge group is enlarged to the bulk gauge group

$$SU(3)_c \times SU(2)_L \times SU(2)_R \times U(1)_X \times P_{LR}, \quad (3)$$

which is known as the RS model with custodial protection (RS<sub>c</sub>) [65, 74–77].  $P_{LR}$  is the discrete symmetry, interchanging the two  $SU(2)_{L,R}$  groups, which is responsible for the protection of the  $Zb_L\bar{b}_L$  vertex. Moreover, for this particular scenario it has been shown that all existing  $\Delta F = 2$  and electroweak (EW) precision constraints can be satisfied, without requiring too much fine-tuning, for the masses of the lightest KK excitations of the order of a few TeV [63], in the reach of the LHC. However, after the ATLAS and the CMS measurements of the Higgs signal strengths, the bounds on the masses of the lightest KK modes arising from Higgs physics have grown much stronger than those stemming from EW precision measurements [78]. In view of this, we have performed a scan for the allowed parameter space of the model by considering all existing constraints, which will be discussed later on.

In the chosen setup, all the SM fields are allowed to propagate in the 5D bulk, except the Higgs field, which is localized near or on the IR brane. In the present study we consider the case in which Higgs boson is completely localized on the IR brane at  $y = L$ . The RS<sub>c</sub> model features two symmetry breakings. First, the enlarged gauge group of the model is broken down to the SM gauge group after imposing suitable boundary conditions (BCs) on the UV brane. Later on the spontaneous symmetry breaking occurs through Higgs mechanism on the IR brane. As a natural consequence in all the extra-dimensional models, we have an infinite tower of KK excitations in this model. For this, each 5D field  $F(x^\mu, y)$  is KK decomposed to generic form

$$F(x^\mu, y) = \frac{1}{\sqrt{L}} \sum_{n=0}^{\infty} F^{(n)}(x^\mu) f^{(n)}(y), \quad (4)$$

where  $F^{(n)}(x^\mu)$  represent the effective four-dimensional fields and  $f^{(n)}(y)$  are called as the 5D profiles or the shape functions.  $n = 0$  case, called as zero mode in the KK mode expansion of a given field, corresponds to the SM particle. Appropriate choices for BCs help to distinguish between fields with and without a zero mode. Fields with the Neumann BCs on both branes, denoted as  $(++)$ , have a zero mode that can be identified with a SM particle while fields with the Dirichlet BC on the UV brane and Neumann BC on the IR brane, denoted as  $(-+)$ , do not have the SM partners. Profiles for different fields are obtained by solving the corresponding 5D bulk equations of motion (EOM). In a perturbative approach as described in [65], EOMs can be solved before the electroweak symmetry breaking (EWSB) and after the Higgs field develops a vacuum expectation value (VEV), the ratio  $v/M_{g^{(1)}}$  of the Higgs VEV  $v$  and the mass of the lowest KK excitation mode of gauge bosons  $M_{g^{(1)}}$  can be taken as perturbation<sup>5</sup>. Starting with the action of 5D theory, we integrate over the fifth dimension  $y$  to obtain the 4D effective field theory, and the Feynman rules of the model are obtained by neglecting terms of  $\mathcal{O}(v^2/M_{g^{(1)}}^2)$  or higher. On similar grounds, the mixing occurring between the SM fermions and the higher KK fermion modes can be neglected as it leads to  $\mathcal{O}(v^2/M_{g^{(1)}}^2)$  modifications of the relevant couplings.

Next, we discuss the particle content of the gauge sector of the RS<sub>c</sub> model and the mixing between SM gauge bosons and the first higher KK modes after the EWSB. For gauge bosons, following the analyses performed in [63, 68], we have neglected the  $n > 1$  KK modes as it is observed that the model becomes non-perturbative already for scales corresponding to the first few KK modes. Corresponding to the enlarged gauge group of the model we have a large number of gauge bosons. For  $SU(3)_c$ , we have  $G_\mu^A$  ( $A = 1, \dots, 8$ ) corresponding to the SM gluons with 5D coupling  $g_s$ . The gauge bosons corresponding to  $SU(2)_L$  and  $SU(2)_R$  are denoted as  $W_{L\mu}^a$  and  $W_{R\mu}^a$  ( $a = 1, 2, 3$ ), respectively, with 5D gauge coupling  $g$ . Where the equality of the  $SU(2)_L$  and  $SU(2)_R$  couplings is imposed by  $P_{LR}$  symmetry. The gauge field

<sup>5</sup> Here we mention that we have employed a different notation for the mass of the first KK gauge bosons than in [65] such that our  $M_{KK}$  corresponds to their  $f$ .

corresponding to  $U(1)_X$  is denoted as  $X_\mu$  with 5D coupling  $g_X$ . All 5D gauge couplings are dimensionful and the relation between 5D and its 4D counterpart is given by  $g_s^{4D} = g_s/\sqrt{L}$ , with similar expressions also existing for  $g^{4D}$  and  $g_X^{4D}$ . Charged gauge bosons are defined as

$$W_{L(R)\mu}^\pm = \frac{W_{L(R)\mu}^1 \mp iW_{L(R)\mu}^2}{\sqrt{2}}. \quad (5)$$

Mixing between the bosons  $W_{R\mu}^3$  and  $X_\mu$  results in fields  $Z_{X\mu}$  and  $B_\mu$ ,

$$\begin{aligned} Z_{X\mu} &= \cos\phi W_{R\mu}^3 - \sin\phi X_\mu, \\ B_\mu &= \sin\phi W_{R\mu}^3 + \cos\phi X_\mu, \end{aligned} \quad (6)$$

where

$$\cos\phi = \frac{g}{\sqrt{g^2 + g_X^2}}, \quad \sin\phi = \frac{g_X}{\sqrt{g^2 + g_X^2}}. \quad (7)$$

Further, mixing between  $W_{L\mu}^3$  and  $B_\mu$  yields the fields  $Z_\mu$  and  $A_\mu$  in analogy to the SM,

$$\begin{aligned} Z_\mu &= \cos\psi W_{L\mu}^3 - \sin\psi B_\mu, \\ A_\mu &= \sin\psi W_{L\mu}^3 + \cos\psi B_\mu, \end{aligned} \quad (8)$$

with

$$\cos\psi = \frac{1}{\sqrt{1 + \sin^2\phi}}, \quad \sin\psi = \frac{\sin\phi}{\sqrt{1 + \sin^2\phi}}. \quad (9)$$

Along with eight gluons  $G_\mu^A(++)$ , after the mixing pattern, we have four charged bosons which are specified as  $W_L^\pm(++)$  and  $W_R^\pm(-+)$  while three neutral gauge bosons are given as  $A(++)$ ,  $Z(++)$  and  $Z_X(-+)$ . Moreover, we mention the following remarks about the masses and profiles of various gauge boson fields that are obtained after solving the corresponding EOMs. Before EWSB, gauge bosons with  $(++)$  BCs have massless zero modes, which correspond to the SM gauge fields, with flat profiles along the extra dimension. On the other hand gauge bosons with  $(-+)$  BCs do not have a zero mode and the lightest mode in the KK tower starts at  $n = 1$ . The profiles of the first KK mode of gauge bosons having a zero mode are denoted by  $g(y)$  and the mass of such modes is denoted as  $M_{++}$  while the first mode profiles of the gauge bosons without a zero mode are given by  $\tilde{g}(y)$  and the mass of such modes is denoted as  $M_{-+}$  before EWSB. There expressions are given by [79],

$$g(y) = \frac{e^{ky}}{N_1} \left[ J_1\left(\frac{M_{g^{(1)}}}{k} e^{ky}\right) + b_1(M_{g^{(1)}}) Y_1\left(\frac{M_{g^{(1)}}}{k} e^{ky}\right) \right], \quad (10)$$

$$\tilde{g}(y) = \frac{e^{ky}}{N_1} \left[ J_1\left(\frac{\tilde{M}_{g^{(1)}}}{k} e^{ky}\right) + \tilde{b}_1(\tilde{M}_{g^{(1)}}) Y_1\left(\frac{\tilde{M}_{g^{(1)}}}{k} e^{ky}\right) \right], \quad (11)$$

where  $J_1$  and  $Y_1$  are the Bessel functions of first and second kinds, respectively. The coefficients  $b_1(M_{g^{(1)}})$ ,  $\tilde{b}_1(\tilde{M}_{g^{(1)}})$  and  $N_1$  are

$$b_1(M_{g^{(1)}}) = -\frac{J_1(M_{g^{(1)}}/k) + M_{g^{(1)}}/kJ_1'(M_{g^{(1)}}/k)}{Y_1(M_{g^{(1)}}/k) + M_{g^{(1)}}/kY_1'(M_{g^{(1)}}/k)}, \quad (12)$$

$$\tilde{b}_1(\tilde{M}_{g^{(1)}}) = -\frac{J_1(\tilde{M}_{g^{(1)}}/k)}{Y_1(\tilde{M}_{g^{(1)}}/k)}, \quad (13)$$

$$N_1 = \frac{e^{kL/2}}{\sqrt{\pi LM_{g^{(1)}}}}. \quad (14)$$

The masses of the lowest KK gauge excitations are numerically given to be  $M_{g^{(1)}} \simeq 2.45 M_{\text{KK}} \equiv M_{++}$  and  $\tilde{M}_{g^{(1)}} \simeq 2.40 M_{\text{KK}} \equiv M_{-+}$ . Notice that the presented KK masses for the gauge bosons are universal for all gauge bosons with the same BCs. After EWSB, the zero mode gauge bosons with  $(++)$  BCs, other than gluons and photon, acquire masses while the massive KK gauge excitations of all the gauge bosons, except KK gluons and KK photons receive mass corrections. Due to the unbroken gauge invariance of  $SU(3)$  and  $U(1)_Q$ , gluons and photon do not obtain masses such that their zero modes remain massless while their higher KK excitations that are massive do not get a mass correction as a result of EWSB and hence remain mass eigenstates. Furthermore, we have mixing among zero modes and the higher KK modes. Considering only the first KK modes, the charged and neutral mass eigenstates are related to their corresponding gauge KK eigenstates via

$$\begin{pmatrix} W^\pm \\ W_H^\pm \\ W'^\pm \end{pmatrix} = \mathcal{G}_W \begin{pmatrix} W_L^{\pm(0)} \\ W_L^{\pm(1)} \\ W_R^{\pm(1)} \end{pmatrix}, \quad \begin{pmatrix} Z \\ Z_H \\ Z' \end{pmatrix} = \mathcal{G}_Z \begin{pmatrix} Z^{(0)} \\ Z^{(1)} \\ Z_X^{(1)} \end{pmatrix}. \quad (15)$$

The expressions of the orthogonal mixing matrices  $\mathcal{G}_W$  and  $\mathcal{G}_Z$  and the masses of the mass eigenstates are given explicitly in [65].

Next, the SM fermions are embedded in three possible representations of  $SU(2)_L \times SU(2)_R$ , that are  $(\mathbf{2}, \mathbf{2})$ ,  $(\mathbf{1}, \mathbf{1})$  and  $(\mathbf{3}, \mathbf{1}) \oplus (\mathbf{1}, \mathbf{3})$ . Which fields belong to which multiplets are chosen according to the guidelines provided by phenomenology. For the realization of the SM quark and lepton sector in the  $RS_c$  model, we refer the reader to [65]. Moreover, other than SM fields, a number of additional vector-like fermion fields with electric charge  $2/3, -1/3$  and  $5/3$  are required to fill in the three representations of the  $SU(2)_L \times SU(2)_R$  gauge group. Since we only consider the fermion fields with  $(++)$  BCs, we do not discuss the new fermions which are introduced with  $(-+)$  or  $(+-)$  choices of the BCs. Furthermore, we will restrict ourselves only to the zero modes in the KK mode expansion of the fermionic fields with  $(++)$  BCs, which are massless before EWSB and up to small mixing effects with other massive modes after the EWSB, due to the transformation to mass eigenstates, are identified as the SM quarks and leptons. We have neglected the higher KK fermion modes because their impact is sub-leading as pointed out previously. The solution of the EOMs of the left and right-handed fermionic zero modes leads to their bulk profiles, which we denote as  $f_{L,R}^{(0)}(y, c_\Psi)$  and their expressions are given by

$$f_L^{(0)}(y, c_\Psi) = \sqrt{\frac{(1 - 2c_\Psi)kL}{e^{(1-2c_\Psi)kL} - 1}} e^{-c_\Psi ky}, \quad f_R^{(0)}(y, c_\Psi) = f_L^{(0)}(y, -c_\Psi). \quad (16)$$

The bulk mass parameter  $c_\Psi$  controls the localization of the fermionic zero modes such as for  $c_\Psi > 1/2$ , the left-handed fermionic zero mode is localized towards the UV brane, while for  $c_\Psi < 1/2$ , it is localized towards the IR brane. Similarly, from the expression of the  $f_R^{(0)}(y, c_\Psi)$ , the localization of the right-handed fermion zero mode depends on whether  $c_\Psi < -1/2$  or  $c_\Psi > -1/2$ . For the SM quarks we will denote the bulk mass parameters  $c_Q^i$  for the three left-handed zero mode embedded into bi-doublets of  $SU(2)_L \times SU(2)_R$ , while for the right-handed zero mode up and down-type quarks which belong to  $(\mathbf{1}, \mathbf{1})$  and  $(\mathbf{3}, \mathbf{1}) \oplus (\mathbf{1}, \mathbf{3})$  representations, respectively [65, 75], we assign bulk mass parameters  $c_{u,d}^i$ , respectively.



The effective 4D Yukawa couplings, relevant for the SM fermion masses and mixings, for the Higgs sector residing on the IR brane are given by [63]

$$Y_{ij}^{u(d)} = \lambda_{ij}^{u(d)} \frac{e^{kL}}{kL} f_L^{(0)}(y=L, c_Q^j) f_R^{(0)}(y=L, c_u^j(c_d^j)) \equiv \lambda_{ij}^{u(d)} \frac{e^{kL}}{kL} f_i^Q f_j^{u(d)}, \quad (17)$$

where  $\lambda^{u(d)}$  are the fundamental 5D Yukawa coupling matrices. Since the fermion profiles depend exponentially on the bulk mass parameters, one can recognize from the above relation that the strong hierarchies of quark masses and mixings originate from the  $\mathcal{O}(1)$  bulk mass parameters and anarchic 5D Yukawa couplings  $\lambda_{ij}^{u(d)}$ . The transformation from the quark flavor eigenbasis to the mass eigenbasis is performed by means of unitary mixing matrices, which are presented by  $\mathcal{U}_{L(R)}$  and  $\mathcal{D}_{L(R)}$  for the up-type left (right) and down-type left (right) quarks, respectively. Moreover, CKM matrix is given by  $V_{\text{CKM}} = \mathcal{U}_L^\dagger \mathcal{D}_L$  and the flavor-changing neutral-currents (FCNCs) are induced already at tree level in this model. This happens because the couplings of the fermions with the gauge bosons involve overlap integrals which contain the profiles of the corresponding fermions and gauge boson leading to non-universal flavor diagonal couplings. These non-universal flavor diagonal couplings induce off-diagonal entries in the interaction matrix after going to the fermion mass basis, resulting in tree level FCNCs. These are mediated by the three neutral electroweak gauge bosons  $Z$ ,  $Z'$  and  $Z_H$  as well as by the first KK excitations of the photon and the gluons, although the last one does not contribute to the processes with leptons in the final state. The expressions of the masses of the SM quarks and the flavor mixing matrices  $\mathcal{U}_{L(R)}$ ,  $\mathcal{D}_{L(R)}$  are given explicitly in terms of the quark profiles and the 5D Yukawa couplings  $\lambda_{ij}^{u(d)}$  in [63].

### 3. Theoretical formalism

The effective weak Hamiltonian for  $b \rightarrow s\mu^+\mu^-$  transition in the  $\text{RS}_c$  model can be written as

$$H_{\text{eff}}^{\text{RS}_c} = -\frac{4G_F}{\sqrt{2}} V_{tb} V_{ts}^* [C_7^{\text{RS}_c} O_7 + C_7'^{\text{RS}_c} O_7' + C_9^{\text{RS}_c} O_9 + C_9'^{\text{RS}_c} O_9' + C_{10}^{\text{RS}_c} O_{10} + C_{10}'^{\text{RS}_c} O_{10}'], \quad (18)$$

where  $G_F$  is the Fermi coupling constant and  $V_{tb}$ ,  $V_{ts}^*$  are the elements of the CKM mixing matrix. The involved operators read

$$\begin{aligned} O_7 &= \frac{e}{16\pi^2} m_b (\bar{s}_{L\alpha} \sigma^{\mu\nu} b_{R\alpha}) F_{\mu\nu}, \\ O_7' &= \frac{e}{16\pi^2} m_b (\bar{s}_{R\alpha} \sigma^{\mu\nu} b_{L\alpha}) F_{\mu\nu}, \\ O_9 &= \frac{e^2}{16\pi^2} (\bar{s}_{L\alpha} \gamma^\mu b_{L\alpha}) \bar{\mu} \gamma_\mu \mu, \\ O_9' &= \frac{e^2}{16\pi^2} (\bar{s}_{R\alpha} \gamma^\mu b_{R\alpha}) \bar{\mu} \gamma_\mu \mu, \\ O_{10} &= \frac{e^2}{16\pi^2} (\bar{s}_{L\alpha} \gamma^\mu b_{L\alpha}) \bar{\mu} \gamma_\mu \gamma_5 \mu, \\ O_{10}' &= \frac{e^2}{16\pi^2} (\bar{s}_{R\alpha} \gamma^\mu b_{R\alpha}) \bar{\mu} \gamma_\mu \gamma_5 \mu, \end{aligned} \quad (19)$$

where  $e$  is the electromagnetic coupling constant and  $m_b$  is the  $b$ -quark running mass in the  $\overline{\text{MS}}$  scheme. In the  $\text{RS}_c$  model the Wilson coefficients in the above effective Hamiltonian can

be written as

$$C_i^{(\prime)RS_c} = C_i^{(\prime)SM} + \Delta C_i^{(\prime)}, \quad (20)$$

where  $i = 7, 9, 10$ . In the SM case, ignoring tiny contribution, when present, the primed coefficients are zero while the unprimed Wilson coefficients  $C_i$  incorporating short-distance physics are evaluated through perturbative approach. The factorizable contributions from operators  $O_{1-6,8}$  have been absorbed in the effective Wilson coefficients  $C_7^{\text{eff}}$  and  $C_9^{\text{eff}}$  [80]. The expressions of these effective coefficients involve the functions  $h(m_q, q^2)$ ,  $F_8^{(7,9)}(q^2)$  defined in [81], and the functions  $F_{1,c}^{(7,9)}(q^2)$ ,  $F_{1,c}^{\prime(7,9)}(q^2)$  given in [82] for low  $q^2$  and in [83] for high  $q^2$ . The quark masses appearing in these functions are defined in the pole scheme. The long distance non-factorizable contributions of charm loop effects can alter the value of  $C_7^{\text{eff}}$  to some extent particularly in the region of charmonium resonances. Modifications  $\Delta C_{9,10}^{(\prime)}$  in the  $RS_c$  model, evaluated at the scale  $\mathcal{O}(M_{g^{(1)}})$  are given by [64]

$$\begin{aligned} \Delta C_9 &= \frac{\Delta Y_s}{\sin^2 \theta_W} - 4\Delta Z_s, \\ \Delta C_9' &= \frac{\Delta Y_s'}{\sin^2 \theta_W} - 4\Delta Z_s', \\ \Delta C_{10} &= -\frac{\Delta Y_s}{\sin^2 \theta_W}, \\ \Delta C_{10}' &= \frac{\Delta Y_s'}{\sin^2 \theta_W}, \end{aligned} \quad (21)$$

where

$$\begin{aligned} \Delta Y_s &= -\frac{1}{V_{tb} V_{ts}^*} \sum_X \frac{\Delta_L^{\mu\mu}(X) - \Delta_R^{\mu\mu}(X)}{4M_X^2 g_{SM}^2} \Delta_L^{bs}(X), \\ \Delta Y_s' &= -\frac{1}{V_{tb} V_{ts}^*} \sum_X \frac{\Delta_L^{\mu\mu}(X) - \Delta_R^{\mu\mu}(X)}{4M_X^2 g_{SM}^2} \Delta_R^{bs}(X), \\ \Delta Z_s &= \frac{1}{V_{tb} V_{ts}^*} \sum_X \frac{\Delta_R^{\mu\mu}(X)}{8M_X^2 g_{SM}^2 \sin^2 \theta_W} \Delta_L^{bs}(X), \\ \Delta Z_s' &= \frac{1}{V_{tb} V_{ts}^*} \sum_X \frac{\Delta_R^{\mu\mu}(X)}{8M_X^2 g_{SM}^2 \sin^2 \theta_W} \Delta_R^{bs}(X). \end{aligned} \quad (22)$$

The sums run over the neutral gauge bosons  $X = Z, Z', Z_H$  and  $A^{(1)}$  with  $g_{SM}^2 = \frac{G_F}{\sqrt{2}} \frac{\alpha}{2\pi \sin^2 \theta_W}$ .  $\Delta C_9^{(\prime)}$  and  $\Delta C_{10}^{(\prime)}$  evaluated at the scale  $M_{g^{(1)}}$  do not need to be evolved to  $\mu_b$  scale. In the case of  $\Delta C_7^{(\prime)}$ , detailed calculation with the set of assumptions consistent with the calculations of  $\Delta C_{9,10}^{(\prime)}$  is given in appendix C of [68], where  $\Delta C_7$  and  $\Delta C_7'$  are evaluated at the  $M_{g^{(1)}}$  scale. The evolution at the scale  $\mu_b$  is given by the following master formula [67]

$$\Delta C_7^{(\prime)}(\mu_b) = 0.429 \Delta C_7^{(\prime)}(M_{g^{(1)}}) + 0.128 \Delta C_8^{(\prime)}(M_{g^{(1)}}). \quad (23)$$

The decay amplitude for  $\Lambda_b \rightarrow \Lambda \mu^+ \mu^-$  can be obtained by sandwiching the effective Hamiltonian displayed in equation (18) within the baryonic states

$$\begin{aligned}
\mathcal{M}_{\text{RS}_c}(\Lambda_b \rightarrow \Lambda \mu^+ \mu^-) = & \frac{G_F \alpha}{\sqrt{2} \pi} V_{tb} V_{ts}^* \left[ \langle \Lambda(k) | \bar{s} \gamma_\mu (C_9^{\text{RS}_c} P_L + C_9'^{\text{RS}_c} P_R) b | \Lambda_b(p) \rangle (\bar{\mu} \gamma^\mu \mu) \right. \\
& + [\langle \Lambda(k) | \bar{s} \gamma_\mu (C_{10}^{\text{RS}_c} P_L + C_{10}'^{\text{RS}_c} P_R) b | \Lambda_b(p) \rangle (\bar{\mu} \gamma^\mu \gamma^5 \mu) \\
& \left. - \frac{2m_b}{q^2} \langle \Lambda(k) | \bar{s} i \sigma_{\mu\nu} q^\nu (C_7^{\text{RS}_c} P_R + C_7'^{\text{RS}_c} P_L) b | \Lambda_b(p) \rangle \bar{\mu} \gamma^\mu \mu \right]. \quad (24)
\end{aligned}$$

The matrix elements involved in the expression of decay amplitude are given in [47] written in helicity basis in terms of FF. The detailed calculation of FFs in lattice QCD is carried out in [23], which will be used in our numerical analysis. The angular decay distribution of the four-fold decay  $\Lambda_b \rightarrow \Lambda(\rightarrow p\pi)\mu^+\mu^-$ , with an unpolarized  $\Lambda_b$ , can be written as [44, 47]

$$\begin{aligned}
\frac{d^4\Gamma}{ds \, d\cos\theta_\Lambda \, d\cos\theta_l \, d\phi} = & \frac{3}{8\pi} [K_{1ss} \sin^2 \theta_l + K_{1cc} \cos^2 \theta_l + K_{1c} \cos \theta_l \\
& + (K_{2ss} \sin^2 \theta_l + K_{2cc} \cos^2 \theta_l + K_{2c} \cos \theta_l) \cos \theta_\Lambda \\
& + (K_{3sc} \sin \theta_l \cos \theta_l + K_{3s} \sin \theta_l) \sin \theta_\Lambda \sin \phi \\
& + (K_{4sc} \sin \theta_l \cos \theta_l + K_{4s} \sin \theta_l) \sin \theta_\Lambda \cos \phi], \quad (25)
\end{aligned}$$

where  $K$ 's represent the angular coefficients which are functions of  $s = q^2$ . Here we concentrate on the observables which have been measured experimentally so that we compare our analysis with experimental data. For the decay under consideration decay rate and longitudinal polarization of the daughter baryon  $\Lambda$  are

$$\frac{d\Gamma}{ds} = 2K_{1ss} + K_{1cc}, \quad F_L = \frac{2K_{1ss} - K_{1cc}}{2K_{1ss} + K_{1cc}}. \quad (26)$$

Forward–backward asymmetry with respect to leptonic and baryonic angles is given as

$$A_{\text{FB}}^l = \frac{3K_{1c}}{4K_{1ss} + 2K_{1cc}}, \quad A_{\text{FB}}^\Lambda = \frac{2K_{2ss} + K_{2cc}}{4K_{1ss} + 2K_{1cc}}. \quad (27)$$

The combined FB asymmetry is

$$A_{\text{FB}}^{\Lambda l} = \frac{3K_{2c}}{8K_{1ss} + 4K_{1cc}}. \quad (28)$$

The uncertainties in the decay rate are larger as it strongly depends on hadronic FF. The other observables being ratio of angular coefficients, are more sensitive to NP effects but less sensitive to hadronic FFs.

#### 4. Constraints and generation of the parameter space of the $\text{RS}_c$ model

In this section we consider the relevant constraints on the parameter space of the  $\text{RS}_c$  model coming from the direct searches at the LHC [84, 85], EW precision tests [78, 86], the latest measurements of the Higgs signal strengths at the LHC [78] and from  $\Delta F = 2$  flavor observables [63].

Starting with the direct searches, current measurements at the LHC for resonances decaying to  $t\bar{t}$  pair constrain the lightest KK gluon mass  $M_{g^{(1)}} > 3.3$  TeV at 95% confidence level [85]. Further, in the  $\text{RS}_c$  model, EW precision measurements permit to have masses of the lowest KK gauge bosons in the few TeV range. For example, a tree-level analysis of the S and T parameters leads to  $M_{g^{(1)}} > 4.8$  TeV for the lightest KK gluon and KK photon masses [86]. Furthermore, a comparison of the predictions of all relevant Higgs decays

in the  $RS_c$  model with the latest data from the LHC shows that the signal rates for  $pp \rightarrow h \rightarrow ZZ^*, WW^*$  provide the most stringent bounds, such that KK gluon masses lighter than  $22.7 \text{ TeV} \times (y_*/3)$  in the brane-Higgs case and  $13.2 \text{ TeV} \times (y_*/3)$  in the narrow bulk-Higgs scenario are excluded at 95% probability [78], where  $y_* = \mathcal{O}(1)$  free parameter is defined as the upper bound on the anarchic 5D Yukawa couplings such that  $|\lambda_{ij}^{u(d)}| \leq y_*$ . This implies that  $y_* = 3$  value, coming from the perturbativity bound of the RS model, will lead to much stronger bounds from Higgs physics than those emerging from the EW precision tests. In general, one can lower these bounds by considering smaller values of  $y_*$ . However one should keep in mind that lowering the bounds up to KK gauge bosons masses implied by EW precision constraints,  $M_{g^{(1)}} = 4.8 \text{ TeV}$ , will require too-small Yukawa couplings,  $y_* < 0.3$  for the brane-Higgs scenario [78], which will reinforce the RS flavor problem because of enhanced corrections to  $\epsilon_K$ . Therefore, moderate bounds on the value of the  $y_*$  should be considered by relatively increasing the KK scale, in order to avoid constraints from both flavor observables and Higgs physics.

Next, in analogy to our previous analysis [70], we explore the parameter space of the  $RS_c$  model by generating two sets of anarchic 5D Yukawa matrices, whose entries satisfy  $|\lambda_{ij}^{u(d)}| \leq y_*$  with  $y_* = 1.5$  and 3. Further, we choose the nine quark bulk-mass parameters  $c_{Q,u,d}$ , which together with the 5D Yukawa matrices reproduce the correct values of the quark masses evaluated at the scale  $\mu = 3 \text{ TeV}$ , CKM mixing angles and the Jarlskog determinant, all within their respective  $2\sigma$  ranges. For muon, we take  $c_\mu = 0.7$  as lepton flavor-conserving couplings are found to be almost independent of the chosen value as far as  $c_l > 0.5$  [64]. Additionally, from the  $\Delta F = 2$  flavor observables, we apply the constraints from  $\epsilon_K$ ,  $\Delta M_K$  and  $\Delta M_{B_s}$  observables, where we set the required input parameters, as given in table 2 of [70], to their central values and allow the resulting observables to deviate by  $\pm 30\%$ ,  $\pm 50\%$  and  $\pm 30\%$ , respectively in analogy to the analysis [63]. For further details on the parameter scan, we refer the reader to [63, 70].

## 5. Numerical analysis

### 5.1. Wilson coefficients

The generated 5D parameter points consisting of Yukawa coupling matrices and bulk mass parameters, fulfilling all the relevant constraints, are used to evaluate the Wilson coefficients in the  $RS_c$  model. In figure 1, we show the dependence of  $|\Delta C_{10}|$  Wilson coefficient on the mass of lowest KK gluon  $M_{g^{(1)}}$  taken in the range 2.45–20 TeV. The red and blue scatter points represent the cases of  $y_* = 1.5$  and 3, respectively. The gray region is excluded by the analysis of EW precision observables. It is clear that the smaller values of  $M_{g^{(1)}}$  give larger deviations. Moreover, for a fixed value of  $M_{g^{(1)}}$  a range of predictions for possible deviations are present for both cases of  $y_*$  such that the maximum allowed deviation for  $|\Delta C_{10}|$  in the case of  $y_* = 1.5$  are generally greater than the case of  $y_* = 3$ . This is due to the fact that in the case of  $y_* = 3$ , the SM fermions are more elementary as their profiles are localized towards the UV brane to a greater extent compared to the  $y_* = 1.5$  case leading to more suppressed FCNC and subsequently smaller deviations in comparison to the case of  $y_* = 1.5$ . Observing the fact that the deviations for all  $|\Delta C_i^{(f)}|$  for  $M_{g^{(1)}} > 10 \text{ TeV}$  are so small, as clear from figure 1 in the case of  $|\Delta C_{10}|$ , that the observables will almost remain unaffected, we limit the range for  $M_{g^{(1)}}$  from 4.8 to 10 TeV, where the lower value is implied by the EW precision constraints. As we are interested in the largest possible deviations of  $|\Delta C_i^{(f)}|$ , for a given allowed value of  $M_{g^{(1)}}$ , so we will take the  $y_* = 1.5$  case and by considering five different

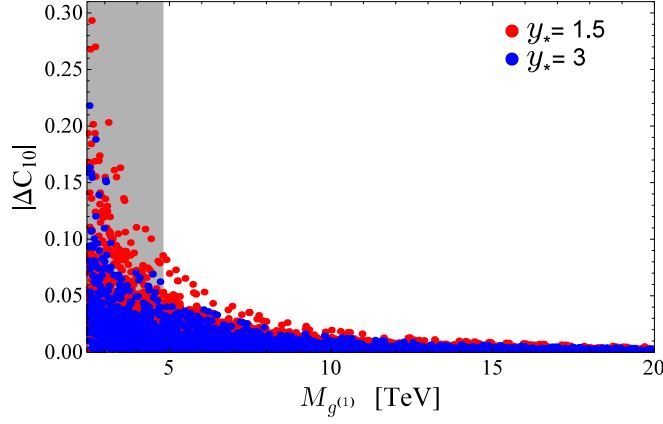


**Figure 1.** The  $RS_c$  contribution to  $|\Delta C_{10}|$  as a function of the KK gluon mass  $M_{g^{(1)}}$  for two different values of  $y_*$ . The gray region is excluded by the analysis of electroweak precision measurements.

values of  $M_{g^{(1)}} \in [4.8, 10]$ , we obtain the maximum possible deviation of each Wilson coefficient. The resultant values will be used for evaluating the effects on the angular observables of interest for each considered value of  $M_{g^{(1)}}$  in next section i.e., section 5.2.

In figure 2, we show the correlation plots between  $|\Delta C_{7,9,10}^{(i)}|$  obtained for the fixed value of  $M_{g^{(1)}} = 4.8$  TeV. The maximum possible deviations from the SM values in this case are

$$\begin{aligned} |\Delta C_7|_{\max} &= 0.011, & |\Delta C_9|_{\max} &= 0.0064, & |\Delta C_{10}|_{\max} &= 0.085, \\ |\Delta C_7'|_{\max} &= 0.0037, & |\Delta C_9'|_{\max} &= 0.047, & |\Delta C_{10}'|_{\max} &= 0.621. \end{aligned}$$

It is found that  $|\Delta C_9|$  and  $|\Delta C_{10}|$  are linearly correlated, as shown in figure 2(f), and same is true for each pair  $|\Delta C_i^{(i)}|$  with  $i = 9, 10$ .

### 5.2. Angular observables

In this section we discuss the numerical results computed for different angular observables both in the SM and for the  $RS_c$  model. The input parameters used in the calculations are included in table 1. The presented results include the uncertainty in the hadronic FFs, which are non-perturbative quantities. For this, we utilize the lattice QCD calculations [23], both in the low and high  $q^2$  ranges, which to date are considered as most accurate in the literature. To improve the accuracy, we have used the numerical values for the short-distance Wilson coefficients, with NNLL accuracy, at the low energy scale  $\mu_b = 4.2$  GeV, given in table 2.

The numerical results for the angular observables in appropriate bins are shown in tables 3 and 4, where a comparison is presented between the predictions obtained for five different values of  $M_{g^{(1)}}$  in the  $RS_c$  model (for  $y_* = 1.5$ ) to that of the SM estimates and with the experimental measurements, where available. The whole spectrum of di-muon mass squared ( $s \in \{s_{\min} = 4m_\mu^2, s_{\max} = (m_{\Lambda_b}^2 - m_\Lambda^2)\}$ ) has not been discussed as the region  $s \in [8, 15]$  GeV<sup>2</sup> is expected to receive sizable corrections from charmonium loops that violate quark–hadron duality. Hence the regions  $s \in [0.1, 8]$  GeV<sup>2</sup> and  $s \in [15, 20]$  GeV<sup>2</sup> have been considered in order to avoid the long distance effects of charmonium resonances arising when lepton pair momenta approaches the masses of  $J/\psi$  family. It can be seen that the results in the  $RS_c$  model for most of the observables show little deviation from the SM predictions.

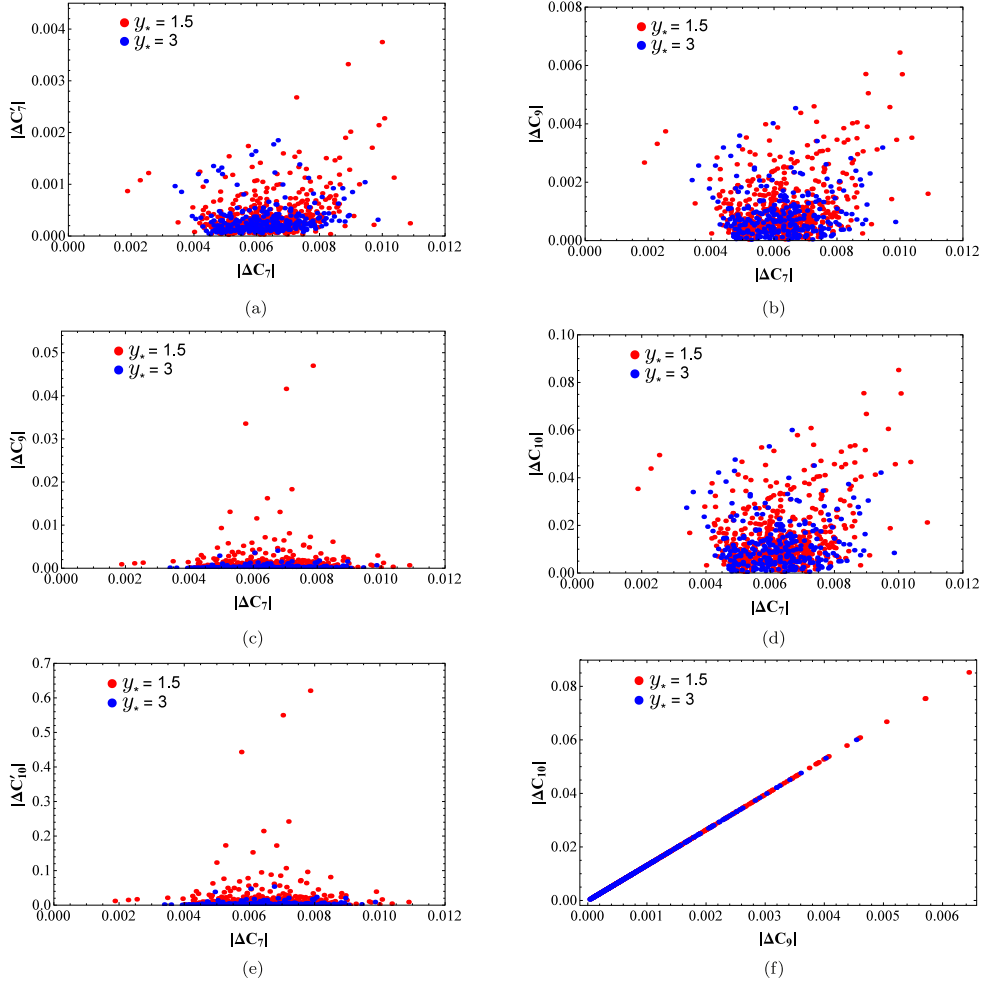


**Figure 2.** Correlation plots between the Wilson coefficients  $|\Delta C_{7,9,10}^{(l)}|$  of the  $RS_c$  model for a fixed value of  $M_g^{(l)} = 4.8$  TeV. The coefficients  $\Delta C_7^{(l)}$  are calculated at the  $\mu_b$  scale. The red and blue points correspond to  $y_* = 1.5$  and 3, respectively.

Maximum deviation from the SM results has been observed for  $M_g^{(l)} = 4.8$  TeV and the difference gradually decreases as one moves from  $M_g^{(l)} = 4.8$  TeV to  $M_g^{(l)} = 10$  TeV.

Next, we compare our results of observables in the SM and the  $RS_c$  model with the measurements from the LHCb experiment [22]. For most of the observables, results in the  $RS_c$  model are close to that obtained for the SM in all bins of  $s$  and this can be seen in tables 3 and 4. The branching ratio for the four-body decay process  $\Lambda_b \rightarrow \Lambda(\rightarrow p\pi)\mu^+\mu^-$  in the  $RS_c$  model (for  $M_g^{(l)} = 4.8$  TeV) shows a slight deviation at low recoil and almost no deviation at large recoil. For the bin [1.1, 6], the branching ratio in the SM and the  $RS_c$  are  $0.199^{+0.12}_{-0.12}$  and  $0.190^{+0.120}_{-0.119}$ , respectively, which are  $1.8\sigma$  and  $1.9\sigma$  away from the measured value  $0.09^{+0.061}_{-0.051}$ . The situation is quite similar for all other bins of large recoil where values of observables do not change much even for  $M_g^{(l)} = 4.8$  TeV. For low recoil bin [15, 20], the SM and the  $RS_c$  model results  $0.753^{+0.069}_{-0.069}$  and  $0.807^{+0.069}_{-0.069}$  deviate from the measured value by  $4.7\sigma$  and  $4.1\sigma$ .

**Table 1.** Default values of the input parameters used in the calculations [23, 87].

$G_F = 1.16638 \times 10^{-5} \text{ GeV}^{-2}$	$m_t^{\text{pole}} = 174.2 \pm 1.4 \text{ GeV}$	$m_\pi = 0.135 \text{ GeV}$
$\alpha_s(m_Z) = 0.1182 \pm 0.0012$	$m_b^{\text{pole}} = 4.78 \pm 0.06 \text{ GeV}$	$m_K = 0.494 \text{ GeV}$
$\alpha(\mu_b) = 1/133.28$	$m_c^{\text{pole}} = 1.67 \pm 0.07 \text{ GeV}$	$m_B = 5.279 \text{ GeV}$
$m_W = 80.385 \pm 0.015 \text{ GeV}$	$m_b = 4.18^{+0.04}_{-0.03} \text{ GeV}$	$m_{\Lambda_b} = 5.619 \text{ GeV}$
$m_Z = 91.1876 \pm 0.0021 \text{ GeV}$	$m_c = 1.27 \pm 0.03 \text{ GeV}$	$\tau_{\Lambda_b} = (1.466 \pm 0.010) \text{ ps}$
$ V_{tb} V_{ts}^*  = 0.04152$	$m_s = 0.096^{+0.008}_{-0.004} \text{ GeV}$	$m_\Lambda = 1.116 \text{ GeV}$
$\alpha_\Lambda = 0.642 \pm 0.013$	$\mu_b = 4.2 \text{ GeV}$	

**Table 2.** The SM Wilson coefficients up to NNLL accuracy given at  $\mu_b = 4.2 \text{ GeV}$  scale.

$C_1 = -0.294$	$C_2 = 1.017$	$C_3 = -0.0059$	$C_4 = -0.087$	$C_5 = 0.0004$
$C_6 = 0.0011$	$C_7 = -0.324$	$C_8 = -0.176$	$C_9 = 4.114$	$C_{10} = -4.193$

It is noted that the differential branching ratio in the  $RS_c$  model is lower than the SM at large recoil and higher than the SM at low recoil.

In case of  $F_L$ , maximum deviation has been observed for the first bin  $[0.1, 2] \text{ GeV}^2$  where predictions in the SM and the  $RS_c$  model are  $\langle F_L \rangle_{SM} = 0.535^{+0.065}_{-0.078}$  and  $\langle F_L \rangle_{RS_c} = 0.552^{+0.069}_{-0.084}$ , respectively which vary from the measured value  $0.56^{+0.244}_{-0.566}$  by  $0.1\sigma$  and  $0.02\sigma$ , respectively. For most of the bins, deviation of  $F_L$  in the  $RS_c$  model from the SM is negligible. For low recoil bin  $[15, 20] \text{ GeV}^2$ , the values in both models  $\langle F_L \rangle_{SM} = 0.409^{+0.033}_{-0.018}$ ,  $\langle F_L \rangle_{RS_c} = 0.403^{+0.034}_{-0.019}$  deviate from the experimental result  $0.61^{+0.114}_{-0.143}$  in the same bin by  $1.6\sigma$ . At lower values of  $s$  up to  $4 \text{ GeV}^2$ , the  $RS_c$  model results deviate from the SM values to a greater extent, whereas almost similar values of the  $RS_c$  model are obtained for the rest of the spectrum.

For  $A_{FB}^\ell$ , small deviation in the  $RS_c$  model exists from the SM at low recoil. In the first bin  $[0.1, 2] \text{ GeV}^2$  our calculated results in both models differ from the measured value by  $0.6\sigma$ . For large  $s$  bin  $[15, 20] \text{ GeV}^2$ , the values in both models  $\langle A_{FB}^\ell \rangle_{SM} = -0.358^{+0.012}_{-0.007}$  and  $\langle A_{FB}^\ell \rangle_{RS_c} = -0.332^{+0.008}_{-0.009}$  are very close to each other and are  $3.2\sigma$  and  $3.0\sigma$  away from the measured value  $-0.05^{+0.095}_{-0.095}$  in the same bin.

For  $A_{FB}^\Lambda$  in the bin  $[15, 20] \text{ GeV}^2$  results of the SM and the  $RS_c$  model are  $\langle A_{FB}^\Lambda \rangle_{SM} = -0.271^{+0.011}_{-0.011}$  and  $\langle A_{FB}^\Lambda \rangle_{RS_c} = -0.247^{+0.011}_{-0.011}$  and deviate from the measured value of LHCb  $-0.29^{+0.076}_{-0.081}$  by  $0.2\sigma$  and  $0.5\sigma$ . For  $A_{FB}^{\ell\Lambda}$ , no sizable deviation from the SM has been observed in any  $s$  bin for the  $RS_c$  model.

## 6. Conclusions

In the work presented here, we have studied the angular observables of the theoretically clean decay  $\Lambda_b \rightarrow \Lambda(\rightarrow p\pi^-)\mu^+\mu^-$  in the SM and the RS model with custodial protection. After performing the scan of the parameter space of the model in the light of current constraints, we have worked out the largest possible deviations in the Wilson coefficients  $|\Delta C_{7,9,10}^\ell|$  from the SM predictions for different allowed values of KK gluon mass  $M_g^{(v)}$ . The resultant deviations are small and do not allow for large effects in the angular observables. Although for maximum possible deviations in Wilson coefficients, for  $M_g^{(v)} = 4.8 \text{ TeV}$ , in the  $RS_c$  model, some

**Table 3.** Numerical results of the observables (low  $s$  region) in the  $\Lambda_b \rightarrow \Lambda(\rightarrow p\pi^+)\mu^+\mu^-$  decay, obtained for the SM and the  $RS_c$  model with  $y_s = 1.5$  case, in different bins of low  $s$ . Experimentally measured values are taken from [22].

		$\langle \frac{d\mathcal{B}}{ds} \times 10^{-7} \rangle$	$\langle F_L \rangle$	$\langle A_{FB}^\ell \rangle$	$\langle A_{FB}^\Lambda \rangle$	$\langle A_{FB}^\Lambda \rangle$
[0, 1, 2]	SM	$0.236_{-0.230}^{+0.230}$	$0.535_{-0.078}^{+0.065}$	$0.097_{-0.007}^{+0.006}$	$-0.310_{-0.008}^{+0.015}$	$-0.031_{-0.002}^{+0.003}$
	$RS_c M_{g^{(0)}} = 4.8$	$0.219_{-0.217}^{+0.218}$	$0.552_{-0.084}^{+0.069}$	$0.093_{-0.006}^{+0.005}$	$-0.313_{-0.004}^{+0.013}$	$-0.030_{-0.002}^{+0.003}$
	$RS_c M_{g^{(0)}} = 6.1$	$0.225_{-0.217}^{+0.219}$	$0.545_{-0.082}^{+0.067}$	$0.095_{-0.006}^{+0.005}$	$-0.313_{-0.006}^{+0.014}$	$-0.030_{-0.002}^{+0.003}$
	$RS_c M_{g^{(0)}} = 7.4$	$0.229_{-0.222}^{+0.224}$	$0.542_{-0.081}^{+0.067}$	$0.095_{-0.007}^{+0.006}$	$-0.312_{-0.007}^{+0.015}$	$-0.030_{-0.002}^{+0.003}$
	$RS_c M_{g^{(0)}} = 8.7$	$0.232_{-0.223}^{+0.224}$	$0.540_{-0.080}^{+0.066}$	$0.096_{-0.007}^{+0.006}$	$-0.312_{-0.007}^{+0.015}$	$-0.031_{-0.002}^{+0.003}$
	$RS_c M_{g^{(0)}} = 10$	$0.233_{-0.225}^{+0.228}$	$0.539_{-0.080}^{+0.066}$	$0.096_{-0.007}^{+0.006}$	$-0.311_{-0.007}^{+0.015}$	$-0.031_{-0.002}^{+0.003}$
	LHCb	$0.36_{-0.112}^{+0.122}$	$0.56_{-0.566}^{+0.244}$	$0.37_{-0.481}^{+0.371}$	$-0.12_{-0.318}^{+0.344}$	—
[2, 4]	SM	$0.180_{-0.123}^{+0.123}$	$0.855_{-0.012}^{+0.008}$	$0.054_{-0.030}^{+0.037}$	$-0.306_{-0.012}^{+0.022}$	$-0.016_{-0.009}^{+0.008}$
	$RS_c M_{g^{(0)}} = 4.8$	$0.171_{-0.117}^{+0.118}$	$0.860_{-0.006}^{+0.008}$	$0.040_{-0.026}^{+0.035}$	$-0.311_{-0.005}^{+0.016}$	$-0.013_{-0.010}^{+0.009}$
	$RS_c M_{g^{(0)}} = 6.1$	$0.173_{-0.117}^{+0.118}$	$0.859_{-0.008}^{+0.008}$	$0.045_{-0.028}^{+0.036}$	$-0.311_{-0.008}^{+0.018}$	$-0.014_{-0.009}^{+0.008}$
	$RS_c M_{g^{(0)}} = 7.4$	$0.175_{-0.118}^{+0.119}$	$0.858_{-0.009}^{+0.008}$	$0.048_{-0.028}^{+0.036}$	$-0.310_{-0.009}^{+0.020}$	$0.015_{-0.009}^{+0.008}$
	$RS_c M_{g^{(0)}} = 8.7$	$0.176_{-0.119}^{+0.119}$	$0.857_{-0.008}^{+0.008}$	$0.050_{-0.029}^{+0.036}$	$-0.310_{-0.010}^{+0.020}$	$-0.015_{-0.009}^{+0.008}$
	$RS_c M_{g^{(0)}} = 10$	$0.177_{-0.120}^{+0.120}$	$0.857_{-0.011}^{+0.008}$	$0.051_{-0.030}^{+0.037}$	$-0.309_{-0.010}^{+0.021}$	$-0.016_{-0.009}^{+0.008}$
	LHCb	$0.11_{-0.091}^{+0.120}$	—	—	—	—
[4, 6]	SM	$0.232_{-0.110}^{+0.110}$	$0.807_{-0.012}^{+0.018}$	$-0.063_{-0.026}^{+0.038}$	$-0.311_{-0.008}^{+0.014}$	$0.021_{-0.009}^{+0.007}$
	$RS_c M_{g^{(0)}} = 4.8$	$0.224_{-0.108}^{+0.108}$	$0.806_{-0.016}^{+0.021}$	$-0.078_{-0.021}^{+0.034}$	$-0.314_{-0.002}^{+0.008}$	$0.024_{-0.009}^{+0.008}$
	$RS_c M_{g^{(0)}} = 6.1$	$0.227_{-0.108}^{+0.109}$	$0.807_{-0.015}^{+0.019}$	$-0.072_{-0.022}^{+0.036}$	$-0.314_{-0.004}^{+0.010}$	$0.023_{-0.009}^{+0.007}$
	$RS_c M_{g^{(0)}} = 7.4$	$0.228_{-0.109}^{+0.109}$	$0.807_{-0.014}^{+0.019}$	$-0.069_{-0.024}^{+0.037}$	$-0.314_{-0.005}^{+0.012}$	$0.023_{-0.009}^{+0.007}$
	$RS_c M_{g^{(0)}} = 8.7$	$0.229_{-0.109}^{+0.109}$	$0.807_{-0.013}^{+0.019}$	$-0.068_{-0.024}^{+0.037}$	$-0.314_{-0.006}^{+0.012}$	$0.022_{-0.009}^{+0.007}$
	$RS_c M_{g^{(0)}} = 10$	$0.230_{-0.110}^{+0.110}$	$0.807_{-0.013}^{+0.019}$	$-0.067_{-0.025}^{+0.037}$	$-0.313_{-0.006}^{+0.013}$	$0.022_{-0.009}^{+0.007}$



Table 3. (Continued.)

	$\langle \frac{d\mathcal{B}}{ds} \times 10^{-7} \rangle$	$\langle F_L \rangle$	$\langle A_{FB}^e \rangle$	$\langle A_{FB}^A \rangle$	$\langle A_{FB}^{\Delta} \rangle$
LHCb	$0.02^{+0.091}_{-0.010}$	—	—	—	—
[6, 8]					
SM	$0.312^{+0.094}_{-0.094}$	$0.724^{+0.025}_{-0.014}$	$-0.162^{+0.025}_{-0.017}$	$-0.317^{+0.007}_{-0.004}$	$0.052^{+0.005}_{-0.007}$
RS $_c _{M_g^{(1)}} = 4.8$	$0.306^{+0.094}_{-0.095}$	$0.720^{+0.026}_{-0.016}$	$-0.174^{+0.021}_{-0.013}$	$-0.314^{+0.002}_{-0.001}$	$0.054^{+0.005}_{-0.007}$
RS $_c _{M_g^{(1)}} = 6.1$	$0.307^{+0.094}_{-0.093}$	$0.721^{+0.026}_{-0.016}$	$-0.170^{+0.022}_{-0.014}$	$-0.317^{+0.004}_{-0.001}$	$0.054^{+0.005}_{-0.007}$
RS $_c _{M_g^{(1)}} = 7.4$	$0.308^{+0.094}_{-0.093}$	$0.722^{+0.025}_{-0.015}$	$-0.168^{+0.023}_{-0.015}$	$-0.317^{+0.005}_{-0.002}$	$0.054^{+0.005}_{-0.007}$
RS $_c _{M_g^{(1)}} = 8.7$	$0.309^{+0.094}_{-0.094}$	$0.723^{+0.025}_{-0.015}$	$-0.166^{+0.024}_{-0.016}$	$-0.317^{+0.006}_{-0.002}$	$0.053^{+0.005}_{-0.007}$
RS $_c _{M_g^{(1)}} = 10$	$0.310^{+0.094}_{-0.094}$	$0.723^{+0.025}_{-0.014}$	$-0.165^{+0.024}_{-0.016}$	$-0.317^{+0.006}_{-0.003}$	$0.053^{+0.006}_{-0.007}$
LHCb	$0.25^{+0.120}_{-0.111}$	—	—	—	—
[1, 1, 6]					
SM	$0.199^{+0.120}_{-0.120}$	$0.818^{+0.011}_{-0.011}$	$0.009^{+0.027}_{-0.018}$	$-0.309^{+0.018}_{-0.010}$	$-0.002^{+0.007}_{-0.005}$
RS $_c _{M_g^{(1)}} = 4.8$	$0.190^{+0.120}_{-0.119}$	$0.824^{+0.010}_{-0.007}$	$-0.005^{+0.025}_{-0.014}$	$-0.312^{+0.012}_{-0.004}$	$0.001^{+0.005}_{-0.006}$
RS $_c _{M_g^{(1)}} = 6.1$	$0.193^{+0.120}_{-0.119}$	$0.821^{+0.010}_{-0.008}$	$0.001^{+0.026}_{-0.015}$	$-0.312^{+0.014}_{-0.006}$	$0.000^{+0.005}_{-0.006}$
RS $_c _{M_g^{(1)}} = 7.4$	$0.195^{+0.120}_{-0.119}$	$0.820^{+0.010}_{-0.010}$	$0.003^{+0.026}_{-0.016}$	$-0.312^{+0.016}_{-0.007}$	$-0.001^{+0.005}_{-0.005}$
RS $_c _{M_g^{(1)}} = 8.7$	$0.196^{+0.120}_{-0.119}$	$0.819^{+0.010}_{-0.010}$	$0.005^{+0.026}_{-0.016}$	$-0.311^{+0.016}_{-0.008}$	$-0.001^{+0.005}_{-0.005}$
RS $_c _{M_g^{(1)}} = 10$	$0.197^{+0.120}_{-0.120}$	$0.819^{+0.011}_{-0.011}$	$0.006^{+0.026}_{-0.017}$	$-0.311^{+0.017}_{-0.008}$	$-0.001^{+0.004}_{-0.005}$
LHCb	$0.09^{+0.061}_{-0.051}$	—	—	—	—

**Table 4.** Numerical results of the observables (high  $s$  region) in the  $\Lambda_b \rightarrow \Lambda(\rightarrow p\pi)\mu^+\mu^-$  decay, obtained for the SM and the  $RS_c$  model with the  $\chi_s = 1.5$  case, in different bins of high  $s$ . Experimentally measured values are taken from [22].

		$\langle \frac{d\beta}{ds} \times 10^{-7} \rangle$	$\langle F_L \rangle$	$\langle A_{FB}^e \rangle$	$\langle A_{FB}^\Lambda \rangle$	$\langle A_{FB}^\Lambda \rangle$
[15, 16]	SM	$0.798^{+0.073}_{-0.073}$	$0.454^{+0.032}_{-0.017}$	$-0.382^{+0.017}_{-0.008}$	$-0.307^{+0.002}_{-0.004}$	$0.131^{+0.004}_{-0.008}$
	$RS_c M_{g^{(1)}} = 4.8$	$0.832^{+0.073}_{-0.073}$	$0.447^{+0.033}_{-0.017}$	$-0.365^{+0.014}_{-0.006}$	$-0.287^{+0.003}_{-0.005}$	$0.132^{+0.004}_{-0.008}$
	$RS_c M_{g^{(1)}} = 6.1$	$0.816^{+0.073}_{-0.073}$	$0.450^{+0.033}_{-0.017}$	$-0.372^{+0.015}_{-0.007}$	$-0.296^{+0.003}_{-0.005}$	$0.132^{+0.004}_{-0.008}$
	$RS_c M_{g^{(1)}} = 7.4$	$0.810^{+0.073}_{-0.073}$	$0.451^{+0.032}_{-0.017}$	$-0.375^{+0.015}_{-0.007}$	$-0.300^{+0.003}_{-0.004}$	$0.132^{+0.004}_{-0.008}$
	$RS_c M_{g^{(1)}} = 8.7$	$0.806^{+0.074}_{-0.074}$	$0.452^{+0.032}_{-0.017}$	$-0.377^{+0.016}_{-0.007}$	$-0.302^{+0.003}_{-0.004}$	$0.132^{+0.004}_{-0.008}$
	$RS_c M_{g^{(1)}} = 10$	$0.804^{+0.074}_{-0.074}$	$0.452^{+0.032}_{-0.017}$	$-0.378^{+0.016}_{-0.008}$	$-0.304^{+0.002}_{-0.004}$	$0.132^{+0.004}_{-0.008}$
	LHCb	$1.12^{+0.197}_{-0.187}$	$0.49^{+0.304}_{-0.304}$	$-0.10^{+0.183}_{-0.163}$	$-0.19^{+0.143}_{-0.163}$	—
[16, 18]	SM	$0.825^{+0.075}_{-0.075}$	$0.418^{+0.033}_{-0.017}$	$-0.381^{+0.013}_{-0.006}$	$-0.289^{+0.005}_{-0.006}$	$0.141^{+0.004}_{-0.008}$
	$RS_c M_{g^{(1)}} = 4.8$	$0.877^{+0.075}_{-0.075}$	$0.411^{+0.033}_{-0.017}$	$-0.356^{+0.010}_{-0.004}$	$-0.265^{+0.005}_{-0.006}$	$0.140^{+0.004}_{-0.009}$
	$RS_c M_{g^{(1)}} = 6.1$	$0.855^{+0.075}_{-0.075}$	$0.414^{+0.033}_{-0.017}$	$-0.366^{+0.011}_{-0.005}$	$-0.276^{+0.005}_{-0.006}$	$0.141^{+0.004}_{-0.008}$
	$RS_c M_{g^{(1)}} = 7.4$	$0.844^{+0.075}_{-0.075}$	$0.415^{+0.033}_{-0.017}$	$-0.371^{+0.012}_{-0.005}$	$-0.280^{+0.005}_{-0.006}$	$0.141^{+0.004}_{-0.008}$
	$RS_c M_{g^{(1)}} = 8.7$	$0.838^{+0.075}_{-0.075}$	$0.416^{+0.033}_{-0.017}$	$-0.374^{+0.012}_{-0.005}$	$-0.283^{+0.005}_{-0.006}$	$0.141^{+0.004}_{-0.008}$
	$RS_c M_{g^{(1)}} = 10$	$0.835^{+0.075}_{-0.075}$	$0.416^{+0.033}_{-0.017}$	$-0.376^{+0.012}_{-0.006}$	$-0.284^{+0.005}_{-0.006}$	$0.141^{+0.004}_{-0.008}$
	LHCb	$1.22^{+0.143}_{-0.152}$	$0.68^{+0.158}_{-0.216}$	$-0.07^{+0.136}_{-0.127}$	$-0.44^{+0.104}_{-0.058}$	—
[18, 20]	SM	$0.658^{+0.066}_{-0.066}$	$0.371^{+0.034}_{-0.019}$	$-0.317^{+0.010}_{-0.010}$	$-0.227^{+0.011}_{-0.011}$	$0.153^{+0.005}_{-0.009}$
	$RS_c M_{g^{(1)}} = 4.8$	$0.726^{+0.066}_{-0.066}$	$0.367^{+0.034}_{-0.020}$	$-0.286^{+0.010}_{-0.010}$	$-0.201^{+0.010}_{-0.010}$	$0.151^{+0.005}_{-0.009}$
	$RS_c M_{g^{(1)}} = 6.1$	$0.698^{+0.066}_{-0.066}$	$0.368^{+0.034}_{-0.019}$	$-0.297^{+0.010}_{-0.010}$	$-0.211^{+0.010}_{-0.010}$	$0.152^{+0.005}_{-0.009}$
	$RS_c M_{g^{(1)}} = 7.4$	$0.685^{+0.066}_{-0.066}$	$0.369^{+0.034}_{-0.019}$	$-0.305^{+0.010}_{-0.010}$	$-0.216^{+0.011}_{-0.011}$	$0.152^{+0.005}_{-0.009}$
	$RS_c M_{g^{(1)}} = 8.7$	$0.677^{+0.066}_{-0.066}$	$0.370^{+0.034}_{-0.019}$	$-0.307^{+0.010}_{-0.010}$	$-0.219^{+0.011}_{-0.011}$	$0.153^{+0.005}_{-0.009}$
	$RS_c M_{g^{(1)}} = 10$	$0.672^{+0.066}_{-0.066}$	$0.370^{+0.034}_{-0.019}$	$-0.309^{+0.010}_{-0.010}$	$-0.221^{+0.011}_{-0.011}$	$0.153^{+0.005}_{-0.009}$

Table 4. (Continued.)


	$\langle \frac{d^3}{ds} \times 10^{-7} \rangle$	$\langle F_L \rangle$	$\langle A_{FB}^c \rangle$	$\langle A_{FB}^A \rangle$	$\langle A_{FB}^B \rangle$
LHCb	$1.24^{+0.152}_{-0.149}$	$0.62^{+0.243}_{-0.273}$	$0.01^{+0.155}_{-0.146}$	$-0.13^{+0.095}_{-0.124}$	—
SM	$0.753^{+0.069}_{-0.069}$	$0.409^{+0.033}_{-0.018}$	$-0.358^{+0.012}_{-0.007}$	$-0.271^{+0.011}_{-0.011}$	$0.143^{+0.005}_{-0.008}$
$RS_c   M_{g^{(1)}} = 4.8$	$0.807^{+0.069}_{-0.069}$	$0.403^{+0.034}_{-0.019}$	$-0.332^{+0.008}_{-0.009}$	$-0.247^{+0.011}_{-0.011}$	$0.142^{+0.005}_{-0.009}$
$RS_c   M_{g^{(1)}} = 6.1$	$0.785^{+0.069}_{-0.069}$	$0.405^{+0.034}_{-0.019}$	$-0.343^{+0.010}_{-0.008}$	$-0.257^{+0.011}_{-0.011}$	$0.143^{+0.005}_{-0.009}$
$RS_c   M_{g^{(1)}} = 7.4$	$0.774^{+0.069}_{-0.069}$	$0.406^{+0.033}_{-0.019}$	$-0.348^{+0.010}_{-0.007}$	$-0.262^{+0.011}_{-0.011}$	$0.143^{+0.005}_{-0.009}$
$RS_c   M_{g^{(1)}} = 8.7$	$0.767^{+0.069}_{-0.069}$	$0.407^{+0.033}_{-0.019}$	$-0.351^{+0.011}_{-0.007}$	$-0.264^{+0.011}_{-0.011}$	$0.143^{+0.005}_{-0.009}$
$RS_c   M_{g^{(1)}} = 10$	$0.764^{+0.069}_{-0.069}$	$0.407^{+0.033}_{-0.019}$	$-0.353^{+0.011}_{-0.007}$	$-0.266^{+0.011}_{-0.011}$	$0.143^{+0.005}_{-0.008}$
LHCb	$1.20^{+0.092}_{-0.099}$	$0.61^{+0.114}_{-0.143}$	$-0.05^{+0.095}_{-0.095}$	$-0.29^{+0.076}_{-0.081}$	—

of the observables receive considerable change in particular bins such as  $\frac{dB}{ds}$  and  $A_{FB}^\ell$  in low recoil bin [15, 20] GeV<sup>2</sup> and  $F_L$  in the bin [0.1, 2] GeV<sup>2</sup> but these deviations are still small enough to explain the large gap between the theoretical and experimental data. Therefore, it is concluded that under the present bounds on the mass of the first KK gluon state  $M_g^{(1)}$ , observables are largely unaffected by the NP arising due to custodially protected RS model. Hence, the current constraints on the parameters of RS<sub>c</sub> are too strict to explain the observed deviations in different observables of  $\Lambda_b \rightarrow \Lambda(\rightarrow p\pi^-)\mu^+\mu^-$  decay.

## Acknowledgments

FMB would like to acknowledge financial support from CAS-TWAS president's fellowship program. The work of FMB is also partly supported by National Science Foundation of China (11521505, 11621131001) and that of MJA by the URF (2015). In addition, AN would like to thank Dr Zaheer Asghar for his help in the calculations done during this work.

## ORCID iDs

Faisal Munir Bhutta  <https://orcid.org/0000-0002-6070-3694>

M Jamil Aslam  <https://orcid.org/0000-0001-9192-066X>

## References

- [1] Aaij R *et al* (LHCb Collaboration) 2014 Test of lepton universality using  $B^+ \rightarrow K^+\ell^+\ell^-$  decays *Phys. Rev. Lett.* **113** 151601
- [2] Aaij R *et al* (LHCb Collaboration) 2017 Test of lepton universality with  $B^0 \rightarrow K^{*0}\ell^+\ell^-$  decays *J. High Energy Phys.* **JHEP08(2017)055**
- [3] Altmannshofer W, Stangl P and Straub D M 2017 Interpreting hints for lepton flavor universality violation *Phys. Rev. D* **96** 055008
- [4] D'Amico G, Nardecchia M, Panci P, Sannino F, Strumia A, Torre R and Urbano A 2017 Flavour anomalies after the  $R_{K^*}$  measurement *J. High Energy Phys.* **JHEP09(2017)010**
- [5] Geng L-S, Grinstein B, Jäger S, Martin Camalich J, Ren X-L and Shi R-X 2017 Towards the discovery of new physics with lepton-universality ratios of  $b \rightarrow s\ell\ell$  decays *Phys. Rev. D* **96** 093006
- [6] Hiller G and Nisandzic I 2017  $R_K$  and  $R_{K^*}$  beyond the standard model *Phys. Rev. D* **96** 035003
- [7] Aaij R *et al* (LHCb Collaboration) 2014 Differential branching fractions and isospin asymmetries of  $B \rightarrow K^{(*)}\mu^+\mu^-$  decays *J. High Energy Phys.* **JHEP06(2014)133**
- [8] Aaij R *et al* (LHCb Collaboration) 2013 Differential branching fraction and angular analysis of the decay  $B_s^0 \rightarrow \phi\mu^+\mu^-$  *J. High Energy Phys.* **JHEP07(2013)084**
- [9] Aaij R *et al* (LHCb Collaboration) 2015 Angular analysis and differential branching fraction of the decay  $B_s^0 \rightarrow \phi\mu^+\mu^-$  *J. High Energy Phys.* **JHEP09(2015)179**
- [10] Aaij R *et al* (LHCb Collaboration) 2013 Measurement of form-factor-independent observables in the decay  $B^0 \rightarrow K^{*0}\mu^+\mu^-$  *Phys. Rev. Lett.* **111** 191801
- [11] Aaij R *et al* (LHCb Collaboration) 2016 Angular analysis of the  $B^0 \rightarrow K^{*0}\mu^+\mu^-$  decay using 3 fb<sup>-1</sup> of integrated luminosity *J. High Energy Phys.* **JHEP02(2016)104**
- [12] Wehle S *et al* (Belle Collaboration) 2017 Lepton-flavor-dependent angular analysis of  $B \rightarrow K^{*\ell^+\ell^-}$  *Phys. Rev. Lett.* **118** 111801
- [13] Ciuchini M, Coutinho A M, Fedele M, Franco E, Paul A, Silvestrini L and Valli M 2017 On flavourful easter eggs for new physics hunger and lepton flavour universality violation *Eur. Phys. J. C* **77** 688
- [14] Hurth T, Mahmoudi F, Martinez Santos D and Neshatpour S 2017 Lepton nonuniversality in exclusive  $b \rightarrow s\ell\ell$  decays *Phys. Rev. D* **96** 095034

- [15] Chiang C-W, He X-G, Tandean J and Yuan X-B 2017  $R_{K^{(*)}}$  and related  $b \rightarrow s\bar{\ell}\ell$  anomalies in minimal flavor violation framework with  $Z'$  boson *Phys. Rev. D* **96** 115022
- [16] Capdevila B, Crivellin A, Descotes-Genon S, Matias J and Virto J 2018 Patterns of new physics in  $b \rightarrow s\ell^+\ell^-$  transitions in the light of recent data *J. High Energy Phys.* **JHEP01(2018)093**
- [17] Kohda M, Modak T and Soffer A 2018 Identifying a  $Z'$  behind  $b \rightarrow s\ell\ell$  anomalies at the LHC *Phys. Rev. D* **97** 115019
- [18] Falkowski A, King S F, Perdomo E and Pierre M 2018 Flavourful  $Z'$  portal for vector-like neutrino dark matter and  $R_{K^{(*)}}$  arXiv:1803.04430
- [19] Mannel T and Recksiegel S 1998 Flavor changing neutral current decays of heavy baryons: the case  $\Lambda_b \rightarrow \Lambda\gamma$  *J. Phys. G: Nucl. Part. Phys.* **24** 979–90
- [20] Chen C-H and Geng C Q 2001 Baryonic rare decays of  $\Lambda_b \rightarrow \Lambda l^+l^-$  *Phys. Rev. D* **64** 074001
- [21] Aaltonen T *et al* (CDF Collaboration) 2011 Observation of the baryonic flavor-changing neutral current decay  $\Lambda_b \rightarrow \Lambda\mu^+\mu^-$  *Phys. Rev. Lett.* **107** 201802
- [22] Aaij R *et al* (LHCb Collaboration) 2015 Differential branching fraction and angular analysis of  $\Lambda_b^0 \rightarrow \Lambda\mu^+\mu^-$  decays *J. High Energy Phys.* **JHEP06(2015)115**
- [23] Detmold W and Meinel S 2016  $\Lambda_b \rightarrow \Lambda\ell^+\ell^-$  form factors, differential branching fraction, and angular observables from lattice QCD with relativistic  $b$  quarks *Phys. Rev. D* **93** 074501
- [24] Cheng H-Y and Tseng B 1996  $1/M$  corrections to baryonic form-factors in the quark model *Phys. Rev. D* **53** 1457
- Cheng H-Y and Tseng B 1997 Erratum:  $1/M$  corrections to baryonic form factors in the quark model [*Phys. Rev. D* **53**, 1457 (1996)] *Phys. Rev. D* **55** 1697
- [25] Mott L and Roberts W 2012 Rare dileptonic decays of  $\Lambda_b$  in a quark model *Int. J. Mod. Phys. A* **27** 1250016
- [26] He X-G, Li T, Li X-Q and Wang Y-M 2006 PQCD calculation for  $\Lambda_b \rightarrow \Lambda\gamma$  in the standard model *Phys. Rev. D* **74** 034026
- [27] Feldmann T and Yip M W Y 2012 Form factors for  $\Lambda_b \rightarrow \Lambda$  transitions in SCET *Phys. Rev. D* **85** 014035
- Feldmann T and Yip M W Y 2012 *Phys. Rev. D* **86** 079901 (erratum)
- [28] Wang Y-M, Li Y and Lü C-D 2009 Rare decays of  $\Lambda_b \rightarrow \Lambda + \gamma$  and  $\Lambda_b \rightarrow \Lambda + l^+l^-$  in the light-cone sum rules *Eur. Phys. J. C* **59** 861–82
- [29] Wang Y-M, Shen Y-L and Lü C-D 2009  $\Lambda_b \rightarrow p, \Lambda$  transition form factors from QCD light-cone sum rules *Phys. Rev. D* **80** 074012
- [30] Wang Y-M and Shen Y-L 2016 Perturbative corrections to  $\Lambda_b \rightarrow \Lambda$  form factors from QCD light-cone sum rules *J. High Energy Phys.* **JHEP02(2016)179**
- [31] Aliev T M, Ozipineci A and Savci M 2002 New physics effects in  $\Lambda_b \rightarrow \Lambda\ell^+\ell^-$  decay with lepton polarizations *Phys. Rev. D* **65** 115002
- [32] Aliev T M, Ozipineci A and Savci M 2003 Model independent analysis of  $\Lambda$  baryon polarizations in  $\Lambda_b \rightarrow \Lambda\ell^+\ell^-$  decay *Phys. Rev. D* **67** 035007
- [33] Aliev T M, Bashiry V and Savci M 2004 Double-lepton polarization asymmetries in  $\Lambda_b \rightarrow \Lambda\ell^+\ell^-$  decay *Eur. Phys. J. C* **38** 283–95
- [34] Turan G 2005 The exclusive  $\Lambda_b \rightarrow \Lambda\ell^+\ell^-$  decay in the general two Higgs doublet model *J. Phys. G: Nucl. Part. Phys.* **31** 525–37
- [35] Giri A K and Mohanta R 2006 Study of FCNC mediated  $Z$  boson effect in the semileptonic rare baryonic decays  $\Lambda_b \rightarrow \Lambda\ell^+\ell^-$  *Eur. Phys. J. C* **45** 151–8
- [36] Aliev T M and Savci M 2007  $\Lambda_b \rightarrow \Lambda\ell^+\ell^-$  decay in universal extra dimensions *Eur. Phys. J. C* **50** 91–9
- [37] Bashiry V and Azizi K 2007 The effects of fourth generation in single lepton polarization on  $\Lambda_b \rightarrow \Lambda\ell^+\ell^-$  decay *J. High Energy Phys.* **JHEP07(2007)064**
- [38] Aslam M J, Wang Y-M and Lü C-D 2008 Exclusive semileptonic decays of  $\Lambda_b \rightarrow \Lambda l^+l^-$  in supersymmetric theories *Phys. Rev. D* **78** 114032
- [39] Wang Y-M, Aslam M J and Lü C-D 2009 Rare decays of  $\Lambda_b \rightarrow \Lambda\gamma$  and  $\Lambda_b \rightarrow \Lambda l^+l^-$  in universal extra dimension model *Eur. Phys. J. C* **59** 847–60
- [40] Aliev T M, Azizi K and Savci M 2010 Analysis of the  $\Lambda_b \rightarrow \Lambda\ell^+\ell^-$  decay in QCD *Phys. Rev. D* **81** 056006
- [41] Azizi K and Katirci N 2011 Investigation of the  $\Lambda_b \rightarrow \Lambda\ell^+\ell^-$  transition in universal extra dimension using form factors from full QCD *J. High Energy Phys.* **JHEP01(2011)087**
- [42] Azizi K and Katirci N 2012 Analysis of  $\Lambda_b \rightarrow \Lambda\ell^+\ell^-$  transition in  $SM_4$  using form factors from full QCD *Eur. Phys. J. A* **48** 73

- [43] Azizi K, Kartal S, Olgun A T and Tavukoglu Z 2012 Comparative analysis of the semileptonic  $\Lambda_b \rightarrow \Lambda \ell^+ \ell^-$  transition in SM and different SUSY scenarios using form factors from full QCD *J. High Energy Phys.* **JHEP10(2012)118**
- [44] Gutsche T, Ivanov M A, Korner J G, Lyubovitskij V E and Santorelli P 2013 Rare baryon decays  $\Lambda_b \rightarrow \Lambda l^+ l^-$  ( $l = e, \mu, \tau$ ) and  $\Lambda_b \rightarrow \Lambda \gamma$ : differential and total rates, lepton- and hadron-side forward–backward asymmetries *Phys. Rev. D* **87** 074031
- [45] Azizi K, Kartal S, Olgun A T and Tavukoglu Z 2013 Analysis of the semileptonic  $\Lambda_b \rightarrow \Lambda \ell^+ \ell^-$  transition in the topcolor-assisted technicolor model *Phys. Rev. D* **88** 075007
- [46] Paracha M A, Ahmed I and Aslam M J 2015 Imprints of CP violation asymmetries in rare  $\Lambda_b \rightarrow \Lambda \ell^+ \ell^-$  decay in family non-universal  $Z'$  model *Prog. Theor. Exp. Phys.* **2015** 033B04
- [47] Böer P, Feldmann T and van Dyk D 2015 Angular analysis of the decay  $\Lambda_b \rightarrow \Lambda(\rightarrow N\pi)\ell^+ \ell^-$  *J. High Energy Phys.* **JHEP01(2015)155**
- [48] Meinel S and van Dyk D 2016 Using  $\Lambda_b \rightarrow \Lambda \mu^+ \mu^-$  data within a Bayesian analysis of  $|\Delta B| = |\Delta S| = 1$  decays *Phys. Rev. D* **94** 013007
- [49] Wang S-W and Yang Y-D 2016 Analysis of  $\Lambda_b \rightarrow \Lambda \mu^+ \mu^-$  decay in scalar leptoquark model *Adv. High Energy Phys.* **2016** 5796131
- [50] Azizi K, Olgun A T and Tavukoglu Z 2017 Impact of scalar leptoquarks on heavy baryonic decays *Adv. High Energy Phys.* **2017** 7435876
- [51] Hu Q-Y, Li X-Q and Yang Y-D 2017 The  $\Lambda_b \rightarrow \Lambda(\rightarrow p\pi^-)\mu^+ \mu^-$  decay in the aligned two-Higgs-doublet model *Eur. Phys. J. C* **77** 228
- [52] Faustov R N and Galkin V O 2017 Rare  $\Lambda_b \rightarrow \Lambda l^+ l^-$  and  $\Lambda_b \rightarrow \Lambda \gamma$  decays in the relativistic quark model *Phys. Rev. D* **96** 053006
- [53] Alnahdi R F, Barakat T and Alhendi H A 2017 Rare  $\Lambda_b \rightarrow \Lambda \ell^+ \ell^-$  decay in the two-Higgs doublet model of type-III *Prog. Theor. Exp. Phys.* **2017** 073B04
- [54] Roy S, Sain R and Sinha R 2017 Lepton mass effects and angular observables in  $\Lambda_b \rightarrow \Lambda(\rightarrow p\pi)\ell^+ \ell^-$  *Phys. Rev. D* **96** 116005
- [55] Das D 2018 Model independent New Physics analysis in  $\Lambda_b \rightarrow \Lambda \mu^+ \mu^-$  decay *Eur. Phys. J. C* **78** 230
- [56] Nasrullah A, Aslam M J and Shafaq S 2018 Analysis of angular observables of  $\Lambda_b \rightarrow \Lambda(\rightarrow p\pi)\mu^+ \mu^-$  decay in the standard and  $Z'$  models *Prog. Theor. Exp. Phys.* **2018** 43B08
- [57] Blake T and Kreps M 2017 Angular distribution of polarised  $\Lambda_b$  baryons decaying to  $\Lambda \ell^+ \ell^-$  *J. High Energy Phys.* **JHEP11(2017)138**
- [58] Randall L and Sundrum R 1999 A large mass hierarchy from a small extra dimension *Phys. Rev. Lett.* **83** 3370–3
- [59] Burdman G 2004 Flavor violation in warped extra dimensions and CP asymmetries in  $B$  decays *Phys. Lett. B* **590** 86–94
- [60] Agashe K, Perez G and Soni A 2005 Flavor structure of warped extra dimension models *Phys. Rev. D* **71** 016002
- [61] Moreau G and Silva-Marcos J I 2006 Flavor physics of the RS model with KK masses reachable at LHC *J. High Energy Phys.* **JHEP03(2006)090**
- [62] Casagrande S, Goertz F, Haisch U, Neubert M and Pfoh T 2008 Flavor physics in the Randall–Sundrum model: I. Theoretical setup and electroweak precision tests *J. High Energy Phys.* **JHEP10(2008)094**
- [63] Blanke M, Buras A J, Duling B, Gori S and Weiler A 2009  $\Delta F = 2$  observables and fine-tuning in a warped extra dimension with custodial protection *J. High Energy Phys.* **JHEP03(2009)001**
- [64] Blanke M, Buras A J, Duling B, Gemmler K and Gori S 2009 Rare K and B decays in a warped extra dimension with custodial protection *J. High Energy Phys.* **JHEP03(2009)108**
- [65] Albrecht M E, Blanke M, Buras A J, Duling B and Gemmler K 2009 Electroweak and flavour structure of a warped extra dimension with custodial protection *J. High Energy Phys.* **JHEP09(2009)064**
- [66] Bauer M, Casagrande S, Haisch U and Neubert M 2010 Flavor physics in the Randall–Sundrum model: II. Tree-level weak-interaction processes *J. High Energy Phys.* **JHEP09(2010)017**
- [67] Blanke M, Shakya B, Tanedo P and Tsai Y 2012 The birds and the Bs in RS: the  $b \rightarrow s\gamma$  penguin in a warped extra dimension *J. High Energy Phys.* **JHEP08(2012)038**
- [68] Biancofiore P, Colangelo P and Fazio F De 2014 Rare semileptonic  $B \rightarrow K^* \ell^+ \ell^-$  decays in  $RS_c$  model *Phys. Rev. D* **89** 095018
- [69] Biancofiore P, Colangelo P, De Fazio F and Scrimieri E 2015 Exclusive  $b \rightarrow s l \bar{\nu}$  induced transitions in  $RS_c$  model *Eur. Phys. J. C* **75** 134

- [70] Lü C-D, Munir F and Qin Q 2017  $b \rightarrow s\bar{s}\bar{d}$  decay in Randall–Sundrum models *Chin. Phys. C* **41** 053106
- [71] D’Ambrosio G and Iyer A M 2017 Flavour issues in warped custodial models:  $B$  anomalies and rare  $K$  decays *Eur. Phys. J. C* **78** 448
- [72] Blanke M and Crivellin A 2018  $B$  meson anomalies in a Pati–Salam model within the Randall–Sundrum background *Phys. Rev. Lett.* **121** 011801
- [73] Azizi K, Olgun A T and Tavukoğlu Z 2015 Comparative analysis of the  $\Lambda_b \rightarrow \Lambda \ell^+ \ell^-$  decay in the SM, SUSY and RS model with custodial protection *Phys. Rev. D* **92** 115025
- [74] Agashe K, Contino R, Da Rold L and Pomarol A 2006 A custodial symmetry for  $Zb\bar{b}$  *Phys. Lett. B* **641** 62–6
- [75] Carena M, Ponton E, Santiago J and Wagner C E M 2006 Light Kaluza Klein states in Randall–Sundrum models with custodial  $SU(2)$  *Nucl. Phys. B* **759** 202–27
- [76] Contino R, Da Rold L and Pomarol A 2007 Light custodians in natural composite Higgs models *Phys. Rev. D* **75** 055014
- [77] Cacciapaglia G, Csaki C, Marandella G and Terning J 2007 A new custodian for a realistic Higgsless model *Phys. Rev. D* **75** 015003
- [78] Malm R, Neubert M and Schmell C 2015 Higgs couplings and phenomenology in a warped extra dimension *J. High Energy Phys.* [JHEP02\(2015\)008](#)
- [79] Gherghetta T and Pomarol A 2000 Bulk fields and supersymmetry in a slice of AdS *Nucl. Phys. B* **586** 141–62
- [80] Du D, El-Khadra A X, Gottlieb S, Kronfeld A S, Laiho J, Lunghi E, Van de Water R S and Zhou R 2016 Phenomenology of semileptonic  $B$ -meson decays with form factors from lattice QCD *Phys. Rev. D* **93** 034005
- [81] Beneke M, Feldmann T and Seidel D 2001 Systematic approach to exclusive  $B \rightarrow V\ell^+ \ell^-$ ,  $V\gamma$  decays *Nucl. Phys. B* **612** 25–58
- [82] Asatryan H H, Asatryan H M, Greub C and Walker M 2002 Calculation of two loop virtual corrections to  $b \rightarrow s\ell^+ \ell^-$  in the standard model *Phys. Rev. D* **65** 074004
- [83] Greub C, Pilipp V and Schupbach C 2008 Analytic calculation of two-loop QCD corrections to  $b \rightarrow s\ell^+ \ell^-$  in the high  $q^2$  region *J. High Energy Phys.* [JHEP12\(2008\)040](#)
- [84] Aad G *et al* (ATLAS Collaboration) 2015 A search for  $t\bar{t}$  resonances using lepton-plus-jets events in proton–proton collisions at  $\sqrt{s} = 8$  TeV with the ATLAS detector *J. High Energy Phys.* [JHEP08\(2015\)148](#)
- [85] Sirunyan A M *et al* (CMS Collaboration) 2017 Search for  $t\bar{t}$  resonances in highly boosted lepton +jets and fully hadronic final states in proton–proton collisions at  $\sqrt{s} = 13$  TeV *J. High Energy Phys.* [JHEP07\(2017\)001](#)
- [86] Malm R, Neubert M, Novotny K and Schmell C 2014 5D perspective on higgs production at the boundary of a warped extra dimension *J. High Energy Phys.* [JHEP01\(2014\)173](#)
- [87] Patrignani C *et al* (Particle Data Group Collaboration) 2016 Review of particle physics *Chin. Phys. C* **40** 100001

# Probing new physics effects in $\Lambda_b \rightarrow \Lambda(\rightarrow p\pi^-)\ell^+\ell^-$ decay via model independent approach

Aqsa Nasrullah<sup>1, \*</sup>, Ishtiaq Ahmed<sup>2</sup>, M. Jamil Aslam<sup>1</sup>, Z. Asghar<sup>3,4</sup>, Saba Shafaq<sup>5</sup>

<sup>1</sup>*Department of Physics, Quaid-i-Azam University, Islamabad 45320, Pakistan.*

<sup>2</sup>*National Centre for Physics, Quaid-i-Azam University, Islamabad 45320, Pakistan.*

<sup>3</sup>*Center for Mathematical Sciences, Pakistan Institute of Engineering and Applied Sciences, Nilore, Islamabad 45650, Pakistan*

<sup>4</sup>*Department of Physics and applied sciences, Pakistan Institute of Engineering and Applied Sciences, Nilore, Islamabad 45650, Pakistan*

<sup>5</sup>*Department of Physics, International Islamic University, Islamabad 44000, Pakistan.*

## Abstract

The New Physics (NP) effects are studied in the rare baryonic decay  $\Lambda_b \rightarrow \Lambda(\rightarrow p\pi^-)\ell^+\ell^-$ , with unpolarized  $\Lambda_b$  using most general model independent approach by introducing new axial(vector), (pseudo)scalar and tensor operators in the weak effective Hamiltonian corresponding to  $b \rightarrow s$  transitions. Recently, for  $\Lambda_b \rightarrow \Lambda(\rightarrow p\pi^-)\mu^+\mu^-$  decay the LHCb collaboration has measured the branching ratio ( $d\mathcal{B}/ds$ ), lepton- and hadron-side forward-backward asymmetries, denoted by  $A_{FB}^\ell$  and  $A_{FB}^\Lambda$ , respectively, and the longitudinal polarization fraction  $F_L$  both in the low- and high-recoil regions. To see whether the new  $VA$ ,  $SP$  and  $T$  couplings can accommodate the available experimental data of these observables, first we have examined their influence on these observables and later we have checked the imprints of these new couplings on a number of interesting but yet not measured observables; namely the combined lepton-hadron forward-backward asymmetry ( $A_{FB}^{\ell\Lambda}$ ), transverse polarization fraction ( $F_T$ ), asymmetry parameters  $\alpha'_s$  and some other angular observables, extracted from certain foldings. It is found that compared to the  $VA$  the  $SP$  couplings favor experimental data for all the four observables but still no individual coupling is able to accommodate all of the available data simultaneously. To achieve this goal, the pairs of new WCs are taken to check their range that simultaneously satisfy constraints of  $B$ -Physics and available LHCb data on  $d\mathcal{B}/ds$ ,  $F_L$ ,  $A_{FB}^\ell$  and  $A_{FB}^\Lambda$  in several bins for the decay channel under consideration. We find that most of the available data could be accommodated by the different pairs of  $VA$  and  $SP$  WCs giving more severe constraints on the parametric space of these WCs that is still satisfied with the  $B$ -physics data.

---

\* aqsanasrullah54@gmail.com